NASA TECHNICAL MEMORANDUM

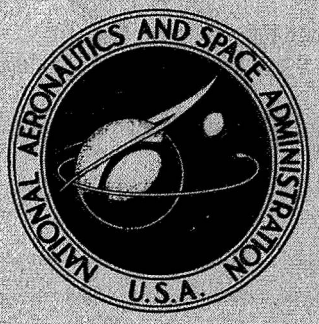

NASA TM X-2507

NASA TM X-2507

SPACE SHUTTLE AEROTHERMODYNAMICS TECHNOLOGY CONFERENCE

Volume II - Heating

Held at
Ames Research Center
Moffett Field, California
December 15-16, 1971

NATIONAL AERONAUTICS AND SPACE ADMINISTRATION • WASHINGTON, D. C. • FEBRUARY 1972

1. Report No.	2. Government Accession No.	3. Recipient's Catalog No.
NASA TM X-2507		

4. Title and Subtitle	5. Report Date
SPACE SHUTTLE AEROTHERMODYNAMICS TECHNOLOGY CONFERENCE VOLUME II - HEATING	February 1972
	6. Performing Organization Code
7. Author(s)	8. Performing Organization Report No. L-8136
	10. Work Unit No.
9. Performing Organization Name and Address NASA Langley Research Center Hampton, Va. 23365	11. Contract or Grant No.
	13. Type of Report and Period Covered Technical Memorandum
12. Sponsoring Agency Name and Address National Aeronautics and Space Administration Washington, D.C. 20546	14. Sponsoring Agency Code

15. Supplementary Notes

Held at NASA Ames Research Center, December 15-16, 1971.

16. Abstract

The conference encompasses four technology efforts, each published as a separate volume.

Volume I - Flow Fields (NASA TM X-2506)

Volume II - Heating (NASA TM X-2507)

Volume III - Aerodynamics (NASA TM X-2508)

Volume IV - Operational Flight Mechanics (NASA TM X-2509)

17. Key Words (Suggested by Author(s))	18. Distribution Statement
Flow fields Heating Aerodynamics Operational flight mechanics Space shuttle Aerothermodynamics	Unclassified - Unlimited

19. Security Classif. (of this report)	20. Security Classif. (of this page)	21. No. of Pages	22. Price*
Unclassified	Unclassified	462	$6.00

*For sale by the National Technical Information Service, Springfield, Virginia 22151

PREFACE

A Space Shuttle Technology Conference on Flow Fields, Heat Transfer, Aerodynamics, and Operational Flight Mechanics was held at the NASA Ames Research Center on December 15 and 16, 1971. The objective of this conference was to review the broad base of aerothermodynamics technology developed for the space shuttle during the period of the Phase B studies and, thereby, help focus attention on the technology required for further space shuttle development. This publication is a compilation of the conference papers. It has been divided into four volumes, one for each of the sessions. Five papers which were omitted from the oral presentation at the conference are included in this publication. Contributing organizations include U.S. Aerospace Contractors, Universities, Canadian and European Space Agencies, in addition to NASA Research Centers.

CONTENTS

VOLUME II.- HEATING

VOLUME III.- AERODYNAMICS

VOLUME IV.- OPERATIONAL FLIGHT MECHANICS

GLOSSARY

ABES	air breathing engines
ACPS	attitude control propulsion system
AEDC	Arnold Engineering Development Center
AFB	air force base
AFFDL	Air Force Flight Dynamics Laboratory
ALT	altitude
APS	auxiliary propulsion system
AR	aspect ratio
ARC	Ames Research Center
ARDC	Air Research and Development Command
BECO	booster engine cutoff
BLOW	booster lift-off weight
BV	body-vertical tail
BW	body-wing
BWV	body-wing-vertical tail
CAL	Cornell Aeronautical Laboratory
CALCS	calculations
CAL HST	Cornell Aeronautical Laboratory hypersonic shock tunnel
CFHT	continuous-flow hypersonic tunnel
CG; C.G.; c.g.	center of gravity
CONFIG	configuration
CRT	cathode ray tube
Cyl	cylinder
2-D	two-dimensional
3-D	three-dimensional

DAC	Douglas Aircraft Company
DCM	data control management
DEX	exit diameter
DIA	diameter
DIAT	diatomic
DIF. REFL.	differential deflection
3DMoC	three-dimensional method of characteristics
DOD	Department of Defense
DOF	degrees of freedom
DWO	delta-wing orbiter
EHT	external hydrogen tank
EOHT	external oxygen-hydrogen tank
EPL	emergency power level
EST	estimated
ETR	eastern test range
F&M	force and moment
FAR; F.A.R.	Federal Aircraft Regulation
FBS	flyback system
F.D.	finite difference
F/O	fuel-oxygen ratio
FO/FS	fail operational/fail safe
FPR	flight performance reserve
FPRE	flat-plate reference enthalpy
FR	fully reusable
FREQ	frequency
GAC	Grumman Aerospace Corporation

GD	General Dynamics
GDC	General Dynamics Corporation
GD/C	General Dynamics/Convair
G.E.	General Electric Company
GLOW	vehicle gross lift-off weight
GTOP	general trajectory optimization program
GW	gross weight
H	hydrogen
HCF	highly compacted fibers
HCR	high cross range
HeT	Mach 20 helium tunnel
HO	hydrogen-oxygen system
H.W.T.	hypersonic wind tunnel
IAC	industrial air center
IBFF	impulse base flow facility
ICD	interface control drawing
IFR	instrument flight rules
ILRV	integral launch and reentry vehicle
ILS	instrument landing system
IND	industrial
IR	infrared
IRAD	Independent Research and Development
KSC	Kennedy Space Center
L.E.	leading edge
LEE	leeward
LH_2	liquid hydrogen

LMSC	Lockheed Missiles & Space Company
LO_2; LOX	liquid oxygen
LRC; LaRC	Langley Research Center
LRU	link retraction unit
MAC	mean aerodynamic chord
MAC Exp	exposed mean aerodynamic chord
MARK I, MARK II	shuttle configurations
MAX	maximum
MC	Monte Carlo
MCAIR	a low-speed wind tunnel
MCAS	Marine Corps Air Station
MDAC	McDonnell Douglas Astronautics Company
MDC	McDonnell Douglas Corporation
MIL SPEC	military specification
MIN	minimum
MM HWT	Martin Marietta Corporation hotshot wind tunnel
MOC	method of characteristics
MPL	minimum power level
MSC	Manned Spacecraft Center
MSFC	Marshall Space Flight Center
MT.	mountain
NA	North American
NAE; N.A.E.	National Aeronautical Establishment
NAR; NARC; NR	North American Rockwell Corporation
NAS	Naval Air Station
NASA	National Aeronautics and Space Administration

NO.; No.	number
NOZ	nozzle
NPL	normal power level
O/F	oxygen-fuel ratio
OLOW	orbiter lift-off weight
OMS	orbiting maneuvering system
P/L	payload
PM	pitching moment
RCC	reinforced carbon carbon
RCS	reaction control system
Ref	reference
REQD	required
RFP	request for porposals
RGAS	real gas
R.H.	right hand engine
RSI	reusable surface insulation
RTV	room-temperature vulcanizing rubber
S&C	stability and control
SCT	shock capturing technique
SF	stick force
S.L.; SL	sea level
SM	service module
SPEC	specification
SRM	solid rocket motors
SS	stainless steel
SSV	space shuttle vehicle
ST	straight

STAR	strings and array computer; self-testing and repair computer
STD	standard
STI	Systems Technology, Incorporated
STOL	short take-off and landing
SW	southwest
SYM	symbol
T/C	thermocouple
T.E.	trailing edge
T.E.D.	trailing edge down
TEMP	temperature
T.E.U.	trailing edge up
THEO	theoretical
TPS	thermal protection system
TRAJ	trajectory
TVC	thrust vector control
Typ	typical
UPWT	Unitary Plan wind tunnel
USAF	U.S. Air Force
VAC HVWT	Vought Aeronautics Company hypervelocity wind tunnel
VAFB	Vandenburg Air Force Base
VDT	variable density tunnel
VFR	visual flight rules
V/STOL	vertical and short take-off and landing
w/o	without
WT	weight
WWD	windward
YM	yawing moment

HEATING SESSION

INTRODUCTION

By James C. Dunavant
Langley Research Center

The importance of the subject of aerodynamic heating need not be stressed to any group concerned with the shuttle. In this symposium, aerodynamic heating, which must include flow fields to a degree, spreads into two sessions. In the first, the flow fields session, much of the work on analytic prediction techniques is directed toward providing a basis for the calculation of boundary-layer heating. The heat-transfer session will approach the flow field from an experimental standpoint and treat the very important viscous boundary-layer problem in more depth.

There has been a multitude of heat-transfer investigations in the shuttle program; many of these in the early part of the program were used in a configuration screening process with the purpose of weeding out those having the poorer heating characteristics. Yet, the shuttle must be an integrated design of all the various disciplines. The concept of minimum heating rate on heat load has found little place in the program and heat transfer must be viewed from the standpoint of weight and cost effects on the total program.

The scope of shuttle heat transfer covers not just the configuration reentry aerodynamic heating but must account for heating imposed by other systems such as rocket plumes, engine base flows, effects of reaction control system jets interacting with the stream flow, and many others.

The papers in the heat-transfer session reflect this expanded subject of heat transfer. In the papers in this session, we will be treating heating to the orbiter and orbiter tank configurations; particular attention will be paid to turbulent heating on the windward surface of the orbiter. In the last technology conference, data were shown which indicated that most of the lower part of the shuttle orbiter was not dominated by nose bluntness effects at all angles of attack and that boundary-layer edge properties are best predicted from oblique-shock properties rather than from properties derived by a normal shock-expansion process. This information proved decisive in the elimination of many of the differences in predicted lower surface turbulent heating levels which are more highly dependent upon boundary-layer edge properties than for laminar flow. Yet, this subject is not fully closed. Some region, possibly small, near the nose will be dominated by nose bluntness. The experimental data flow fields and calculation procedures remain to be fully developed and used to explore this effect over the full range of the orbiter reentry corridor. Although no papers deal directly with the correlation or prediction of transition on the orbiter, boundary-layer transition has been looked at not from the standpoint of how transition location is best predicted from data and correlations, but from the point of view of what effect the entire range of transition prediction methods and correlations that have been used in shuttle studies would have on thermal environment of the shuttle.

We were indeed fortunate in having a newly developed method of measuring heat transfer available at the start of the Phase B studies. I am speaking now of the phase-change technique which has been extensively used for the many configurations tested. Certainly, the same job

could not have been done with the older slower heat-transfer model construction and test techniques. An analysis of factors affecting the accuracy of data taken during the Phase B studies has been made and there are several points to be made regarding the phase-change data. Although this technique has proved to be a viable measurement method, the thermal properties of the most commonly used model material upon which the heat rates are directly dependent have proved to be quite elusive and this fact has had considerable effect on the heat-transfer results. Beyond this, a number of common practices have been used in reduction of heat transfer which should be resolved before examining data from different facilities under a format for determining heating-rate uncertainties.

The lee surface flow will get special attention because our prediction tools are less well developed for these flows and the large acreage of the lee surface makes it a big driver in the thermal-protection-system weight. The effects of surface roughness on the orbiter in producing boundary-layer transition and in increasing turbulent heating rates will be shown. The subjects of plume and base heating will be examined in two papers and lastly, a radical new method of experimentally measuring heat transfer will be described.

EXPERIMENTAL AND THEORETICAL AERODYNAMIC HEATING AND FLOW FIELD ANALYSIS OF A SPACE SHUTTLE ORBITER

By R. K. Matthews, T. D. Buchanan,
W. R. Martindale, ARO, Inc., and
J. D. Warmbrod, NASA-MSFC

Arnold Engineering Development Center
Arnold Air Force Station, Tennessee

INTRODUCTION

Extensive Space Shuttle wind tunnel tests have recently been completed at the von Karman Facility of the AEDC. In support of these tests theoretical analysis has also been conducted. This paper summarizes the results of this work on the McDonnell Douglas Delta Wing Orbiter (MDAC-DWO) and shows comparisons of the data with the applicable theories.

The tests were conducted in the continuous hypersonic Tunnel B at Mach 8 and in the hypervelocity hotshot Tunnel F at Mach 10.5. Photographic data are used to illustrate the regions of peak heating on the lee-side and to show the vortical nature of the flow. Windward centerline data include measurements of shock angle, surface pressure, flow field pitot pressure and total temperature, and heat-transfer rate coefficient distributions. Shock angles, surface pressures, and local Mach number distributions are compared with tangent cone theory over an angle of attack range from 10 to 60 deg. The measured heat-transfer rate coefficient distributions are compared to both laminar and turbulent theories and boundary layer transition data are compared to the McDonnell Douglas criteria.

In this paper all heat-transfer coefficients are based on $T_{aw} = T_o$ and are divided by the stagnation point heat-transfer coefficient (Ref. 1) on a 0.011-ft radius sphere (a 1-ft radius sphere scaled to the model scale). A complete set of the data discussed in this paper will be presented in a series of SADSAC reports to be published in the near future.

SYMBOLS

h	heat-transfer coefficient based on $T_{aw} = T_o$
h_{ref}	reference heat-transfer coefficient based on the stagnation point heating of a 1 foot scaled sphere (0.011 ft.)
L	model length (54.2 cm)
M_∞	free-stream Mach number
M^*	local Mach number at $y = y^*$
p	model surface pressure
p_p	flow field pitot pressure (see Fig. 8)
p_{t_2}	stagnation pressure downstream of a normal shock
Re_L	free-stream Reynolds number based on a model length of 54.2 cm (21.35 in.)
r	the radius used in the axisymmetric calculation (see Fig. 10a)
T_o	free-stream stagnation temperature
T_p	measured flow field stagnation temperature
X	distance from nose along model axis (see Fig. 8)
Y	distance normal to model surface (see Fig. 8)
y^*	minimum value of y where $T_p/T_o = 1.0$
α	angle of attack, deg
δ_s	the angle between the model surface and the bow shock at a given model station, deg
θ_s	the angle between the free-stream flow direction and the bow shock at a given model station, deg
σ	the angle between the model surface and the model axis at a given station, deg

LEE SURFACE PHASE CHANGE PAINT PHOTOGRAPHS

(Figure 1)

Typical phase-change paint photographs of the model lee-side at α = 20, 40, and 60 deg are shown in Figure 1. Photographs at two Reynolds numbers are shown for α = 40 deg. Isotherm lines are indicated by the black model surface (Stycast)® showing through the white paint (Tempilaq)®. In all four pictures the canopy is clearly a "hot region". The level of the peak heating on the canopy will be shown in a later figure. A second "hot region" can be seen on the centerline meridian between the nose and the canopy. For an orbiter at α = 20 and 40 deg Hefner and Whitehead (Ref. 2) also observed peak heating in this region and attributed it to vortices emanating from the model nose area. It was shown in Ref. 2 that the peak heating in this region increased as Reynolds number increased but this trend could not be confirmed by the present data. Comparison of the α = 40 photographs in Figure 1 does show that for the Reynolds number range of the present test the isotherm patterns have essentially the same shape. However, it should be pointed out that the present isotherm patterns are significantly elongated compared to those in Ref. 2 and this supports the conclusion of Whitehead and Bertram (Ref. 3) that nose shaping is a dominant factor in the lee-side meridian heating.

Tunnel B $M_\infty = 8.0$

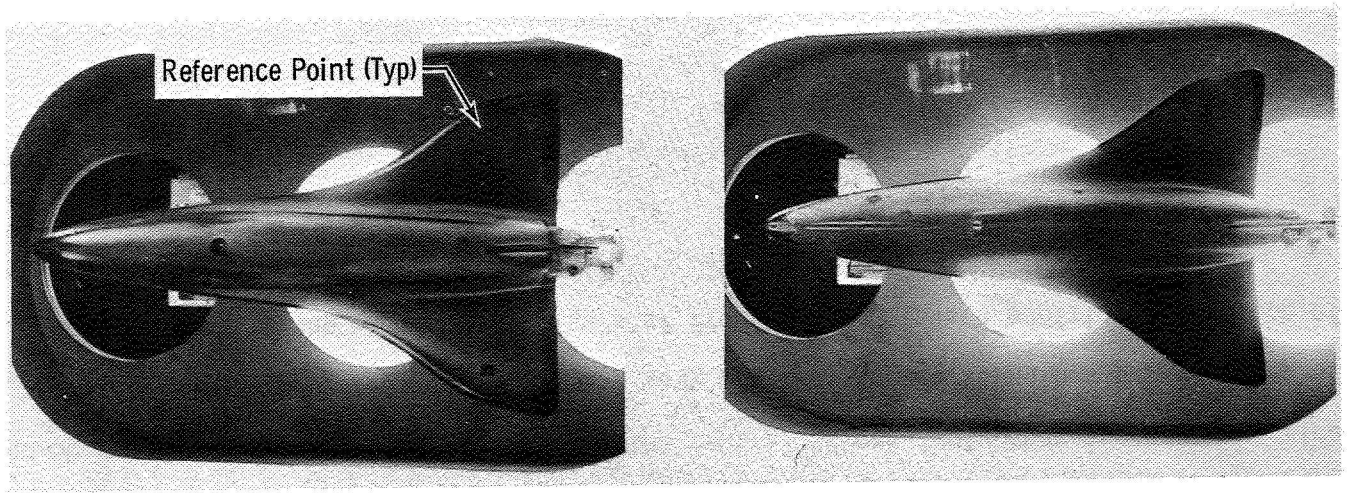

a. $\alpha = 20$ deg, $h/h_{ref} = 0.0217$, $Re_L = 4.5 \times 10^6$

b. $\alpha = 40$ deg, $h/h_{ref} = 0.0175$, $Re_L = 4.5 \times 10^6$

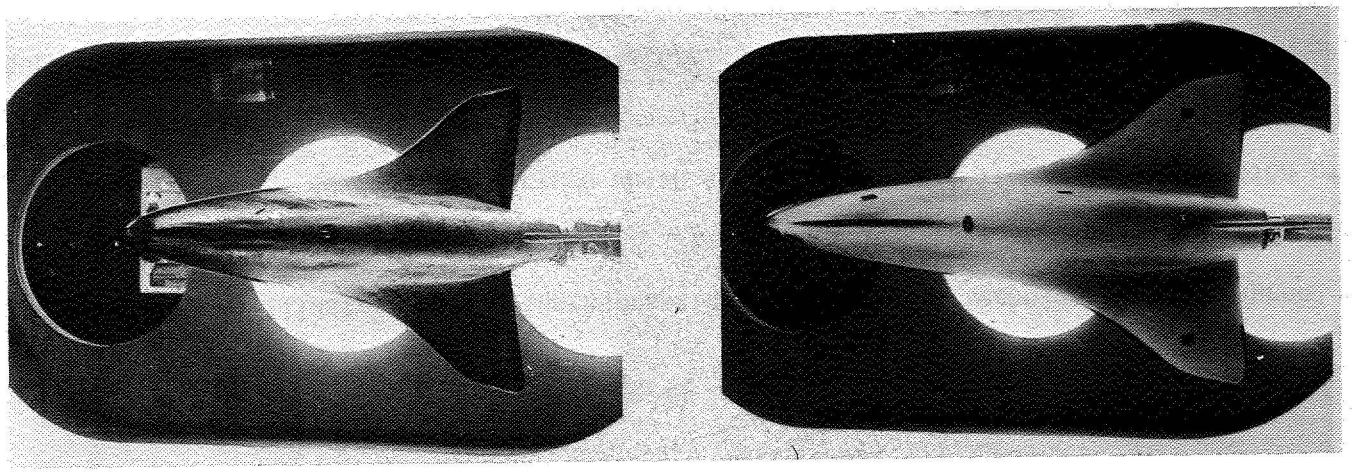

c. $\alpha = 60$ deg, $h/h_{ref} = 0.0114$, $Re_L = 4.5 \times 10^6$

d. $\alpha = 40$ deg, $h/h_{ref} = 0.0179$, $Re_L = 6.6 \times 10^6$

Fig. 1 Lee Surface Phase Change Paint Photographs

LEE SURFACE THERMOGRAPHIC PHOSPHOR PHOTOGRAPHS

(Figure 2)

Typical photographs illustrating the thermographic phosphor paint technique used in Tunnel F for obtaining heat-transfer data are shown in Figure 2. Lee-side photographs at α = 20, 40, and 50 deg are presented as well as an α = 40 deg tare picture which shows the general lighting and emission of the paint with no temperature gradients. Note, for example, that the intensity of the left wing tip in the tare picture is similar to that of the wind-on picture. Relative dark regions in the wind-on pictures are indicative of "hot regions" as was the case in Figure 1.

Again the canopy and the region upstream of the canopy are clearly shown to be "hot regions". At α = 40 and 50 deg dark streaks on either side of the central streak imply that secondary vortices are present. Also, of some academic interest, is the wavy shape of the dark regions particularly at α = 50 deg. Referring back to the α = 60 deg picture of Figure 1 one can see additional evidence of this phenomenon.

Tunnel F $M_\infty = 10.5$

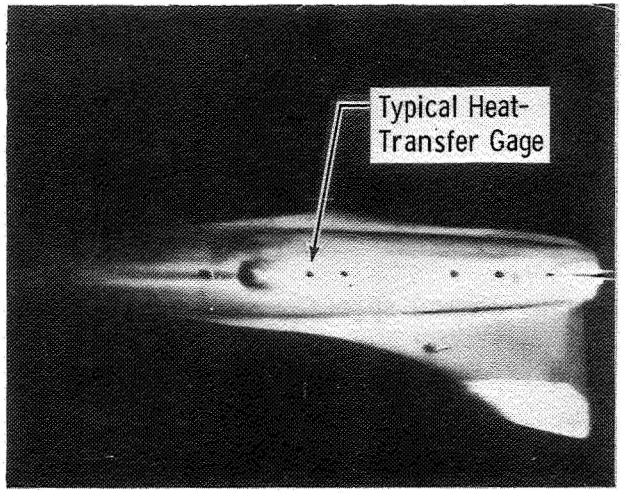

a. $\alpha = 20$ deg, $Re_L = 9.1 \times 10^6$

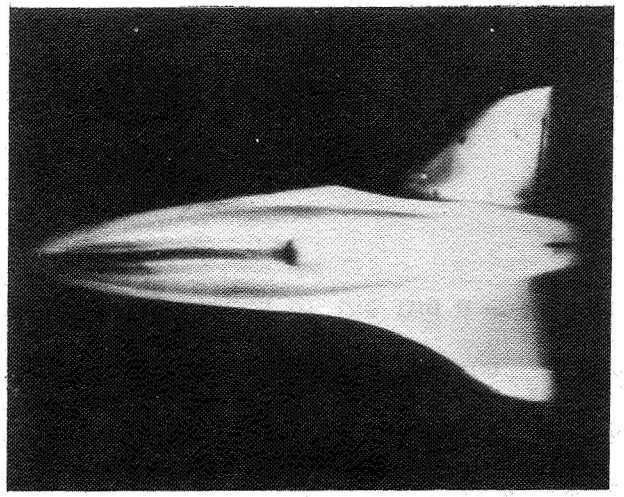

b. $\alpha = 40$ deg, $Re_L = 9.4 \times 10^6$

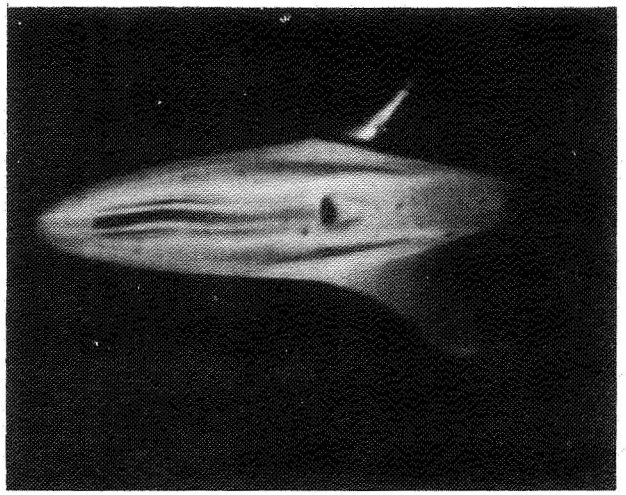

c. $\alpha = 50$ deg, $Re_L = 7.3 \times 10^6$

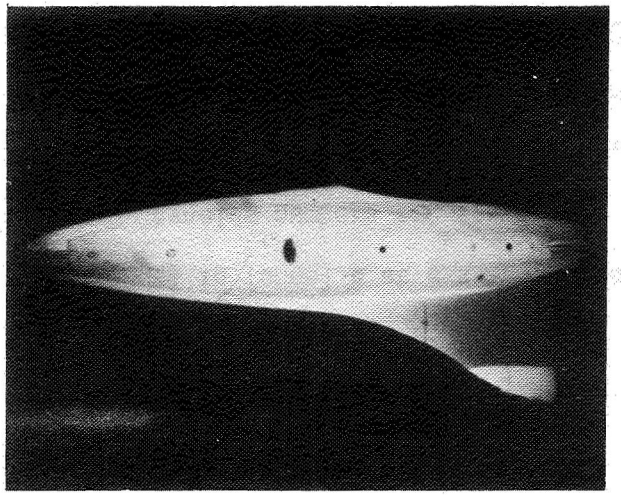

d. $\alpha = 40$ deg, Tare Picture

Fig. 2 Lee Surface Thermographic Phosphor Photographs

SIDE PANEL PHASE-CHANGE PAINT PHOTOGRAPHS

(Figure 3)

Phase-change paint photographs showing a side view of the model in Tunnel B at α = 20, 40, and 60 deg are presented in Figure 3. As before, photographs at two Reynolds numbers are shown for α = 40 deg. At α = 20 deg a single elongated "hot region" is evident on the body above the wing. At α = 40 deg there is a series of elongated "hot regions" on the body below the canopy. This implies that a series of vortices exist in this region. The dark area toward the aft of the body (α = 40 deg) was not caused by the paint melting and should be disregarded in the interpretation of this photograph. At α = 60 deg the location and extent of the "hot region" is somewhat similar to that at α = 40 deg. Comparison of the α = 20 and 60 deg photographs indicates that the surface area covered by the "hot region" increased as angle of attack increased. Conversely the extent of the "hot region" appears to have decreased slightly as Reynolds number increased as seen by comparison of the two α = 40 deg photographs.

Tunnel B $M_\infty = 8.0$

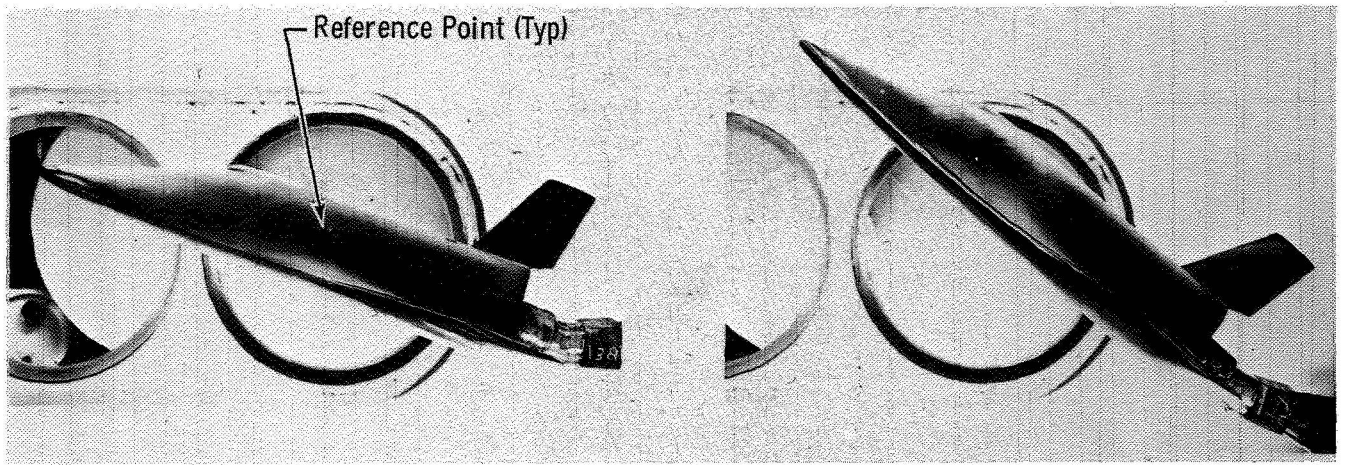

a. $\alpha = 20$ deg, $h/h_{ref} = 0.0341$, $Re_L = 4.5 \times 10^6$

b. $\alpha = 40$ deg, $h/h_{ref} = 0.0132$, $Re_L = 4.5 \times 10^6$

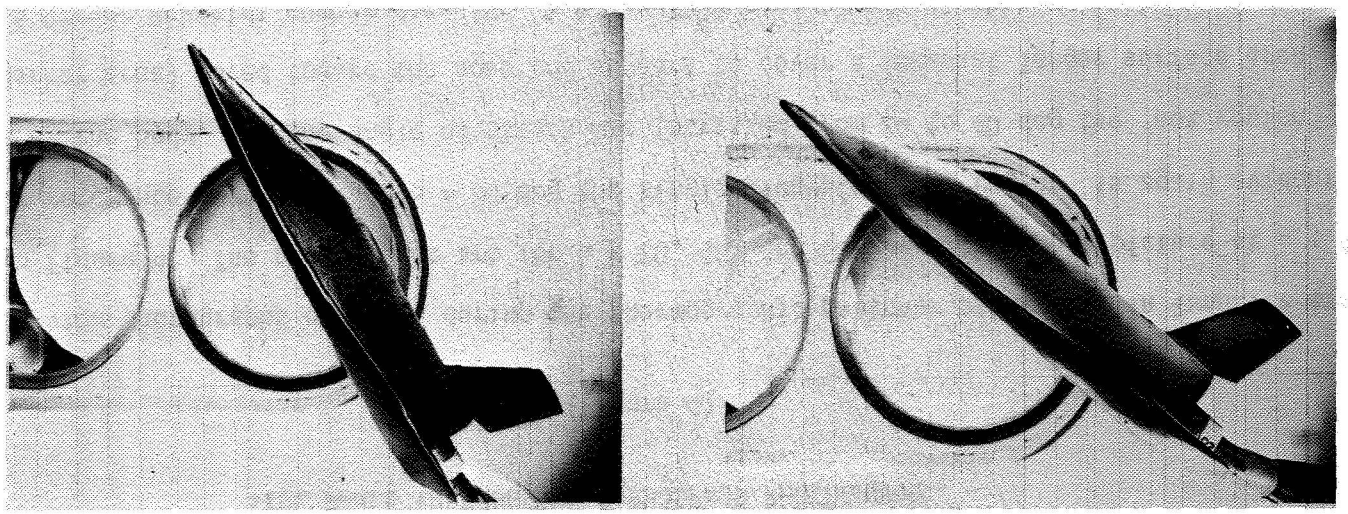

c. $\alpha = 60$ deg, $h/h_{ref} = 0.0077$, $Re_L = 4.5 \times 10^6$

d. $\alpha = 40$ deg, $h/h_{ref} = 0.0093$, $Re_L = 6.6 \times 10^6$

Fig. 3 Side Panel Phase-Change Paint Photographs

SIDE PANEL THERMOGRAPHIC PHOSPHOR PHOTOGRAPHS

(Figure 4)

Side view photographs obtained during the thermographic phosphor paint test in Tunnel F are presented in Figure 4. The photographs are for α = 20, 40, and 50 deg with a tare picture at α = 40 deg shown for reference purposes. At α = 20 deg the single elongated "hot region" is again evident along the side of the body. As the angle of attack was increased from 20 to 40 deg the "hot region" (i.e., darker area) moved toward the nose and appears to cover a somewhat larger surface area. These Mach 10.5 higher Reynolds number data ($Re_{\ell} \approx 9.0 \times 10^6$) have trends similar to those observed at Mach 8 at a Reynolds number of 4.5×10^6.

Tunnel F $M_\infty = 10.5$

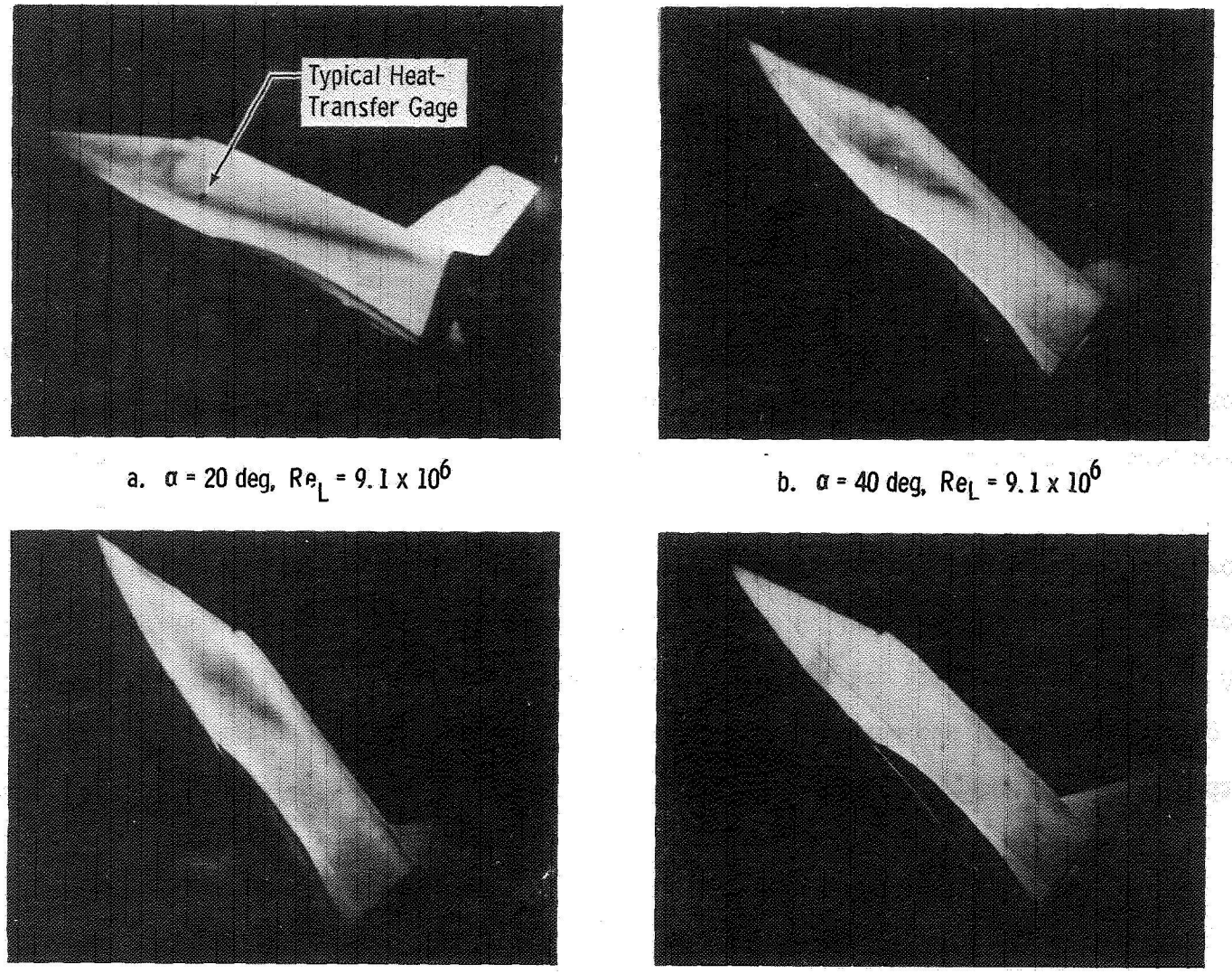

a. $\alpha = 20$ deg, $Re_L = 9.1 \times 10^6$

b. $\alpha = 40$ deg, $Re_L = 9.1 \times 10^6$

c. $\alpha = 50$ deg, $Re_L = 7.3 \times 10^6$

d. $\alpha = 40$ deg, Tare Picture

Fig. 4 Side Panel Thermographic Phosphor Photographs

COMPARISON OF WINDWARD AND LEE-SIDE CENTERLINE HEATING DISTRIBUTIONS

Tunnel B, $M_\infty = 8.0$, $Re_L = 4.5 \times 10^6$

(Figure 5a)

Mach 8 (Tunnel B) lee-side meridian data fairings are compared with windward centerline data fairings for α = 20, 40, and 60 deg in Figure 5a. As previously pointed out the canopy heating is quite severe despite the fact that it is in the shadow of the bottom surface at α = 40 and 60 deg. As can be seen at α = 20 deg the peak heating on the canopy ($h/h_{ref} \approx 0.1$) exceeded that on the windward centerline for a Reynolds number of 4.5×10^6. However, as the angle of attack increased there was a slight decrease in the lee-side heating levels.

The location of the side panel "hot regions" was shown in Figures 3 and 4 and the peak heating levels are shown in the lower right side of the graphs in this figure. The side panel peak heating was $h/h_{ref} = 0.04$ and this value occurred at α = 20 deg.

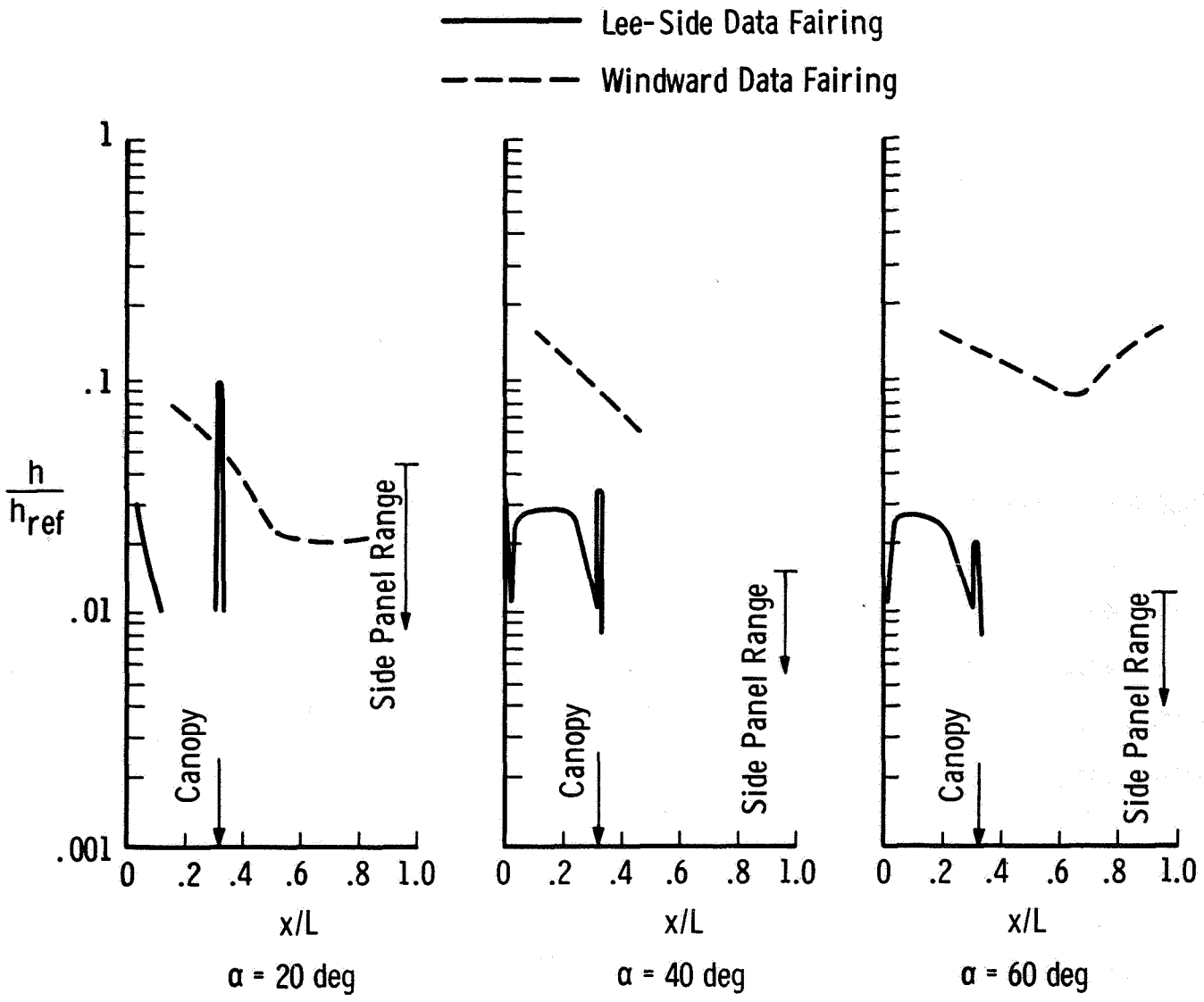

a. Tunnel B, $M_\infty = 8.0$, $Re_L = 4.5 \times 10^6$

Fig. 5 Comparison of Windward and Lee-Side Centerline Heating Distributions

COMPARISON OF WINDWARD AND LEE-SIDE CENTERLINE HEATING DISTRIBUTIONS

Tunnel F, $M_\infty = 10.5$

(Figure 5b)

Mach 10.5 (Tunnel F) lee-side meridian data fairings are compared with windward centerline data fairings for α = 20, 40, and 50 deg in Figure 5b. These thermographic phosphor data fairings also show relatively high heating on the canopy and nose region as did the phase-change paint data fairings (Tunnel B) which were presented in Figure 5a. However, the canopy peak heating level was not obtained. This figure and the photographic data presented in Figures 1 and 3 do show that except for the canopy and nose region the lee-side surface area experiences heating values of h/h_{ref} less than 0.008.

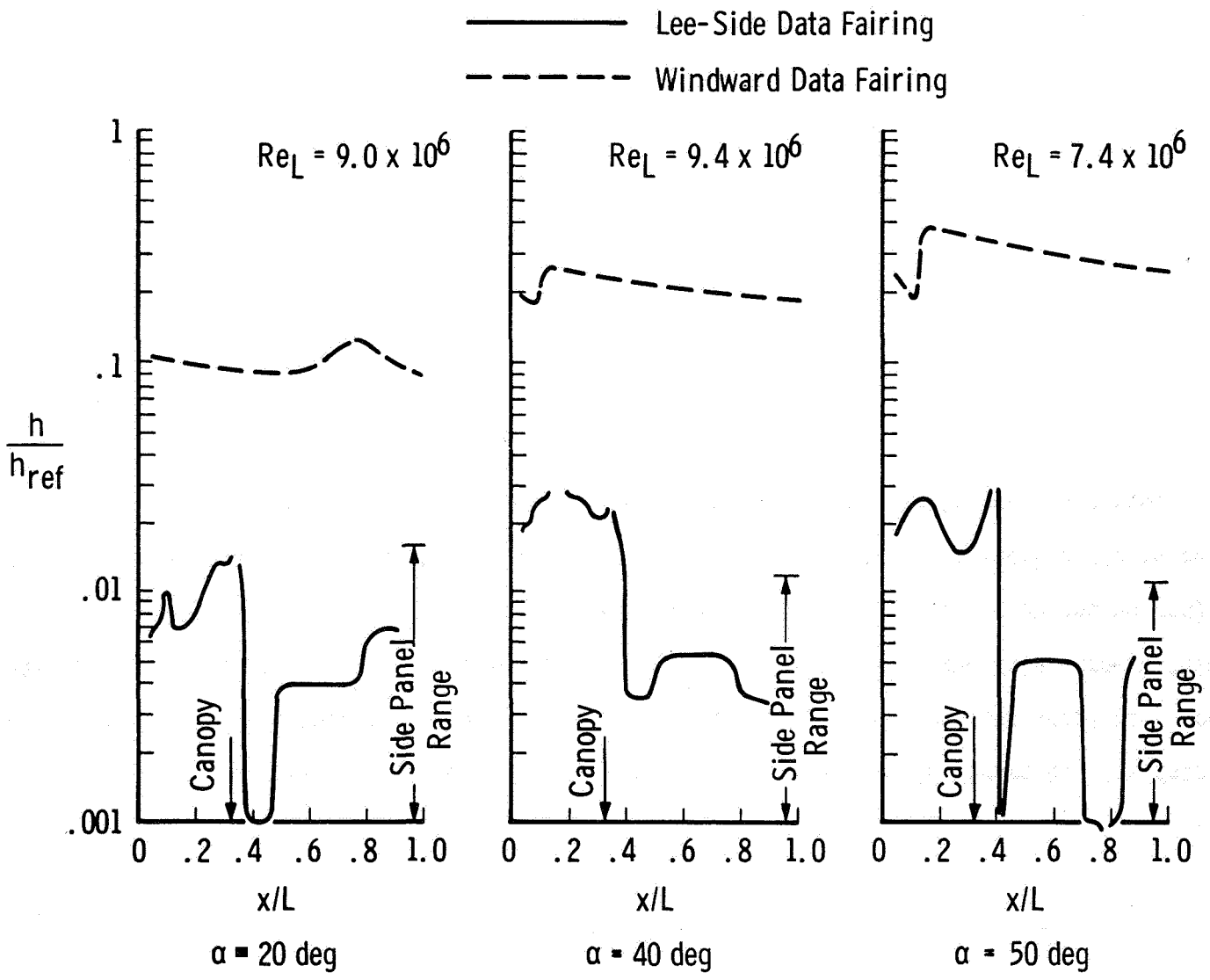

b. Tunnel F, $M_\infty = 10.5$

Fig. 5 Concluded

COMPARISON OF EXPERIMENTAL AND THEORETICAL SHOCK ANGLES

(Figure 6)

Shock angle measurements for both M_∞ = 8 and 10.5 are presented in Figure 6. The data are presented in terms of the incremental angle between the local body slope and the local bow shock. This angle is between 3 and 6 deg for all angles of attack. For $\alpha \leq 40$ deg the data agree within $\pm$ 2 deg with the tangent cone theory. For angles around shock detachment (i.e., α = 50 and 60 deg) the data are compared to the α = 30 deg fairing and as can be seen the incremental shock angle is relatively insensitive to model angle of attack. No significant Mach number effects were observed.

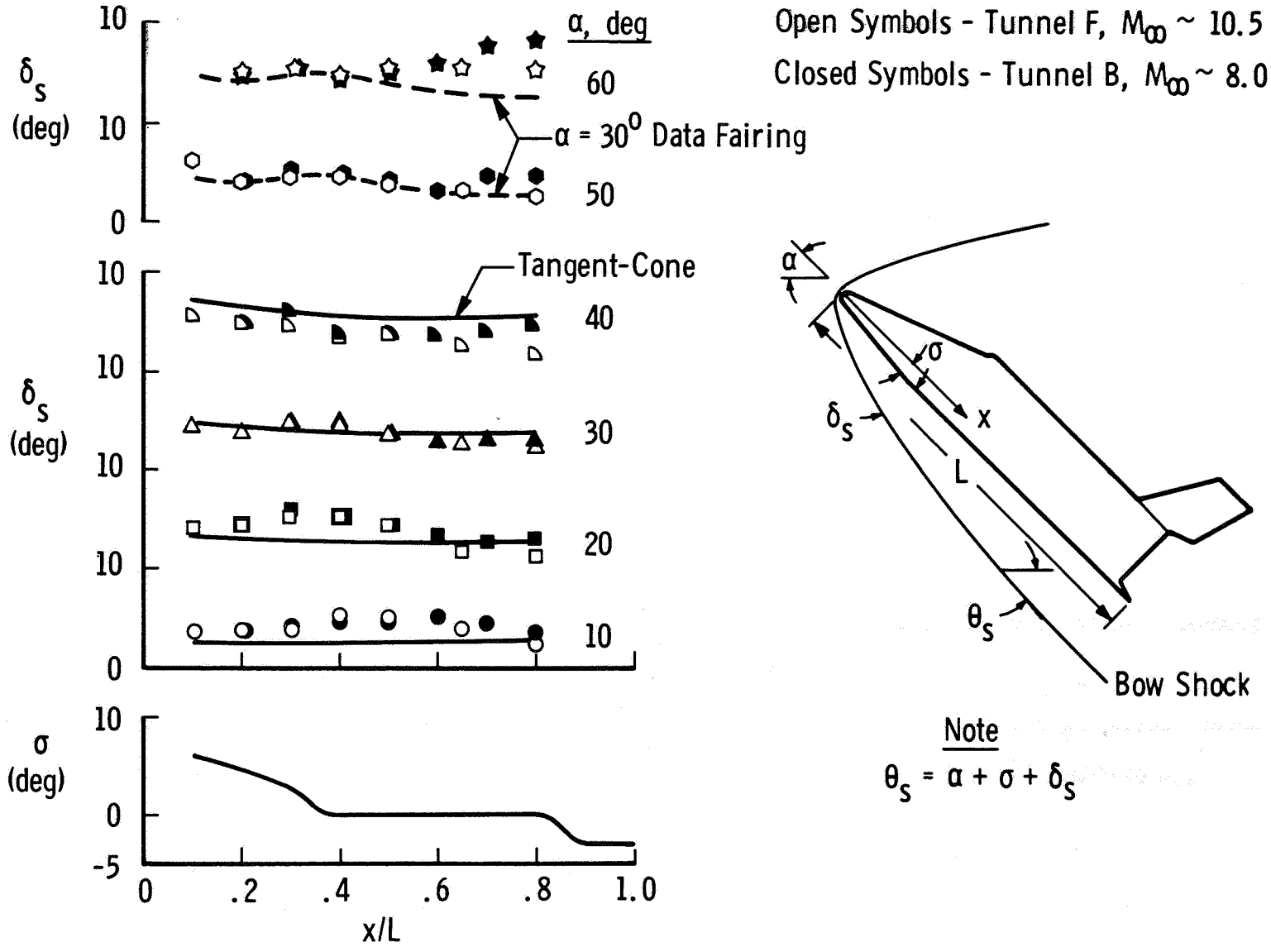

Fig. 6 Comparison of Experimental and Theoretical Shock Angles

MDAC ORBITER - WINDWARD CENTERLINE PRESSURE DISTRIBUTIONS

(Figure 7)

In Figure 7 windward centerline pressure distributions at M_∞ = 8 and 10.5 are compared with tangent cone and modified Newtonian theories. Considering its simplicity, modified Newtonian theory shows satisfactory agreement with the data for both Mach numbers and for all angles of attack (i.e., $10 \leq \alpha \leq 60$). However, at the intermediate angles tangent cone theory shows better agreement with the data.

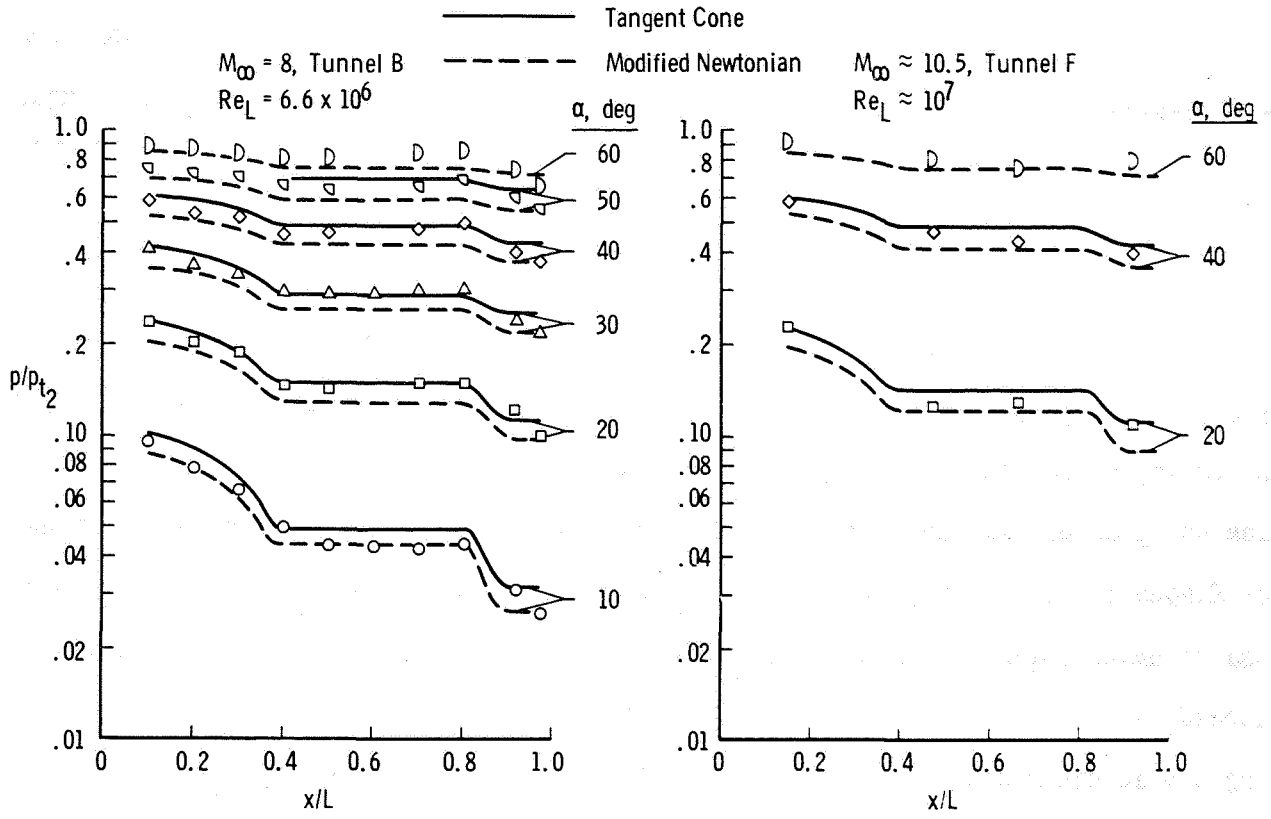

Fig. 7 MDAC Orbiter - Windward Centerline Pressure Distributions

TYPICAL PITOT PRESSURE AND TOTAL TEMPERATURE PROFILES

(Figure 8)

Mach 8 windward centerline flow field data were obtained at four model stations (x/L = 0.3, 0.5, 0.7 and 0.92) and at α = 10 through 60 deg. Typical flow field rake measurements at α = 20 deg and x/L = 0.5 are shown in Figure 8. The rake consisted of a column of 15 pitot pressure probes and an adjacent column of 6 total temperature probes. The pitot pressure distribution shown is representative of the case where the entropy layer has not yet been completely swallowed by the boundary layer. To determine an approximate lower bound of the inviscid flow the total temperature profiles were used to define at value of y* (the minimum value of y where $T_p/T_o \approx 1.0$)[1]. The measured pitot pressure at y* and the local surface pressure at the corresponding station were used to calculate M*, the local flow field Mach number. These Mach numbers are presented in the next figure.

---

[1]The actual boundary layer thickness (δ) may be slightly less than y* since continuous profiles would be required to define δ.

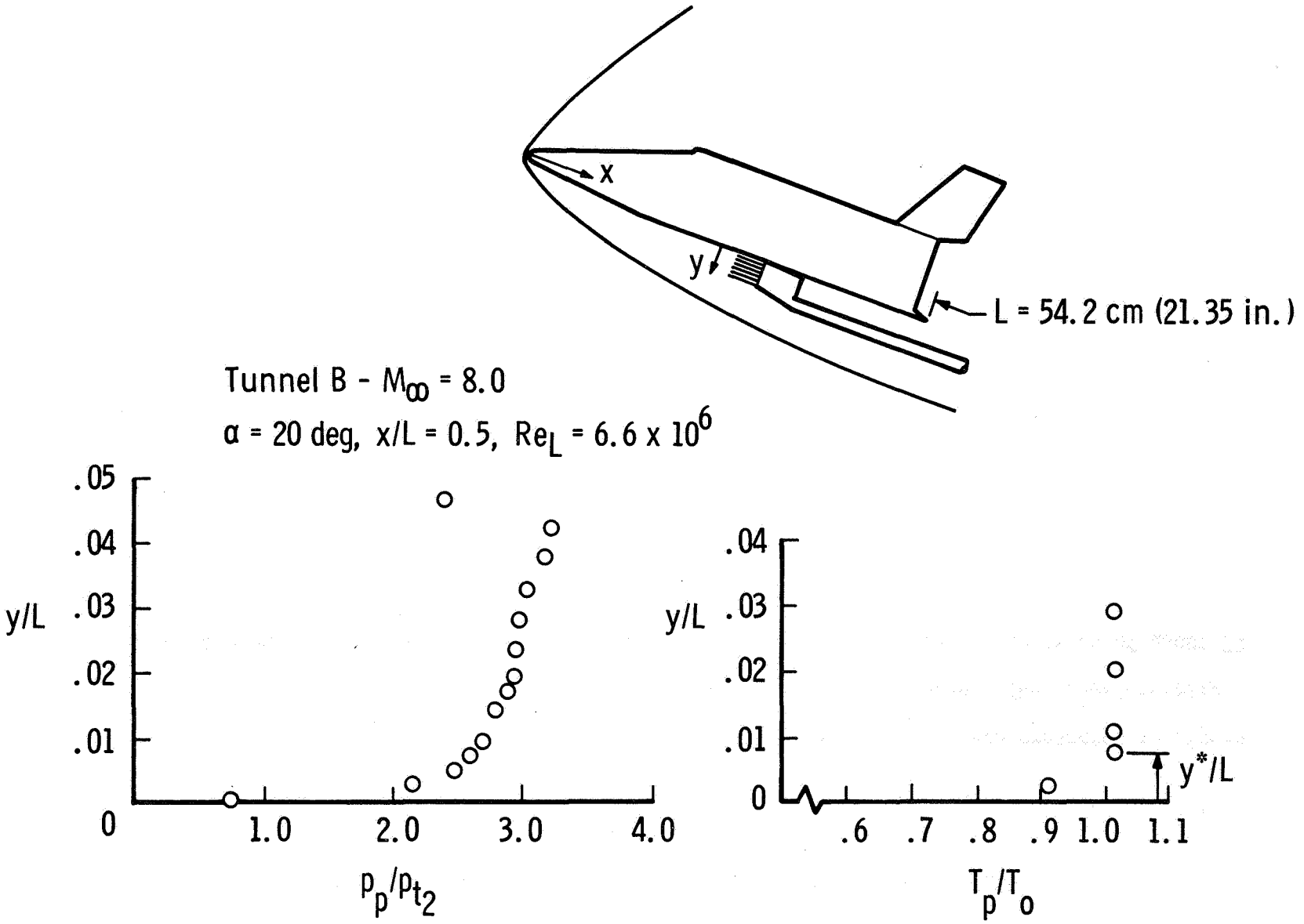

Fig. 8 Typical Pitot Pressure and Total Temperature Profiles

MDAC ORBITER - WINDWARD CENTERLINE MACH NUMBER DISTRIBUTIONS

(Figure 9)

Measured local Mach number (M*) distributions at α = 10 through 60 deg are presented in Figure 9. These distributions are compared to tangent cone theory where applicable. The experimentally determined Mach numbers appear to be somewhat below the theory with a maximum deviation of about 20 percent.

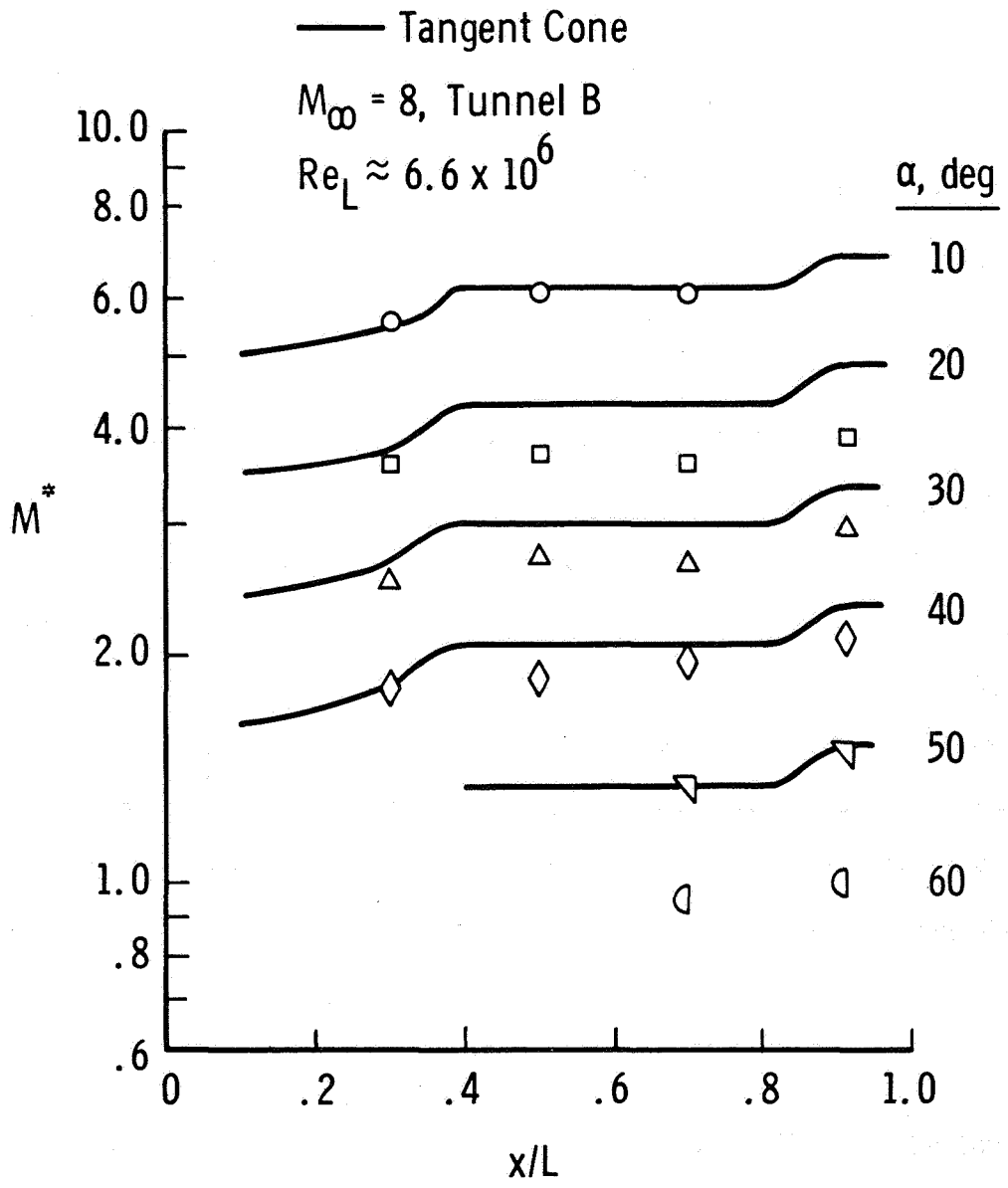

Fig. 9 MDAC Orbiter - Windward Centerline Mach Number Distributions

COMPARISON OF EXPERIMENTAL AND THEORETICAL WINDWARD CENTERLINE HEATING DISTRIBUTIONS

Tunnel B, $M_\infty = 8$

(Figure 10a)

Heat-transfer coefficient distributions obtained at α = 10 and 20 deg and using the phase-change paint technique are presented in Figure 10a. The 10-degree angle-of-attack data are compared to two-dimensional and axisymmetric laminar local similarity theory (Ref. 4) and two-dimensional Spalding-Chi turbulent theory (Ref. 5) using the Colburn Reynolds analogy factor (1.25). Local flow properties were calculated using a fairing of the experimental pressure data and a shock angle of 15 degrees. The radius (r) used in the axisymmetric calculation is shown superimposed on the orbiter planform sketch. Since the laminar data are bracketed by the 2-D and the axisymmetric solutions, only a small amount of streamline divergence is indicated at this angle of attack. The turbulent data are in good agreement with the Spalding-Chi theory. The boundary layer trips consisted of 0.076 cm diam steel spheres located 2.54 cm from the model nose with 3 diam spacing between centers.

The 20-degree angle-of-attack data are compared to axisymmetric laminar theory and turbulent Spalding-Chi theory corrected to axisymmetric values by the method of Ref. 6. These corrections were less than 10 percent at all points. A shock angle of 23 degrees was assumed. The laminar data agree with the axisymmetric theory both in magnitude and distribution. The turbulent data are about 20 percent above the Spalding-Chi theory.

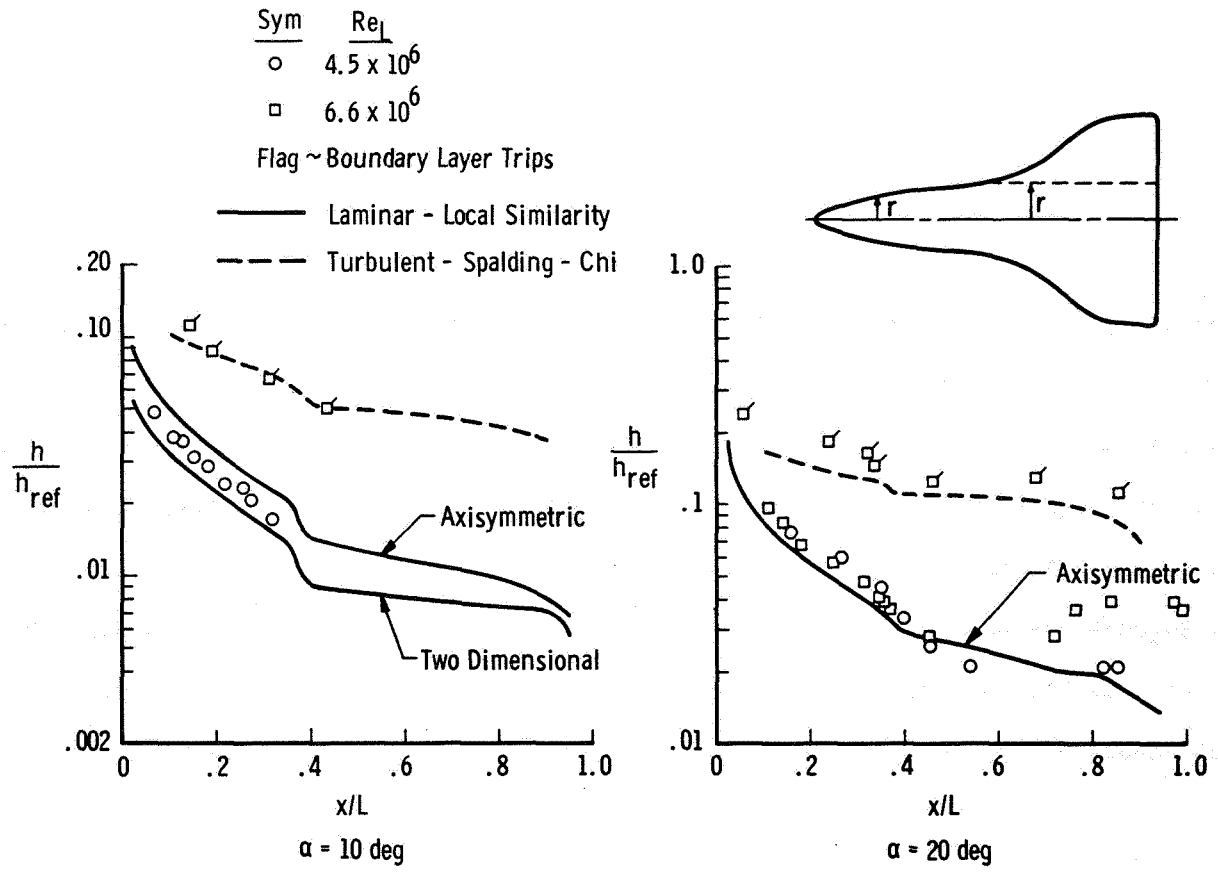

a. Tunnel B, $M_\infty = 8$

Fig. 10 Comparison of Experimental and Theoretical Windward Centerline Heating Distributions

COMPARISON OF EXPERIMENTAL AND THEORETICAL WINDWARD CENTERLINE HEATING DISTRIBUTIONS

Tunnel F, $M_\infty \approx 10.7$

(Figure 10b)

Tunnel F heat-transfer rate gage data at 10 and 20 degree angle of attack are compared to theoretical solutions calculated in the same manner as those of the preceding figure. The laminar data show good agreement with the theoretical laminar solutions. At the highest Reynolds number there was about 30-40 percent difference between data and theory. At the lowest Reynolds number the data appear to be transitional. In Ref. 7 it was shown that surface roughness which was not large enough to move the end of transition significantly upstream could considerably increase the heating rates downstream of the roughness. The small surface roughness caused by the heat gages and surface pressure taps may have had a similar effect on the present data at the lowest Reynolds number.

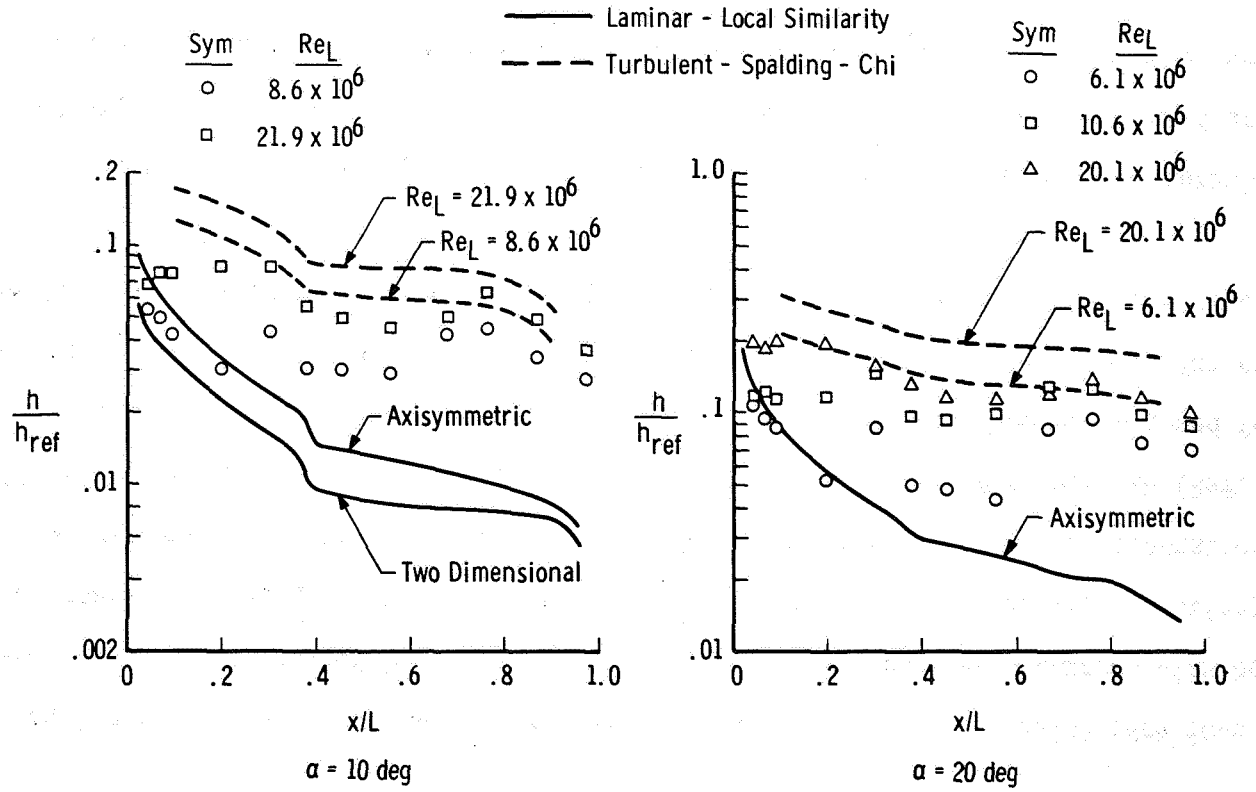

b. Tunnel F, $M_\infty \approx 10.7$

Fig. 10 Continued

COMPARISON OF EXPERIMENTAL AND THEORETICAL WINDWARD CENTERLINE HEATING DISTRIBUTIONS

Tunnel B, $M_\infty = 8.0$

(Figure 10c)

Heat-transfer coefficient distributions obtained using the phase-change paint technique (Tunnel B) at $\alpha = 40$ and 60 deg are presented in Figure 10c. The experimental data are compared with both laminar and turbulent theories. The theoretical distributions were obtained from numerical solutions of the governing three-dimensional laminar and turbulent boundary layer equations for the stagnation line of a swept cylinder following Kaups and Keltner (Ref. 8) and Hunt, Bushnell, and Beckwith (Ref. 9). The turbulent eddy viscosity model used was that of Adams (Ref. 10). Conical flow was assumed for the 40 degree angle-of-attack calculations while parallel shock flow was used at 60 degrees. The cross flow velocity gradient was obtained by approximating the local body lower surface with a spherical segment and using the method of South (Ref. 11).

Agreement between theory and experiment is within 15 percent for the laminar and turbulent cases at both angles of attack. The boundary layer trips used at these angles of attack consisted of small ($\approx$ 0.064-cm) clusters of grit spaced approximately one inch apart on the entire windward surface.

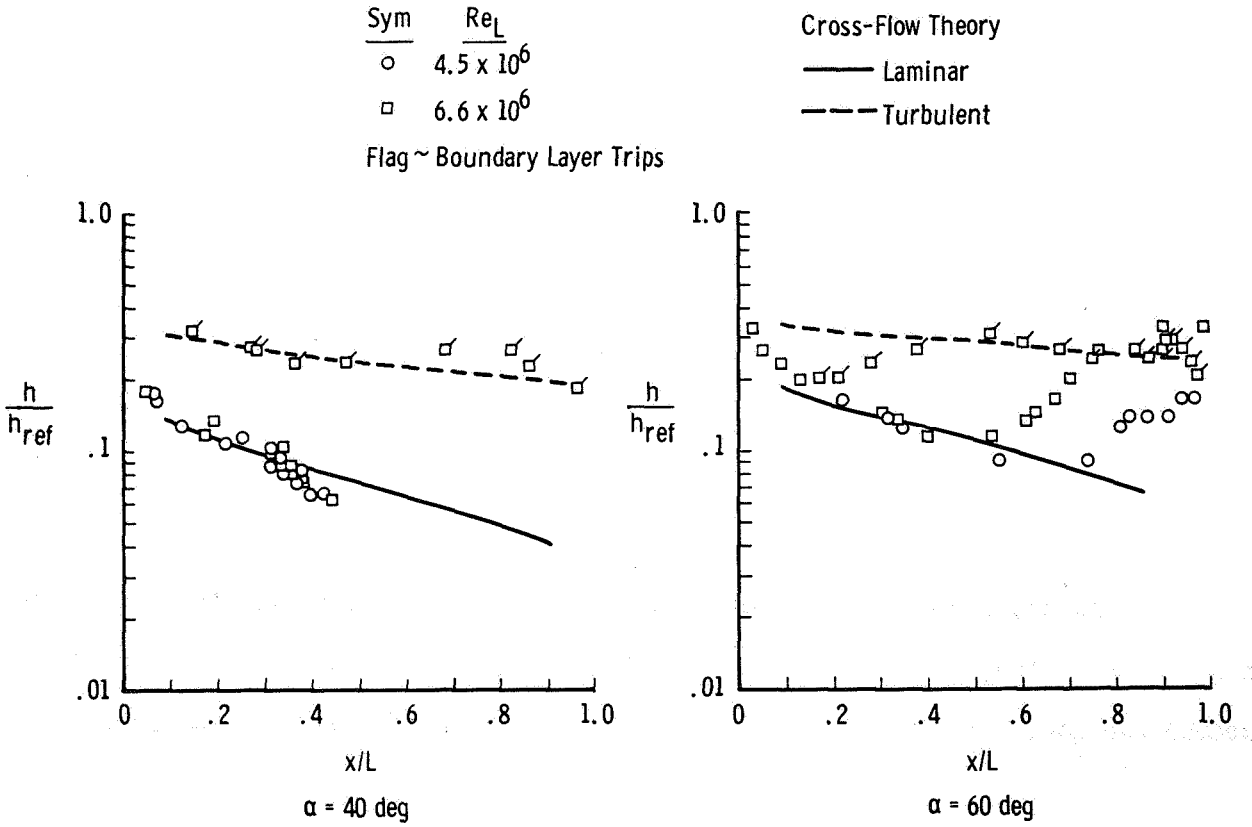

c. Tunnel B, $M_\infty = 8.0$

Fig. 10 Continued

COMPARISON OF EXPERIMENTAL AND THEORETICAL WINDWARD CENTERLINE HEATING DISTRIBUTIONS

Tunnel F, $M_\infty = 10.5$

(Figure 10d)

Tunnel F heat-transfer rate gage data at 40 and 60 degree angles of attack are compared to theoretical solutions calculated in the same manner as those of the previous figure. In general, there is about a 25 percent difference between the data and the turbulent theory.

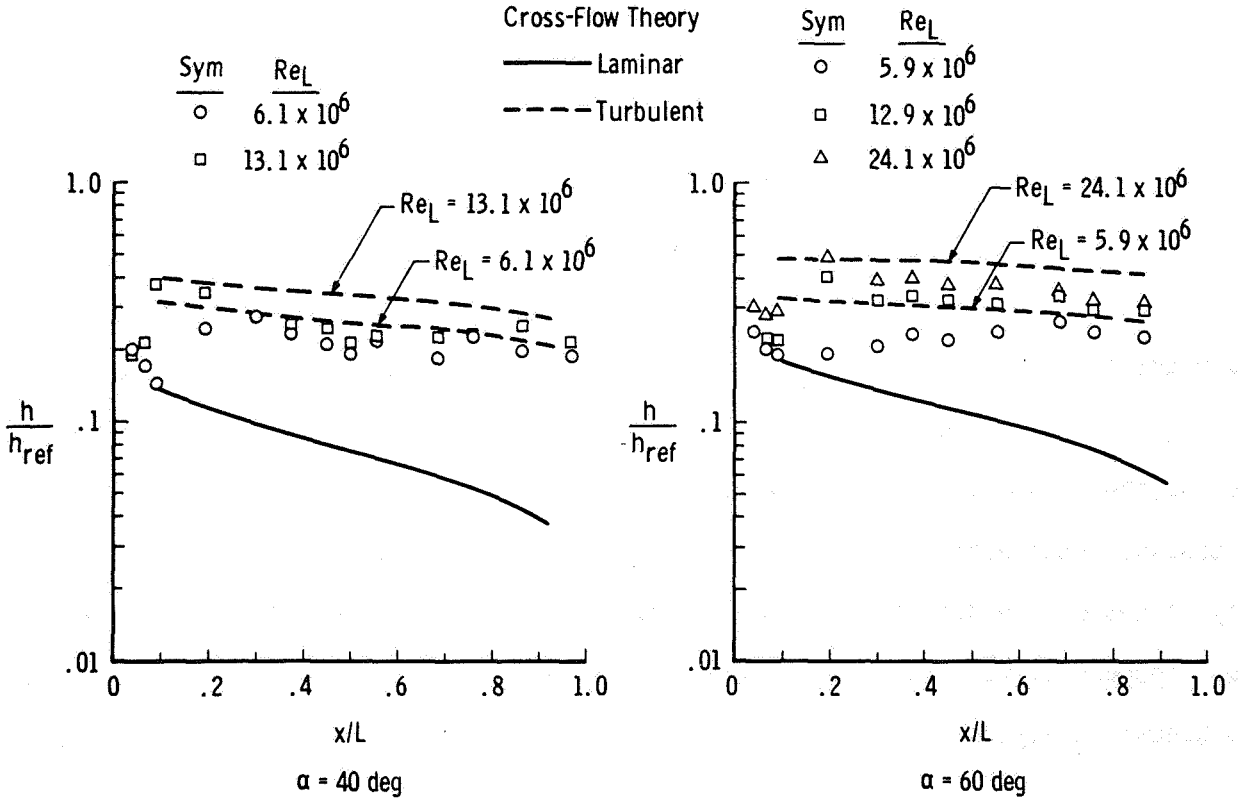

d. Tunnel F, M_∞ = 10.5

Fig. 10 Concluded

TRANSITION ONSET CORRELATION

(Figure 11)

Hamilton (Ref. 12) has shown that turbulent heating can have a significant impact on the design of a thermal protection system and therefore a proper transition criteria is needed. The transition criteria recommended by the aerothermodynamic working group was developed by Masek (Ref. 13) and this criteria is compared with the present Mach 8 data in Figure 11. The momentum-thickness at transition was determined by the same theoretical methods used for computing the laminar heating rates. For $\alpha \leq 50$ deg the data scatter about the transition criteria line but for $\alpha = 60$ deg the data are about 30 percent below the line. Since the Tunnel F data may have been artificially tripped they are not included in this figure.

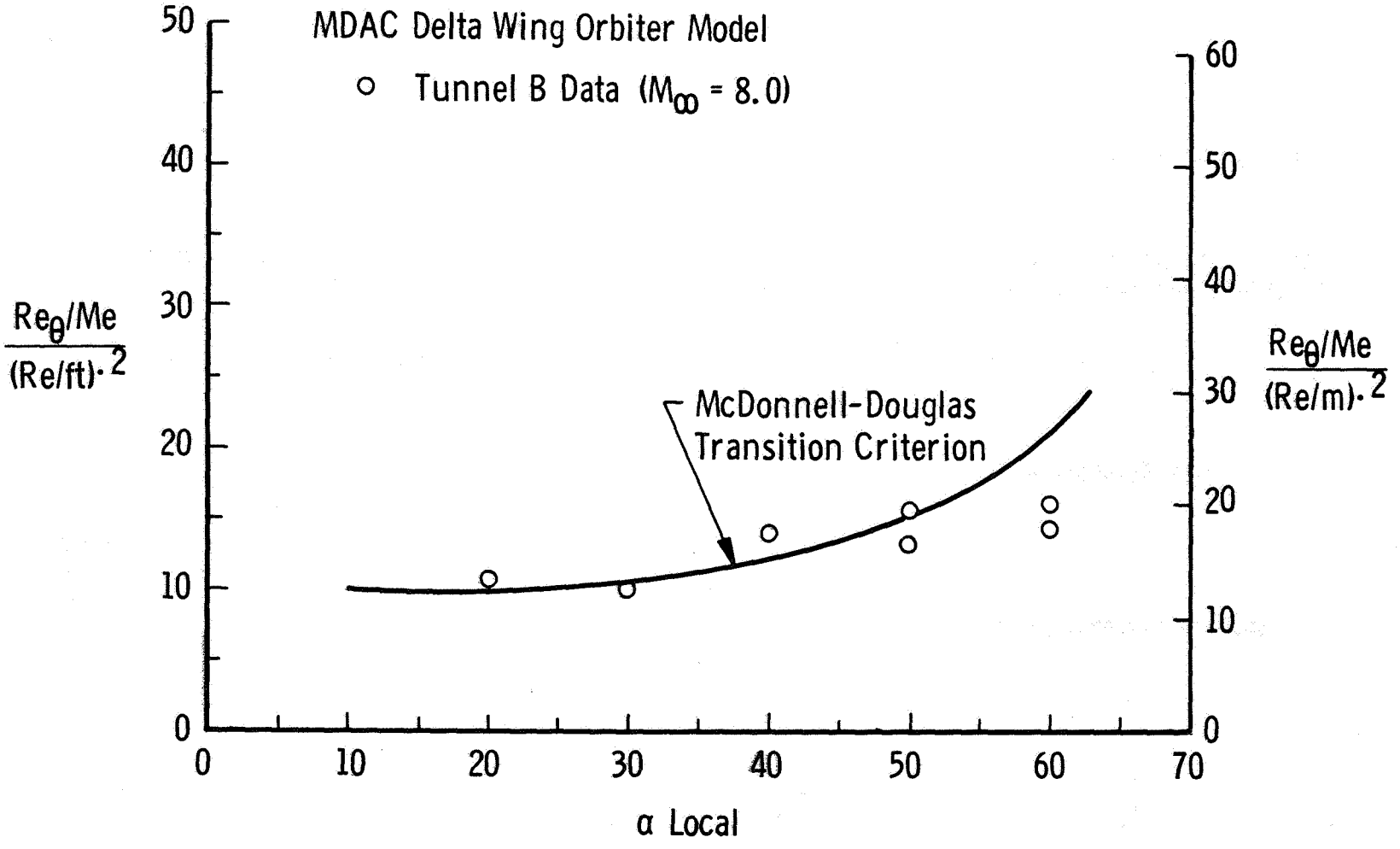

Fig. 11 Transition Onset Correlation

CONCLUSIONS

LEE SIDE

1) Hot regions on canopy $(h/h_{ref})_{max} \approx 0.1$ and on nose $(h/h_{ref})_{max} \approx 0.03$.

2) Hot streaks on side panel $(h/h_{ref})_{max} \approx 0.04$; move forward as angle of attack increases.

WINDWARD CENTERLINE

3) The angle between the body and shock was $\sim$ 3 to 6 deg and varied only slightly with angle of attack.

4) Pressure distributions were between tangent cone and modified Newtonian theory.

5) At α = 10 and 20 deg 2-D and axisymmetric theory agreed with both the laminar and turbulent data in Tunnel B. At the higher Reynolds number in Tunnel F there was about 30-40 percent difference between data and theory.

6) At α = 40 and 60 deg cross flow theory and experimental data were within 15 percent in Tunnel B and 25 percent in Tunnel F.

REFERENCES

1. Fay, J. A.; and Riddell, F. R.: Theory of Stagnation Point Heat Transfer in Dissociated Air. Journal of the Aeronautical Sciences, Vol. 25, 1958, pp. 73-85.
2. Hefner, Jerry H.; and Whitehead, Allen H., Jr.: Lee-Side Heating Investigations, Part I - Experimental Lee-Side Heating Studies on a Delta-Wing Orbiter. NASA Space Shuttle Technology Conference, NASA TM X-2272, Vol. I, March 1971, pp. 267-287.
3. Whitehead, Allen H., Jr.; and Bertram, Mitchel H.: Alleviation of Vortex-Induced Heating to the Lee-Side of Slender Wings in Hypersonic Flow. AIAA Journal, Vol. 9, 1971, pp. 1870-1872.
4. Dewey, C. Forbes, Jr.; and Gross, Joseph F.: Exact Similar Solutions of the Laminar Boundary-Layer Equations. Advances in Heat Transfer, Vol. 4, New York: Academic Press, Inc., 1967, pp. 317-446.
5. Neal, Luther, Jr.; and Bertram, Mitchel H.: Turbulent-Skin-Friction and Heat-Transfer Charts from the Spalding-Chi Method. NASA TN-D-3969, May 1967.
6. Vaglio-Laurin, R.: Heat Transfer on Blunt Nosed Based in General Three-Dimensional Hypersonic Flow. Heat Transfer and Fluid Mechanics Institute, University of California, Los Angeles, California, June 11-13, 1959.
7. Sterrett, J. R.; Morrisette, E. L.; Whitehead, A. H., Jr.; and Hicks, R. M. Transition Fixing for Hypersonic Flow. NASA TN D-4129, October, 1967.
8. Kaups, K.; and Keltner, G.: Laminar Compressible Boundary Layer on a Yawed Infinite Wing. McDonnell-Douglas Report No. LB 32706, March 1967.

9. Hunt, J. L.; Bushnell, D. M.; and Beckwith, I. E.: Finite Difference Analysis of the Compressible Turbulent Boundary Layer on a Swept Blunt Slab Leading-Edge Blowing. Paper No. 19 in "Analytic Methods in Aircraft Aerodynamics," NASA SP-228, 1970, pp. 417-472.

10. Adams, J. C., Jr.: Numerical Calculation of the Three-Dimensional Turbulent Boundary Layer on Sharp Cone at Incidence in a Supersonic Flow. Paper presented at Workshop on Fluid Dynamics of Unsteady, Three-Dimensional, and Separated Flows, Georgia Institute of Technology, June 10-11, 1971.

11. South, J. C., Jr.: Calculation of Axisymmetric Supersonic Flow Past Blunt Bodies with Sonic Corners Including a Program Description and Listing. NASA TN D-4563, May 1968.

12. Hamilton, Harris H.: Turbulent Heating on Space Shuttle Orbiters During Reentry. Space Transportation System Technology Symposium, NASA TM X-52876, Vol. I, July, 1970, pp. 463-484.

13. Masek, R. V.: "Boundary Layer Transition on Lifting Entry Vehicle Configurations at High Angle-of-Attack. Space Transportation System Technology Symposium, NASA TM X-52876, Vol. I, July, 1970, pp. 445-462.

A REVIEW OF THE GRUMMAN ORBITER WIND TUNNEL HEAT TRANSFER TESTS

By A. R. Mendelsohn, M. Bourbin, M. Jew,
and C. W. Osonitsch

Grumman Aerospace Corporation
Bethpage, New York

INTRODUCTION

Aerodynamic heat transfer and flow visualization tests of the Grumman Space Shuttle Orbiter have been conducted in the NASA Langley Continuous Flow, Variable Density and Mach 20 Helium Tunnels. The orbiter was tested alone and with various side and tandem mounted tanks. Test conditions spanned a Reynolds number range which resulted in both laminar and turbulent flows.

Experimental studies have also examined the heat transfer problems associated with integration of the Auxiliary Propulsion System into the Orbiter. Tests in the Grumman Hypersonic Shock Tunnel have investigated heating to cavities and heating from single and multiple hydrogen-oxygen plumes while tests run as part of the configuration evaluation have examined the heating to wing pods. The plume work, reported in Reference 1, is beyond the scope of this presentation.

In reviewing this program, the attempt is made to show how the collaborating information from heat transfer data, flow visualizations and supporting theories led to a better understanding of the orbiter's aerothermodynamic environment. The review begins by justifying this experimental program, and proceeds with the discussion of the flow field and heat transfer to the windward surface, to the leeward surface, to cavities and finally to the orbiter with tanks.

TPS SENSITIVITY

(Figure 1)

The current Orbiter consists of an all aluminum structure entirely protected by ablators. Sufficient ablator is applied to limit the ablator structural interface temperature to 450°K (350°F). Prior to this, thermal protection systems consisted of both reradiating surface panels and hot structure of titanium, super alloys, refractory metals, ceramics and graphitic composites. The selection of a material in a given area of the vehicle and the subsequent TPS weight was extremely dependent on and sensitive to aero-heating predictions. Much advantage was gained from trajectory optimization and large weight differences arose due to differences in flow field assumptions, heating correlations, transition criteria and interpretation of tunnel data. The reliability of a minimum weight TPS design rested with the ability to define the aero-heating environment.

On the other hand, as figure 1 shows, the current TPS is relatively insensitive to trajectory and heating variables. Large weight savings are to be found by relaxing crossrange requirements or going to an all ablative protected titanium structure. However, adoption of either of these options leaves unchanged the weak dependence of TPS on trajectory and heating methodology.

It now appears that only one option within the framework of the current baseline TPS would again introduce the strong reliance on the reentry environment. While the feasibility of this option from a cost stand point remains to be shown, it does offer a large potential weight savings. That is, the option of using unprotected titanium in regions of peak temperatures lower than 590°K but staying with ablators in all other areas.

Since the latter option is not now being actively pursued, it might be falsely assumed that the requirements on accurate aero-heating description are somewhat relaxed. While not sensitive to accurate description on the gross scale, an undetected, underestimated local problem might spell the difference between mission success and failure.

TPS SENSITIVITY

- Baseline TPS (11300 kg)
  SLA 561 Over Al (T_{Back} = 450°K Max)

	Wt Savings
• Trajectory Variables	
Δ Downrange (13900 to 8330 km)	2%
Δ Trajectory Algorithm ($\dot{q}_0$ to T_{max})	6%
Δ Crossrange (2040 to 370 km)	26%
• Aeroheating	
Δ No Turbulent Heating	9%
Δ Double Lee Side $\dot{q}/\dot{q}_0$	−8%
• Structure	
Δ 590° K Backface (Ti)	27%
Δ 590° K Backface + Bare Ti	52%

Figure 1

ORBITER CONFIGURATION

(Figure 2)

The orbiter configuration tested in the Langley Continuous Flow Hypersonic Tunnel*(CFHT), the Variable Density Tunnel (VDT) and the Mach 20 Helium Tunnel (HeT) is shown in figure 2. The configuration is the GAC H-33, a medium L/D (L/D_{max} = 1.9, L/D at α design of 27° = 1.57), external hydrogen tank vehicle. Since the configuration is only slightly larger than the current HO designs (41.1m in length vs 33.6m) and is geometrically similar, the data is still of general interest.

Phase change paint and thin skin thermocouple heat transfer data as well as oil flow, schlieren and electron beam visualizations were gathered in the varied facilities. The following table summarizes the type of data with the facility and where appropriate, the model material.

LANGLEY DATA MATRIX

CFHT (1/150 scale)	VDT (1/200 scale)	HeT (1/150 scale)
o Phase change paint - Stycast o Thin skin thermocouples - Ni fuselage/SS wing o Thermocouple strips(1) - SS	o Phase change paint - Stycast - Material "G"(2) o Thermocouple strips(1) - SS o Oil Flow o Schlieren	o Oil flow o Electron beam

(1) Thermocouple strips are thin strips of stainless steel placed flush on the surface of a phase change paint model. The model material under the strip is removed to minimize conduction losses.

(2) A GAC epoxy which exhibits higher temperature resistance, lower $k\rho c$, more uniform properties, and better casting characteristics than STYCAST.

* The CFHT model, an earlier version of the H-33, differed somewhat from the configuration shown in figure 2, having a tapered aft fuselage, a more contoured forebody planform and a straight trailing edge.

ORBITER CONFIGURATION

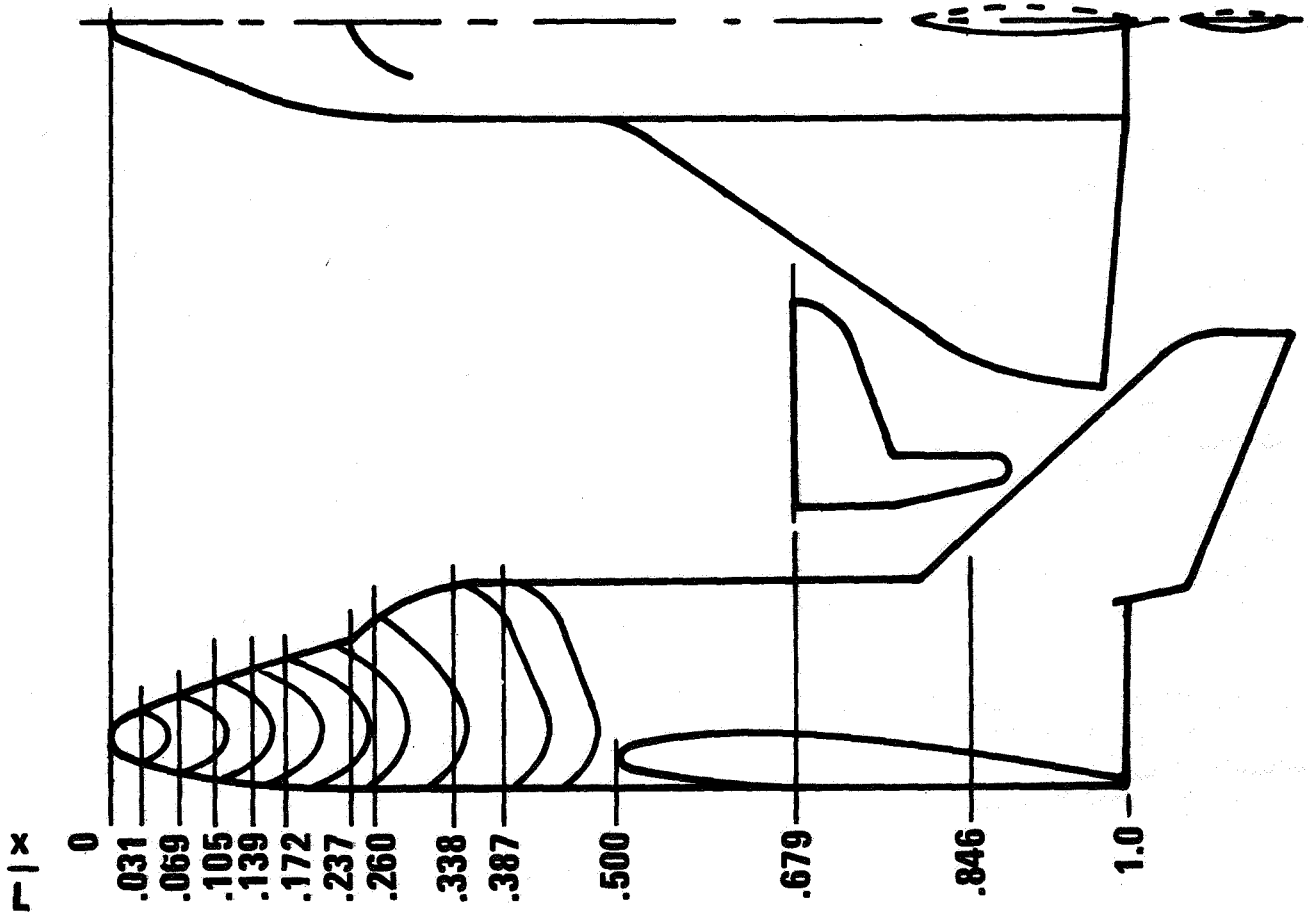

Figure 2

WINDWARD OIL FLOW

(Figure 3)

Oil flow patterns on the windward surface of the Orbiter at $\alpha = 27°$ and $M_\infty = 8$ are shown in figure 3 for two Reynolds numbers, $Re_\infty/m = 4.35 \times 10^6$ and 1.64×10^7. The surface streamlines near the center of the flat forebody tend to run fore and aft with little divergence. The cross flow outboard of this central core, in the rounded chine region, is uniform and quite pronounced.

The streamlines entering the wing fillet region, having a higher pressure than those from the fuselage, overexpand inward and, together with the fuselage streamlines, flow toward the low pressure aft central region of the wing. The initial inward overexpansion of the streamlines from the fillet region is consistent with the patterns observed on blunt nosed delta wings (Ref 2). While not obvious from the oil flows presented, phase change paint data indicates that the streamline convergence increases with Reynolds number. This dependence is conceivable since the pheonomenon, the confluence of a new and a developed boundary layer, is not of the usual boundary layer kind.

The flow on the wing outboard of the fillet, spans greater than 1/3, tend to flow in a more orderly spanwise pattern. This observation supports the argument that the inflow effect is primarily due to the abrupt change in configuration at the wing-fuselage junction. Previous orbiter configurations had tapered rather than cylindrical forebodies which allowed a smoother blending of the two streams. Streamline convergence was not observed. However, data from an early GD booster (Oct. 1970), a cylindrical forebody delta wing configuration, showed trends similar to those observed here.

Shock impingement on the wing as a result of the intersection of forebody bow and wing shocks is not visible on the oil flow. Calculation and observation of leeside oil flow shows that this impingement takes place at 70% span, just outboard of the most outboard fore and aft reference line.

WINDWARD OIL FLOW IN VDT

$\alpha = 27^0, M_\infty = 8, L_{MODEL} = .205$ m

$Re_\infty/m = .436 \times 10^7$

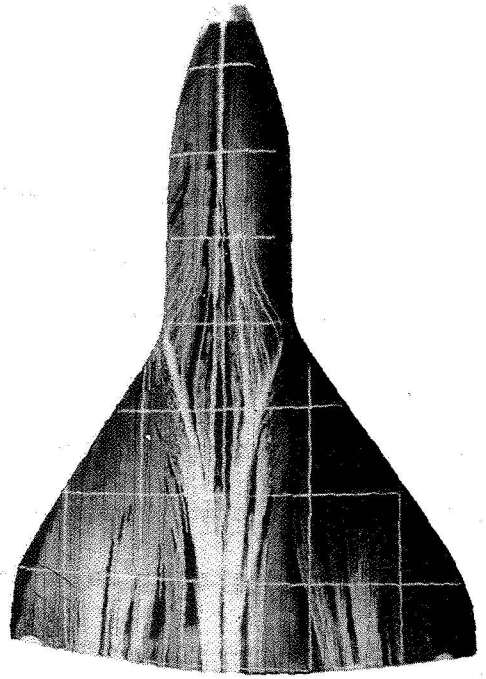

$Re_\infty/m = 1.64 \times 10^7$

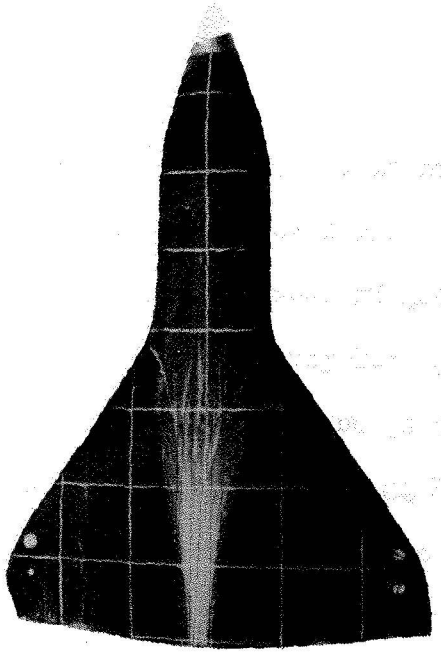

Figure 3

COMPARISON OF WINDWARD SURFACE HEAT TRANSFER DISTRIBUTIONS AT TWO REYNOLDS NUMBERS

(Figure 4)

Heat transfer distributions on the windward side of the orbiter at 27° angle of attack, based on phase change paint patterns, are compared for two Reynolds numbers. Of particular interest are the wing distributions. At the low Reynolds number, the heating is indicative of an orderly chordwise flow with little interaction between wing and fuselage. At the higher Reynolds numbers the heating mirrors the complex oil patterns emanating from the wing fillet. Transition and turbulent heating are found to occur uniformly over the entire aft section. Bow shock impingement on the wing at the 70% span location has a more pronounced effect on the heat transfer for the high Reynolds number case.

COMPARISON OF WINDWARD SURFACE HEAT TRANSFER DISTRIBUTIONS AT TWO REYNOLDS NUMBERS

$\alpha = 27^0$, $M_\infty = 8$

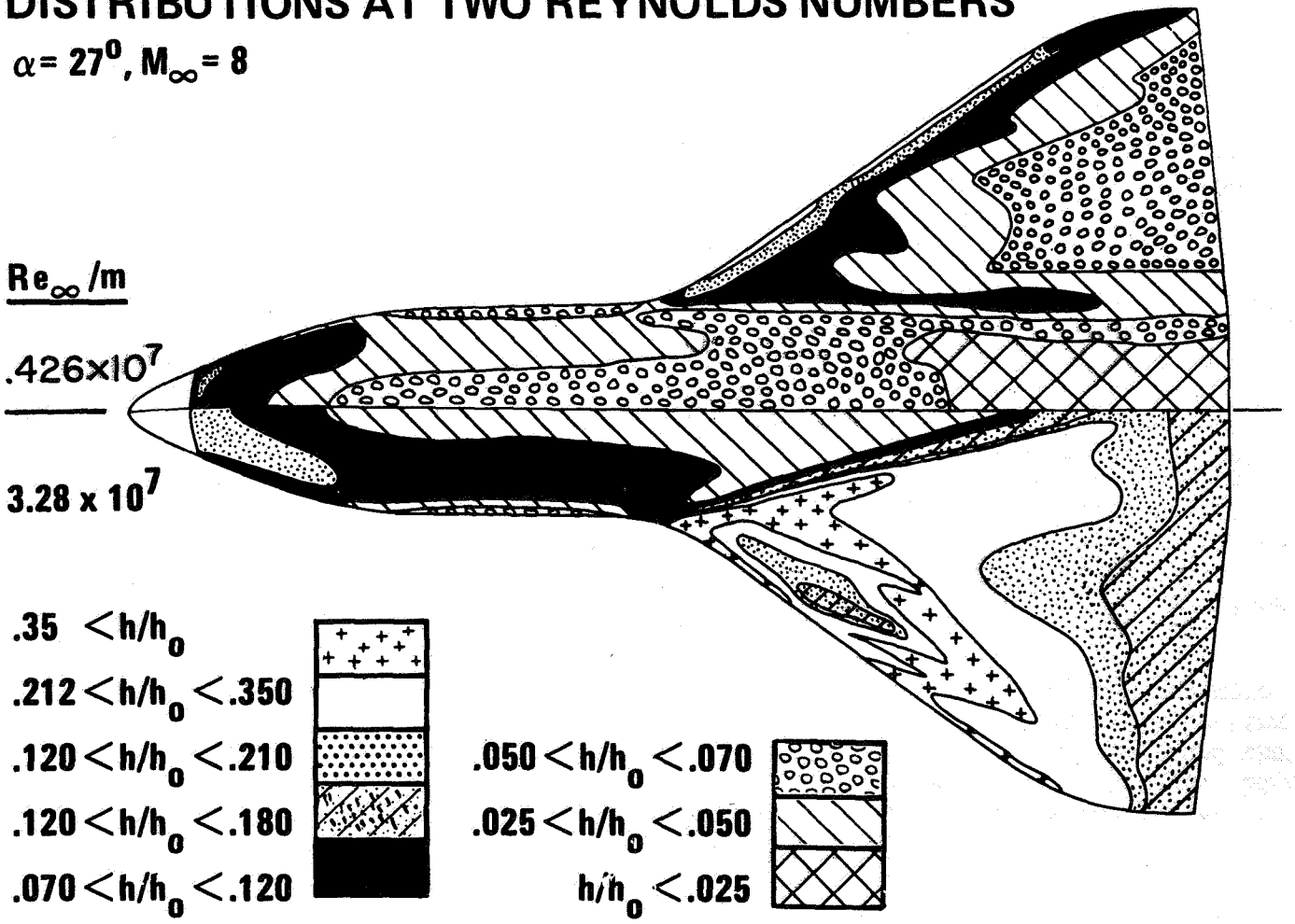

Figure 4

EFFECT OF ANGLE OF ATTACK ON LAMINAR HEAT TRANSFER DISTRIBUTION

(Figure 5)

Analysis of the laminar windward centerline heat transfer distributions for angles of attack of 0°, 20°, 27°, and 40° was correlated using the reference enthalpy technique. Edge properties were evaluated based upon a tangent-cone flowfield assumption. It was found that the coupling of the parameters derived from a conical flowfield with the flat plate heating relation, used without benefit of the conical heating correction factor, provided the more successful correlations.

The figure compares the analytical predictions with the measured heating distributions. Along the windward centerline at 0°, the analytical prediction is excellent for $s/L < .25$ and overpredicts for $s/L > 0.25$. The measured heating rates aft of $s/L=0.25$ are affected by the significant inflow component from the nose and wing leading edge as seen from oil flow studies. The inflow results in a thickening of the boundary layer and a decrease in heat transfer which cannot be predicted by this analysis. At the higher angles of attack (20°, 27°, 40°) the inflow is negligible and the agreement between analysis and data is quite satisfactory in the region of $s/L > 0.10$. However, at these higher angles of attack, the analysis underpredicts the data in the region near the nose ($s/L < 0.10$). The difference between data and analysis in this region is less than full conical heating values ($\sqrt{3}$) and varies between $h_{data}/h_{analysis} = 1.06$ at $\alpha = 40°$ to $h_{data}/h_{analysis} = 1.36$ at $\alpha = 20°$.

When the orbiter is at zero angle of attack, the flow on the lee surface centerline separates just forward of the canopy and reattaches on the canopy. Forward of the flow separation point, heat transfer was correlated in the same manner as for the windward centerline. However, aft of the reattachment point, the flowfield assumption found most suitable was one which considered an isentropic expansion from the maximum reattachment pressure to the local pressure as determined from modified Newtonian considerations. Heat transfer in this region was correlated using the reference enthalpy technique for a flat plate. Agreement between data and theory is good.

EFFECT OF ANGLE OF ATTACK ON LAMINAR HEAT TRANSFER DISTRIBUTION

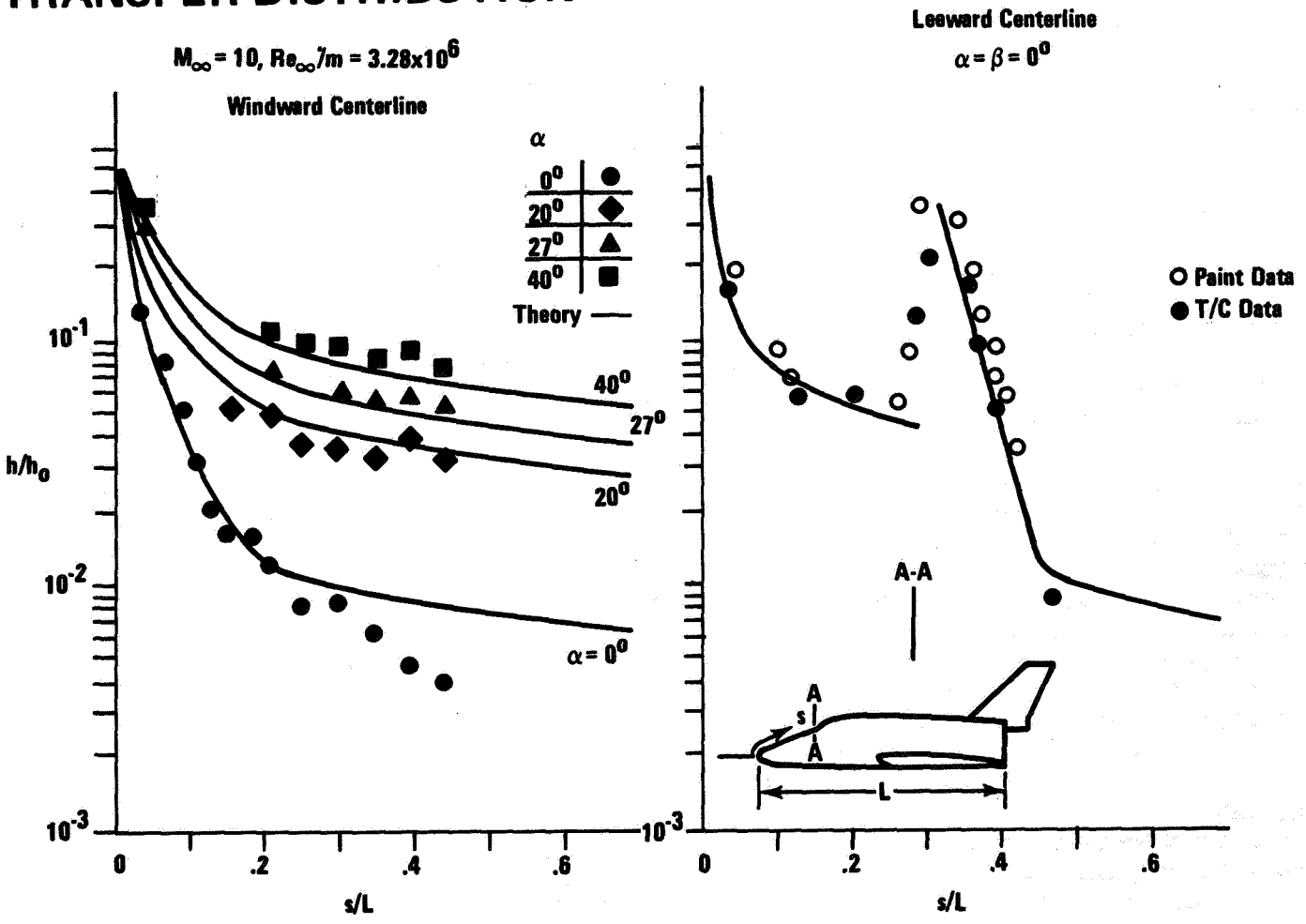

Figure 5

EFFECT OF REYNOLDS NUMBER ON WINDWARD CENTERLINE HEAT TRANSFER

(Figure 6)

Examination of the heat transfer data from phase change paint and thermocouple strip models, on the windward centerline at $\alpha = 27°$, indicated that the flow was entirely laminar for the first 20% of the fuselage, at unit freestream Reynolds numbers up to 3.28×10^7/meter. At the lowest test Reynolds numbers, laminar flow persisted over the entire windward centerline. Increasing the Reynolds number to 1.64×10^7/meter resulted in transition onset beginning at the aft 30% of the fuselage. Fully developed turbulent flow was obtained only on the aft 15% of the fuselage at the highest test Reynolds number.

The measured heat transfer data from the phase change paint models and the thermocouple strip models are in good agreement for test Reynolds numbers up to 2.46×10^7/meter. The results show an orderly decrease in heating with increase in distance up to $x/L = 0.35$ after which the heating increases to a maximum value at $x/L = 0.55$ and then decreases once more with distance until transition onset occurs. This increase in heating, which is centered about $x/L = 0.55$ is invariant with Reynolds number. It is postulated to be the result of a localized increase in pressure brought about by the complex flow at the wing/fuselage junction. At the highest test Reynolds number, 3.28×10^7/meter, the phase change paint and thermocouple results are not in agreement in the region $0.25 < x/L < 0.8$. The thermocouple results follow the trends exhibited at the lower Reynolds numbers whereas the phase change paint results indicate a plateau of constant heating level. This anomaly is attributed to transition induced on the phase change paint models by the paint roughness, a phenomena not experienced by the thermocouple strip model.

The correlation of the above results was achieved using strip theory. For the laminar flow conditions, the reference enthalpy technique for evaluating the thermodynamic and transport properties was used in conjunction with the Blasius skin friction relation and the Colburn form of the Reynolds analogy factor. Turbulent heat transfer was evaluated using the Spalding-Chi skin friction correlation and the Colburn form of the Reynolds analogy factor with the local length Reynolds number evaluated based upon a transition onset distance. For these heating calculations, the local flow conditions at the edge of the boundary layer were assumed to be prescribed by a sharp cone whose semi-vertex angle was equivalent to the local body angle of attack. The plateau observed in the high Reynolds number phase change paint model run was successfully correlated using turbulent swept cylinder heat transfer theory.

In general, the agreement between theory and test was favorable with the exception of the region near the nose, which theory consistently underpredicted. However, as the Reynolds number was increased, the heat transfer distribution in this region approached full conical heating values and could be correlated by mutliplying the flat plate results by $\sqrt{3}$.

EFFECT OF Re NO. ON WINDWARD CENTERLINE HEAT TRANSFER DISTRIBUTION

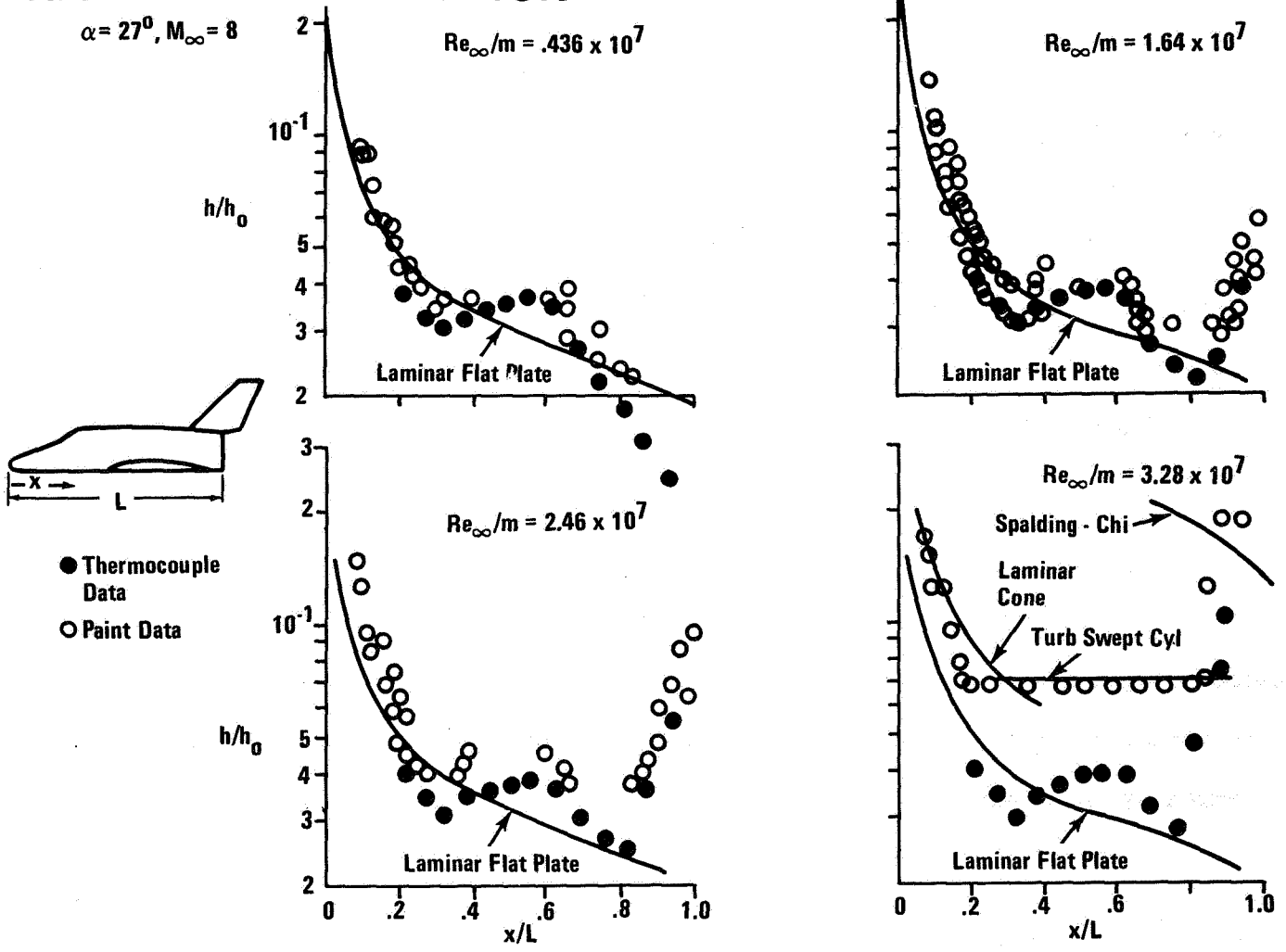

Figure 6

WINDWARD CENTERLINE HEAT TRANSFER CORRELATION

(Figure 7)

The windward centerline heat transfer results, theory and test, are shown in terms of the correlation parameters Stanton number versus local Reynolds number. Indicated on the curve is the predicted transition onset Reynolds number based on the criteria recommended by the Thermal Panel of NASA Aerothermodynamic/Configuration Working Group.

$$(Re_e/M_e)/(Re_x/X)^{0.2} = f(\delta)$$

The transition onset criteria agrees reasonably well with the data trend. However, the often assumed criteria of fully developed turbulent flow at twice the onset transition Reynolds number appears somewhat conservative. The fully turbulent heat transfer data is also seen to agree well with the Panel's recommended methodology.

Extrapolating the above results to the full scale orbiter indicates that as much as 60% of the underbody centerline will be in transitional or turbulent flow with maximum heating rates approximately $4\frac{1}{2}$ times laminar values.

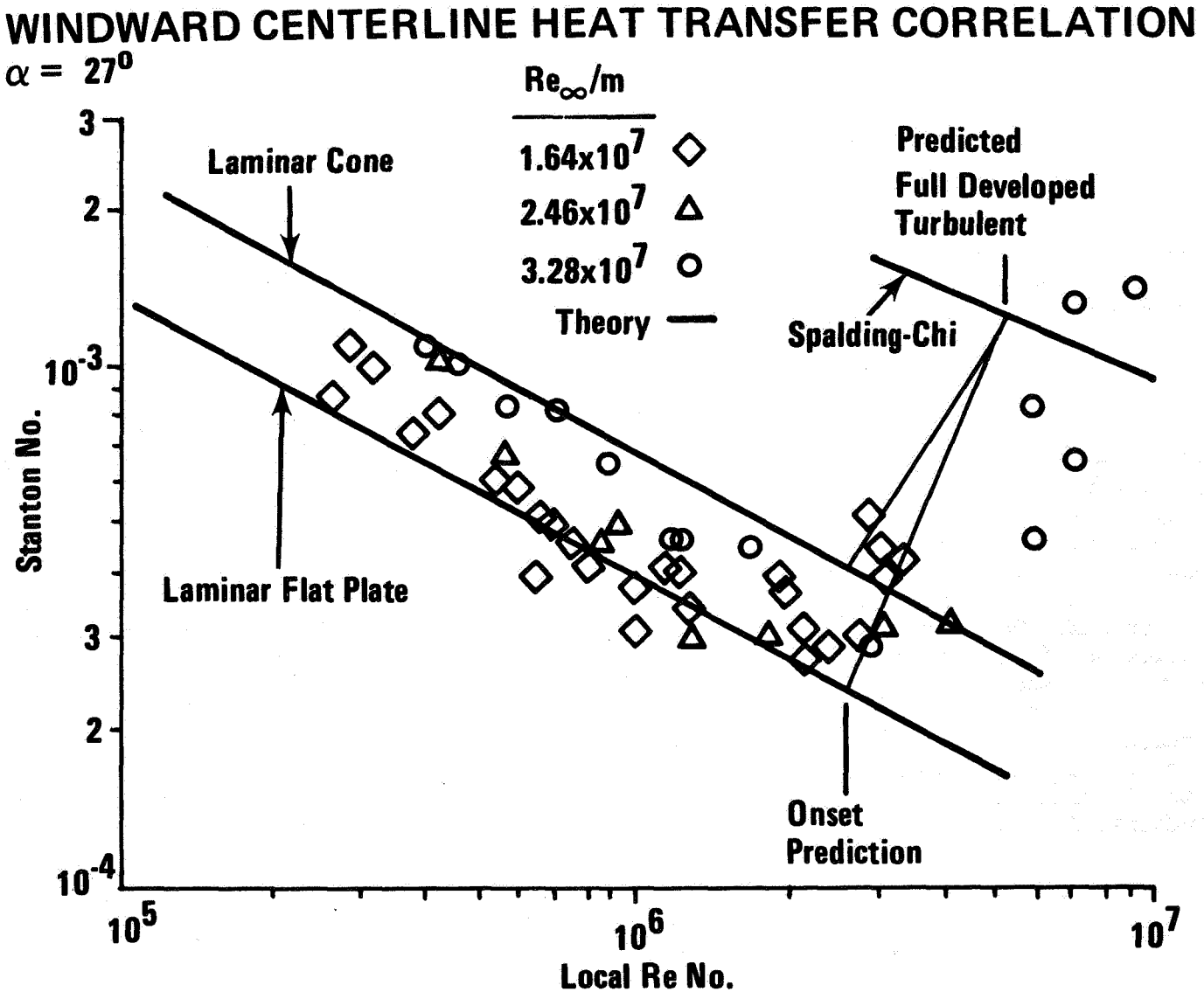
WINDWARD CENTERLINE HEAT TRANSFER CORRELATION
α = 27°
Re∞/m
1.64x10^7
2.46x10^7
3.28x10^7
Theory
Laminar Cone
Laminar Flat Plate
Predicted
Full Developed
Turbulent
Spalding-Chi
Onset
Prediction
Stanton No.
Local Re No.
3
2
10^-3
3
2
10^-4
10^5
10^6
10^7

Figure 7

EFFECT OF REYNOLDS NUMBER ON WINDWARD WING HEAT TRANSFER, 50% SEMISPAN

(Figure 8)

Heat transfer distributions along the windward side of the wing at the 50% semispan show a definite dependence on Reynolds number. At the lowest test Reynolds number, the condition of the flow was laminar. It was found that the data within the first 20% of the wing chord could be adequately predicted using strip theory if a parallel shock expansion from the leading edge stagnation line pressure to a modified Newtonian pressure ($Cp/Cp_o = \sin^2\alpha$) was assumed. However, aft of the 20% chord line, this procedure underpredicted the data. When a tangent-wedge flow field assumption was employed, the strip theory results agreed reasonably well with the data trend. With increasing Reynolds number, the data trend did not exhibit the usual decrease with increasing length for laminar flow, thus indicating the start of transition. At the highest test Reynolds number it was found that the heat transfer distribution within the first 20% of the wing chord was adequately described using laminar strip theory with tangent-wedge pressures. Aft of the 20% chord line the data shows heating values of the same order as found on the fuselage centerline, thus indicating that turbulent flow persists across the entire windward surface. The heat transfer in this region can be adequately predicted using the turbulent skin friction correlation of Spalding-Chi if transition onset is assumed to begin at the leading edge.

The data and theory lines for the highest Reynolds number case are shown in terms of the dimensionless parameters Stanton number versus local Reynolds number. The plot indicates that transition onset occurs at a local Reynolds number of 3×10^5. The local Mach Number at onset is 2.4.

EFFECT OF Re NO. ON WINDWARD WING HEAT TRANSFER DISTRIBUTION, 50% SPAN

$\alpha = 27^0$, $M_\infty = 8$

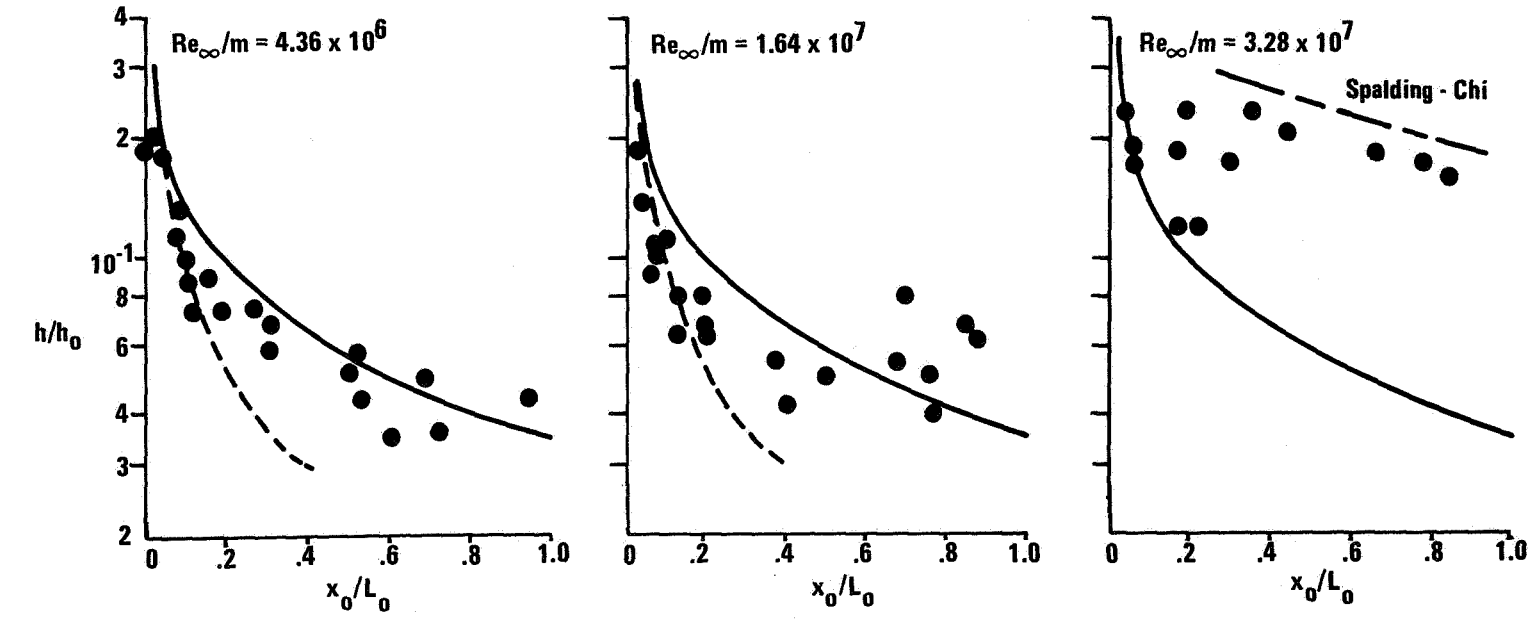

Figure 8

LEESIDE OIL FLOW PATTERN

(Figure 9)

Figure 9 shows photographs of oil flow patterns on the leeside of the Orbiter at an angle of attack of 27°. The patterns shown were observed in the VDT at $M_{oo} = 8$, $Re_{oo}/m = 1.64 \times 10^7$. Attention is directed to three areas which have been singled out for further amplification.

The first is the area in the vicinity of the chines between the canopy and wing. The parallel streamlines in this region suggest correlation of side body heat transfer data using a skewed plane, strip theory approach. The second area of interest is the wing APS pod. The oil pattern graphically shows the disturbance caused by this protuberance. The third area is about the wing, aft fuselage and tail region. The wing separation pattern, coupled with the shear layer re-attachment line on fuselage and tails, suggests a relationship between these regions and the possibility of an analogy with the flow on the leeside of a simple delta wing.

LEE SIDE OIL FLOW IN VDT

$\alpha = 27^0$, $Re_\infty/m = 1.64 \times 10^7$, $M_\infty = 8$

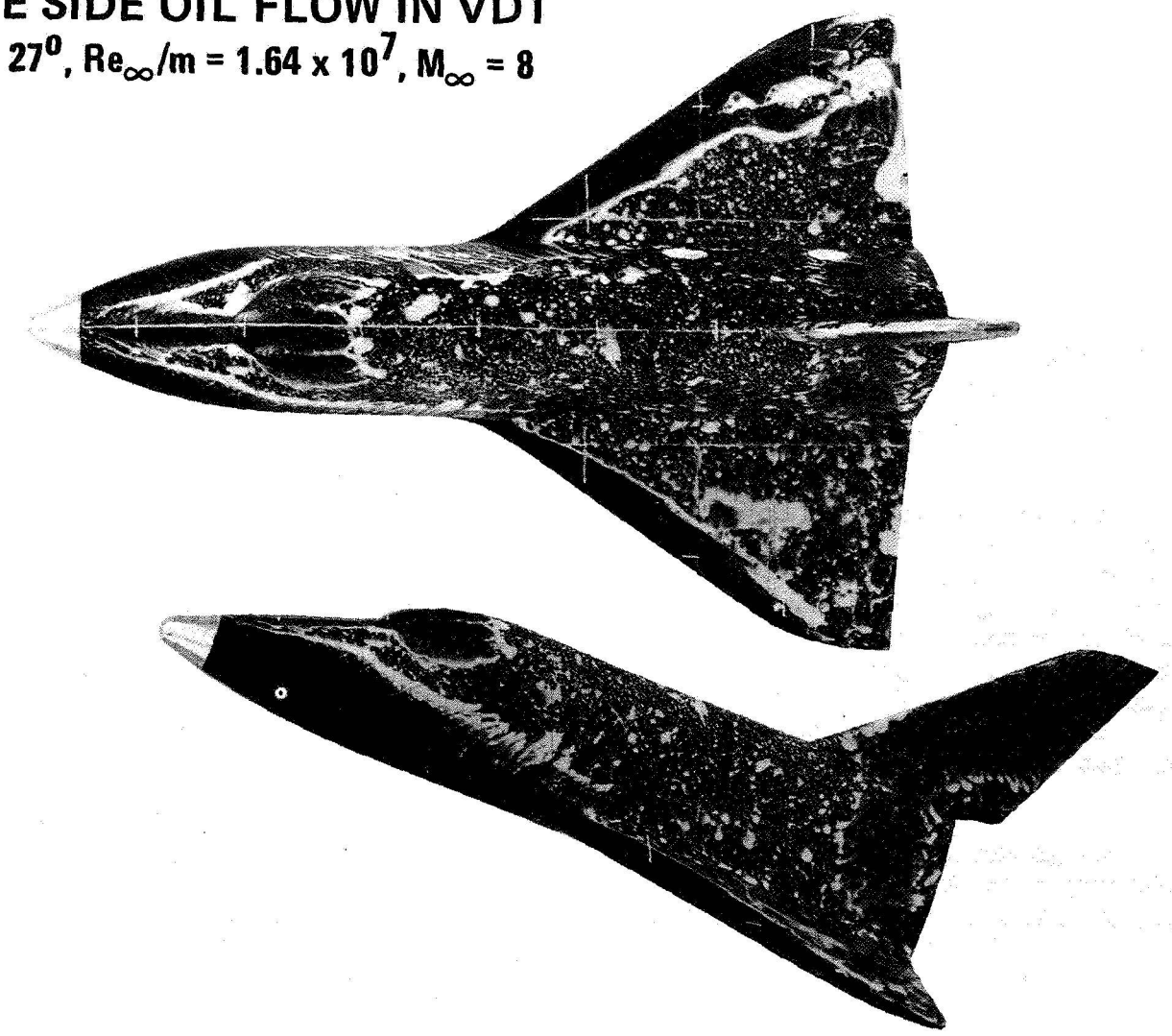

Figure 9

SIDE FUSELAGE HEATING

(Figure 10)

Predicting heating in the region of the lee generator is problematic because of both vortical and separation phenomena. However, a section of the leeside, the side fuselage, can be predicted using two dimensional strip theory on a skewed cross section of the fuselage.

The skewed section investigated is located in the region between the canopy and the wing. The section is generated by cutting the fuselage reference line with a plane inclined at an angle which is twice the angle of attack. This cutting plane is suggested by oil flow results such as those in figure 9 in which the upper surface streamlines are inclined at an angle which is approximately 2α. Local flow properties around the periphery of the skewed section were calculated by assuming Prandtl-Meyer expansion from a normal shock processed stagnation point. Simple strip theory is used to predict heat transfer up to the point of separation. Modification of attached flow heating by the Chapman cavity value of .56 after this point allows extension of the approach into the separated region. The method breaks down over the topmost contoured section.

The skewed plane as well as the theory data comparison are shown in figure 10. The data was normalized with the measured centerline heating value, the theoretical heat transfer coefficient was normalized with a calculated centerline value. This approach gives reasonable agreement.

SIDE BODY HEATING SKEWED SECTION/STRIP THEORY

$\alpha = 27^0, M_\infty = 8, Re_\infty/m = 3.28 \times 10^7$

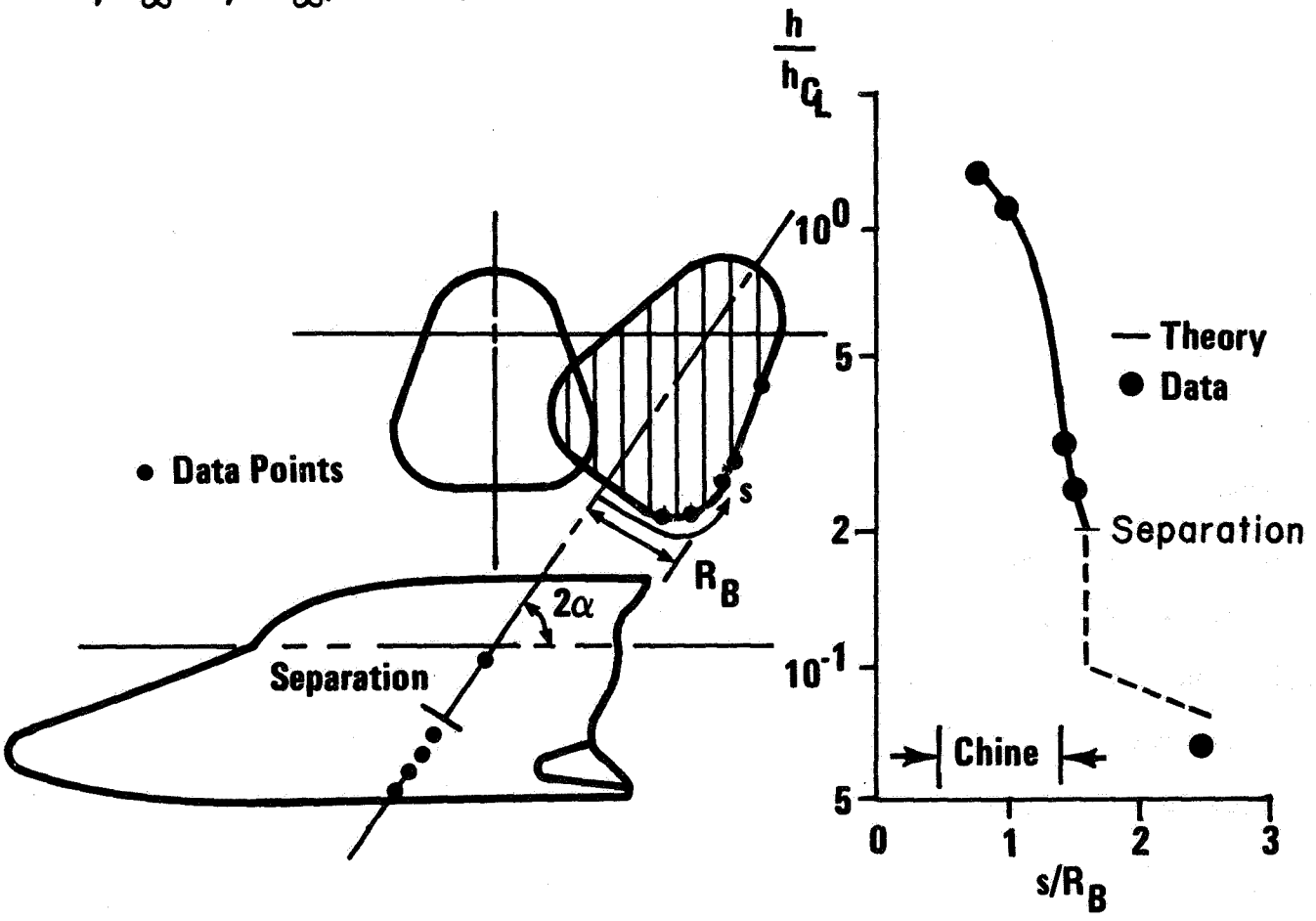

Figure 10

EFFECT OF APS POD ON HEAT TRANSFER

(Figure 11)

A typical APS pod was mounted on the lee side of the wing at 86% span and tested in the VDT at 27° angle of attack. The oil flow photograph shows that the flow which approaches the pod comes in perpendicular to the wing leading edge, in the plane of the wing. The flow over the wing in the region adjacent to the inboard side of the pod is separated while the region of flow disturbance lies within the confines of a shock layer generated by a finite swept cylinder. Locations of regions of increased or decreased heating conform to the oil patterns. That is, the highest heating amplifications on the wing are adjacent to the outboard side of the pod; heating is reduced on the wing immediately adjacent to the inboard side of the pod; and, the pod generated shock layer effects the aft end of the wing, elevating heating by a factor of two.

EFFECT OF APS POD ON HEAT TRANSFER

$\alpha = 27^0$, $M_\infty = 8$, $Re_\infty/m = 3.28 \times 10^7$

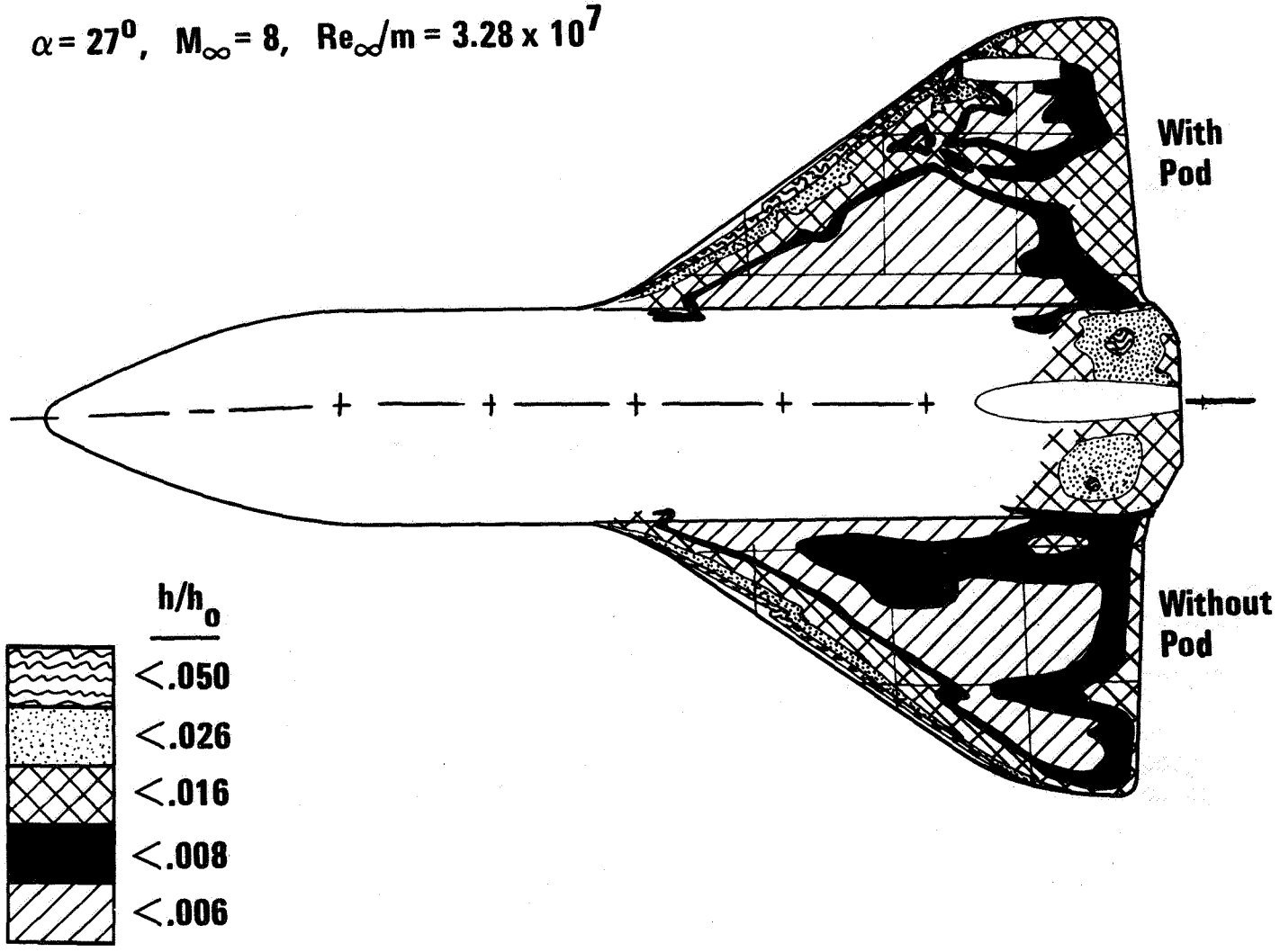

Figure 11

LEESIDE WING AND FUSELAGE FLOW FIELD

(Figure 12)

Heat transfer data (figure 11) and surface streamline patterns (figure 10) indicate a local region of high heating and a shear layer re-attachment line on the aft portion of the fuselage and vertical tail. Although the flow field in this region is complex, both three dimensional in nature and dominated by strong viscous - inviscid interaction, a simple flow model appears to characterize the main features of the flow. Examination of the separation patterns on the leeside of sharp delta wings reveals a marked similarity with the leeside wing patterns. This similarity suggested using the approach Cross (Ref 3) had taken in successfully predicting the leeside flow field of sharp delta wings; that is, using a two dimensional analysis in the cross flow plane. Figure 12 is a schematic of the assumed separation / re-attachment geometry.

The wing flow field is divided into two regions, the boundary being the bow shock intersection point on the wing leading edge. It then appears that the flow on the aft portion of the fuselage is dominated by the outboard wing flow. Wing separation geometry and a detached shear layer can be generated using local flow properties. After postulating the re-attachment point of the shear layer, laminar heating on the aft fuselage was calculated using the results of Bushnell and Weinstein (Ref 4) for re-attachment heating on a deflected flap. The result was found to predict the region of high localized heating to a reasonable degree.

The lack of any evidence of re-attachment heating on the forward portion of the fuselage is believed due to the presence of a thick three dimensional boundary layer in the region of the wing-fuselage junction. The flow model presented, rather than one which assumes wing fillet generated vortices, may better explain the hot streaks seen along the aft side of some configurations.

LEE SIDE WING & FUSELAGE FLOW FIELDS

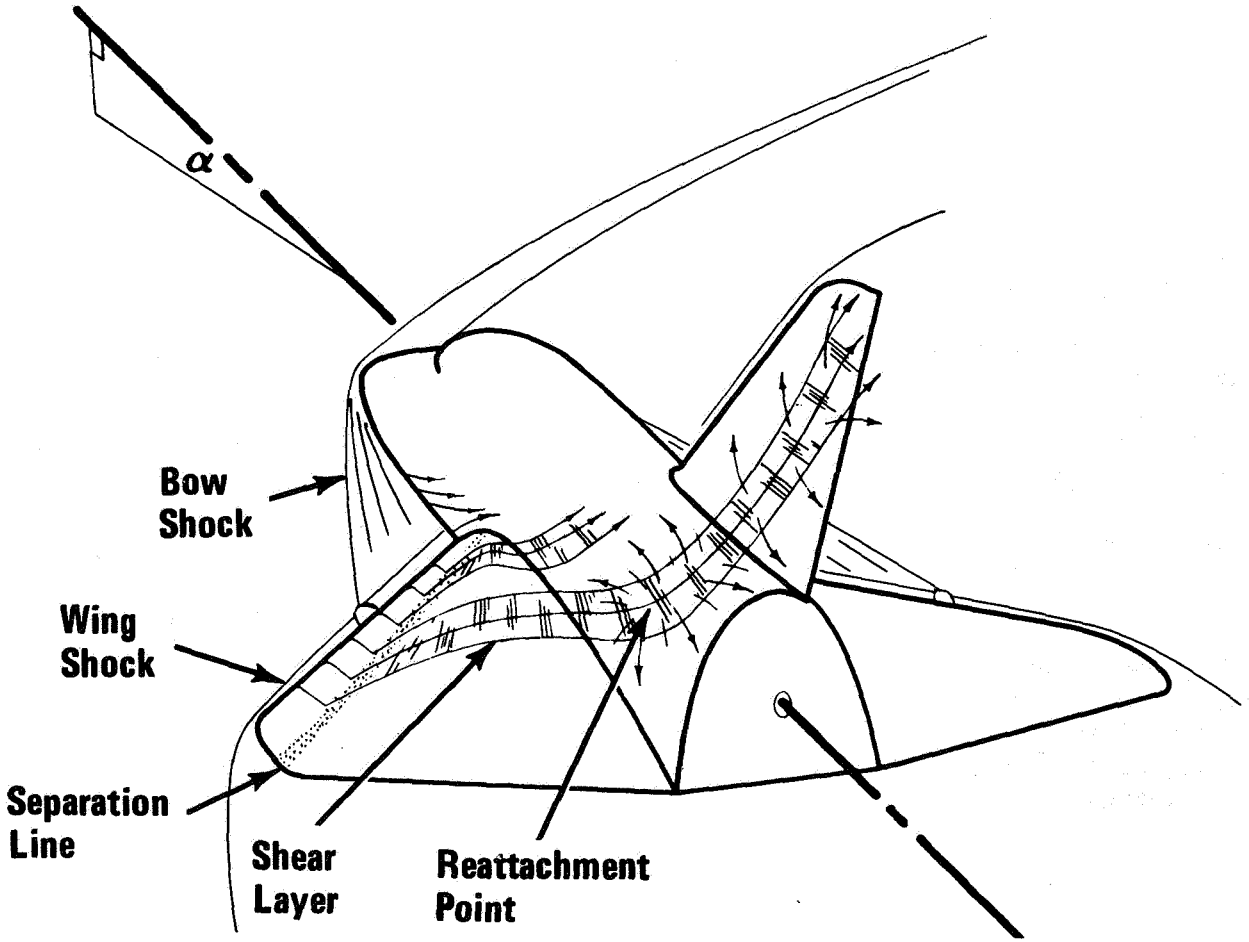

Figure 12

APS CAVITY

(Figure 13)

The possibility exists of having open ports on the windward surface of the Orbiter to accommodate APS nozzles. Previous cavity flow investigations, conducted primarily on two dimensional slots or annular slots in axisymmetric flows have shown increased heating downstream of the cavity and high peak heating in the immediate vicinity of re-attachment on the downstream cavity wall. Tests were deemed necessary to ascertain the magnitude of heating to the APS related configuration, a circular cavity in a flat plate surface.

The model chosen for these exploratory experiments in the GAC Hypersonic Shock Tunnel was a simple flat plate-wedge with a cylindrical hole in the middle of the flat plate surface (figure 13). Thin film heat transfer gages were positioned on the flat plate surface and also on the glass insert for the cavity. A hole was drilled through the model from the front wedge surface into the lower portion of the cavity. This provided a passage for (hot) tunnel air from the lower portion of the model to enter the cavity and simulate the effects of mass bleed. To increase the pressure at the upstream end of the mass bleed passage, an "L" shaped flange was located on the wedge surface immediately downstream of the passage opening.

The model was positioned such that the flat plate was a compression surface (10 degrees). For all test runs, the free stream Mach number was 10.5, the tunnel flow stagnation temperature was 1770°K, the local Mach number and Reynolds number over the flat plate surface was 6.9 and 2.82×10^6 per meter, respectively. Three configurations were tested: the flat plate with no cavity; the plate with the cylindrical cavity, but with the air bleed passage blocked; and the cavity with the uncalibrated air bleed passage open. The undisturbed flow over the plate with no cavity in the surface, with or without mass bleed, could then be compared with the reference conditions. Two or more test runs were made for each configuration to ensure the reliability of the data. These tests are completely described in Ref. 5.

APS CAVITY HEATING MODEL

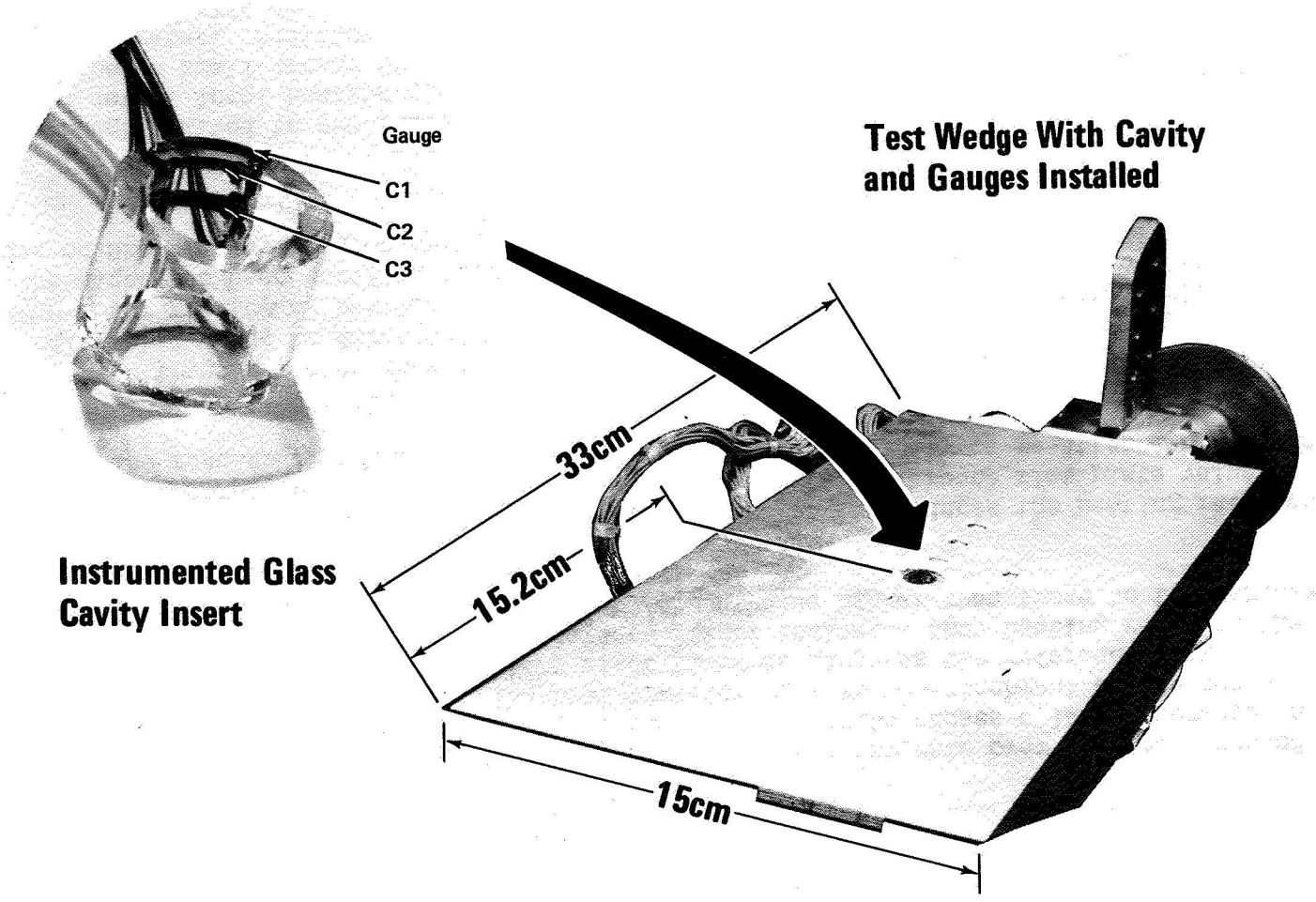

Figure 13

APS CAVITY EXPERIMENTAL RESULTS

(Figure 14)

Within the accuracy of the measurements, the heat transfer rate over the instrumented portion of the flat plate surface remains constant. The cavity causes a large increase in heating on the downstream surface. The heat transfer rate at re-attachment on the downstream lip of the cavity is approximately eight times as large as the reference flat plate heating rate. Extrapolating this data to flight indicates that heating rates to the downstream lip could be as high as 9.08×10^2 kw/m^2, a value higher than those to the vehicle's stagnation point and wing leading edges.

As shown in figure 14, the bleed flow through the cavity reduces the heating rates on the surface downstream of the cavity to values less than the reference flat plate values. The bleed also results in a much lower heating rate in the vicinity of re-attachment on the cavity wall.

The heat transfer rates measured inside the cavity are in excellent agreement with those calculated using an Aeronautical Research Associates of Princeton analytical technique for predicting heating rate distributions in three dimensional open cavities. This technique has been verified in reentry flight test and is available and applicable for use on Shuttle cavity flow problems.

CONCLUSIONS

Although limited to one particular set of test conditions, these exploratory tests indicated severe local heating at the downstream lip of a circular cavity. The tests also revealed that a small amount of mass flow through the cavity can greatly reduce these peak heating rates. Additional tests are required to obtain quantitative trends with Mach number, Reynolds number, cavity size, etc.

APS CAVITY HEAT TRANSFER DISTRIBUTIONS

$M_\infty = 10.5, \alpha = 10^0$

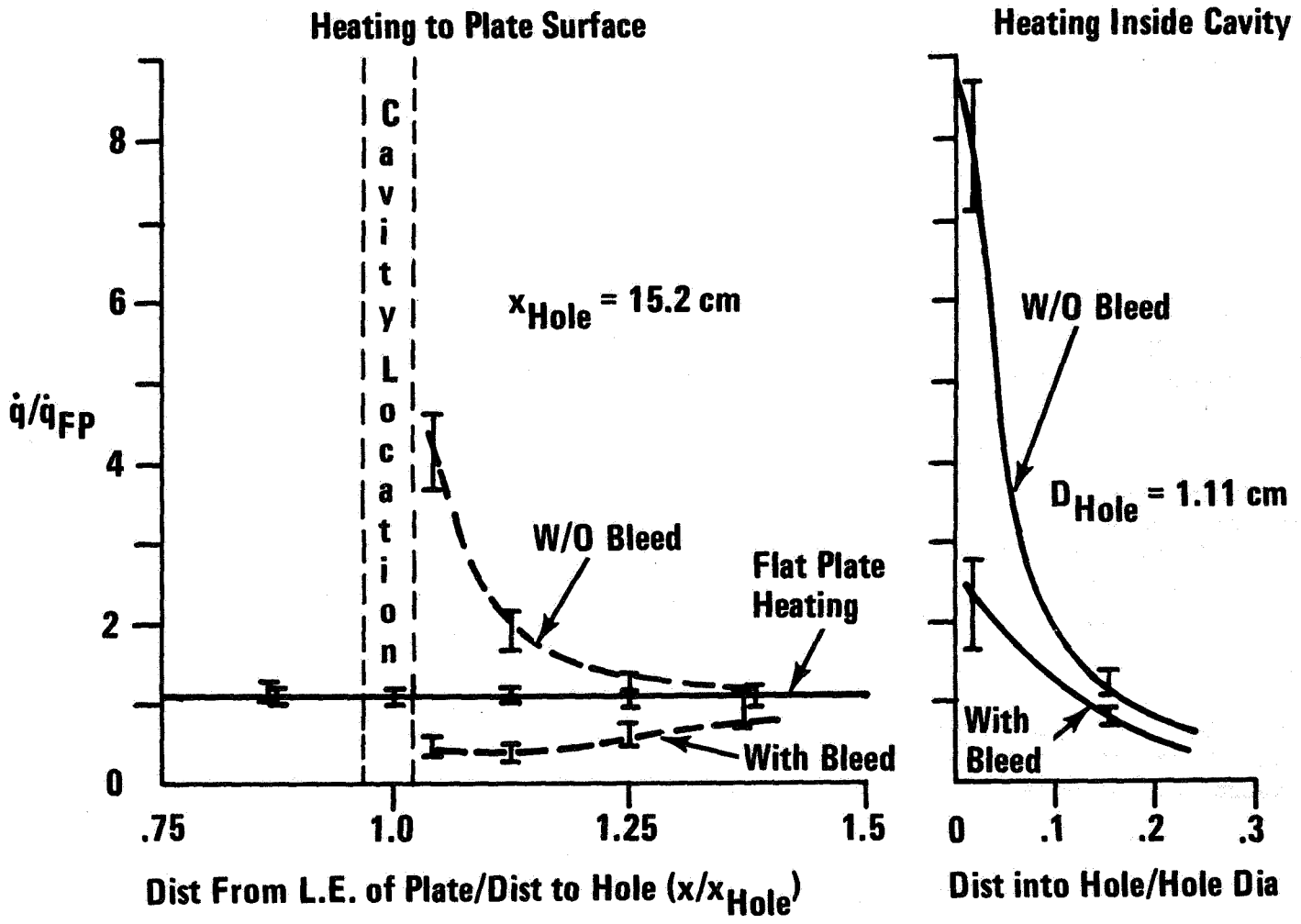

Figure 14

ORBITER/TANK COMBINATIONS

(Figure 15)

In addition to testing the basic orbiter, the orbiter was examined with various external side mounted tanks as shown in figure 15. The configurations were tested under conditions which would give laminar flow over the orbiter. This then allows appropriate scaling to the ascent flight case where maximum heating rates occur at orbiter engine burnout under conditions which are clearly laminar.

In the first entry in the CFHT, test series H-0602, cylindrical tanks with conical, hemispherical and contoured forebody geometries were mounted above the wing planform and tested at various fuselage stations. Thermocouple and phase change paint data were obtained on both the fuselage and tanks at 0° and 5° angle of attack. The objective of this program was to find the fuselage - tank combination with the minimum interference heating effects and to generate data to aid in the development of interference heating prediction methods.

The second entry in the CFHT, test series H-0603, concentrated on the tank selected from the previous series, the contoured tank. Structural and propulsion constraints forced the tank forward which in turn resulted in a slightly re-shaped contoured faring. Oil flow and electron beam visualizations were obtained on this configuration in the Helium Tunnel.

H TANKS TESTED IN CFHT

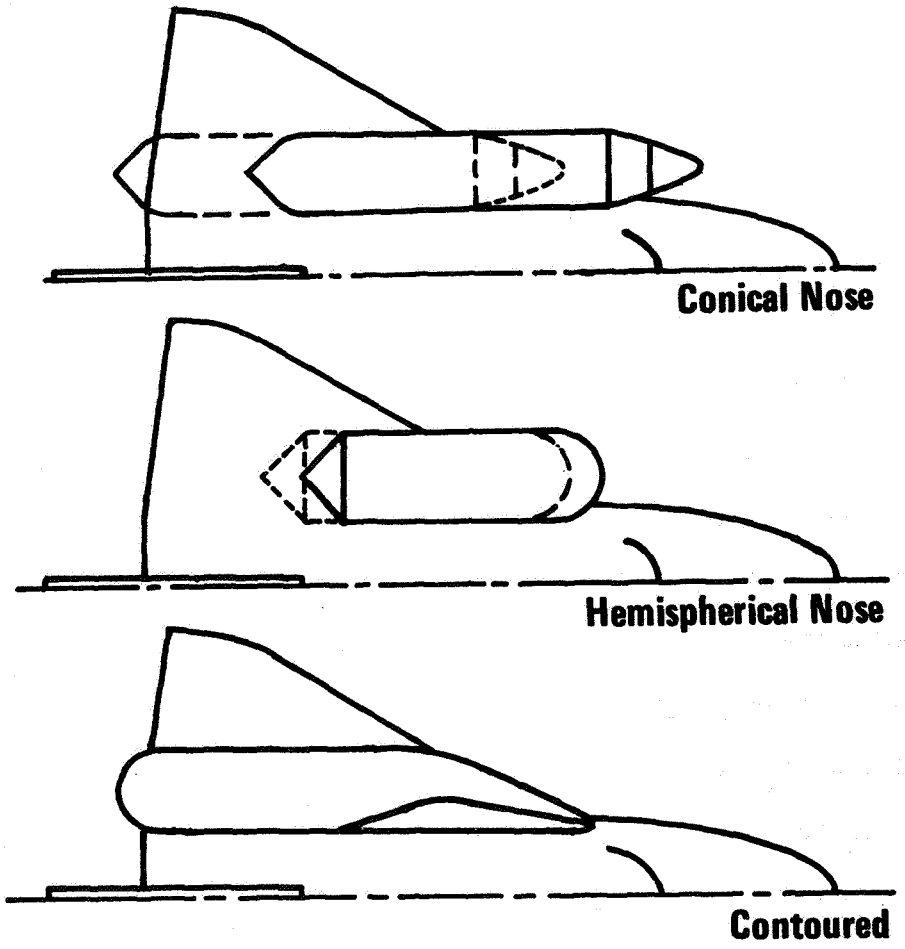

Figure 15

H TANK COMPARISON

(Figure 16)

The complexity of the flow field about an orbiter with side mounted tanks, as seen in the oil flow photographs of figure 16 makes it virtually impossible to predict detail heat transfer distributions. While measured heat transfer data is available (Langley tests), a qualitative approach is chosen here to compare tank configurations. The next three figures provide a visual comparison of the heating to the various orbiter/tank configurations. Shown are top and side views of the phase change paint models (T_{pc} = 368°K) after being subjected to identical conditions (M_{∞} = 10.35, $Re_{\infty}/m = 3.28 \times 10^6$, $\alpha = 0°$) for the same period of time (17 seconds) in the CFHT. Dark areas are regions of higher heating. Quantitative data, in the form of amplification factors on the fuselage, are given on figure 20.

OIL FLOW ABOUT CONTOURED H TANK/ORBITER

$\alpha = 0^0$

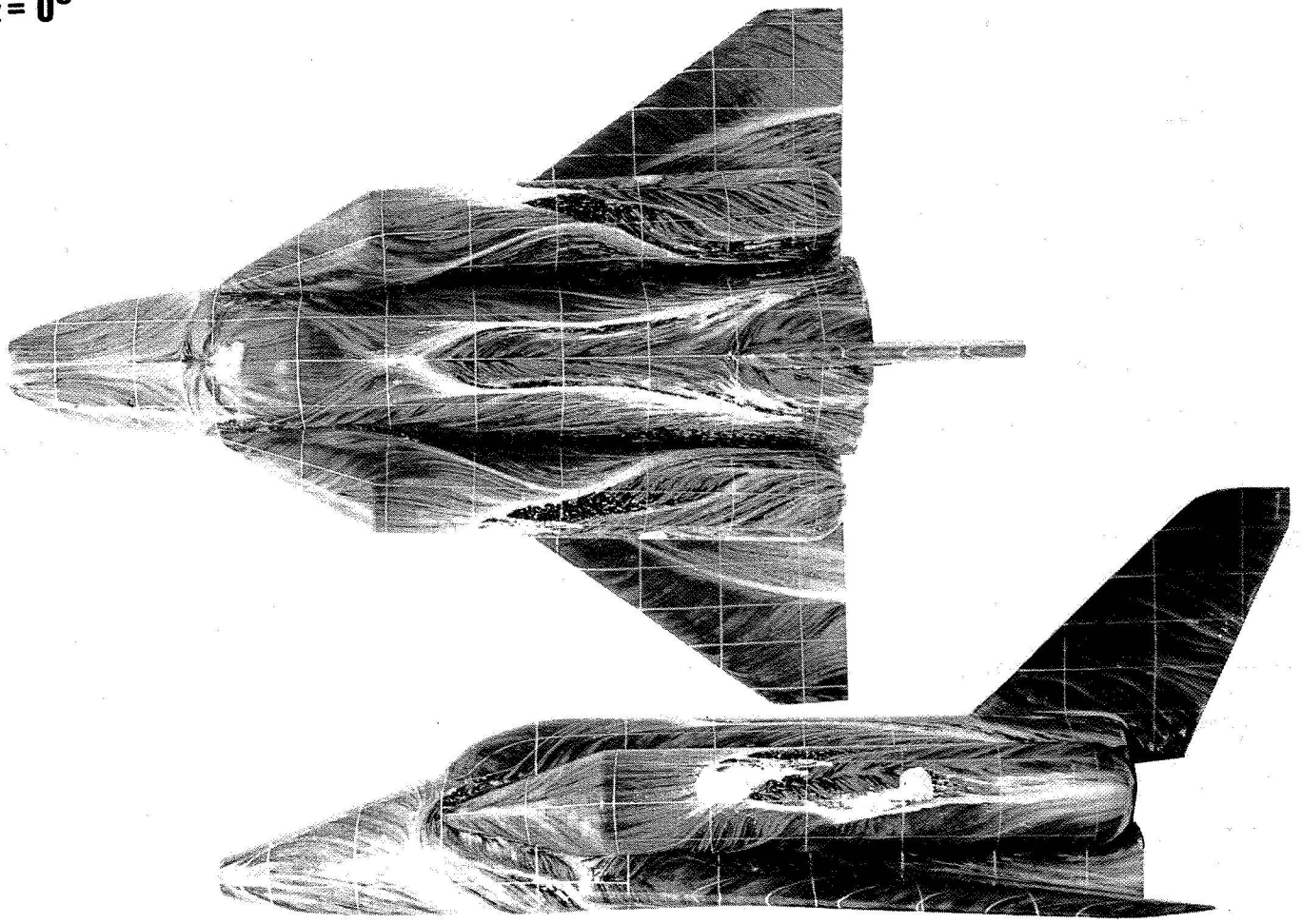

Figure 16

CONICAL TANK

(Figure 17)

Figure 17 shows the conical nose tanks in the forward and aft position. In the forward position, the orbiter bow shock intersects the conical shock from the tank on the inboard side. These shocks of opposite families product a slip stream which impinges on the inboard side of the tank and rereflects off the fuselage and tank. Maximum amplification factors, the ratio of heat transfer with flow disturbed to that with the flow undisturbed, on the tank and fuselage are 60 and 45, respectively.

Moving the tanks aft decreases the maximum amplification factor on the tank to 33, but raises the fuselage factor to 70. The decrease is attributable to the fact that the shock causing the amplification is now the weaker canopy shock rather than the bow shock. The increase on the fuselage is due to the much lower undisturbed reference value. In both positions, a hot streak is seen on an outboard aft section of the tank which is due to the reflection from the intersection of the bow and conical shock. The lee centerline hot spot is probably due to induced vortices from the complex flow field while the streak in the lower portion of the horizontal tail can be attributed to the conical shock. Higher heating between the wing and underside of the tank is also visible.

PHASE CHANGE PAINT HEAT TRANSFER PATTERNS

Conical Nose H Tank, $\alpha = 0^0$

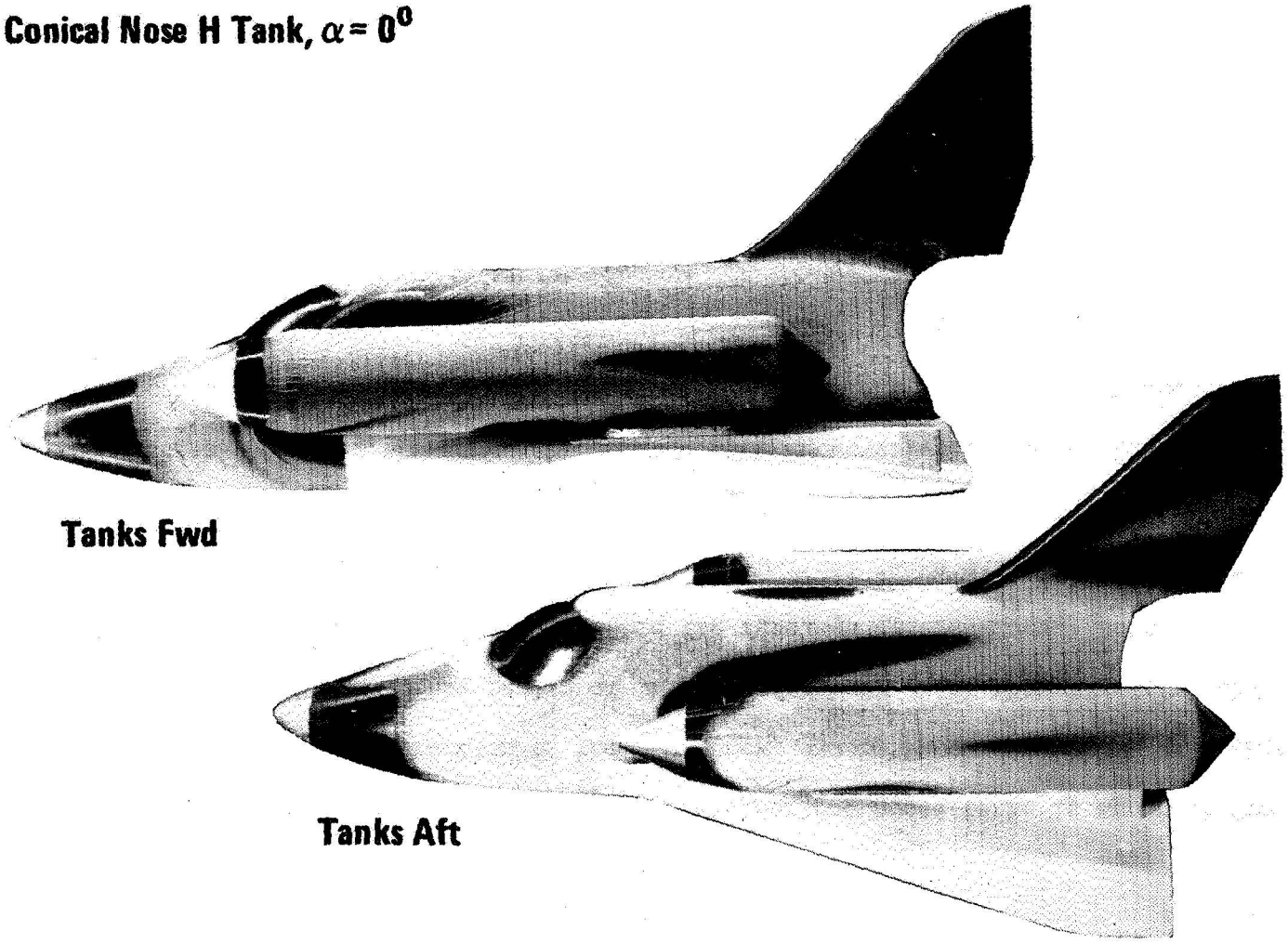

Tanks Fwd

Tanks Aft

Figure 17

HEMISPHERICAL TANKS

(Figure 18)

The complexity of the flow field for the hemispherical nosed tanks is apparent from figure 18. The mutual interaction of the bow shock, canopy shock and strong tank shock produce a local flow field in the region of the tank forebody which abruptly drive the streamlines on the side of the fuselage toward the fuselage undersurface. Both thermocouple and paint data indicate that the hemispherical tanks affect the greatest area of the fuselage with high heating values. The severity of the heating to the fuselage changes little as the tanks are shifted aft. However, heating to the hemispherical nose does decrease for tanks aft since the tanks lie within the bow shock envelope.

PHASE CHANGE PAINT HEAT TRANSFER PATTERNS

Hemispherical Nose H Tanks, $\alpha = 0^0$

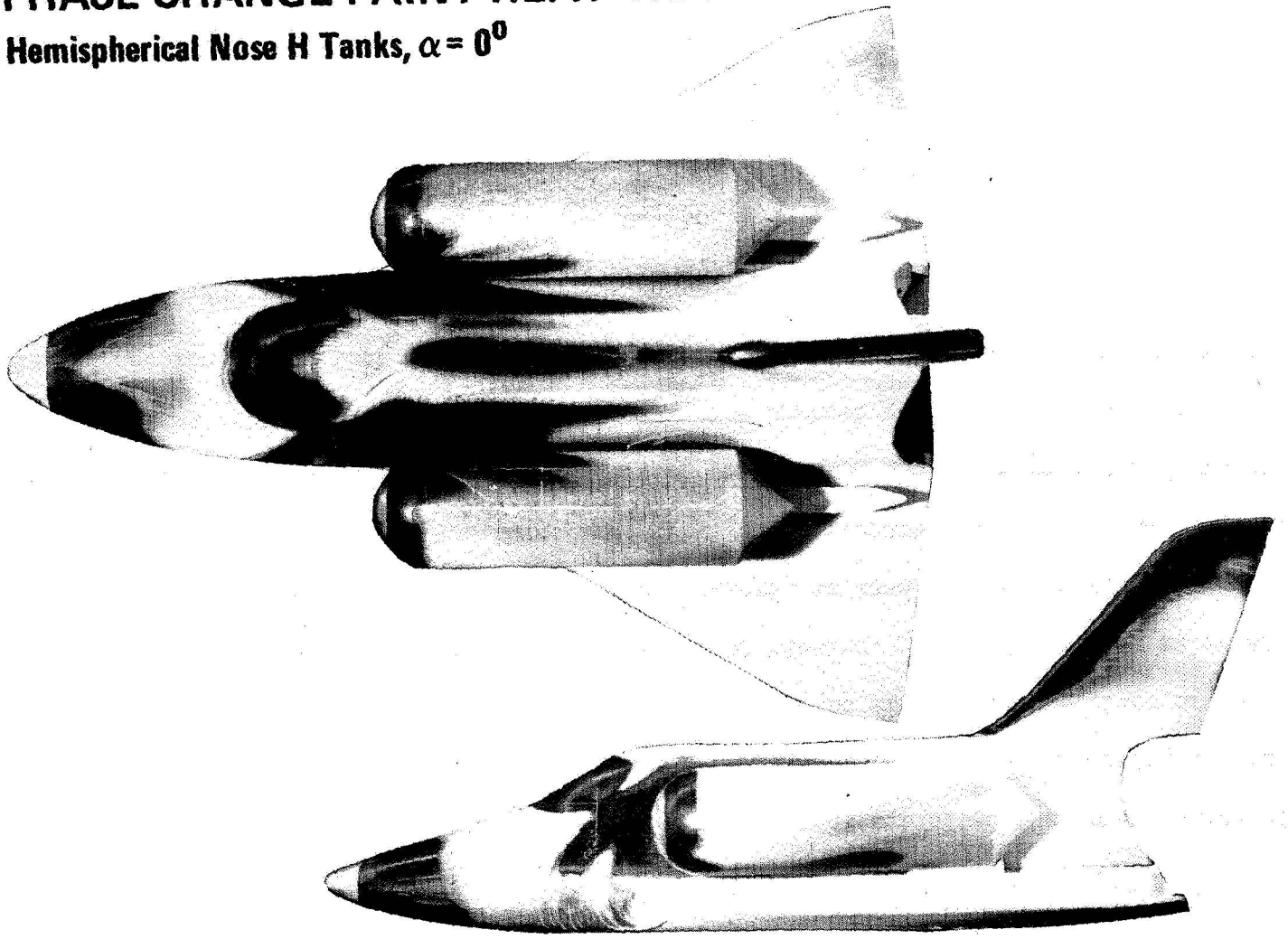

Figure 18

CONTOURED TANKS

(Figure 19)

Of all the configurations investigated, the contoured tank exhibited the lowest value of peak heating amplification, only 8.3, and caused the least disturbance to the fuselage. The hot streak on the lee centerline, aft of the canopy, and on the aft outboard surface of the tank, present on the other configurations, is noticeably missing. The model filler material between the contoured section of the tank and the fuselage, as seen in the top view, is different from the model material and,therefore, provides no comparative data in that region.

The heating ratio h/h_o on the contoured fairing peaks along the windward ray at a value of .155 and agrees well with swept cylinder theory. The highest values of h/h_o on the cylindrical section of the tank are of the order of .03 and lie on the tank surface nearest the wing-fuselage junction.

PHASE CHANGE PAINT HEAT TRANSFER PATTERNS

Contoured H Tanks, $\alpha = 0^0$

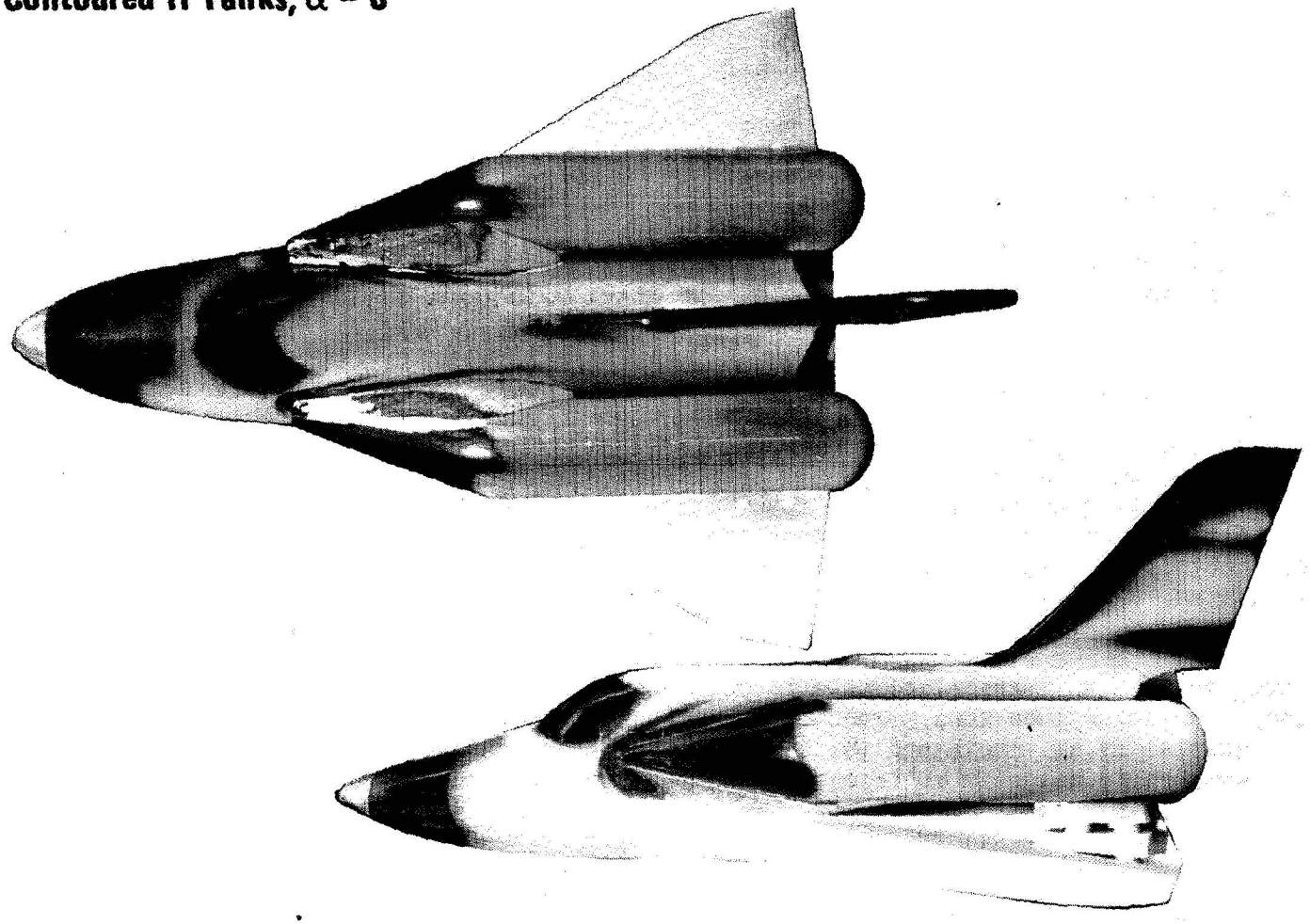

Figure 19

HEATING AMPLIFICATIONS ON ORBITER FUSELAGE DUE TO PRESENCE OF SIDE-MOUNTED TANKS

(Figure 20)

Figure 20 shows the maximum fuselage amplification factors, as measured by thermocouples along the side of the fuselage, as a function of axial position. It is evident that heating to the vehicle and tanks is lowest for the contoured tank configuration. What is not apparent is which configuration is lightest, considering structural as well as heat protection factors.

A study was performed to compare the weight of contoured to conical tanks. Hemispherical tanks were ruled unacceptable from a heat transfer standpoint. It was first determined that for either conical or contoured nose tanks, a dry nose design is significantly lighter. That is, having the nose cone act merely as a fairing over a cylindrical tank with hemispherical end domes is lighter than carrying hydrogen in the nose as well as the cylindrical region. Next, for the dry nose design, the structural weightof the contoured fairing was found to be 1100 pounds greater than that for the conical nose cone. However, this deficit was completely offset by the greater amount of TPS required on tank and vehicle for the conical configuration.

The factor which tipped the scales in favor of the contoured tank was an increased payload capability of 600 pounds associated with lower boost drag. Drag data was obtained for a full boost configuration with both sets of tanks in the Ames 6'x 6' Wind Tunnel and corrected for booster power on base drag. The contoured tank configuration had a 6.7% lower total boost drag in the high q portion of the trajectory.

HEATING AMPLIFICATIONS ON ORBITER FUSELAGE DUE TO PRESENCE OF SIDE-MOUNTED TANKS

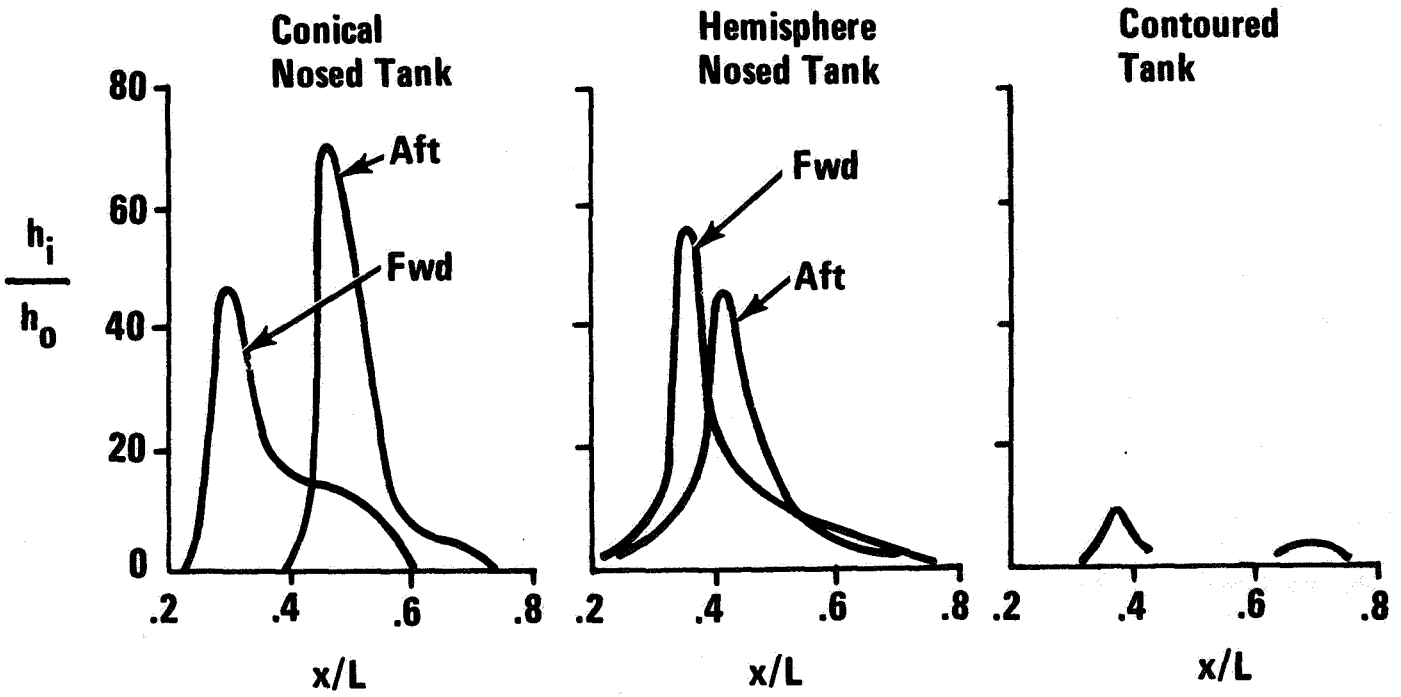

Figure 20

HO TANK/ORBITER

(Figure 21)

By the time test series HO604 began in the VDT, the H concept had been dropped in favor of the HO. A typical HO tank was quickly fabricated to be tested with the orbiter to obtain interference heating and schlieren data. This tank is geometrically similar to the MSC 040A tank, but scaled to HO size, is of slightly smaller diameter (9.7m vs. 11.7m). The distance from the nose of the tank to the nose of the orbiter is approximately twice as great as that for the 040A. This mated configuration was tested at $M_\infty = 8$, $Re_\infty/m = 4.36 \times 10^6$ at angles of attack of -5°, 0°, 5°, and 15°.

The side view schlierens, shown in figure 21, indicated that the bow shock from the tank will impinge on the orbiter with the orbiter in any realistic position and at any realistic angle of attack. The magnitude of the impingement and the interference patterns are examined in subsequent figures.

HO TANK/ORBITER

Configuration

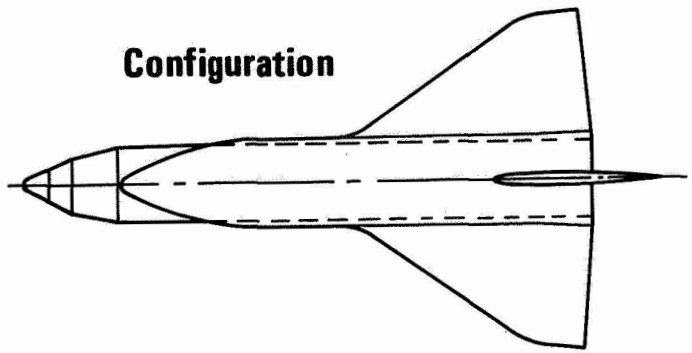

M_∞ = 8 Schlieren

$\alpha = 0^0$

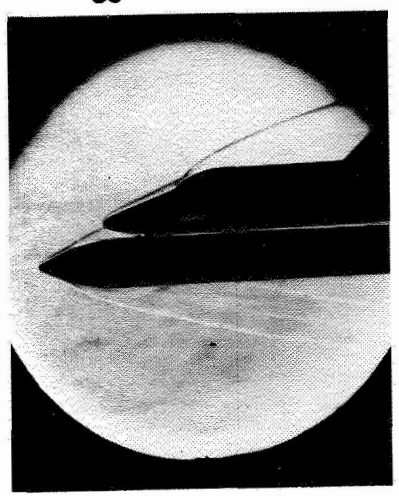

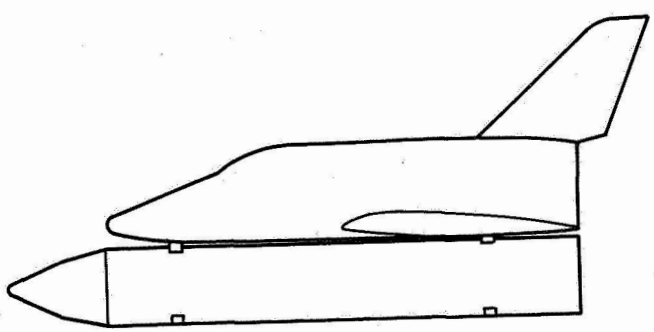

$\alpha = 15^0$

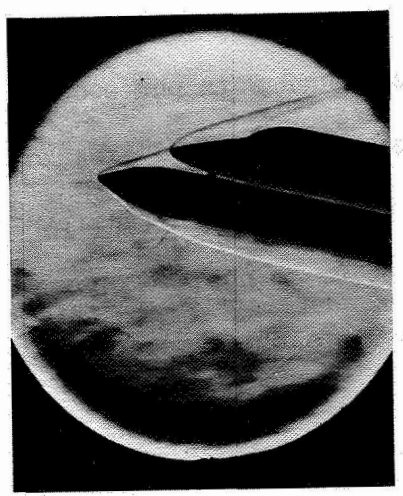

Figure 21

HO TANK/ORBITER ELECTRON BEAM FLOW VISUALIZATION

(Figure 22)

Electron beam flow visualizations of the mated HO tank configuration at zero angle of attack were taken in the NASA Langley $M_{\infty} = 20$ Helium Tunnel. Comparison of mated and orbiter alone visualizations indicate that the HO tank has virtually no effect on the surface streamline on the side of the orbiter. The orbiter, however, plays a dominate role on the HO tank surface streamlines; the effects of orbiter nose and wing generated shocks are clearly visible.

HO TANK/ORBITER ELECTRON BEAM FLOW VISUALIZATION

$\alpha = 0^0$, $M_\infty = 20$

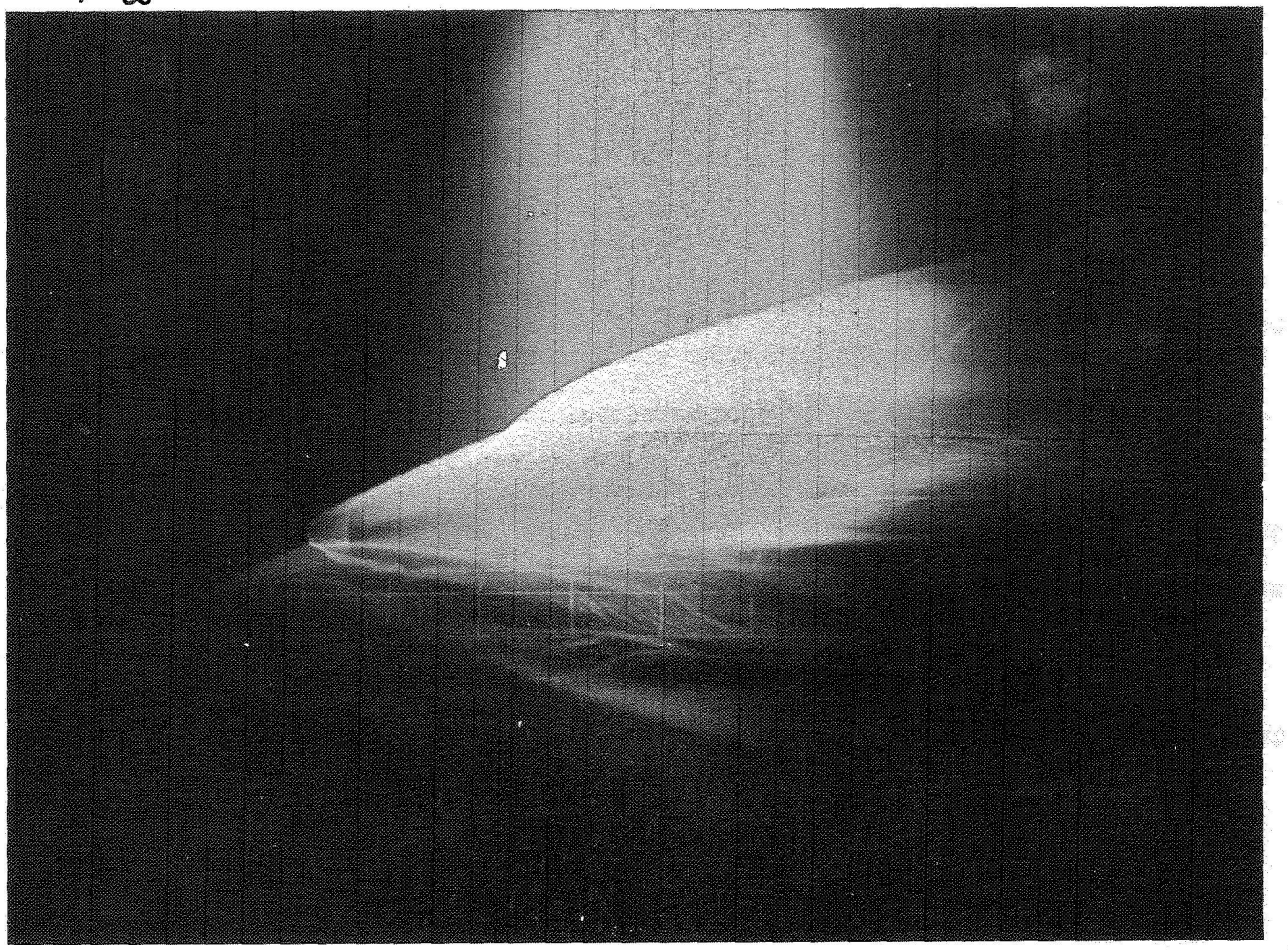

Figure 22

INTERFERENCE HEATING ON HO/ORBITER CONFIGURATION

(Figure 23)

The mated HO Tank Orbiter configuration was tested in the VDT at 0° and 15°* angle of attack at an Re /m = 4.36×10^6 and M = 8. Figure 23 shows the phase change paint heat transfer patterns for the zero angle of attack case, comparing the orbiter nose region with and without the tanks. The bow shock from the HO Tank impinges on the windward side of the Orbiter just aft of the geometric stagnation point. The change in the side body heat transfer pattern is small and in some regions actually lower than the Orbiter alone heating. The reflecting shock between tank and orbiter gives rise to amplifications as high as 10. Lesser amplifications, on the order of 5, are seen in the vicinity of the interstage bulkhead. The inset figure compares the centerline heat transfer during ascent with reentry values. Although the ascent amplification factors appear high, the reentry situation is seen to give the higher heating values.

Centerline amplification factors on the tank are somewhat higher than on the Orbiter because the first reflected shock which strikes the tank is stronger than the subsequent reflection which strikes the Orbiter in the peak amplification region. The effect of the orbiter bow shock on the tank side, the curved streak seen in the flow visualization photo as well as the paint pattern, is seen to be minimal.

* α = 15° data not available at this time.

INTERFERENCE HEATING ON HO/ORBITER CONFIGURATION

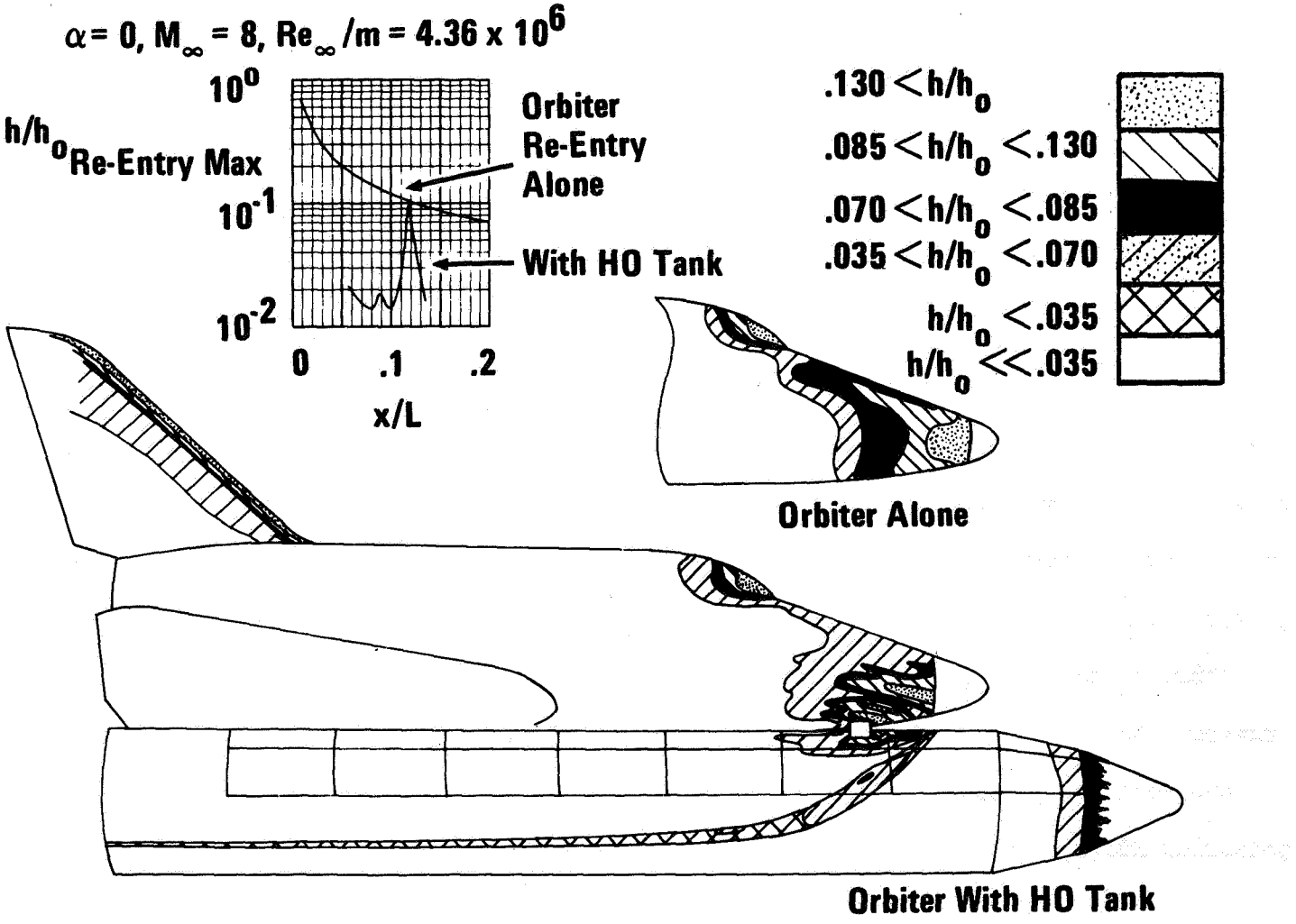

Figure 23

CONCLUSIONS

Much of the data presented in this report tends to substantiate the methodology suggested by the NASA Aerothermodynamic/Configurations Working Group. However, some of the flow and heating results, such as the Reynolds number dependent inflow phenomenon seen on the windward side of the wing, have not appeared on previously tested orbiters. While some might argue that any anomalous behavior is unique to this particular configuration, the geometric similarity between this configuration and the current class of HO orbiters makes it mandatory that these "anomalies" be evaluated in terms of current designs. Several postulated flow models, such as the aft wing and fuselage separation and reattachment model, offer the possibility of greater insight into the complex orbiter flow field.

REFERENCES

1. Leng, J., Osonitsch, C.W., and Konopka, W.H., "Experimental Study of Plume Impingement Heating from Orbiter Main Engines", GAC Rpt. 552-1200RD- 31, May, 1971.
2. Bertram, H.M. and Everhart, P.E., "An Experimental Study of the Pressure and Heat Transfer Distribution on a 70° Sweep Slab Delta Wing in Hypersonic Flow", NASA TR R-153, December 1963.
3. Cross, E.J., "Analytical Investigation of the Expansion Flow Field over a Delta Wing at Hypersonic Speeds", ARL 68-0027, February 1968.
4. Bushnell, D.M. and Weinstein, L.M., "Correlation of Peak Heating for Reattachment of Separated Flow", J. Spacecraft and Rockets, Vol. 5, No. 9, September 1968.
5. Kaufman, L.G., et al, "Hypersonic Heating Distributions Caused by a Circular Cavity in a Flat Plate Surface", GAC Research Dept. Memo RM-497, March 1971.

HIGH REYNOLDS NUMBER TURBULENT HEATING TO TWO SIMPLIFIED SHUTTLE CONFIGURATIONS

By Charles B. Johnson

NASA Langley Research Center
Hampton, Virginia

INTRODUCTION

In the space shuttle symposium held in March 1971, preliminary transition and heating data from one facility for two simplified shuttle configurations were presented. (See ref. 1.) Since that time, the work has continued and the results to date are presented with the main emphasis on (1) the effect of the two geometries having different amounts of cross flow and how the different cross flows affect heating and transition, (2) the experimental level of turbulent heating and the ability to predict the level of turbulent heating, and (3) a comparison of the transitional and turbulent heating in three facilities with two model scale sizes to investigate the facility effects and scale-size effect on transition and turbulent heating. The three facilities in which the configurations were tested are the Langley Mach 8 variable-density hypersonic tunnel and the Arnold Engineering Development Center tunnel B and tunnel F at Mach numbers of 8 and 10.5, respectively.

SYMBOLS

A	maximum mixing-length constant
h	heat-transfer coefficient
h_o	stagnation-point heat-transfer coefficient
l	mixing length
M_∞	free-stream Mach number
$R_{e,x}$	local Reynolds number based on distance
$R_{e,\theta}$	local Reynolds number based on momentum thickness
R_∞/m	unit Reynolds number
r_n	nose radius
x	surface distance
α	angle of attack
δ	boundary-layer thickness in physical plane

SOME OF MODELS TESTED

(Figure 1)

Figure 1 shows several of the models tested at the Arnold Engineering Development Center (AEDC) and at the Langley Research Center (LRC). The large model shown at the left is one of the 60.96-cm- (2-ft-) long delta-body configurations tested at AEDC. In addition to the large delta body, a straight-body configuration of the same length was tested at AEDC. The large, straight configuration is not shown; however, a small-scale version of the straight configuration is shown between two of the small delta-body models. The three small models at the right were tested in the LRC Mach 8 facility. The two small models (dark models) at the left were used with phase-change paint and are made from Stycast. The metallic model on the right is a thin-skin thermocouple model made of stainless steel. The large models were tested at AEDC in tunnel B and tunnel F. The models tested in tunnel B were made from Stycast and RTV rubber. The same size models tested in tunnel F were made of stainless steel and had 6.35-mm- (0.25-in-) diameter heat gages mounted flush to the surface. The majority of the heat gages for the models tested in tunnel F were in a row down the center line of the model. Similarly, the small thermocouple model had all the instrumentation down the center line of the model.

SOME OF MODELS TESTED

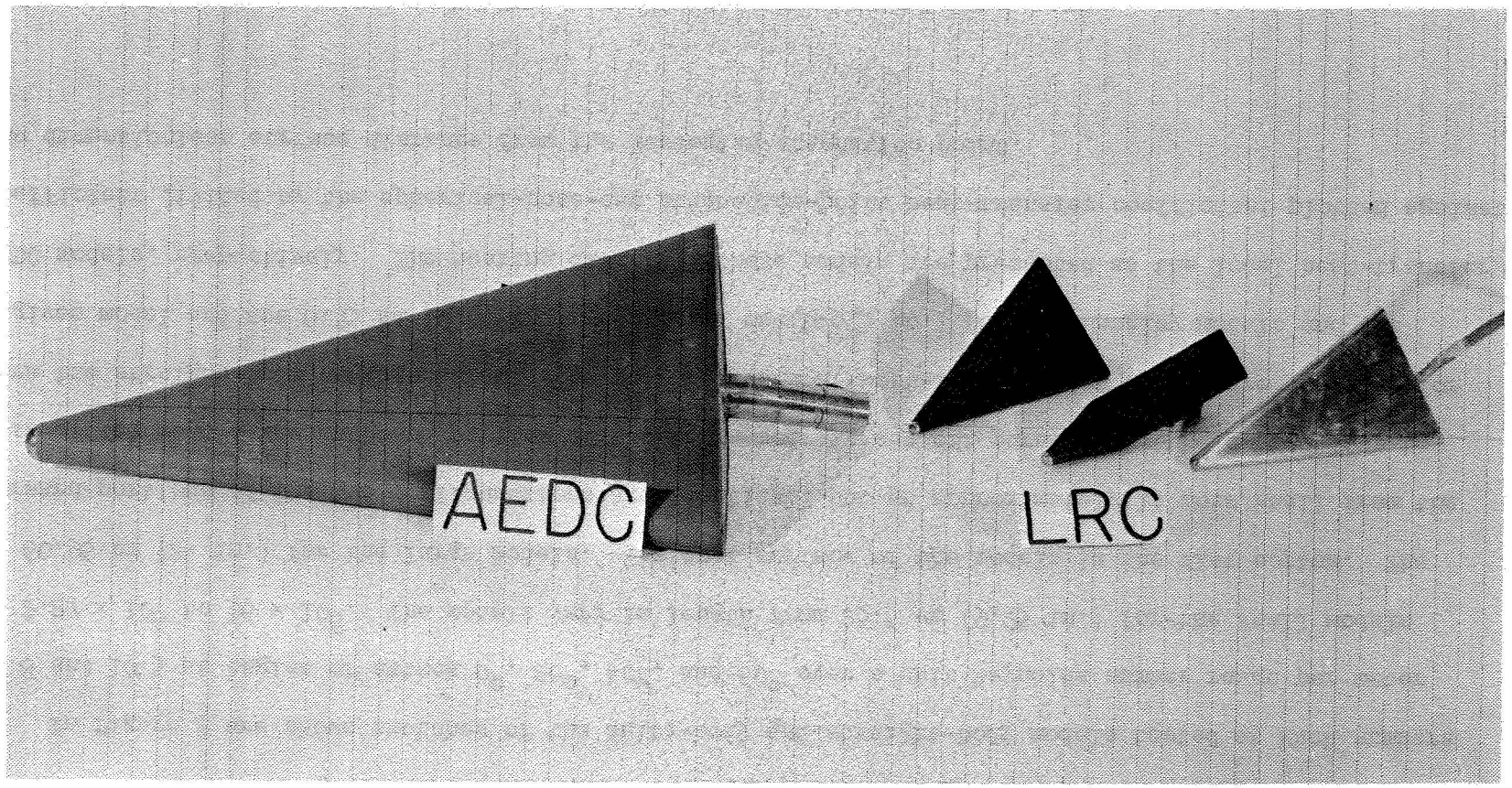

Figure 1

DELTA-BODY AND STRAIGHT-BODY MODELS FOR HEAT-TRANSFER STUDIES

(Figure 2)

In figure 2 are shown sketches of the delta-body and straight-body models tested at Mach numbers of 8 and 10.5 at angles of attack 0°, 20°, 40°, and 60° over a unit Reynolds number range per meter of 2.27×10^6 to 36×10^6. The models vary in length from 23.5 cm (9.25 in.) for the small models to 60.96 cm (24 in.) for the large models. The test surface of the models is the flat bottom. The forward portions of the two configurations are identical; but at approximately 13 nose radii from the nose of the model, the outboard portion of the delta body is cut off parallel to the center line to form the straight-body configuration. The nose radius and swept-leading-edge radius are the same for a given model and are 6.35 mm (0.25 in.) and 17.145 mm (0.675 in.) for the Langley models and the AEDC models, respectively. The heating data from these models are presented as the local heat-transfer coefficient divided by the spherical-nose-cap stagnation-point heat-transfer coefficient plotted against the dimensionless surface distance from the Newtonian stagnation point.

DELTA-BODY AND STRAIGHT-BODY MODELS FOR HEAT-TRANSFER STUDIES

M_∞ = 8 AND 10.5

$0 \leq \alpha \leq 60^0$

$2.27 \times 10^6 \leq R_\infty/m \leq 36 \times 10^6$

$r_n = \begin{cases} 6.35 \text{ mm } (.25 \text{ in.}) \\ 17.145 \text{ mm } (.675 \text{ in.}) \end{cases}$

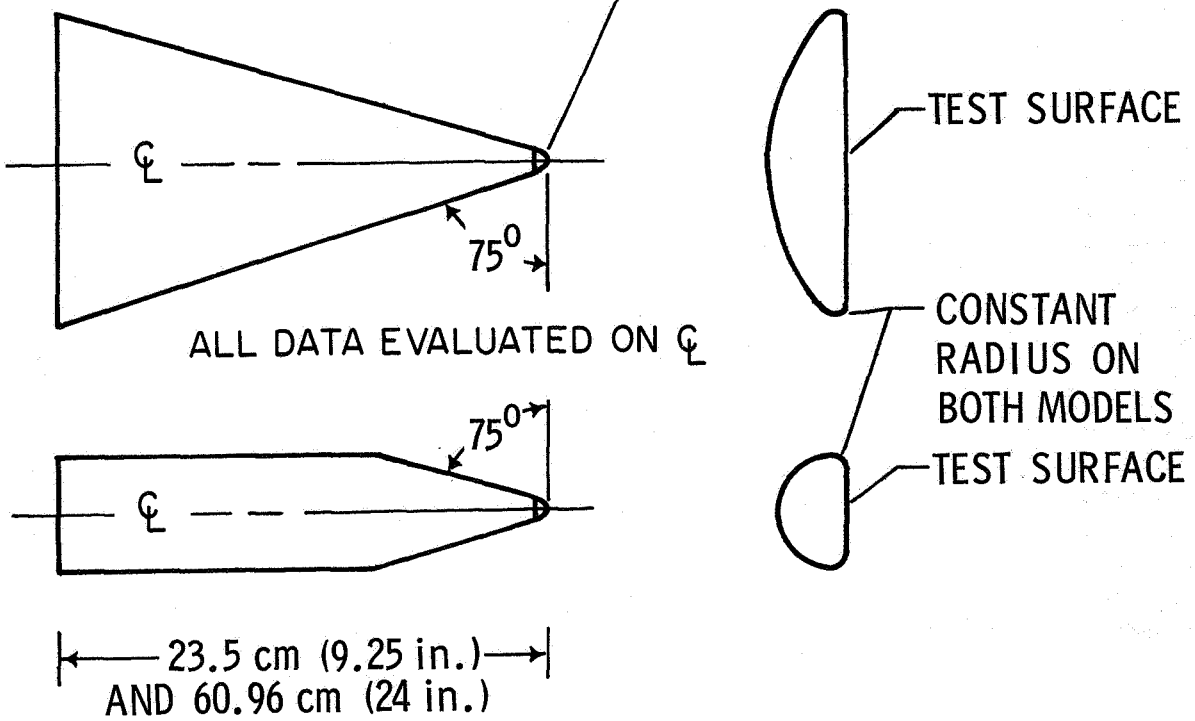

Figure 2

HEATING-RATIO DATA AT MACH 8

(Figure 3)

Figure 3 shows the heating-ratio data from two facilities at 20° angle of attack at a free-stream Mach number of 8. The local Mach number in the turbulent-flow region at this angle of attack varies from about 2.0 to 4.3, depending on the value of entropy at the edge of the boundary layer. The convention of open symbols representing data from the delta configurations and closed symbols representing the data from the straight configurations is used in all figures. All the data presented in this paper are taken on the plane of symmetry (center-line data) and are plotted against the number of nose radii from the geometrical stagnation point. The circles and squares indicate phase-change-paint data from the AEDC tunnel B, whereas data indicated by the diamonds and the upper left-hand quadrant of a circle are from the thin-skin thermocouple model tested in the LRC Mach 8 facility. The phase-change-paint data from tunnel B show very little difference for a given unit Reynolds number between the straight and delta configurations. The onset of transition for the higher Reynolds number from both facilities is considerably more upstream than that for the lower Reynolds number. The high Reynolds number data from the Langley facility show an onset of transition and a rise in the transition region nearly the same as the high Reynolds number data from tunnel B; a similar relationship is noted for the low Reynolds number data. The highest unit Reynolds number of the Langley data is approximately 3 times that of the AEDC data but the AEDC model is larger than the Langley model by a factor of 3, which indicates that the local transition Reynolds number is about the same for the two facilities.

The solid lines indicate the results from a boundary-layer integral theory (ref. 2) in which variable entropy is used by assuming a conical flow field for the surface pressures and a curved shock entropy distribution. The skin friction used in Reynolds analogy for heat transfer is calculated for a two-dimensional flow. The heating prediction in the transition region starts at a known experimental value of heat transfer and rises to a theoretical value of fully turbulent flow at the end of transition with the heat transfer assumed to vary as a hyperbolic tangent function within this region. The fully turbulent heating prediction is based on the Van Driest II ($R_{e,\theta}$, refs. 2 and 3) theory which uses a Reynolds number based on momentum thickness to determine the skin friction. It can be seen that at the highest unit Reynolds number of 36×10^6, the theory gives reasonable prediction of the level of the fully turbulent data; however, at the lower unit Reynolds number of 19×10^6, the theory overpredicts the level of heating. It is interesting to note that if an entropy distribution resulting from the laminar-boundary-layer calculation is used, the theory predicts a lower level of heating which is in close agreement with the data.

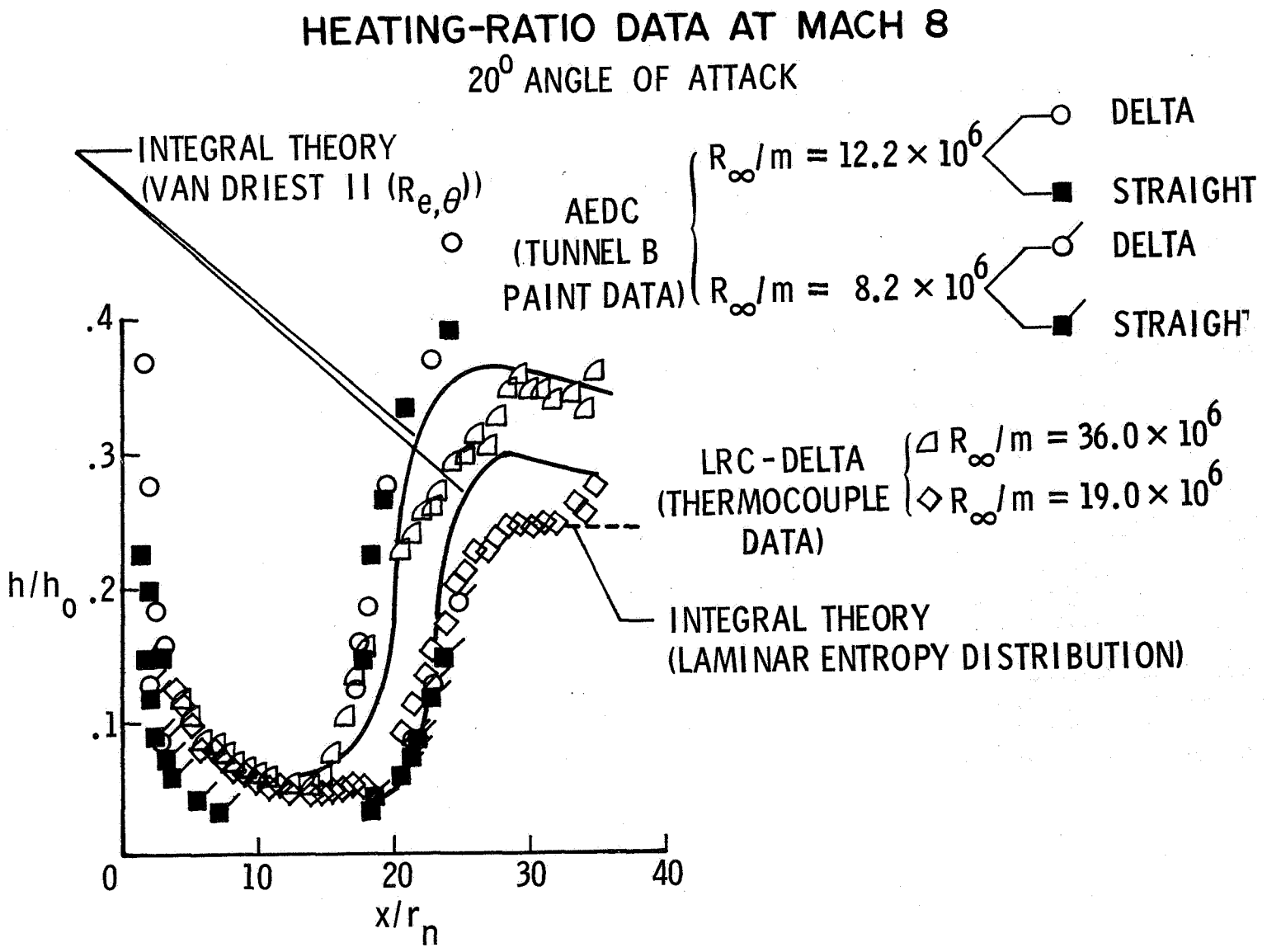
HEATING-RATIO DATA AT MACH 8
20° ANGLE OF ATTACK
INTEGRAL THEORY
(VAN DRIEST II ($R_{e,\theta}$))
AEDC
(TUNNEL B
PAINT DATA)
$R_\infty/m = 12.2 \times 10^6$
DELTA
STRAIGHT
$R_\infty/m = 8.2 \times 10^6$
DELTA
STRAIGHT
LRC-DELTA
(THERMOCOUPLE
DATA)
$R_\infty/m = 36.0 \times 10^6$
$R_\infty/m = 19.0 \times 10^6$
INTEGRAL THEORY
(LAMINAR ENTROPY DISTRIBUTION)
h/h_0
.4
.3
.2
.1
0
10
20
30
40
x/r_n

Figure 3

REYNOLDS NUMBER EFFECT ON HEATING AND TRANSITION

(Figure 4)

Figure 4 shows the effect of Reynolds number on heating and the onset of transition at 20° angle of attack and a free-stream Mach number of 8. The local Mach number in the region of turbulent flow varies from about 2.0 to 4.3, depending on the value of the entropy at the edge of the boundary layer. The data symbols shown in figure 4 are for the small Stycast models tested with phase-change paint in the LRC Mach 8 facility. Again the convention of using the open and closed symbols for data from the delta and the straight configuration, respectively, is used. The results show that the laminar heating distribution from the complete range of unit Reynolds number (2.27×10^6 to 36.0×10^6) falls on a single curve, as would be expected. The laminar distribution was the same for both the straight and delta configurations due to the similarity of the forward portions of the two models. A comparison of the heating results for the delta and straight configurations after the onset of transition, shown by the open and closed symbols, indicates that there is very little difference in the level of the transitional heating or in the location of the onset of transition between the two configurations. As would be expected, the onset of transition moves forward on the model as the Reynolds number increases. For the three highest Reynolds numbers the slope of the heating in the transition region is about the same, but for the three lowest Reynolds numbers there is a decrease in slope in the transition region which indicates that the length of the transition region decreases with increasing Reynolds number. The hatched regions in figure 4 represent the phase-change-paint data from tunnel B, shown in figure 3, at unit Reynolds numbers per meter of 12.2×10^6 and 8.2×10^6. In figure 3, the onset of transition for the LRC Mach 8 facility thin-skin thermocouple data and the tunnel B data is at about the same location for the highest Reynolds number. However, in figure 4 the phase-change-paint data at a unit Reynolds number of 36×10^6 from the LRC Mach 8 facility indicate transition more forward than the tunnel B data. The more upstream location of the onset of transition indicates that the phase-change paint could be tripping the boundary layer and causing transition to occur closer to the nose than for the thin-skin thermocouple model. For the data at a unit Reynolds number of 19.0×10^6, the boundary layer is thicker and any surface roughness due to the paint does not appear to affect the location of transition, as shown in figure 4 by the agreement in the onset of transition for the paint data from tunnel B and the LRC Mach 8 facility.

REYNOLDS NUMBER EFFECT ON HEATING AND TRANSITION

20^0 ANGLE OF ATTACK AT MACH 8; PAINT DATA

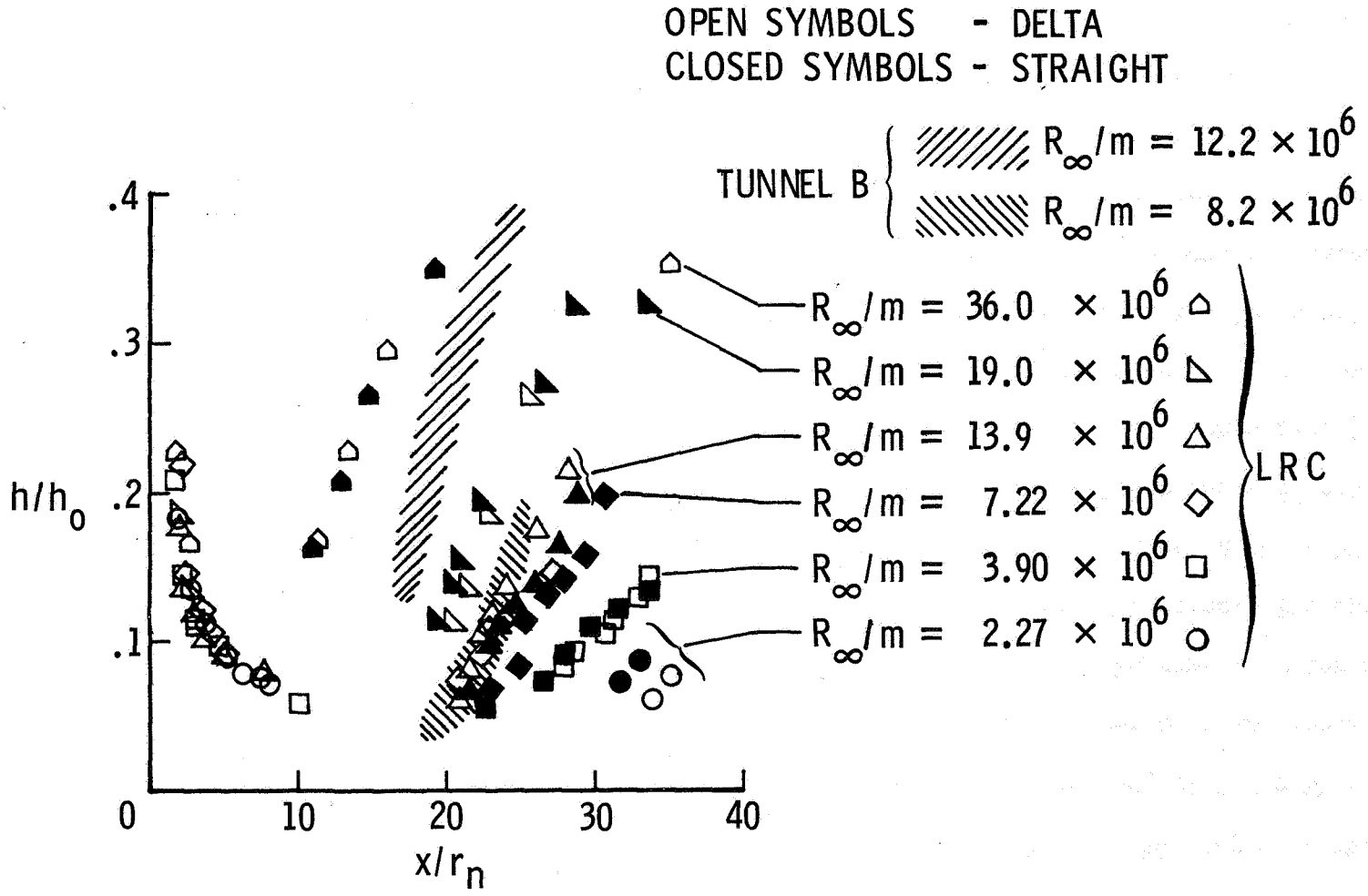

Figure 4

A COMPARISON OF HEATING RATIOS ON A DELTA BODY

(Figure 5)

Figure 5 shows phase-change-paint heating data from two delta-body models at 40° angle of attack, tested in tunnel B at a unit Reynolds number of 12.2×10^6; one delta body was made of RTV rubber and the other was made from Stycast. The tunnel B tests had a free-stream Mach number of 8 and local Mach number of about 2.1 based on oblique shock calculations. Both models indicate the same location of the onset of transition and nearly the same rise to the fully turbulent level of heating. The upper range of hatching represents data from a delta configuration obtained with heat gages in the AEDC tunnel F at a Mach number of 10.5 and a unit Reynolds number of 36×10^6. The lower range of hatching is data from a delta body obtained by a thin-skin thermocouple technique in the LRC Mach 8 facility at the same unit Reynolds number (36×10^6) as the tunnel F data. The prediction of heating is from a variable-entropy boundary-layer integral method previously described (see ref. 2). For two heating predictions, the Van Driest II theory is used (1) with the Reynolds number based on momentum thicknesses (refs. 2 and 3) and (2) with the Reynolds number based on the distance from the virtual origin (ref. 4). The virtual origin was based on the unpublished work on flat plates and cones by Aubrey M. Cary, Jr., and Mitchel H. Bertram of LRC in which they correlated about 1200 nonadiabatic data points of turbulent heating and skin friction and found the best virtual origin to be 0.825 times the distance to the end of transition. The third heating prediction uses the Spalding-Chi theory (ref. 5) based on the distance from the virtual origin. All theories reasonably predict the maximum heat-transfer data ($h/h_o \approx 0.7$) at the start of fully turbulent flow.

A COMPARISON OF HEATING RATIOS ON A DELTA BODY

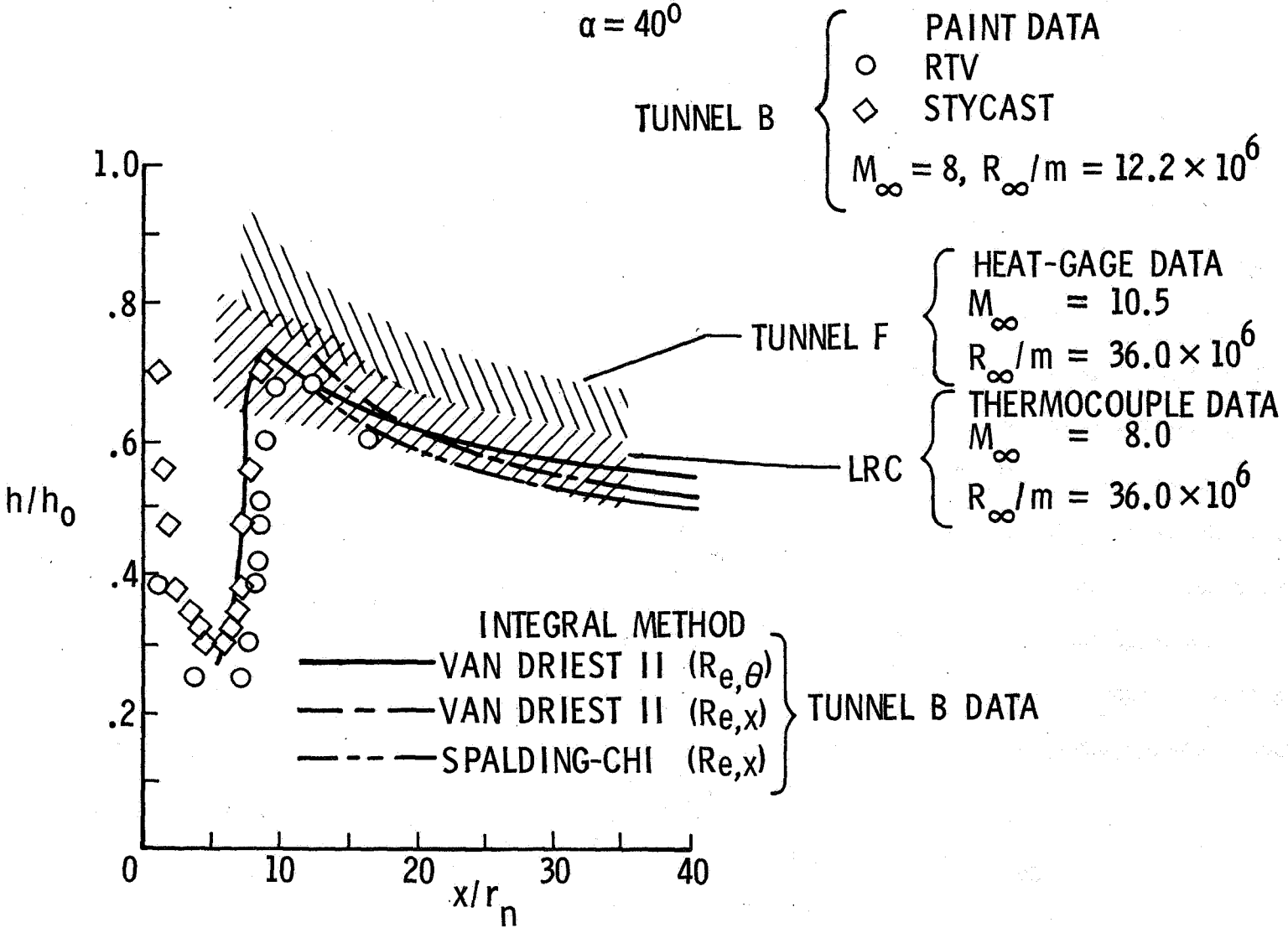

Figure 5

HEATING RATIOS ON DELTA- AND STRAIGHT-BODY CONFIGURATIONS

(Figure 6)

In figure 6 are shown the phase-change-paint heating data on the delta- and straight-body configurations from tunnel B at a unit Reynolds number of 8.2×10^6 and a 40° angle of attack. Again, the open symbols are for the delta configuration and the closed symbols are for the straight-body configuration. The data from the two configurations show approximately the same onset of transition and the same rise in the transition region with the exception of the overshoot in the heating at the end of the transition region for the straight configuration. The hatching represents data from a delta configuration obtained with heat gages in the AEDC tunnel F at a unit Reynolds number of approximately 10.3×10^6 and a free-stream Mach number of 10.5. The range of tunnel F data falls within the range of phase-change-paint data found on the delta configuration tested in tunnel B. The theoretical predictions show agreement with both the tunnel F and tunnel B data. The methods of theoretical predictions are the same as those described for figure 5.

HEATING RATIOS ON DELTA AND STRAIGHT-BODY CONFIGURATIONS

$\alpha = 40^0$

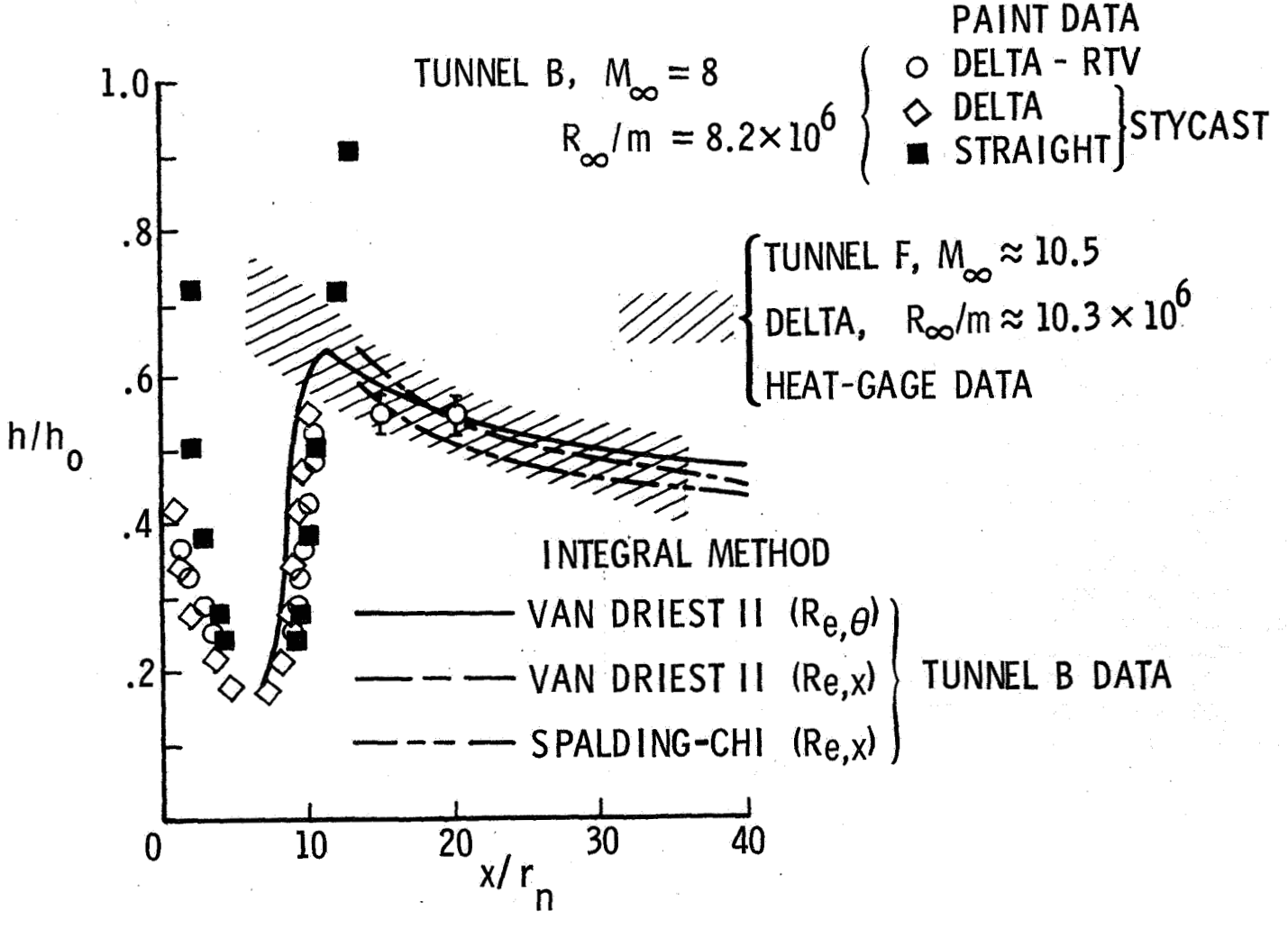

Figure 6

TUNNEL F TURBULENT HEATING DATA AT TWO ANGLES OF ATTACK

(Figure 7)

Figure 7 shows the heat-transfer data, measured with heat gages, from the AEDC tunnel F at two angles of attack (20° and 40°), over a range of free-stream unit Reynolds numbers of 30.1×10^6 to 38.3×10^6 per meter and a free-stream Mach number of about 10.5. The local Mach number in the region of fully turbulent flow varies from 4.1 to 5.0 at $\alpha = 20^\circ$ and is approximately equal to 2.2 at $\alpha = 40^\circ$. Again, the open symbols are for the delta configuration and the closed symbols are for the straight configuration. It can be seen from the level of heating that the straight configuration, in general, has a slightly higher level of heating than the delta configuration. The results from both configurations at both angles of attack indicate that almost all the data are fully turbulent. The extreme upstream location of the onset of transition may be caused by heat gages tripping the boundary layer. In addition, there is considerable scatter in the data which is due to (1) the type of instrumentation, (2) the possibility that the gages may be slightly recessed or slightly protruding, and (3) a high turbulence intensity in the boundary layer. The integral method (Van Driest II ($R_{e,\theta}$), refs. 2 and 3) for the 40° angle-of-attack conditions reasonably predicts the heating level and distribution for the straight configuration and slightly overpredicts the heating for the delta configuration. The integral method for the 20° angle-of-attack conditions overpredicts the data; however, when the entropy distribution resulting from the laminar-boundary-layer calculation is used, the prediction of the data is good. The theoretical results at $\alpha = 20^\circ$ indicate that the model used for entropy swallowing should be modified for the condition of "in-flow" at low angles of attack.

TUNNEL F TURBULENT HEATING DATA AT TWO ANGLES OF ATTACK

$M_\infty \approx 10.5$

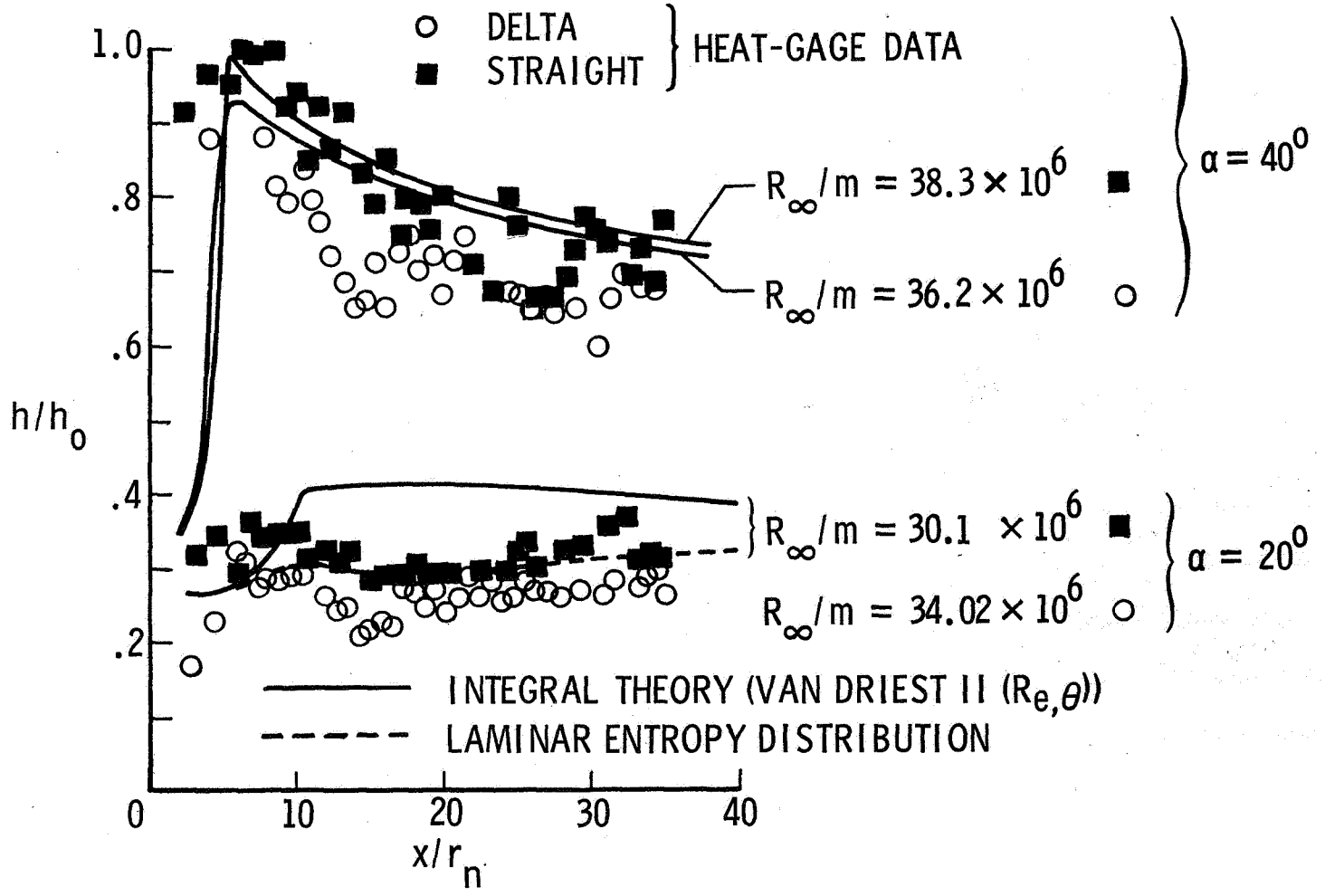

Figure 7

TUNNEL F TURBULENT HEATING DATA AT TWO ANGLES OF ATTACK

(Figure 8)

The data shown in figure 8 are measured in the AEDC tunnel F with heat gages using the same configurations and at the same free-stream Mach number as shown in figure 7. The difference in the data between figures 7 and 8 is that the data in figure 8 are at a lower unit Reynolds number (from 9.35×10^6 to 11.4×10^6). Even at the lower unit Reynolds number, the data in figure 8 at 40° angle of attack indicate that transition is far upstream on the body and almost all data are turbulent. The data at 20° angle of attack indicate some laminar and transitional data but again most of the data are fully turbulent. The large amount of fully turbulent data at a unit Reynolds number as low as 11×10^6 is again indicative of either tripped boundary layer or an extremely high turbulence level in the boundary layer. The data at 40° angle of attack show close agreement between the results found on the delta and the straight body. The 20° angle-of-attack data show that the straight body has a higher level of heating than the delta configuration, the same results that were found for both the 20° and 40° angle-of-attack data in figure 7. As was found in figure 7, the prediction of the integral method for the 40° angle-of-attack conditions agrees with the data; but for the 20° angle-of-attack conditions, the prediction is above the data. However, when the entropy distribution from the laminar-boundary-layer solution is used, the prediction agrees with the data, again indicating that the model used for entropy swallowing should be modified for the condition of "in-flow" found at the low angles of attack.

TUNNEL F TURBULENT HEATING DATA AT TWO ANGLES OF ATTACK

$M_\infty \approx 10.5$

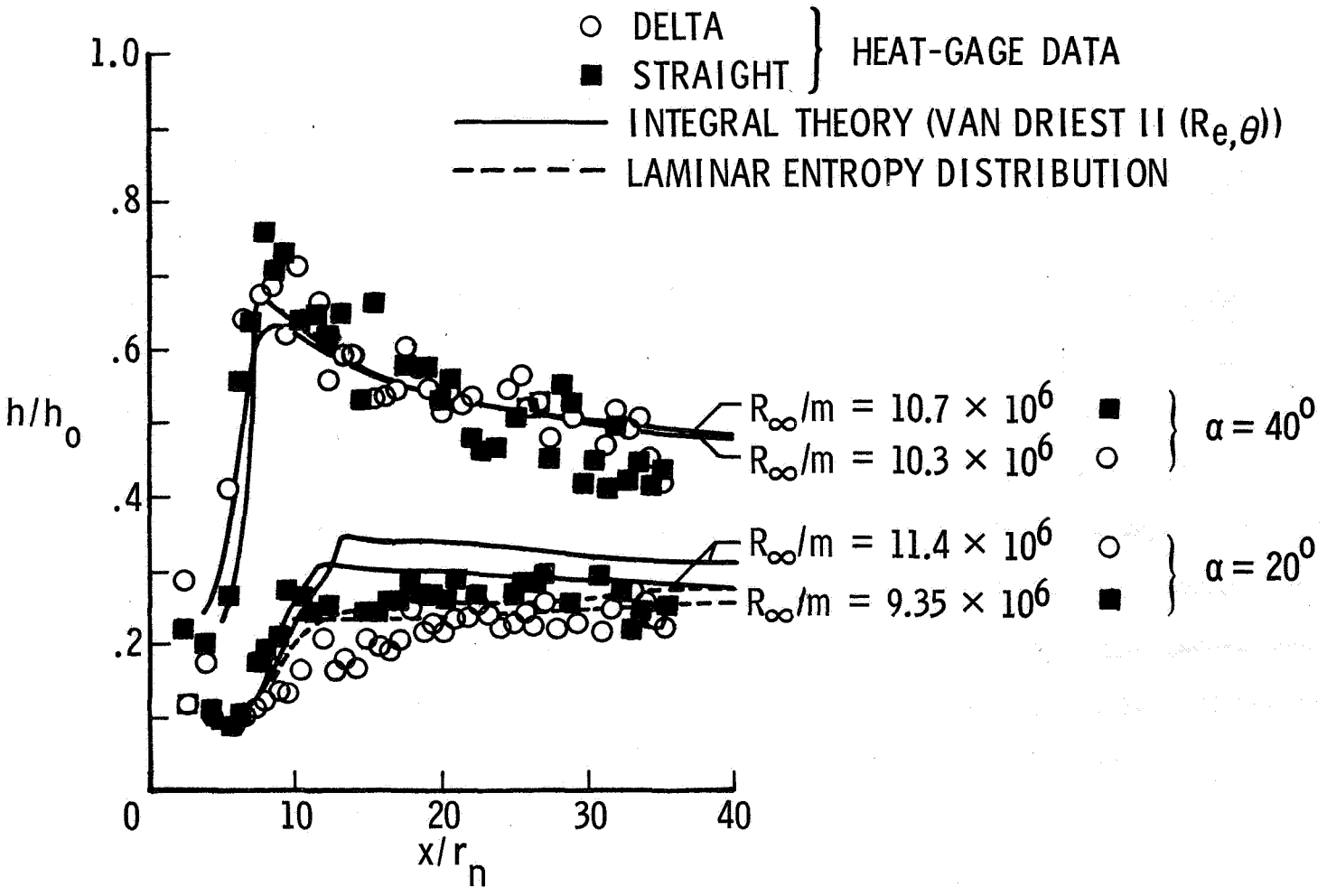

Figure 8

HIGH-ANGLE-OF-ATTACK HEATING DATA FROM TUNNEL F

(Figure 9)

The data in figure 9 are measured in the AEDC tunnel F using heat gages on the delta and straight configurations at 60° angle of attack and a unit Reynolds number of about 36×10^6. The free-stream Mach number is about 10.8 but the local Mach number based on oblique shock conditions is about 1.0. The data at 60° angle of attack appear to be fully turbulent, about the same as the results found in the previous 20° and 40° angle-of-attack data from tunnel F, again indicating the possibility of a tripped boundary layer. In general, the level of heating from the straight configuration is slightly higher than that from the delta-body configuration, as was noted in most of the other tunnel F data. The theoretical prediction of heating is based on oblique shock conditions using a measured shock angle from schlieren photographs of the delta configuration and using measured pressure distributions on the delta configuration. The prediction of heating is reasonably good for the Van Driest II ($R_{e,\theta}$, refs. 2 and 3) and Spalding-Chi ($R_{e,\theta}$, refs. 2 and 5, and $R_{e,x}$, ref. 5) predictions. However, the reference-enthalpy prediction is high for the $R_{e^{\cdot},\theta}$ (ref. 3) prediction and is low for the $R_{e,x}$ (ref. 6) prediction.

HIGH-ANGLE-OF-ATTACK HEATING DATA FROM TUNNEL F

$\alpha = 60^0$; $M_\infty \approx 10.8$

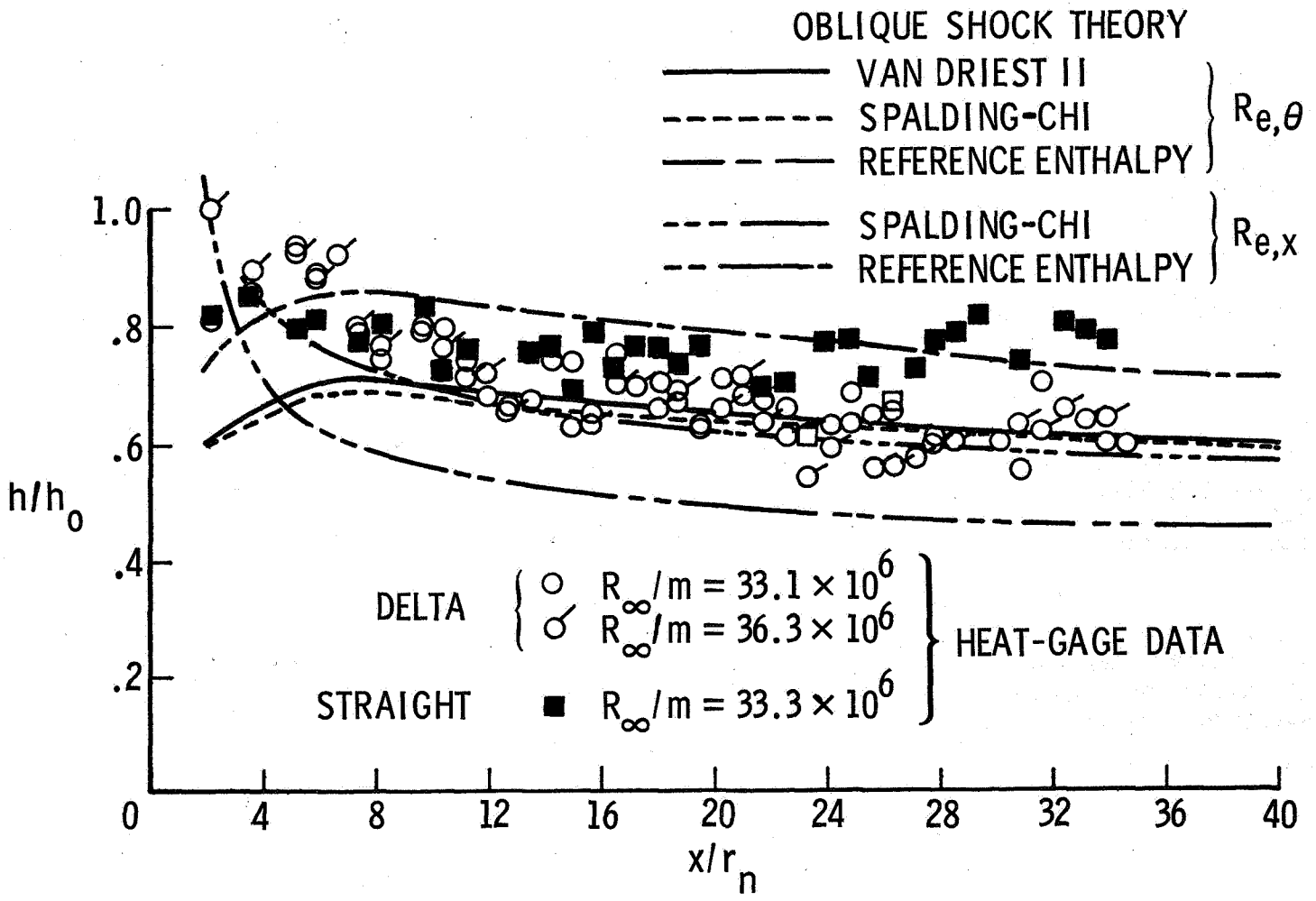

Figure 9

EFFECT OF PAINT ROUGHNESS

(Figure 10)

The data from tunnel F indicated transition very near the nose and also exhibited considerable scatter at angles of attack of 40° and 60°. This trend in the data indicated the possibility that irregularities in the surface fit of the heat gages could be perturbing the boundary layer. Furthermore, tunnel F schlieren photographs at 40° angle of attack showed weak shock waves coming off the surface of the model with about the same spacing as the heat-gage installation.

Because of the indicated roughness on the tunnel F models and because of the previously mentioned roughness condition with the phase-change paint (see fig. 4), an investigation of roughness effects on a smooth thin-skin thermocouple model of the delta configuration was conducted in the LRC Mach 8 facility. Initially the roughness tests were conducted with phase-change paint sprayed on the steel model to simulate varying degrees of roughness; however, the data were always taken by using the thin-skin thermocouple technique. The untripped data from the clean model shown in figure 10, at $\alpha = 40^\circ$ and $R_\infty/m = 36 \times 10^6$, are indicated by the crossed circles. The first application of 533.3° K (500° F) paint was sprayed on the model roughly, resulting in a very rough model surface. The data from the rough paint application, shown by the triangles, indicated that transition occurred very near the nose and also that the level of heating was higher than the untripped data. Next, 533.3° K (500° F) paint was applied to the surface smoothly; this resulted in about the same onset of transition as untripped data, but again the level of the fully turbulent heating was higher than the undisturbed data. It should be noted that in both applications of this paint, the paint did not melt but left a uniform roughness over the entire surface of the model which resulted in a higher level of turbulent heating than was found for the smooth unpainted model. The final simulated roughness was an application of a lower temperature phase-change paint (312.8° K (103° F)) which was known to melt over the thin-skin area, where the thermocouples were, prior to the time the data were taken. The results on the model with the melted paint showed an onset of transition about the same as for the clean (unpainted) model and the model covered with the smooth high-temperature paint. However, the level of turbulent heating on the model with the smooth melted paint was lower than that found on the model coated with the unmelted high-temperature paint. In addition, the level of turbulent heating on the model with the smooth melted paint was the same as that on the clean unpainted model. Therefore, it appears that a distributed roughness over the area of turbulent flow can raise the level of turbulent heating as much as 20 percent.

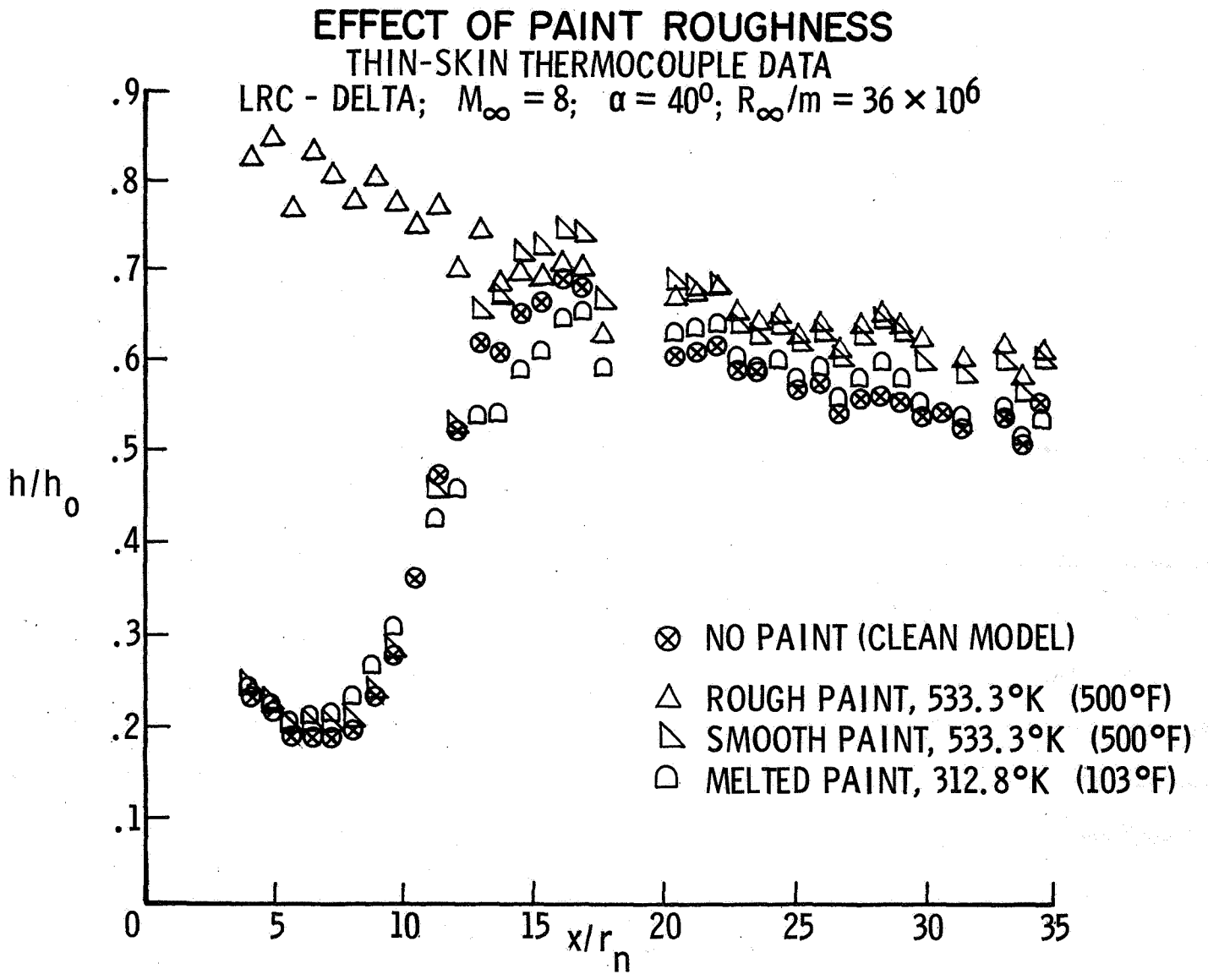
EFFECT OF PAINT ROUGHNESS
THIN-SKIN THERMOCOUPLE DATA
LRC - DELTA; $M_\infty = 8$; $\alpha = 40^0$; $R_\infty/m = 36 \times 10^6$
h/h_0
.9
.8
.7
.6
.5
.4
.3
.2
.1
0
5
10
15
20
25
30
35
x/r_n
NO PAINT (CLEAN MODEL)
ROUGH PAINT, 533.3°K (500°F)
SMOOTH PAINT, 533.3°K (500°F)
MELTED PAINT, 312.8°K (103°F)

Figure 10

EFFECT OF WIRE-TRIP ROUGHNESS

(Figure 11)

In figure 11 is shown the effect (at $\alpha = 40^{\circ}$ and $R_{\infty}/m = 36 \times 10^{6}$) of discrete roughness elements near the nose of the configuration tested in the LRC Mach 8 facility. The data on the untripped model are shown by the crossed circles. The roughness was placed on the same steel thermocouple model used for the paint-roughness test (fig. 10) by using two different sizes of wire trips. First, a 0.254-mm (0.010-in.) wire was placed around the model in two rows 0.794 cm (0.3125 in.) and 1.27 cm (0.50 in.) from the nose. The presence of these two wire trips resulted in transition moving far upstream on the configuration, as shown by the triangles in figure 11, but the level of turbulent heating was the same as that found on the untripped model. Next, a smaller wire (0.0762 mm (0.003 in.)) was placed around the model in a single row 0.9525 cm (0.375 in.) from the nose. The smaller wire trip had an onset of transition somewhat downstream of the double trip but again upstream of the natural transition location. Again the level of turbulent heating on the model with the single trip was the same as the level found on the untripped model. It appears that the level of fully turbulent heating is the same for the tripped and untripped tests primarily because the surface over the area of fully turbulent flow was smooth in all three cases. Thus even though the boundary layer is severely disturbed by the trips, the level of heating in the downstream fully turbulent region returns to natural or an undisturbed level of heating.

EFFECT OF WIRE-TRIP ROUGHNESS

THIN-SKIN THERMOCOUPLE DATA

LRC - DELTA; $M_\infty = 8$; $\alpha = 40^0$; $R_\infty/m = 36 \times 10^6$

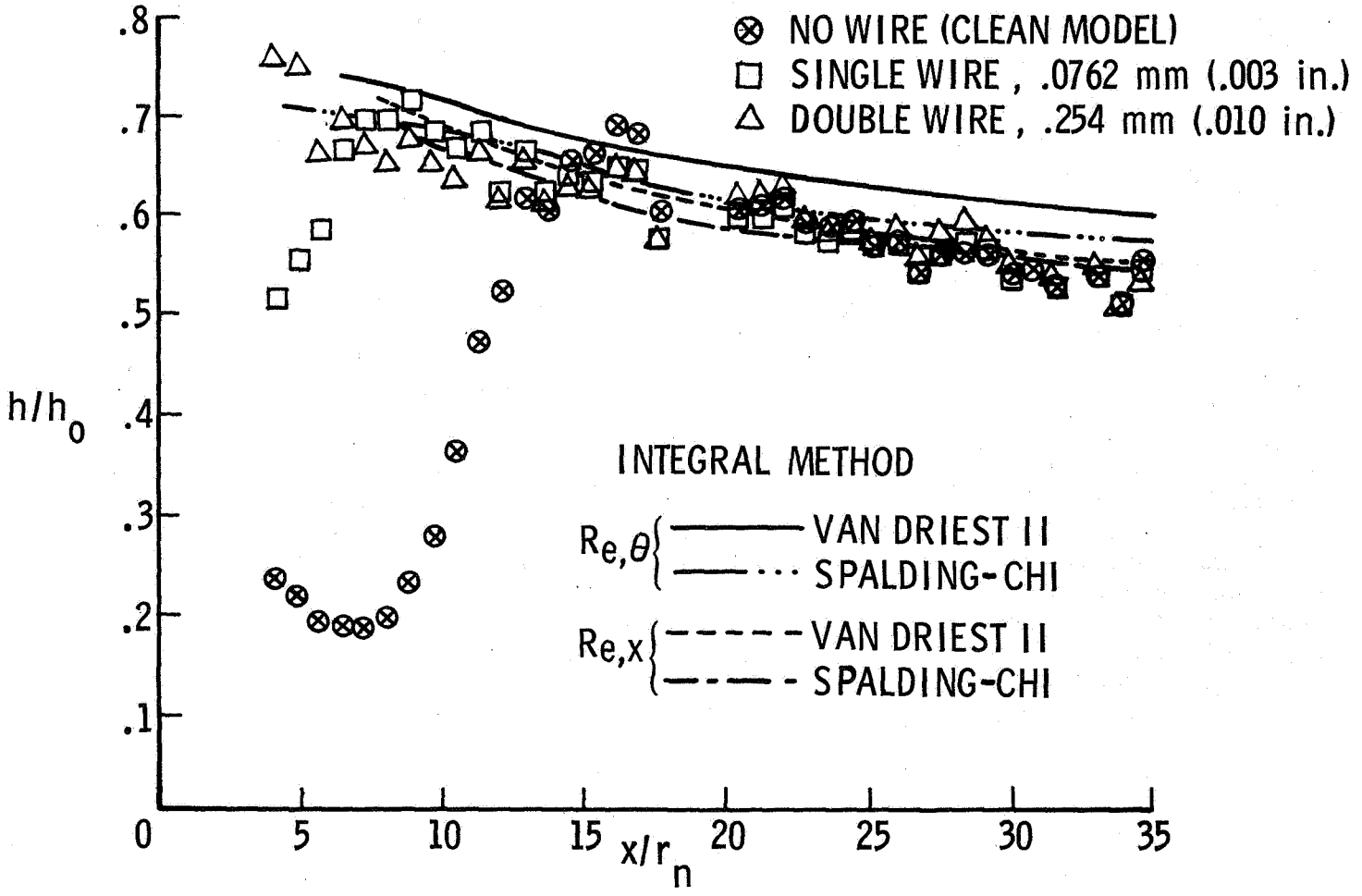

Figure 11

THE EFFECT OF ROUGHNESS AT LOWER REYNOLDS NUMBER

(Figure 12)

Tests in the LRC Mach 8 facility similar to those of figures 10 and 11 were conducted at a lower unit Reynolds number ($\alpha = 40^\circ$, $R_\infty/m = 19 \times 10^6$). The data from the untripped model is shown by the crossed circles. Again, when the two 0.254-mm (0.010-in.) wires were on the model (same location as fig. 10) transition moved very near the nose of the configuration as shown by the isosceles triangles in figure 12. The smooth 533.3° K (500° F) paint and the 0.0762-mm (0.003-in.) wire had an onset of transition that was almost the same as natural transition. However, in the transition region the slope of the tripped data to the fully turbulent level was much steeper than the untripped data. The level of turbulent heating for the tripped and untripped boundary layer was about the same. It should be noted that the level of the heating with the 533.3° K (500° F) paint was nearly the same as for the smooth untripped model. It appears that at this lower unit Reynolds number the ratio of the roughness height to the boundary-layer thickness decreases to the point that the evenly distributed paint roughness does not affect the level of turbulent heating.

A calculation was made using a nonsimilar boundary-layer approach which solved the longitudinal and spanwise momentum equations as well as the continuity and energy equations. The equations used are exact for the developing-line-of-symmetry case (degenerate three-dimensional boundary layer) and include models for the turbulent shear terms. The nonsimilar solution utilized experimental longitudinal and spanwise pressure distributions obtained on the same size model at the same conditions and in the same facility. The prediction of the nonsimilar solution technique (developed at Langley by Dennis M. Bushnell and Ivan E. Beckwith) is shown for two mixing-length assumptions ($A = 0.075$ and $A = 0.05$). These predictions should correspond to the untripped data shown in figure 12. The comparison between data and theory indicates that the present three-dimensional developing-line-of-symmetry turbulent boundary layer possesses a turbulence level corresponding to a fairly low value of mixing-length constant ($A = (l/\delta)_{max} \approx 0.06$). Thus, before the nonsimilar boundary layer can accurately predict turbulent heating with flow divergence, much data and theory must be compared to check the dependence of the mixing-length-constant variation with unit Reynolds number and angle of attack. The integral-theory prediction is shown for (1) the Van Driest II ($R_{e,\theta}$, refs. 2 and 3) theory based on the natural transition data and (2) the Spalding-Chi theory ($R_{e,\theta}$, refs. 2 and 5) based on the onset of transition at 1 nose radius from the stagnation point.

THE EFFECT OF ROUGHNESS AT LOWER REYNOLDS NUMBER

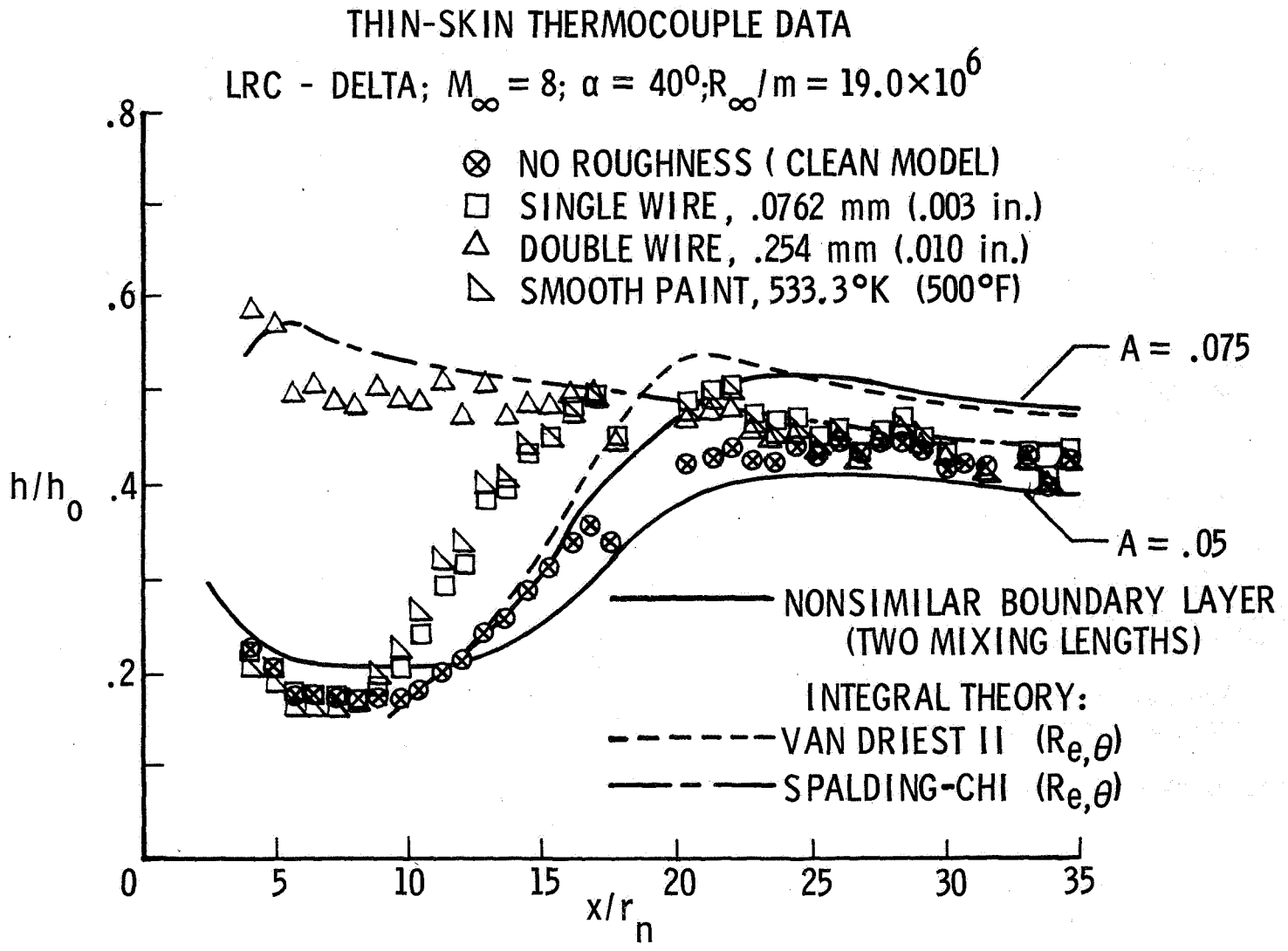

Figure 12

CONCLUDING REMARKS

Concluding remarks concerning results found on the two simplified configurations are as follows:

A variation in the degree of cross flow, as found for the delta and straight configurations, showed the same onset of transition and the same heating distribution in the transition region.

The level of turbulent heating, at a given free-stream unit Reynolds number can vary from one facility to another by as much as 20 percent. The difference in the level of turbulent heating may be due to (1) roughness on the model surface and (2) a high level of turbulent intensity in the boundary layer.

With a difference of a factor of 3 in model scale size, transition in the AEDC tunnel B and the LRC Mach 8 facility occurs at about the same local Reynolds number.

The boundary layer at high angles of attack can be easily tripped by roughness. In addition, roughness over the entire vehicle can raise the level of turbulent heating about 15 percent, but when discrete trips are placed near the nose, the boundary layer recovers to a level of turbulent heating that is the same as the undisturbed data.

Theoretical predictions of turbulent heating made by using a simple boundary-layer integral method are good at angles of attack of 40° and 60°. At 20° angle of attack, the theoretical predictions of heating are quite sensitive to entropy distribution at the edge of the boundary layer.

A nonsimilar turbulent-boundary-layer solution with cross flow was made, and it was found that the level of heating was strongly dependent on the value of the mixing-length parameter.

REFERENCES

1. Johnson, Charles B. (With appendix by George C. Ashby, Jr.): Boundary-Layer Transition and Heating Criteria Applicable to Space Shuttle Configurations From Flight and Ground Tests. Vol. I of NASA Space Shuttle Technology Conference, NASA TM X-2272, 1971, pp. 97-156.

2. Johnson, Charles B.; and Boney, Lillian R.: A Simple Integral Method for the Calculation of Real-Gas Turbulent Boundary Layers With Variable Edge Entropy. NASA TN D-6217, 1971.

3. Hopkins, Edward J.; Keener, Earl R.; and Louie, Pearl T.: Direct Measurements of Turbulent Skin Friction on a Nonadiabatic Flat Plate at Mach Number 6.5 and Comparisons With Eight Theories. NASA TN D-5675, 1970.

4. Van Driest, E. R.: The Problem of Aerodynamic Heating. Aeronaut. Eng. Rev., vol. 15, no. 10, Oct. 1956, pp. 26-41.

5. Spalding, D. B.; and Chi, S. W.: The Drag of a Compressible Turbulent Boundary Layer on a Smooth Flat Plate With and Without Heat Transfer. J. Fluid Mech., vol. 18, pt. 1, Jan. 1964, pp. 117-143.

6. Zoby, Vincent E.; and Rumsey, Charles B.: Analysis of Free-Flight Laminar, Transitional, and Turbulent Heat-Transfer Results at Free-Stream Mach Numbers Near 20 (Reentry F). NASA TM X-2335, 1971.

EFFECTS OF ROUGHNESS ON HEATING AND BOUNDARY-LAYER TRANSITION

PART I - EFFECTS OF SIMULATED PANEL JOINTS ON BOUNDARY-LAYER TRANSITION

By H. Lee Seegmiller
NASA Ames Research Center
Moffett Field, California

INTRODUCTION

The exterior surfaces of proposed space shuttle orbiters are composed of a large number of individual thermal protection panels which require provision for refurbishment and thermal expansion. Although the desirability of maintaining a smooth exterior surface to delay transition to turbulent flow is widely appreciated, little information exists to guide the designer regarding the effects of the distributed roughness arising from panel joints. In order to obtain some information regarding these effects, tests have been performed in the Ames 3.5-foot hypersonic wind tunnel using models of the North American Rockwell 134B delta-wing shuttle configuration with two types of simulated panel joints.

MODELS OF DELTA-WING ORBITER

(Figure 1)

The three models are shown in the figure. The model with the smooth lower surface was used to obtain baseline data for comparison with the two models having simulated panel joints. One of the models with joints simulated panels on the orbiter .635 m (25 inches) square separated by slots 20.3 mm (.8 inch) wide and 5.1 mm (.2 inch) deep. The second model simulated a series of transverse panels .635 m (25 inches) wide separated by a raised retaining strip or batten 25.4 mm (1 inch) wide by 2.5 mm (.1 inch) high. A better appreciation of the scale of the simulated joints may be had by noting that on the test model which was over .4 meters in length, the height of the raised joint was less than 1/2 the thickness of a human hair. The three models were instrumented with thermocouples which were placed in a row on the lower surface centerline. Additional thermocouple measurements were obtained at the rear of the models off the centerline.

MODELS OF DELTA-WING ORBITER

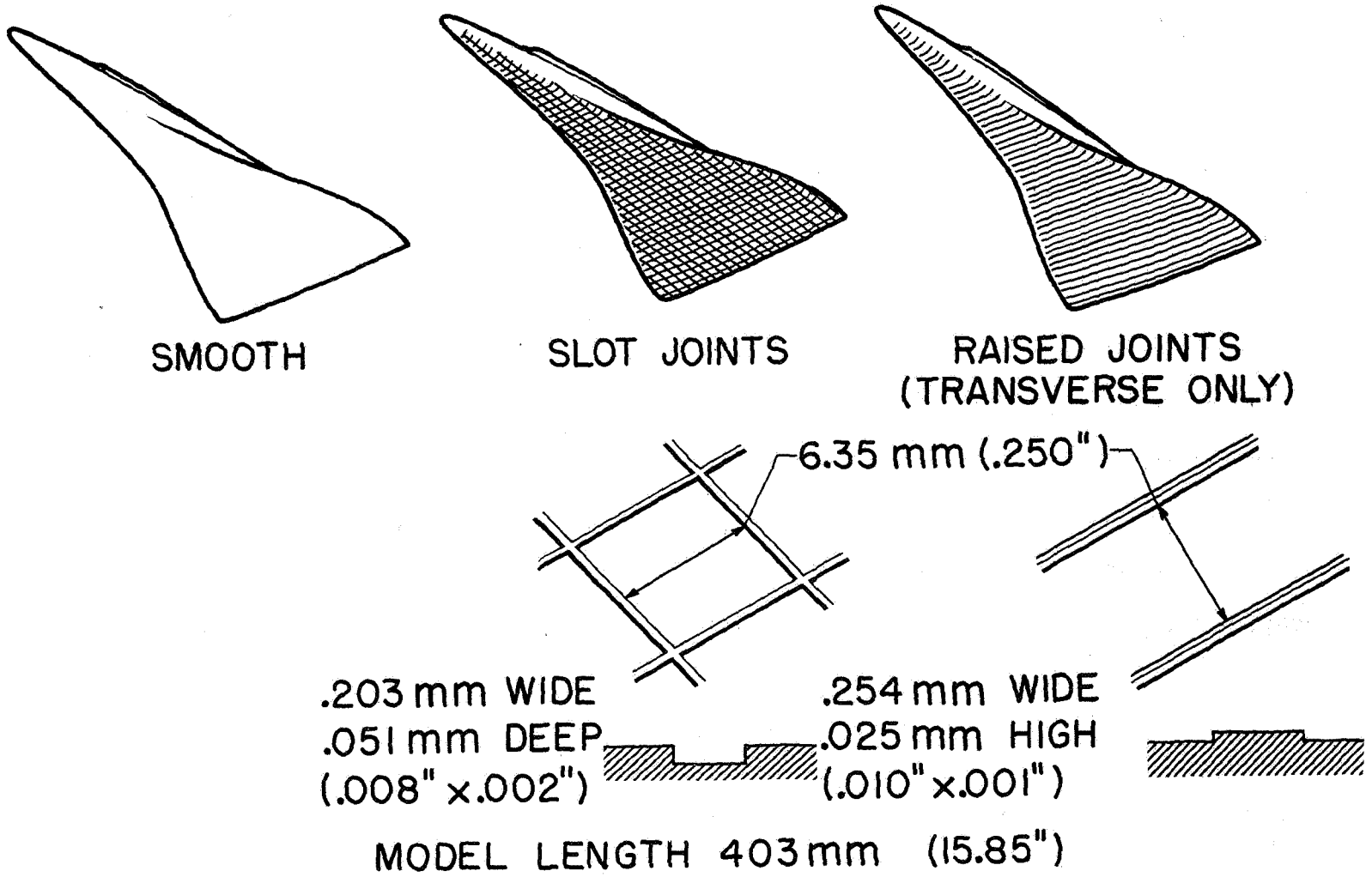

Figure 1

SURFACE-FLOW VISUALIZATION

(Figure 2)

Before beginning a discussion of the effects of panel joints on boundary-layer transition, it is important to understand as completely as possible the flow over a smooth model. For this reason, results of an oil-flow study and comparisons of heat-transfer measurements with theory are presented in the next few slides for the model without joints. Surface-flow streamlines made visible with an oil-flow technique (see reference 1) are shown for the model at an angle of attack of 30°. The forward 1/3 of the model is covered with a smoothly expanding flow of relatively uniform divergence. The presence of the wing leading edge at an X/L of about .5, however, causes a turning and compression of the expanding flow which becomes nearly two-dimensional over the rear of the model. Although the fuselage-wing leading-edge juncture is smoothly faired, it is seen that a rather complex flow exists. Further evidence of this complexity may be indicated by an otherwise unexplained local decrease in heating which was observed in this region. Local perturbations of the boundary layer caused by a flow interference of this type may have a significant and undesirable effect on transition.

SURFACE-FLOW VISUALIZATION, NAR DELTA-WING ORBITER (129)

$\alpha = 30°$; $Re_{l_\infty} = 2.7 \times 10^6$

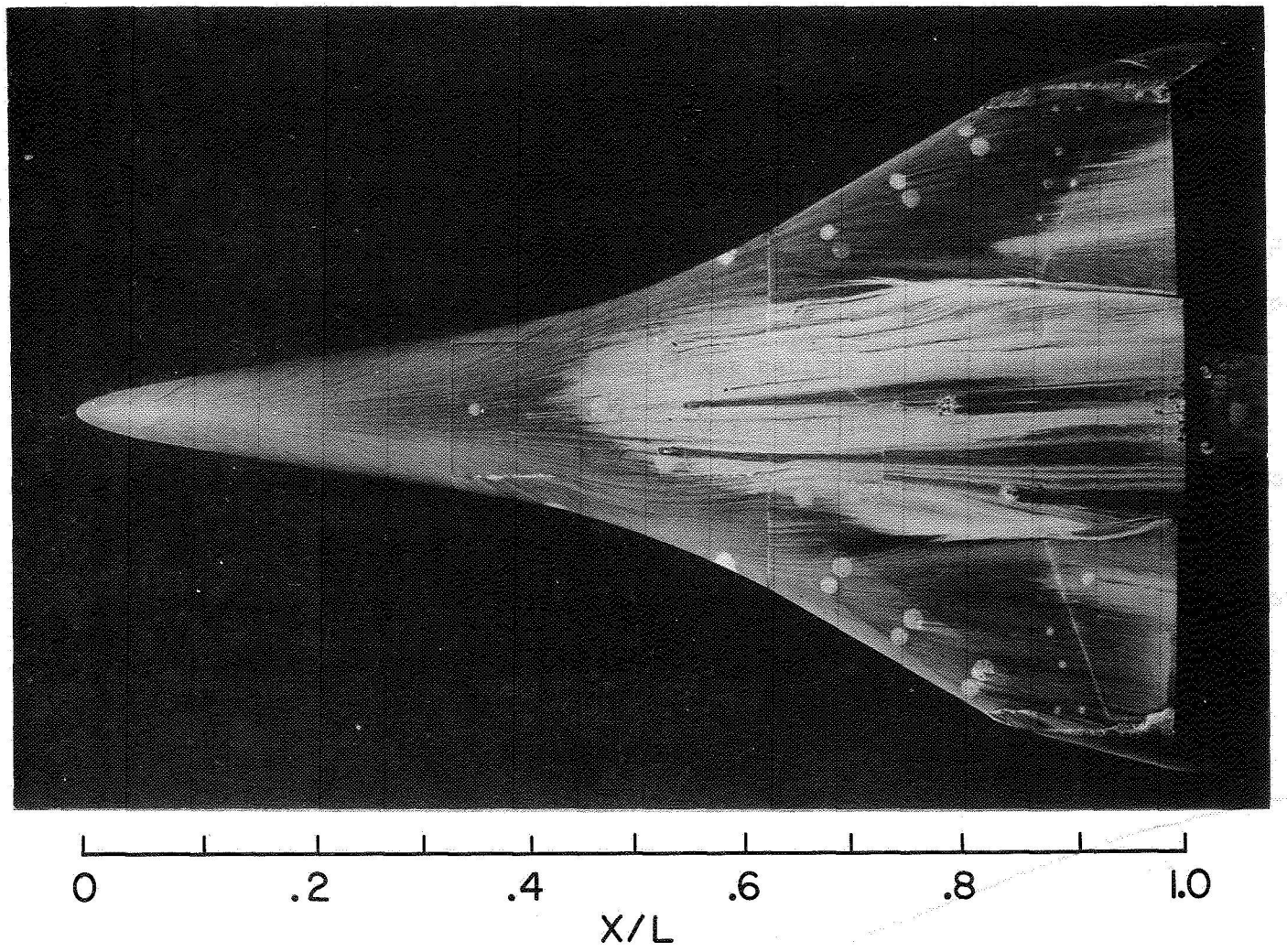

Figure 2

LONGITUDINAL HEATING DISTRIBUTION, $Re_{l_\infty} = 6.5 \times 10^6$

(Figure 3)

Representative heating distributions for the model without joints are shown in the next 3 slides for comparison with theory. In this figure a laminar distribution obtained at a Reynolds number of 6.5×10^6 is compared with a local swept cylinder theory. This theory assumes a cylinder having a sweep angle equal to the local body surface inclination and a diameter equal to the local body width. The cylinder cross-flow velocity gradients are modified by the method of reference 2 to account for the flattened lower surface contour and chine radius of the model. Relatively good results are obtained with this prediction technique for the forward portion of the model. The previously mentioned effect of the wing on the fuselage flow may be seen in the local decrease in heating which occurs at an X/L of .54.

LONGITUDINAL HEATING DISTRIBUTION

NAR DELTA ORBITER

$\alpha = 30°$; $Re_{l\infty} = 6.5 \times 10^6$; $L/R_s = 132$

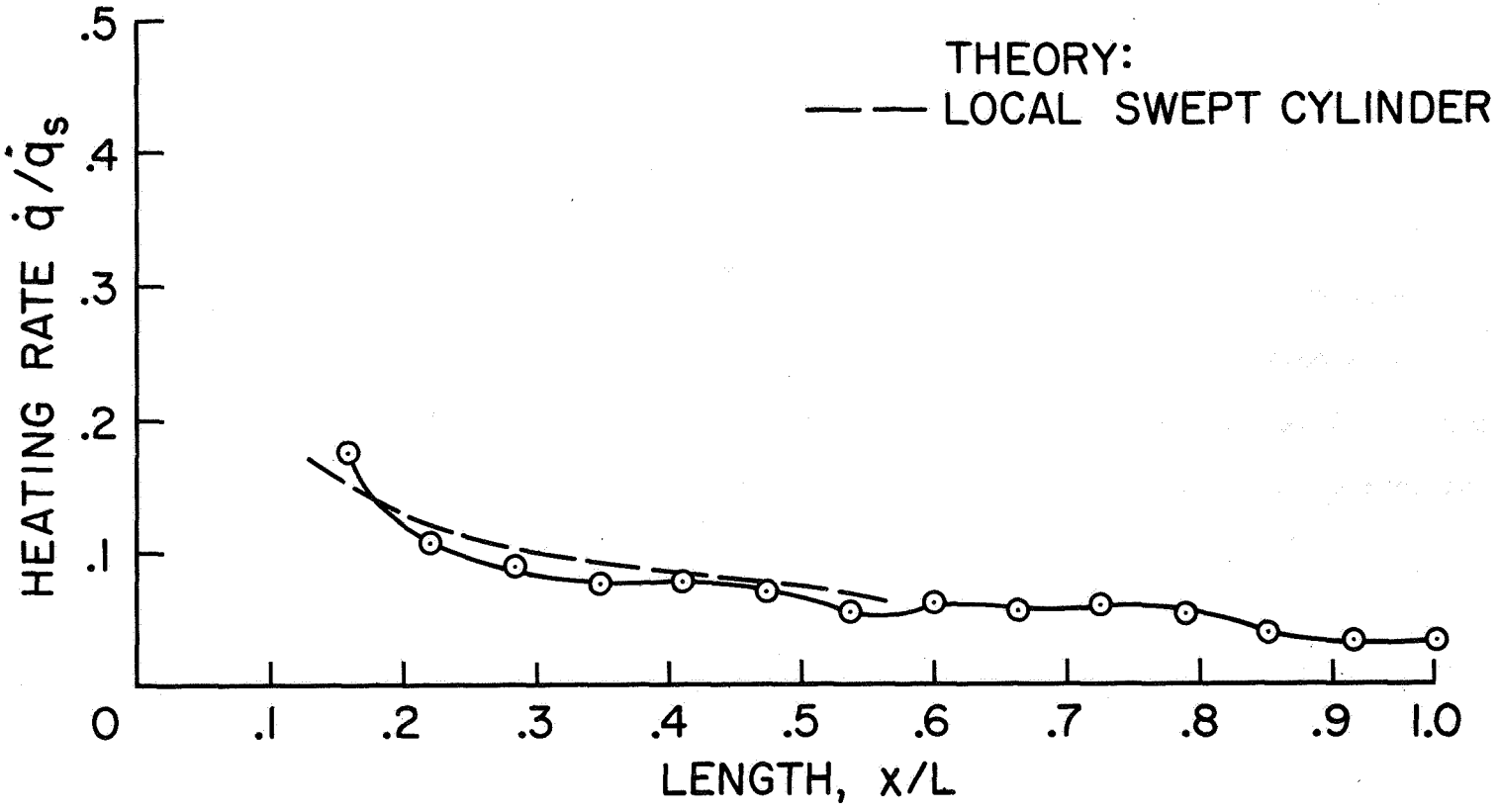

Figure 3

LONGITUDINAL HEATING DISTRIBUTION, $Re_{l_\infty} = 8.2 \times 10^6$

(Figure 4)

In this figure, the turbulent theory of reference 3 is compared with data from a test in which a substantial run of turbulent flow was obtained. Model surface pressures were computed with the method of reference 4 which uses a conical flow approximation with measured shock angles. Results for Reynolds analogy factors of 1.0 and the Colburn form (reference 5) are shown. The wing-fuselage flow interference effects referred to previously are also seen in this figure.

LONGITUDINAL HEATING DISTRIBUTION

NAR DELTA ORBITER

$\alpha = 30°$; $Re_{l\infty} = 8.2 \times 10^6$; $L/R_s = 132$

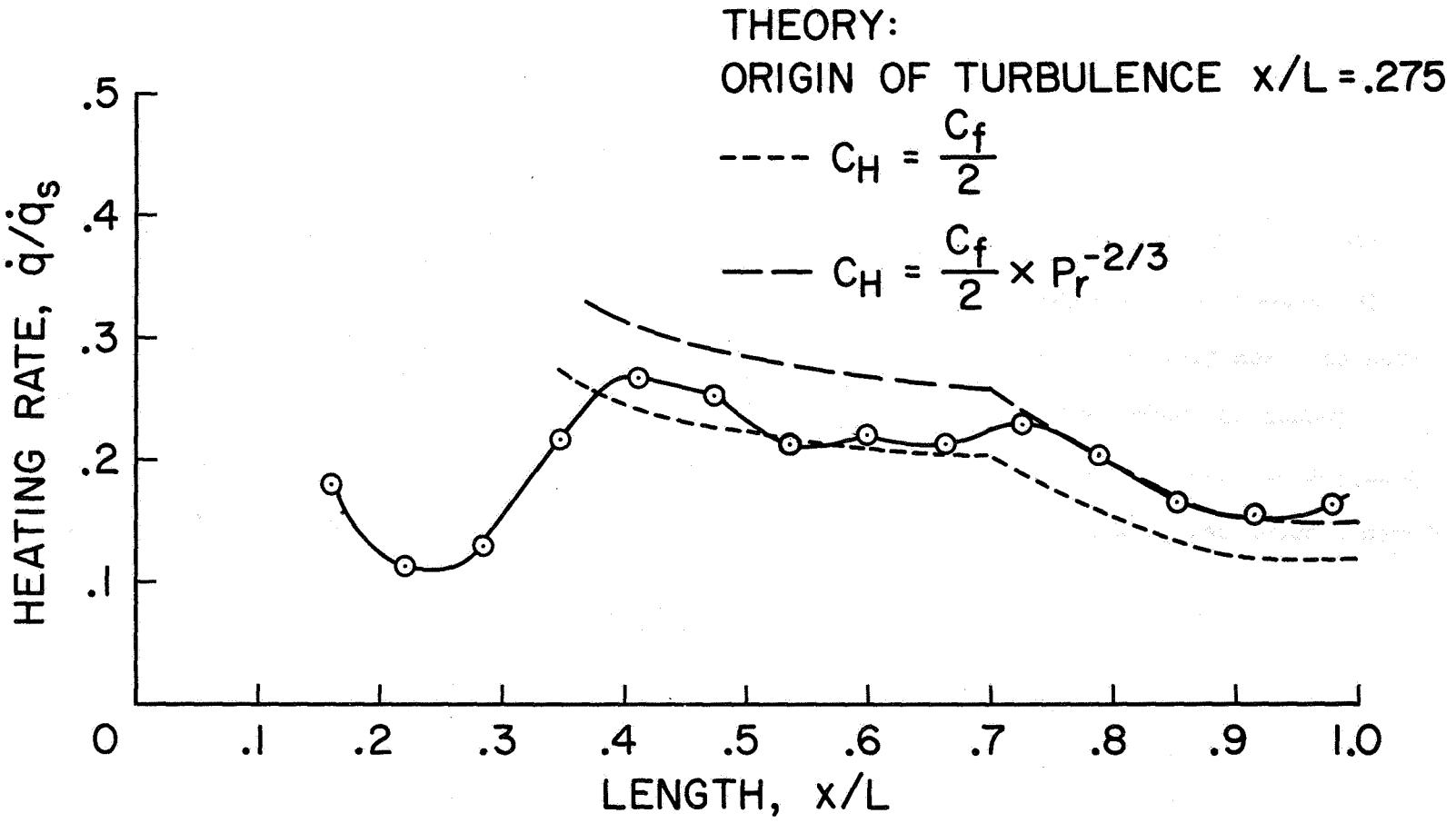

Figure 4

LONGITUDINAL HEATING DISTRIBUTION, $Re_{l_\infty} = 7.8 \times 10^6$

(Figure 5)

The heating distribution shown in this figure is compared with the theory of reference 3 using the Colburn form of the Reynolds analogy. Although the data for this particular test are believed to represent a boundary layer which was tripped by roughness caused from the impact of tunnel heater particles, they are shown because of the extensive run of turbulent flow that was obtained. The origin of turbulence was arbitrarily assumed to be the nose of the model in the theoretical calculations. The influence of the body boattail starting at an X/L of .7 may be clearly seen.

LONGITUDINAL HEATING DISTRIBUTION

NAR DELTA ORBITER

$\alpha = 30°$; $Re_{l\infty} = 7.8 \times 10^6$; $L/R_s = 132$

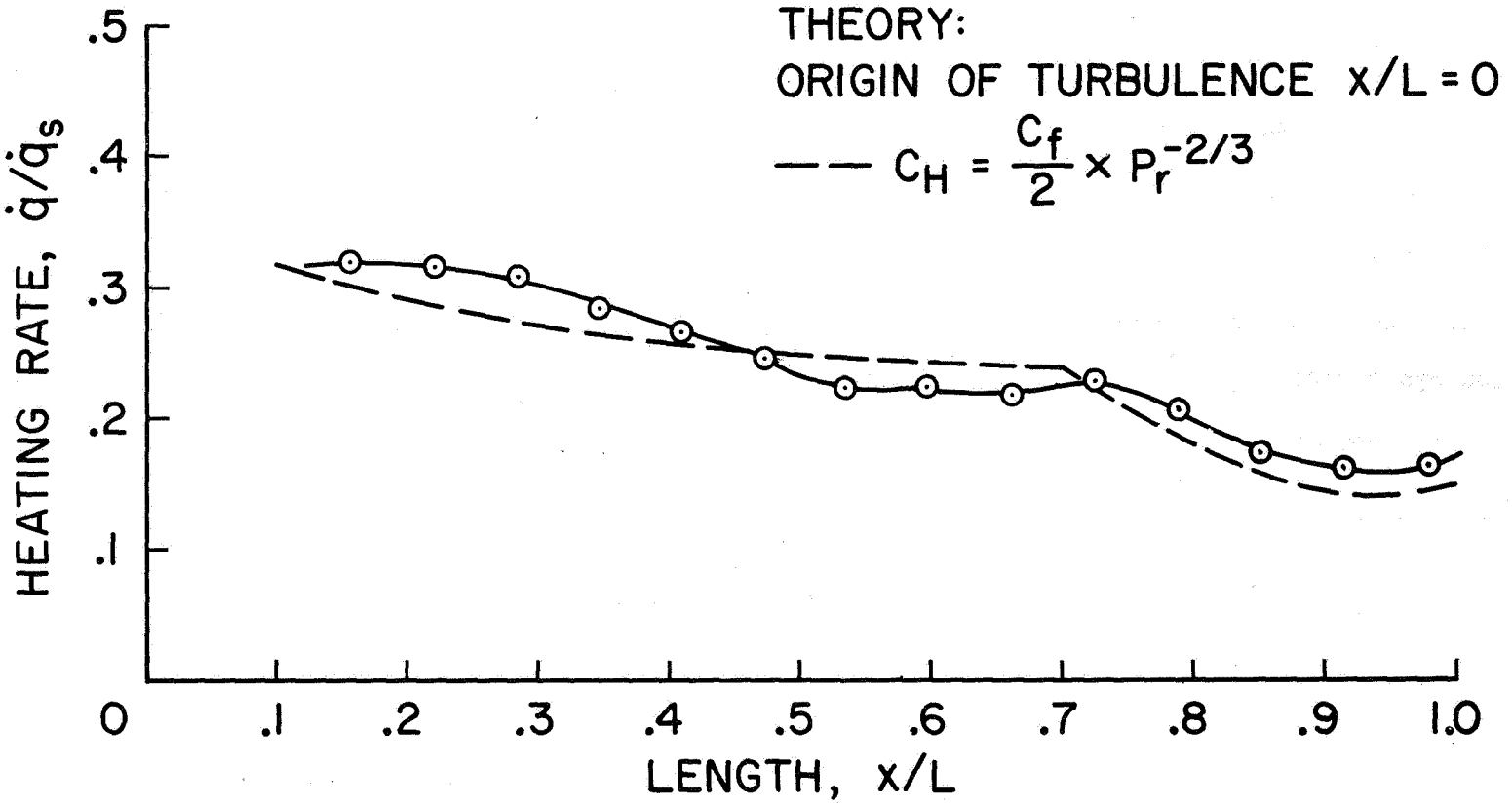

Figure 5

EFFECT OF SIMULATED HEAT-SHIELD PANEL JOINTS

ON BOUNDARY-LAYER TRANSITION

(Figure 6)

The effect of the two simulated panel joint configurations on the delta orbiter model in the Reynolds number range of 6.5 to 9.0 x 10^6 are shown in this figure. The slot joints did not trip the boundary layer and laminar flow was maintained at a Reynolds number of 7.8 x 10^6. The raised joints, however, caused transition to occur at a model station of about .5 at a Reynolds number of 6.8 x 10^6. Increasing the Reynolds number to 9.0 x 10^6 caused a forward movement of transition and a substantial increase in the level of heating as a more fully developed turbulent flow was obtained.

EFFECT OF SIMULATED HEAT-SHIELD PANEL JOINTS ON BOUNDARY-LAYER TRANSITION

NAR DELTA ORBITER

$\alpha = 30°$; $M_\infty = 7.4$; $L/R_s = 132$

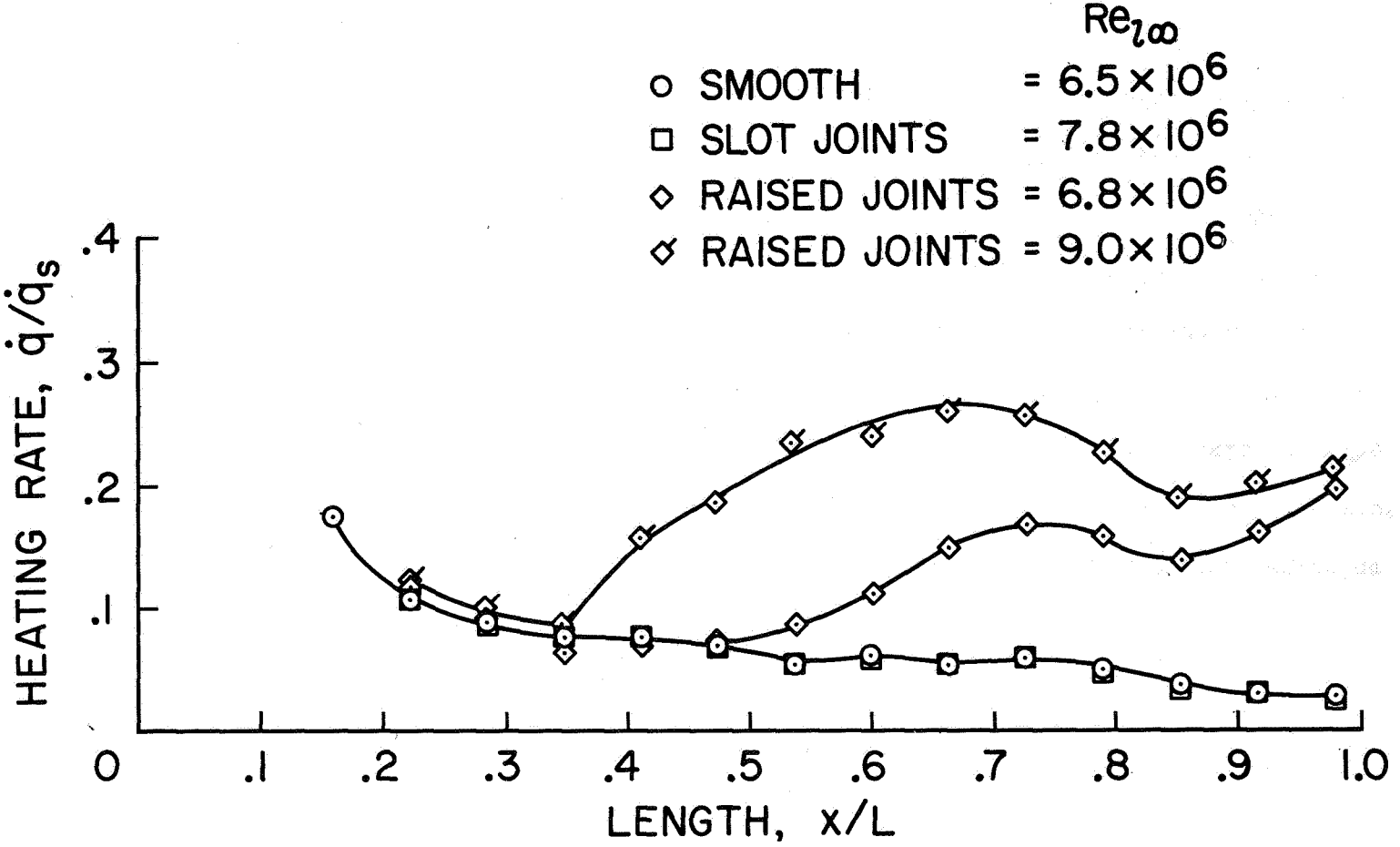

Figure 6

EFFECT OF PANEL JOINTS ON LOCATION OF TRANSITION ONSET

(Figure 7)

The effect of the two simulated panel joint configurations on the location of the beginning of transition are summarized in this figure. An important result of these tests is that the slot joints are not sufficiently disturbing to the boundary layer to cause premature transition. The raised joints, however, initiate transition at a Reynolds number approximately one half that at which laminar flow was obtained on the smooth and slot joint models. The transition criteria of references 6 and 7 are shown for comparison with the data. The MDAC criteria was computed for the divergence terms associated with both the forward fuselage flow, using a sweepback angle of 81.5°, and the wing flow, using a sweepback angle of 60°. It is seen that the two criteria predict the beginning of transition at Reynolds numbers below those obtained in these tests - even for the model with the raised joints.

EFFECT OF PANEL JOINTS ON LOCATION OF TRANSITION ONSET

NAR DELTA ORBITER

$\alpha = 30°$

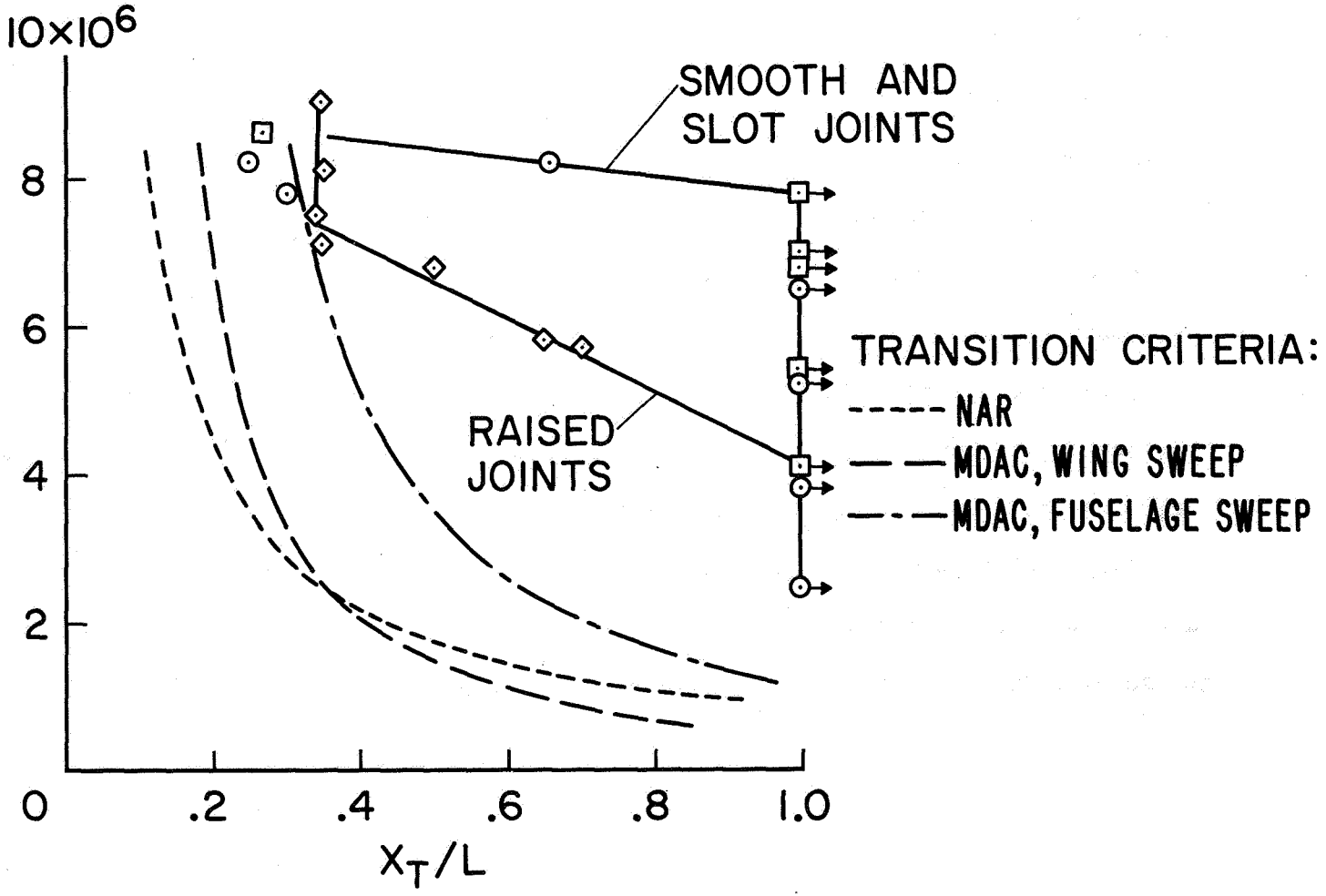

Figure 7

EFFECT OF TRANSITION REYNOLDS NUMBER

ON HEAT-SHIELD TEMPERATURE

(Figure 8)

Before an attempt is made to apply the present results to a shuttle vehicle, it is important to recognize that the test conditions do not fully simulate the entry environment and that other factors in addition to panel-joint roughness influence the stability of the orbiter boundary layer. Although the model edge Mach number is approximately correct, the wall to total enthalpy ratio of .43 is considerably greater than the values below .1 which are prevalent during entry. These and other factors such as structural waviness, vibration, opening for attitude control jets, landing gear etc., must all be carefully considered. As an aid in assessing the possible impact of the panel joint roughness, this figure shows radiation equilibrium temperatures at the rear of the shuttle for laminar and turbulent flow during entry. Using the results of the previous figure, the effect of premature transition to turbulent flow is illustrated. With transition occurring at a Reynolds number of 4×10^6 because of the panel joint roughness rather than at 8×10^6 for a smooth surface, the rearward portion of the orbiter is exposed to transitional or turbulent flow for nearly 300 additional seconds and the peak heat shield temperatures are increased nearly 139°C (250°F) from about 872°C (1600°F) to about 1011°C (1850°F). Although in this example scaling factors other than Reynolds number have been ignored, the results illustrate the importance of avoiding a raised panel joint configuration in the design of the heat shield.

EFFECT OF TRANSITION REYNOLDS NUMBER ON HEAT SHIELD TEMPERATURE OF DELTA ORBITER

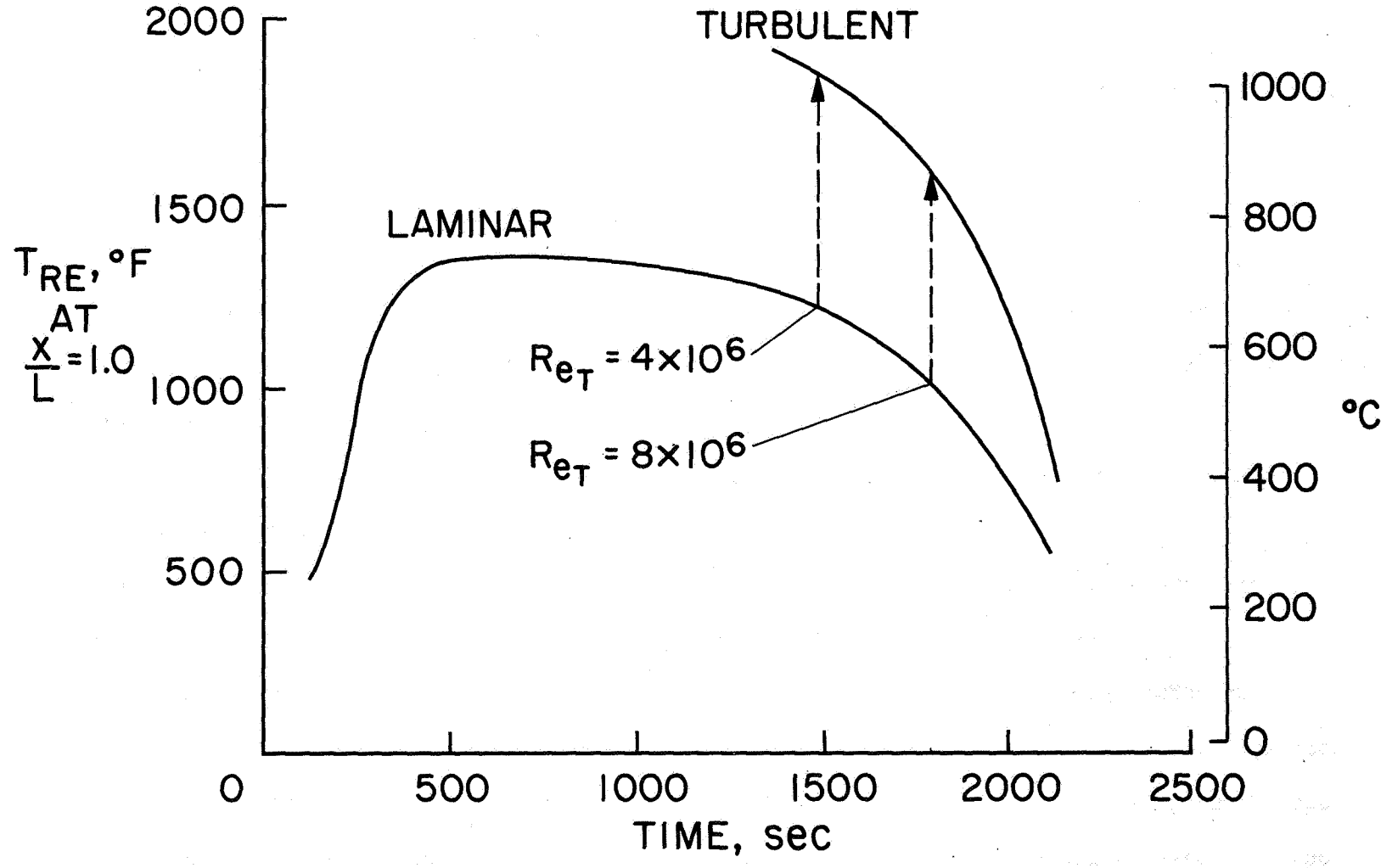

Figure 8

A series of tests has been conducted using models of a delta-wing orbiter to determine the effects of two simulated panel joint configurations on boundary-layer transition. Although the present test conditions of Mach number 7.4 and wall enthalpy ratio of .43 do not fully simulate the entry environment, the results illustrate the importance of the distributed roughness arising from heat-shield panel joints. The results are summarized as follows:

1. Premature boundary-layer transition was observed on a model having simulated heat-shield panels with raised joints.
2. Laminar flow was maintained on a model with a slot-type panel joint to a Reynolds number nearly twice that at which transition occurred with the raised joint model.
3. Significant increases in both the peak surface temperatures and the time during which turbulent flow occurs on the orbiter could result from the distributed roughness of raised heat-shield panel joints.
4. Laminar and turbulent heating levels for the smooth model were well predicted with available theories.
5. The transition criteria used by two Phase B contractors were found to predict the beginning of transition at Reynolds numbers below those obtained in the present tests, even for the models with simulated panel joints. The question of whether the criteria are overly conservative for flight conditions, however, cannot be answered at this time.
6. In spite of a smoothly faired wing-fuselage juncture on this highly swept delta model, evidence of a complex interference between the wing and fuselage flow was observed.

REFERENCES

1. Seegmiller, H. Lee: Surface-Flow Visualization Investigation of a Delta Wing Shuttle Configuration at a Mach Number of 7.4 and Several Reynolds Numbers. NASA TM X-62036, June 1970.
2. Bertram, Mitchel H.; and Henderson, Arthur, Jr.: Recent Hypersonic Studies of Wings and Bodies. ARS J., Vol. 31, No. 8, August 1961, pp. 1129-1139.
3. Spalding, D. B.; and Chi, S. W.: The Drag of a Compressible Turbulent Boundary Layer on a Smooth Flat Plate with and without Heat Transfer. J. Fluid Mech., Vol. 18, pt. 1, Jan. 1964, pp. 117-143.
4. Cleary, Joseph W.: Approximation for Distribution of Flow Properties in the Angle-Of-Attack Plane of Conical Flows. NASA TN D-5951, Aug. 1970.
5. Colburn, Allan P.: A Method of Correlating Forced Convection Heat Transfer Data and a Comparison With Fluid Friction. Trans. of the American Institute of Chemical Engineers, Vol. 29, 1933, pp. 174-210.
6. Masek, R.V.: Boundary Layer Transition on Lifting Entry Vehicle Configurations at High Angle-of-Attack. Space Transportation System Technology Symposium, NASA TM X-52876, Vol. I, 1970, pp. 445-462.
7. Moote, Jack D.: A Minimum Heating Flight Mode for High Lateral Range Space Shuttle Entries Including the Effects of Transition. Space Transportation System Technology Symposium, NASA TM X-53876, Vol. I, 1970, pp. 531-546.

EFFECTS OF ROUGHNESS ON HEATING AND BOUNDARY-LAYER TRANSITION

PART II - EFFECTS OF DISCRETE ROUGHNESS ON HEATING

By George G. Mateer
NASA Ames Research Center
Moffett Field, California

INTRODUCTION

In part one of this paper the effect of uniform, two-dimensional roughness on transition was investigated. Another type of roughness encountered on the shuttle is three-dimensional and discretely distributed (eg. bolt and rivet heads, tank attachments, and protruding corner of landing gear doors or thermal protection panels). Numerous investigations into the effects of discrete roughness on heating have been made on simple shapes such as plates and cones. Although much of this data has been correlated into parametric relationships that account for changes in Mach and Reynolds numbers, roughness, size, etc., it has not been demonstrated that these correlations can be applied to the space shuttle. Therefore, a preliminary investigation on the effects of roughness on heating was conducted on the windward surface of a typical delta-wing orbiter. The purpose of the experiment was to determine what parameters were needed to characterize the influence of roughness, and to relate roughness effects on the shuttle to those on simple shapes.

NOTATION

k	roughness height
l	distance between the roughness element and location of the turbulence wedge (figure 4)
L	model length
M	Mach number
$\dot{q}$	heating rate
$Re/_l$	Reynolds number per unit length
R	nose radius
T	temperature
u	velocity along streamline
x	distance along model centerline
α	angle of attack
δ	boundary layer thickness
μ	viscosity
ρ	density
ψ	turbulence wedge spreading angle (figure 6)

Subscripts

ℓ	centerline value
e	boundary layer edge
k	value at top of roughness element
s	stagnation point
t	total condition
w	wall condition
∞	freestream condition

MODEL AND TEST CONDITIONS

(Figure 1)

A model of North American's earliest delta wing configuration (NA129) was used in these tests. It is sketched on figure 1. The roughness elements were circular cylinders 0.3 cm in length and of varying diameters. The elements were located on the windward surface 17.5 cm from the nose and 0.8 cm apart. The axes of revolution were parallel to the centerline of the model.

The test data were obtained in the Ames 3.5-foot hypersonic wind tunnel at a freestream Mach number of 7.4. Angles of attack were 15^{o}, 25^{o}, and 35^{o}.

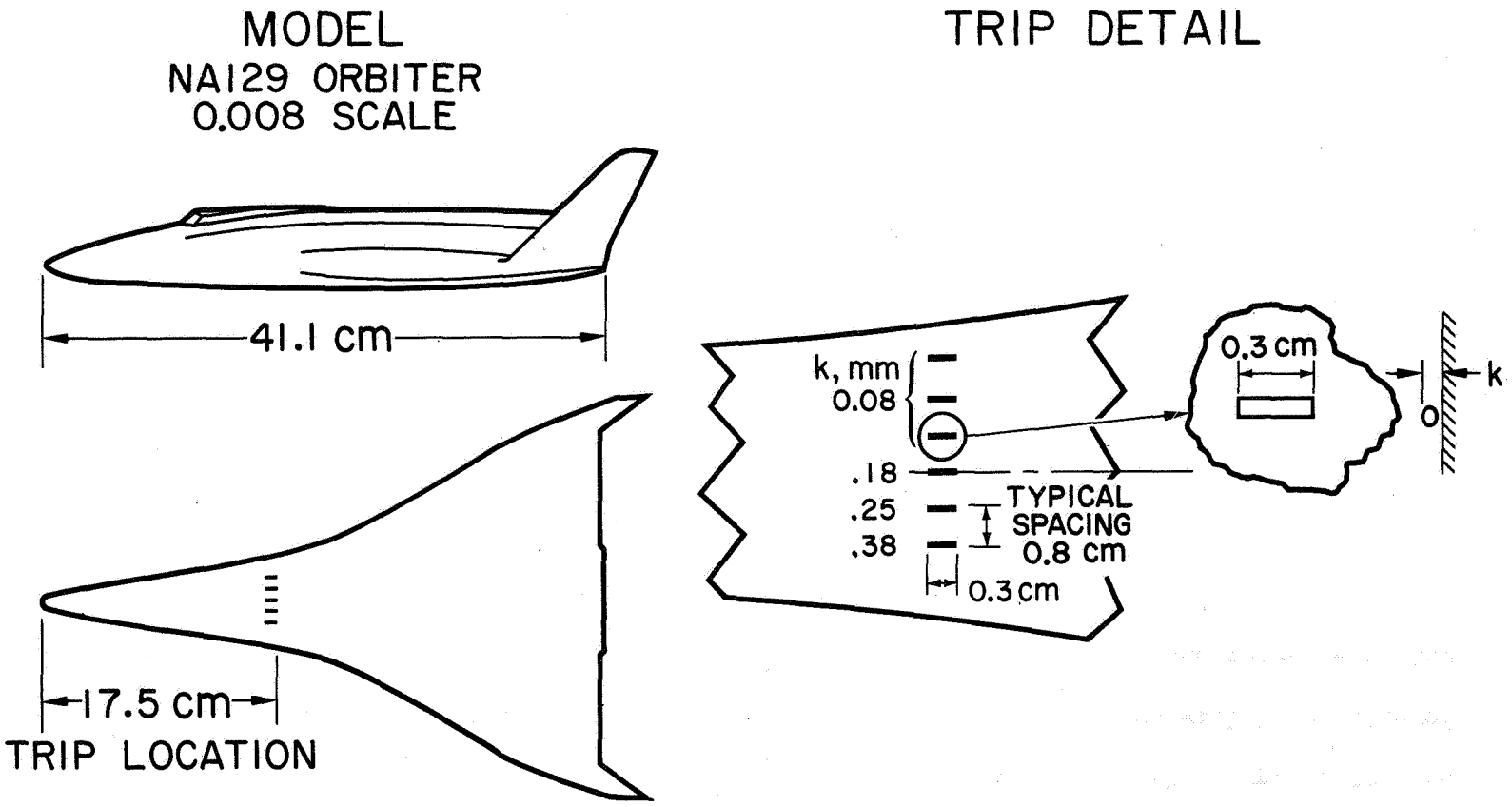

TEST CONDITIONS

$M_\infty = 7.4$ $\quad T_t = 722\,°K$ $\quad T_w = 346\text{-}394\,°K$

$\left(\frac{Re}{l}\right)_\infty = 6.9 \times 10^6 - 2.8 \times 10^7\ m^{-1}$

$\alpha = 15°,\ 25°,\ 35°$

Figure 1

WINDWARD SURFACE PHASE-CHANGE PAINT PHOTOGRAPH

(Figure 2)

The phase-change paint technique was used to obtain the test data and a typical photograph of the melt pattern at 25^{o} angle of attack is shown. The corresponding freestream unit Reynolds number was 1.3×10^{7} per meter. This figure illustrates that an effect of roughness of this type is to produce a turbulence wedge downstream. In what follows three aspects of wedge formation will be considered; (1) the size of roughness required to form a wedge, (2) the location of the wedge relative to the roughness, and (3) the growth of the wedge.

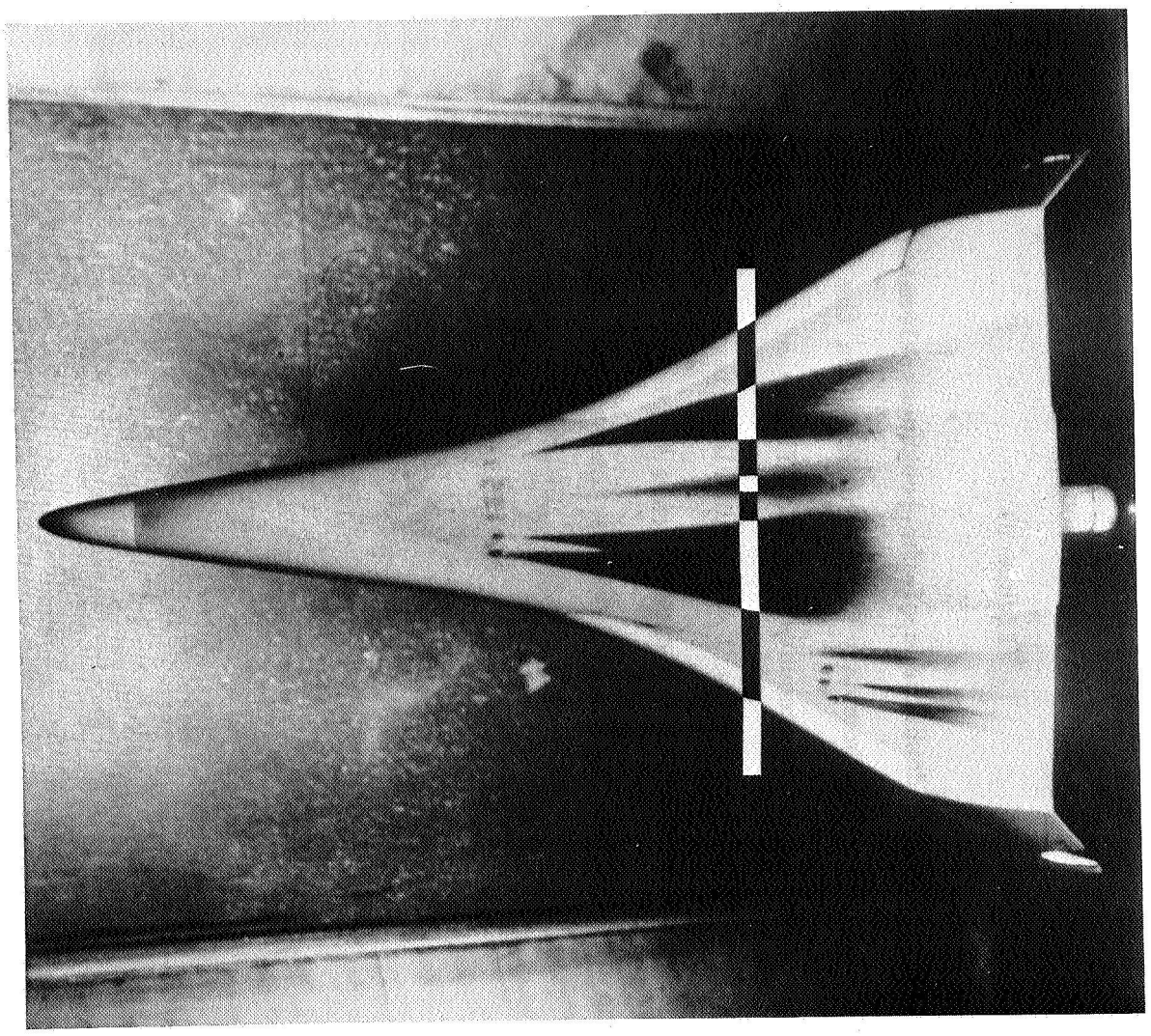

Figure 2

HEATING AFT OF ROUGHNESS

(Figure 3)

A lateral heating distribution downstream of the roughness elements for the model and test conditions of the previous figure is shown. The boundary layer thickness on the centerline was calculated by a method described in reference 1, which accounts for the effects of crossflow. The measured laminar heating distribution and a calculated (refs. 1 & 2) turbulent level on the centerline are also shown. A comparison of the rough and smooth heating data reveals that the maximum heating rate inside all of the wedges is about the same as the turbulent level on the smooth model, irrespective of the size of the roughness element.

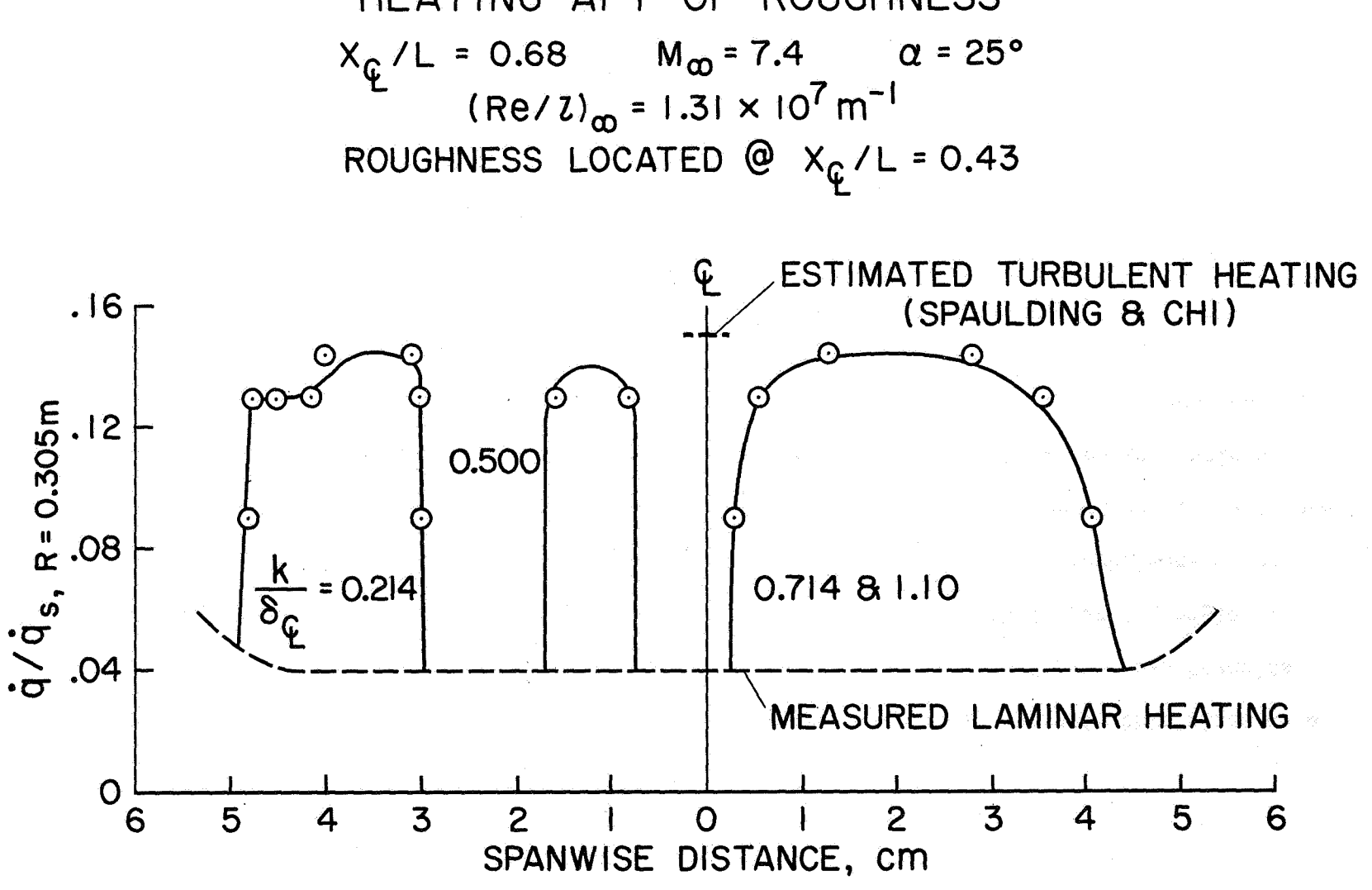
HEATING AFT OF ROUGHNESS
$X_{\mathcal{L}}/L = 0.68$ $M_\infty = 7.4$ $\alpha = 25°$
$(Re/\ell)_\infty = 1.31 \times 10^7\ m^{-1}$
ROUGHNESS LOCATED @ $X_{\mathcal{L}}/L = 0.43$
$\mathcal{L}$
ESTIMATED TURBULENT HEATING
(SPAULDING & CHI)
$\dot{q}/\dot{q}_s$, R = 0.305m
.16
.12
.08
.04
0
0.500
$\frac{k}{\delta_{\mathcal{L}}} = 0.214$
0.714 & 1.10
MEASURED LAMINAR HEATING
6 5 4 3 2 1 0 1 2 3 4 5 6
SPANWISE DISTANCE, cm

Figure 3

SEPARATION BETWEEN ROUGHNESS AND TURBULENCE

(Figure 4)

The distance between the roughness element and the turbulence wedge is shown in this slide as a function of the roughness Reynolds number defined in reference 3. The value of roughness Reynolds number at which a wedge first appears at a given location (l), decreases with increasing angle of attack. As the size of the roughness or the unit Reynolds number increases, the turbulence wedge moves closer to the roughness until $l \approx 0$ (a condition denoted as "effective roughness" in reference 3). The sensitivity of l to changes in roughness Reynolds number increases with decreasing angle of attack. Although not shown, the trend of existing data for flat plates (e.g. ref. 4) shows that l is even more sensitive to roughness Reynolds number than these shuttle data at $\alpha = 15^{o}$.

SEPARATION BETWEEN ROUGHNESS AND TURBULENCE

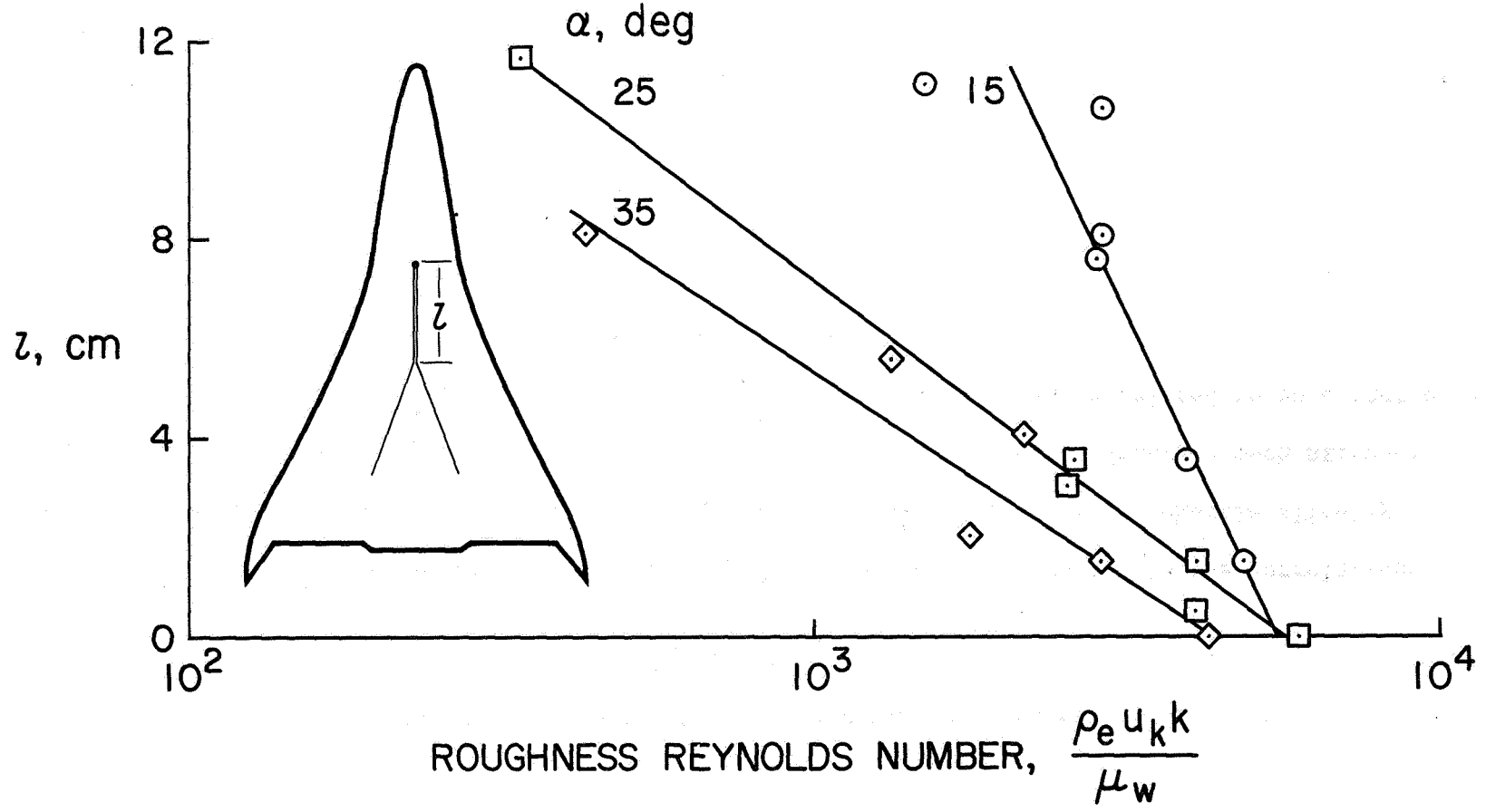

Figure 4

COMPARISON OF EFFECTIVE ($\ell \approx 0$) REYNOLDS NUMBERS

(Figure 5)

A comparison of the effective Reynolds numbers from the previous figure with the correlations ($\alpha = 0^{\circ}$) of reference 3 is shown. Effective roughness Reynolds numbers for the shuttle slightly increase with Mach number, whereas, the correlations for plates and cones indicate a much stronger effect of Mach number. The difference in the effect of Mach number could be related to an effect of angle of attack not accounted for in the correlations based on data at $\alpha = 0^{\circ}$.

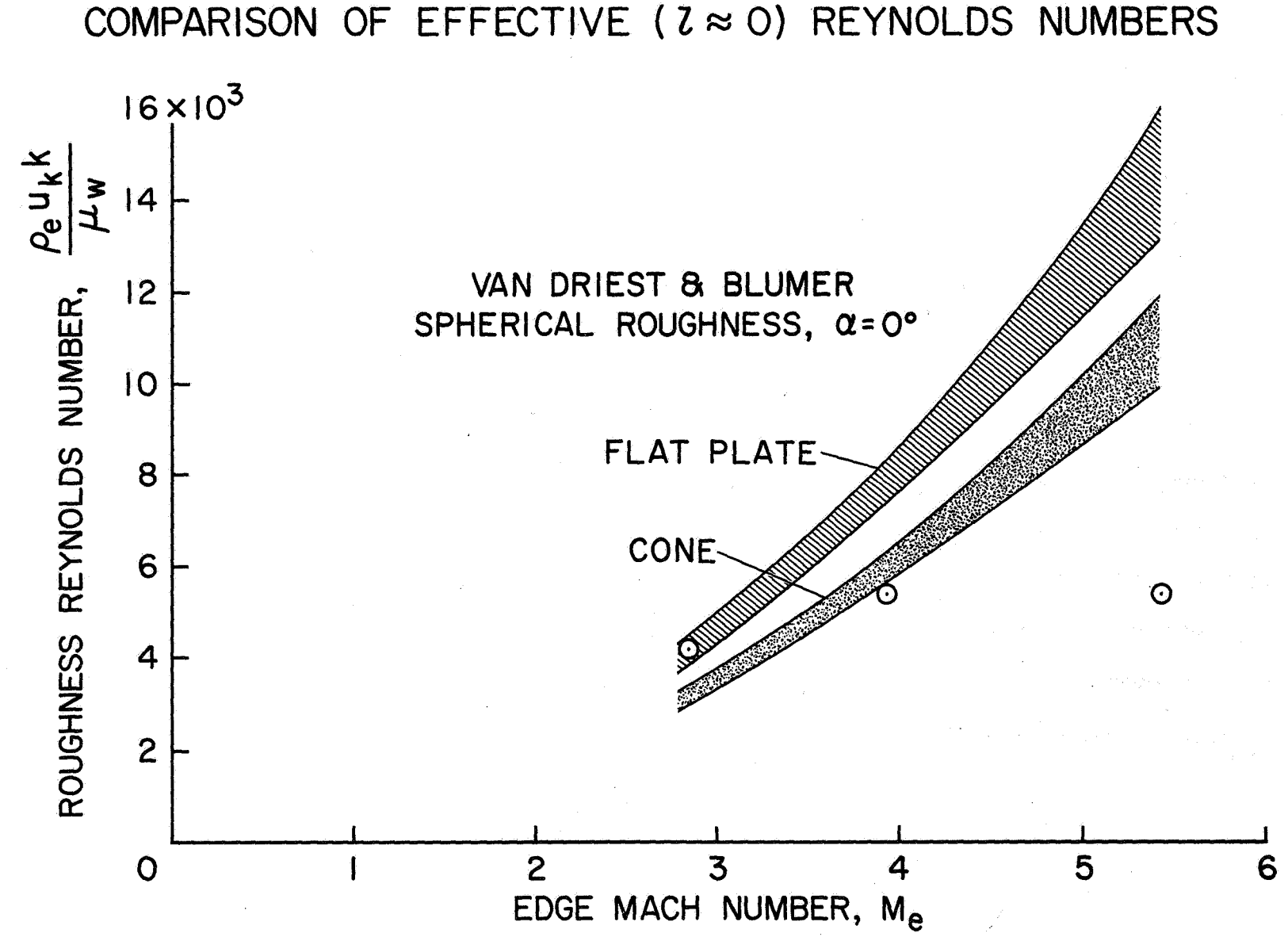
COMPARISON OF EFFECTIVE ($\ell \approx 0$) REYNOLDS NUMBERS
ROUGHNESS REYNOLDS NUMBER, $\frac{\rho_e u_k k}{\mu_w}$
16×10^3
14
12
10
8
6
4
2
0
1
2
3
4
5
6
EDGE MACH NUMBER, M_e
VAN DRIEST & BLUMER
SPHERICAL ROUGHNESS, $\alpha = 0°$
FLAT PLATE
CONE

Figure 5

EFFECT OF ANGLE OF ATTACK ON TURBULENCE SPREADING ANGLE

(Figure 6)

The growth of a turbulence wedge may be characterized by a spreading angle as defined in this figure. The angle is shown as a function of angle of attack and was found to be independent of roughness height. The additional data for angles of attack other than 15°, 25°, and 35° were also obtained from phase-change paint tests on similar models in the same facility where the roughness was not controlled and the height was not known. The spreading angle increases from the flat plate value for angles of attack greater than 15° and may level off or decrease slightly for $\alpha > 35^{\circ}$. In contrast, the spreading angle from unpublished flat plate data that we are studying is relatively constant at 10° regardless of the local Mach number. The low speed data of ref. 5 also indicate a spreading angle of 10°.

EFFECT OF ANGLE OF ATTACK ON TURBULENCE SPREADING ANGLE

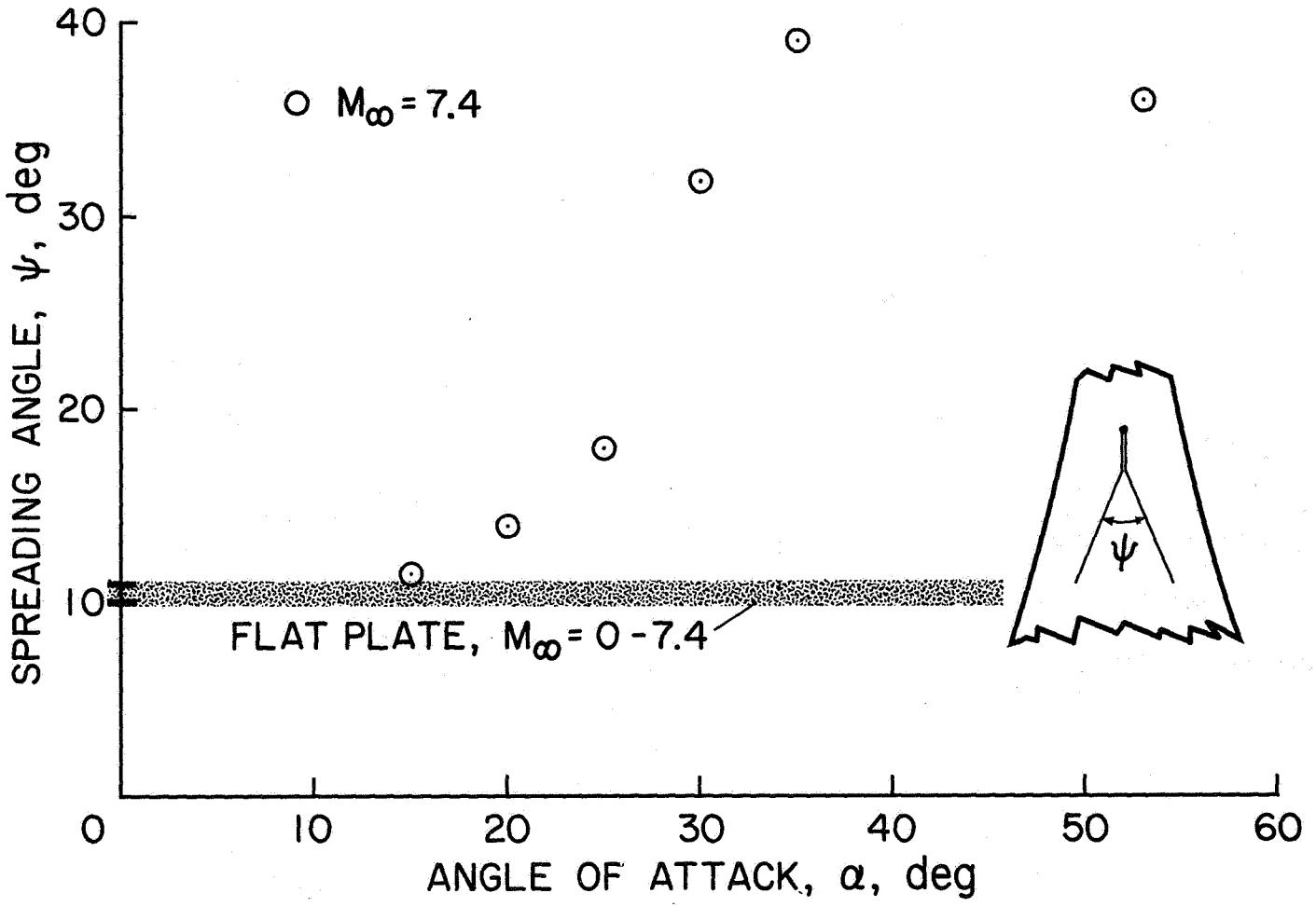

Figure 6

CONCLUSIONS

Specific conclusions that can be drawn from the present data are:

1. Heating rates inside the observed turbulence wedges are comparable to estimated smooth model turbulent levels and independent of the size of the roughness generating the wedge.
2. The separation distance between roughness and the accompanying turbulence wedge is a function of unit Reynolds number, roughness height, and angle of attack.
3. Depending on the angle of attack, effective roughness Reynolds numbers are less than or equal to those on flat plates at the same edge Mach number.
4. The spreading angle of a turbulence wedge increases with angle of attack.

It appears that existing roughness correlations for flat plates and cones may not be applicable to the complex shuttle configurations. Furthermore, additional tests will have to be performed to determine whether wall temperature effects can be adequately accounted for through the use of a roughness Reynolds number alone.

REFERENCES

1. Marvin, J. G., Seegmiller, H. L., Lockman, W. K., Mateer, G. G., Pappas, C. C. and DeRose, C. E., "Surface Flow Patterns and Aerodynamic Heating on Space Shuttle Vehicles," AIAA Paper No. 71-594, June 1971.
2. Spaulding, D. E., and Chi, S. W., "The Drag of a Compressible Turbulent Boundary Layer on a Smooth Flat Plate with and without Heat Transfer," J. Fluid Mech., Vol. 18, pt. 1, Jan. 1964, pp. 117-143.
3. Van Driest, E. R., and Blumer, C. B., "Boundary Layer Transition at Supersonic Speeds --- Three Dimensional Roughness Effects (Spheres)," JAS, Vol. 29, No. 8, August 1962.
4. Hicks, R. M., Harper, W. R., Jr., "A Comparison of Spherical and Triangular Boundary-Layer Trips on a Flat Plate at Supersonic Speeds," NASA TM X-2146, December 1970.
5. Gregory, N., and Walker, W. S., "The Effect on Transition of Isolated Surface Excrescences in the Boundary Layer," Aero. Res. Council, Part I, R & M No. 2779, London (1951), p. 1-23.

LEE-SIDE FLOW PHENOMENA ON SPACE SHUTTLE CONFIGURATIONS AT HYPERSONIC SPEEDS

PART I – FLOW SEPARATION AND FLOW FIELD VISCOUS PHENOMENA OF A DELTA-WING SHUTTLE ORBITER CONFIGURATION

By J. W. Cleary
NASA Ames Research Center
Moffett Field, California

INTRODUCTION

An analysis of heating on the leeward surface of shuttle vehicles and on shielded components such as the canopy and vertical tail is difficult because of a lack of knowledge of the flow field on the lee side. Experimental results have been published (references 1 to 3, e.g.) for simple conical type bodies that show the lee side of the flow field consists essentially of a region of separated flow lying adjacent to the surface and beneath an unseparated inviscid type flow. The separated flow may have vortices that are either symmetrically or asymmetrically disposed and, depending on angle of attack, imbedded shock waves may exist at about where the circumferential flow separates from the surface. In addition to these complexities, the flow over the lee side of shuttle-type vehicles may be affected by nose bluntness, body curvature, and the effects of interference from the canopy and the wing.

Pitot-pressure surveys of the flow field can give useful information on these complexities of the flow that is helpful to an analysis of heating. The present experimental effort endeavors, by means of pitot-pressure surveys, to investigate the more significant aspects of the lee-side flow field of a typical delta-wing orbiter. Measurements of pitot-pressure distributions are presented to demonstrate the effects of varying three fundamental parameters: (1) flow-field axial and spanwise positions, (2) angle of attack, and (3) Reynolds number. The measurements are supplemented by shadowgraphs of the flow and oil streaks of the surface streamlines. The tests were conducted in the Ames 3.5-foot hypersonic wind tunnel in air at a Mach number of 7.4.

DELTA-WING ORBITER MODEL INSTRUMENTED WITH FLOW-FIELD RAKES

$M_\infty = 7.4$, $Re_{\infty_L} = 1.5 \times 10^6$ to 9.0×10^6, $\alpha = 0°$ to $60°$, $L = 40.4$ cm, $b = 27.2$ cm

(Figure 1)

The pitot-pressure investigation of the flow field was conducted on the delta-wing-body configuration shown in figure 1. This configuration is a .0075-scale model of the shuttle orbiter proposed by North American Rockwell Corporation and is designated the 134 full-scale vehicle. The wing is swept back 60° and has 7° dihedral. The model was instrumented with pitot-pressure rakes on the windward and leeward sides. The pitot probes were mounted with their axes parallel to the model reference axis which is parallel to the middle half of the windward and leeward sides of the body. As shown in figure 1, the rakes were attached to a platform at $y/\frac{b}{2} = 0$, .21, .41, .59, and .78 with the probes at $x/L = .98$. In addition, the rakes were attached to the body on centerline with the probes at $x/L = .35$ and .60.

The probes are stainless steel tubing with inside and outside diameters of 1.07 mm and 1.58 mm, respectively. The probes are spaced 4 outside diameters apart on the leeward rake and 2 diameters apart on the windward rake. A body axes system of coordinates is used to define the position of the probes.

While measurements were made on centerline for angles of attack from 0° to 60°, lee-side results for angles of attack of 15° and 30° only are presently being presented. Results are given for Reynolds numbers based on model length from 1.5×10^6 to 9.0×10^6 and for a free-stream Mach number of 7.38. Because, in general, the probes were not alined with the local flow and flow angles are not known, the data are presented in uncorrected form. Effects of probe misalinement are discussed next.

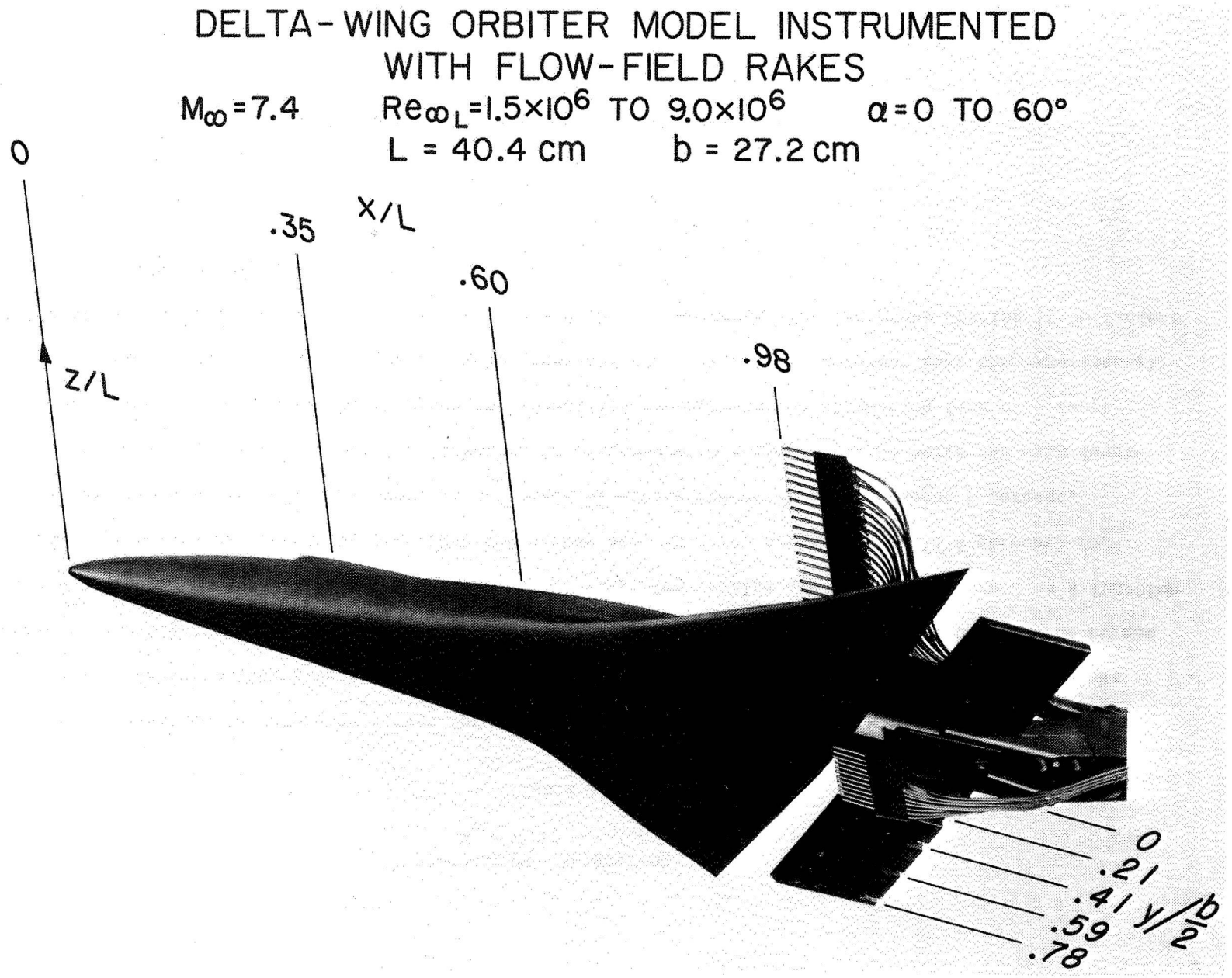
DELTA-WING ORBITER MODEL INSTRUMENTED
WITH FLOW-FIELD RAKES
$M_\infty = 7.4$
$Re_{\infty_L} = 1.5\times10^6$ TO 9.0×10^6
$\alpha = 0$ TO $60°$
L = 40.4 cm
b = 27.2 cm
0
.35
X/L
.60
.98
Z/L
0
.21
.41
.59
.78
Y/(b/2)

Figure 1

PITOT-PROBE CALIBRATION
$M_\infty = 7.4$, $\gamma = 1.4$

(Figure 2)

It is asserted in reference 4 that for supersonic Mach numbers, pitot probes of the type used in the present investigation give accurate measurements for flow misalinement angles up to 20°. In the present investigation, the measurements of probes outside the flow field and exposed to the free stream give a check on this assertion for a Mach number of 7.4. The results are shown in figure 2 as a function of angle of attack and it can be seen that the probes are, in fact, accurate (within 4 percent) for angles of attack up to 20°. Moreover, at 30° angle of attack the error is only about 9 percent.

For interest, the experimental calibration is compared with a simple cosine curve and with swept-cylinder theory. The latter theory gives the normalized pressure on the stagnation line of a swept cylinder and is analogous to successive probes that are adjacent. It is apparent that the experimental calibration is more accurate than sweep theory and this is evidence that the probe spacing is sufficient to give interference-free measurements.

PITOT-PROBE CALIBRATION

$M_\infty = 7.4 \quad \gamma = 1.4$

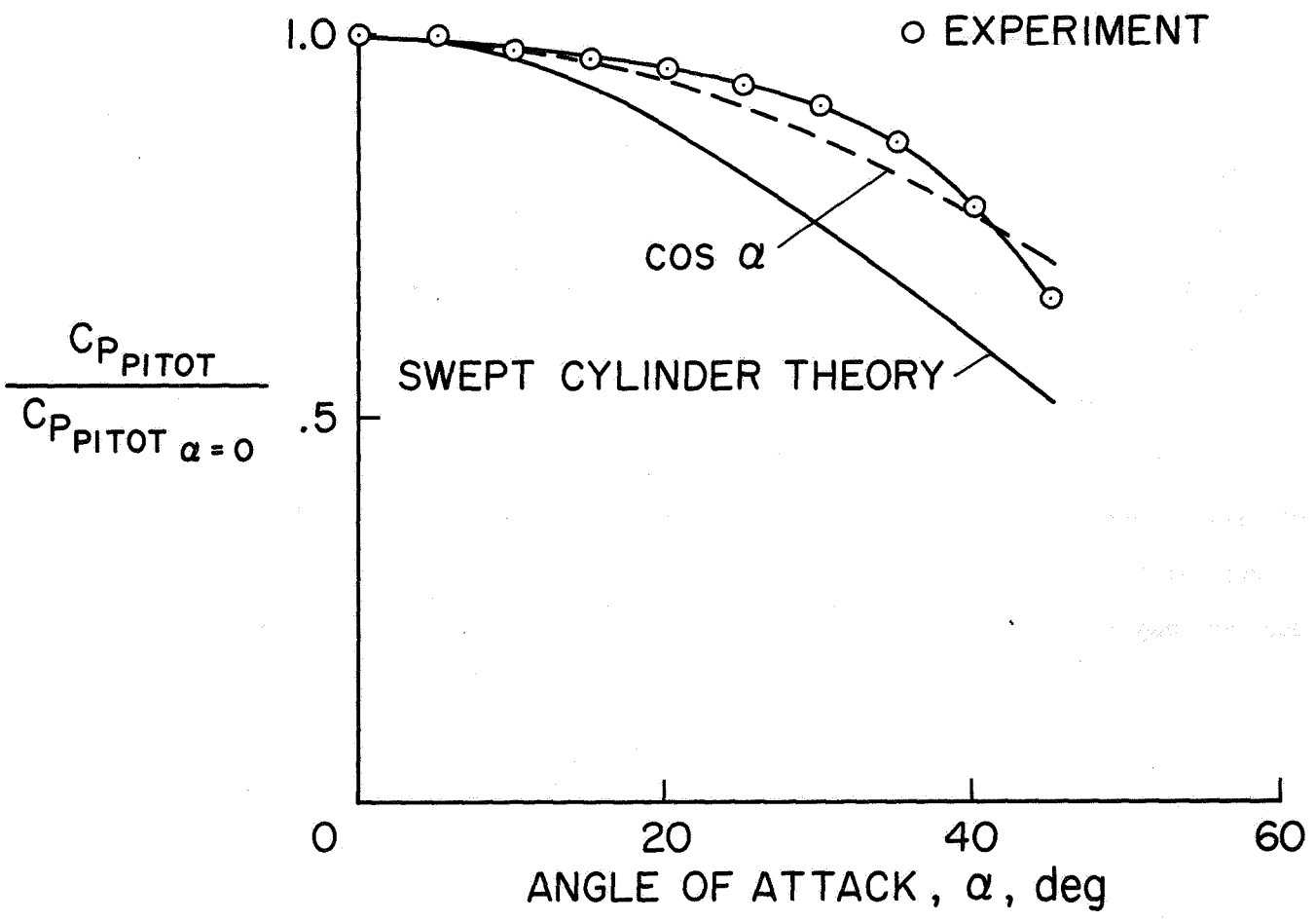

Figu

PITOT-PROBE CHARACTERISTICS

$M_\infty = 7.4, \quad \gamma = 1.4$

(Figure 3)

In order to relate the pitot-pressure measurements to imbedded shock-wave phenomena that can occur in the flow field, pitot pressures were estimated as a function of total flow-deflection angle for single and two oblique-shock systems and for isentropic flow (limiting case of multiple shock waves). The results, shown in figure 3, were obtained from oblique-shock theory.

Later it will be shown that for the lee side, the measured coefficients of pitot pressure are less than about 4 even in the unseparated region of the flow field. From figure 3, it is concluded that for these low values of pitot-pressure coefficient, the imbedded waves are weak and shock-wave deflections of the flow are small. Large flow deflection angles for stronger waves that are associated with the upper branches of the curves of figure 3 are precluded by a priori knowledge of the lee-side flow from shadowgraphs. These shadowgraphs are presented next with the surface flow superimposed.

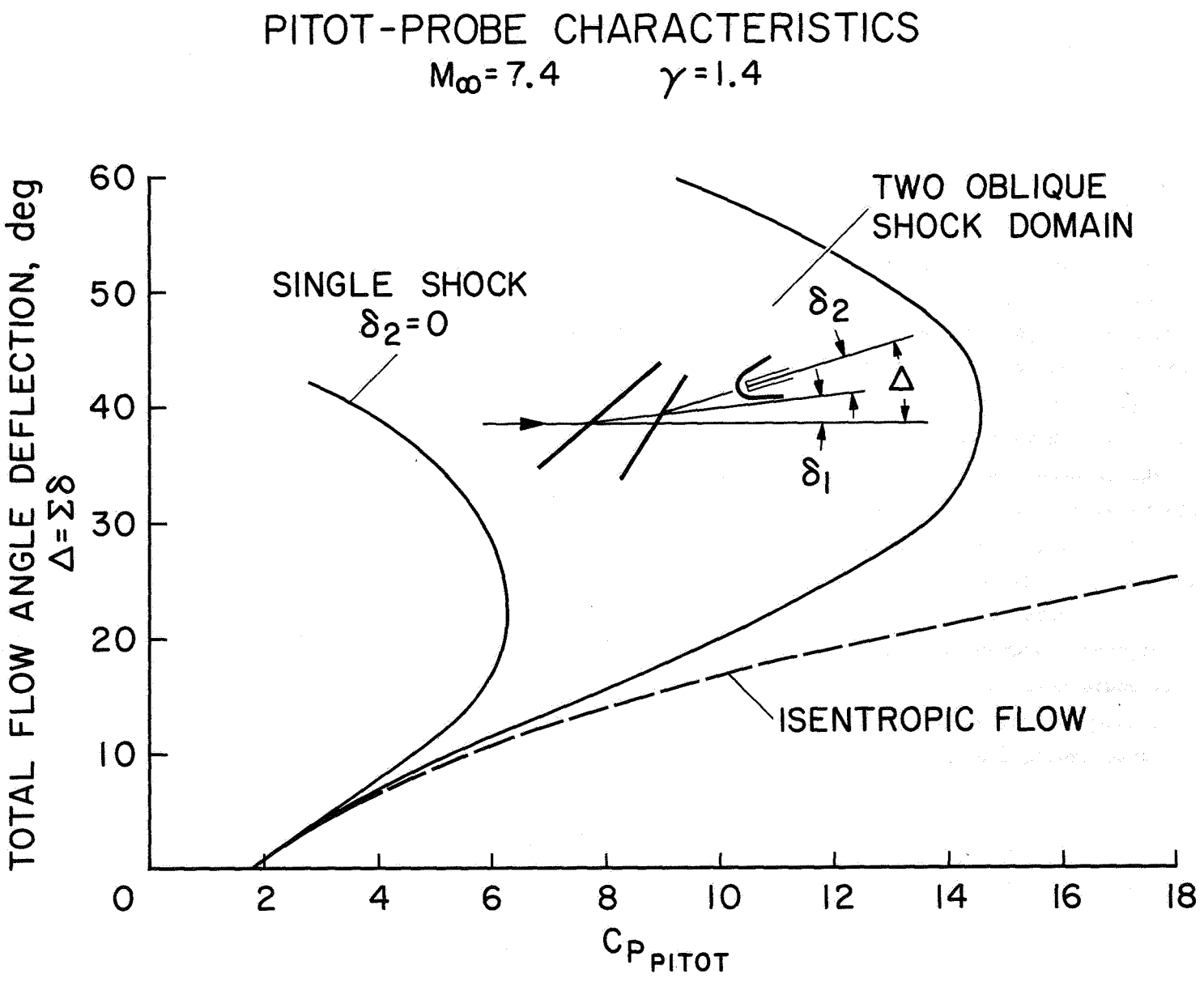
PITOT-PROBE CHARACTERISTICS
$M_\infty = 7.4$ $\gamma = 1.4$
TOTAL FLOW ANGLE DEFLECTION, deg
$\Delta = \Sigma\delta$
60
50
40
30
20
10
0
2
4
6
8
10
12
14
16
18
$C_{P_{PITOT}}$
SINGLE SHOCK
$\delta_2 = 0$
TWO OBLIQUE
SHOCK DOMAIN
δ_2
Δ
δ_1
ISENTROPIC FLOW

Figure 3

SIDE VIEW OF THE FLOW
$M_\infty = 7.4$, $\alpha = 15°$, $Re_{\infty_L} = 9 \times 10^6$

(Figure 4)

Shadowgraphs and oil streaks of the surface flow are helpful to an analysis of the pitot-pressure measurements. Therefore, a superposition of the surface flow on a shadowgraph is presented in figure 4 for an angle of attack of 15°. The shaded background of the figure is not relevant to the flow since it results from a window imperfection. The shadowgraph is from reference 5 wherein more complete results are compiled for angles of attack from 0° to 60°. The figure indicates that the flow separates on the lee side of the body forward of the wing and moreover, the wing acts as a shield to keep the flow separated over the aft surface of the body. However, it is shown that there is sufficient recovery of the flow in the flow field to impose a complicated surface pattern to the flow over the tail even though it is shielded by the body. For this angle of attack, a leading-edge wave can be seen over the outer semispan of the tail and therefore, the flow is believed to be locally supersonic. In addition, a separation line is visible forward of the 20° flared surface that appears characteristic of supersonic shock-induced flow separation. Near the root of the tail the flow is locally subsonic and a different flow pattern is evident.

The wave that appears to be emanating from the trailing edge of the tail is a trace of the inboard edge of the imbedded wing leading-edge wave and a continuation of this wave is visible on the windward side. For $\alpha = 15°$, a weak disturbance from the canopy is barely visible on the lee side that parallels the bow wave.

SIDE VIEW OF THE FLOW

$M_\infty = 7.4 \qquad \alpha = 15° \qquad Re_{\infty_L} = 9 \times 10^6$

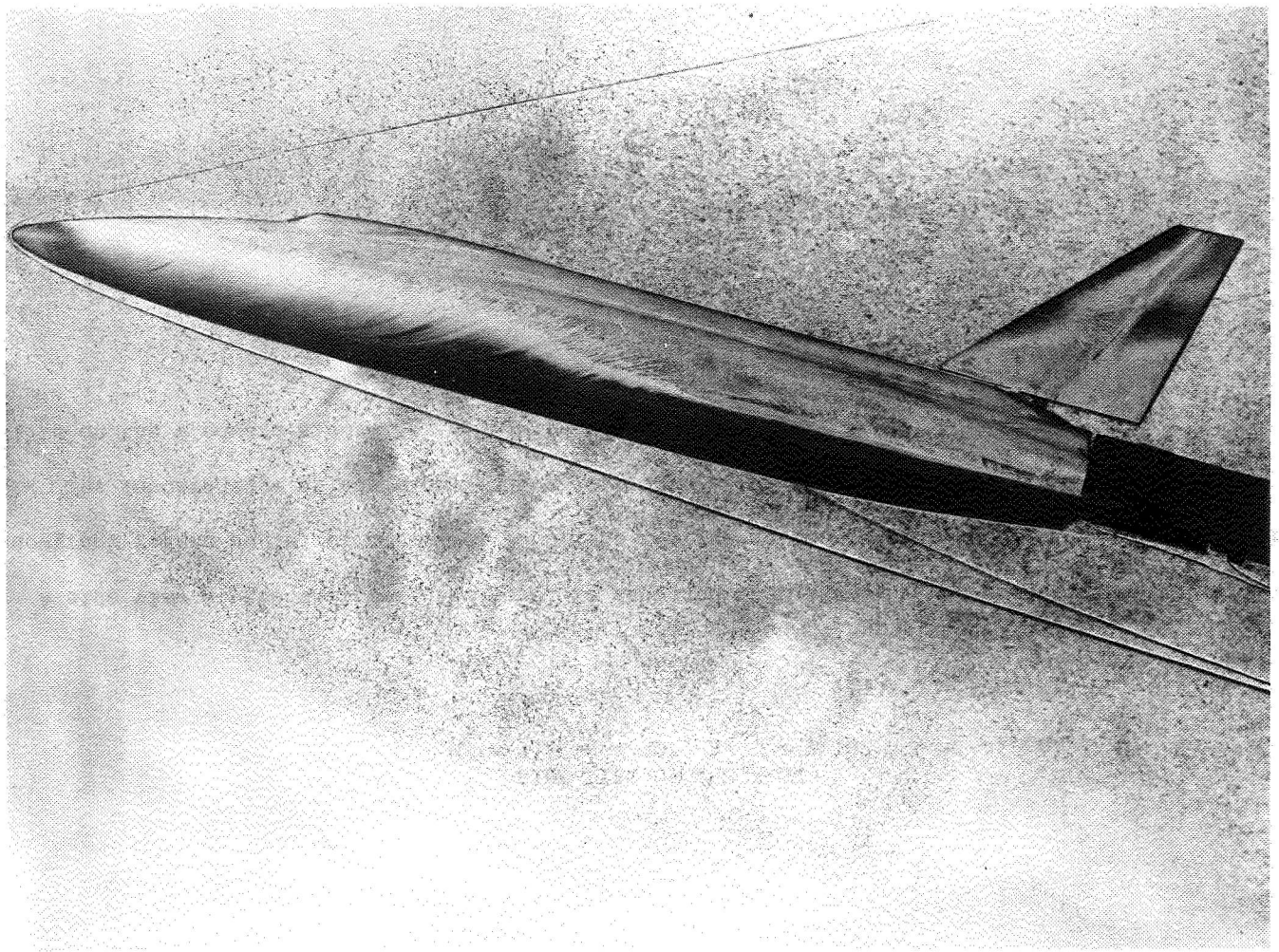

Figure 4

SIDE FIEW OF THE FLOW
$M_\infty = 7.4$, $\alpha = 30°$, $Re_{\infty_L} = 9x10^6$

(Figure 5)

A side view of the flow over the model is depicted in figure 5 by the composite surface flow and shadowgraph for an angle of attack of 30°. The flow appears separated on the lee side and over the tail. The inboard edge of the wing leading edge wave is visible on the lee side, but it is not visible on the windward side.

SIDE VIEW OF THE FLOW

$M_\infty = 7.4$ $\alpha = 30°$ $Re_{\infty_L} = 9 \times 10^6$

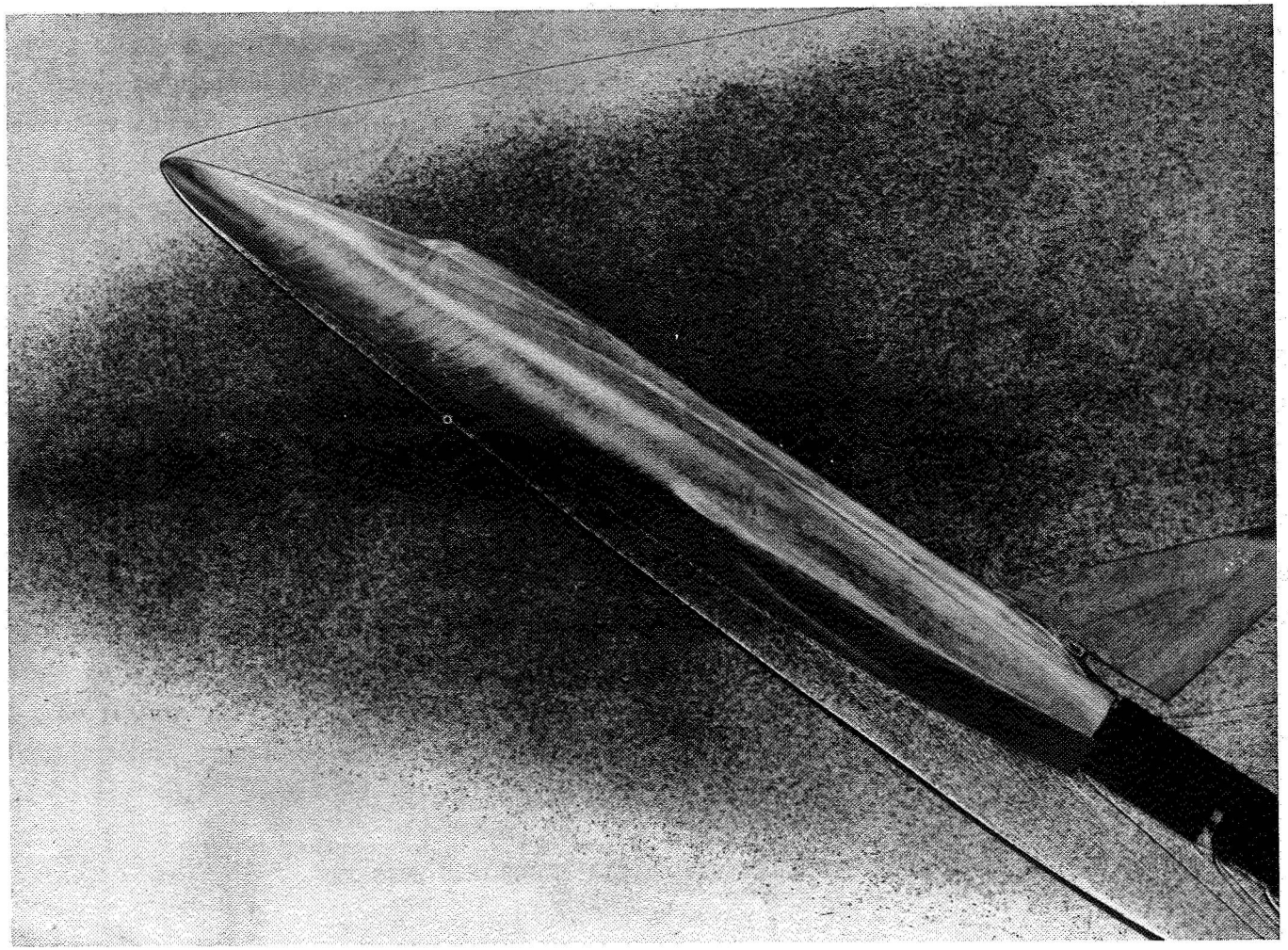

Figure 5

LEE-SIDE CENTERLINE PITOT-PRESSURE DISTRIBUTIONS
$M_\infty = 7.4$, $\alpha = 15°$
(Figure 6)

Pitot-pressure distributions of the lee-side flow field are presented in figure 6 for $\alpha = 15°$ and Reynolds numbers from 1.5×10^6 to 9.0×10^6. In addition, the surface flow is depicted for a Reynolds number of 9×10^6 and the shock-wave shape for Reynolds numbers of 4×10^6 and 9×10^6. At the canopy station, $x/L = .35$, the data indicate a blast-wave type distribution of pitot pressure between the body and the canopy wave. On this basis, the flow does not appear separated, i.e., $dC_{P_{PITOT}}/d(z/L) > 0$ at the wall. Since the oil streaks terminate in a manner indicative of separated flow (but for a slightly greater Reynolds number), it is concluded that the boundary layer was thick and that separation of the flow was incipient. Further aft at $x/L = .60$ and .98, the distributions indicate separated flow over about half the depth of the flow field.

Measurements of heating (reference 6) on the windward centerline demonstrate that the flow was laminar for present test conditions at a Reynolds number of 1.5×10^6 but transition to turbulent flow occurred near midlength for Reynolds numbers of about 7×10^6. Therefore, it is believed that the present pitot-pressure distributions for a Reynolds number of 1.5×10^6 are characteristic of flow that was initially laminar at separation. On the same basis, the flow may have been transitional or turbulent at separation for Reynolds numbers of 6×10^6 and 9×10^6. Characteristic of a turbulent boundary layer, better recovery of the flow is shown by the pitot-pressure distributions at $x/L = .98$ for the higher Reynolds numbers. From the extent of the exposure of the vertical tail to the unseparated flow, it is believed that a significant effect of Reynolds number on heating would occur over the outer semispan. Clearly, the hypersonic assumption of shielding of the flow by the body would lead to an erroneous heating estimate. Nonetheless, the effects of Reynolds number on the unseparated flow field and on the shock-wave shape in particular, appear small for the test range of Reynolds number.

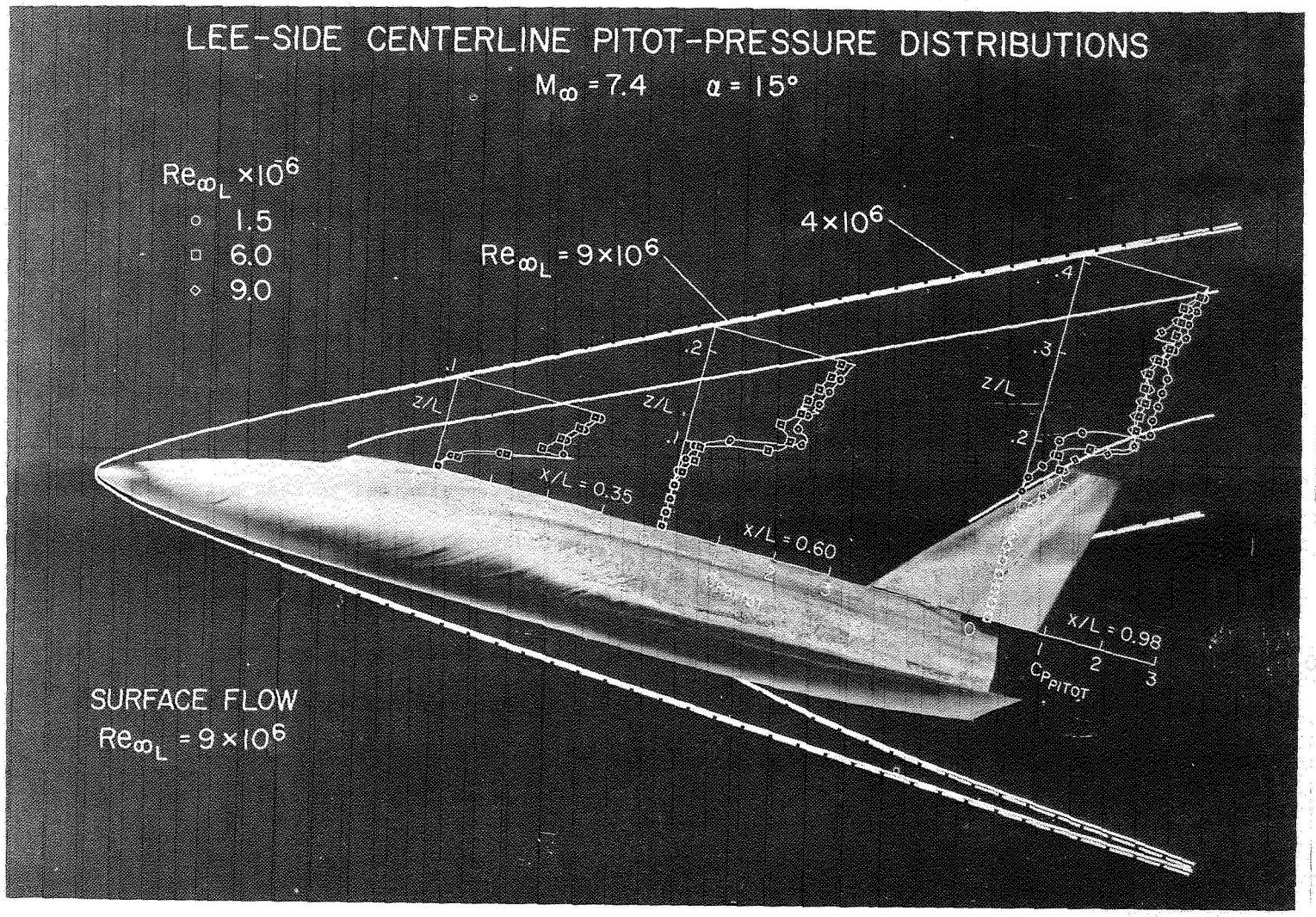
LEE-SIDE CENTERLINE PITOT-PRESSURE DISTRIBUTIONS
$M_\infty = 7.4$ $\alpha = 15°$
$Re_{\infty_L} \times 10^6$
○ 1.5
□ 6.0
◇ 9.0
$Re_{\infty_L} = 9 \times 10^6$
4×10^6
z/L
x/L = 0.35
x/L = 0.60
x/L = 0.98
$C_{P_{PITOT}}$
SURFACE FLOW
$Re_{\infty_L} = 9 \times 10^6$

Figure 6

LEE-SIDE CENTERLINE PITOT-PRESSURE DISTRIBUTIONS
$M_\infty = 7.4$, $\alpha = 30°$

(Figure 7)

Pitot-pressure distributions on the lee side of the body together with the surface streamlines and the shock-wave shape are presented in figure 7 for an angle of attack of 30°. In agreement with the surface flow, the pitot-pressure distributions indicate the flow is separated ($dC_{p_{PITOT}}/d(z/L) = 0$ at the wall) for all three axial stations. Increasing Reynolds number from 1.5×10^6 to 6×10^6 appears to have only small effects on the vertical extent of the separated flow. The flow is separated over the entire span of the vertical tail and it is clear from the extent of the separated flow that the imbedded wave from the wing leading edge is not continuous over the body. Reasons for the reversals in the distributions of pitot pressure at the edge of the separated flow at $x/L = .35$ and .60 are not clear but may result from three-dimensional flow effects of the nose and canopy.

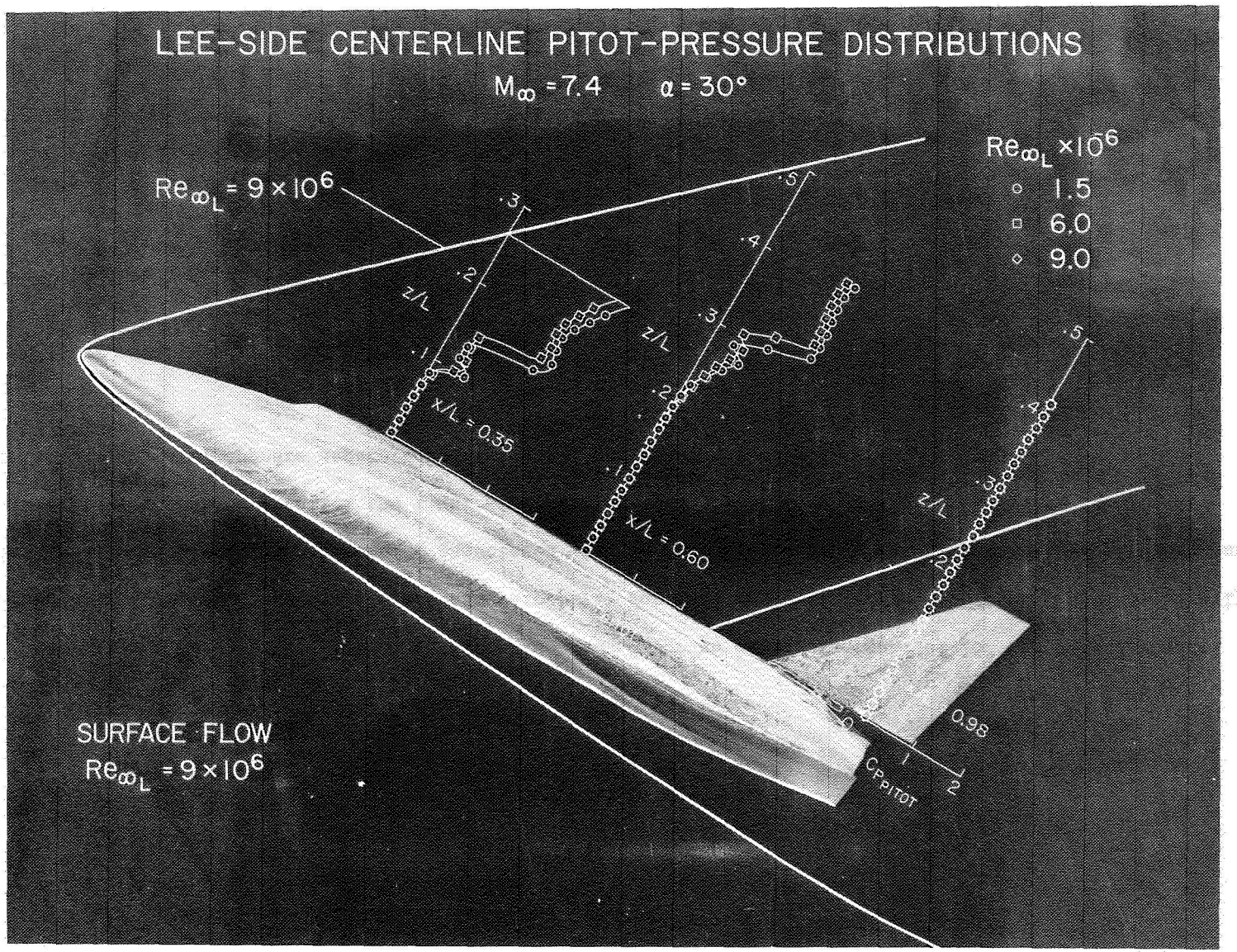
LEE-SIDE CENTERLINE PITOT-PRESSURE DISTRIBUTIONS
$M_\infty = 7.4$ $\alpha = 30°$
$Re_{\infty_L} \times 10^6$
1.5
6.0
9.0
$Re_{\infty_L} = 9 \times 10^6$
z/L
x/L = 0.35
x/L = 0.60
0.98
$C_{P_{PITOT}}$
SURFACE FLOW
$Re_{\infty_L} = 9 \times 10^6$

Figure 7

OBLIQUE VIEW OF THE FLOW
$M_\infty = 7.4$, $\alpha = 15°$, $Re_{\infty_L} = 9 \times 10^6$

(Figure 8)

An oblique view of the flow is depicted in figure 8 for an angle of attack of 15° and with the model rolled 45° with respect to the free-stream velocity. For this angle of attack, the canopy wave is clearly visible and traces of discontinuities associated with the intersecting bow and wing leading-edge waves can be seen that appear to parallel the right wing leading edge. The flow, as indicated by the termination of the oil streaks, appears separated over the aft region of the wing.

OBLIQUE VIEW OF THE FLOW

$M_\infty = 7.4$ $\alpha = 15°$ $Re_{\infty_L} = 9 \times 10^6$

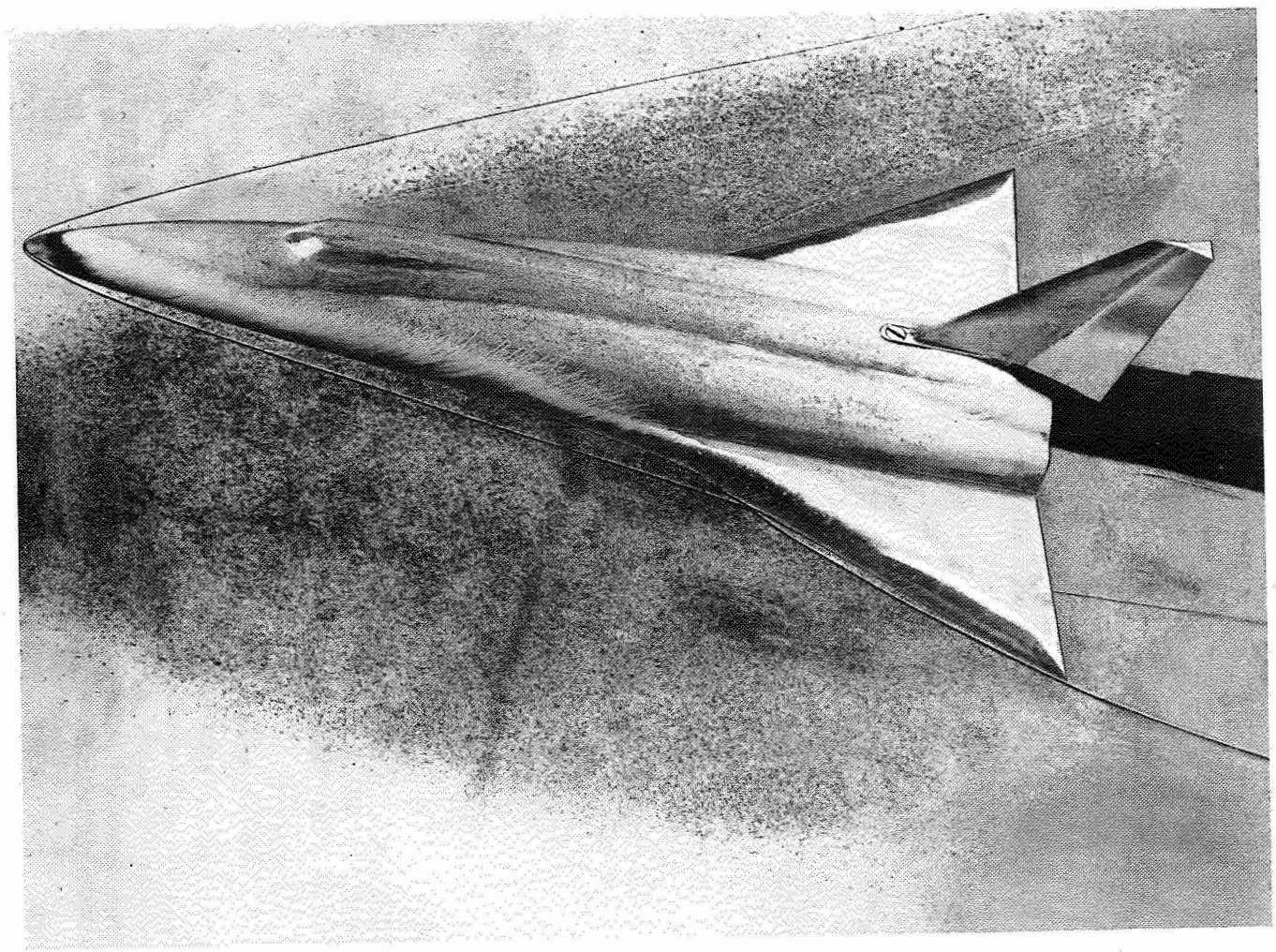

Figure 8

OBLIQUE VIEW OF THE FLOW
$M_\infty = 7.4$, $\alpha = 30°$, $Re_{\infty_L} = 9 \times 10^6$

(Figure 9)

An oblique view of the flow is shown in figure 9 for an angle of attack of 30° with the model rolled 45° with respect to the free-stream velocity.

OBLIQUE VIEW OF THE FLOW

$M_\infty = 7.4 \qquad \alpha = 30° \qquad Re_{\infty_L} = 9 \times 10^6$

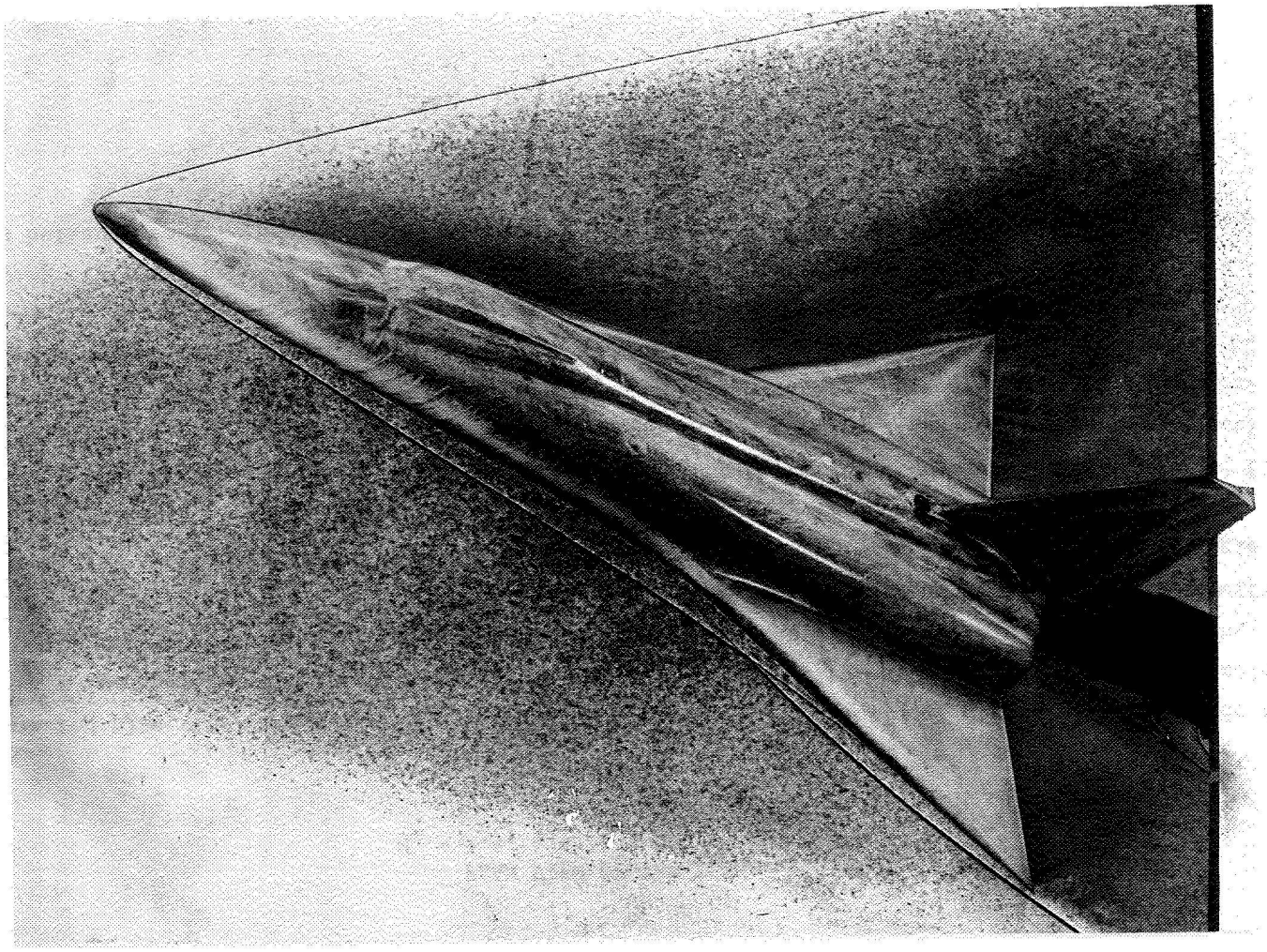

Figure 9

PLAN VIEW OF THE FLOW
$M_\infty = 7.4$, $\alpha = 15°$, $Re_{\infty_L} = 9 \times 10^6$

(Figure 10)

A projected plan view of the flow is presented in figure 10 for an angle of attack of 15°. Aside from the effects of leading-edge bluntness, the leading-edge wave of the wing appears attached to the leading edge. The flow remains attached for a significant extent of the chord but appears separated over the aft surface of the wing. Moreover, the interaction of the intersecting bow and leading-edge waves with the boundary layer and the separated flow produces a unique pattern to the surface flow for this angle of attack.

For $\alpha = 15°$, a faint reattachment line can be seen in the chordwise direction of the separated flow near mid-semispan. It is believed this line is associated with a contact discontinuity (vortex sheet) that impinges on the surface and originates from the intersecting waves. A separation line is visible further outboard that is associated with the chordwise intersection of the defracted bow wave with the boundary layer. The phenomena is not unlike that observed in reference 7 on the windward surface of a straight wing orbiter. Because of the favorable effects of sweepback, the effect of the interaction on heating is believed small. However, the phenomena poses a complicating aspect to the heating estimate.

PLAN VIEW OF THE FLOW

$M_\infty = 7.4 \qquad \alpha = 15° \qquad Re_{\infty_L} = 9 \times 10^6$

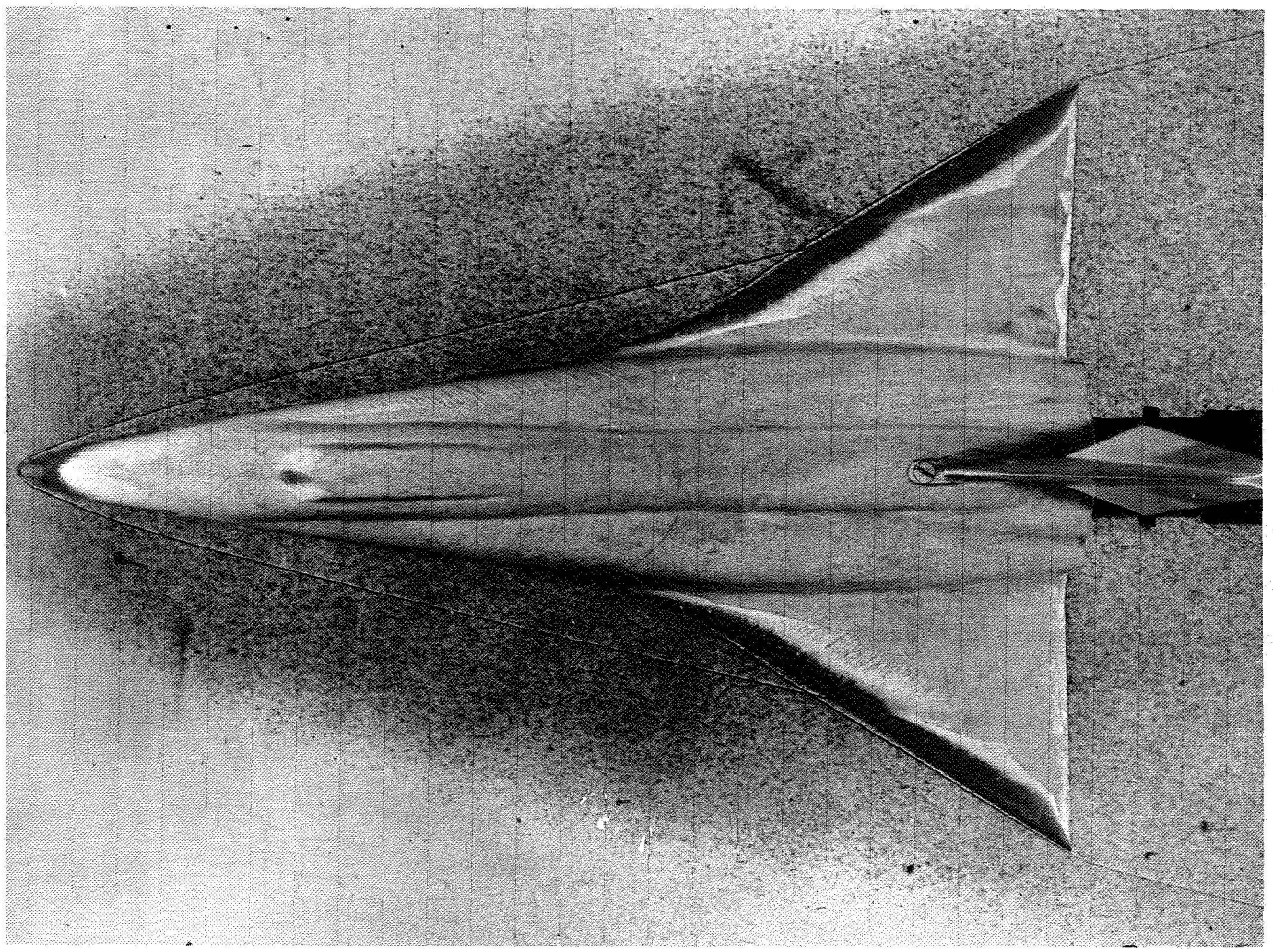

Figure 10

PLAN VIEW OF THE FLOW
$M_\infty = 7.4$, $\alpha = 30°$, $Re_{\infty_L} = 9x10$

(Figure 11)

The projected plan view of the flow presented in figure 11 for an angle of attack of 30° indicates that the leading-edge wave of the wing is detached from the leading edge. The flow appears attached over the leading edge but separated over a considerable extent of the wing surface. An interaction of the bow wave with the surface flow is not apparent from the oil streaks.

PLAN VIEW OF THE FLOW

$M_\infty = 7.4$ $\alpha = 30°$ $Re_{\infty_L} = 9 \times 10^6$

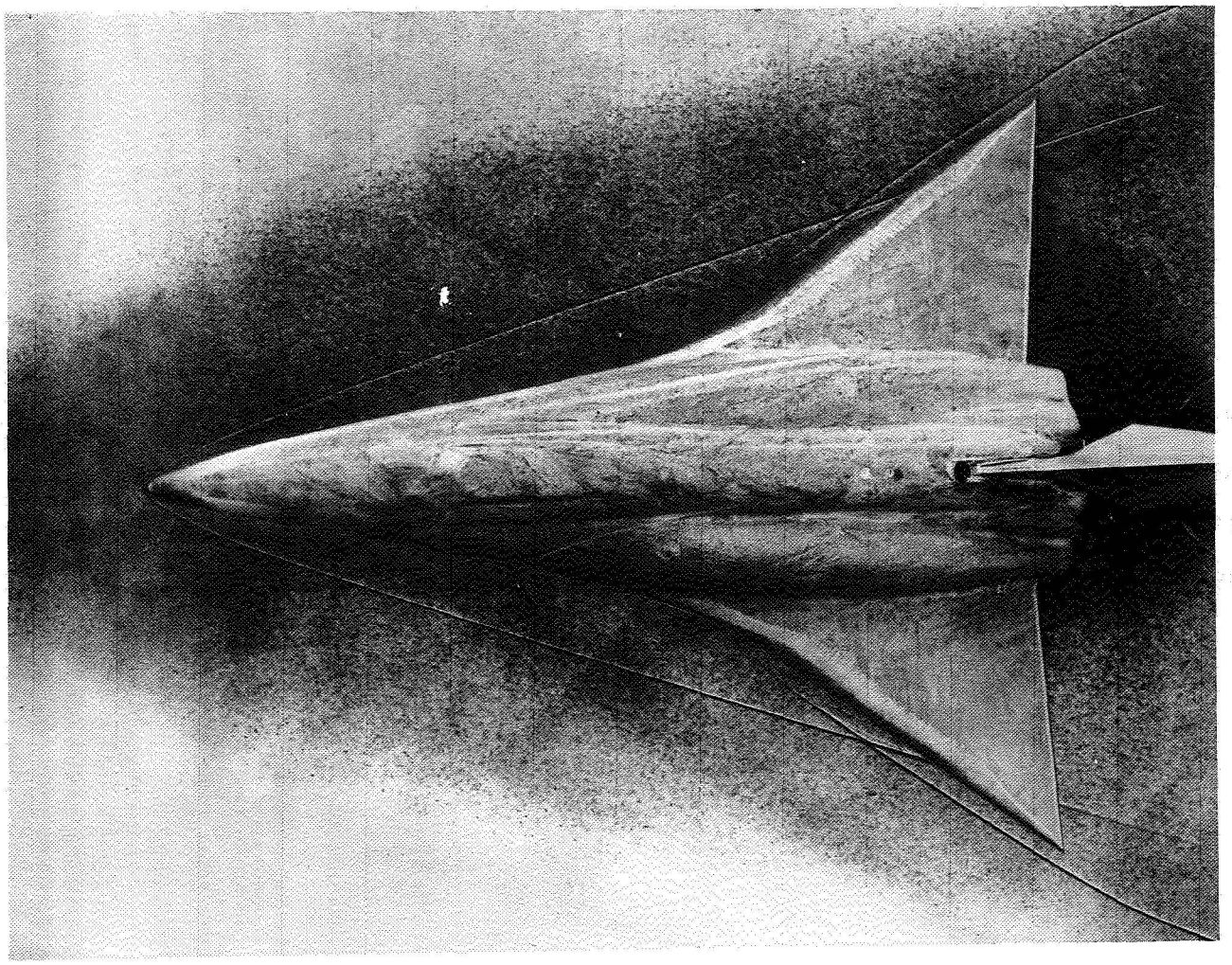

Figure 11

LEE-SIDE FLOW AT THE SPANWISE PITOT TRAVERSE STATIONS
$M_\infty = 7.4$, $\alpha = 15°$, $Re_{\infty_L} = 9 \times 10^6$

(Figure 12)

The spanwise positions of the pitot-traverse stations with respect to the flow is shown in figure 12 for an angle of attack of 15°. This figure shows that the station nearest the wing tip $y/\frac{b}{2} = .78$ is outboard of the influence of the bow wave and is therefore, exposed only to flow passing through the wing leading-edge wave. It is clear the remaining stations are within the bow wave and subject to the complicating aspects of this and perhaps other features of the flow.

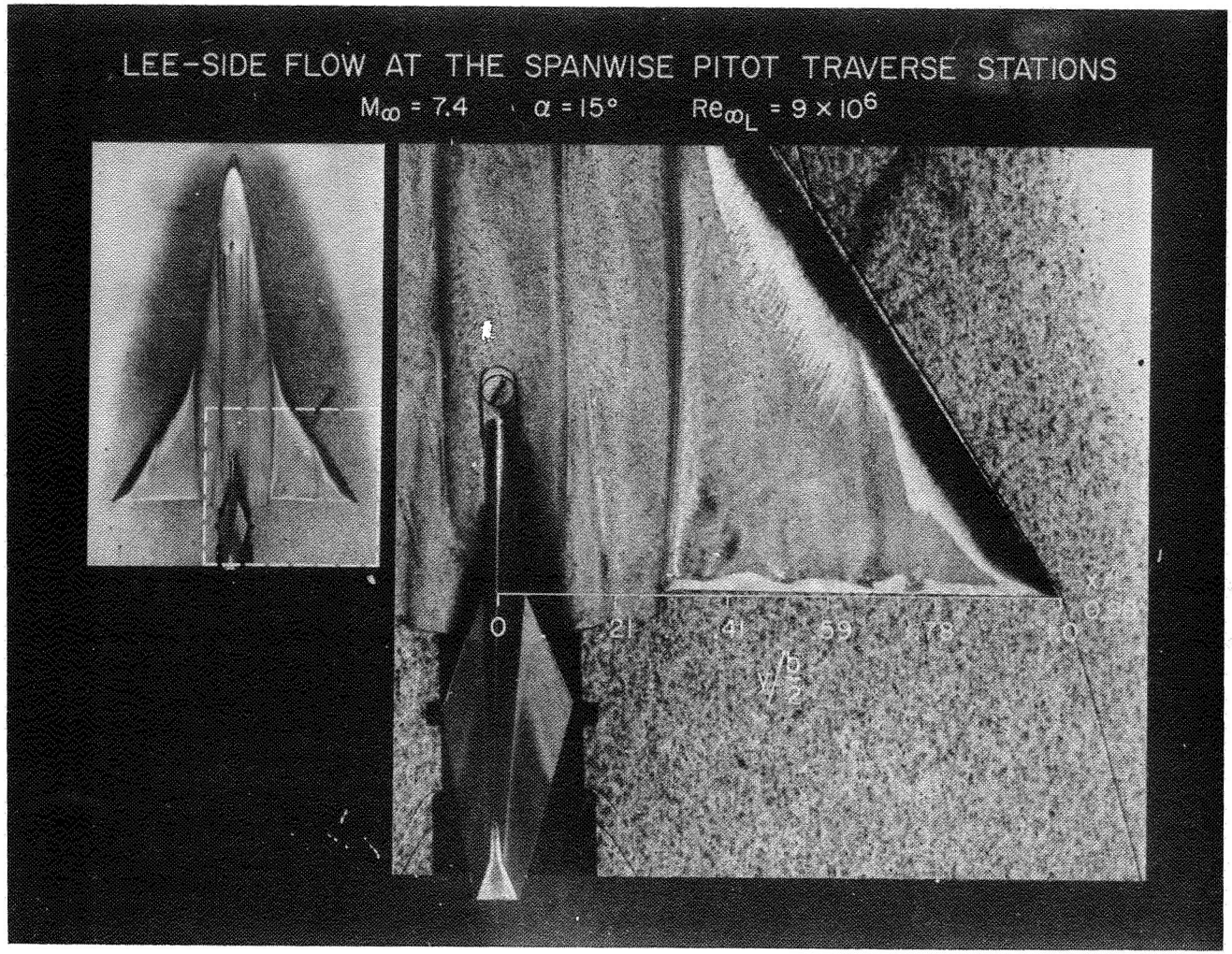
LEE-SIDE FLOW AT THE SPANWISE PITOT TRAVERSE STATIONS
$M_\infty = 7.4$ $\alpha = 15°$ $Re_{\infty_L} = 9 \times 10^6$
0
2
41
59
78
0
$\frac{b}{2}$

Figure 12

LEE-SIDE FLOW AT THE SPANWISE PITOT TRAVERSE STATIONS
$M_\infty = 7.4$, $\alpha = 30°$, $Re_{\infty_L} = 9 \times 10^6$

(Figure 13)

Figure 13 shows the spanwise positions of the pitot-traverse stations with respect to the flow for an angle of attack of 30°. For this angle of attack, all traverse stations are within the influence of the bow wave.

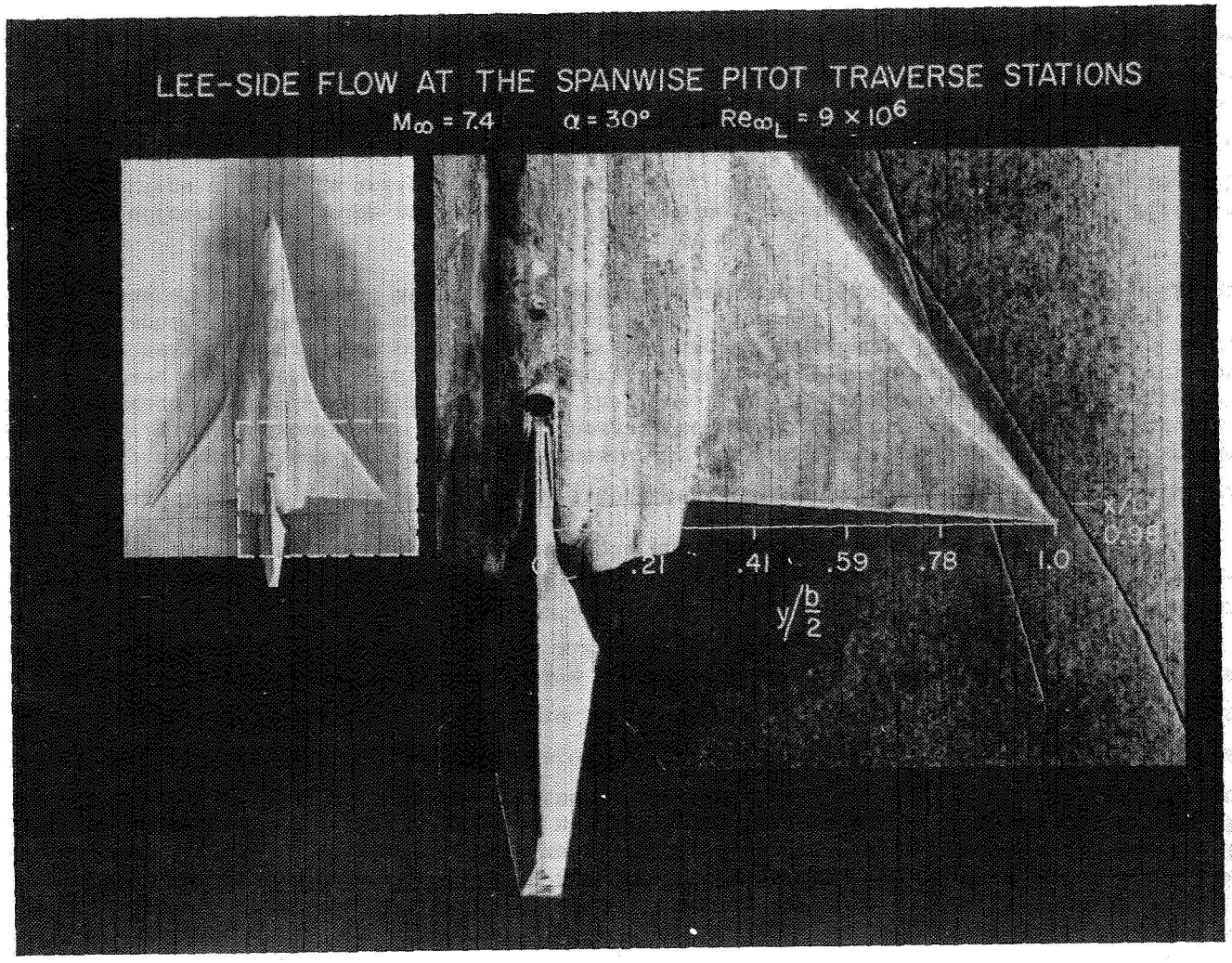
LEE-SIDE FLOW AT THE SPANWISE PITOT TRAVERSE STATIONS
$M_\infty = 7.4$ $\alpha = 30°$ $Re_{\infty_L} = 9 \times 10^6$
.21
.41
.59
.78
1.0
$y/\frac{b}{2}$

Figure 13

LEE-SIDE DISTRIBUTIONS OF PITOT PRESSURE AT SPANWISE LOCATIONS
$M_\infty = 7.4$, $\alpha = 15°$, $x/L = .98$

(Figure 14)

Pitot-pressure distributions are presented in figure 14 on the lee side at five spanwise stations for $x/L = .98$ and $\alpha = 15°$. Discontinuities of the flow field that are believed to be shock waves are faired as horizontal lines. This aspect of fairing the data was influenced by other data not presented and knowledge of the flow field from shadowgraphs; it is, of course, not known in some cases that discontinuities are, in fact, imbedded waves. The body and wing surface are denoted by hatched lines. At $y/\frac{b}{2} = .78$, the distribution of pitot pressure is of the blast-wave type and terminates at the wing leading-edge wave. Here the flow appears only slightly separated. At the next station inboard $y/\frac{b}{2} = .59$ the layer of separated flow is thicker than outboard and 2 imbedded waves are indicated. The wave adjacent to the separated flow is believed to be an interference wave and the next wave above it is the wing leading-edge wave. The bow wave crosses this station at $z/L = .39$. Proceeding inboard to the middle station, $y/\frac{b}{2} = .41$, the separated-flow layer thickens. Imbedded waves are not indicated above the separated flow but a compressive type disturbance is evident at about $z/L = .3$. At this station the bow wave is above the outermost probe and therefore, is not shown.

At the inboard stations $y/\frac{b}{2} = .21$ and 0 the distributions are over the body; distributions for $y/\frac{b}{2} = 0$ were given previously and are shown here for completeness. At both stations the separated flow extends over about half the shock-layer thickness. In the outer unseparated region of the flow, the canopy wave is shown as a weak wave just beneath the bow wave that terminates the flow field. A compressive disturbance is evident beneath the canopy wave but since it could not be detected on shadowgraphs, it is not shown as a discontinuity. This disturbance may be a recompression of the flow over the canopy and such a disturbance is, in fact, visible in schlieren photographs of reference 8 at a Mach number of 2. Clearcut evidence of body vortices is not apparent from the distributions at the 2 inboard stations. These vortices require extensive surveys to delineate their location.

Although large effects of Reynolds number on the flow are not evident, there are detailed differences particularly for stations within the influence of the bow wave, $y/\frac{b}{2} \leq .59$. At the nearest station inboard of where the bow wave crosses the wing $y/\frac{b}{2} = .59$, increasing Reynolds number decreases the thickness of the separated flow. Perhaps of some significance is the defect of pitot pressure incurred in the flow field, $0.1 \lesssim z/L \lesssim .3$, at station $y/\frac{b}{2} = .41$ as the Reynolds number is increased. This station is approximately in line with the fillet and therefore, the defect of pitot pressure appears related to the influence of the wing-fillet-body juncture.

LEE-SIDE DISTRIBUTIONS OF PITOT PRESSURE AT SPANWISE LOCATIONS

$M_\infty = 7.4$ $\alpha = 15°$ $x/L = 0.98$

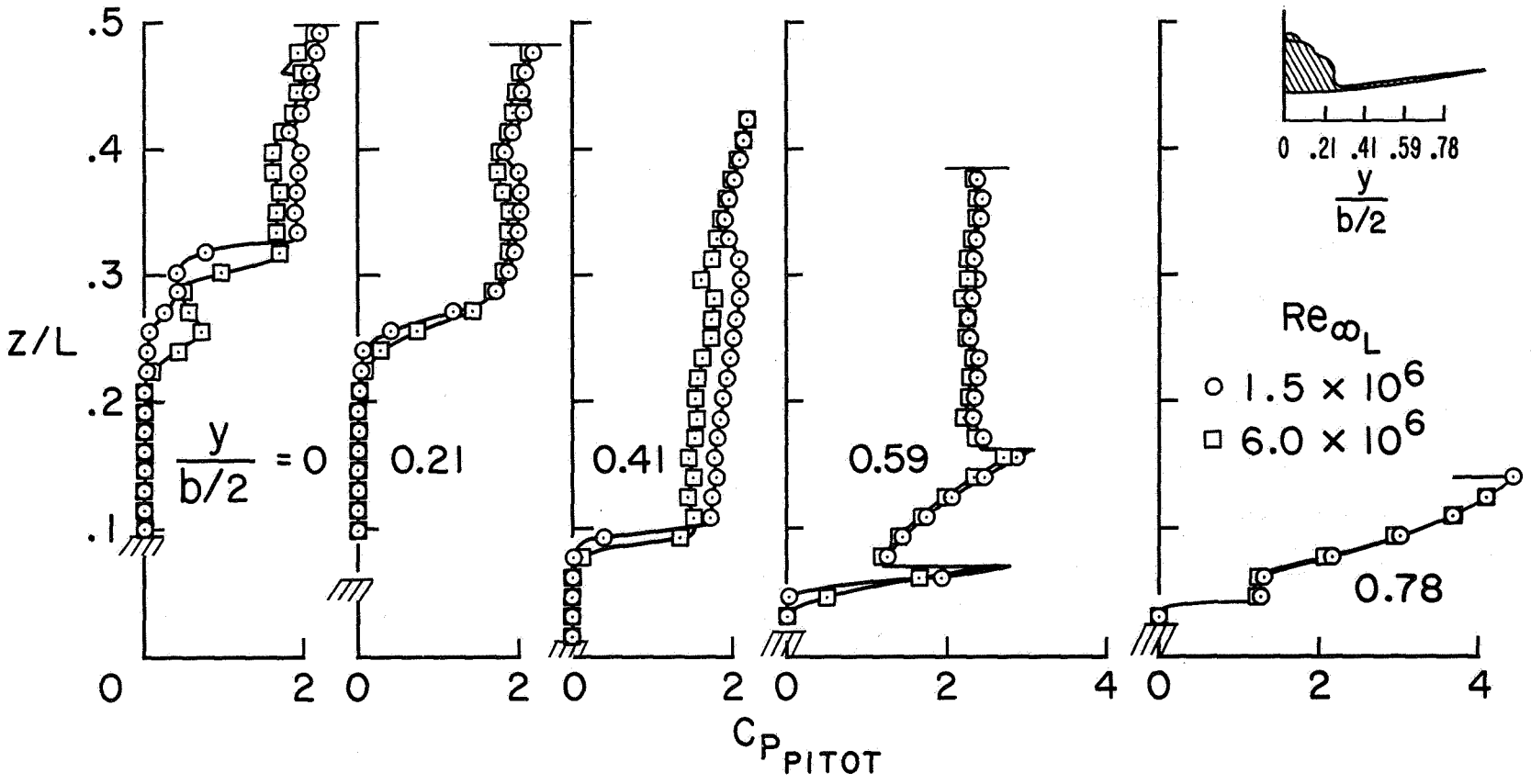

Figure 14

LEE-SIDE DISTRIBUTIONS OF PITOT PRESSURE AT SPANWISE LOCATIONS
$M_\infty = 7.4$, $\alpha = 30°$, $x/L = .98$
(Figure 15)

Pitot-pressure distributions at the spanwise stations are given for an angle of attack of 30°. Results for the 5 stations are within the lateral scope of the bow wave and this wave is above the vertical scope of the rake. At the outermost station, $y/\frac{b}{2} = .78$, the wave at $z/L = .19$ is believed to be an interference wave and that at $z/L = .27$ is the wing leading-edge wave. Inboard at $y/\frac{b}{2} = .59$, the interference wave crosses at a lower elevation $z/L = .12$.

The imbedded wave shown for $y/\frac{b}{2} = .41$ adjacent to the edge of the separated flow is tentatively identified as a body wave extending rearward over the wing. Such waves have been observed on the lee side of conical bodies at large angles of attack (see references 1 and 2). At the 2 inboard stations over the body $y/\frac{b}{2} = 0$ and .21 the flow appears essentially separated over the full extent of the rake, $z/L = .51$.

In general, the data do not show significant effects of Reynolds number on flow separation at the 5 spanwise stations. On the other hand and similar to results given for $\alpha = 15°$, increasing Reynolds number decreases slightly the pitot pressure in the unseparated region. Reasons for this decrease are not clearly known but may be a result of a general increase in the level of turbulence of the lee-side flow.

LEE-SIDE DISTRIBUTIONS OF PITOT PRESSURE AT SPANWISE LOCATIONS

$M_\infty = 7.4$ $\alpha = 30°$ $X/L = 0.98$

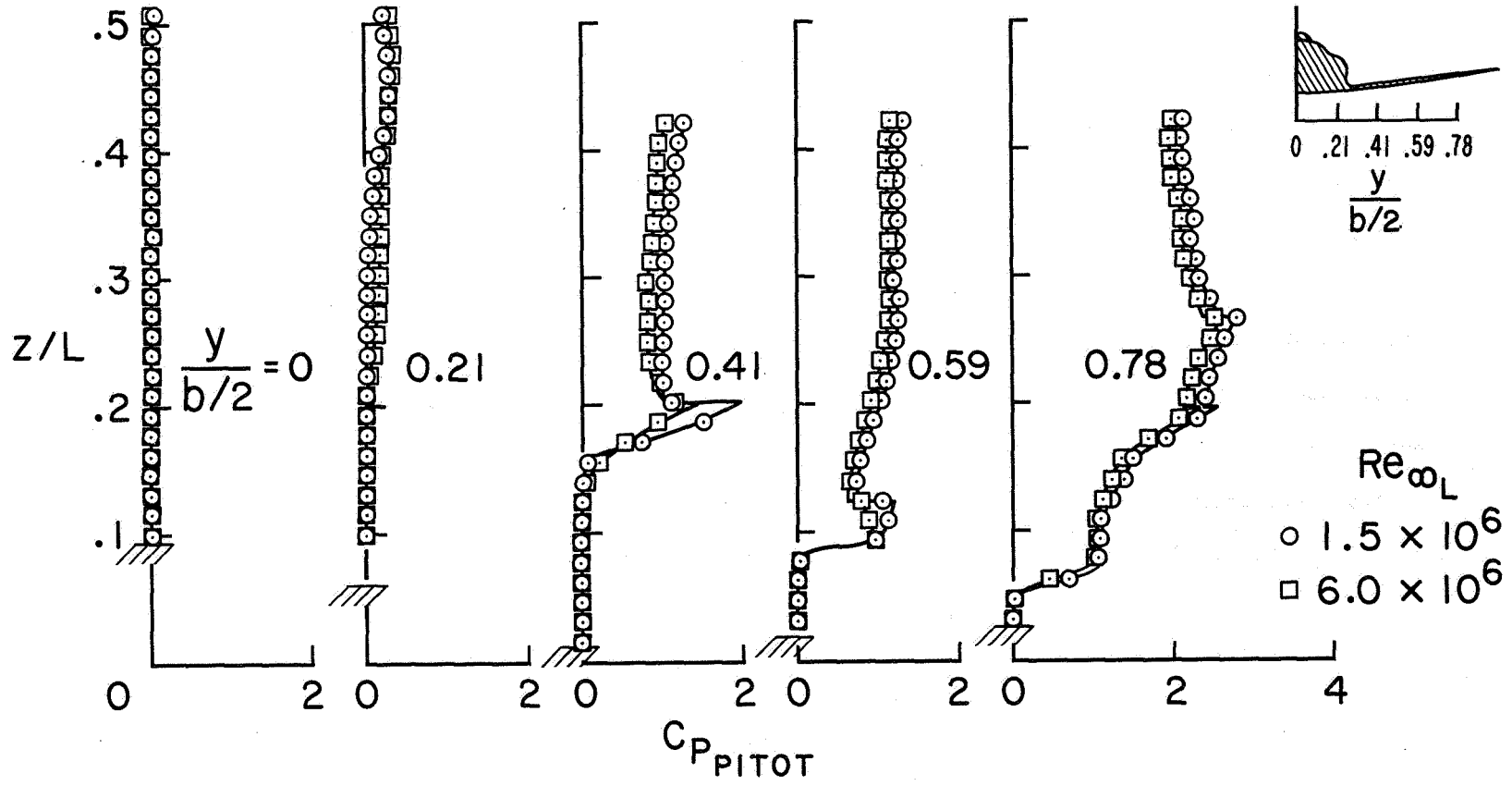

Figure 15

DELTA-WING ORBITER FLOW-FIELD STRUCTURE

$M_\infty = 7.4$, $\alpha = 15^\circ$, $x/L = .98$

(Figure 16)

A cross-section of the delta-wing-orbiter flow-field structure is presented in figure 16 for $x/L = .98$ and $\alpha = 15^\circ$. The results are based on an interpretation of the pitot-pressure measurements and on shadowgraphs and are given for both windward and leeward flow fields. While agreement is shown in the major aspects of the flow-field definition between pitot-pressure measurements and shadowgraphs, it is clear that a concrete definition of the structure requires extensive surveys. Therefore, the results are given as a tentative illustration.

The bow and wing leading edge waves are fairly well defined but the imbedded interference wave is identified by only one point and is arbitrarily faired to the intersection of the bow and leading edge waves. No attempt is given to justify the stability of this intersecting shock configuration; if proven unstable the interference shock could be faired as an oblique leg to the bow wave. The canopy wave in the outer part of the flow field appears concentric with the bow wave but terminates inboard of the middle station $y/L = .14$.

The separated flow boundary is given for the condition $C_{P_{PITOT}} \leq .2$. This boundary encloses the subsonic flow region but is slightly supersonic at the inner edge. A significant increase in the depth of the separated flow near the wing-body juncture when approaching the body with decreasing y/L is an interesting feature of the flow field structure.

DELTA-WING ORBITER FLOW-FIELD STRUCTURE

$M_\infty = 7.4$ $\alpha = 15°$ $x/L = 0.98$

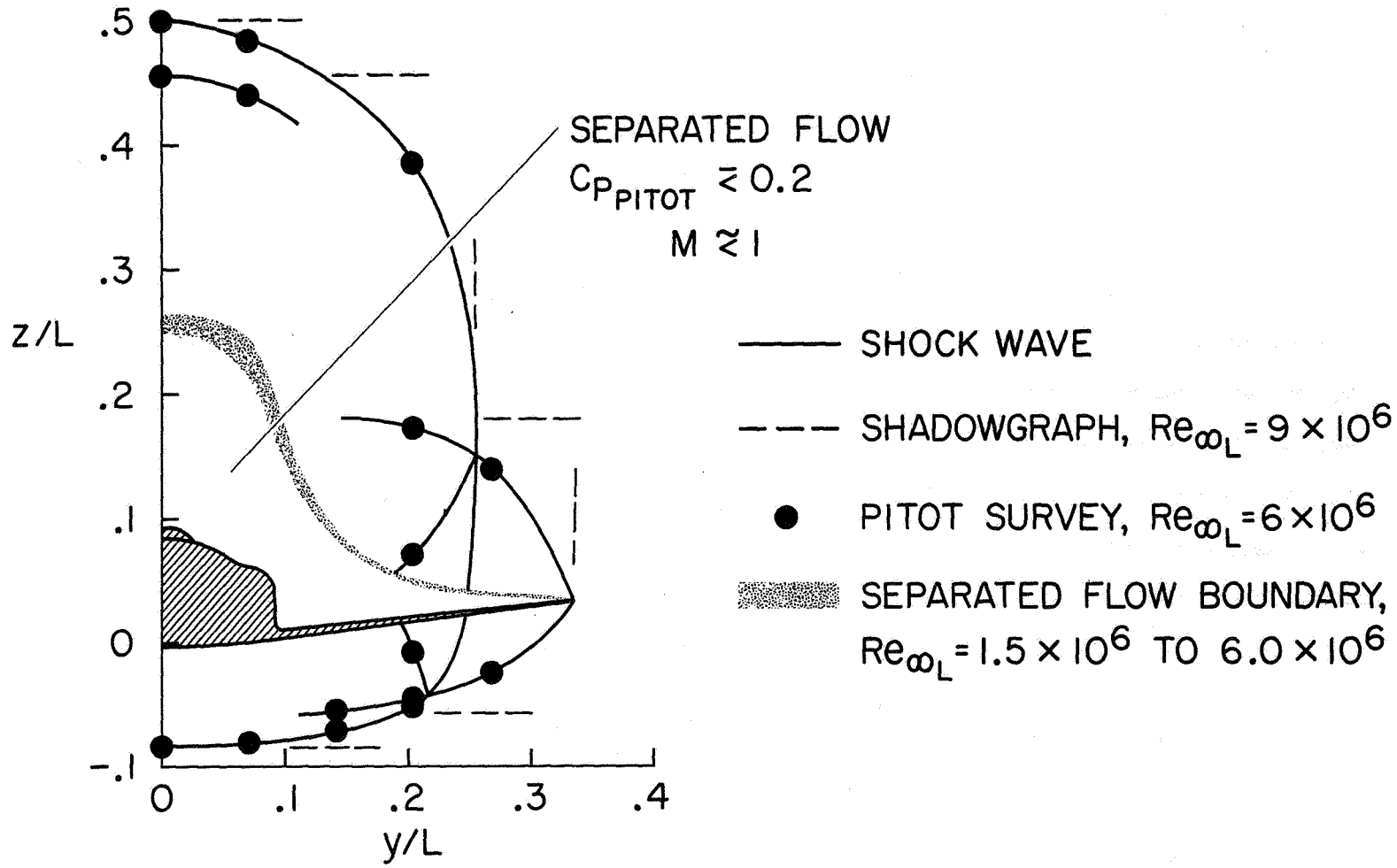

Figure 16

DELTA-WING ORBITER FLOW-FIELD STRUCTURE

$M_\infty = 7.4$, $\alpha = 30^\circ$, $x/L = .98$

(Figure 17)

Figure 17 presents the flow-field structure for an angle of attack of 30°. The shock-wave pattern is similar to that for $\alpha = 15^\circ$ (figure 16) except the wing leading-edge wave is detached and there is an imbedded wave over the wing body juncture. The wing body juncture wave is not well defined and since it is not observed at the next station outboard, it is faired beyond the scope of the rake at that station. On the lee side, the interference wave is defined by 2 points that appear in line with the intersection of the bow and leading-edge waves. For $\alpha=30^\circ$ the flow appears extensively separated particularly over the body but the effects of Reynolds number on the separated flow do not appear large.

DELTA-WING ORBITER FLOW-FIELD STRUCTURE

$M_\infty = 7.4$ $\alpha = 30°$ $x/L = 0.98$

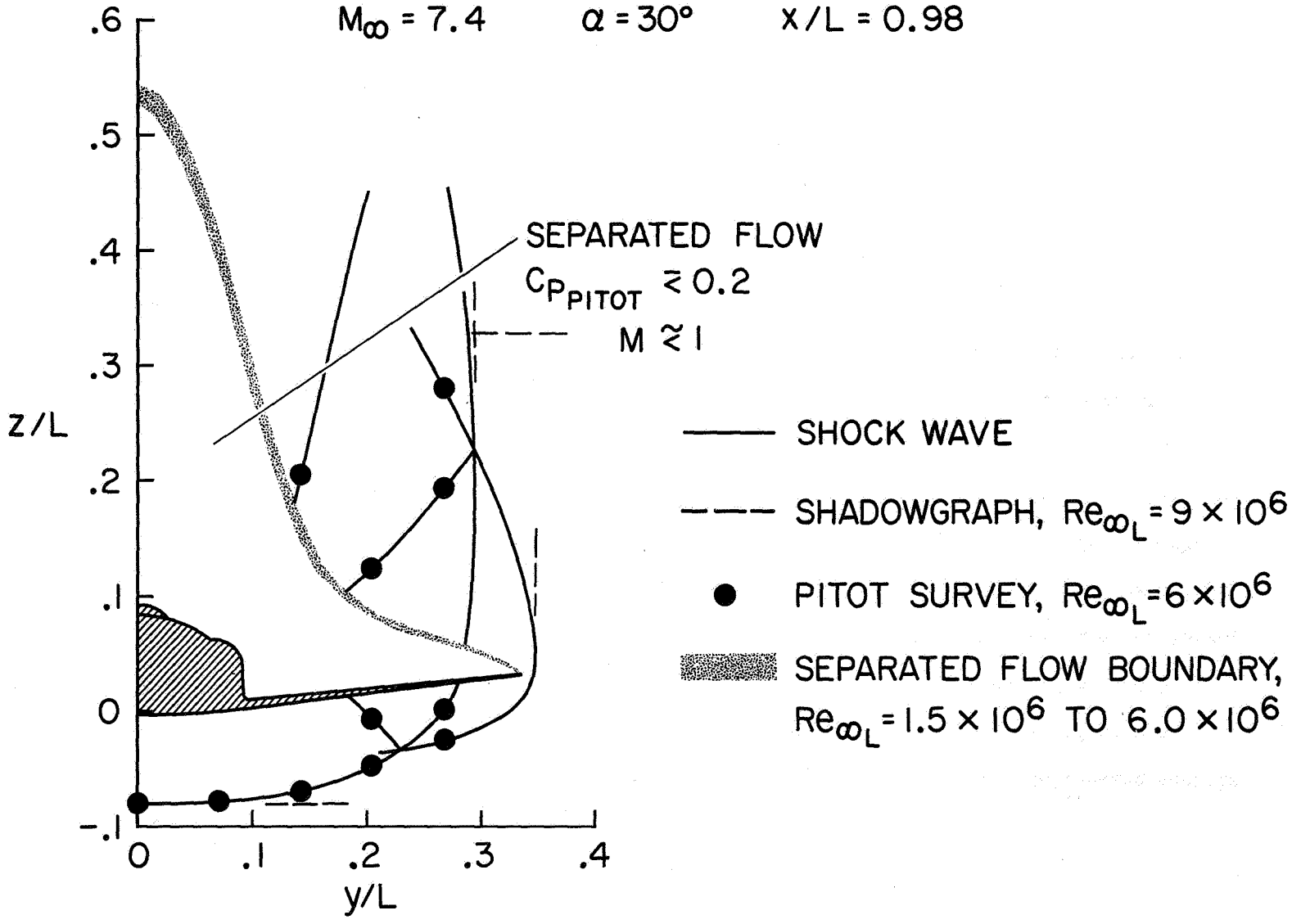

Figure 17

CONCLUDING REMARKS

Results of a pitot-pressure investigation of the flow field on the lee side of a delta-wing shuttle orbiter are presented. The results delineate the extent of the lee-side separated flow and give a tentative cross-sectional definition to the shock-wave structure for angles of attack of 15° and 30°.

It is shown that while, in general, the effects of Reynolds number on the flow field are not large, detailed effects are observed that may have significant bearing on the heating estimate. Two examples are cited for an angle of attack of 15°; these are: (1) The scope of the vertical tail exposed to the unseparated flow increases with increasing Reynolds number and (2) the depth of the separated flow adjacent to where the bow wave crosses the wing appears to decrease with increasing Reynolds number. In addition, it is shown that at a spanwise station outboard of the wing-fuselage juncture, increasing Reynolds number decreased the pitot pressure in the unseparated flow. This defect of pitot pressure appears associated with the flow over the wing-fillet-fuselage juncture.

REFERENCES

1. Rainbird, W. J.: Turbulent Boundary Layer Growth and Separation on a Yawed Cone. AIAA Journal, Vol. 6, No. 12, Dec. 1968, pp. 2410-2416.

2. Tracy, R.: Hypersonic Flow Over a Yawed Circular Cone. Hypersonic Research Project Memo. 69, California Institute of Technology, Aug. 1963.

3. Cleary, Joseph W.: Effects of Angle of Attack and Bluntness on the Shock-Layer Properties of a 15° Cone at a Mach Number of 10.6. NASA TN D-4909, 1968.

4. Liepman, H.W.; and Roshko, A.: Elements of Gasdynamics. GALCIT, Aeronautical Series, John Wiley and Sons, N.Y., 1957.

5. Cleary, Joseph W.: Hypersonic Shock-Wave Phenomena of a Delta-Wing Space-Shuttle Orbiter. NASA TMX-62,076, Oct., 1971.

6. Marvin, J.G.; Seegmiller, H.L.; Lockman, W.K.; Mateer, C.G.; Pappas, C.C.; and Derose, C.E.: Surface Flow Patterns and Aerodynamic Heating on Space Shuttle Vehicles. AIAA Paper 71, 594, 1971.

7. Seegmiller, H.L., Shock Interference and Density Ratio Effects Part I, Flow Field Visualization, Thermocouple Measurements, and Analysis, Paper No. 5. NASA TMX-2272.

8. Cleary, Joseph W.: Subsonic, Transonic, and Supersonic Stability and Control Characteristics of a Delta-Wing Orbiter. NASA TMX-62,066, Sept. 1970.

LEE-SIDE FLOW PHENOMENA ON SPACE SHUTTLE CONFIGURATIONS AT HYPERSONIC SPEEDS

PART II – STUDIES OF LEE-SURFACE HEATING AT HYPERSONIC MACH NUMBERS

By Jerry N. Hefner and Allen H. Whitehead, Jr.

NASA Langley Research Center
Hampton, Virginia

INTRODUCTION

In the March 1971 Space Shuttle Technology Conference, the present authors reported that severe lee-surface heating existed on an early design delta-wing orbiter in wind-tunnel tests at angles of attack between 20° and 50° at Mach 6 (ref. 1). However, numerous pertinent and important questions remain unanswered. These include: (1) the behavior of vortex-induced heating at unit Reynolds numbers relatively low in comparison to those reported in the previous shuttle conference, (2) the relationship between lee-surface pressures and heating, (3) the effect of Mach number on the heating, and (4) the influence of geometry and nose bluntness on vortex formation and heating.

This paper presents results of a continuing experimental investigation to answer questions regarding lee-surface heating and flow phenomena on shuttle-type geometries. The delta-wing orbiter model chosen for this study is the same model used in the initial lee-surface heating study reported in the March 1971 Space Shuttle Technology Conference. Lee-surface heating data, obtained at relatively low unit Reynolds numbers at Mach 6 and 19, are discussed with emphasis on the peak heating behavior. Surface pressures measured along the lee meridian of the delta-wing orbiter are presented and analyzed in conjunction with the heating. The effects of nose bluntness and lee-surface geometry on the heating are discussed and general guidelines are presented for modifying the lee-surface geometry of the shuttle to reduce vortex-induced heating. The application of the wind-tunnel results to realistic shuttle flight conditions is discussed.

LEE-SURFACE HEATING CHARACTERISTICS

(Figure 1)

The results presented in the March 1971 Space Shuttle Technology Conference are summarized briefly. As indicated by the oil-flow pattern, the lee-surface flow is characterized by relatively large areas of flow separation and numerous vortices interacting with the upper surfaces (interaction of vortices with a surface creates a "featherlike" oil smear). A schematic depicting the formation and shedding of the lee-side vortices together with the inviscid streamline behavior is shown. The measured heating distribution for a free-stream Reynolds number based on body length ($R_{\infty,L}$) of 5.2×10^6 and Mach number of 6 is presented in terms of the ratio of the local heat-transfer coefficient (h) to the stagnation heat-transfer coefficient (h_{ref}) on a 0.305-m-radius sphere scaled by the same factor as the particular model. The heating is plotted versus the ratio of surface distance to overall model length (x/L) and shows that high meridian heating is associated with the vortex-interaction regions and much of the heating is above that for an angle of attack (α) of 0°. (Note that this high heating is referred to as the peak lee-surface heating even though higher heating may occur in the attached flow region on the nose, $x/L < 0.1$.) This vortex-induced heating along the lee meridian is probably caused by the thinning of the viscous shear layer (which acts as an insulator against the high-energy inviscid flow) as a result of outflow caused by the vortices. A similar explanation was given in reference 2 for vortex-induced heating on a planar delta wing at low incidence and is discussed in detail in reference 3.

The severity of the vortex-induced peak heating on the delta-wing orbiter is strongly influenced by Reynolds number and the position of the peak heating is sensitive to angle of attack. Radiation equilibrium surface temperatures (T_w), examples of which are shown, were found to exceed the structural limits for titanium in many instances; this result was dependent upon the choice of the maximum heat-transfer rate and the trajectory used in the calculation procedure. (The maximum heat-transfer rate used in calculating the surface temperatures was 136 kW/m^2.)

LEE-SURFACE HEATING CHARACTERISTICS

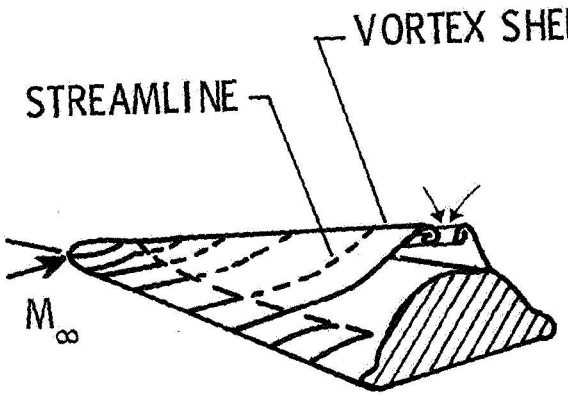

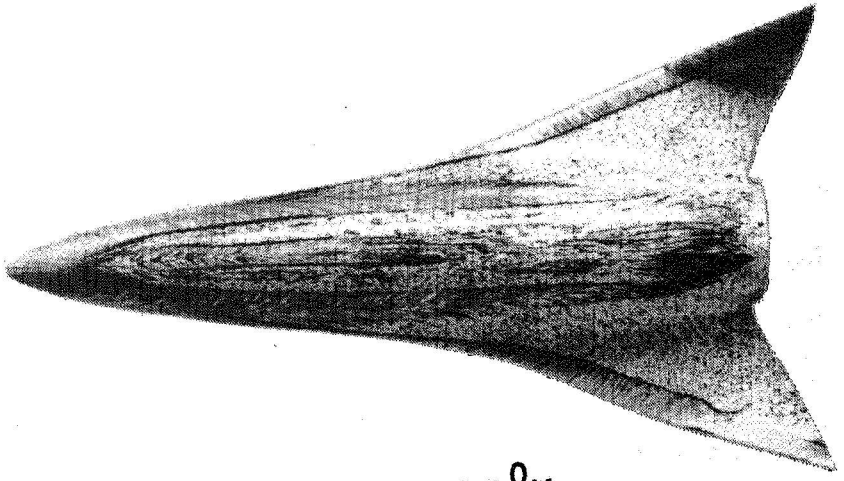

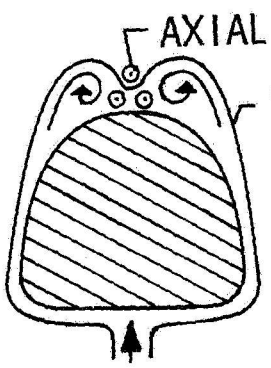

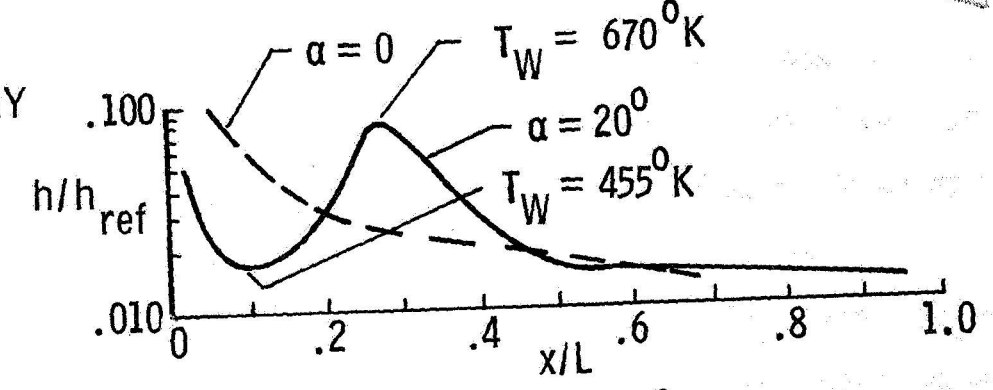

SHOWN PREVIOUSLY:

1) SEVERE HEATING CAN OCCUR - ABOVE THAT AT $\alpha = 0^0$
2) PEAK HEATING IS EXTREMELY SENSITIVE TO REYNOLDS NUMBER
3) POSITION OF PEAK HEATING SENSITIVE TO ANGLE-OF-ATTACK

Figure 1

EFFECT OF REYNOLDS NUMBER ON HEATING

(Figure 2)

The effect of decreasing Reynolds number on the heating along the lee meridian of the 0.00397-scale delta-wing orbiter for two angles of attack is shown. Note the absence of peak heating for $x/L < 0.5$ at $\alpha = 20^{\circ}$ for body length Reynolds numbers ($R_{\infty,L}$) of 1.2×10^6 and 0.7×10^6. (The peak heating at $x/L \approx 0.75$ for $R_{\infty,L} = 1.2 \times 10^6$ is not believed to be vortex-induced heating since oil-flow patterns indicate separated flow in this region; also, for $R_{\infty,L} = 0.7 \times 10^6$, the phase-change paint did not melt below a value of $h/h_{ref} \approx 0.012$.) A "threshold" Reynolds number exists, in this instance based on body length, between 1.2×10^6 and 2.2×10^6 where peak heating decreases abruptly. Oil-flow studies at these lower Reynolds numbers still exhibit the "featherlike" reattachment regions identified at the higher Reynolds numbers. Therefore, the lack of peak heating and the existence of a threshold Reynolds number cannot be attributed to an elimination of the lee-side vortices. At $\alpha = 35^{\circ}$, the test Reynolds numbers are apparently above the threshold for that angle of attack since no abrupt decrease in peak heating was observed with decreasing Reynolds number.

EFFECT OF REYNOLDS NUMBER ON HEATING

$M_\infty = 6$, .00397 - SCALE DELTA-WING ORBITER

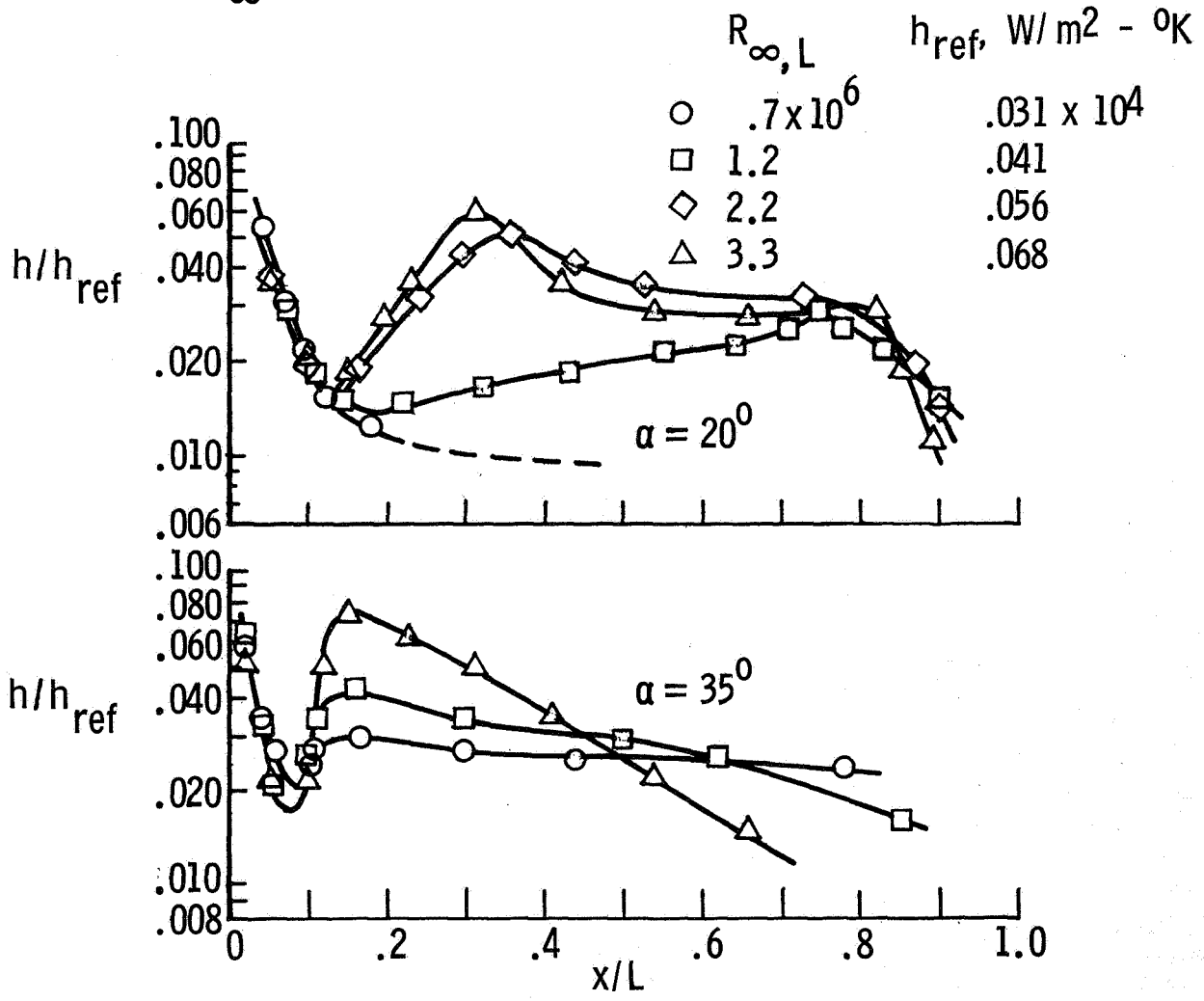

Figure 2

VORTEX – INDUCED PEAK HEATING

(Figure 3)

An analysis of the heating data in terms of boundary-layer properties and flow phenomena is difficult when heating is reduced only in the form of h/h_{ref} since h_{ref} is primarily useful in evaluating laminar heating for attached flows. Therefore, the variation of the vortex-induced peak heating in terms of free-stream Stanton number (N_{ST_∞}) is presented in addition to peak h/h_{ref} as a function of the free-stream Reynolds number based on the distance to the position of peak heating $(R_{\infty,x})$. The data presented were obtained on two different scale models of the same delta-wing orbiter with the 0.00397-scale model having a relative nose bluntness (ratio of nose radius to body length (r/L)) half as large as that for the 0.00635-scale model. Even though the relative nose bluntnesses for the two models differed by a factor of 2, very little effect has been observed on the magnitude (figure 3) or position (not shown on this figure) of the peak heating for Reynolds numbers above the threshold, which, in this instance, is based on the distance to the position of peak heating and is approximately equal to 0.7×10^6. Therefore, vortex-induced peak heating for the present delta-wing orbiter is concluded to be a weak function of nose bluntness for Reynolds numbers above the threshold. However, nose bluntness apparently influenced the threshold Reynolds number since the data at $\alpha = 20^\circ$ indicate that a threshold occurred only for the scale model with the relatively smaller nose bluntness.

Although the peak h/h_{ref} increases significantly with $R_{\infty,x}$, the peak heating in terms of Stanton number for a constant angle of attack is a relatively weak function of Reynolds number and increases only slightly. It should be emphasized that all of the peaks were obtained at conditions above the threshold Reynolds number; a maximum heating (differentiated from peak heating) for the area beyond the attached flow region on the nose, $x/L > 0.1$, is indicated where the test conditions were below the threshold and no peak occurred. A similar heating behavior has been observed with decreasing Reynolds number in the reattachment regions of separated boundary layers when the reattaching flow is transitional (ref. 4). Although the analogy between reattachment heating and vortex-induced heating should not be extended too far, the observed Reynolds number behavior suggests that the flow in the region of peak heating for these tests is transitional; the rapid decrease in heating with further reductions in Reynolds number is associated with the flow becoming laminar. One might suppose that the Reynolds numbers are too low for transitional flow to exist; however, some vortices are known to be highly unstable and thus may produce transitional flow at relatively low Reynolds numbers somewhat similarly to that for wake flow (ref. 5). Further studies are necessary to determine both the specific cause of the rapid decrease in heating below the threshold and the dimension on which to base this threshold Reynolds number.

VORTEX-INDUCED PEAK HEATING

M_∞ = 6, DELTA-WING ORBITER

α, deg

○ 20
□ 35
} .00635 - SCALE, r/L = 0.02

● 20
■ 35
} .00397 - SCALE, r/L = 0.01

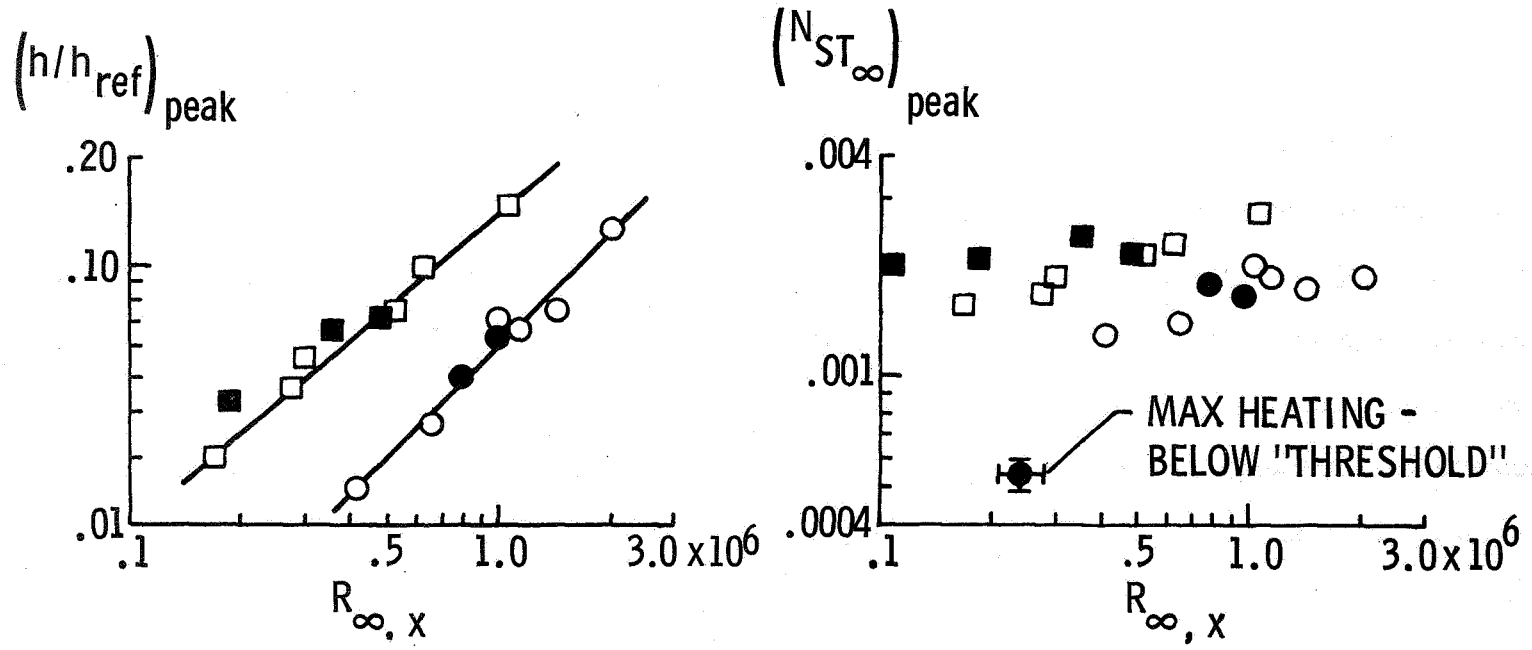

Figure 3

LEE – MERIDIAN PRESSURES

(Figure 4)

Surface pressures, measured along the lee meridian and presented as the ratio of local static pressure to free-stream static pressure (p/p_∞), show no abrupt increases in the regions of peak heating. The surface pressures are insensitive to the effects of the vortices for the present tests. In fact, at the position of peak heating, the pressures decrease with increasing Reynolds number and remain nearly constant with increasing angle of attack. In contrast, the peak heating increased with both Reynolds number and angle of attack. These results are therefore compatible with the explanation of peak heating previously discussed on figure 1 in that peak heating is caused by thinning of the viscous shear layer.

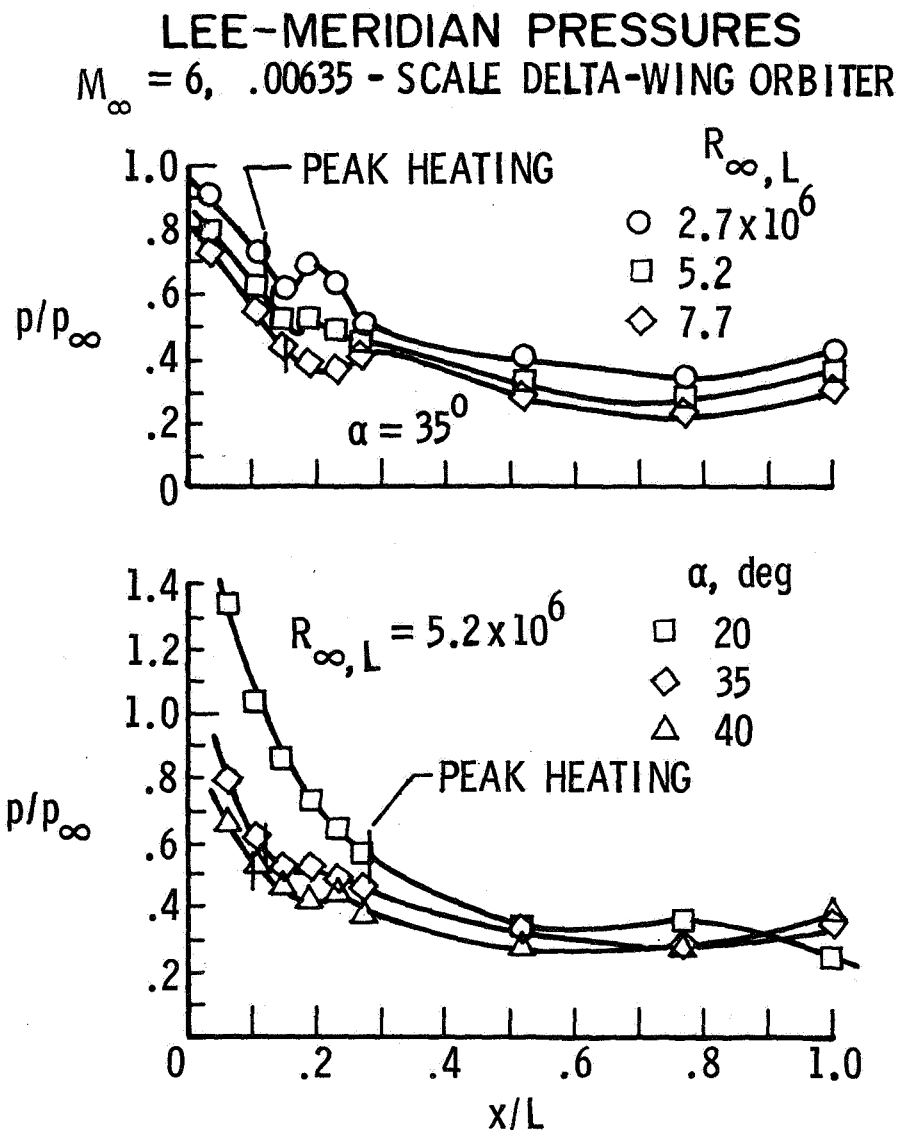
LEE-MERIDIAN PRESSURES
M_∞ = 6, .00635 - SCALE DELTA-WING ORBITER
PEAK HEATING
$R_{\infty,L}$
2.7×10^6
5.2
7.7
$\alpha = 35^0$
p/p_∞
1.0
.8
.6
.4
.2
0
$R_{\infty,L} = 5.2 \times 10^6$
α, deg
20
35
40
PEAK HEATING
1.4
1.2
1.0
.8
.6
.4
.2
0
.2
.4
.6
.8
1.0
x/L

Figure 4

LEE-SURFACE HEATING AT VARIOUS MACH NUMBERS

(Figure 5)

Lee-Surface heating data obtained at both Mach 19 and Mach 6 on the 0.00397-scale delta-wing orbiter are shown for $R_{\infty,L} \approx 0.7 \times 10^6$. No heating peaks for $x/L < 0.5$ were found for either $\alpha = 20^\circ$ or $\alpha = 37^\circ$ at Mach 19 and the heating level was significantly lower than that for $\alpha = 0^\circ$. The heating was also lower than that found at Mach 6. Oil-flow patterns at Mach 19 were found to be similar to those at Mach 6 with the exception that the "featherlike" signature, characteristic of vortex flows, was not clearly defined. This should not necessarily be attributed to the lack of lee-surface vortices since the surface shear may have been too low to move the oil and, hence, the characteristic featherlike pattern was not formed. Since no peak heating occurred, the Reynolds number for the Mach 19 data was undoubtedly below the threshold. This is a reasonable conclusion since the Mach 19 Reynolds number was below the Mach 6 threshold value for $\alpha = 20^\circ$ and the local Reynolds number at Mach 19 was, of course, much lower than that at Mach 6. These high Mach number results are not sufficient to define the effect of Mach number since the influence of Reynolds number complicates the analysis. Additional studies to determine the Mach number effect are necessary since the effect of Mach number is required for an application of wind-tunnel results to flight conditions.

LEE-SURFACE HEATING AT VARIOUS MACH NUMBERS

$R_{\infty,L} \approx .7 \times 10^6$, .00397 - SCALE DELTA-WING ORBITER

	α, deg	M_∞	h_{ref}, W/m^2 - ^oK
○	0	19	.027 x 10^4
□	20	19	.027
◇	37	19	.027
■	20	6	.031
◆	35	6	.031

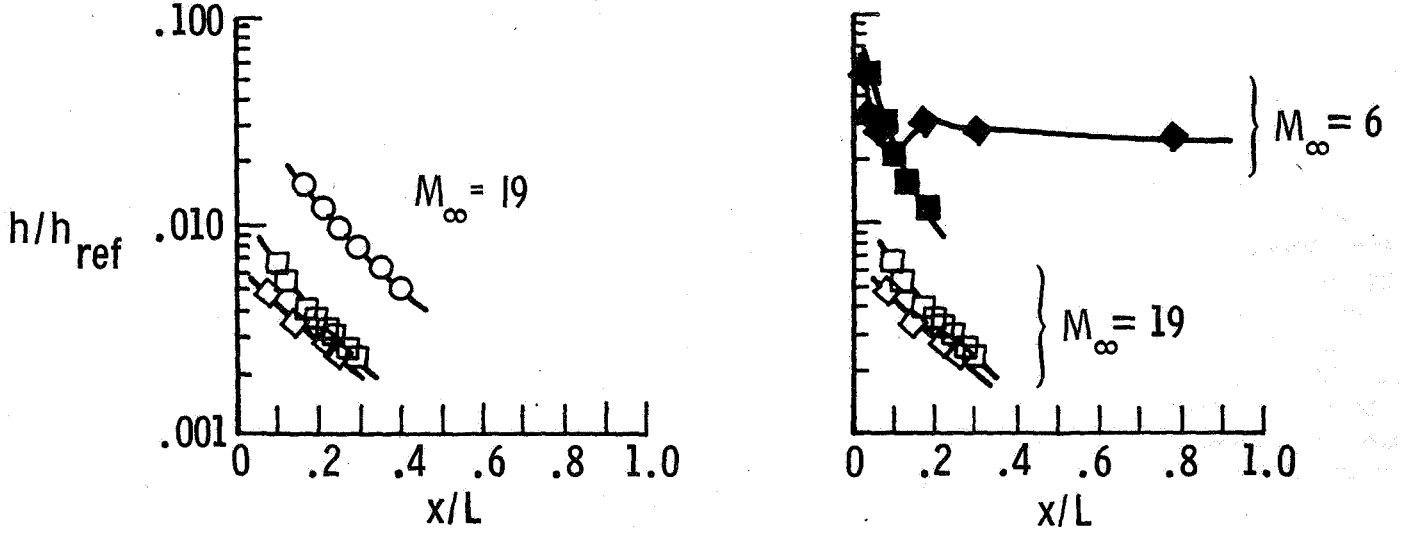

Figure 5

EFFECT OF LEE-SURFACE GEOMETRY ON HEATING

(Figure 6)

Although a complete knowledge of the lee-surface geometry influence is not presently available, variations in the lee-surface geometry strongly influence vortex-induced heating. Dramatic reductions in vortex-induced heating have been realized by altering the planform shape and lee-surface geometry of several planar delta wings at low incidence (refs. 2 and 6). The potential of varying the lee-surface geometry on the shuttle to reduce heating is shown for several configurations at Mach 6 and Mach 8. The Mach 6 data show the results of a modification to the existing delta-wing orbiter model. The rationale behind this modification primarily involved the alteration of the lee-surface geometry to encourage the vortices, if present, to break away from the lee surface. The initial slope of the lee meridian was increased and broken sharply with the hope that the vortices would lift off the surface at the geometry discontinuity. As the data reveal, the heating level was reduced significantly along 50% of the leeward meridian.

Further verification of the concept of reducing lee-surface heating by modifying the upper-surface geometry to induce vortex lift-off can be found in reference 7 and in unpublished data obtained in the Langley Mach 8 variable-density tunnel by H. D. Schultz and K. W. McGee of Lockheed Missiles & Space Company. The profiles of the orbiters tested at Mach 8 are shown on the figure. The configuration of Shultz and McGee with relatively large initial slope angle and sharp break in contour generated relatively low lee-surface heating in comparison to the configuration of Connor, which used a more gradually changing contour. Therefore, it seens advantageous in terms of heating to shape the upper surface of the shuttle with a relatively large initial slope that breaks sharply to encourage vortex lift-off. Although some of the current shuttle concepts utilize profiles somewhat similar to those which produced the lower lee-surface heating, additional guidelines for configuring the shuttle to insure reductions in vortex-induced heating are needed.

EFFECT OF LEE-SURFACE GEOMETRY ON HEATING

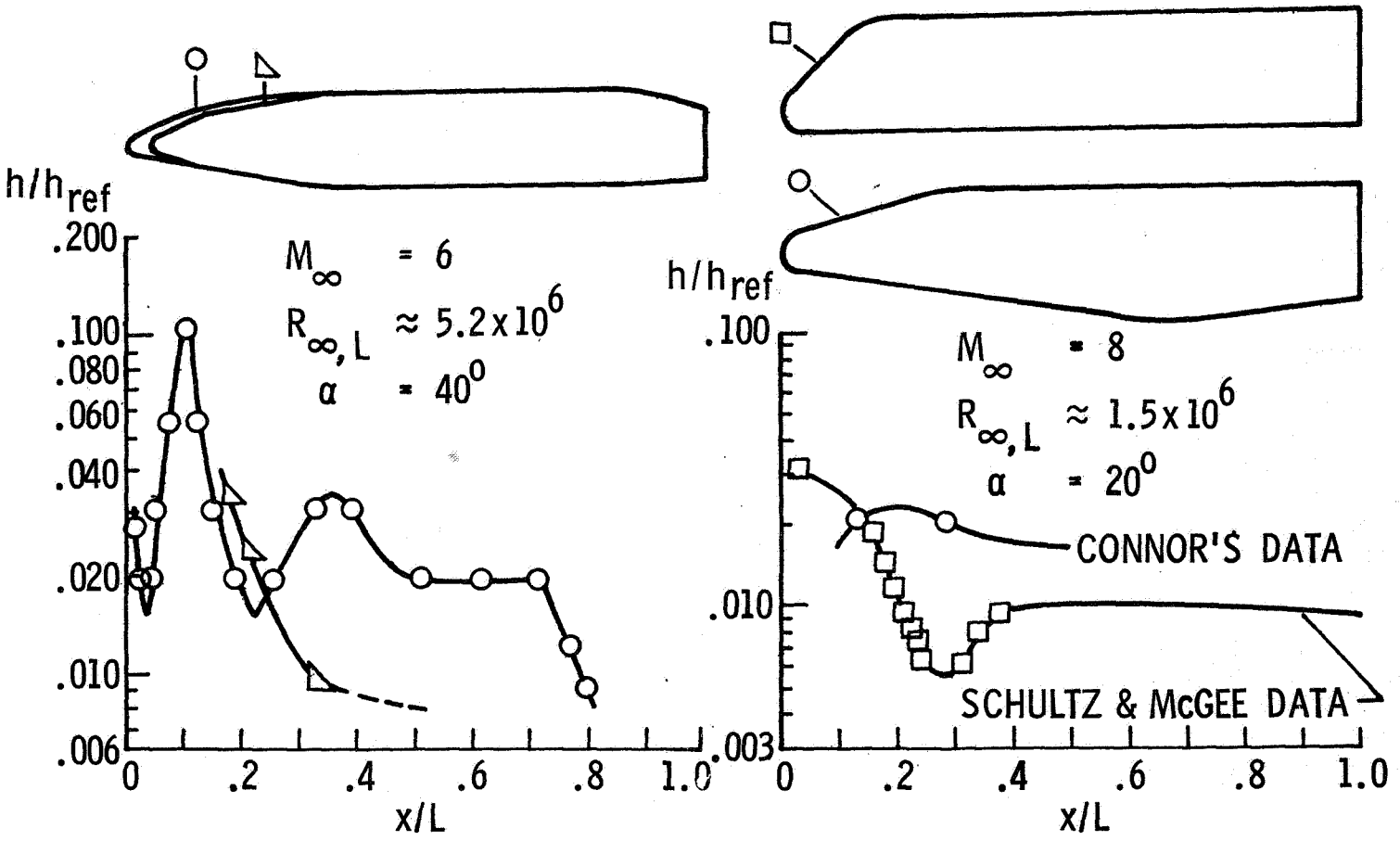

Figure 6

APPLICATION OF WIND-TUNNEL RESULTS TO FLIGHT ENVIRONMENTS

(Figure 7)

Lee-surface vortex-induced heating should be expected on the shuttle in flight. However, it is difficult to determine quantitatively the severity of the vortex-induced heating since the heating is influenced by numerous interrelated parameters (i.e., Mach number, Reynolds number, angle of attack, geometry, and probably real-gas effects and wall cooling). Furthermore, this complicated interrelation of parameters precludes satisfactory theoretical heating predictions at this time.

Application of the present wind-tunnel results at Mach 6 and 19 to projected shuttle flight trajectories (ref. 8) is instructive in indicating the severity of the lee-surface heating in flight. The radiation equilibrium surface temperatures were calculated for the maximum vortex-induced heating rates obtained experimentally on the lee surface of the 0.00397-scale delta-wing orbiter at $\alpha = 20^{\circ}$ for several Reynolds numbers. The maximum heat-transfer rate used in the calculation of surface temperatures was assumed to be 136 kW/m^2 for Mach 6 and 790 kW/m^2 for Mach 19 based on typical high cross-range trajectories (ref. 8). At the higher Reynolds numbers at Mach 6, which are approaching the projected flight Reynolds numbers, the surface temperatures are significantly greater than the established structural limit for titanium. Below the threshold Reynolds number, however, the surface temperatures are appreciably lower. The insert shows the important influence of threshold Reynolds number on the surface temperatures. At Mach 19, the surface temperatures for $R_{\infty,L} = 0.7 \times 10^6$ were below the structural limit for titanium; undoubtedly, this Reynolds number was below the threshold Reynolds number for the particular test conditions. Although it is not known how much below the threshold Reynolds number the Mach 19 conditions were, an extrapolation of the wind-tunnel results to the flight Reynolds numbers indicates that the most severe vortex-induced heating will occur at the lower hypersonic Mach numbers. Since the lee-surface heating problem is extremely complex, completely definitive studies of lee-surface heating across the Mach number range cannot be obtained until the shuttle geometries have been partially frozen. However, utilization of lee-surface shaping guidelines, which are now under development, are recommended for the reduction of vortex-induced lee-surface heating.

APPLICATION OF WIND TUNNEL RESULTS TO FLIGHT ENVIRONMENTS

.00397 - SCALE DELTA-WING ORBITER

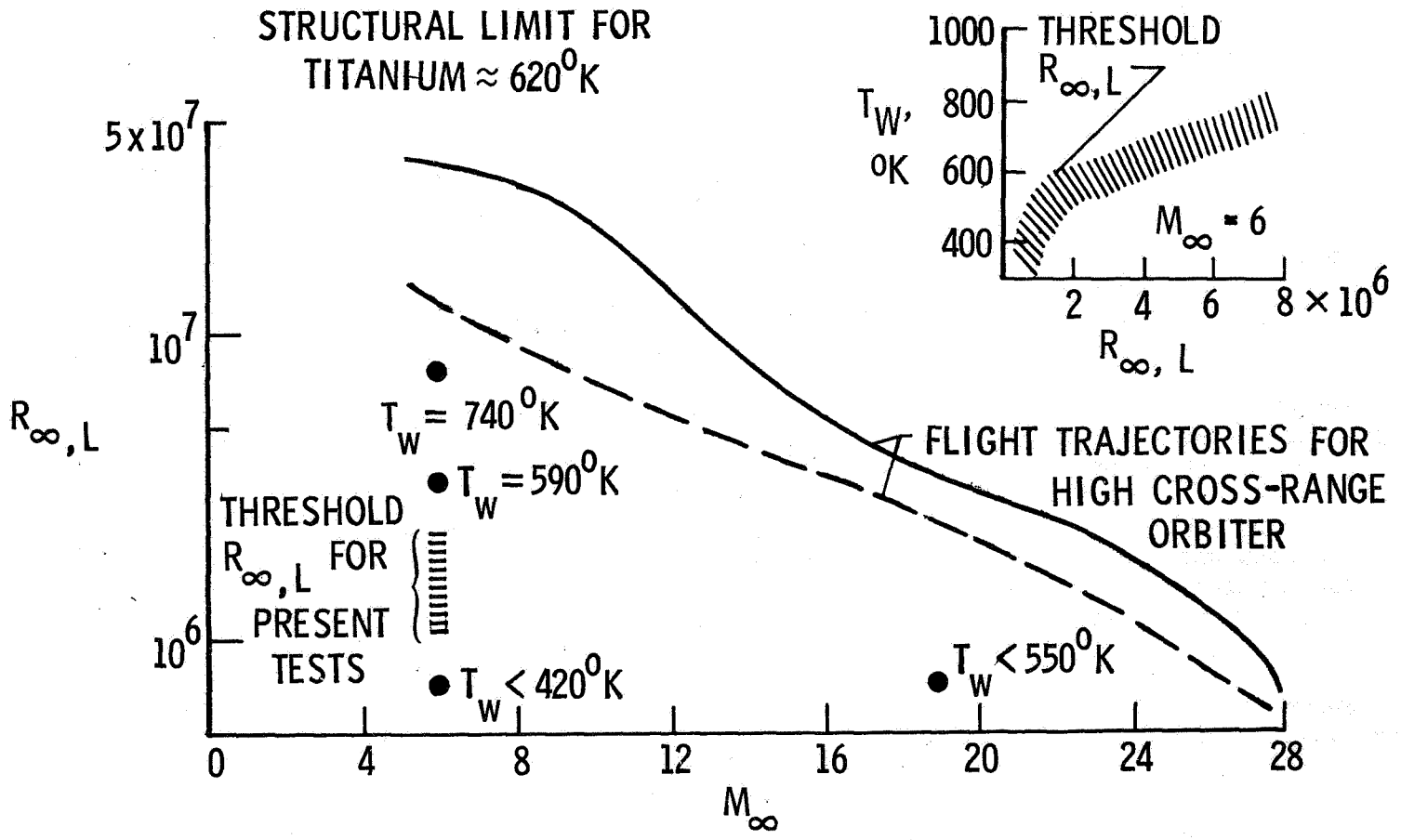

Figure 7

CONCLUSIONS

Results of a continuing experimental lee-surface heating investigation at Mach 6 and 19 on a delta-wing orbiter have been presented with the following conclusions:

(1) The severity of vortex-induced heating is strongly influenced by Reynolds number and there exists a threshold Reynolds number below which peak heating decreases abruptly with decreasing Reynolds number.

(2) Relatively low lee-surface heating was found for the test conditions at Mach 19 which were undoubtedly below the threshold Reynolds number. However, these results were insufficient to define Mach number effects on heating since the Reynolds number influence was interrelated with Mach number.

(3) Vortex-induced peak heating is a relatively weak function of nose bluntness for Reynolds numbers above the threshold. A variation in nose bluntness by a factor of 2 had little effect on the magnitude or position of peak heating. However, the data indicate that nose bluntness influences the threshold Reynolds number.

(4) Variations in lee-surface geometry strongly influence vortex-induced peak heating. Modifying the upper surface of the shuttle to encourage vortex lift-off reduced the vortex-induced heating; additional guidelines to insure this reduction in heating are necessary.

(5) At the position of peak heating, the pressures decrease slightly with increasing Reynolds number and remain nearly constant with increasing angle of attack. In contrast, the peak heating increased with Reynolds number and angle of attack.

(6) Vortex-induced heating should be expected on the shuttle in flight with the most severe lee-surface heating probably occurring at the lower hypersonic Mach numbers. A quantitative determination of this heating is very difficult since it is influenced by numerous interrelated parameters; continuing research is indicated.

REFERENCES

1. Hefner, Jerry N.; and Whitehead, Allen H., Jr.: Lee-Side Heating Investigations. Part I – Experimental Lee-Side Heating Studies on a Delta-Wing Orbiter. NASA Space Shuttle Technology Conference. NASA TM X-2272, Vol. I, 1971, pp. 267-287.

2. Whitehead, Allen H., Jr.; and Bertram, Mitchel H.: Alleviation of Vortex-Induced Heating to the Lee Side of Slender Wings in Hypersonic Flow. AIAA J., vol. 9, no. 9, Sept. 1971, pp. 1870-1872.

3. Whitehead, Allen H., Jr.; Hefner, Jerry N.; and Rao, D. M.: Lee Surface Vortex Effects Over Configurations in Hypersonic Flow. AIAA Preprint No. 72-77, Jan. 1972.

4. Holloway, Paul F.; Sterrett, James R.; and Creekmore, Helen S.: An Investigation of Heat Transfer Within Regions of Separated Flow at a Mach Number of 6.0. NASA TN D-3074, 1965.

5. Chang, Paul K.: Separation of Flow. Pergamon Press, Inc., c.1970, pp. 396-400.

6. Rao, Dhanvada Madhava: Hypersonic Lee-Surface Heating Alleviation on Delta Wing by Apex-Drooping. AIAA J., vol. 9, no. 9, Sept. 1971, pp. 1875-1876.

7. Connor, L. E.: Heat Transfer Tests of the Lockheed Space Shuttle Orbiter Configuration Conducted at the Langley Research Center Mach 8 Variable Density Tunnel. TM 54/20-241, Lockheed Missiles & Space Co., Dec. 1969.

8. Arrington, James P.: Entry Maneuver/Aerothermodynamic Interactions for High Cross-Range Candidate Orbiters. Space Transportation System Technology Symposium – Aerothermodynamics and Configurations, NASA TM X-52876, Vol. I, 1970, pp. 509-530.

AEROTHERMODYNAMIC MEASUREMENTS FOR SPACE SHUTTLE CONFIGURATION IN HYPERSONIC WIND TUNNELS

John J. Bertin, Frank E. Williams, and Robert C. Baker
The University of Texas, Austin, Texas

Winston D. Goodrich
NASA Manned Spacecraft Center, Houston, Texas

William C. Kessler
McDonnell Douglas Astronautics Corporation, St. Louis, Missouri

Presented at the

Space Shuttle Aerothermodynamics Technology Conference

December 15 - 16, 1971

Ames Research Center

Moffett Field, California

AEROTHERMODYNAMIC MEASUREMENTS FOR SPACE SHUTTLE CONFIGURATIONS IN HYPERSONIC WIND TUNNELS

By John J. Bertin, Frank E. Williams, and Robert C. Baker
The University of Texas, Austin, Texas

Winston D. Goodrich
NASA Manned Spacecraft Center, Houston, Texas

William C. Kessler
McDonnell Douglas Astronautics Corporation, St. Louis, Missouri

INTRODUCTION

(Figure 1)

Prediction of the heating-distribution history for the space shuttle vehicle during reentry requires the analysis of a complex, three-dimensional flow field complicated by shock-induced perturbations. To study the resultant flow field, an experimental program with subsequent data analysis has been conducted. The primary objective of the current study was to examine the effect of configuration geometry, angle of attack, and free-stream flow conditions on the heat-transfer distribution as influenced by three-dimensional effects and the wing-fuselage shock-interaction and resultant wing-impingement phenomena. In addition, the data provided information regarding the flow field in the vicinity of the nose and boundary-layer transition in the plane of symmetry of the fuselage.

The University of Texas-coordinated experimental program, which was conducted by using the Vought Aeronautics Company Hypervelocity Wind Tunnel (VAC HVWT) and the Martin-Marietta Corporation Hot-Shot Wind Tunnel (MM HWT), included a Mach number range from 10 to 17 and a unit Reynolds number range from 10^6 to 2×10^7 per foot. The data included measurements of the surface-pressure and the heat-transfer-rate distributions (using models instrumented with thermocouples and models painted with thermographic phosphor) and schlieren and shadowgraph photographs. Posttest photographs of the painted models supplemented the heat-transfer data. In addition, extensive use was made of data obtained in the Cornell Aeronautical Laboratory (CAL) 96-inch Hypersonic Shock Tunnel under another NASA Manned Spacecraft Center contract.

INTRODUCTION

SCOPE OF THE INVESTIGATION

- BOW-GENERATED SHOCK WAVE, WING-GENERATED SHOCK WAVE, AND RESULTING INTERACTION
- FUSELAGE FLOW FIELD, INCLUDING BOUNDARY-LAYER TRANSITION
- DESIGN CORRELATIONS FOR A STRAIGHT WING

CONTROLLED PARAMETERS

- CONFIGURATION GEOMETRY
- ANGLE OF ATTACK : 0° TO 70°
- FREE-STREAM CONDITIONS

M_∞ : 8 TO 17

Re_∞/m : 3×10^5 TO 6×10^7

FACILITIES

- CAL 96-in. HYPERSONIC SHOCK TUNNEL
- MARTIN-MARIETTA HOT-SHOT WIND TUNNEL
- VAC HYPERVELOCITY WIND TUNNEL

Figure 1

ORBITER CONFIGURATIONS

(Figure 2)

The experimental program was conducted in two phases. In one phase, 0.0067-scale models coated with thermographic phosphor were subjected to hypersonic streams in the MM HWT. In the second phase, 0.0045-scale models instrumented with thermocouples and with pressure orifices were subjected to hypersonic streams in the VAC HVWT. The nose geometries were conceptually similar for the models used in a given tunnel, although the geometries differed considerably for the two tunnels. For the MM HWT models (e.g., the fuselage-wing configuration F4:W3 shown), the nose was of a conic nature with a spherically blunted apex. For the VAC HVWT models (e.g., the F3:W2 shown), the relative dimensions for the nose cross sections were identical to the fuselage cross section; that is, the body was homothetic. As viewed from above, the nose is a semicircle, having a radius equal to one-half the body width. Thus, the nose geometry was an "uncontrolled" variable between the test programs in the two facilities.

ORBITER CONFIGURATIONS

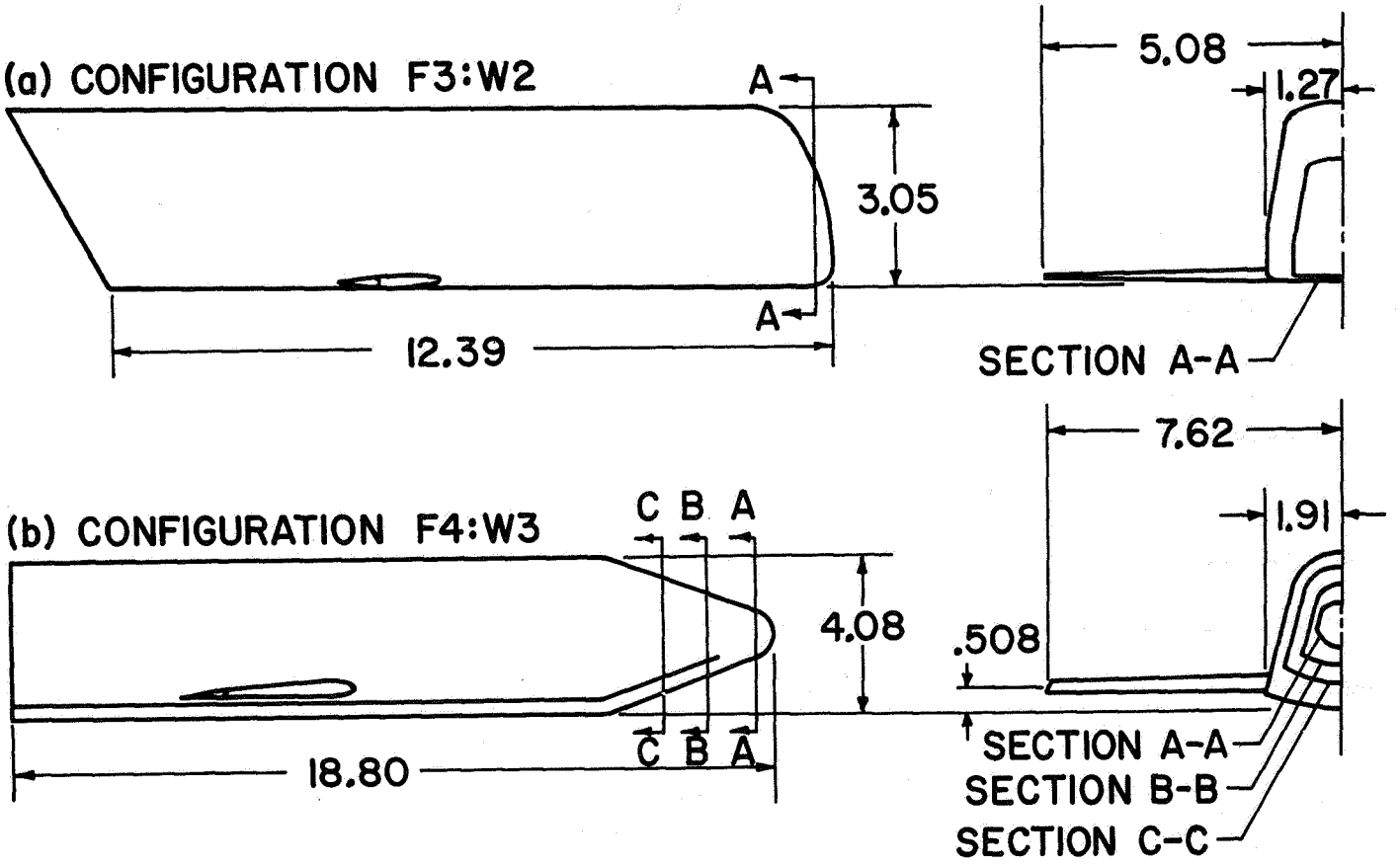

NOTE: DIMENSIONS ARE IN CENTIMETERS.

Figure 2

CONTROLLED GEOMETRIC PARAMETERS

(Figure 3)

The planned variables of configuration geometry were the fuselage cross section and the wing planform, which included two fuselage cross sections and two wing planforms that were common to the programs in the two facilities. An NACA 0012-64 airfoil section (ref. 1) served as the nominal cross section for the wings. A delta-wing planform has been built for use in the VAC HVWT, but the data for this configuration are not yet available. In discussing the data, the model will be identified by the specific fuselage cross section and wing planform combination of the configuration discussed (e.g., F4:W2). This identification method uniquely describes the geometry of the model for which the data were taken because the nose configuration was the only other geometric parameter that was varied. As noted previously, the nose configuration is peculiar to the program (and, hence, to the tunnel) from which the data came.

CONTROLLED GEOMETRIC PARAMETERS

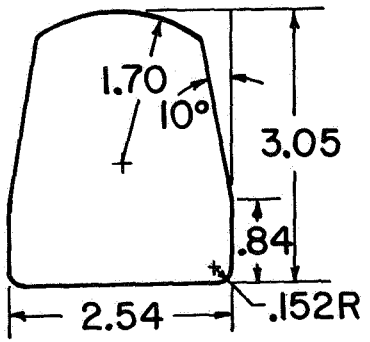

F3 FUSELAGE

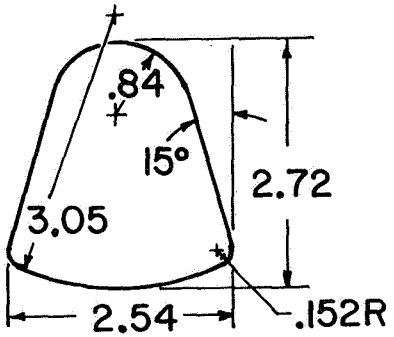

F4 FUSELAGE

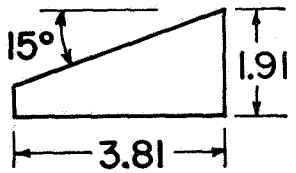

W2 WING

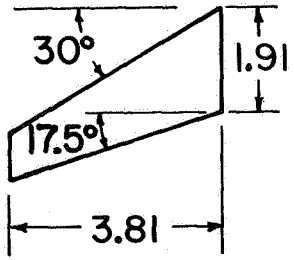

W3 WING

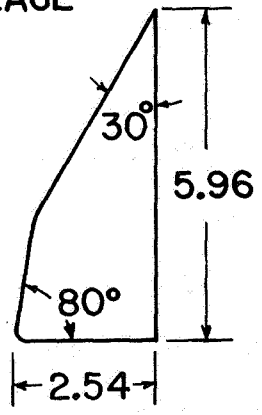

W4 WING

NOTE: DIMENSIONS (cm) ARE FOR MODELS USED IN THE VAC HVWT. TO OBTAIN DIMENSIONS FOR MM HWT MODELS, MULTIPLY BY 1.5.

Figure 3

COMPARISON OF FLOW-VISUALIZATION PHOTOGRAPHS

(Figure 4)

The shock-wave photographs from the two tunnels are compared for the F3:W2 at an angle of attack of 50°. The shock-wave patterns were made visible by using the schlieren technique in the MM HWT and by using the shadowgraph technique in the VAC HVWT. The flow conditions for which the photographs were taken include $M_\infty = 11.9$ and $Re_\infty/ft = 4.2 \times 10^6$ in the VAC HVWT and $M_\infty = 13.5$ and $Re_\infty/ft = 0.7 \times 10^6$ in the MM HWT. The location of the wing impingement associated with the intersection of the fuselage-generated shock wave with the wing-generated shock wave is essentially the same for both configurations. Outboard of the interaction region, the traces of the wing shock are essentially the same. However, as will be discussed next, the photographic traces of the bow-generated shock waves differ significantly for the two configurations.

COMPARISON OF FLOW VISUALIZATION PHOTOGRAPHS
F3:W2 AT $\alpha = 50°$

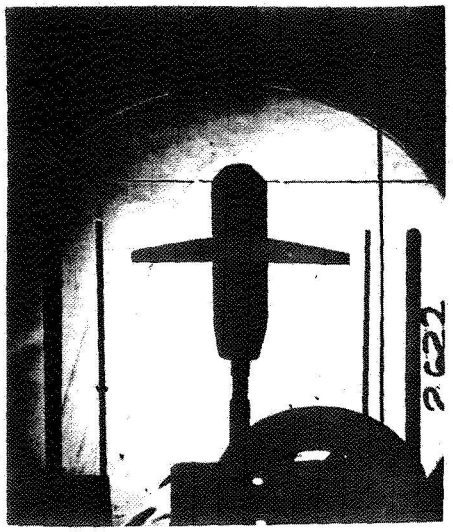

(a) **MM HWT**

$M_\infty = 14$

$Re_\infty/m = 2.1 \times 10^6$

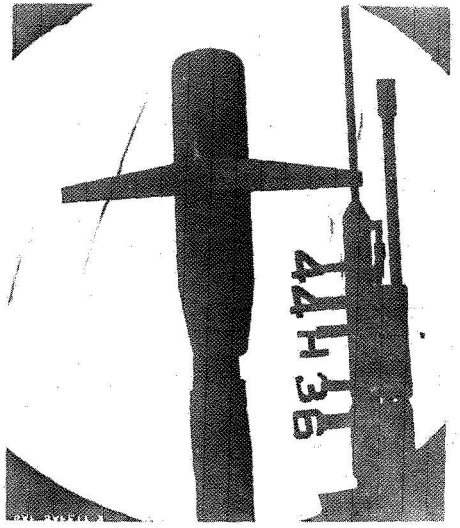

(b) **VAC HVWT**

$M_\infty = 12$

$Re_\infty/m = 12.6 \times 10^6$

Figure 4

EFFECT OF NOSE GEOMETRY ON THE BOW SHOCK WAVE

(Figure 5)

When comparing the photographic traces of the shock-wave patterns, it was noted that, at an angle of attack of 40°, the MM HWT model generated a broader bow shock wave than did the VAC HVWT model, although the MM HWT model was more slender in terms of the rate at which the cross-sectional area increases with distance from the apex. After eliminating the possibility that these differences might be due to the free-stream Mach number or to real-gas effects as discussed in reference 2, it was concluded that the differences were due to configuration geometry. The MM HWT nose fairing makes a 20° angle with the underbelly of the fuselage. Therefore, at an angle of attack of 40°, the inviscid flow on the ramp is subsonic while the flow on the underbelly of the fuselage is supersonic. (Recent tests in a Mach 5 stream at the University of Texas indicate that the ramp flow is subsonic for this configuration for angles of attack in excess of 20°.) Because the entire underbelly of the VAC HVWT model is very flat, at an angle of attack of 40°, the inviscid flow is generally supersonic except near the stagnation point. For an angle of attack of 60°, the fuselage flow fields are entirely subsonic for both configurations, and the observed traces for the bow shock waves are virtually identical. The resultant intersection of the wing-generated shock wave with the fuselage-generated shock wave was not influenced by the differences in the nose geometry at either angle of attack.

EFFECT OF NOSE GEOMETRY ON THE BOW SHOCK WAVE

F3:W2

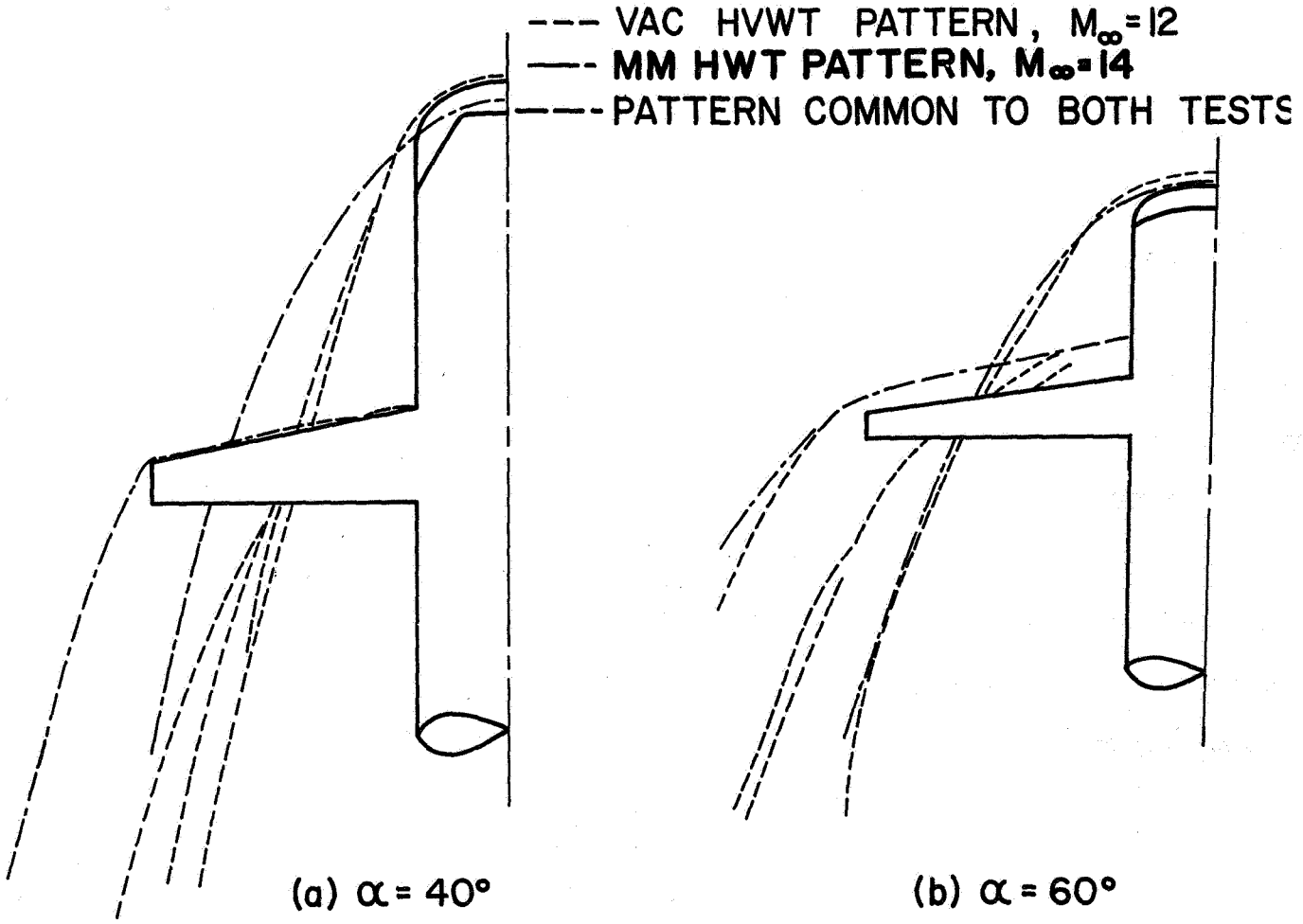

Figure 5

PRESSURE MEASUREMENTS ON THE WINDWARD-MOST ELEMENT OF THE FUSELAGE

(Figure 6)

Pressure measurements from the third orifice in the plane of symmetry of the fuselage (i.e., $s = 2.25\ W_b$), presented as a function of angle of attack, are compared with pressure data for "infinite" cylinders. Measurements from the third orifice were chosen for this comparison because upstream data were influenced by the stagnation-region flow while flow-field perturbations introduced by the wing affect the downstream data. Also included for comparison with these measurements are the pressures calculated for three simple flow models, specifically: modified Newtonian flow, tangent-cone flow, and tangent-wedge flow. These "theoretical" models assume the flow is turned by a straight-line surface element through an angle α from the free-stream direction. The values calculated by using the equation for modified Newtonian flow provide the best correlation with the data at this fuselage station. The agreement between the data and the calculated values for the tangent-cone assumption is considered satisfactory at the lower angles of attack.

PRESSURE MEASUREMENTS ON THE WINDWARD-MOST ELEMENT OF THE FUSELAGE

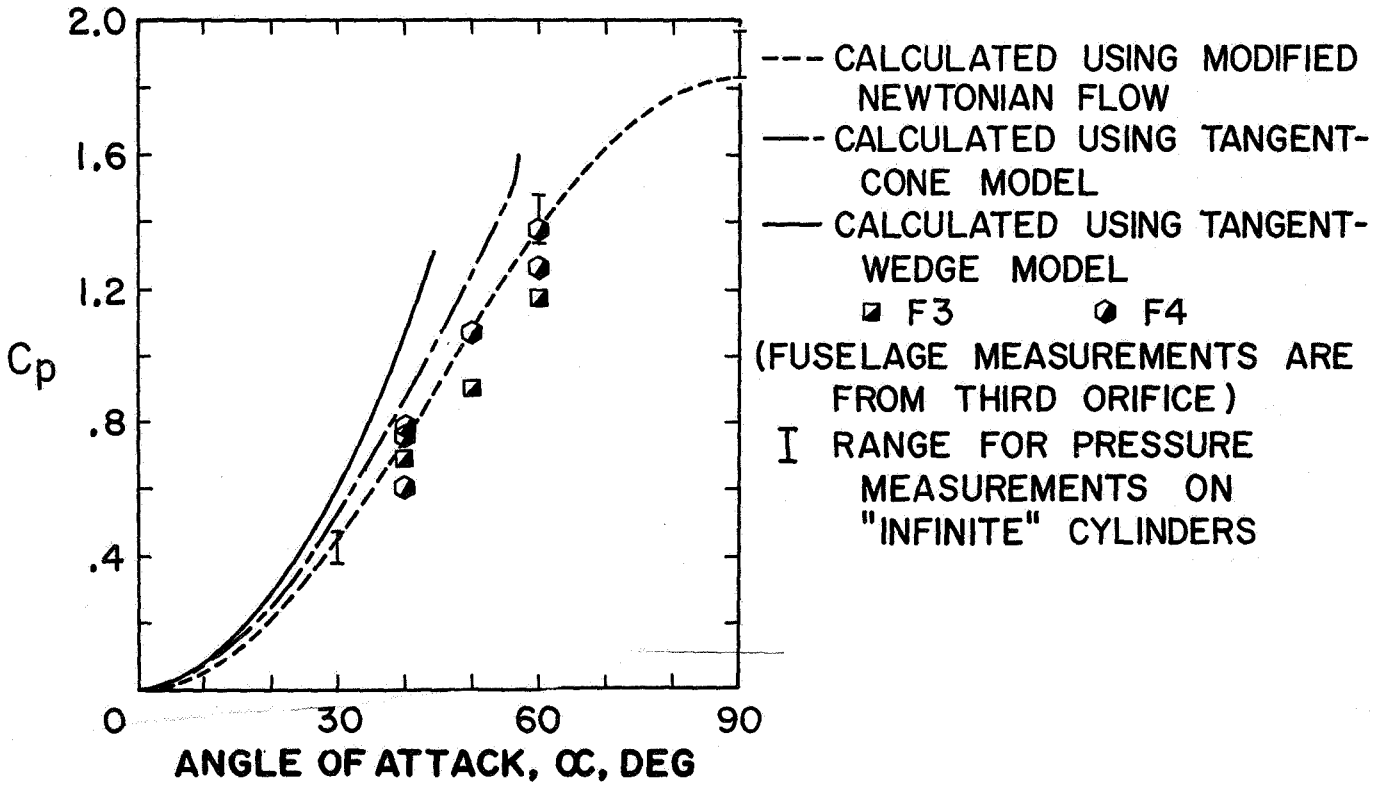

Figure 6

EFFECT OF REYNOLDS NUMBER ON PLANE-OF-SYMMETRY FLOW FIELD

(Figure 7)

The surface-pressure and the heat-transfer-rate distributions measured in the pitch plane of the F4:W2 are presented for an angle of attack of 40°. The local heat-transfer measurements have been divided by the theoretical stagnation-point heat-transfer rate (ref. 3) for a sphere the diameter of which is equal to the characteristic width of the fuselage $W_b(\dot{q}_{t,ref})$ and for a sphere having a 1-foot radius scaled to model size $(\dot{q}_{t,R = 1\ foot})$. The pressure distribution is essentially independent of the Reynolds number. The heat-transfer data obtained at the lower Reynolds number indicate that the boundary layer remained laminar along the entire length of the fuselage. The locally high heating for the thermocouple at the trailing edge of the wing is largely due to a flow-field perturbation caused by the wing and partially by experimental uncertainty. Both the experimental heat-transfer distribution and the shadowgraph indicate that boundary-layer transition occurred at the higher Reynolds number.

Theoretical heat-transfer distributions for a laminar boundary layer, which have been calculated based on simple flow models, are included for comparison. The flow models are designated as swept-cylinder, normal-shock-expansion, tangent-cone, and tangent-wedge models. The philosophy used to calculate the inviscid flow properties and the appropriate metric for the spreading of the boundary layer is described in reference 2. The laminar measurements are best correlated by using a combination of flow-field models, such as the normal-shock-expansion model near the nose and the tangent-cone approximation at downstream points. For many engineering applications, the heating rates calculated by using the swept-cylinder theory are in reasonable agreement with the laminar heat-transfer measurements for these configurations, especially where a degree of conservatism will be used in the design procedures.

EFFECT OF REYNOLDS NUMBER ON PLANE-OF-SYMMETRY FLOW FIELDS

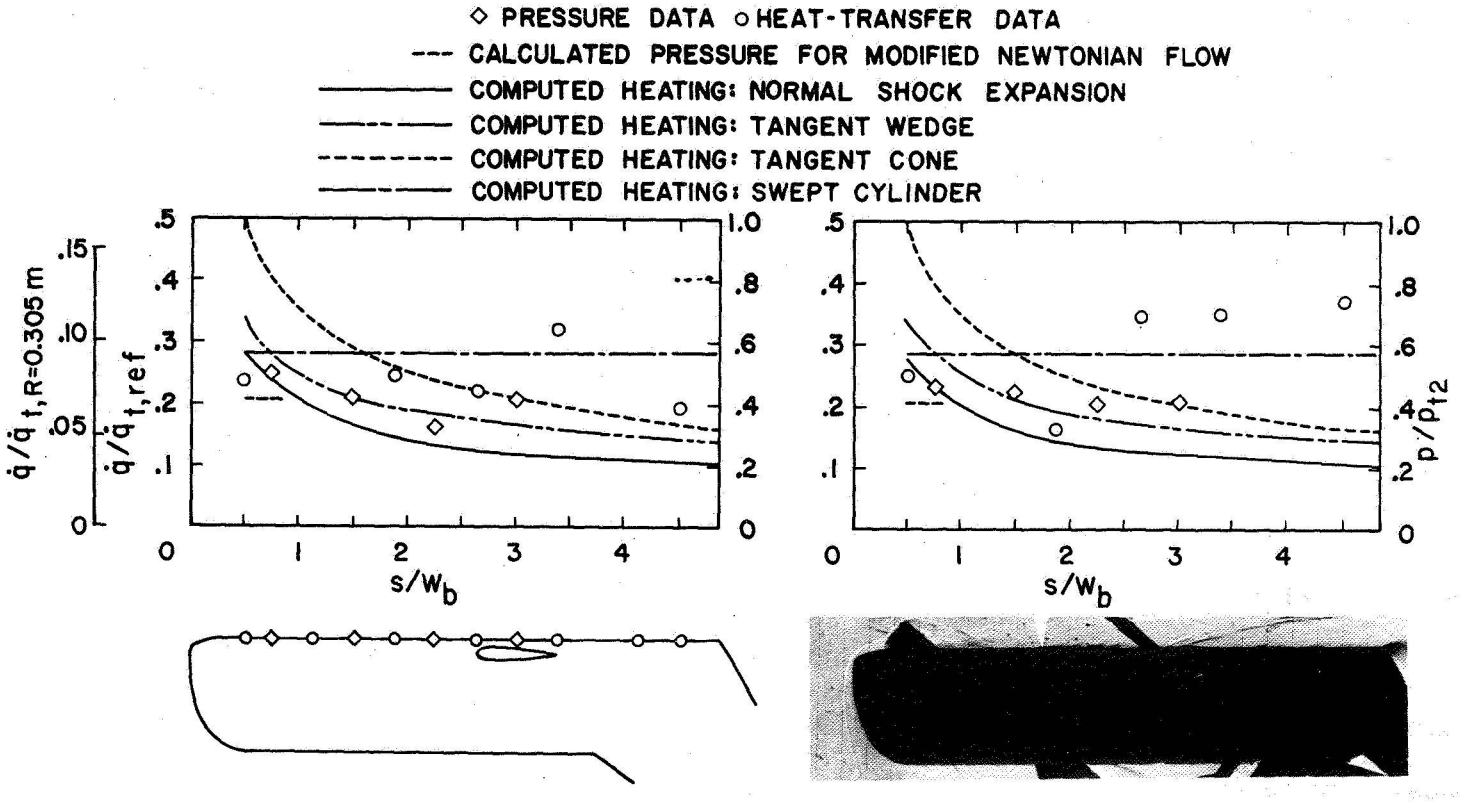

(a) $M_\infty = 17$, $Re_\infty/m = 5.8 \times 10^6$

(b) $M_\infty = 12$, $Re_\infty/m = 13.7 \times 10^6$

F4:W2 at $\alpha = 40°$

Figure 7

EFFECT OF FUSELAGE CROSS SECTION ON PLANE-OF-SYMMETRY FLOW FIELD

(Figure 8)

The effect of the transverse curvature on the surface-pressure and on the heat-transfer distributions in the plane of symmetry for an angle of attack of 40° is indicated. No difference is discernible between the pressure distributions for the two different fuselages. Heat-transfer data from the plane of symmetry, however, indicate that transition occurred earlier on the F4 fuselage (which has a rounded underbelly) than on the F3 fuselage (which has a flat underbelly). The heat-transfer distributions measured at an angle of attack of 50° (which are not presented herein) indicate the same relation between the transition locations for these two configurations. Transition occurring earlier for a configuration with a rounded cross section than for a flat-bottomed configuration was also observed in the heat-transfer distributions measured on a simulated "infinite" cylinders in a companion program (ref. 4).

The surface pressures and the heat-transfer rates measured in the pitch plane of the F3 fuselage at an angle of attack of 40° are presented for two different straight wings. Although the wing planforms are significantly different, the surface-pressure and the heat-transfer-rate distributions are essentially the same. Similar wing-planform independence was observed for these configurations at angles of attack of 50° and 60°.

EFFECT OF FUSELAGE CROSS SECTION ON PLANE-OF-SYMMETRY FLOW FIELDS

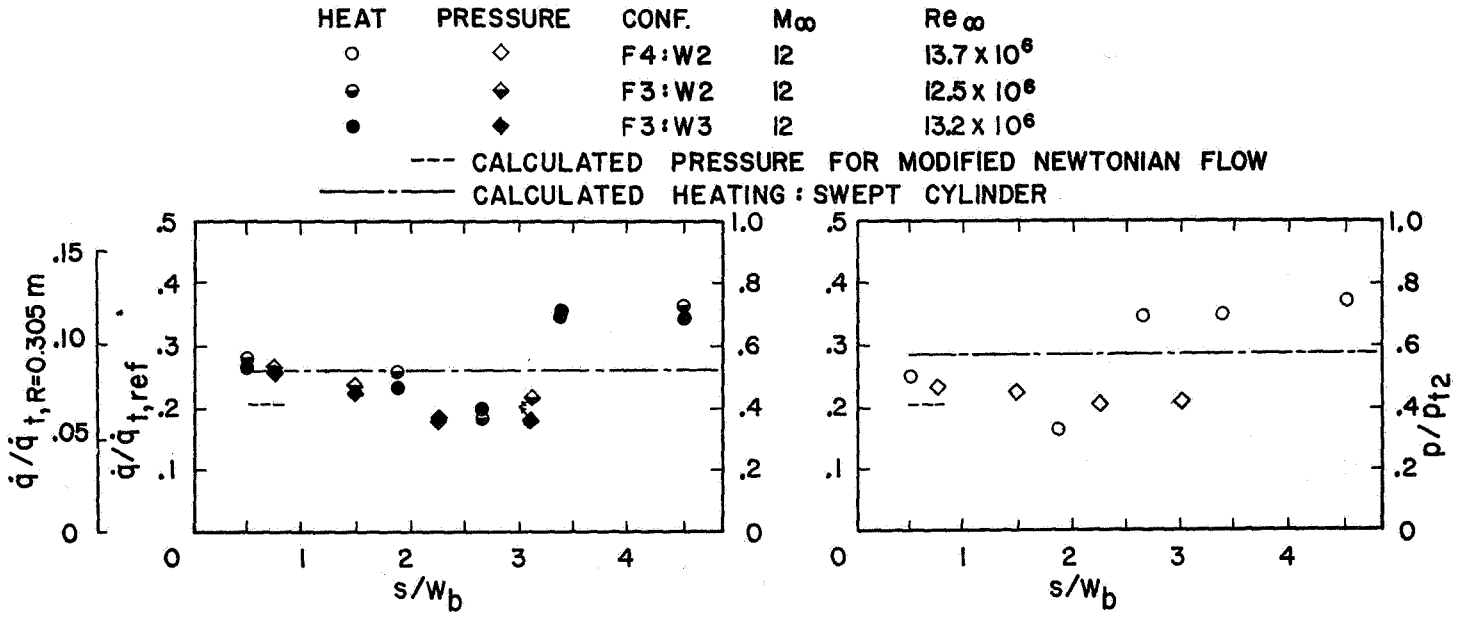

Figure 8

TRANSITION CORRELATION

(Figure 9)

Despite the limited instrumentation, the transition locations (which were defined to be at the last thermocouple for which the heating rate indicated laminar flow) are reasonably consistent. As noted, the transition location on the flat-bottomed F3 fuselage was downstream of the location on the rounded F4 fuselage for a given test condition. Therefore, the use of $Re_{x,tr}$ to define transition yields different criteria for the two fuselages. Using $Re_{\theta,tr}$ (or $Re_{\delta^*,tr}$), a "single" criterion is obtained for both configurations. Thus, the transition criteria should use parameters that at least partially account for the spreading of the flow.

A comparison of the current transition measurements with other data is presented in reference 2. In terms of the parameter

$$\log_{10}\left(\frac{Re_{\delta^*,tr}}{\left(Re_x/ft\right)^{0.25}}\right)$$

the current transition results lie below the empirical correlation of reference 5 (although no other data were presented in ref. 5 at the low, local Mach number of the present tests). Using a different correlation (i.e., that suggested in ref. 6), the present data indicate that

$$\frac{Re_{\theta,tr}}{M_e\left(Re_x/ft\right)^{0.2}} \sim 11 \text{ to } 14$$

when the parameters are calculated using the normal-shock-expansion techniques or

$$\frac{Re_{\theta,tr}}{M_e\left(Re_x/ft\right)^{0.2}} \sim 5 \text{ to } 10$$

if the tangent-cone flow model is used to evaluate the parameters.

The introduction of vorticity caused by the strongly curved character of the bow shock wave may contribute to the apparently premature occurrence of transition in the present tests, which is consistent with the literature experience with blunt cones.

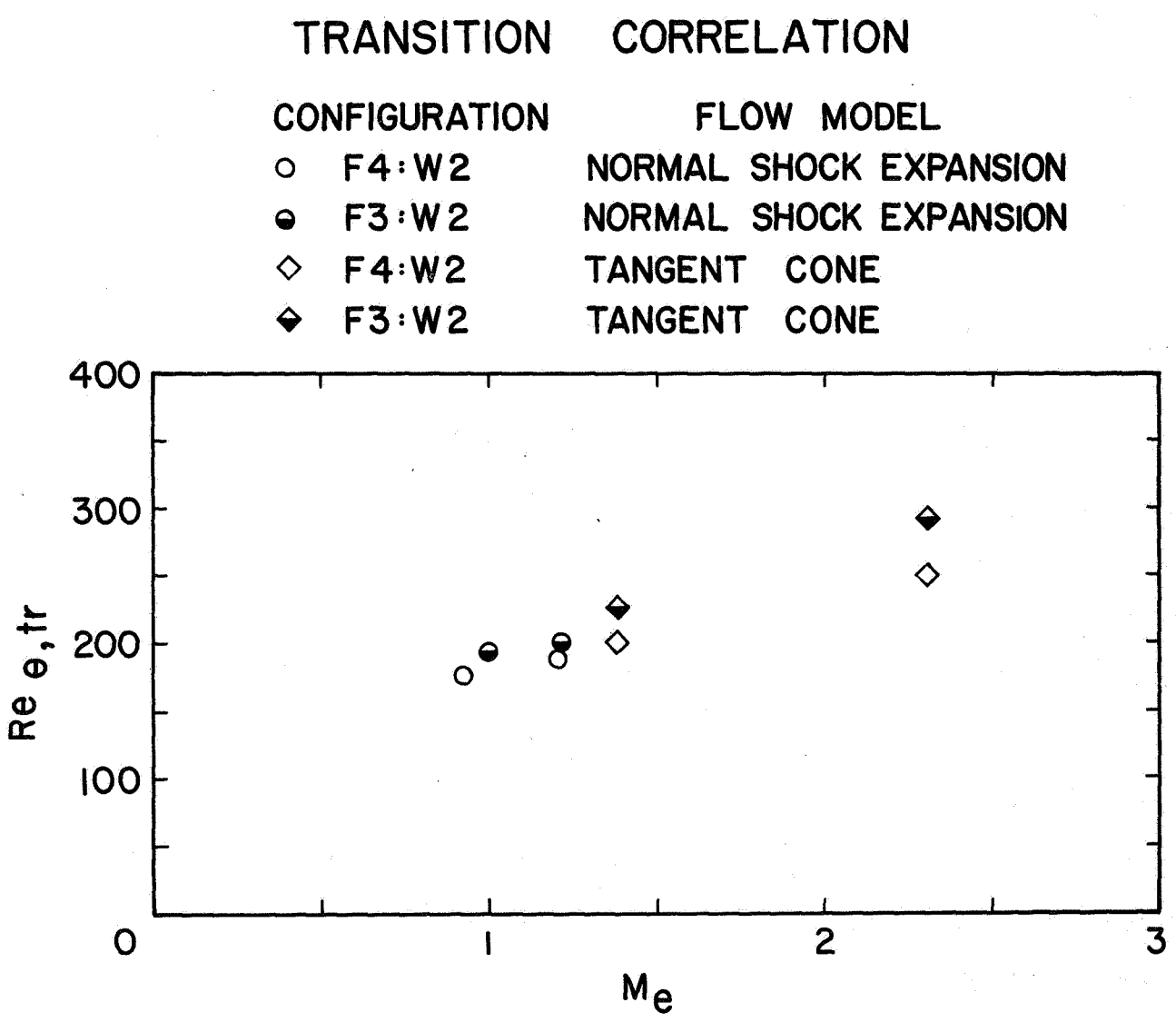
TRANSITION CORRELATION
CONFIGURATION
FLOW MODEL
F4:W2
NORMAL SHOCK EXPANSION
F3:W2
NORMAL SHOCK EXPANSION
F4:W2
TANGENT CONE
F3:W2
TANGENT CONE
400
300
200
100
0
1
2
3
Re e,tr
Me

Figure 9

UNPERTURBED HEAT-TRANSFER RATES NEAR THE WING LEADING EDGE

(Figure 10)

A suggested philosophy for generating design curves for the unperturbed heat-transfer distributions for "straight" wings is discussed in the next five figures. Wind-tunnel data are used to generate semiempirical relations for the maximum heat-transfer rate as a function of configuration and of angle of attack. Flat-plate relationships are used to compute the subsequent downstream variation in heating.

Using measurements from the CAL 96-inch Hypersonic Shock Tunnel, the heat-transfer rates measured at three sensors near the leading edge are shown here as a function of angle of attack. One sensor is located at the leading edge; two sensors are at $0.01c_{\ell}$ from the leading edge along the chord line (one windward and one leeward). The local heat-transfer rate is very sensitive to position. Although the sensors are only $0.01c_{\ell}$ apart, the heating measured at the leading edge is approximately five times that measured at the leeward sensor. As the angle of attack increases, the peak heating location moves from the leading-edge sensor to the windward surface. In addition to the fairings of the heat-transfer data for a particular sensor, a design curve has been drawn to denote the maximum heating rate as a function of the angle of attack. To generate such a curve, the sensors must be closely spaced, the positions must be accurately known, and experimental errors (e.g., conduction losses) must be minimal. The type of instrumentation used on the CAL model is believed to satisfy these requirements.

UNPERTURBED HEAT-TRANSFER RATES NEAR THE WING LEADING EDGE

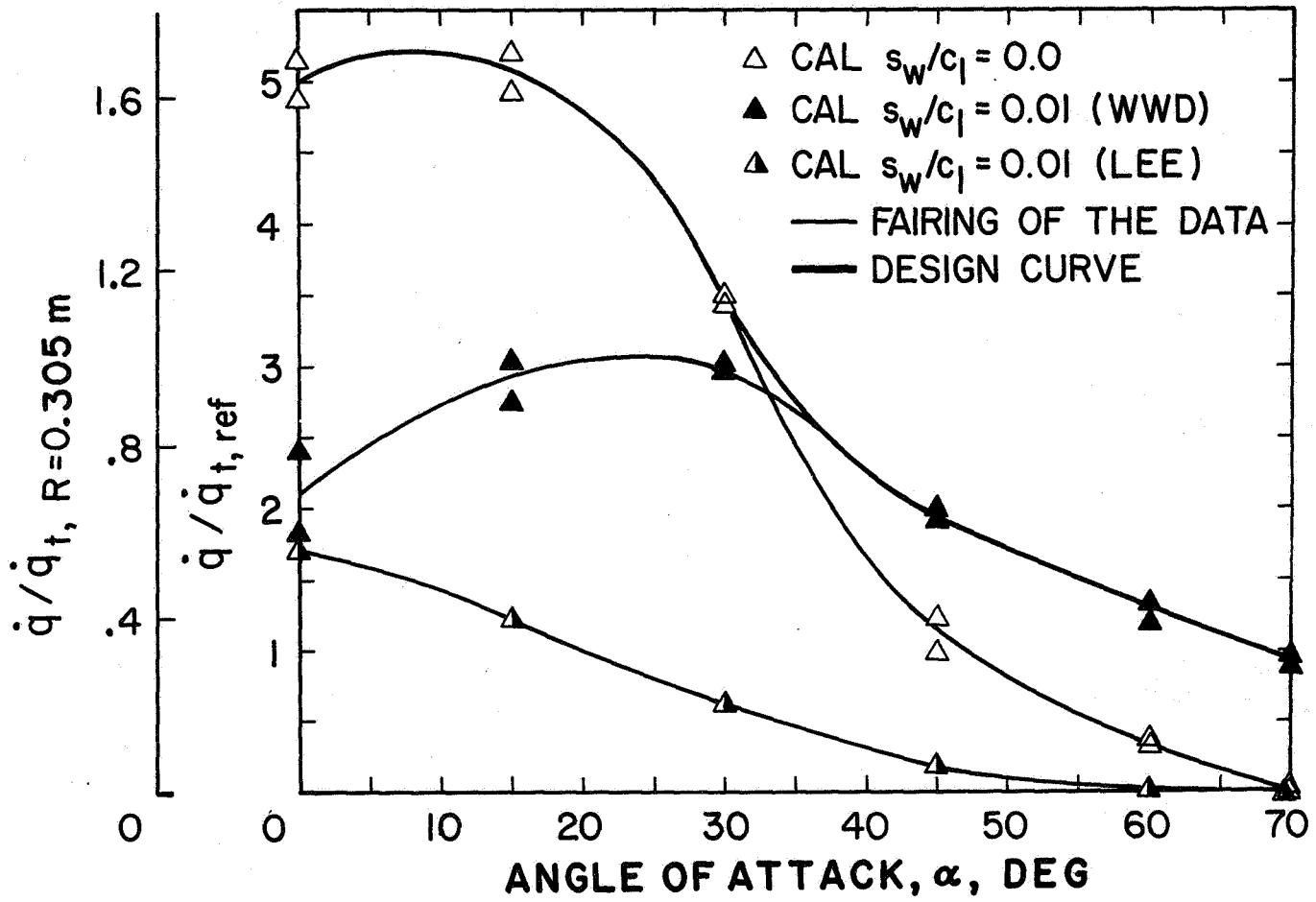

Figure 10

EFFECTIVE RADIUS OF CURVATURE FOR PEAK HEATING AS A FUNCTION OF ANGLE OF ATTACK

(Figure 11)

At an angle of attack of 0°, the nondimensionalized heat-transfer rate to the leading edge of the swept wing satisfies the relationship

$$\frac{(\dot{q})_{\alpha = 0^\circ}}{\dot{q}_{t,ref}} = 0.707(\cos \Lambda)^{1.2} \sqrt{\frac{0.5W_b}{R_{eff,\alpha = 0^\circ}}} \tag{1}$$

Thus, using the measured heating rate, the effective radius of curvature for an angle of attack of 0° can be calculated. The effective radius of curvature for any other angle of attack can be calculated, assuming that

$$\left(\frac{\dot{q}}{\dot{q}_{\alpha = 0^\circ}}\right)_{peak} = \sqrt{\frac{R_{eff,\alpha = 0^\circ}}{R_{eff}}} \tag{2}$$

The effective radius of curvature, shown here as a function of the angle of attack, was computed by using the measured values of the peak heating rate presented in the ninth slide. Because heating data were not available for an angle of attack of 90°, this effective radius of curvature was calculated by using the relationship

$$\frac{R_{eff,\alpha = 90^\circ}}{c_\ell} = \frac{1.157}{0.745 + 3.14 \frac{r_c}{c_\ell}} \tag{3}$$

The value thus calculated for an angle of attack of 90° falls on a reasonable extrapolation of the effective radius-of-curvature relationship based on the heating-rate measurements.

The results presented herein are based on the data for a particular straight-wing configuration (ref. 7). A more general approach should take into account planform area (probably in conjunction with the aspect ratio). The need to account for planform area would become more critical at higher angles of attack. Attempts to generate more general curves by including data for other wing geometries failed. The inability to incorporate other data into the procedure will be discussed subsequently.

EFFECTIVE RADIUS OF CURVATURE FOR PEAK HEATING AS A FUNCTION OF ANGLE OF ATTACK

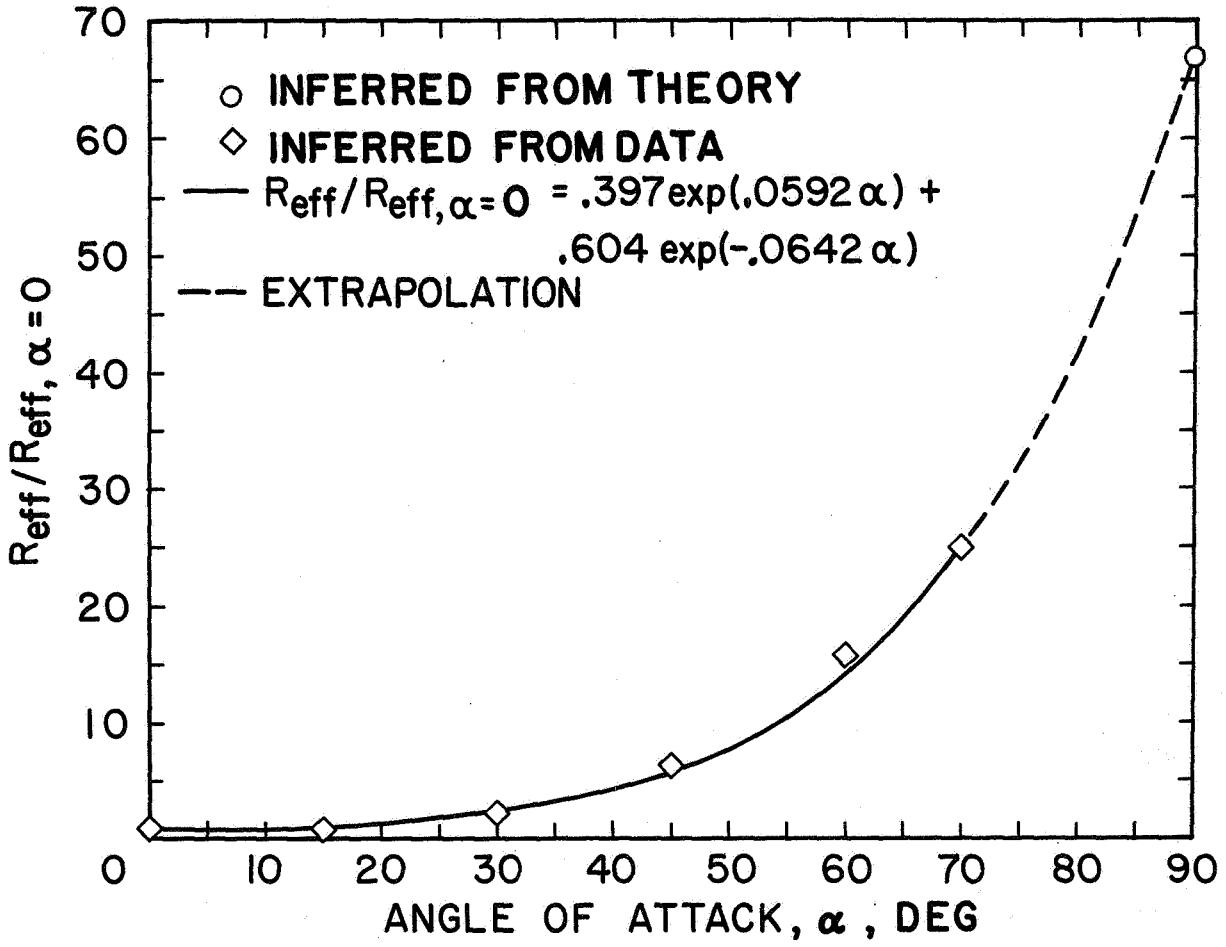

Figure 11

DESIGN CURVES FOR THE UNPERTURBED PEAK HEATING TO A STRAIGHT WING

(Figure 12)

A series of design curves presenting a peak heating rate as a function of the angle of attack and of the sweep angle can be generated by combining the information contained in the two previous figures. These design relationships, shown here, may be represented by the relationship

$$\frac{\dot{q}}{\dot{q}_{t,ref}} = 0.707(\cos \Lambda)^{1.2} \sqrt{\frac{0.5W_b}{R_{eff}}} \qquad (4)$$

As noted previously, a more general approach should take into account the planform area of the wing.

DESIGN CURVES FOR THE UNPERTURBED PEAK HEATING TO A STRAIGHT WING

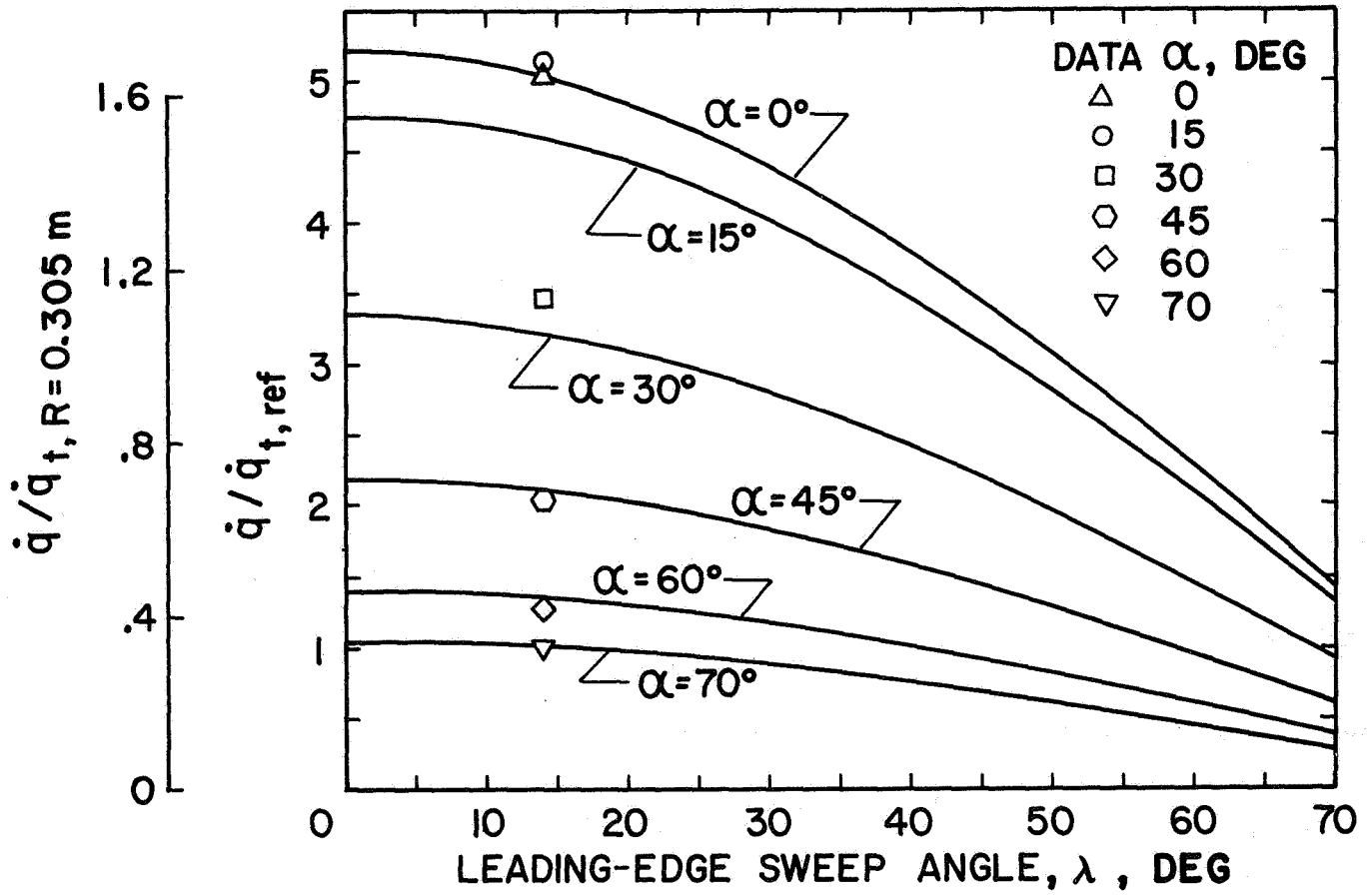

Figure 12

PROBLEMS ENCOUNTERED WITH PEAK-HEATING MEASUREMENTS

(Figure 13)

As noted, attempts were made to incorporate the effect of wing planform area by using heat-transfer measurements from other configurations. The following data were considered.

1. Thin-skin heat-transfer measurements on a straight-winged orbiter in the VAC HVWT (Λ of 15° and 30°)

2. Thin-skin heat-transfer measurements on a North American-Rockwell delta-wing orbiter in the Arnold Engineering Development Center (AEDC) Tunnel B (Λ of 60°)

3. Thin-skin heat-transfer measurements on a General Dynamics Corporation (GDC) booster in AEDC Tunnel B (Λ of 52.5°)

Typical data from these programs are compared here with the design curves generated by using the measurements from the CAL 96-inch Hypersonic Shock Tunnel. The relative insensitivity to position and to angle of attack of the heat-transfer rates measured on the GDC booster is attributed to thermal-conduction effects associated with thin-skin measurements in a sharply curved area of a small-scale model. Posttest inspection of the VAC HVWT models revealed that the thermocouples were not on the leading edge but in the leeward region. Conduction-related errors are thought to be less important for the VAC HVWT model because the run time is very short and because the nickel skin is only 0.004 inch thick.

The important conclusion to be drawn from this figure is that certain types of experimental information are best obtained by using a particular type of instrumentation or model rather than that data from one facility are much better than those from another. In this instance, the need for an accurate definition of the rapidly varying heat transfer over a limited portion of the model places different requirements on the test program than does the gross characterization of heat transfer over an entire configuration.

PROBLEMS ENCOUNTERED WITH PEAK-HEATING MEASUREMENTS

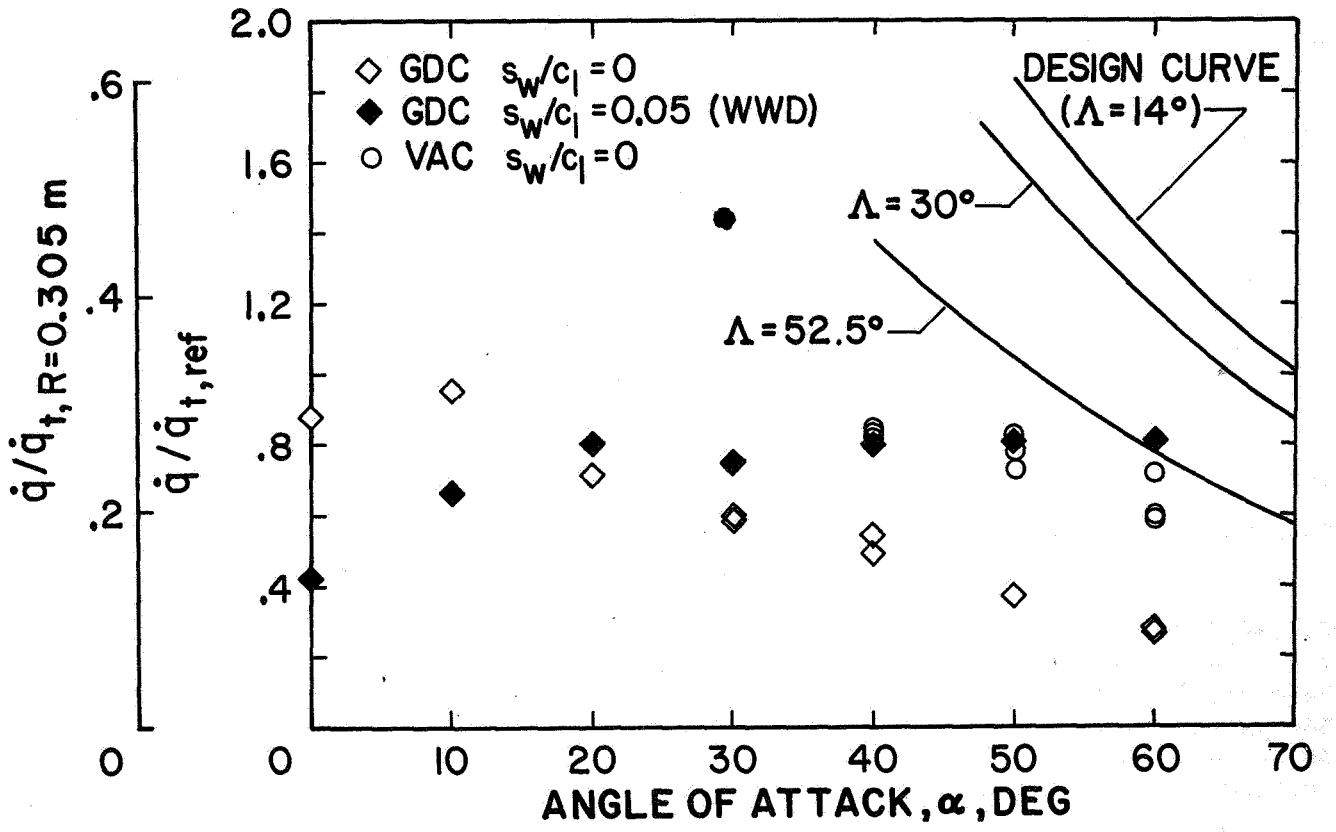

Figure 13

CHORDWISE HEAT-TRANSFER DISTRIBUTION FOR THE STRAIGHT WING

(Figure 14)

The experimental chordwise heat-transfer distributions for the F4:W2 configuration at an angle of attack of 40° and for the CAL model at an angle of attack of 45° are compared here with the theoretical distribution. The theoretical values were calculated by using the Eckert-reference-temperature method (ref. 8) in the "flat-plate" relation. "Flat-plate" is within quotation marks because the properties at the edge of the boundary layer were not assumed to be constant (as would be the case for a flat plate) but were allowed to vary in the chordwise direction in accordance with the measured pressures.

The heat-transfer data, which are presented as a function of the chordwise coordinate s_w (nondimensionalized by division by the root chord c_r), are within ±20 percent of the theory with the following exceptions.

1. The lower Reynolds number measurements at all thermocouples for which $z_r = 0.2b$ (filled and half-filled triangular symbols)

2. The measurements at the midchord thermocouples at $z_r = 0.4b$, where z_r is the lateral distance measured from the root chord of the wing and b is the span (root to tip) of one wing

The first exception is attributed to flow perturbations at the fuselage-wing juncture. This wing-root interference could also be seen in the pressure data and in the posttest photograph of the model (ref. 2). The severity of the perturbation is a function of the geometry of the wing-fuselage juncture and the flow conditions (as indicated principally by the Reynolds number). The second exception is attributed to the impinging flow resulting from the interaction of the wing-generated shock wave with the fuselage-generated shock wave. This localized heating increase is verified by the posttest photograph of the model. However, the fact that a majority of the measurements are within ±20 percent of the theoretical values is considered significant for design purposes. Further, a single, relatively smooth curve could be faired through the data from the two tunnels to generate an empirical heat-transfer-rate distribution (especially if the fact that the angles of attack differ by 5° is considered).

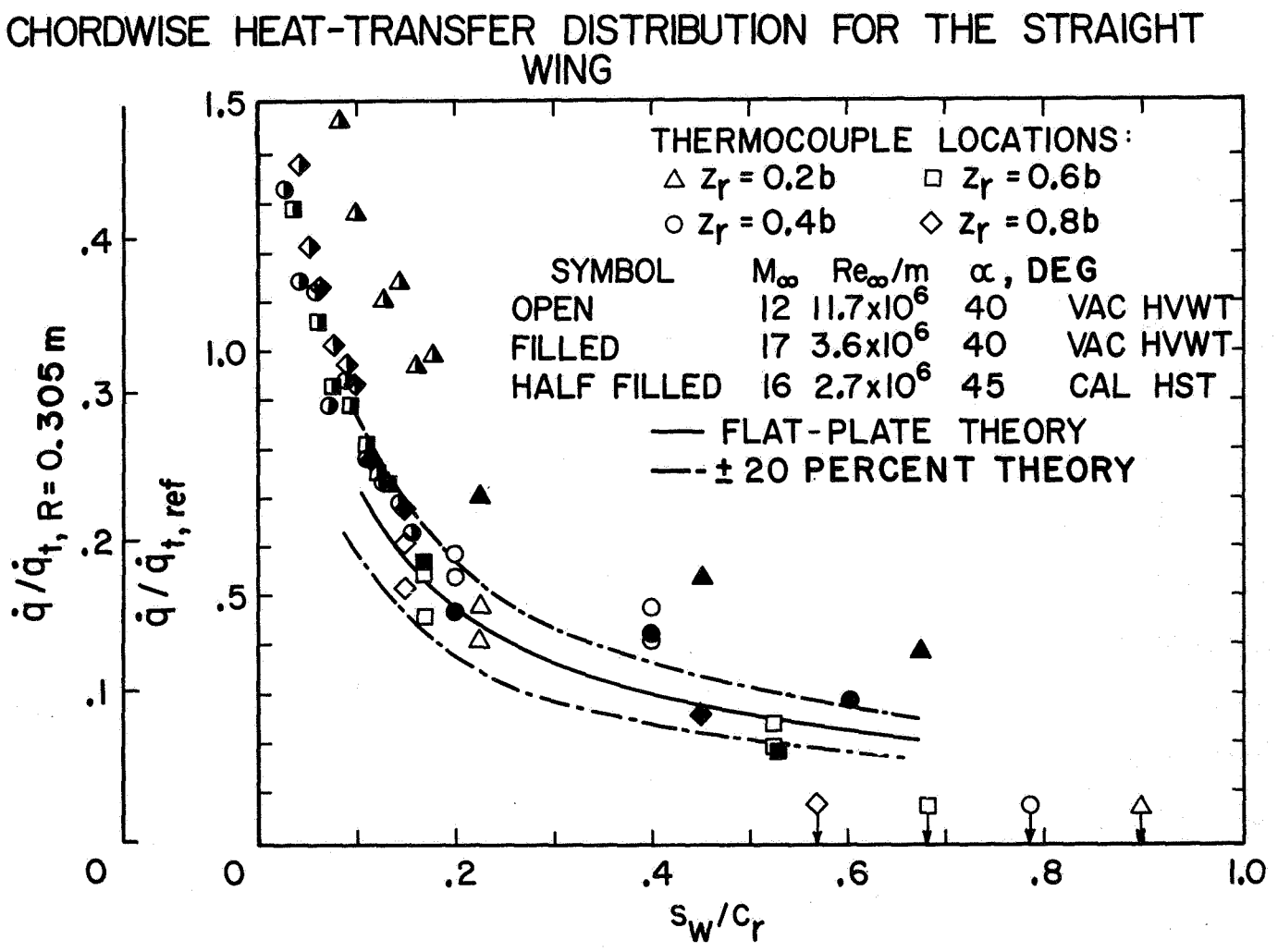
CHORDWISE HEAT-TRANSFER DISTRIBUTION FOR THE STRAIGHT WING
THERMOCOUPLE LOCATIONS:
△ z_r = 0.2b
□ z_r = 0.6b
○ z_r = 0.4b
◇ z_r = 0.8b
SYMBOL M_∞ Re_∞/m α, DEG
OPEN 12 11.7×10^6 40 VAC HVWT
FILLED 17 3.6×10^6 40 VAC HVWT
HALF FILLED 16 2.7×10^6 45 CAL HST
FLAT-PLATE THEORY
± 20 PERCENT THEORY
$\dot{q}/\dot{q}_{t,R=0.305\,m}$
$\dot{q}/\dot{q}_{t,ref}$
s_w/c_r
0
.1
.2
.3
.4
.5
1.0
1.5
.2
.4
.6
.8
1.0

Figure 14

INTERACTION OF WING-GENERATED SHOCK WAVE WITH FUSELAGE-GENERATED SHOCK WAVE

(Figure 15)

The flow structure resulting from the interaction of the fuselage-generated shock wave and the resulting impingement on the surface of the wing depends on the vehicle geometry and on the angle of attack. The experimental results indicate that a similar flow-structure model is valid for the W2 wing for angles of attack of 40° and 50°. The results shown here suggest the "Type V" shock/shock-interaction model of Edney (ref. 9). Such a model is consistent with the data for the straight-wing configuration tested in the MM HWT (e.g., the schlieren photograph and the post-test photograph of the model). Photographs of the shockwave structure from the VAC HVWT tests are also consistent with a Type V interaction. Sufficient thermocouples were not available on the VAC HVWT models to determine if the heat-transfer data were consistent with the interaction model.

INTERACTION OF WING-GENERATED SHOCK WAVE WITH FUSELAGE-GENERATED SHOCK WAVE

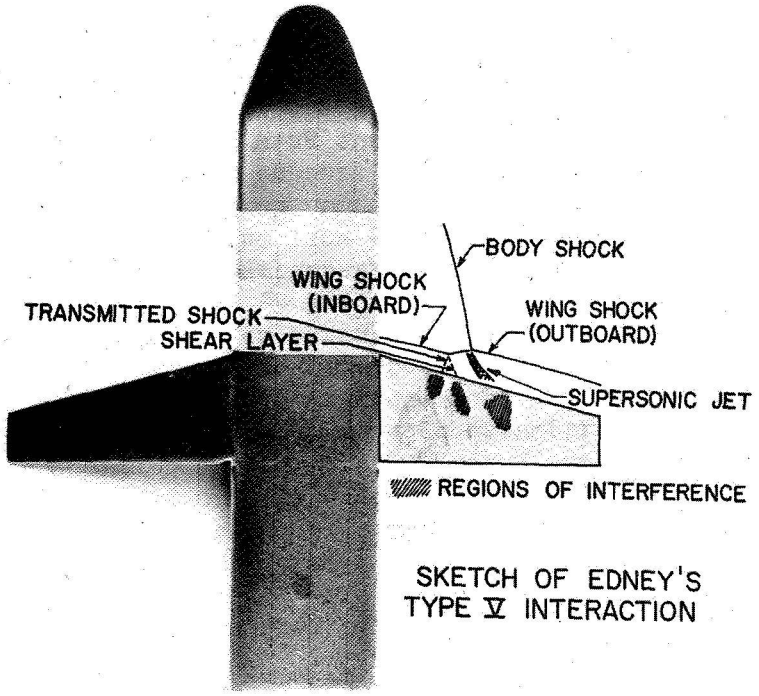

SKETCH OF EDNEY'S TYPE V INTERACTION

POST TEST PHOTOGRAPH OF MM HWT MODEL

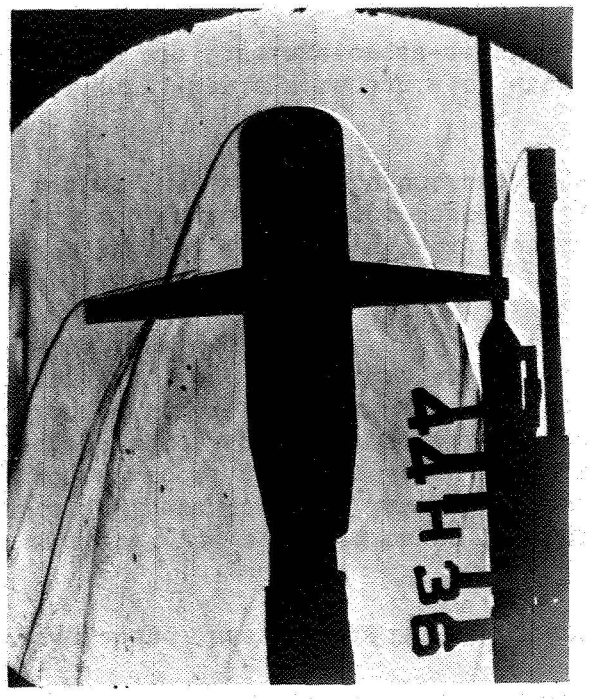

FLOW-FIELD PHOTOGRAPH FROM VAC HVWT

Figure 15

CONCLUDING REMARKS

For the test conditions of the current study, the significant conclusions are as follows.

1. The longitudinal curvature (as well as the transverse shape) has a significant effect on the bow shock wave.

2. The heat-transfer distribution along the plane of symmetry was computed using the University of Texas nonsimilar boundary-layer code. The results indicate that the inviscid flow properties are best estimated by using the normal-shock-expansion model near the nose, while the tangent-cone or the tangent-wedge assumptions provide adequate prediction at downstream points. In addition, these data indicate that a wing-shock interaction perturbs the heating along the fuselage at high angles of attack but not at low angles of attack. The demarcation angle of attack is dependent on curvature of the windward surface of the fuselage.

3. The local perturbations that were observed in the pressure data on the wing were a strong function of the flow geometry (i.e., configuration geometry and angle of attack) but only a weak function of Mach number or Reynolds number. At the highest angle of attack tested (i.e., 60°), the body shock appears to merge with the wing shock, muting the local perturbations in surface pressure on the wing surface.

4. The shock-intersection and wing-impingement locations vary little with angle of attack. At a given angle of attack, these locations are weak functions of the fuselage-cross-section corner radius.

5. Perturbations in the heating, which were observed in the corner formed by the junction of the wing and the rounded underbelly of the fuselage, were a function of the Reynolds number.

6. Large differences in wing-leading-edge heat-transfer data exist at modest to low angles of attack. These differences are attributable to instrumentation type and instrumentation location. Extreme care must be exercised in obtaining such data.

REFERENCES

1. Abbott, Ira H.; and Von Doenhoff, Albert E.: Theory of Wing Sections. Dover Publications, Inc. (New York), 1959.

2. Bertin, J. J.; Williams, F. E.; Baker, R. C.; Smith, C. L.; and Pope, T. C.: Aerothermodynamic Measurements for Space-Shuttle Configurations in Hypersonic Wind Tunnels. Univ. of Tex. (Austin) Aerospace Eng. Rept. 71006, Sept. 1971.

3. Fay, J. A.; and Riddell, F. R.: Theory of Stagnation Point Heat Transfer in Dissociated Air. J. Aeron. Sci., vol. 25, no. 2, Feb. 1958, pp. 73-85, 121.

4. Bertin, J. J.; Lamb, J. P.; and Center, K. R.: Flow Field Measurements for Infinite Cylinders In a Hypersonic Wind Tunnel: Windward and Leeward Flow Field. Univ. of Tex. (Austin) Aerospace Eng. Rept. 71007, Dec. 1971.

5. Anon.: NASA Space Shuttle Technology Conference, vol. 1. Aerothermodynamics, Configurations, and Flight Mechanics. NASA TM X-2272, 1971.

6. Kipp, H. W.; and Masek, R. V.: Aerodynamic Heating Constraints on Space Shuttle Vehicle Design. Space Technology and Heat Transfer Conference, ASME Paper 70-HT/SpT-45, June 1970.

7. Rogers, C. E.: Experimental Investigation of Leading-Edge Shock Impingement and Interaction Heating on a 1/80 Scale Model of a NASA Straight Wing Orbiter Configuration at Mach Numbers 8 and 16. Cornell Aeronautical Lab. Rept. AA-2977-Y-1, Aug. 1971.

8 Eckert, E. R. G.: Engineering Relations for Friction and Heat Transfer to Surfaces in High Velocity Flow. J. Aeron. Sci., vol. 22, no. 8, Aug. 1955, pp. 585-587.

9. Edney, B: Anomalous Heat Transfer and Pressure Distributions on Blunt Bodies at Hypersonic Speeds in the Presence of an Impinging Shock. FFA Rept. 115, The Aeron. Res. Inst. of Sweden, 1968.

DETERMINATION OF AEROTHERMODYNAMIC ENVIRONMENT UNCERTAINTIES WITH APPLICATION TO SPACE SHUTTLE VEHICLES

by C. A. Scottoline
Space Division, North American Rockwell Corporation
Downey, California

INTRODUCTION

The Space Shuttle Vehicle is sensitive to cost, and therefore weight. To help minimize the cost of the Thermal Protection System (TPS), conservatism in the definition of aerothermodynamic environments must be controlled. This may be done by identifying and analyzing the uncertainties associated with environment prediction. This paper discusses the basic categories of environment uncertainties, the determination of uncertainty profiles, and TPS design sensitivity to environment uncertainties.

BASIC CATEGORIES OF AEROTHERMODYNAMIC ENVIRONMENT UNCERTAINTIES

(Figure 1)

Aerothermodynamic environment uncertainties can be categorized into four basic groups. The first category is aerodynamic heating methods. Wind tunnel data correlations provide information on geometry dependent heating characteristics and the effects of important flow parameters such as Mach number and Reynolds number. Uncertainties in the tunnel data correlations can be determined with a suitable amount of data. The determination of uncertainties associated with the extrapolation of these correlations to flight conditions (real gas effects, different streamline divergence, etc.) is not straightforward because of minimal availability of flight data. This is an important area for future work.

The other three categories are concerned with trajectory dispersions, atmospheric variations and vehicle attitude variations. This paper deals primarily with the determination of wind tunnel data correlation uncertainties, however some preliminary results are presented for TPS design sensitivity to the above environment uncertainties, when lumped together.

BASIC CATEGORIES OF AEROTHERMODYNAMIC ENVIRONMENT UNCERTAINTIES

✓ AERODYNAMIC HEATING METHODS

- WIND TUNNEL DATA CORRELATIONS
  - GEOMETRY DEPENDENT HEATING CHARACTERISTICS
  - EFFECTS OF SIMULATABLE FLOW PROPERTIES (M, Rey)
- EXTRAPOLATION OF DATA CORRELATIONS TO FLIGHT CONDITIONS
  - NON-SIMULATABLE REAL GAS CONDITIONS
  - STREAMLINE DIVERGENCE, CROSS FLOW, PRESSURE GRADIENT

TRAJECTORY DISPERSIONS

ATMOSPHERIC VARIATIONS

ATTITUDE VARIATIONS

Figure 1

DETERMINATION OF WIND TUNNEL DATA "UNCERTAINTY PROFILES"

(Figure 2)

The development of a typical wind tunnel data uncertainty profile is shown in the opposing figure. The data (heating in this case), obtained from the configuration of interest, are analyzed to determine the "best estimate" mean correlation. For heating data, the mean correlations represent geometry factors times an appropriate theory. For laminar flow, the Eckert Flat Plate Reference Enthalpy theory is used; for turbulent flow, the Spalding and Chi theory is used. Using theory as a basis for the correlations gives greater confidence in the extrapolation of the results to flight conditions.

The deviation of the data from the correlation ("scatter") is analyzed in terms of the percentage of data that are greater or less than a factor times the mean correlation, yielding the normalized "uncertainty profile."

The data deviations are presented on an arithmetic probability plot. Data with a small slope indicates low uncertainty, whereas data with a large slope indicates high uncertainty. All data points have been weighted equally.

It is important to note that it is necessary (but not sufficient) that the "best estimate" mean correlation include all important parameters ascribed to the physical phenomena for confidence in the uncertainty profile to be high. Since many of the phenomena are geometry dependent, data must be available for the actual configuration.

DETERMINATION OF WIND TUNNEL DATA "UNCERTAINTY PROFILES"

FUSELAGE ℄ HEATING DATA

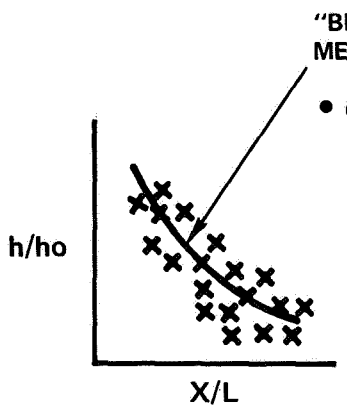

- GEOMETRY FACTOR X THEORY
  LAMINAR: ECKERT FPRE
  TURBULENT: SPALDING & CHI

- DETERMINE "BEST ESTIMATE" MEAN CORRELATION
- DATA POINTS EQUALLY WEIGHTED
- ANALYZE DATA SCATTER ABOUT MEAN CORRELATION
- CORRELATION MUST INCLUDE ALL IMPORTANT PARAMETERS
- PRESENT DATA ON ARITHMETIC PROBABILITY PLOT

"UNCERTAINTY PROFILE"

(h/ho)/(h/ho) MEAN =
HEATING FACTOR, F

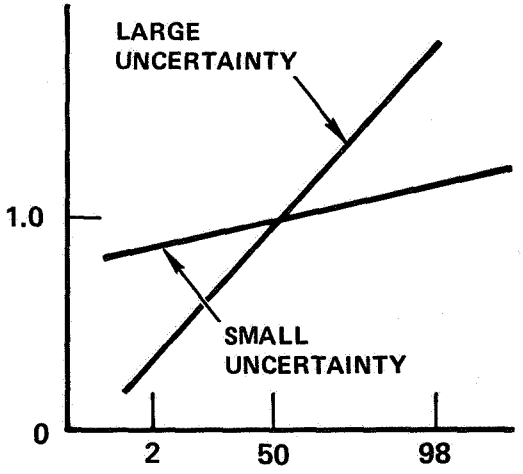

PERCENT DATA COVERED

OR

PROBABILITY THAT MEASURED HEATING WILL BE LESS THAN F X MEAN CORRELATION

Figure 2

LAMINAR AND TURBULENT HEATING UNCERTAINTY PROFILES

(Figure 3)

The opposing figure shows results of uncertainty analysis of laminar data from shuttle configurations and turbulent data from both shuttle and non-shuttle configurations. (See Appendix for data identification). Four important observations can be made:

(1) Both sets of turbulent data have the same normalized uncertainty profile.

(2) Both sets of turbulent data and the laminar data lie along a straight line on the arithmetic probability plot, in excellent agreement with a Gaussian distribution.

(3) The standard deviations for the laminar and turbulent data are about the same and are moderate.

(4) Since the number of data points included is sufficiently large, there is high confidence in the uncertainty profiles developed.

It is concluded that the existing laminar and turbulent data from the NR shuttle tests are of good quality and that high confidence level laminar and turbulent uncertainty profiles have been developed for the NR Delta Wing Orbiter lower surface.

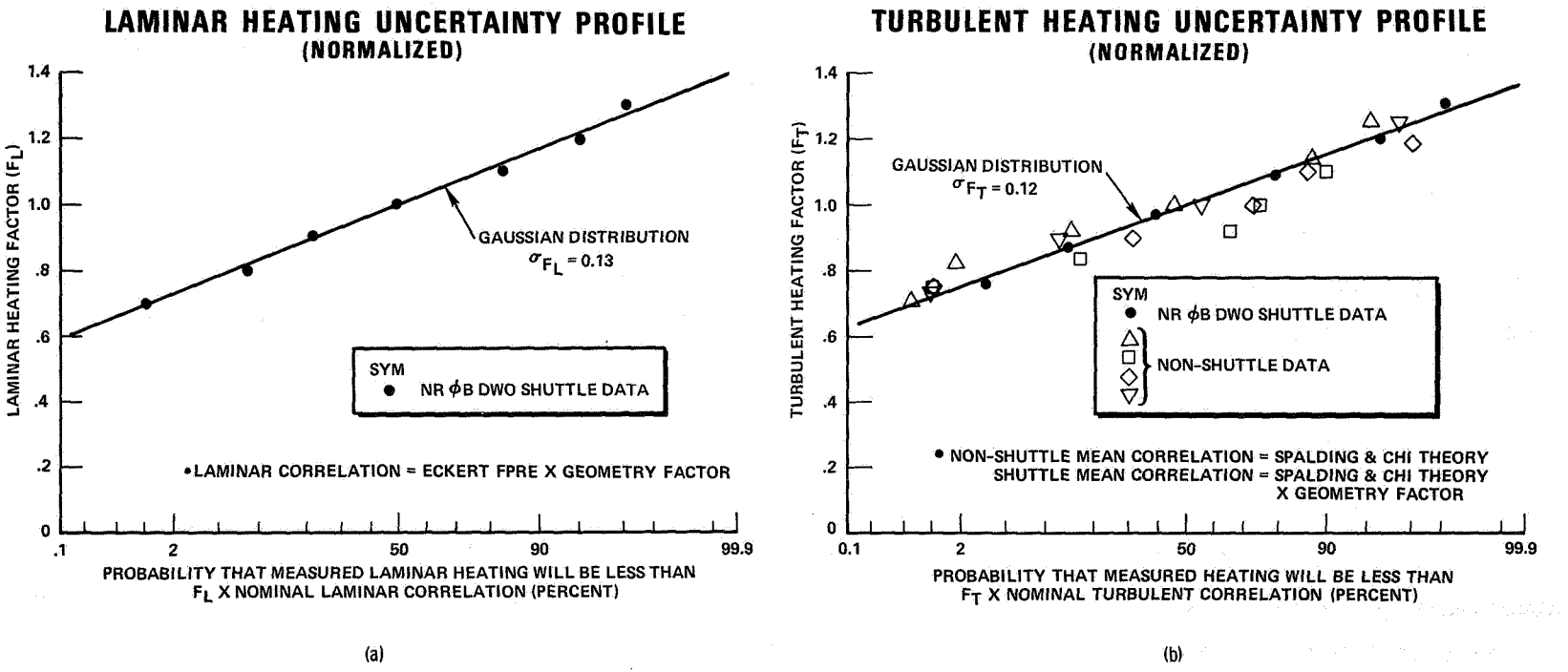
LAMINAR HEATING UNCERTAINTY PROFILE
(NORMALIZED)
LAMINAR HEATING FACTOR (F_L)
1.4
1.2
1.0
.8
.6
.4
.2
0
GAUSSIAN DISTRIBUTION
$\sigma_{F_L} = 0.13$
SYM
NR ϕB DWO SHUTTLE DATA
•LAMINAR CORRELATION = ECKERT FPRE X GEOMETRY FACTOR
.1
2
50
90
99.9
PROBABILITY THAT MEASURED LAMINAR HEATING WILL BE LESS THAN
F_L X NOMINAL LAMINAR CORRELATION (PERCENT)
(a)
TURBULENT HEATING UNCERTAINTY PROFILE
(NORMALIZED)
TURBULENT HEATING FACTOR (F_T)
1.4
1.2
1.0
.8
.6
.4
.2
0
GAUSSIAN DISTRIBUTION
$\sigma_{F_T} = 0.12$
SYM
NR ϕB DWO SHUTTLE DATA
NON-SHUTTLE DATA
• NON-SHUTTLE MEAN CORRELATION = SPALDING & CHI THEORY
SHUTTLE MEAN CORRELATION = SPALDING & CHI THEORY
X GEOMETRY FACTOR
0.1
2
50
90
99.9
PROBABILITY THAT MEASURED HEATING WILL BE LESS THAN
F_T X NOMINAL TURBULENT CORRELATION (PERCENT)
(b)

Figure 3

NR DELTA WING ORBITER BOUNDARY LAYER TRANSITION CORRELATION (WIND TUNNEL DATA)

(Figure 4)

The prediction of boundary layer transition is recognized as having a high degree of uncertainty, and the confidence level of the uncertainty profile derived from transition data will depend on the validity of the correlation. The NR shuttle transition data obtained to date have been correlated in terms of Re_θ/M_e, accounting for actual cross-flow and streamlined divergence as exists under wind tunnel conditions. (See Appendix for data identification).

The opposing figure shows that between $\delta = 15°$ and $\delta = 53°$, the correlation of fuselage lower surface centerline data is essentially independent of flow deflection angle (δ). Since most of the data were obtained at locations where the vehicle bottom was flat, flow angle is, for the most part, the same as angle of attack.

Between local unit Reynolds numbers of 5.4×10^6 and 3.6×10^7 meter^{-1} (Re/FT = 1.6×10^6 to 1.1×10^7), the correlation is insensitive to the local unit Reynolds number. A potentially important transition parameter, that has been identified by stability theory, is the ratio of H_w/H_r, however, since the NR data to date have been obtained over a narrow band of H_w/H_r, this parameter has not been included in the correlation at this time.

A phenomenum not accounted for is the possible wing/body interaction which may cause transition "sticking" in the vicinity of the wing leading edge. There is a need for data over a wider range of H_w/H_r in order to determine the effect of this parameter on shuttle transition.

NR DELTA WING ORBITER
BOUNDARY LAYER TRANSITION CORRELATION
(WIND TUNNEL DATA)

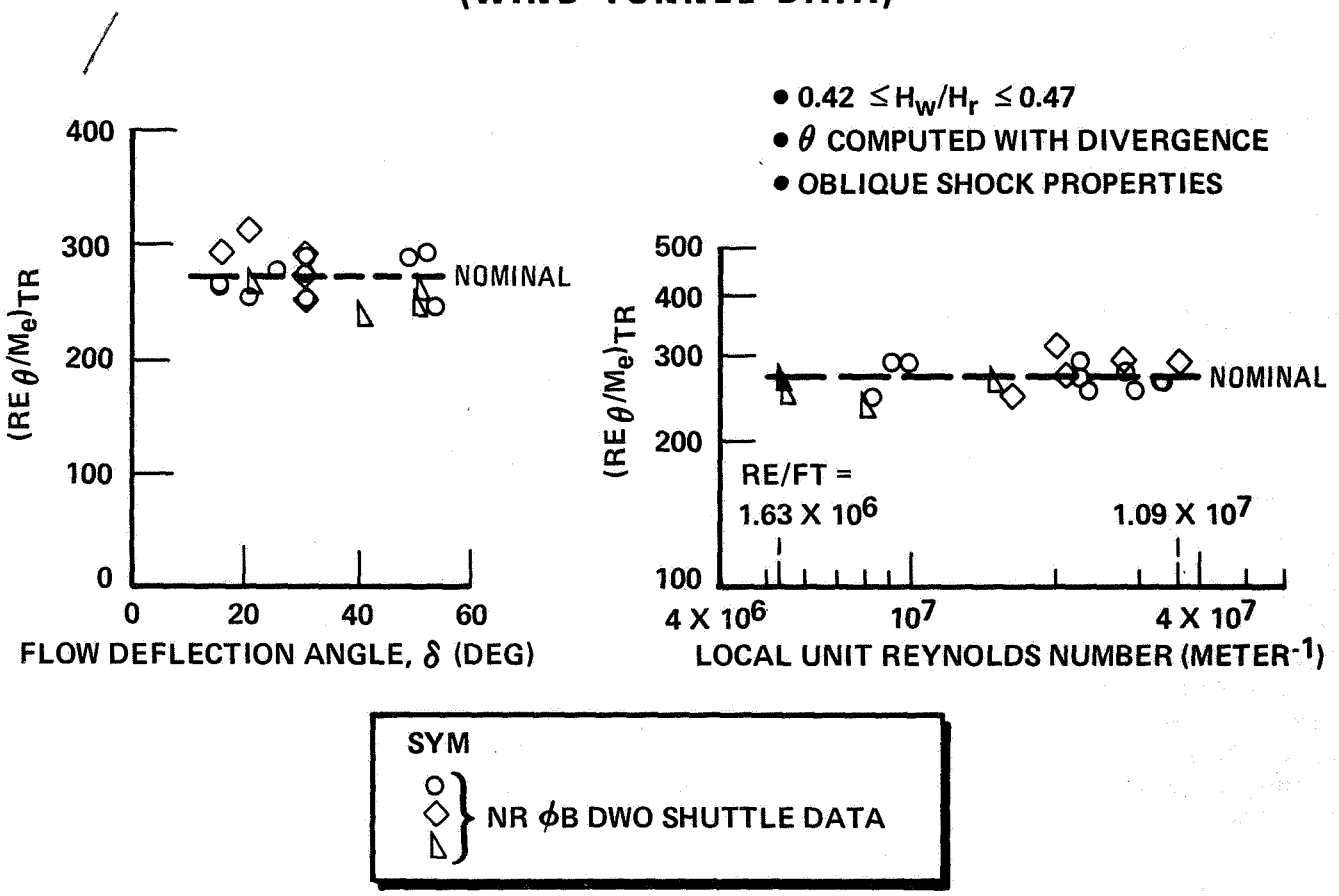

Figure 4

BOUNDARY LAYER TRANSITION UNCERTAINTY PROFILES

(Figure 5)

The transition uncertainty profiles were developed in the same manner as with the heating data. Shown in the opposing figure are both the "absolute" and the "normalized" uncertainty profiles for NR delta wing orbiter transition data and slab delta transition data. (See Appendix for data identification).

Examining the chart, it can be seen that the uncertainty profiles are quite different for the two types of configurations. The NR shuttle data conforms well to a Gaussian distribution, whereas, the slab delta data does not. These differences point out a major requirement in determining uncertainty profiles. The correlation used must account for all important parameters and all variables used in the correlation must be accurately computed. One of the biggest problems encountered in the analysis of transition data from a variety of sources is in the non-uniformity of local flow property determination by various investigators. The local conditions for the NR data were computed in a uniform manner, whereas, the slab delta data were taken directly from the open literature, where there was no information given as to how local properties were determined. Another possible explanation for the greater deviation from a Gaussian distribution for the slab delta correlation is that the correlation does not include enough parameters for this configuration and data. Since transition is highly geometry dependent, it is expected that the absolute values of mean correlations would vary between configurations.

The mean value of $(R_{e_\theta}/M_e)_{TR}$ was 272 from the shuttle data and 220 from the slab delta data.

The standard deviation in predicted transition length (x) was 19% for shuttle data and 59% for the slab delta data.

Because of the relatively small standard deviation and the Gaussian distribution of the shuttle data, it is felt that the data are good and that the uniformity of analysis has helped to better order the data. Since there are only 21 shuttle data points, the confidence in these probability plots is not as great as with the heating data. A 95% confidence level statement about shuttle $(R_{e_\theta}/M_e)_{TR}$ could be made as follows (assuming that the correlation included all important parameters):

"At least 95% of a large number of data points will have values greater than 215 for $(R_{e_\theta}/M_e)_{TR}$ for flow angles between 15° and 53°."

As stated earlier, uncertainty profiles are formulated assuming that the correlation accounts for all important parameters. In the above case of transition, there are potentially important parameters that have not been included in this correlation, (such as H_w/H_r), and therefore, these results must be considered preliminary.

BOUNDARY LAYER TRANSITION UNCERTAINTY PROFILES

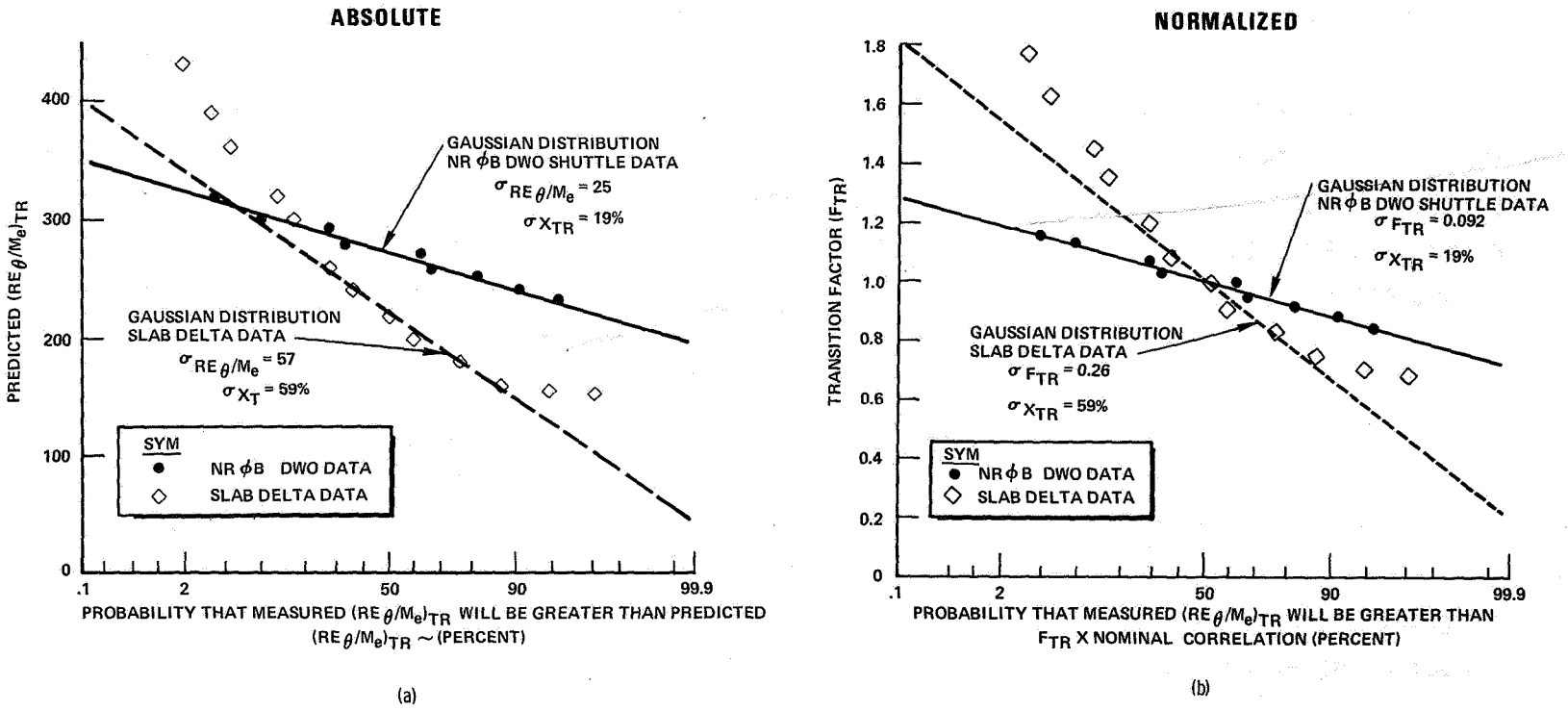

Figure 5

PRELIMINARY INVESTIGATION OF THE SENSITIVITY OF TPS DESIGN (RSI)
TO ENVIRONMENT UNCERTAINTIES
(NR ØB DWO)

(Figure 6)

The effect of environment uncertainties on TPS design was studied for a Reusable Surface Insulation (RSI) system (titanium sub-structure), where the TPS weight is sensitive to total heat load. The opposing figure shows the results of this exercise.

The following categories of environment uncertainties were accounted for:

- wind tunnel data correlations
- trajectory dispersions
- atmospheric variations
- angle-of-attack variations

As can be seen, a 95% confidence level environment costs a weight bias of 30% above that for all nominal environments. A popular combination is one using nominal heating methods and a nominal trajectory/atmosphere/attitude with a conservative transition criteria. This combination gives a 10% weight increase above the all nominal case. As a matter of interest, an all turbulent environment causes TPS weights that are 1.5 times heavier than for an all laminar environment (not shown).

These results are considered preliminary as some of the uncertainties associated with the "basic" combinations used to generate the weight uncertainty profile shown were assigned, but they are felt to be a reasonable initial estimate for the ØB concept orbiters.

PRELIMINARY INVESTIGATION OF THE SENSITIVITY OF TPS DESIGN (RSI) TO ENVIRONMENT UNCERTAINTIES

(NR ØB DWO)

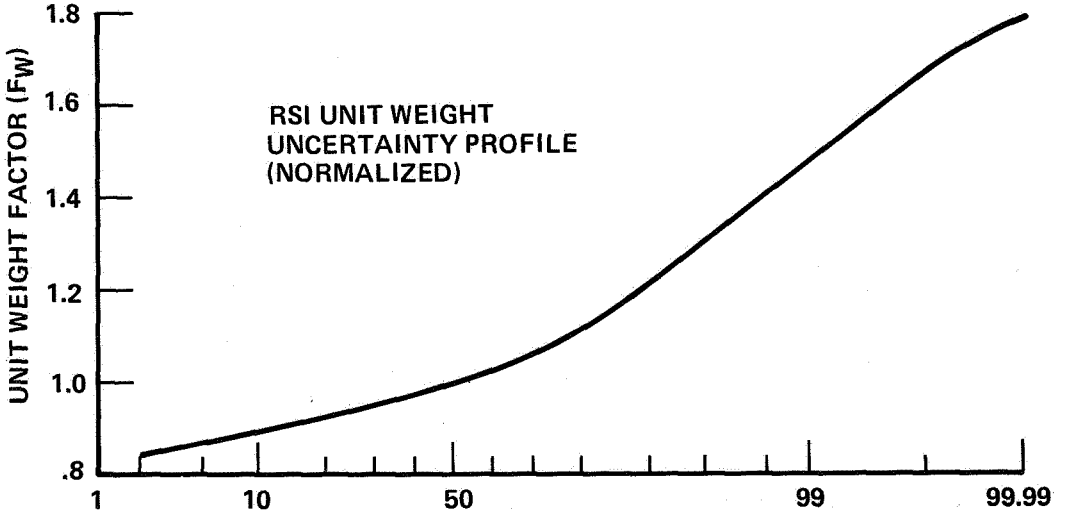

RESULTS OF WT UNCERTAINTY ANALYSIS FOR SPECIFIC CASES

HEATING METHODS	TRANSITION	TRAJ/ ATMOS/ ATTITUDE	LUMPED PROBABILITY	Q/Q_N	$F_W = W/W_N$	
2%	ALL LAMINAR	NOMINAL	2%	0.61	0.84	BASIC
NOMINAL	NOMINAL	NOMINAL	50%	1.0	1.0	
98%	98%	DISPERSED	98%	2.7	1.4	
98%	ALL TURBULENT	DISPERSED	99.99%	5.5	1.8	
NOMINAL	98%	DISPERSED	95%	2.2	1.3	
NOMINAL	98%	NOMINAL	78%	1.4	1.1	

Figure 6

CONCLUSIONS

- UNCERTAINTY PROFILE DETERMINATION HAS BEEN DEMONSTRATED FOR WIND TUNNEL DATA CORRELATIONS
- CORRELATIONS MUST PROPERLY ACCOUNT FOR PHYSICAL PHENOMENA
- HIGH CONFIDENCE LEVEL UNCERTAINTY PROFILES HAVE BEEN DEVELOPED FOR LAMINAR AND TURBULENT WIND TUNNEL DATA CORRELATIONS ON NR DWO LOWER SURFACE
- PRELIMINARY RESULTS INDICATE MODERATE TPS COSTS FOR HIGH CONFIDENCE LEVEL ENVIRONMENT
- UNCERTAINTIES IN OTHER TUNNEL DATA CORRELATIONS (e.g., LEESIDE HEATING) AND IN THE EXTRAPOLATION OF WIND TUNNEL DATA TO FLIGHT CONDITIONS NEED TO BE DETERMINED

APPENDIX: DATA IDENTIFICATION

FIGURE	SYM	CONFIGURATION	α	LOCATION	M∞	DATA SOURCE	NO. PTS
3 (Laminar)	●	SSV-134C	30°	Fuselage C_L & wing	7.9	LRC-VDT, Paint	
↓		SSV-161B		lower surface @ 50%	7.4	ARC 3.5' HWT, T/C	321
				exposed semi-span	8.0	AEDC-B, T/C	
3 (Turbulent)	●	SSV-134C	20-50°	Fuselage C_L	7.9	LRC-VDT, Paint	
↓		SSV-161B			7.4	ARC 3.5' HWT, T/C	94
					8.0	AEDC-B, T/C	
	△	Sharp flat plate	0-20°	C_L	7-11	Ref. 1	170
	□	Blunt flat plate	0-20°	C_L	7-11	Ref. 1	100
	◇	Apollo SM	0°	SM & Adaptor	3-5	LRC-UPWT & Flight	100
↓	▽	Shock tube wall		Wall	2.5-3.5	Ref. 2	110
4	○	SSV-134C	15-53°	Fuselage C_L	7.4	ARC 3.5' HWT, T/C	
	◇	SSV-161B	15-53°		7.4	ARC 3.5' HWT, T/C	21
↓	◺	SSV-161B	20-50°	↓	8.0	AEDC-B, T/C	
5	●	SSV-134C	15-53°	Fuselage C_L	7.4	ARC 3.5' HWT, T/C	
		SSV-161B	15-53°		7.4	ARC 3.5' HWT, T/C	21
		SSV-161B	20-50°	↓	8.0	AEDC-B, T/C	
↓	◇	Slab Delta	15-51°	C_L	>5	Ref. 3	54

REFERENCES

1. Wallace, J. E., "Hypersonic Turbulent Boundary-layer Studies at Cold Wall Conditions," Proceedings of the 1967 Heat Transfer and Fluid Mechanics Institute, pp 427-451, Stanford University Press

2. Hopkins, R. A. and R. M. Nerem, "An Experimental Investigation of Heat Transfer from a Highly Cooled Turbulent Boundary Layer," AIAA Journal, Vol. 6, No. 10, Oct. 1968, pp. 1912-1918

3. Masek, R. V., "Boundary Layer Transition on Lifting Entry Vehicle Configurations at High Angle of Attack," NASA TMX-52876, Volume I, Space Transportation System Technology Symposium, I - Aerothermodynamics and Configurations, July 1970, pp. 445-462

SPACE SHUTTLE BOOSTER MULTI-ENGINE BASE FLOW ANALYSIS

Homer H. Tang**, Charles P. Gardiner***,
William A. Anderson†, John Navickas††

McDonnell Douglas Astronautics Company

Huntington Beach, California

ABSTRACT

A comprehensive review of currently available analytical techniques pertinent to several prominent aspects of the base thermal problem of the space shuttle booster is given in this paper. Because of the vast quantity of work in the areas of radiation physics and plume flow, emphasis is given to only the remaining aspects directly related to significant phenomena observed in some flight and ground test programs and which are directly applicable to the formulation of a versatile analysis. A brief review of existing experimental results, with important effects identified, is given in summary form. A tractable engineering analysis, capable of predicting the power-on base pressure, base heating, and other base thermal environmental conditions, such as base gas temperature, is presented here and used for an analysis of various space shuttle booster configurations.

The analysis consists of a rational combination of theoretical treatments of the prominent flow interaction phenomena in the base region. These theories consider jet mixing, plume flow, axisymmetric flow effects, base injection, recirculating flow dynamics, and various modes

of heat transfer. Such effects as initial boundary-layer expansion at the nozzle lip, reattachment, recompression, choked vent flow, and nonisoenergetic mixing processes are included in the analysis. A unified method has been developed and programmed to numerically obtain compatible solutions for the various flow-field components in both flight and ground test conditions. Preliminary prediction for a 12-engine space shuttle booster base thermal environment has been obtained for a typical trajectory history. Theoretical predictions have also been obtained for some clustered-engine experimental conditions. Results indicating comparisons show good agreement between the data and theoretical predictions.

*This research was sponsored by the McDonnell Douglas Astronautics Company's Independent Research and Development Program. The authors gratefully acknowledge the contributions of Professor Glen W. Zumwalt, MDAC Consultant, for his effort in development of the present analysis and of F. I. Clayton and G. P. Johnson in the experimental review section.

Supervisor, * Engineer/Scientific Specialist, † Sr. Engineer/Scientist, Aero/Thermodynamics and Nuclear Effects Department, Research and Development.

††Senior Engineer/Scientist, Space Shuttle Booster Program

Section 1
INTRODUCTION

Evaluation of the base heating environments for launch vehicles is one of the most challenging problems that has been facing aerothermodynamicists since the mid-1950's, when relatively large launch vehicles were first developed. With the advent of clustered engines, the problem has become even more complex, and analytical solutions are still elusive.

The need to accurately evaluate multi-engine base flow characteristics, such as base pressure, base heating, and other pertinent flow field properties, will become increasingly appreciated during development phases of the space shuttle program because of the following reasons: (1) An optimum space shuttle configuration will depend on accurate estimates of the aerodynamic forces throughout the flight envelope that are directly related to base pressure (drag) for power-on and power-off flight conditions. (2) The base region of a vehicle, such as the space shuttle booster, is probably the most difficult region in which to predict aerodynamic forces and heating rates throughout the flight envelope. Flow-field phenomena, such as plume induced separation, recirculating flow dynamics coupled with plume interaction, and mixed mode convective-radiative heat transfer, are possible areas for special consideration since they further complicate an already complex problem. (3) Most aerothermodynamic design work in this area is based on subscale, or flight test, data correlations and semi-empirical design methods, which can result in unnecessary vehicle base heat shield weight penalties and, too often, in costly redesign efforts.

Heat transfer to the base of a multi-engine vehicle can occur through two modes: convection and radiation. On large vehicles, particularly those burning RP-1 (kerosene) with oxygen or air aluminized solid propellant, these two modes are both important. For vehicles powered

by LH_2-LOX clustered engines, the radiative heating mode predominates at low altitudes and the convective heating mode associated with a choked reverse flow becomes more important at high altitudes. In general, the above statements are subject to other considerations, such as the base configuration, nozzle arrangement, trajectory, and flight operation with engine cutoff, restart, and many other alternatives.

A list of possible heating sources for a Delta six-solid retrofit vehicle, for example, includes the following:

A. Main engine effects:
   1. Radiation from the Mach disk in the main engine plume.
   2. Radiation from afterburning of turbine exhaust gases on the base plane.
   3. Radiation from the exhaust gases of the main engine.
   4. Vernier plume radiation (including the Mach disk).
   5. Convection from the afterburning of turbine exhaust gases on the base plane.
   6. Convection and recirculation of main engine gases.
   7. Radiation from shock waves at vernier and main engine plume interaction.

B. Solid motor effects:
   1. Radiation from solid particles (Al_2O_3) in the plume.
   2. Radiation from the gaseous region of the solid motor plume.
   3. Radiation from the Mach disk in the solid motor plume.
   4. Convection from recirculated gases.
   5. Radiation from shock waves at interaction of the solid motor plume and the main engine plume.
   6. Radiation from shock waves at interaction between adjacent solid motor plumes.

There is no existing method or flow model that can account for all of the above listed heat sources simultaneously. Usually, each source or a small group of sources is treated independently of the others, and their cumulative interaction effects are neglected. For instance, radiation and convection evaluations are uncoupled. Simplifying assumptions are usually imposed, such as neglecting the free shear layer (which is important in evaluating the convective heating) during computation of the radiative heating contributions from the plume flow.

This paper provides a brief review of existing theoretical methods and some typical experimental data presented in summary form. In particular, emphasis is directed toward consideration of current space shuttle concepts, such as (1) the S-IC multi-engine type booster, and (2) the "pressure-fed" booster using an ablative, or active cooling, base-insulation system. Consequently, a versatile base flow analysis that considers possible base bleeding effects due to the products of ablative or active cooling systems, in addition to the conventional clustered-engine effects, becomes increasingly appropriate for space shuttle applications.

Based upon the above considerations, the Chapman-Korst type base flow analyses are particularly useful for current space shuttle configurations. A detailed review is therefore given for this group of analyses, which are mainly used for convective heating evaluations. Also, the analytical approach developed at MDAC is described and several data-theory comparisons are presented to demonstrate the applicability of the present analysis.

Section 2
REVIEW OF THE EXISTING METHODS

It is known that multi-engine base flow fields are very complex. Such flows can vary from the aspiration case at low altitudes, where the flow from the surrounding region will be drawn into the base stagnation region, to the recirculation case at high altitudes, where the engine exhaust plumes expand and interact, producing the recirculated flow pattern, which will continue with increased altitude. Recirculated mass flow rates may become sufficiently large to choke available vent areas, in which case the flow in the base stagnation region becomes independent of external conditions. For a vehicle using a liquid propellant, the fuel-rich turbine exhaust is often dumped into the base, and this exhaust then contributes to additional convective heating as a result of afterburning.

The results of many investigators indicate further that many variables are involved in determining a power-on, multi-engine, base thermal environment.[1-4] Parameters, such as nozzle area ratio, nozzle half-angle, base-to-nozzle exit distance, nozzle boundary layer and wall temperature, rocket spacing, effective specific heat ratio, rocket chamber pressure and temperature, base vent factor, free-stream Mach number versus altitude, and surface boundary layers, are all important considerations. Consequently, it is difficult to obtain general semi-empirical correlations that include several of the above parameters simultaneously. However, some correlations based on certain chosen parameters are available.

Sergeant[5] shows that the base convective heating rate can correlate with chamber pressure in a power-law manner; i. e., $q \sim P_c^{0.8}$. The base heating deviates from the $P_c^{0.8}$

relationship, however, at points removed from the cluster's center. Consequently, other investigators (including Sergeant) found that it is more useful to correlate the heating with heat shield pressure (or base pressure).

Other investigaters have pointed out that the nozzle boundary-layer mass flow may be more than sufficient to account for the reversed mass flow under choked conditions.[5, 6, 7] It has also been theoretically and experimentally demonstrated that the nozzle wall temperature has a marked effect on convective base heating under these conditions. Therefore, if the entrainment process between the plume and the surrounding flow is small, the effects of free shear layer mixing might be neglected and only the appropriate boundary layer profiles at the nozzle exit used. It remains to be seen, however, whether or not sufficient boundary-layer mass flow can be accounted for in the reverse flow experienced by either a full-scale model or actual flight vehicle.

Other complexities are usually associated with the plume-plume interaction and plume flow radiations. Many multiplume interaction methods are, generally speaking, based on an inviscid approach, using either a method of characteristics or a multitube analysis.[8, 9] The method is not in itself an independent base heating method, but it provides necessary information to supplemental analytical methods. For example, as shown in References 4 and 10, evaluations of such heat sources as radiation from the Mach disk, radiation from the gaseous region of solid motor plumes, and convection from the recirculated mass flow resulting from plume interaction require the plume interaction results to describe the basic flow-field conditions.

For the reasons mentioned in the introduction section, the following review will concentrate on jet mixing layer analyses. A recent survey of supersonic base flow theories[11] and the latest analytical work[12] indicate that the application of the Chapman-Korst mixing layer theory is a highly practical method that gives reasonable results for this approach.

Although the qualitative formulation of the Chapman-Korst flow model originated with Chapman,[13] it was first exploited to obtain quantitative results in a base pressure theory published by Korst.[14] Consequently, the commonly used title is the "Chapman-Korst Flow Model." A thorough review of the model (with several modified theories) is given by Tang, Gardiner, and Barnes.[15] It should be noted that the most significant contribution of this flow model is the dividing streamline concept, together with the jet-type boundary conditions. Because of this, many modified theories have been developed to generalize the applications of this model.[16-25]

It is obvious that there are many advantages in adapting the Chapman-Korst flow model for the base-heating evaluation, not because it is the most accurate, but because it has been generalized to many applications, with considerable success. These extensions also provide usable auxiliary tables of the various integral quantities involved, making calculations comparatively simple and rapid. The following paragraphs contain a review of some base-heating analyses using a Chapman-Korst mixing layer model. A summary is given in Table 1.

The method of Dixon, Richardson, and Page[26] is intended primarily for use in base-drag predictions and shows good agreement between the base pressure solutions and some of the cold-flow wind tunnel data. The method has not been compared with flight data, and analysis of base gas temperature has not been made. Addy, at approximately the same time as Dixon, developed a similar analysis, including an additional base temperature evaluation.[27]

Table 1.

SUMMARY OF SOME BASE F 'SES USING CHAPMAN-KORST JET-MIXING THEORY

Authors	Configuration		Effects Neglected	Effects Included	Flow Model	Major Outputs
Dixon Richardson Page (Ref. 26)	Cylindrical axisymmetric body with one jet	Korst, two-stream, supersonic, isoenergetic	Initial boundary layer, reverse flow	Axial pressure gradient, base-bleed	Iterating P_b	Base-pressure, mass-entrainment rate
Addy (Ref. 27)	Cylindrical axisymmetric body with one jet	Korst, two-stream, supersonic, nonisoenergetic	Initial boundary layer, heat transfer	Base-bleed	Interacting P_b and T_b, Korst's criterion (oblique shock)	Base pressure, base temperature
Hong (Ref. 12	Cylindrical axisymmetric body with one jet	Korst-Zumwalt two-stream, supersonic, nonisoenergetic	Initial boundary layer, reverse flow	Base-Bleed	Iterating P_b and T_b Goethert's criterion reattachment	Base pressure, base gas temperature, mass entrainment rate
Fong (Ref. 28)	Pseudo two-dimensional body with one jet	Chapman-Korst two-stream, supersonic, nonisoenergetic	Reverse flow, heat transfer	Initial boundary layer chemistry (equilibrium)	Iterating P_b and T_b Nash factor of 0.65 for reattachment	Base pressure, plume-induced separation distance
Lamb Abbud Lenzo (Ref. 29)	Planar approximation, for four-engine configuration	Korst, two-stream (plume-plume), supersonic, isoenergetic	Initial boundary layer, heat transfer	Reverse flow impingement, Goethert's criterion	Iterating the cut-off length and recompression pressure	Base pressure and distributions
Goethert (Ref. 2)	Cylindrical axisymmetric body with four jets	Korst, two-dimensional, one-stream, supersonic	Ambient flow, base-bleed	Nozzle boundary layer	Limited to choked reversal flow, supersonic exhaust jet discharging into still air	Base pressure, convective heating rate (by correlating $q/p^{0.8}$ relation)
Page Dixon (Refs. 3 and 43)	Cylindrical axisymmetrical with multiple nozzles	Korst, two-dimensional, one-stream, supersonic isoenergetic	Initial boundary layer, base-bleed	Reverse flow, stagnating heating	Matching P_b with either sudden expansion or equivalent two-dimensional base-pressure analysis. T_b is obtained, using a reflected image approximation, Goethert's criterion	Base pressure, convective heating rate
Marion Daniels Herstine Burge (Ref. 30)	Axisymmetric body with cluster nozzles	Korst, two-dimensional, one-stream, supersonic isoenergetic	Initial boundary layer, base-bleed	Choked reverse flow	Iterating P_b to satisfy the choked vent flow rate	Base pressure

The method of Hong has included the base gas temperature consideration and compared it successfully with both ground and flight test data.[12] However, the effects of the initial boundary layer of nozzle and vehicle surface have been neglected. These effects are very important for multijet configurations.

The method of Fong is intended mainly for plume-induced separation distance evaluation.[28] Although thermochemical effects have been included, heat transfer (such as base heating) has not been considered.

The method of Lamb for a clustered four-engine configuration has emphasized the fluid dynamic aspects of the recirculated flow.[29] Base pressure and distribution are obtained as a function of ambient pressure and nozzle geometry, which includes height above the base, lateral spacing, and expansion ratio. The plume-plume interaction is evaluated in the 45-degree meridian planes. No heat-transfer aspects have been considered.

Goethert in 1961 pioneered a first multirocket base flow analysis, using Korst's two-dimensional base-pressure theory.[2] A number of phenomena had been considered, such as characteristic altitudes for the change of the base flow pattern, particularly the critical altitudes for flow reversal from atmospheric air flowing into the backflow of hot exhaust gases toward the base. Other significant flow parameters, such as base pressure, convection heat flux, and base thrust increments, were also evaluated. Although convective heat flux was determined by the use of $q/p^{0.8}$ correlation, Goethert's paper indeed provides many guidelines for later theoretical developments.

The method of Marion, Daniels, Herstine, and Burge, uses a simple two-dimensional, one-stream, isoenergetic base-pressure analysis to evaluate multiple-nozzle base flow in the

choked vent flow condition.[30] Base pressure is obtained by iterating the mass entrainment rate to satisfy the choked vent-flow condition.

The method of Page and Dixon uses a number of methods to simulate various flight regimes of interest.[3] Their method is basically a Korst-type, one-stream, two-dimensional, supersonic analysis, supplemented by the use of a sudden expansion analysis, a reflected image approximation, and a stagnation heating relation. Because the change in analytical components is required for various flow regimes, the compatibility of various methods requires further examination.

Section 3
PRESENT ANALYSIS

From the above review, it is clear that a complete solution satisfying the complex interaction between the inner multijet and the outer jet has not as yet been obtained. The main reason is that it is very difficult to match the complete inner and outer solutions simultaneously. The present method represents one more forward step in achieving this objective. Realizing the complexities involved, two compatible analyses were developed to solve the outer one-jet and the inner multijet problems separately. Solutions were then obtained by matching the common parameters, such as base pressure, mass flow rate, and base gas temperature. At present, two separate programs are both operational for implementing the above analyses. Flight simulation predictions (given in a later section) have been obtained by matching the cross-plotted results computed from these two programs. A unified program to automatically perform this task is warranted for future development, and it is under consideration. The basic analyses are discussed below:

THE OUTER JET

The outer jet results in a free shear layer generated by the boundary layer that separates from the vehicle aft surface. For cylindrical bodies, it is fortuitous that simple solutions (such as those in Reference 31) can be obtained by applying a Mangler-type transformation to the planar base flow analysis of Chapman-Korst. The application in laminar flow is straightforward and similar to various boundary-layer studies, whereas the application in turbulent flow is not.

For laminar flow, the Mangler transformation is not only geometric, but it changes the form of the continuity equation without changing the energy and momentum equations. This is possible because the laminar kinematic viscosity μ is a state variable. For turbulent

boundary-layer flow, the kinematic viscosity is negligible. However, the transformation does not hold, as noted by various authors including de Soto and Wolf,[32] because of the dependence of the apparent or eddy viscosity ϵ on the spatial position[33] and other variables.

For turbulent free shear flow, certain forms of the eddy viscosity, $\epsilon \sim u_a r$, for example, lead to similarity solutions for various flow conditions. Only with this restriction on ϵ, can the axisymmetric differential equations (e. g., continuity and momentum) transform immediately to the planar forms. Similarly, the energy equation is not changed when the turbulent Prandtl number is unity; i. e., $Pr = \bar{P}r = 1$.

Transformation of the Axisymmetric Governing Equations

Since planar base pressures are obtained using an integral approach, the following demonstrates that, for the eddy viscosity model above and isoenergetic flow, the axisymmetric governing equations in integral forms can also be transformed to the planar forms.

The coordinate system (Figure 1) is of the Korst-Zumwalt type.[23] With the use of the control volume shown in Figure 2, mass conservation gives the following (note that flow conditions at 2a and 3a in Equation (1) are identical):

$$\int_0^{y_{2a}} \frac{r}{r_1} \frac{\rho u}{(\rho u)_{2a}} dy + \frac{\sec \theta_{12}}{2r_1} \left[\left(r_1 + y_n \cos \theta_{12} \right)^2 - \left(r_1 + y_{2a} \cos \theta_{12} \right)^2 \right]$$

$$= \int_{y_j}^{y_{3a}} \frac{r}{r_1} \frac{\rho u}{(\rho u)_{3a}} dy + \frac{\sec \theta_{12}}{2r_1} \left[\left(r + y_n \cos \theta_{12} \right)^2 - \left(r + y_{3a} \cos \theta_{12} \right)^2 \right] \qquad (1)$$

Similarly, the conservation of momentum (neglecting the x-momentum of the base bleed) gives

$$\int_{o}^{y_{2a}} \frac{r}{r_1} \frac{\rho u^2}{(\rho u^2)_{2a}} dy + \frac{\sec \theta_{12}}{2r_1} \left[(r_1 + y_n \cos \theta_{12})^2 - (r_1 + y_{2a} \cos \theta_{12})^2 \right]$$

$$= \int_{-\infty}^{y_{3a}} \frac{r}{r_1} \frac{\rho u^2}{(\rho u^2)_{3a}} dy + \frac{\sec \theta_{12}}{2r_1} \left[(r + y_n \cos \theta_{12})^2 - (r + y_{3a} \cos \theta_{12})^2 \right] \quad (2)$$

Combining Equations (1) and (2) gives

$$\int_{o}^{y_{2a}} \frac{r}{r_1} \frac{\rho u^2}{(\rho u)_{2a}} dy - \int_{o}^{y_{2a}} \frac{r}{r_1} \frac{\rho u^2}{(\rho u^2)_{2a}} dy = \int_{y_j}^{y_{3a}} \frac{r}{r_1} \frac{\rho u}{(\rho u)_{3a}} dy$$

$$- \int_{-\infty}^{y_{3a}} \frac{r}{r_1} \frac{\rho u^2}{(\rho u^2)_{3a}} dy \quad (3)$$

Kirk postulates that the flow pattern changes abruptly from a boundary-layer type to a mixing (free shear layer) type without losses in momentum and mass.[34] This postulate allows the evaluation of the qualities on the left-hand side of Equation (3), using the normal boundary-

layer definitions of displacement thickness and momentum thickness. Referencing to the conditions at Position 2 (Figure 2) and neglecting the transverse curvature effects

$\left(\delta_2^{**} \cos\theta_{12} \ll 2r_1\right)$, gives

$$\delta_2^{**} = \int_0^{y_{2a}} \frac{r}{r_1} \frac{\rho u}{(\rho u)_{2a}}\, dy - \int_0^{y_{2a}} \frac{r}{r_1} \frac{\rho u^2}{\left(\rho u^2\right)_{2a}} dy$$

Equation (3) becomes

$$\delta_2^{**} = \int_{y_j}^{y_{3a}} \frac{r}{r_1} \frac{\rho u}{(\rho u)_{3a}}\, dy - \int_{-\infty}^{y_{3a}} \frac{r}{r_1} \frac{\rho u^2}{\left(\rho u^2\right)_{3a}} dy \tag{4}$$

The base-bleed mass flows between the dividing streamline y_j and the reattachment streamline y_d, therefore leading to

$$\frac{Gr_1}{2(\rho u)_{3a}} = \int_{y_d}^{y_j} \frac{r}{r_1} \frac{\rho u}{(\rho u)_{3a}}\, dy \tag{5}$$

Combining Equations (4) and (5) yields

$$\delta_2^{**} + \frac{Gr_1}{2(\rho u)_{3a}} = \int_{-\infty}^{y_{3a}} \frac{r}{r_1} \frac{\rho u}{(\rho u)_{3a}} dy - \int_{-\infty}^{y_{3a}} \frac{r}{r_1} \frac{\rho u^2}{(\rho u^2)_{3a}} dy$$

$$- \int_{-\infty}^{y_d} \frac{r}{r_1} \frac{\rho u}{(\rho u)_{3a}} dy \qquad (6)$$

Equation (6), together with an appropriate reattachment criterion and jet mixing theory, can be used to calculate the base pressure and other quantities of interest. Simplicity of computation is achieved by introducing the geometric transformations:

$$\bar{x} = \int_0^x \left(\frac{r}{r_1}\right)^2 dx, \quad \bar{y} = \frac{r}{r_1} y, \quad \bar{u} = u, \quad \bar{v} = \frac{r_1}{r} \left(v + \frac{1}{r} \frac{\partial r}{\partial x} y u\right) \qquad (7)$$

Substituting Equations (7) and (6) gives the governing equation for the equivalent planar flow:

$$\bar{\delta}_2^{**} + \frac{\overline{Gr}_1}{2(\rho u)_{3a}} = \int_{-\infty}^{\bar{y}_{3a}} \frac{\rho \bar{u}}{(\rho \bar{u})_{3a}} d\bar{y} - \int_{-\infty}^{\bar{y}_{3a}} \frac{\rho \bar{u}^2}{(\rho \bar{u}^2)_{3a}} d\bar{y} - \int_{-\infty}^{\bar{y}_d} \frac{\rho \bar{u}}{(\rho \bar{u})_{3a}} d\bar{y} \qquad (8)$$

Equation (8) is identical to the governing equation given in Reference 35 for planar flow; Equation (8) also shows that the initial momentum thickness and base-bleeding rate are invariant under the transformation. Also in the present case, the x-axis is located along the dividing streamline so that the velocities are invariant under the transformation. These

conditions allow the use of the results of planar jet mixing theory for the equivalent flow.

Axisymmetric Base Pressure

Analytical difficulties occur in base-flow calculations when the flow converges toward the axis of symmetry. Zumwalt's model assumed that a minute sting attached to the base approximates the no-sting base model. Recently, Mueller[36] demonstrated that a better approach is to use the experimental results of Chapman (see Figure 3 of Reference 36) to determine the radial location of the recompression point; i.e.; where the oblique shock recompression begins (shown as r_3 in Figure 2). Values of r_3/r_1 vary from 0.55 at M = 2 to an asymptotic value of 0.42 at higher Mach numbers. However, $r_3/r_1 = 0.5$ can be used for most practical calculations. For a conical, inviscid flow field, r is a linear function of x; i. e.,

$$\frac{r}{r_1} = 1 - \left(\frac{x}{x_3}\right)\left(1 - \frac{r_3}{r_1}\right) \tag{9}$$

Substituting Equation (9) into Equation (7) and then evaluating at the recompression point gives

$$\bar{x}_3 = x_3\left[\frac{r_3}{r_1} + \frac{1}{3}\left(1 - \frac{r_3}{r_1}\right)^2\right] \tag{10}$$

Since the following geometric relations apply

$$\bar{x}_3/L_B = \bar{x}_3/(r_1 - r_3) = \csc \bar{\theta}_{12}$$

and

$$x_3/(r_1-r_3) = \csc \theta_{12}$$

where L_B is the base height, Equation (10) becomes

$$\sin \theta_{12} = \left[\frac{r_3}{r_1} + \frac{1}{3}\left(1 - \frac{r_3}{r_1}\right)^2\right] \sin \bar{\theta}_{12} \tag{11}$$

where θ_{12} and $\bar{\theta}_{12}$ are the dividing-streamline turning angles for the axisymmetric and the equivalent planar flow, respectively; therefore, any inviscid theory, such as Prandtl-Meyer flow, can be used to obtain the resulting pressures of the external streams after completing their corresponding turning angles. The resulting pressure is assumed to be equal to the base pressure and consistent with other base-pressure analyses. The present theory compares well with results obtained by other more complicated theories.[36, 37] The comparisons are given in Reference 25.

In Figure 1, the coordinate systems for axisymmetric and equivalent planar flow are shown.

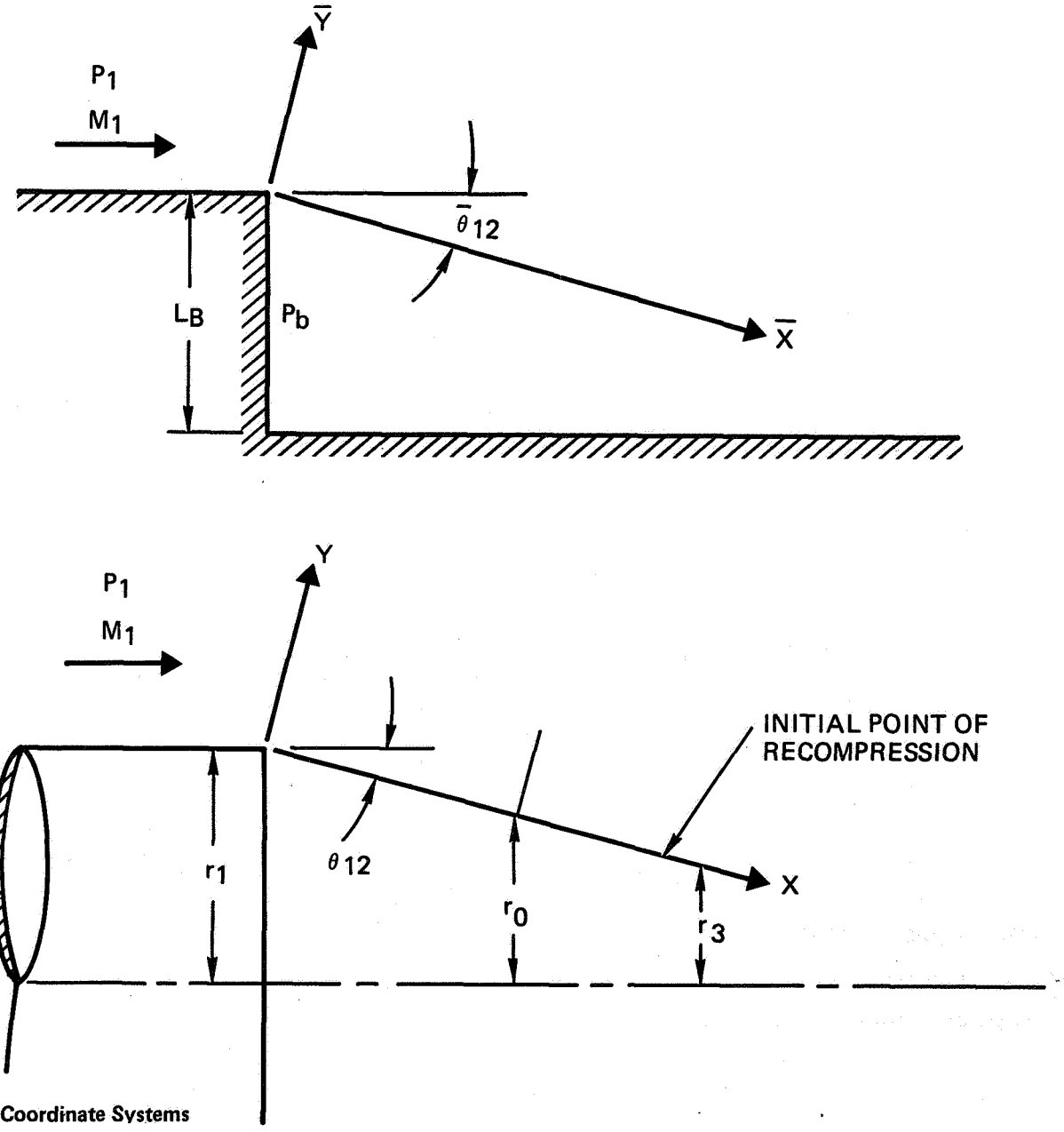

Figure 1. The Coordinate Systems

The control volume in an axisymmetric base flow region is indicated by dashed lines in Figure 2. The double dashed line is the outer edge of the free shear layer (called outer jet in the text). Other flow-field conditions, such as trailing shock, rear stagnation point, and base-bleed, are also shown.

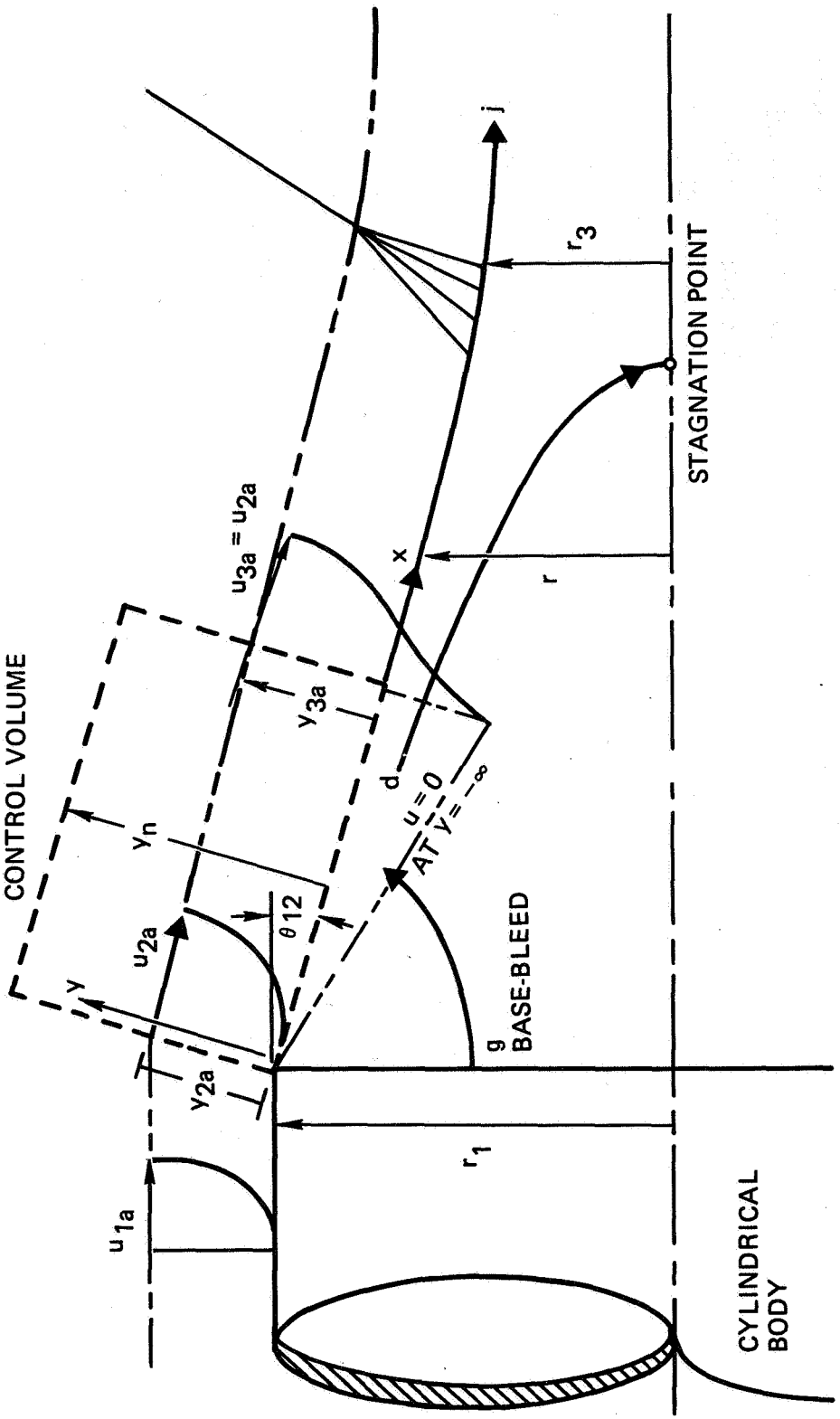

Figure 2. Control Volume in Base Regions

THE INNER JETS

The inner jets consist of all the plume flows generated by the particular multi-engine configuration of interest. Engine plumes usually involve several flow field regimes. The basic structure includes an inviscid core, a viscous shear layer, and several shock-wave patterns, depending on ambient conditions. Major effects on plume flow fields, such as shock wave interactions, chemical reactions, radial oxidizer-to-fuel ratio gradients, viscous mixing, nozzle boundary layer, noncontinuum flow regimes, and condensation, are usually considered in conventional plume flow analyses.[38,39] Because of these complexities, it is a very difficult task to combine a complete plume flow analysis with a complicated base flow analysis to obtain exactly compatible solutions. Consequently, assumptions have been used as follows:

A. The inviscid flow (called the inviscid core in plume flow analyses) originating from the nozzle obeys an isentropic expansion process from the nozzle exit conditions to the required base pressure conditions. These inviscid edge conditions are needed for describing the appropriate mixing-layer properties.

B. The viscous free shear layer can be evaluated, using the Chapman-Korst type asymptotic turbulent jet-mixing velocity profile. Detailed properties, such as density and temperature throughout the mixing layer, can be evaluated from the velocity profiles by applying the nonisoenergetic Crocco relationship.[40] Initial boundary-layer effects upon the mixing-layer properties are accounted for approximately by using the technique of defining the virtual origin of the mixing layer with coordinate shifts, which depend upon the expanded boundary-layer momentum and displacement thicknesses.[16,41]

C. The convective heating from the recirculating flow is uncoupled from the radiative heating from plume exhausts, jet shocks, and/or afterburning along fuel-rich jet boundaries of the liquid fuel engines.[6] This assumption is somewhat justified because the convective heating is more sensitive to the flow field near the base

structure whereas the radiative heating is more sensitive to the downstream plume flow.

Within the limitation of the above assumptions, the present work was initially developed with a 12-engine booster configuration in mind. A schematic base geometry of rectangular arrangement, such as that indicated in Figure 3a, was therefore used originally. For this rectangular positioning of similar rocket nozzles, versatile analysis techniques may be applied to account for nozzle flow interactions in an approximate, readily useful, manner. This involves examination of three basic venting configurations, which recur throughout the rectangular pattern of the nozzle positions. These basic venting configurations are illustrated in Figure 3b and form the basis of the present multirocket nozzle analysis. The three venting configurations of importance are specified by (1) nozzles completely surrounded by four other nozzles (no vent area), (2) nozzles bounded by three other nozzles (single-vent area), and (3) nozzles bounded by two other nozzles (double-vent area).

Without coupling with the outer jet, the inner-jet analysis alone can be used directly to describe multi-engine base-flow characteristics for high-altitude environments. Such uncoupling of the inner and outer jet analyses is appropriate for situations where the rocket nozzles exhaust into a nearly quiescent ambient atmosphere or where the interaction with the surrounding atmosphere is of secondary importance in comparison with the internal nozzle-exhaust interactions. It will be also noted that many ground-test simulations involve weak inner-outer iterations and may be considered uncoupled. This situation is discussed in greater detail below.

An important streamline associated with overall base-flow characteristics emanates from the nozzle and meets similar streamlines coming from surrounding nozzles along a common

streamline interaction axis[3, 5] as illustrated in Figure 4a.

A flow model in the plane passing through the nozzle axis and the common streamline interaction axis is formulated to approximately describe the base flow characteristics surrounding the nozzle. The postulated flow model, given in Figure 4b, indicates the various components of the analysis:

A. Inviscid flow originating from the nozzle.
B. Downstream shock wave recompression.
C. Initial boundary-layer expansion at the nozzle lip.
D. Nonisoenergetic mixing layer properties and important streamlines.
E. Reattachment.
F. Base flow recirculation and venting.
G. Base wall heat transfer.

The numbers used in Figure 4b correspond directly to the above regions of interest. The techniques for treating the above components of the flow model are discussed below. The solution method for a particular configuration is an iterative procedure involving two variables, the base pressure-to-nozzle exit pressure ratio and the recirculation stagnation temperature ratio. Simultaneous variations in these two parameters are carried out to satisfy (1) the mass balance required by venting into the external outer-jet environment and (2) the energy balance required by heat-transfer effects in the recirculating flow. Bearing in mind that the base pressure-to-nozzle exit pressure ratio and the recirculation stagnation temperature ratio are specified initially as guesses may assist in following the logical sequence of techniques for treating the various flow-field components given below.

Inviscid Flow

The inviscid edge conditions needed for describing the mixing-layer properties are obtained by isentropically expanding the nozzle exit conditions to satisfy the required base pressure ratio. The inviscid edge Mach number, which is perhaps the most significant parameter describing the state of the flow, is obtained from the nozzle exit conditions and base pressure ratio by using the following relationship:[42]

$$M_e^2 = \frac{2}{\gamma-1}\left\{\frac{\left(1+\frac{\gamma-1}{2}M_{ex}^2\right)}{\left(\frac{P_b}{P_{ex}}\right)^{\left(\frac{\gamma-1}{\gamma}\right)}}-1\right\} \tag{12}$$

where γ is the specific heat ratio.

Other parameters, such as density, temperature, and velocity, may be obtained from the Mach number by using other flow relationships. For example, the Crocco number used frequently in mixing-layer expressions[15, 40] is given by

$$C_e^2 = \frac{1}{1+\frac{2}{(\gamma-1)M_e^2}} \tag{13}$$

Application of two-dimensional Prandtl-Meyer solutions[15] for inviscid flow provides an approximate streamline direction for the overall expanded inviscid flow. The flow subsequently impinges on the common streamline interaction axis to form a downstream recompression shock wave process, which is treated in the manner described below.

Downstream Shock Wave Recompression

A wedge shock flow is used to specify the recompressed inviscid flow properties. These properties are specified as a function of the shock wave angle θ_s and the oncoming Mach number M_e. For example, Reference 42 indicates

$$\tan \delta = \frac{2 \cot \theta_s (M_e^2 \sin^2 \theta_s - 1)}{2 + M_e^2 (\gamma + 1 - 2\sin^2 \theta_s)} \tag{14}$$

$$\frac{P_4}{P_e} = \frac{2\gamma M_e^2 \sin^2 \theta_s - (\gamma - 1)}{\gamma + 1} \tag{15}$$

where δ is the flow deflection and P_4 is the downstream pressure.

The value of the shock wave angle for which the deflection δ is equal to the turning angle θ_e of the inviscid flow from the nozzle axis is used in the pressure equation above to evaluate the recompression pressure P_4. This recompression pressure P_4 is an important quantity for dealing with the reattachment processes to be discussed later.

Initial Boundary-Layer Expansion

Since properties of the mixing layer are influenced by initial boundary-layer characteristics at the nozzle lip, expanded boundary-layer properties are required to properly describe the beginning of the mixing layer. The expanded boundary layer properties are evaluated by applying convenient expressions developed from a small expansion analysis.[15] Comparison with detailed numerical results, using individual streamtube expansions throughout the boundary layer, has verified the usefulness of the small expansion analysis for describing overall

boundary-layer properties. The displacement thickness and momentum thickness ratios due to expansion of the initial boundary layer at the nozzle lip are therefore given, respectively, by the following expressions:

$$\frac{\delta_e^*}{\delta_{ex}^*} = \frac{(\rho u)_{ex}}{(\rho u)_e} \tag{16}$$

$$\frac{\delta_e^{**}}{\delta_{ex}^{**}} = \frac{(\rho u)_{ex}}{(\rho u)_e}\left(\frac{M_{ex}}{M_e}\right)^2 \tag{17}$$

The above expanded boundary-layer properties are important for describing the virtual origin coordinate shifts of the mixing-layer analysis.[15,41] The virtual origin coordinate shifts are given below for the turbulent mixing-layer case:

$$x_o = \frac{\sigma\delta_e^{**}}{(1 - C_e^2)I_{1j}} \tag{18}$$

$$y_o = \delta_e^* + \delta_e^{**} \tag{19}$$

where

$$\eta = \sigma \frac{y}{x} \tag{20}$$

Mixing-Layer Properties and Important Streamlines

Consistent with the anticipated heat-transfer rates, size, and turbulence levels of current rockets, a nonisoenergetic turbulent mixing layer is utilized in the current analysis. Solutions using laminar mixing layers may have rather limited application for scale-model tests (if free laminar shear layers remain stable) and necessarily require extensive computing times for integrating the detailed conservation equations[15] across the mixing layer.

The mixing-layer velocity profile of the error function shape, which was analytically derived and experimentally verified for two-dimensional[14] and the axisymmetric mixing layers[22] can be used in the analysis and is given below:

$$\phi = \frac{1}{2}(1 + \operatorname{erf}\eta) \tag{21}$$

According to the latest experimental results obtained by Hong[12], the following relation is given for the spreading parameter:

$$\sigma = 12\left(1 + 0.119\, M_{2e}\right) \tag{22}$$

As noted by Hong, the velocity profile of the inner jet may not follow the error function shape given by Equation (21) as closely as the external jet. Although it has been widely known that an integral method is not very sensitive to small changes in profile shape, a refinement can be achieved by replacing Equation (21) with an improved profile derived by Lamb, Greenwood, and Gaddis,[43] using an iterative procedure. As they indicated, the resulting velocity profile should improve the accuracy for flow-field conditions with significant density variation and a strong secondary stream.

The total enthalpy profile is obtained by using the Crocco relation:

$$\Lambda = \phi + \Lambda_B(1 - \phi) = \Lambda_B + (1 - \Lambda_B)\phi \tag{23}$$

where $\Lambda = h_o/h_{oe}$ is the total enthalpy ratio of the jet. The density profile for a constant pressure mixing region is given as

$$\frac{\rho}{\rho_e} = \frac{1 - C_e^2}{\Lambda - \phi^2 C_e^2}\lambda \tag{24}$$

where

$\lambda = \dfrac{C_p \mathcal{M}}{C_{p_e} \mathcal{M}_e}$ is the molal specific heat ratio of the jet.

$\mathcal{M}$ = molecular weight

It is usually now necessary to provide some thermodynamic properties for air and engine exhaust gas in order to evaluate the density profile and other integrals used in the analysis. For the present paper, $\lambda = 1$ has been used.

With $\lambda = 1$, Equation (24) is reduced to

$$\frac{\rho}{\rho_e} = \frac{1 - C_e^2}{\Lambda - \phi^2 C_e^2} \tag{25}$$

where Λ is now a temperature ratio instead of an enthalpy ratio; i.e., $\Lambda = T_o/T_{oe}$.

There are two important streamlines in a mixing layer analysis. One is called a "separating (or dividing) streamline," and the other is called a "reattaching (or discriminating) streamline." The latter is either identical to or related to the former, depending on whether there is a base-bleed or not. Therefore, it is necessary to locate the separating streamline first. To do this, the coordinate shift should be determined. Since initial boundary-layer effects have been accounted for by employing the virtual origin concept used to obtain Equations (18) and (19), the "restricted" mixing theory of Korst for negligible initial boundary layer is directly applicable.[44] When the X-momentum entrained by the recirculating flow is ignored, the conservation equation[15] gives the following relation for the coordinate shift η_m in terms of the edge similarity coordinate η_e:

$$\eta_e - \eta_m = \int_{-\infty}^{\eta_e} \frac{\rho u^2}{(\rho u^2)_e} d\eta = \left(1 - C_{2e}^2\right) \int_{-\infty}^{\eta_e} \frac{\phi^2 \lambda}{\Lambda - C_e^2 \phi^2} d\eta \tag{26}$$

Separating (Dividing) Streamline

The separating "j" streamline based on the virtual origin coordinates can now be found. This streamline separates the nozzle main flow (which continuously flows downstream at the separation corner) from that entrained from the recirculated flow region.

Using similarity coordinates and Equations (24) and (26), the resulting equation obtained from the mass conservation law is given below. This allows one to determine the separation streamline.

$$\int_{\eta_j}^{\eta_e} \frac{\phi \lambda}{\Lambda - C_e^2 \phi^2} d\eta = \int_{-\infty}^{\eta_e} \frac{\phi^2 \lambda}{\Lambda - C_e^2 \phi^2} d\eta \tag{27}$$

Defining

$$I_1 \equiv \int_{-\infty}^{\eta} \frac{\phi \lambda}{\Lambda - C_e^2 \phi^2} d\eta \tag{28}$$

$$I_2 \equiv \int_{-\infty}^{\eta} \frac{\phi^2 \lambda}{\Lambda - C_e^2 \phi^2} d\eta \tag{29}$$

where λ and Λ are defined in Equations (22) and (24); Equation (27) now becomes

$$I_{ij} = I_{1e} - I_{2e} = \int_{-\infty}^{\eta_e} \frac{\phi \lambda}{\Lambda - C_e^2 \phi^2} d\eta - \int_{-\infty}^{\eta_e} \frac{\phi^2 \lambda}{\Lambda - C_e^2 \phi^2} d\eta \tag{30}$$

For isoenergetic $\Lambda = 1$ and perfect gas flow $\lambda = 1$, the integrals I_1, and I_2, and I_{1j} are reduced to the same expressions that were used by Korst except that they are now referred to the virtual origin.

Reattaching (Discriminating) Streamline

The reattaching "d" streamline is the other important streamline considered. This is the streamline that divides the mass flow in the mixing layer near the recompression region into (1) the portion that passes through the downstream pressure rise to escape, and (2) the portion that is turned back into the base region to be recirculated or vented. When there is no base-bleed or mass exchange between the inner and the outer jet, the j and d streamlines are iden-

tical and they bound an enclosed recirculated region. Otherwise, the j and d streamlines are related by the amount of mass pumping in or out of the recirculated region, in accordance with the following relation:

$$\dot{m}_{mix} = \pm \int_{y_j}^{y_d} (2\pi r)^i \rho u \, dy \tag{31}$$

the positive sign refers to $y_d > y_j$; i.e., mass is being pumped into the recirculated region from the plume mixing layer, and then it either goes out through the pumping process of the other mixing stream or vents out by a base suction arrangement. Also, i = 0 for two-dimensional flow, and i = 1 for axisymmetric flow.

To locate the d streamline, conservation laws are used to determine its pressure ratio P_{o_d}/P_d at the cut-off location (the beginning point of the recompression zone). This will be discussed in the following section. To locate the d streamline, a trial value of the stagnation pressure of the d streamline P_{o_d}/P_d is used to evaluate the remaining properties (by using the average value of γ, isentropic flow relations, and Crocco's relationship):

$$\frac{T_{od}}{T_d} = \left(\frac{P_{od}}{P_d}\right)^{\frac{\gamma-1}{\gamma}} = \left(\frac{P_{od}}{P_e}\right)^{\frac{\gamma-1}{\gamma}} \tag{32}$$

$$M_d^2 = \frac{2}{\gamma - 1}\left(\frac{T_{od}}{T_d} - 1\right) \tag{33}$$

$$\sqrt{\frac{T_d}{T_e}} = \frac{\frac{M_d}{M_e}(1-\Lambda_b)\frac{T_{oe}}{T_e} + \sqrt{\frac{M_d}{M_e}(1-\Lambda_b)\frac{T_{oe}}{T_e} + 4\frac{T_{od}}{T_d}\Lambda_b\frac{T_{oe}}{T_e}}}{2\frac{T_{od}}{T_d}} \tag{34}$$

$$\frac{U_d}{U_e} \equiv \phi_d = \frac{M_d}{M_e}\sqrt{\frac{T_d}{T_e}} \tag{35}$$

The d streamline location η_d is determined by inverting the asymptotic velocity profile given in Equation (21). Utilization of the above streamlines permits considerations of the net mass and energy fluxes across the mixing layer.

Reattachment (Recompression) Process

Many approaches have been offered for treating reattachment, and they are usually based on local flow-field characteristics near the reattachment region.[12, 15, 43] Empirical correlations, such as the Nash factor relationship,[19] which is useful for examining recompression pressure-rise phenomena, permit identification of the discriminating streamline stagnation pressure in terms of pressures that may be determined from the overall inviscid flow outside the mixing layer. Note that when the reattachment streamline Mach number is greater than unity, the flow is often assumed, as in many previous base-flow analyses, to first pass through the equivalent of a normal shock. The value of P_{o_d} in this case is, therefore, the stagnation pressure behing a normal shock. This is known as Goethert's criterion.

It may also be worthwhile to note that there are a number of analytical models for treating the overall mass, momentum, and energy conservation within control volumes around the reattachment point by approximating various integral behaviors over the control volume (such as References 41 and 44) based upon rational assumptions related to the physical properties of the flow. The analytical aspects of such an approach are now given below.

Selecting a control volume as shown in Figure 5, a mass balance is employed on the cut-off location X_r, where the recompression process begins. Using the isentropic flow properties in each streamtube across point A to point D, and integrating for the total mass flow, gives

$$\int_o^{r_r} (2\pi r)^i dr = -\int_{r_d}^{r_r} \frac{(2\pi y)^i}{\cos\theta_d}\, dy \tag{36}$$

Substituting geometric relations into Equation (36) yields

$$\frac{x_r}{L} = \frac{\sigma \tan\theta_d}{\Delta\eta \cos\epsilon_d}\left[1 - \frac{1}{(1+\cos\theta_d)^{\frac{1}{1+i}}}\right] \tag{37}$$

In Equation (37), θ_d can be computed only when P_{o_d} has already been determined, where θ_d can be related to η_d by the following expression:

$$\theta_d = \theta_e + \tan^{-1}\frac{\eta_m}{\sigma} - \tan^{-1}\frac{\eta_d}{\sigma} \tag{38}$$

When P_{od} is known, η_d can be computed as mentioned previously, and consequently, θ_d and then X_r/L can be evaluated. The value of P_{od} can also be determined by employing the momentum balance to the same control volume given in Figure 5. To do this, three basic assumptions and their applications (similar to those of Reference 41) are given below:

A. The momentum coming in through the shear layer flow undergoes a change in direction but not in magnitude. In other words, if the flow were isentropic and the recirculated flow redirected uniformly parallel, the magnitude of the momentum would remain unchanged. An axial momentum balance neglecting shear effects yields:

$$\dot{p} + \dot{p}\cos\theta_d = \int_o^L (2\pi r)^i \left| [\, p(\ell) - p_e \,] \sin\theta_d + \tau(\ell)\cos\theta_d \right| d\ell \tag{39}$$

where

$$\dot{p} = \int_{-\infty}^{y_d} \rho u^2 (2\pi r)^i dy \quad ; \quad r^i = (\ell \sin\theta_d)^i$$

B. The pressure distributions along surfaces $\overline{DR}$ and $\overline{FR}$ are specified by a quadratic function; i.e.,

$$\frac{P(\ell)}{P_e} - 1 = \left(\frac{P_{od}}{P_e} - 1 \right) (1 - \xi)^2 \tag{40}$$

where

$$\xi = \ell/L \, .$$

Since $\tau(L)/P_e << P_{od}/P_e$ has been confirmed by many shear layer analyses, it is therefore suitable to ignore the shear stress contribution in Equation (39), which then yields the following location for the cutoff station:

$$\frac{x_r}{L} = \frac{\sigma\left(\frac{P_{od}}{P_e} - 1\right)\sin\theta_d}{3.4^i\gamma M_e^2\,(1+\cos\theta_d)\,I_{2d}\cos\epsilon_d} \tag{41}$$

Equating Equations (41) and (37) gives

$$\frac{P_{od}}{P_e} = 1 + \frac{3.4^i\gamma M_e^2(1+\cos\theta_d)I_{2d}}{\Delta\eta\cos\theta_d}\left[1 - (1+\cos\theta_d)^{-\frac{1}{1+i}}\right] \tag{42}$$

If the value computed from Equation (42) is not the same as that assumed in Equation (32), the iterative process to determine the final value will be continued until a satisfactory solution has been obtained. Note that the energy balance has already been accounted for by the implicit use of Crocco's relation in the derivation of Equation (41).

Base-Flow Recirculation and Venting

The base-flow recirculation region is usually approximated as a "dead-air" zone with constant pressure and temperature, but with no velocity components. As an initial assumption, this approximation is useful for specifying the inner-edge properties of the mixing layer as well as the static pressure upstream of the reattachment point. The amount of mass recirculated upstream is determined by the reattachment analysis and provides an approximate indication of the "dead-air"zone validity.

With regard to specifying base heat-transfer properties, conditions in the recirculating flow near the base wall are required to determine the convective heat transfer across the base wall boundary layer. For this purpose, the initial assumptions of a "dead-air" region may not provide sufficient information to treat the overall base-heat transfer. Techniques for analyzing jet impingement on flat surfaces[29] prove useful in estimating the flow properties associated with the recirculated flow impingement on the base. Constant density, or isentropic flow, approximations in the recirculated flow may be useful for treating base flow characteristics in portions of the flow near stagnation points or regions with small viscous transport interactions. Currently, conditions of the recirculated mass flow, as given in the following analysis, are used in conjunction with the mass venting characteristics to approximately specify the required overall recirculation properties used for dealing with the base wall heat transfer.

The mass flow that is to be vented into the surrounding atmosphere through the outer jet mixing layer originates from two sources: (1) the initial boundary layer and (2) the inner jet-mixing layer. The total recirculation mass flow can be given by adding these two sources to give

$$\frac{\dot{m}}{(\rho u)_{ex} R_n^2} = (2\pi)^i \left[\frac{\delta_{ex}^{**}}{R_n} \left(\frac{r_{BL}}{R_n} \right)^i + \frac{(\rho u)_e}{(\rho u)_{ex}} \frac{\cos \epsilon_d}{\sigma} \frac{x_r}{R_n} \left(\frac{r_{mix}}{R_n} \right)^i \int_{\eta_j}^{\eta_d} \frac{\rho u}{(\rho u)_e} \, d\eta \right] \tag{43}$$

where $r_{BL} = R_n + \delta$ and r_{mix} are the integrated mean radius of the j and d streamline locations from the common streamline interaction axis. The value of $\dot{m}$ computed from Equation (43) and its corresponding assumed base pressure p_b are used to match the corresponding mass flow computed in the outer jet solution; i. e. ,

$$\dot{m} + G + \dot{m}_b = 0 \tag{44}$$

where $\dot{m}_b$ is the base-bleed mass flow rate, if any.

Base Wall Heat Transfer

The principal contributions to the base wall heat transfer may be attributed to the radiative and convective phenomena of exhaust rocket plumes and the recirculating flow in regions behind the base of the vehicle. For recirculating regions that do not absorb substantial amounts of the incident radiation, the radiation reaching the base wall may be treated independently of the convective phenomena existing in the base recirculating flow (and vice versa). Techniques for determining of the radiative heat fluxes reaching the base wall have been considered elsewhere The current approach for determining the convective heat transfer is indicated in the two following subsections.

Energy Transfer

Two forms of energy transfer are associated with the jet-mixing layer, one resulting from the total enthalpy gradient across the mixing layer and the other associated with the mass flow entrainment and initial boundary layer. The conservation of energy in the base region thus allows one to determine the net heat transfer rate to the base surface (or the nozzle wall if so desired). In this Section, the two types of mixing-layer energy transport are described.

The transferred energy and the shear work and heat from the mixing-layer edge boundary to the inner base region (across the dividing streamline) between $x = 0$ and $x = x_r$ for inner jets may be expressed as

$$\Omega_c = \int_{y_j}^{y_e} (2\pi r)^i \rho u \left(h_{oe} - h_o \right) dy \qquad (45)$$

The energy carried by the entrained mass flow between the d and j streamlines into the base region is

$$\Omega_d = \int_{y_j}^{y_d} (2\pi r)^i \rho u h_o dy \tag{46}$$

The additional energy carried into the base by the equivalent mass flow associated with the initial boundary layer can be evaluated as follows:

$$\Omega_{BL} = (2\pi r_{BL})^i \int_o^\infty \rho u \left(h_o - h_{oe} \right) dy \tag{47}$$

The total energy transfer is then obtained by summing Equations (45) and (46) and (47). With some algebraic manipulation the final result is as follows:

$$\frac{\Omega}{(\rho u)_{ex} R_n^2 h_{oe}} = (2\pi)^i \left\{ \frac{\delta_{ex}^{**}}{R_n} \frac{r_{BL}}{R_n} \frac{(h_o)_{ex}}{(h_o)_e} + \frac{(\rho u)_e}{(\rho u)_{ex}} \frac{\cos \epsilon_d}{\sigma} \frac{x_r}{R_n} \left(\frac{r_{mix}}{R_n} \right)^i \right.$$
$$\left. \left[\int_{\eta_j}^{\eta_d} \frac{\rho u}{(\rho u)_e} \frac{h_o}{h_{oe}} d\eta + \int_{\eta_j}^{\eta_d} \frac{\rho u}{(\rho u)_e} \left(1 - \frac{h_o}{h_{oe}} \right) d\eta \right] \right\} \tag{48}$$

Many terms given in Equation (48) are defined in the preceding section. In addition, by defining another kind of integral I_3, the two integrals in Equation (48) can also be evaluated as

$$\int_{\eta_j}^{\eta_d} \frac{\rho u}{(\rho u)_e} \frac{h_o}{h_{oe}} \, d\eta = \frac{x_r}{\sigma} \left(1 - C_e^2\right) \left(I_{3d} - I_{3j}\right) \tag{49}$$

$$\int_{\eta_j}^{\eta_d} \frac{\rho u}{(\rho u)_e} \left(1 - \frac{h_o}{h_{oe}}\right) d\eta = \frac{x_r}{\sigma} \left(1 - C_e^2\right) \left[\left(I_{1e} - I_{1j}\right) - \left(I_{3e} - I_{3j}\right)\right] \tag{50}$$

where

$$I_3 \equiv \int_{-\infty}^{\eta} \frac{\phi \lambda \Lambda}{(\Lambda - C_e^2 \phi^2)} d\eta = \Lambda_b I_1 + \left(1 - \Lambda_b\right) I_2 \tag{51}$$

Base Wall Heat Transfer

To treat the base wall heat transfer, it is convenient to have a detailed description of the recirculation flow properties near the base, with an appropriate compressible boundary layer analysis to specify the convective heat-transfer distributions. Because of the complexity of the geometries for the actual recirculation region and the base wall boundary layer, however, approximate approaches such as that of Dixon and Page[45] become useful for estimating the magnitude of the base wall heat transfer. By using a modified Sibulkin heat-transfer equation. the base stagnation point is considered in an approximate manner. The expression for estimating the base wall convective heat transfer rate as given by Reference 45 is

$$q_{stag} = 0.763 \sqrt{\rho \mu \frac{U_{vent}}{r_{vent}}} \frac{c_p T_{oa}}{P_r^{0.6}} \left(1 - \frac{T_w}{T_{oa}}\right) \tag{52}$$

where

U_{vent} is the vent velocity between the nozzles

r_{vent} is the radius from the stagnation point to the vent area between the nozzles

The properties are evaluated at the nozzle-exit static temperature whenever appropriate. It will be noted that the above expression approximates the base stagnation-point velocity gradient by assuming that the gradient is linear between the stagnation point and the vent area. To approximately account for velocity components in the recirculating flow, the current analysis utilizes a linear combination of the vent velocity and the recirculated discriminating streamline velocity. An estimated heat-transfer rate may thus be obtained for a nonvented, purely recirculated, flow that would otherwise vanish, using the above expression without the indicated recirculation flow considerations.

An energy balance in the base region yields

$$\Omega + \bar{\Omega} + Q_b + Q_n = 0 \tag{53}$$

where Ω is the total energy transfer across the outer jet and Q is the heat transfer to either the nozzle's outer surface or the base. The nozzle's outer surface heat transfer has not been treated in the present analysis, and results shown in a later section are obtained using the following approximate equation for recirculation cases ($Q_b = q_{stag} A_b$):

$$\Omega + Q_b = 0 \tag{54}$$

Correspondingly, for aspiration cases the following approximate equation is used

$$\bar{\Omega} + Q_b = 0 \tag{55}$$

In Figure 3a, a rectangular positioning of similar rocket nozzles is shown. This configuration simulates a space shuttle booster configuration used in the Phase B study. Each nozzle is identified by a number: 0, 1, or 2, corresponding to the base flow patterns indicated in Figure 3b. In Figure 3b, three types of base flow patterns are shown (in a self-explanatory fashion), indicating the approximate vent area between nozzles associated with the venting mass flow from each quadrant of the flow field.

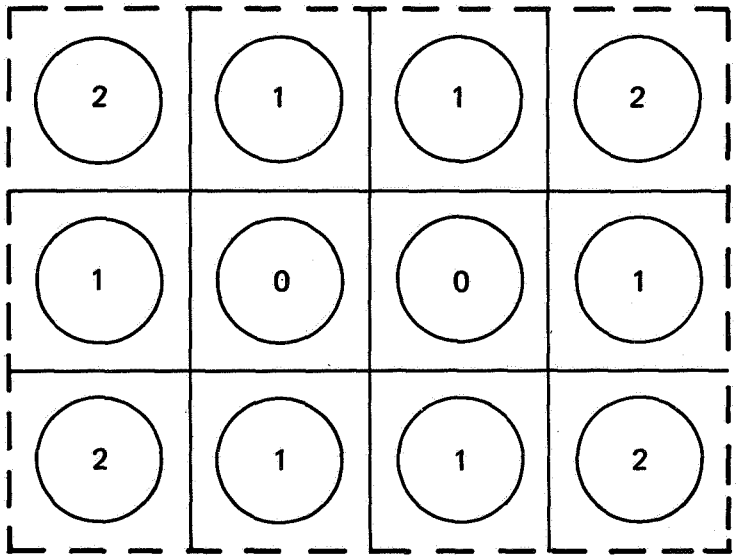

(a) MULTI-ENGINE NOZZLE CONFIGURATION AND OVERALL PATTERN

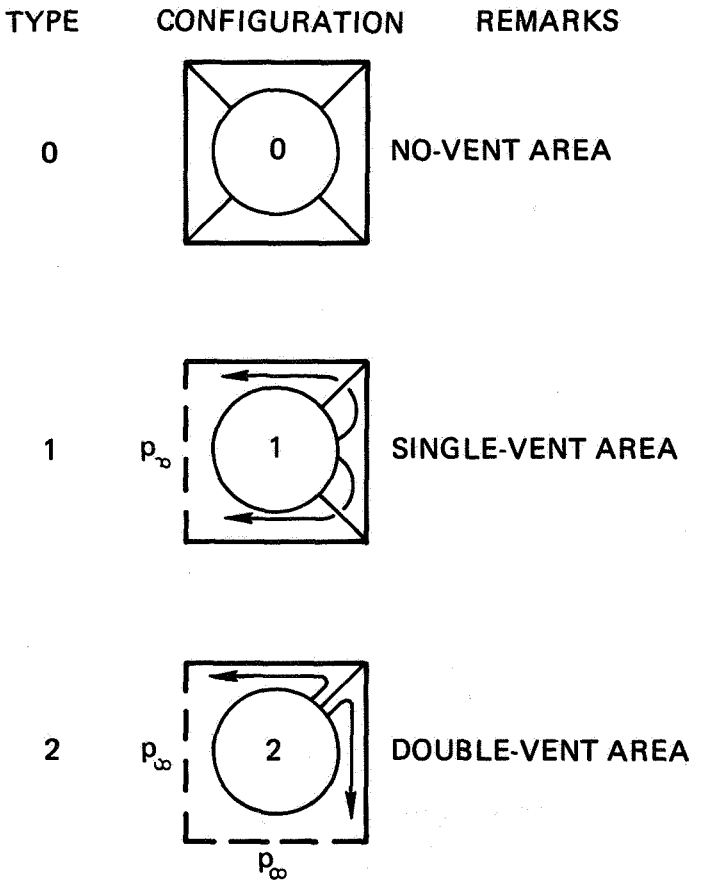

(b) BASIC VENTING CONFIGURATIONS

Figure 3. Various Venting Configurations

In Figure 4a, an illustration showing the common streamline axis is given. Because of the symmetry associated with this axis, flow-field solutions between it and the various nozzle axes are approximately identical. Consequently, this axis is useful in treating the recirculating flow contained between the nozzles. The detailed flow-field components associated with the above cross-sectional planes are given in Figure 4b.

In Figure 4b, a schematic base flow model is shown to indicate various components used in the theoretical formulation. These are:

A. Inviscid flow originating from the nozzle.
B. Downstream shock wave recompression.
C. Initial boundary-layer expansion at the nozzle lip.
D. Nonisoenergetic mixing-layer properties and important streamlines.
E. Reattachment.
F. Base flow recirculation and venting.
G. Base wall heat transfer.

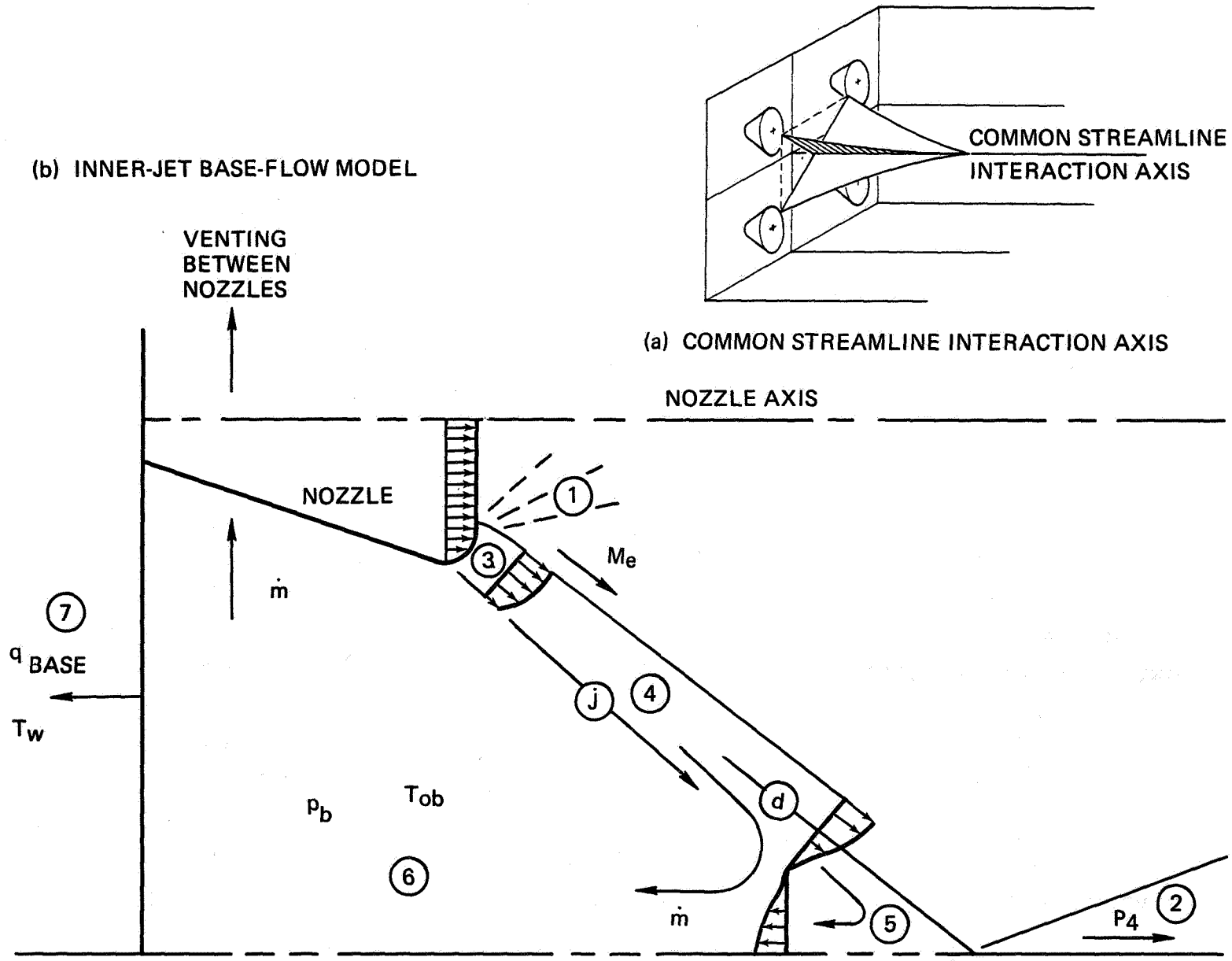

Figure 4. *Common* **Streamline Interaction Axis and Inner-Jet Base Flow Model**

Figure 5 shows the coordinates and nomenclature used in the present analysis. The virtual origin is indicated at (x_o, y_o). The inviscid coordinates X and Y are related to the intrinsic coordinates x and y by the following equations:

$$X \cong x$$
$$Y \cong y - y_m(x) ; \qquad y_m(0) = 0$$

Figure 5 also shows the control volume used for the reattachment evaluation (ADRF). Axisymmetric mass and momentum flux quantities are obtained by revolving the flow field properties around the axis specified by FR.

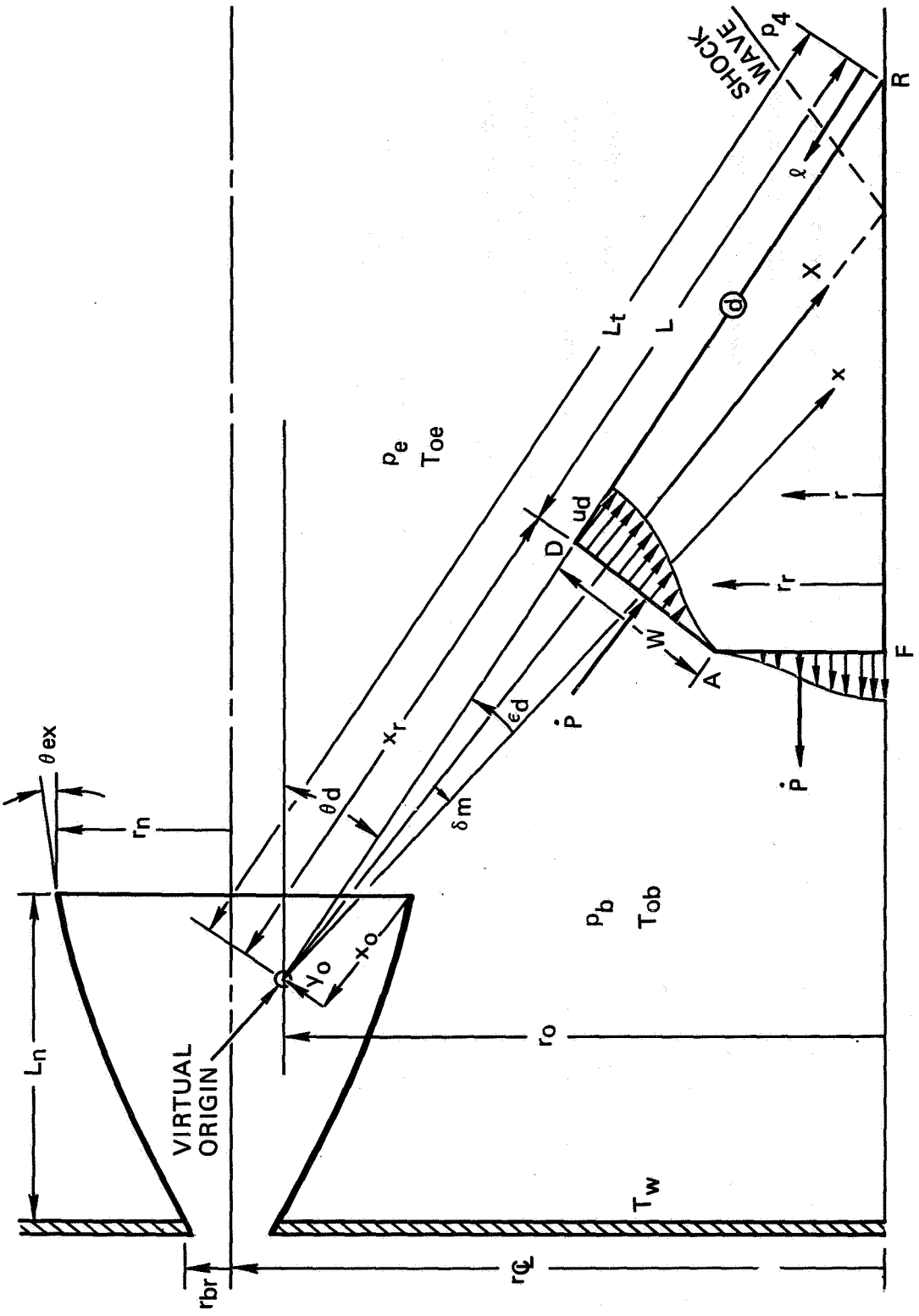

Figure 5. Inner-Jet Base Flow Field and Reattachment Control Volume (ADRF)

Section 4
EXPERIMENTAL REVIEW

Experimental data used to investigate various multi-engine base flow phenomena are of crucial importance since the base heating problem is very complex and sensitive to various controllable parameters, such as geometry. Experimental data can therefore provide a better understanding of the problem.

Since a large quantity of data is available for various configurations, a summary of the most recent experiments is useful to examine the over-all effects of key parameters, such as altitude, propellant, and configuration. Table 2 presents a partial breakdown of available data sources. Experimental results for three different boosters (S-I, S-IC, and S-II) are presented below to demonstrate the following points of interest:

For S-I: to identify the various heating modes and base flow-field conditions

For S-IC: to demonstrate the importance of reverse-flow radiative heating

For S-II: to demonstrate the sole existence of convective heating.

Table 2

BASE HEATING DATA SUMMARY

VEHICLE	CONFIGURATION (* MAX HEATING)	PROPELLANT	ENGINE PARAMETERS						TYPE PROGRAM	FACILITY	ALTITUDE-KM (nmi)	FLIGHT TIME (sec)	APPROX MAX HEATING- W/cm^2 (Btu/ft^2 sec)			APPROX BASE PRESSURE $-N/cm^2$ (psia)
			F/O	A/A*	P_{CH}-N/CM2 (psia)	T_{CH}-°K (°R)	DEX-CM (in.)	NOZ EXIT HALF-ANGLE					CONVECTIVE	RADIATIVE	TOTAL	
THOR DSV-2A	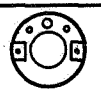	RJ-1/LOX	2.27:1	8:1	410 (595)	3,250 (5,840)	116.0 (45.6)	4.7	FLIGHT		0 TO 75 (0 TO 40)	147			18 (16)	10.1 TO 0 (14.7 TO 0)
		RJ-1/LOX	2.2:1	7.9:1	393 (570)	3,220 (5,800)	12.7 (5.0)		10.7% SUBSCALE TEST	AEDC CELL T-1	1.5 TO 25.0 (0.8 TO 13.5)				18 (16)	
TITAN II		N_2O_4/ AEROZINE							FLIGHT						12 (10)	
TITAN IIIC	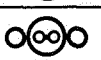	N_2O_4/ AEROZINE PLUS SOLIDS							FLIGHT				12 (10)	12 (10)		
SATURN S-IV		GASEOUS H_2/O_2	5:1		240 (350)	2,920 (5,260)	10.9 (4.3)		1/10 SUBSCALE TEST	CAL	40 TO 67 (22 TO 36)		4.8 (4.3)		4.8 (4.3)	0.028 TO 0.052 (0.04 TO 0.075)
		AIR							1/27.7 SUB-SCALE TEST	AEDC	37 TO 55 (20 TO 30)		4.8 (4.3)		4.8 (4.3)	
SATURN S-II		LH_2/LOX	5:1	27.5:1	435 (632)		204.0 (80.0)		FLIGHT		67 TO 174 (36 TO 94)	370	13.5 (12.0)		13.5 (12.0)	0.0275 (0.04)
		GASEOUS H_2/O_2	5:1	27:1	435 (632)		8.1 (3.2)		1/25 SUB-SCALE TEST	CAL	49 TO 73 (26.5 TO 40.0)		>13.5 (12.0)		>(13.5) (12.0)	0.062 (0.09)
SATURN S-IC		RP-1/LOX	2.26:1	16:1	690 (1,000)	3,350 (6,040)	356.0 (140.0)		FLIGHT		0 TO 64 (0 TO 35)	160		23 (20)	23 (20)	10.1 TO 0 (14.7 TO 0)
					690 (1,000)				1/45 SUB-SCALE TEST	NASA LANGLEY 8 X 6 FT	0 TO 11.1 (0 TO 6.0)			1 (1)	13.5 (12.0)	
SATURN S-IV		LH_2/LOX	5.5:1	40:1	207 (300)	3,100 (5,600)	100.0 (40.0)		FLIGHT		40 TO 67 (22 TO 36)		1.8 (1.6)		1.8 (1.6)	0.0137 (0.021)
		GASEOUS H_2/O_2	5.5:1	40:1	207 (300)	3,100 (5,600)	10.2 (4.0)		1/10 SUB-SCALE TEST	CAL	37 TO 67 (20 TO 36)		3.4 (3.0)		3.4 (3.0)	0.0028 TO 0.052 (0.004 TO 0.075)
SATURN S-I	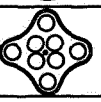	RP-1/LOX	2.35:1	8:1	400 (576)	3,450 (6,240)	116.0 (45.7)		FLIGHT		0 TO 40 (0 TO 22)	140	5.7 (5.0)	80 (70)	100 (90)	10.1 TO 0 (14.7 TO 0)
									SUBSCALE							
THOR DSV-2C		RJ-1/LOX PLUS TP-H 8038 SOLIDS	2.27:1	8:1 5.9:1	410 (595) 355 (515)	3,250 (5,840) 3,270 (5,860)	116.0 (45.6) 60.5 (23.8)	4.7 15.0	FLIGHT		0 TO 91.5 (0 TO 50.0) 0 TO 9.2 (0 TO 5.0)	147 42		20.5 (18.0)	13.5 (12.0)	10.1 TO 0 (14.7 TO 0)
		RJ-1/LOX PLUS TP-H 8038 SOLIDS	2.2:1	6:1 7.9:1	393 (570) 370 (540)	3,200 (5,800)	12.7 (5.0)	15.0	10.7 SUB-SCALE TEST	AEDC	1.5 TO 25.0 (6.8 TO 13.5)				9.1 (8.0)	
THOR DSV-2L	SAME AS DSV-2C	RJ-1/LOX PLUS TP-H 7038 SOLIDS	2.27:1	8:1 7.5:1	410 (595) 355-500 (515-720)	3,250 (5,840) 3,650 (6,540)	116.0 (45.6) 58.5 (23.0)	4.7 16.4	FLIGHT		0 TO 91.5 (0 TO 50.0) 0 TO 5.2 (0 TO 2.8)	220 38	11 (10)	19 (17)	20.5 (18.0)	
THOR DSV-3L		RJ-1/LOX PLUS 3TP-H 8038 AND 3TP-H 7036 SOLIDS	2.27:1	8:1 5.9:1 7.5:1	410 (595) 355 (515) 355-500 (515-720)	3,250 (5,840) 3,270 (5,860) 3,650 (6,540)	116.0 (45.6) 60.5 (23.2) 58.5 (23.0)	4.7 15.0 16.4	FLIGHT		0 TO 91.5 (0 TO 50.0) 0 TO 4.6 (0 TO 2.5) 2.1 TO 14.0 (1.1 TO 7.6)	220 42 37	19.3 (17.0)	22 (19)	34 (30)	

Figure 6 is a typical plot of reduced data for the Saturn S-I. The initial large heat input is due to the launch procedure of holding the vehicle down until all engines have reached full thrust. During this time, there is a large radiation heat input from the exhaust gases, which are deflected by the launch pad. After release, the heat input drops to the normal low-altitude rate. In the region of a 15- to 20-km altitude for this vehicle, the reversed flow resulting from the interaction of the inboard engine plumes chokes in the vent areas. Leading up to this is a progressively more-severe plume interaction, which results in (1) increased mass flow of the reversed exhaust gases and (2) increasing high-temperature zones in the plume interaction regions. The former increases the gas temperature in the base area, and the latter increases the radiation to the base area. It is interesting to note that the convective mode of heat transfer is almost entirely one of cooling, particularly at lower altitudes. This is because the flow is principally from the outside toward the inside as the inboard flame-shield base pressure is less than the outer heat-shield base pressure. Other flight data for this vehicle indicate that late in flight, the convective component is positive (heating) albeit quite small. Also shown is the range of ground test data obtained. The simulation seems good for total heating but not for radiation. This points up one of the major problems in scaling hydrocarbon engine exhausts; namely, afterburning.[46]

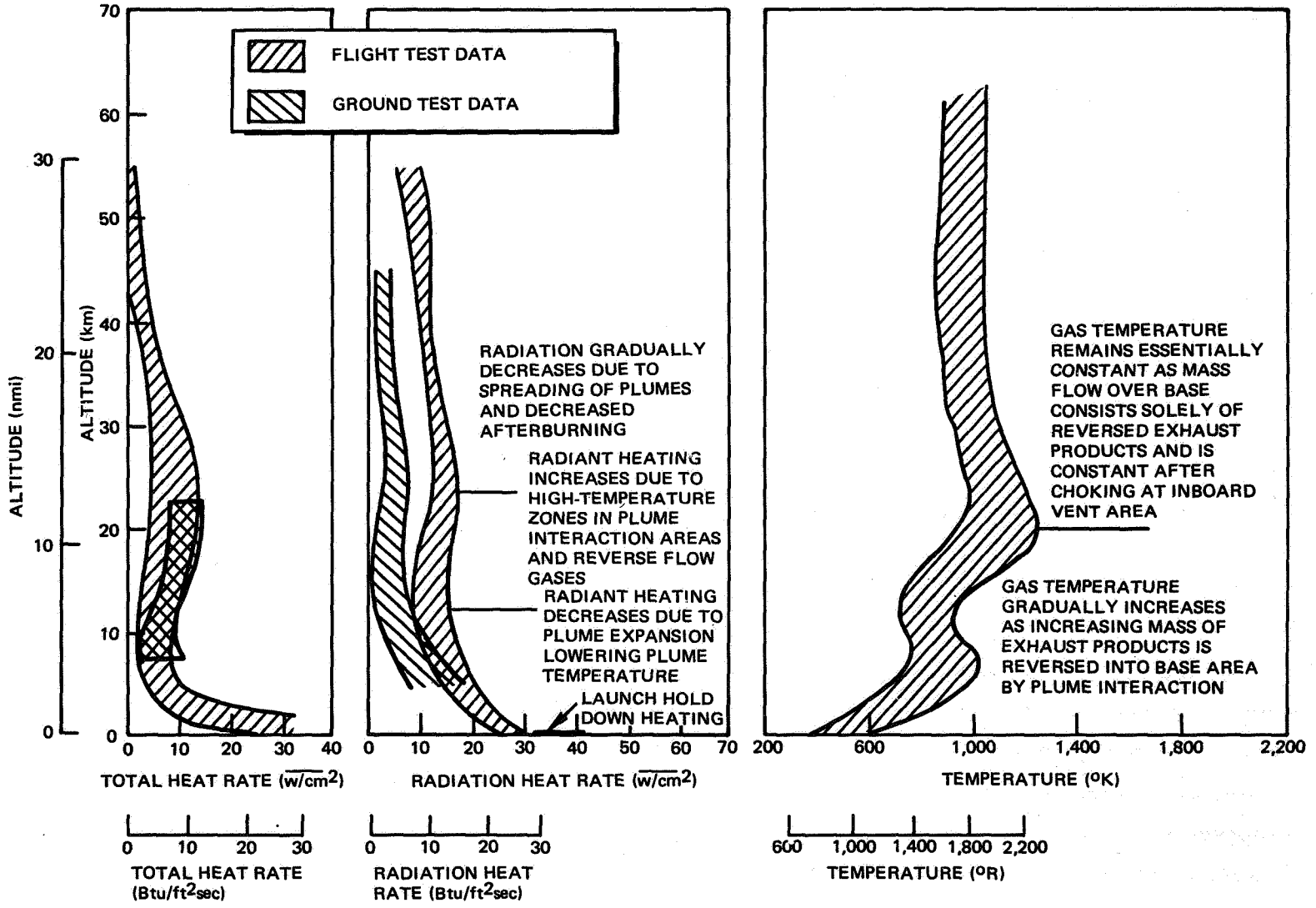

Figure 6. Saturn I/S-I Inner Base Heat Shield Heating

The Saturn S-IC stage has a configuration that is different from the S-I with five engines in a cross pattern. Figure 7 compares the heating rates of the S-I and S-IC. As can be seen, the launch heating is considerably less even though the holddown time appears to be longer; i. e., 6 versus 3 seconds. On the other hand, the heating due to reverse flow was considerably higher (at about 20 km). Other data indicate that the principal mode of heating in this regime is radiation from the hot gases reversed into the base and from the plumes.[47] This contention is supported by the ground test data shown, which indicate that the convective heating should be virtually zero at 20 km. The ground test data are convective only because gaseous H_2 and O_2 were used as propellants for the model.

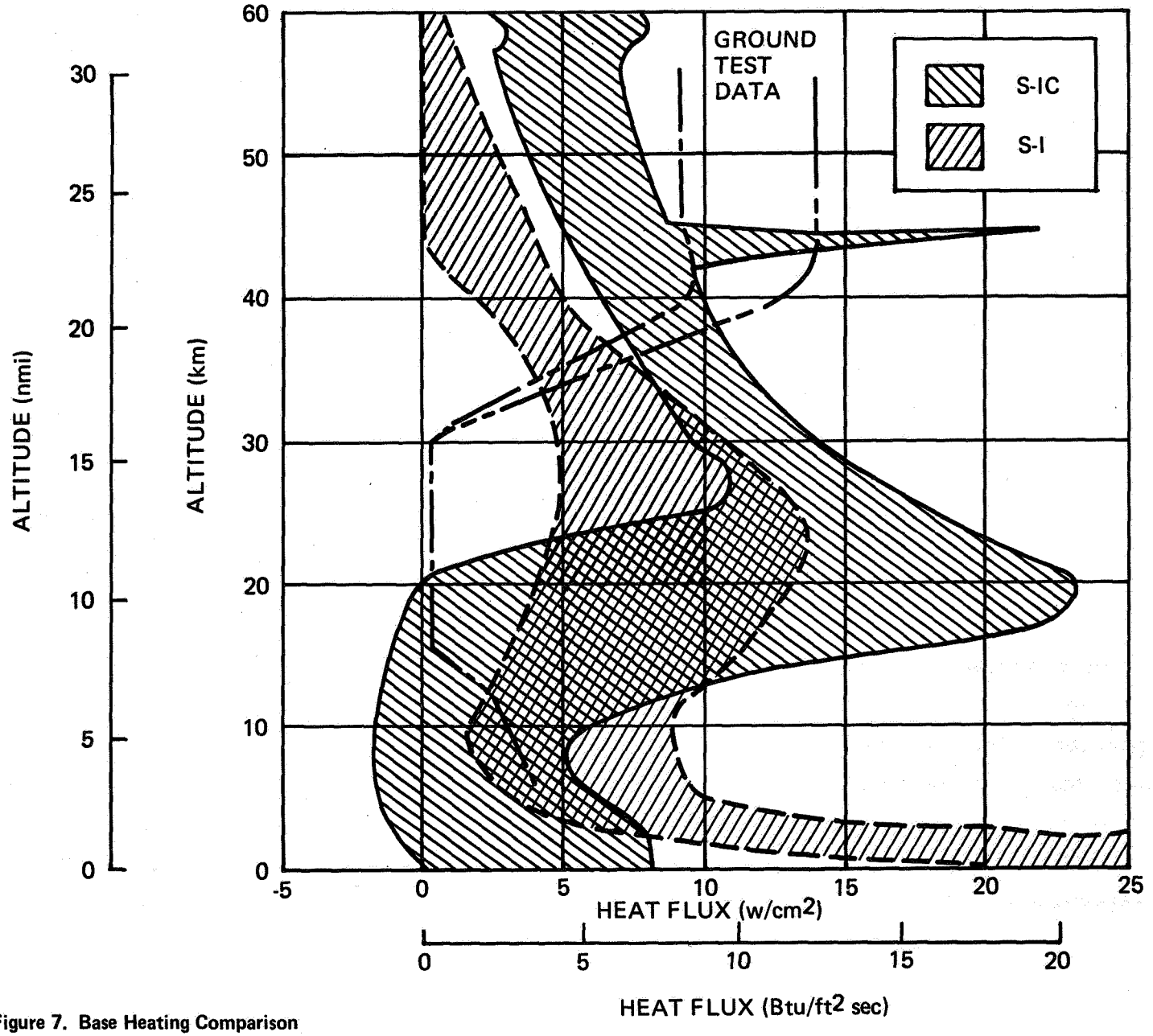

Figure 7. Base Heating Comparison

The S-II and S-IV utilize LOX and LH_2 as propellants. Consequently, their plume emissivities are very low, and radiation heating is only a minor component. Since these stages operate predominantly outside the atmosphere, afterburning also is negligible. Therefore, any base heating that arises is due to convection by the reversed exhaust gases. Also, since the operational altitudes are high, the reversed flow resulting from plume impingement will always be choked. Thus, both base-pressure and base-heating rates should be relatively constant with time or altitude. Figure 8 shows a plot of S-II data indicating such behavior.

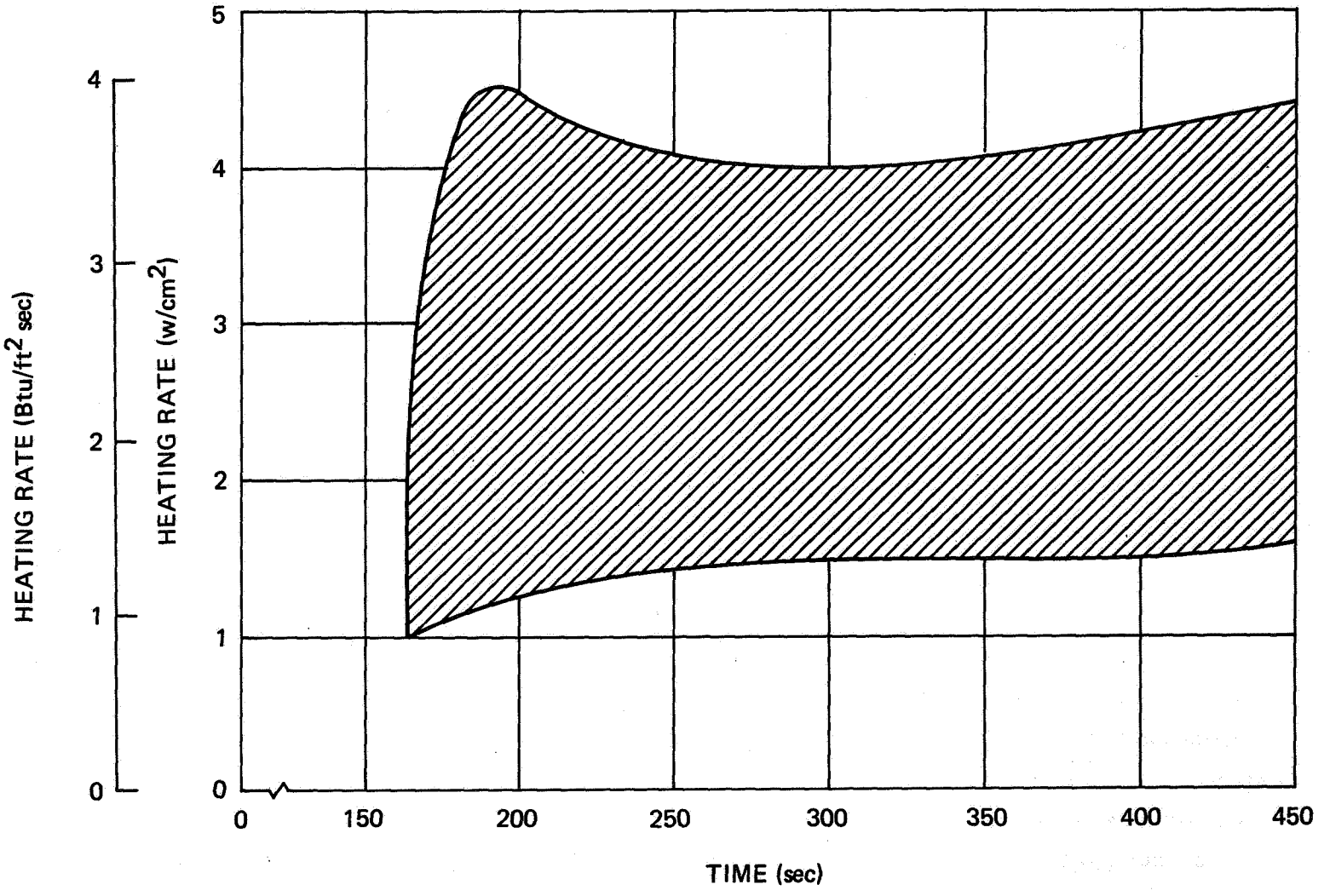

Figure 8. S-II Base Heating Rate History

Section 5

THEORETICAL PREDICTIONS AND DATA COMPARISONS

SATURN V/S-IC STAGE

Since the S-IC booster is one of the prime candidates for current space shuttle booster applications, a special effort has been conducted to use the present method to evaluate its base thermal environment. This is presented in two parts. Part 1 evaluates the convective heating, and Part 2 estimates the radiative heating. Both parts include comparisons with flight test data. A detailed discussion of the computational procedures is given in the two subsections that follow.

Convective Heating

By using typical Saturn V trajectory data,[48] it is possible to specify approximately the external flow surrounding the Saturn V vehicle. The pertinent regimes for comparison purposes involve the portion of the trajectory below 60 km (about 200 kft), where the launch vehicle Mach number does not exceed a value of 8.

By considering the size of the launch vehicle,[48] which is approximately 110.6 m (363 ft) long with a base diameter of 10.1 m (33 ft), the above trajectory information permits a determination of the typical Reynolds numbers experienced by the vehicle. Consequently, the boundary layer properties at the base of the vehicle may be specified and utilized, together with an estimate of the effective mass bleeding into the outer base region from the combined inner-rocket-nozzle venting processes, to estimate the pressure existing in the effective "outer-annulus" region surrounding the inner jet portions of the base flow. For this purpose, the outer-jet base flow program has been utilized, and it yields the results indicated in Figure 9. It will be noted that the results are relatively insensitive to the equivalent mass bleed-venting process of the inner jets.

Application of the outer-annulus pressure ratio results given in Figure 9 to the particular trajectory of interest permits an estimate of the outer-annulus pressure for the present data comparison. It will be noted that results of this procedure generally indicate that the magnitude of the predicted outer-annulus pressure is less than the ambient atmospheric pressure experienced by the Saturn V throughout the trajectory.

Estimates for the outer jet flow having been completed, the inner-jet flow results become of interest. By specifying the inner jet results in terms of the outer-jet "annulus" pressure, the properties associated with the inner jet may be predicted by matching the outer-annulus properties as previously specified along the trajectory.

The inner-jet base heating for both recirculation and aspiration cases is indicated in Figure 10. For aspiration, cooling is experienced because of the cooler outside annulus gases being drawn into the base region. Note that for sufficiently low outside-annulus pressures, the vented flow between the nozzles "chokes," and consequently the internal flow pattern as well as base heating remains constant for lower outside-annulus pressures. The corresponding inner base-pressure variation with the outer-annulus pressure exhibits a similar choked flow behavior. Figure 11 shows the present prediction for convective base heating compared with the experimental data. It is seen that the prediction curve falls within the data bounds (indicated by two dashed lines). The present predictions account for aspiration flow below 12 km (40 kft) with recirculation flow above 21 km (70 kft). Figure 12 shows the results of the base pressure prediction compared with data. The predictions, as shown, are lower. This is probably due to geometry effects, such as engine fairings, located in the base recirculation flow region.

In Figure 9, the parameterized results for the ratio of predicted outer-jet annulus pressures to the ambient atmospheric pressure are presented for a variety of flight-vehicle Mach numbers and Reynolds numbers. Extreme values for the equivalent mass bleeding (or suction) corresponding to the inner-jet venting processes are also considered in the predicted results.

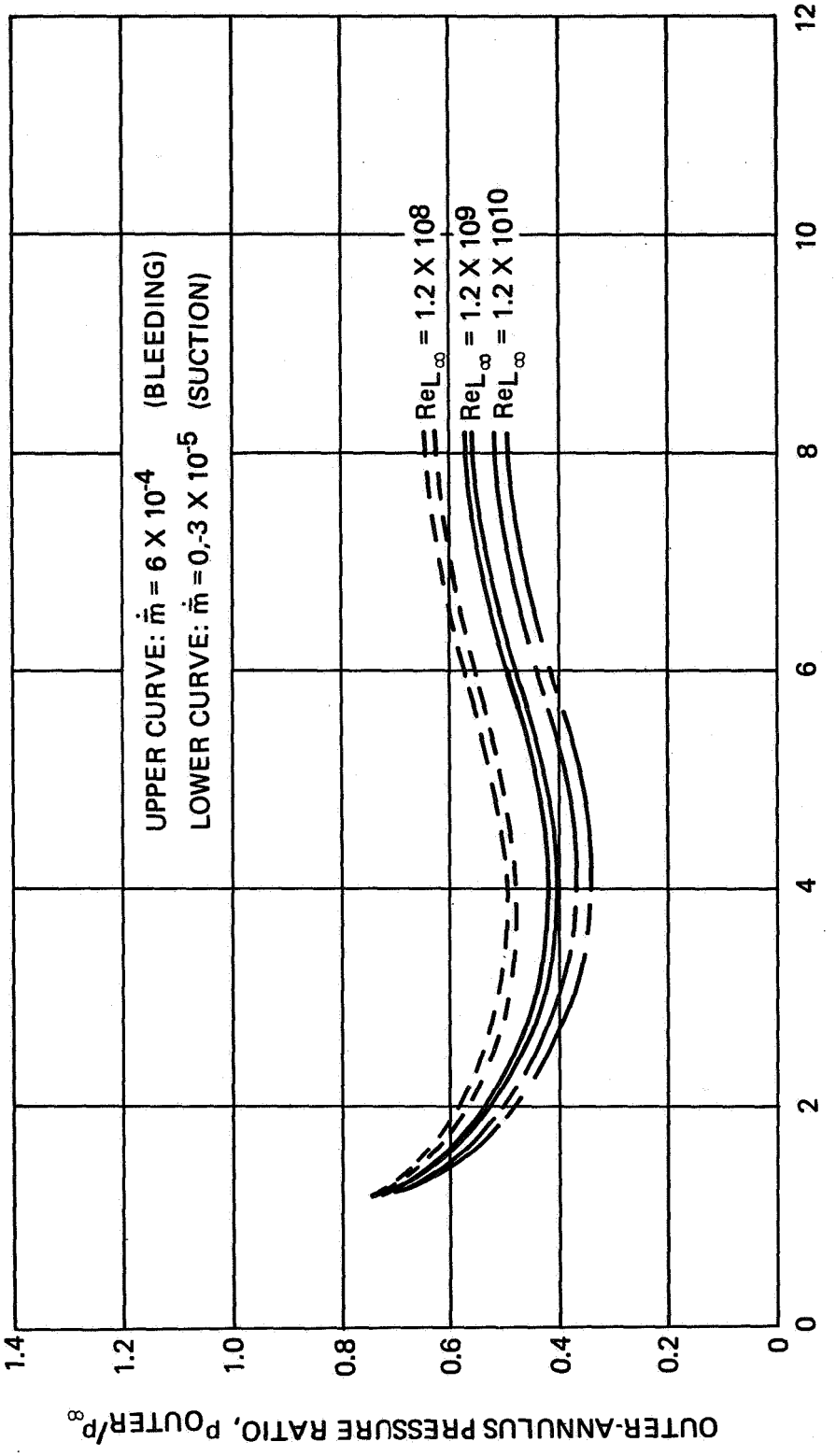

Figure 9. Predicted Outer-Annulus Pressure Versus Mach Number

In Figure 10, the predicted inner-jet base heat transfer results are presented in terms of the outer-jet annulus pressure. The results indicate the predicted cooling rates associated with low-altitude aspiration as well as the predicted positive heating rates associated with the high-altitude recirculation flow patterns.

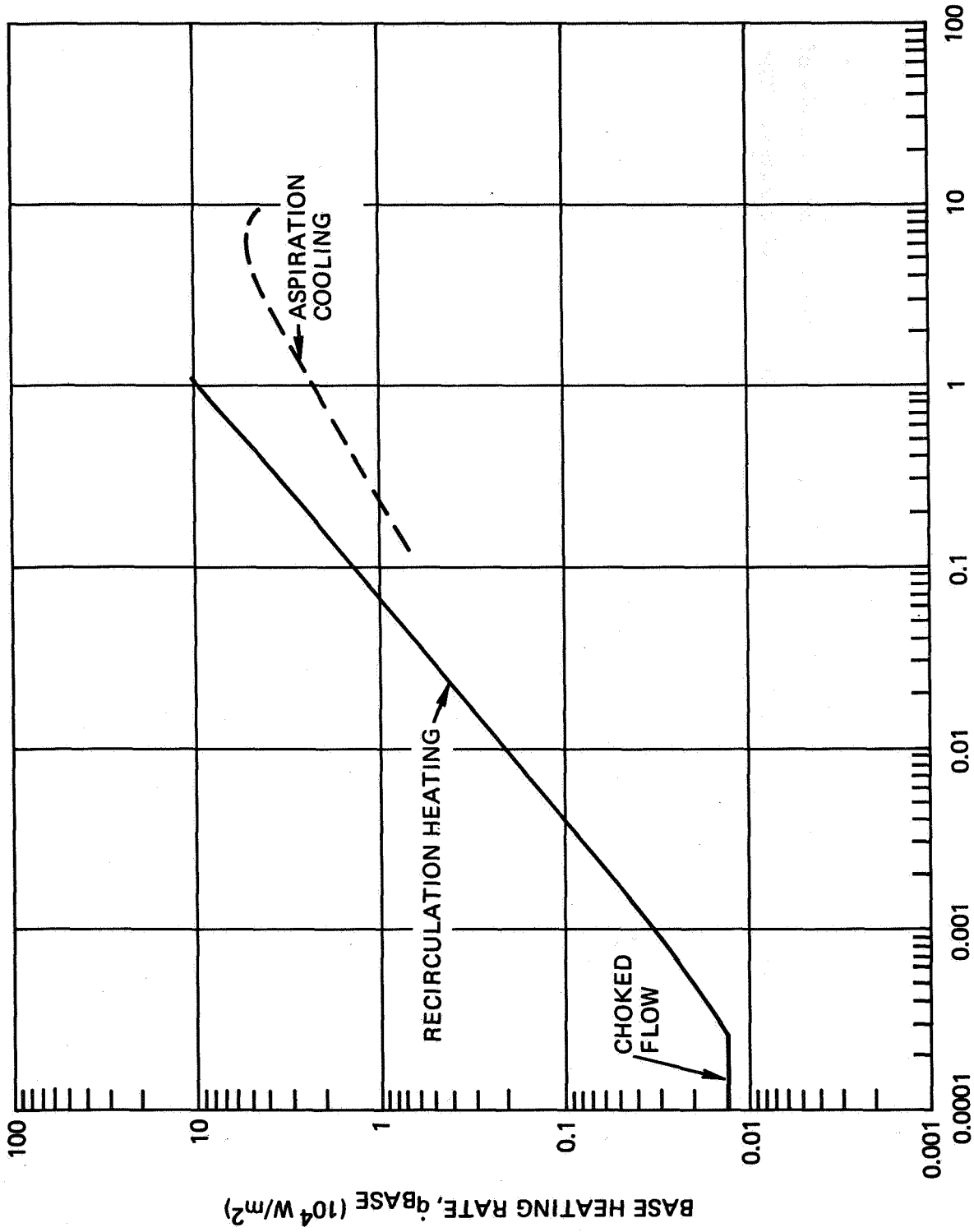

Figure 10. Predicted Base Heating Versus Outer-Annulus Pressure

In Figure 11, a comparison of the present predictions with the experimental data bounds of the Saturn V launch vehicle are presented for the base convective heat transfer rates. The predictions are well within the data bounds and exhibit the general trends of the data.

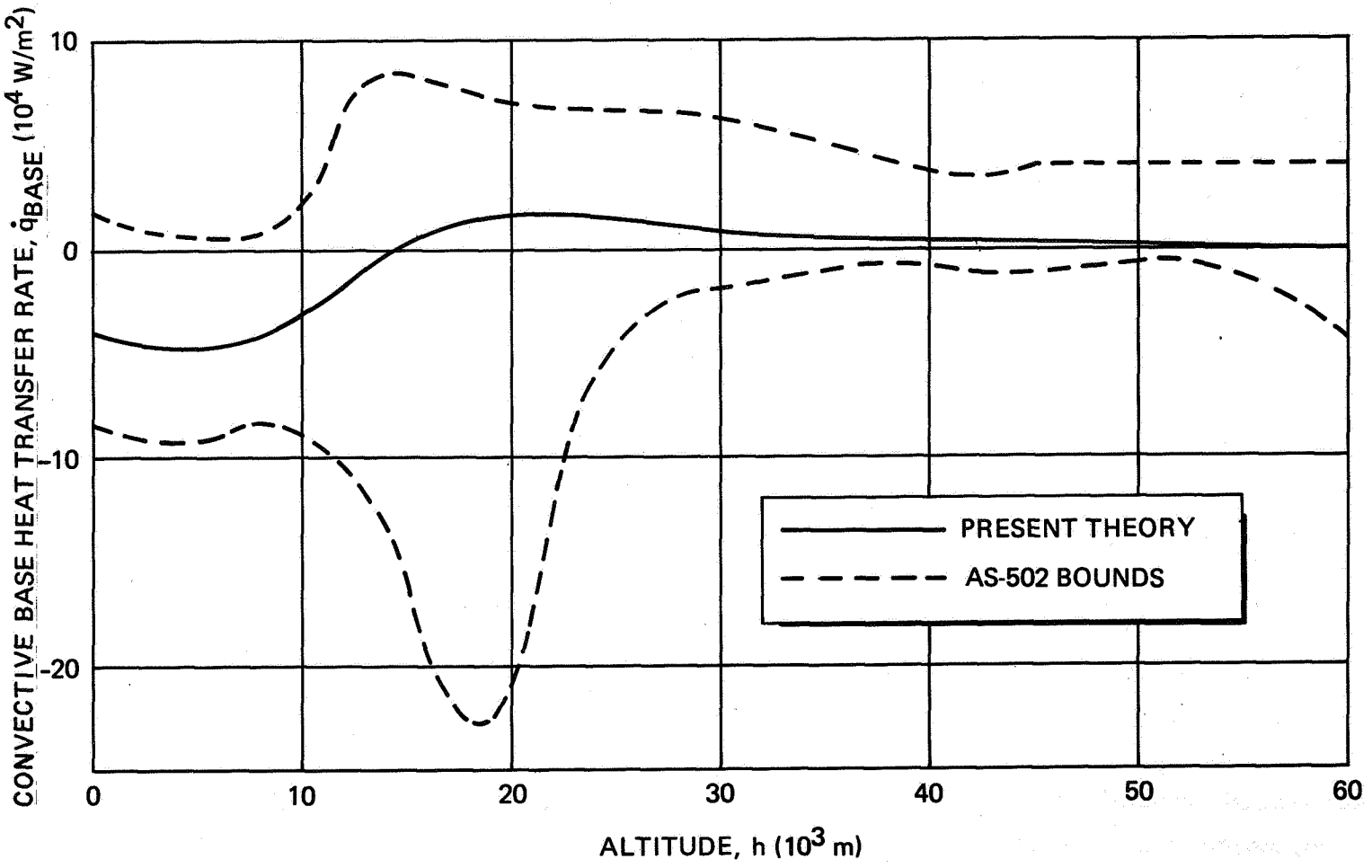

Figure 11. Base Heating Comparison

In Figure 12, present predictions for the base pressure are compared with the Saturn V launch vehicle data as a function of altitude. The predicted results are generally below the level of the data, and this may be attributable to estimates of the outer-jet annulus pressures, which do not account for specific rocket nozzle geometry and probable strong plume interaction effects in the recirculation region.

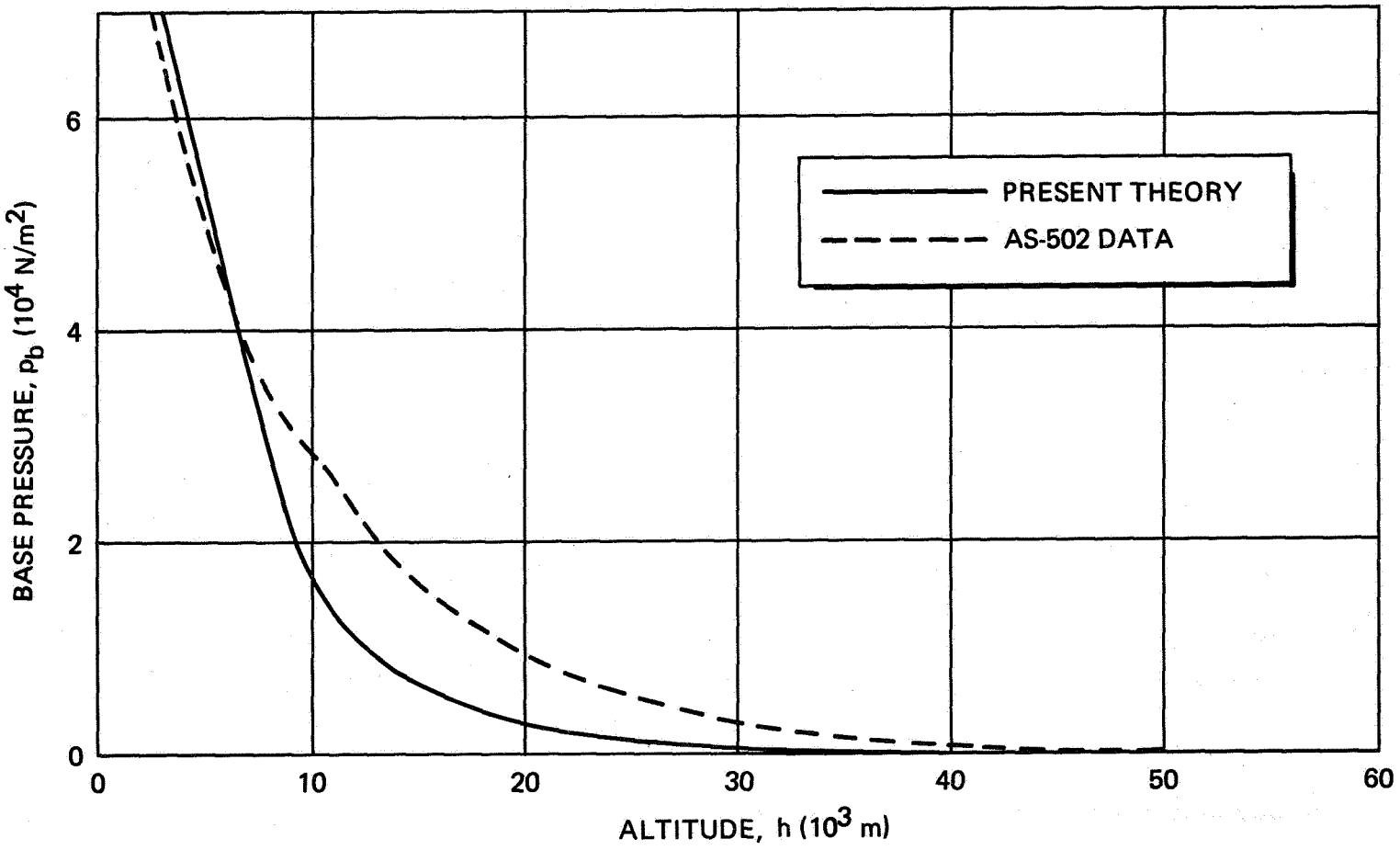

Figure 12. Base Pressure Comparison

Radiation Heating

Radiative base heating is very significant for the Saturn V/S-IC stage. Since the Saturn V/S-IC engines and base configuration are being considered as candidates for the space shuttle, model test data and flight results for the Saturn V/S-IC stage were evaluated to establish the validity of the available data, to extend these data to the shuttle conditions, and to determine the means to evaluate the radiative base heating experimentally. The base flow-field information obtained from the convective base heating analysis in the preceding section and an MDAC plume-flow analysis were used in this data evaluation.

The outside surface of the engine nozzle at the nozzle exit plane was chosen for analysis, since this is the area of maximum radiation heating. To estimate the time of flow reversal and the radiation configuration factors between the plumes and the engine nozzle, F-1 engine plumes at varying altitudes have been generated from an MDAC plume-flow program. From the shape of the exhaust plumes, the beginning time of flow reversal was estimated to be 6.1 km (3.3 nmi). To calculate the nozzle radiation heating rates, the configuration factors between the plumes and the middle engine nozzle were calculated at sea level and at a 6.1 km (3.3 nmi) altitude, using a radiation configuration factor computer program. The sea level plume was approximated by a cylindrical shape equal in diameter to the engine nozzle's exit diameter. The calculated plume boundary has been used for the 6.1 km (3.3 nmi) altitude. The calculated configuration factors around the nozzle circumference are shown in Figure 13. After the flow reversal, carbon particles are carried into the base region by the reversed flow, and the configuration factor between the particles and the nozzle becomes essentially 1.0.

The sharp increase in the nozzle heating rate after flow reversal at 6.1 km (3.3 nmi) altitude is caused by the cloud of solid particles carried into the base area. The measured flight gas temperature[49] at the time of maximum radiation heating was 1,480° K (2,660° R).

The maximum effective radiation temperature required to give the 23.0 watt/cm^2 (26.0 Btu/ft^2-sec) heating rate is 1,510° K (2,720° R) for a cloud radiating with a configuration factor of 1.0 and an emissivity of 1.0.

Both the measured maximum gas temperature and the temperature at the plume boundary at the time of flow reversal, estimated from flight data, compare favorably with the temperature required to give the maximum measured radiation heating rates.

Based on the available flight data and the available analytical methods, it can be concluded that plume radiation can be estimated up to the point of flow reversal. The plume temperatures must be estimated or determined experimentally. Scale model data for the Saturn V/S-IC stage appear to be valid, and scale testing may provide a convenient means to determine the effective plume temperatures. The heating of the vehicle structure resulting from flow reversal can best be determined experimentally. Lacking experimental data, the maximum radiation heating can be estimated by considering the plume boundary temperature at the time of flow reversal as the effective radiation temperature.

An effective plume temperature at sea level was estimated to be 1,620° K (2,920° R) from the F-1 engine scale tests.[50] The effective plume temperature in a fuel-rich LO_2/RP-1 engine is largely determined by combustion at the plume boundary. The model test data indicate that the average plume temperature is higher than could be predicted, disregarding the plume boundary combustion. Based on this average temperature, a plume emissivity of 1.0, and the maximum sea level configuration coefficient shown in Figure 13, a nozzle heating rate of 9.1 watts/cm^2-sec (8.0 Btu/ft^2-sec) was obtained. The plume emissivity of 1.0 is based

on an analysis presented in Reference 51. Although the effective plume emissivity can be lower than 1.0, especially at higher altitudes, it appears to be a good estimate, especially at sea level, for the Saturn V/S-IC F-1 engine.

Flight data for the Saturn V-S-IC -502 and -503 stages[49] are shown in Figure 14. These data represent upper values of a number of instruments located around the nozzle periphery. The calculated nozzle heating rates of 9.1 watts/cm^2-sec (8.0 Btu/ft^2-sec), based on the model plume temperature and calculated configuration factors, compare favorably with the flight data. From Figure 13, the configuration factor increases from 0.26 at sea level to 0.36 at a 6.1 km (3.3 nmi) altitude. However, the nozzle heating rate remains essentially constant. This can occur only if the plume surface temperature or the surface emissivity decreases. For the emissivity of 1.0, the surface temperature could decrease to 1,530° K (2,750° R) at the 6.1 km (3.3 nmi) altitude.

The radiation configuration factors between the outside of the center engine nozzle and the outside engine plumes were calculated at sea level and 6.1 km (3.3 nmi) altitude, as shown in Figure 13. The configuration factors at sea level were calculated, assuming a cylindrical plume equal in diameter to the engine nozzle exit. The configuration factors at 6.1 km (3.3 nmi) altitude were calculated using the configuration of a calculated plume.

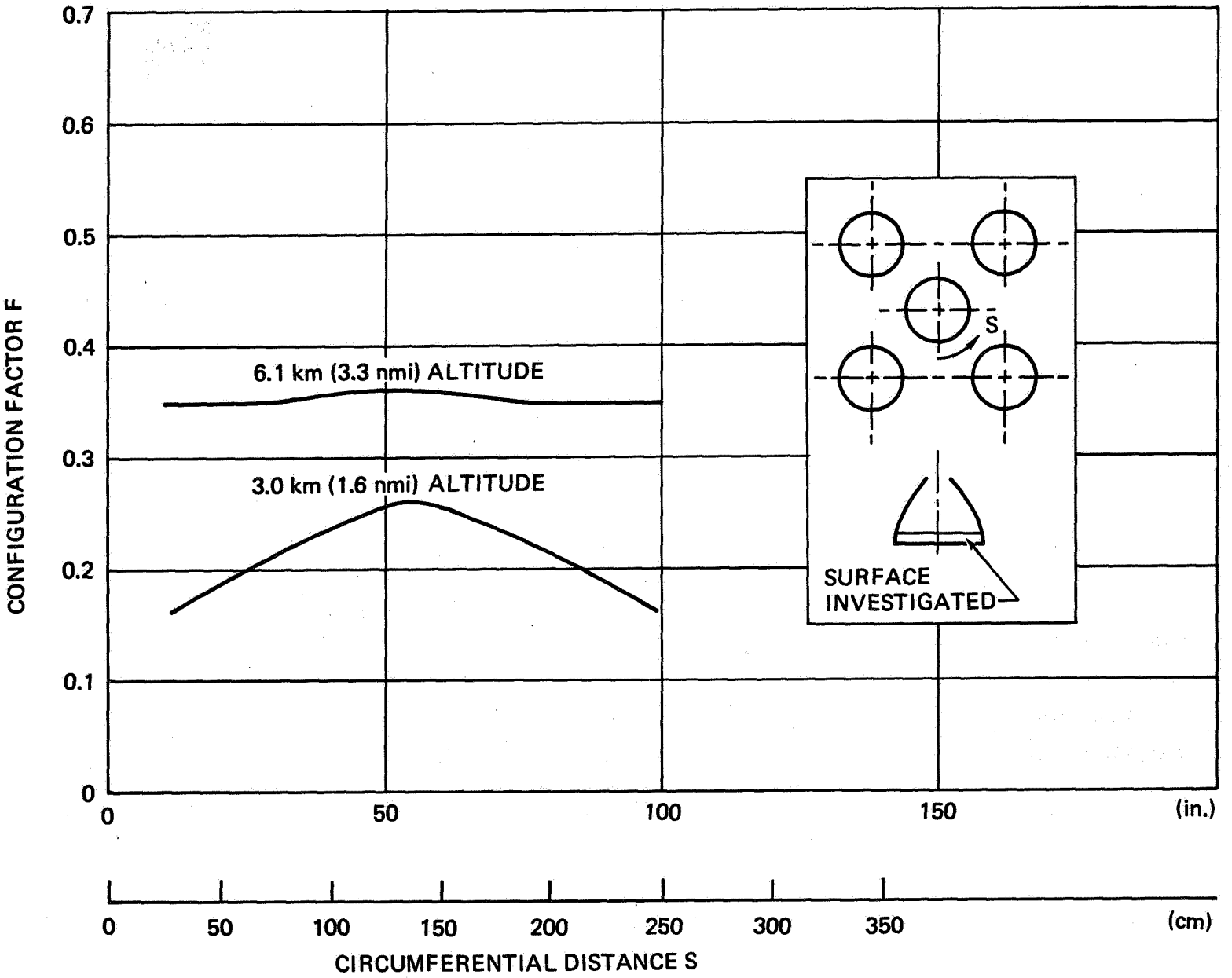

Figure 13. Saturn F-1 Engine Nozzle Configuration Factors

Saturn V/S-IC stage flight data[49] are shown in Figure 14. These data represent the upper values of a number of instruments located on the engine bell. The initiation of convective heating at the 6.1 km (3.3 nmi) altitude indicates the initiation of flow reversal. The increase in radiation heating after 9.0 km (4.9 nmi) altitude is caused by radiation from the particle cloud ingested into the base area by reversed flow. The heating peak at 45.0 km (24.0 nmi) altitude is caused by the middle engine shutdown.

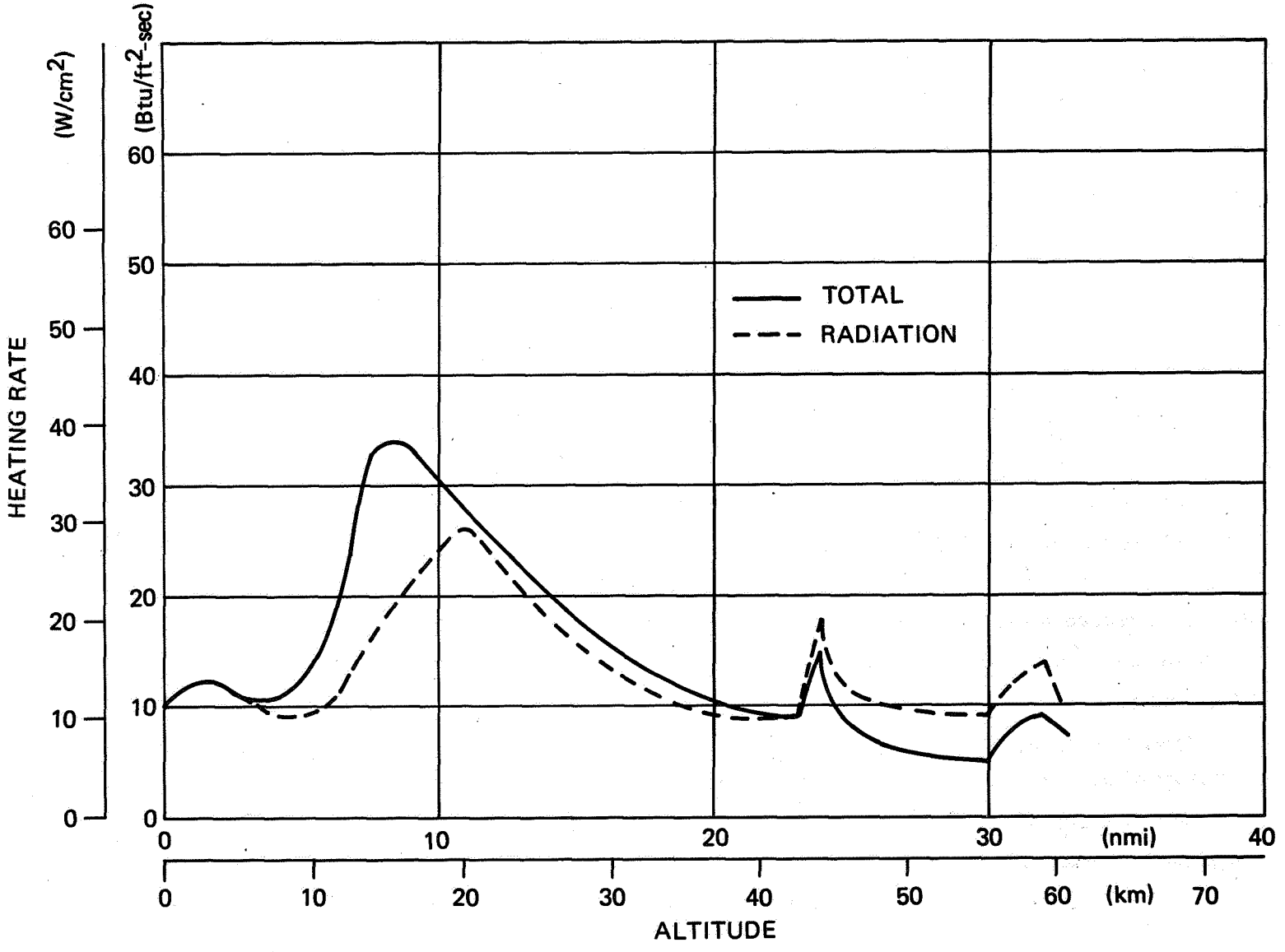

Figure 14. Saturn V F-1 Engine Bell Heating Rates

VARIOUS LOX-LH_2 FUELED BOOSTERS AND SUBSCALE MODELS

As has been suggested, perhaps the easiest case to theoretically analyze and experimentally correlate is the high-altitude LOX and LH_2 clustered-engine case. Considerable ground testing[5, 52-60] and flight testing have been performed for the Saturn S-IV and S-II vehicles. Figure 15 presents a crude summary of both flight and ground test data for S-IV and S-II. The agreement among all of the data is startling, considering the differences in configuration between the S-IV and the S-II, and the fact that the various data were measured at various locations on the base. Some length dependence would be expected, and it does exist; i. e., the heating at the base heat shield edges of the S-IV is generally in the lower portions of the scatter band. It would appear, however, to the first order, that the predominant dependence is upon base pressure. By closer examination of the measurement locations, the length dependence can be isolated as has been done previously by Sargeant.[5] The solid line is predicted by the present inner-jet program, using the above experimental conditions. The agreement seems quite good.

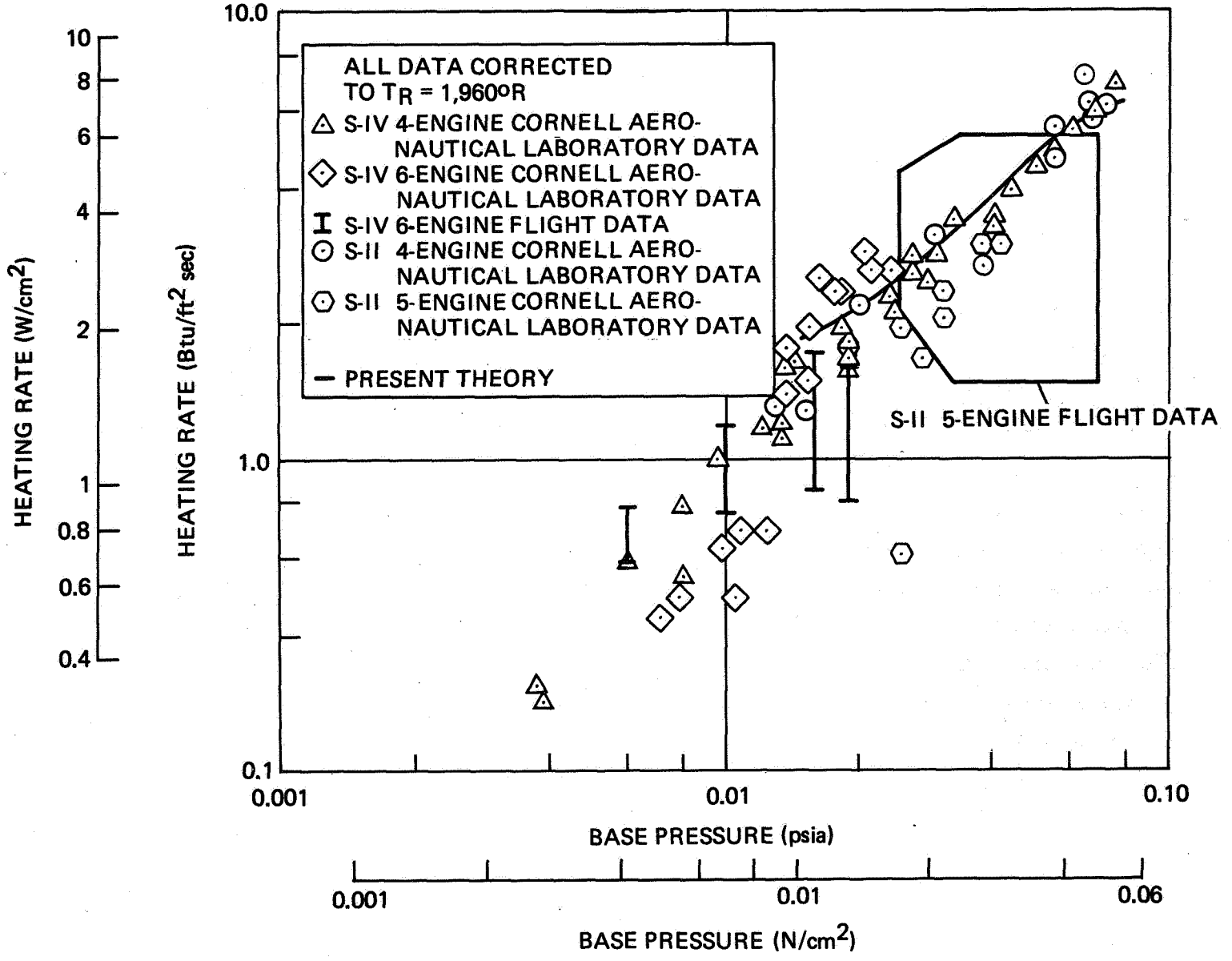

Figure 15. Base Heating Comparison for LOX/LH_2 Clustered Engines and Choked Flow

RECENT SHUTTLE BOOSTER MODEL TESTS

A series of 62 short-duration combustion technique test runs were made on a four-engine 5-11 model, and the test results are presented in Reference 61. The distance between the centerline of the engines was 1.5 times the diameter of the rocket nozzle at the exit plane (d_e). The heat-shield locations were 1.35 and 1.73 times d_e. The model was equipped to make heat-transfer and static-pressure measurements on the heat shield. The model was modified so dams could be placed in the four vent areas. The nozzle area ratio A_e/A^* was 27, which generates a Mach 3.468 flow with a specific heat ratio of 1.24 for a chamber temperature of 6200° R, a chamber pressure of 600 psia, and an oxidizer-to-fuel ratio of 6.

The results of these tests with no dams are cross-plotted and presented in Figure 16. The multi-engine base-flow computer program was used to generate the theory that is shown with the data. The theory predicts somewhat lower heating rates than the data show, but it agrees quite well with the general trend indicated by the data.

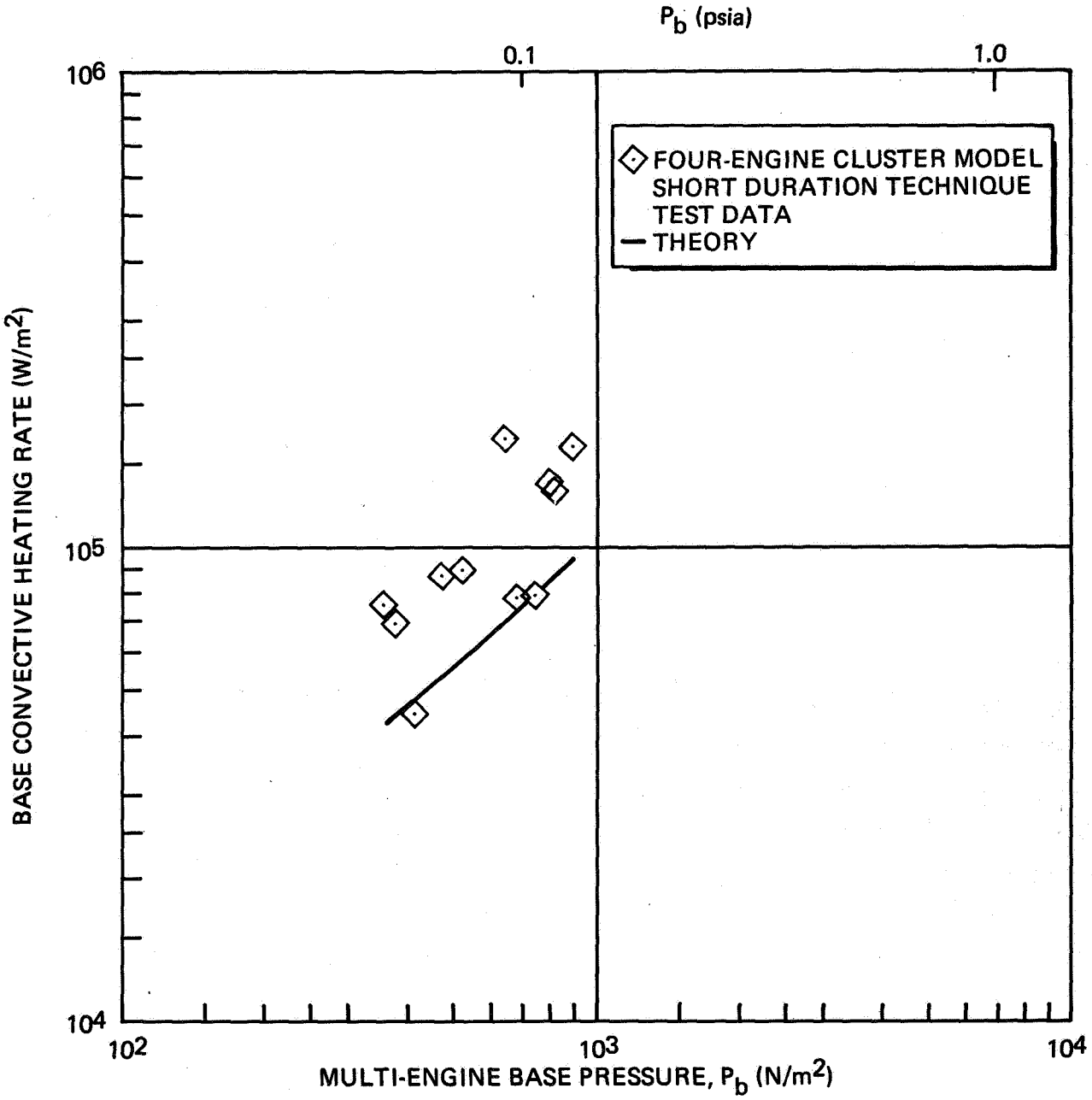

Figure 16. Base-Heating Comparison for Recent Shuttle Booster Tests

TWELVE-ENGINE SHUTTLE BOOSTER PREDICTIONS

Finally, the present method is used to predict, preliminarily, the convective base heating for a Phase B shuttle booster configuration. The particular space shuttle booster configuration considered uses twelve engines arranged in a rectangular pattern with 1.33 nozzle-diameters between the nozzle axes. Chamber conditions for the individual engines are given by a chamber pressure of 3000 psia and a chamber temperature of 6509°R. The engines operate on a liquid-oxygen and liquid-hydrogen mixture ratio of 6 and a nozzle-expansion ratio of 35. Results of the theoretical predictions are given in Figure 17, and they show a trend similar to that indicated in Figures 15 and 16.

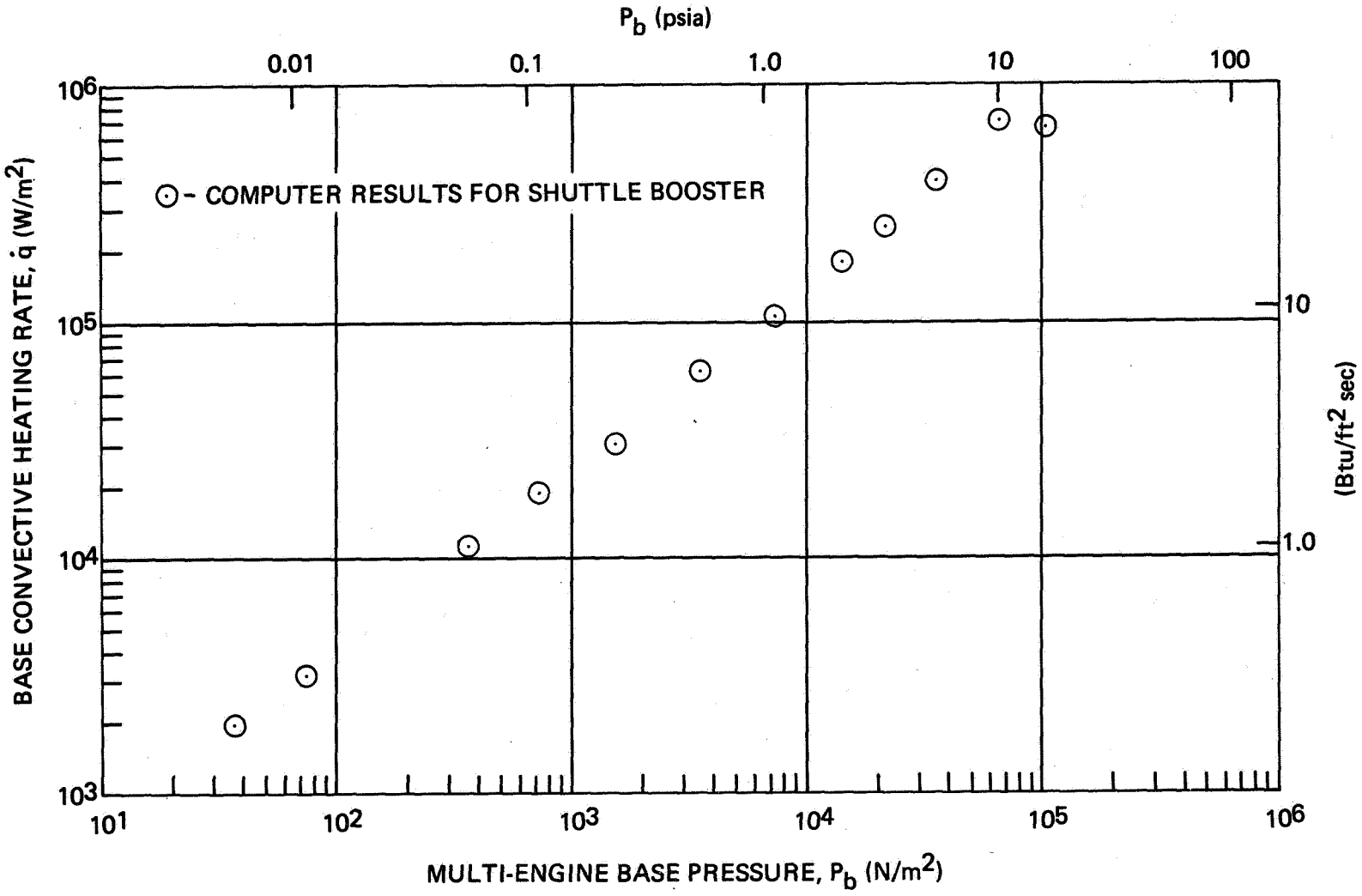

Figure 17. Preliminary Predictions for Twelve-Engine Shuttle Booster

Appendix
NOMENCLATURE

A	area
a	speed of sound
C_e	Crocco number
C_p	specific heat at constant pressure
h	enthalpy
G	base-bleed rate into the outer jet
I_1, I_2, I_3	integrals defined in Equations 28, 29, and 51, respectively
M	Mach number
$\mathcal{M}$	molecular weight
$\dot{m}$	mass flow rate
L	Length or distance from cut-off station to the reattachment point.
L_t	total distance from virtual origin to the reattachment point
p	pressure
P_r	Prandtl number
q	heat transfer rate
R or r	radius
Re	Reynolds number
r_o	axisymmetric radius for virtual origin of shear layer
r_r	axisymmetric radius of the recirculating flow at the cut-off station
$r_{\mathbb{Q}}/r_n$	rocket nozzle centerline spacing ratio

r_{br}/r_n	rocket base radius ratio
T	temperature
u, v	velocities in x, y directions, respectively
x, y	coordinate of the intrinsic system
X, Y	coordinate of the inviscid system
x_o	axial coordinate shift for virtual origin of shear layer
y_o	transverse coordinate shift for virtual origin of shear layer
x_r	virtual axial distance to the cut-off station
W	mixing layer width at the cut-off station
$\Lambda_b \equiv T_{ob}/T_{oex}$	recirculation stagnation temperature ratio
θ_e	turning angle of the inviscid flow measured from the rocket nozzle axis
θ_{ex}	flow direction outward from rocket axis at nozzle exit
θ_d	reattaching d-streamline angle measured from the rocket nozzle axis
ϵ_m	viscous-inviscid coordinate shift angle at cut-off station
ϵ_d	viscous angle associated with the d-streamline at cut-off station
γ	specific heat ratio
μ	kinematic viscosity
ϵ	eddy viscosity
ρ	density
η	similarity transformed variable
η_m	viscous-inviscid coordinate shift

Ω	energy transfer
δ	shear layer thickness
δ^*	displacement thickness
δ^{**}	momentum thickness
σ	jet spreading parameter
ϕ	dimensionless velocity
ψ	stream function

Subscripts

1, 2, 3, 4	various cross sections indicated in Figures 2 and 46
a, d, j	inviscid streamline adjacent to mixing layer
BL	boundary layer
b or B	base conditions
e	edge of shear layer
ex	nozzle exit conditions
mix	mixing layer
n	nozzle conditions
o	stagnation conditions or conditions indicated locally in the text
R	rear stagnation point
r	cut-off station of the recompression region
vent	venting conditions
w	wall
∞	freestream
stag	stagnating

REFERENCES

1. M. A. Hetrick, Jr. Space Shuttle Base and Engine Compartment Environment. Paper presented at Space Technology and Heat Transfer Conference, Los Angeles, California, 21-24 June 1970.

2. B. H. Goethert. Base Flow Characteristics of Missiles with Cluster-Rocket Exhausts. Journal of Aerospace Engineering, March 1961, p. 28.

3. R. H. Page and R. J. Dixon. Base Heating on Multiple Propulsion Nozzle Missile. AIAA Preprint 63-179, June 1963.

4. G. A. Etemad and K. D. Korkan. Base Flow Characteristics and Thermal Environment of Launch Vehicles with Strap-On Solid Rocket Motors. Journal of the Astronautical Sciences, Vol. XV, No. 1, 1968.

5. R. J. Sergeant. Base Heating Scaling Criteria for a Four-Engine Rocket Cluster Operating at High Altitudes. AIAA paper 65-826, AIAA Aerothermochemistry of Turbulent Flows Conference, San Diego, California, 13-15 December 1965.

6. H. P. Liepman. Survey of Base Flow Recirculation and Base Heating Problems. Symposium Proceedings, 1-2 December 1959, Simulated Altitude Testing of Rockets and Missile Components, AEDC-TR-60-6, March 1960, pp. 3-1-1 to 3-1-17.

7. J. E. Hubbart. Analysis of Saturn II Base Heat Model. Informal Report, Georgia Institute of Technology, 1965.

8. R. C. Farmer, R. J. Prozan, L. R. McGimsey, and A. W. Ratliff. Verification of a Mathematical Model Which Represents Large, Liquid Rocket-Engine Exhaust Plumes. AIAA Paper No. 66-650, presented at AIAA Second Propulsion Joint Specialist Conference, 13-17 June 1966.

9. C. W. Chu, A. F. Niemann, Jr., and S. A. Powers. Calculation of Multiple Rocket Engine Exhaust Plumes by the Method of Characteristics, Part I. AIAA Paper No. 66-651, 1966.

10. R. M. Huffaker and D. J. Carlson. Radiation from Rocket Exhaust Plumes, AIAA Paper No. 66-652, presented at AIAA Second Propulsion Joint Specialist Conference, Colorado Springs, Colorado, 13-17 June 1966.

11. P. W. Carpenter and W. Tabakoff. Survey and Evaluation of Supersonic Base Flow Theories. The Institute of Space Sciences, University of Cincinnati, NASA N 68-36011 (CR-97129), 1968.

12. Y. S. Hong. Base Flow Analysis of an Axisymmetric Body with a Central Jet. Air Force Report No. SAMSO-TR-70-415, 20 November 1968.

13. D. R. Chapman. Analysis of Base Pressure at Supersonic Velocities and Comparison with Experiment. NACA TN-2137, 1950.

14. H. H. Korst. A Theory for Base Pressure in Transonic and Supersonic Flow. Journal of Applied Mechanics, Vol. 23, 1956, p. 593.

15. H. H. Tang, C. P. Gardiner, and J. W. Barnes. Jet Mixing Theory Extensions and Applications in Separated Flow Problems. Douglas Aircraft Company, DAC-59181, February 1967.

16. W. G. Hill, Jr., and R. H. Page. Initial Development of Turbulent, Compressible Free Shear Layers. Journal of Basic Engineering, March 1969, pp. 67-73.

17. A. F. Charwat and J. K. Yakura. An Investigation of Two-Dimensional Supersonic Base Pressure. Journal of the Aeronautical Sciences, Vol. 25, No. 2, February 1958.

18. P. Carriere. Recherches Recentes Effectuees a l'ONERA Sur les Problemes de Recollement. Paper presented at 7th Symposium of Mechanics of Fluids, Jurata, Poland, September 1965 (ONERA Technical Paper No. 275, 1968).

19. J. F. Nash. An Analysis of Two-Dimensional Turbulent Base Flow, Including the Effect of the Approaching Boundary Layer. ARC-RM-3344, July 1962.

20. H. MacDonald. The Turbulent Shear Layer Reattachment with Special Emphasis on the Base Pressure Problem, The Aeronautical Quarterly, Vol. 15, August 1964.

21. J. B. Roberts. On the Prediction of Base Pressure in Two-Dimensional Supersonic Turbulent Flow. A.R.C., R and M, 3434, 1966.

22. G. W. Zumwalt. Analytical and Experimental Study of the Axially Symmetric Supersonic Base Pressure Problems. Ph. D. Dissertation, Department of Mechanical Engineering, University of Illinois, 1959.

23. G. W. Zumwalt and H. H. Tang. Transient Base Pressure Study of an Axisymmetric Supersonic Missile Flying Head-On Through a Blast Wave. SC-TM-65-218, Sandia Corporation, May 1965.

24. H. H. Korst and W. L. Chow. Nonisoenergetic Turbulent (Pr = 1) Jet Mixing Between Two Compressible Streams at Constant Pressure. NASA CR-149, April 1966.

25. H. G. Timmer, C. L. Arne, T. R. Stokes, and H. H. Tang. Ablation Aerodynamics for Slender Reentry Bodies. AFFDL-TR-70-27, March 1970.

26. R. J. Dixon, J. M. Richardson, and R. H. Page. Turbulent Base Flow on an Axisymmetric Body with A Single Exhaust Jet. AIAA Paper No. 69-650, June 1969.

27. A. L. Addy. Analysis of the Axisymmetric Base-Pressure and Base-Temperature Problem with Supersonic Interacting Freestream-Nozzle Flows Based on the Flow Model of Korst, et al., Report No. RD-TR-69-12, U. S. Army Command, Redstone Arsenal, Alabama, July 1969.

28. M. C. Fong, and C. F. Ehrlich, Jr. Propulsion Effects on Aerodynamic Characteristics of Lifting Reentry Vehicles. AFFDL-TR-70-12, March 1970.

29. J. P. Lamb, K. A. Abbud, and C. S. Lenzo. A Theory for Base Pressure on Multinozzle Rocket Configurations. Journal of Spacecraft and Rockets, April 1970, pp. 451-457.

30. E. D. Marion, D. J. Daniels, G. L. Herstine, and G. W. Burge. Exhaust Reversal From Cluster Nozzles—A New Flow Model. ARS Report No. 2706-62, November 1962.

31. H. McDonald. An Analysis of Turbulent Base Pressure Problem in Supersonic Axisymmetric Flow. The Aeronautical Quarterly, May 1965, pp. 97-121.

32. S. deSoto and H. Wolf. Application of the Mangler Transformation in Boundary Layer Flow. ARS Journal, April 1961, pp. 553-555.

33. L. Prandtl. Bemerkungen zur Theorie der Freien Turbulenz. Z.A.M.M., Vol. 22, 1942, pp. 241-243.

34. F. N. Kirk. An Approximate Theory of Base Pressure in Two-Dimensional Flow at Supersonic Speeds. Royal Aeronautical Establishment, TN-Aero-2377, 1959.

35. H. H. Tang and J. W. Barnes. A Combining Parameter for Base Pressure Evaluation. AIAA Journal, Vol. 5, No. 9, September 1967, pp. 1723-1724.

36. T. J. Mueller. Determination of the Turbulent Base Pressure in Supersonic Axisymmetric Flow. Journal of Spacecraft and Rockets, Vol. 5, No. 1, January 1968, pp. 101-107.

37. H. H. King. A Tabulation of Base Flow Properties for Cones and Wedges. RN-17, Electro-Optical Systems, Inc., Pasadena, California, January 1964.

38. J. L. Sims and T. F. Greenwood. Plume Flow Field Analysis for Liquid Propellant Rocket Engines. Research Achievements Review, Vol. III, Report 4, pp. 34-49; also TMX-53799, NASA, 1968.

39. T. F. Greenwood, D. Seymour, R. Prozan, and A. W. Ratliff. Analysis of Liquid Rocket Engine Exhaust Plumes. Journal of Spacecraft, February 1971, pp. 123-128.

40. T. F. Greenwood. Separated Base Flow Heat Transfer Analysis. Brown Engineering Company, Inc., Technical Note R-168, November 1965.

41. D. C. Reda and R. H. Page. Supersonic Turbulent Flow Reattachment Downstream of a Two-Dimensional Backstep. AIAA Paper No. 70-108, January 1970.

42. Ames Research Staff. Equations, Tables, and Charts for Compressible Flow. NACA Report 1135, 1953.

43. J. P. Lamb, T. F. Greenwood, and J. L. Gaddis. Improved Linearized Velocity Profiles for Turbulent Free Shear Layers. ASME Paper No. 69-WA/APM-28, November 1969.

44. T. J. Kessler. Two-Stream Mixing With Finite Initial Boundary Layers. AIAA Journal, February 1969, pp. 363-364.

45. R. J. Dixon and R. H. Page. Theoretical Analysis of Launch Vehicle Base Flow. AGARD Conference Proceedings No. 4 on Separated Flows. Belgium, May 1966.

46. M. A. Beheim and L. J. Obery. Wind Tunnel Studies of Booster Base Heating. IAS Paper 62-166, June 1962.

47. C. R. Mullen and R. L. Bender. Saturn V. S-IC Stage Model and Flight Test Base Thermal Environment. AIAA Paper 69-318, March 1969.

48. Saturn V Launch Vehicle Flight Evaluation Report AS-502, Apollo 6 Mission. Saturn V Flight Evaluation Working Group. NASA-MSFC Report MPR-SAT-68-1, 25 June 1968.

49. Saturn V Launch Vehicle Flight Evaluation Report—AS-503, Apollo 8 Mission. Saturn V Flight Evaluation Working Group. NASA-MSFC Report MPR-SAT-69-1, 1969.

50. Radiative and Structural Characteristics of Rocket Engine Exhaust Plumes. Rocketdyne Report R-6742, September 29, 1966.

51. W. C. Rochelle. Review of Thermal Radiation from Liquid and Solid Propellant Rocket Exhausts. NASA TMX-53579, February 1967.

52. W. D. Rickard. High-Altitude Investigations on the Saturn S-II Stage Using Short-Duration Techniques. Part I, Parametric Studies. Cornell Aeronautical Laboratory Report No. HM-1510-Y-17 (1), April 1965.

53. R. J. Sergeant. The Application of Short-Duration Techniques to the Experimental Study of Base Heating. Part II, A Study of Reynolds Number and Temperature Effects on Base Heating for a Four-Engine Hot Rocket Configuration Operating at High Altitude. Cornell Aeronautical Laboratory Report No. HM-1510-Y-1 (II), April 1965.

54. D. L. Dearing. The Saturn S-IV Stage Base Thermal Environment Flight and Scale Model Data Comparison. AIAA Paper 66-45, January 1966.

55. K. C. Hendershot. The Application of Short-Duration Techniques to the Experimental Study of Base Heating. Cornell Aeronautical Laboratory, Report No. HM-1510-Y-18, May 1965.

56. K. D. Bird, C. L. Matthis, and J. W. Reece. The Application of Short-Duration Techniques to the Experimental Study of Base Heating. Part 1, High-Altitude Testing Technique and Experimental Results for a Four-Engine Rocket Configuration. Cornell Aeronautical Laboratory, Report No. HM-1510-Y-1 (I), April 1962.

57. L. Bogdan and R. K. Muench. Density Measurements in the Reverse Flow Field of a Four-Engine Rocket Cluster Model Using an Electron Beam Technique. Cornell Aeronautical Laboratory, Report No. HM-2045-Y-1, October 1967.

58. J. Llinas and W. C. Rustay. Temperature and Density Measurements in the Base Region of a Clustered Rocket Model Using an Electron Beam Technique. Cornell Aeronautical Laboratory, Report No. HM-2107-Y-1, 1968.

59. J. Llinas. High-Altitude Base Region Thrust Investigations on a Saturn S-IV Six-Engine Stage Model Using Short-Duration Techniques. Cornell Aeronautical Laboratory, Report No. HM-2045-Y-3, September 1967.

60. W. D. Rickard. High-Altitude Investigations on the Saturn S-II Stage Using Short-Duration Techniques. Part 2, Prototype Base Environment. Cornell Aeronautical Laboratory, Report No. HM-1510-Y-17 (II), February 1966.

61. E. B. Brewer. Shuttle Booster Base Heating Test Results. NASA-MSFC Memo S&E-AERO-AT-71-11, 18 May 1971.

AN ANALYSIS OF THE BOOSTER PLUME IMPINGEMENT ENVIRONMENT DURING THE SPACE SHUTTLE NOMINAL STAGING MANEUVER

by

C. J. Wojciechowski
M. M. Penny
Lockheed Missiles & Space Company, Inc.
Huntsville, Alabama

T. F. Greenwood
NASA-Marshall Space Flight Center
Huntsville, Alabama

and

I. H. Fossler
NASA-Manned Spacecraft Center
Houston, Texas

INTRODUCTION

This paper presents preliminary results of two studies conducted to define the booster plume impingement environment during the Space Shuttle staging maneuver for the Phase B parallel-staged orbiter/booster configuration. These studies included experimental and analytical investigations. The experimental investigations were conducted in the Marshall Space Flight Center (MSFC) Impulse Base Flow Facility (IBFF) under the direction of personnel of the Aero-Astrodynamics Laboratory. Analytical pretest predictions and the post-test analysis were conducted by Lockheed-Huntsville personnel. A second experimental program was conducted by Grumman Aircraft Company (GAC) personnel in their Detonation Tube Plume Simulation Facility (ref. 1). Lockheed-Huntsville personnel, at the request of the Engineering Analysis Office of the Manned Spacecraft Center (MSC), conducted an analytical/experimental data comparison using available state-of-the-art analytical techniques (refs. 2, 3, 4, and 5).

The multiple-engine arrangement used for the orbiter main-stage propulsion presents a formidable task to model analytically. Several methods to simulate the plume shapes have been used in the past. For the Space Shuttle staging studies performed to date for MSC and MSFC, Lockheed-Huntsville used the equivalent engine concept (first used for Saturn exhaust plume studies) to simulate the multiple-engine exhaust plume. The equivalent engine (1) has the same mass flow as the multiple-engine arrangement; (2) has been shown to predict the overall

multiple-engine exhaust plume shape; and (3) predicts, except for localized plume intersection shock effects, the multiple engine plume trends. Therefore, the integrated plume impingement forces and moments obtained using the equivalent engine exhaust plume simulation should provide a reasonable approximation to those resulting from the multiple engine. Subsequent heating analysis should, in most cases, give a good indication of the heating rates resulting from the multiple-engine exhaust plume.

A combined analytical and experimental study to investigate the Space Shuttle nominal staging environment was begun in a cooperative effort by the MSC Engineering Analysis Office and the MSFC Aero-Astrodynamics Lab. The objectives shown were to (1) obtain plume impingement pressure and heating rate data for use in full-scale design studies; (2) determine the degree to which the equivalent engine exhaust plume will simulate the multiple engine exhaust plume; and (3) determine the applicability of the current analytical techniques to predict the staging plume impingement environment.

TEST MODELS USED IN THE GRUMMAN SPACE SHUTTLE ORBITER PLUME HEATING TESTS

(Figures 1 and 2)

An experimental study of the plume impingement heating on the space shuttle booster afterbody resulting from the space shuttle orbiter engine plumes was conducted in the Grumman Aircraft Company's (GAC) Detonation Tube Plume Simulator Facility (ref. 1). The 1/100-scale model tests consisted of one and two orbiter engine firings on a flat plate, a flat plate with a fin, and a cylinder model. The plume impingement heating rates on these surfaces were measured using thin-film heat-transfer gages.

The tests were conducted at a back pressure in the test chamber of $\approx 5 \times 10^{-5}$ mm Hg which corresponds to an altitude of 111,000 km. The engines were 1/100-scale model orbiter main-stage propulsion engines with the provision to run either engine alone or both together. The engine chamber pressure for the tests was 6.895×10^{6} N/m^2 (1000 psia) which together with the 1/100-scale of the models (figures 1 and 2) yields a model to full-scale Reynolds number ratio of 1/300. The steady state run time was approximately 3 msec. The engines were located three nozzle exit radii above the flat plate and cylinder models and the root chord of the vertical fin was located 9.21 exit radii downstream.

CYLINDER TEST MODEL USED IN THE GAC SPACE SHUTTLE ORBITER PLUME HEATING TESTS

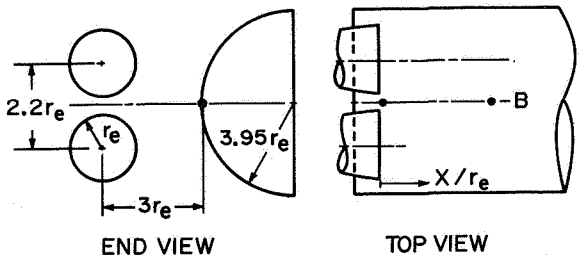

- DENOTES TYPICAL LOCATION OF HEAT TRANSFER GAGES; GAGES ARE LOCATED 3r_e APART

Figure 1

FLAT PLATE TEST MODEL USED IN THE GAC SPACE SHUTTLE ORBITER PLUME HEATING TESTS

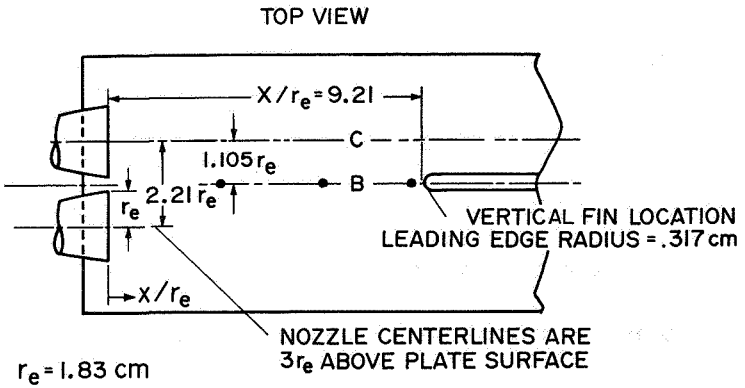

- DENOTES TYPICAL LOCATION OF HEAT TRANSFER GAGES; GAGES ARE LOCATED 3r_e APART

Figure 2

MODEL AND TEST CONDITIONS FOR THE SPACE SHUTTLE NOMINAL STAGING TESTS CONDUCTED IN THE MSFC IBFF TEST FACILITY

(Figure 3)

This test program was conducted in two phases: (1) exhaust plume surveys of the equivalent and multiple engine exhaust plumes; and (2) monitoring the impingement pressure and heating rates on the booster surfaces subjected to the orbiter exhaust plume impingement.

The test were to simulate staging at an altitude of 73,200 m (240,000 feet) with a vehicle Mach number of 11.65. Because the model engine chamber pressure was one-third of full-scale combustion pressure, studies were conducted to determine a plume back pressure which would closely simulate the plume shape at the desired staging conditions. The study results indicated that the test should be conducted at a pressure altitude of 79,300 m (260,000 feet).

The engines were 3% scaled models of the Aerojet orbiter mainstage engine. The booster model shown in figure 3 was a 3% scaled version of the proposed General Dynamics low-delta-wing configuration.

Plume surveys of the exhaust plume obtained radial distributions of the pitot total pressures and stagnation-point heating rates at several plume axial stations. The booster surface impingement data (pressure and heating rates) were obtained for a matrix of positions such that the booster impingement and heating rates were mapped over a region of interest for current staging trajectories.

TEST MODEL USED IN THE MSFC/IBFF SPACE SHUTTLE NOMINAL STAGING TESTS

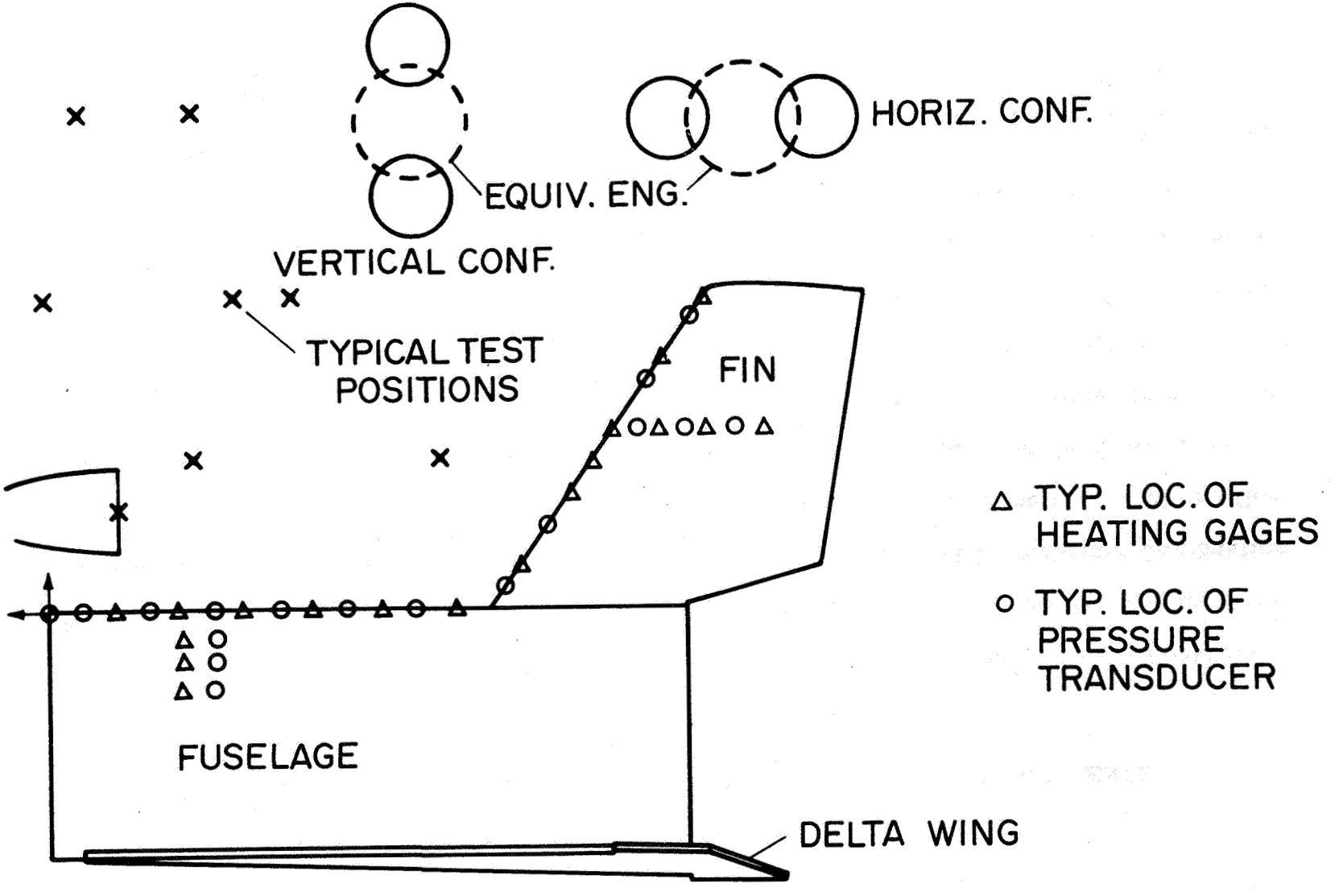

Figure 3

SUMMARY OF TEST CONDITIONS FOR THE MSFC IBFF AND GAC TESTS

(Figure 4)

The plume flowfield properties used in the analysis were computed using the Lockheed-Huntsville Method-of-Characteristics (MOC) Computer Program (refs. 2 and 3). The thermochemistry properties were computed using the NASA-Lewis Chemical Equilibrium Combustion (CEC) Computer Program (ref. 6). The thermochemistry properties of the nozzle-plume flow field were computed assuming the flow to be in chemical equilibrium. For the GAC plume analysis, the Chapman-Jouguet detonation option of the CEC program was utilized to obtain the initial chemical state conditions downstream of the detonation wave. The detonation tube plume simulation technique yields a plume total enthalpy which is approximately 20% higher than the full-scale engine. For the IBFF tests the initial conditions were computed by assuming gaseous propellants at 298^{o}K entered the combustion chamber. The oxidizer-to-fuel ratio for both test programs was 6.0. The nozzle internal shock waves which were present in both test programs were included in the analysis. A summary of the test conditions for the GAC and MSFC IBFF tests is presented in figure 4.

SUMMARY OF TEST CONDITIONS FOR THE GAC AND MSFC IBFF TESTS

GAC TESTS	MSFC IBFF TESTS
ENGINE DATA	**ENGINE DATA**
1/100 SCALE OF PROPOSED PHASE B SHUTTLE ENGINE	1/33.3 SCALE OF PROPOSED PHASE B SHUTTLE ENGINE
PROPELLANTS - O_2 (GAS), H_2 (GAS)	PROPELLANTS - O_2 (GAS), H_2 (GAS)
O/F = 6.0	O/F = 6.0
CHAM. PRESS. = 1/3 FULL SCALE	CHAM. PRESS. = 1/5 FULL SCALE
CHAM. ENTHALPY = 1.2 FULL SCALE	CHAM. ENTHALPY = FULL SCALE
$A/A^{\bullet}$ = 168	A/A* = 166
MODEL	**MODEL**
1/100 FULL SCALE	1/33.3 FULL SCALE
FLAT PLATE, CYLINDER, VERTICAL FIN	FUSELAGE AFT SECTION, VERTICAL FIN
Re = 1/300 FULL SCALE	Re = 1/167 FULL SCALE

Figure 4

ANALYTICAL/TEST DATA COMPARISONS FOR THE GAC CYLINDER TESTS

(Figure 5)

The analytical plume impingement heating rates were computed using the Lockheed-Huntsville Plume Impingement Computer Program (refs. 4 and 5). Shown on figure 5 are the experimental and analytical heating rate distributions on the GAC cylinder model along its centerline (Row B) for the single-engine and two-engine firings. The analytical results were calculated using yawed infinite cylinder theory (refs. 7 and 8) with the velocity gradient calculated from the pressure distributions in the crossflow direction (ref. 9). The analytical results for the two-engine firing were calculated using an equivalent engine plume in which the overall mass flow and exit momentum are preserved. In general, overall good agreement is indicated between the test data and the laminar yawed infinite cylinder theory. The rise in the analytical results at $x/r_e = 10$ is due to the nozzle internal shock wave impinging on the cylinder in this region.

ANALYTICAL/TEST HEATING RATE COMPARISONS FOR THE GAC CYLINDER TESTS

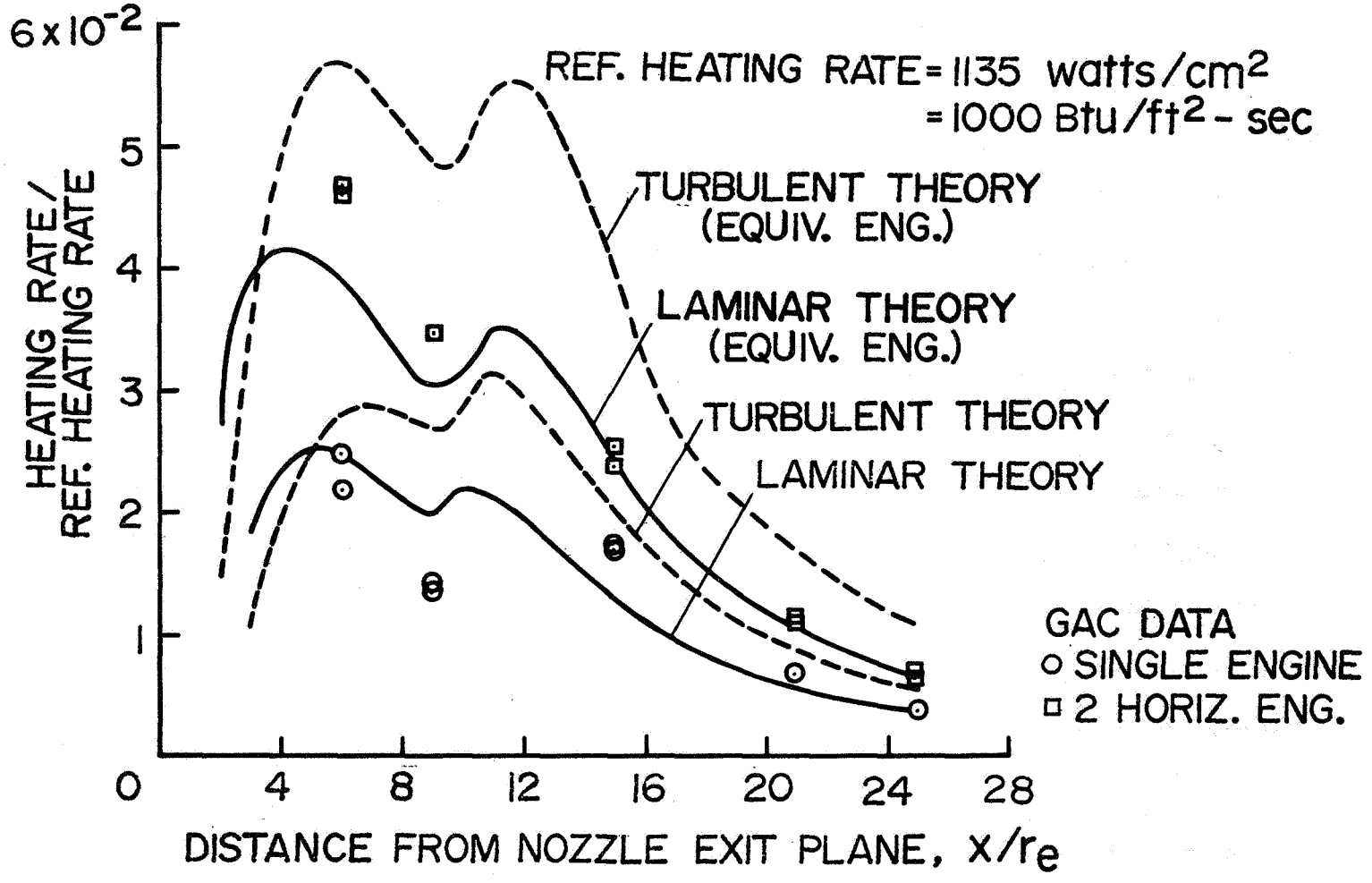

Figure 5

ANALYTICAL/TEST DATA COMPARISONS FOR THE GAC FLAT PLATE TESTS

(Figures 6 and 7)

Shown in figure 6 are the experimental and analytical heating rate distributions for the GAC flat plate test. The heating rate distributions are along the engine centerline (Row C) for the single engine firing. For analytical purposes, the boundary layer on the flat plate was idealized as being two dimensional. The analytical results were obtained using the Eckert Reference Enthalpy method (ref. 10) modified for pressure gradients in the streamline direction (refs. 11 and 12). The increase in heating shown in the analytical results at the x/r_e value of 10.5 is due to the nozzle internal shock impinging on the flat plate in this region. Since the theoretical convective heat-transfer rate is inversly proportional to the square root of the streamline distance, the flat-plate heat-transfer theory will overpredict the heating rates in the initial impingement region due to the small streamline distance. Therefore, in the initial impingement region, i.e., from x/r_e = 3 to 6, the laminar line was obtained using the laminar swept cylinder theory with the velocity gradients calculated from the pressure gradients in the crossflow direction.

ANALYTICAL/TEST HEATING RATE COMPARISONS FOR THE GAC FLAT PLATE TESTS

(SINGLE ENGINE FIRING)

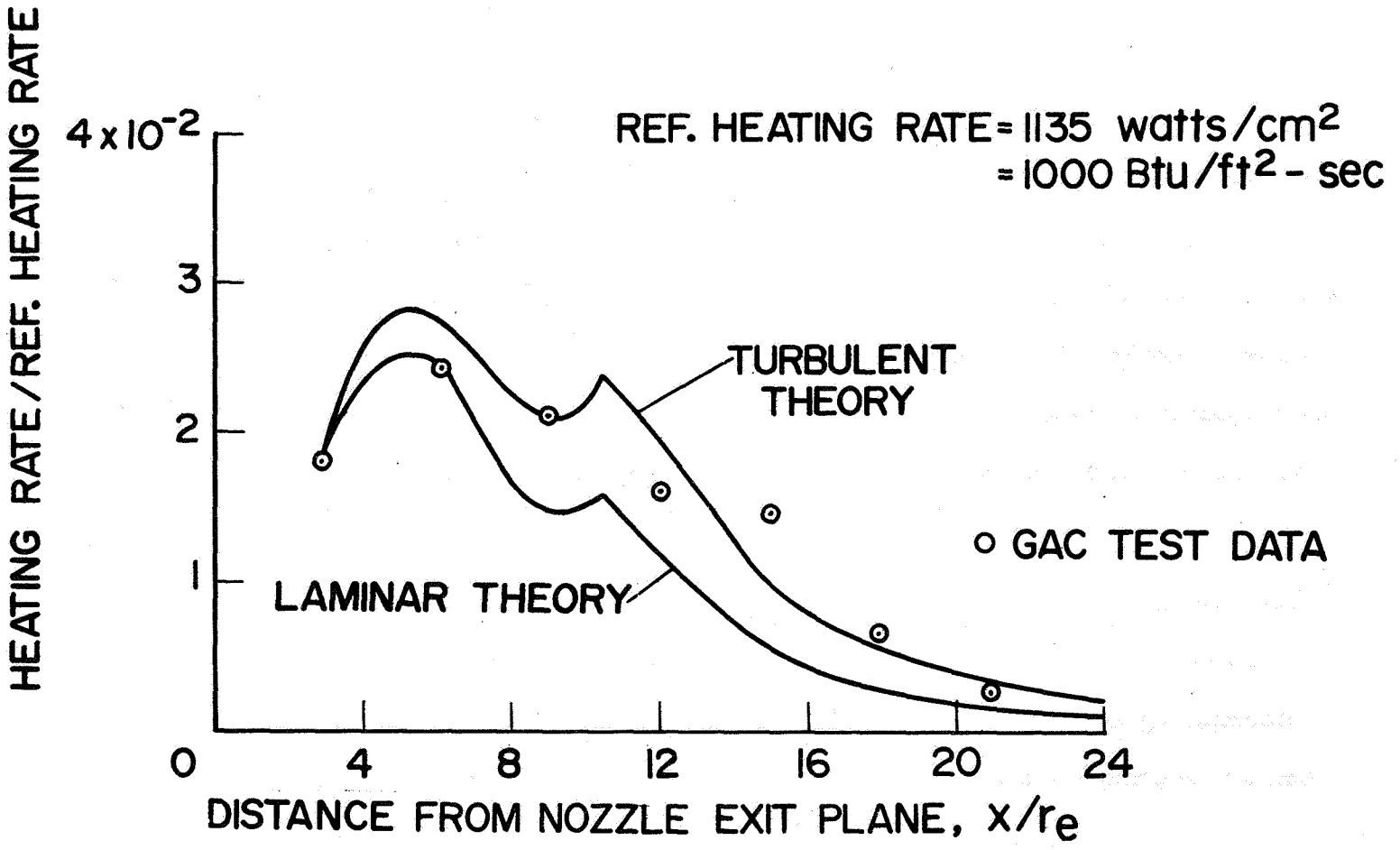

Figure 6

Shown in figure 7 are the experimental and analytical heating rate distributions for two engines firing. The heating rate distributions are along the centerline row (Row B) between the two engines. The analytical results presented were calculated using the equivalent engine plume to approximate the two-engine plume. The comparisons in this case are very similar to the single engine results.

Since the flat-plate theory used considered only streamwise pressure gradients and not crossflow pressure gradients, it is expected that the analytical results would underpredict the data in the region where large crossflow pressure gradients exist, i.e., in the region between $x/r_e = 6$ and $x/r_e = 16$. Therefore, since overall good agreement is indicated between the test data and the turbulent results, it should not be concluded that the boundary layer is turbulent. It is planned to add the capability to the plume impingement program to calculate the effects on convective heating of crossflow pressure gradients.

ANALYTICAL/TEST HEATING RATE COMPARISONS FOR THE GAC FLAT PLATE TESTS (TWO ENGINES FIRING)

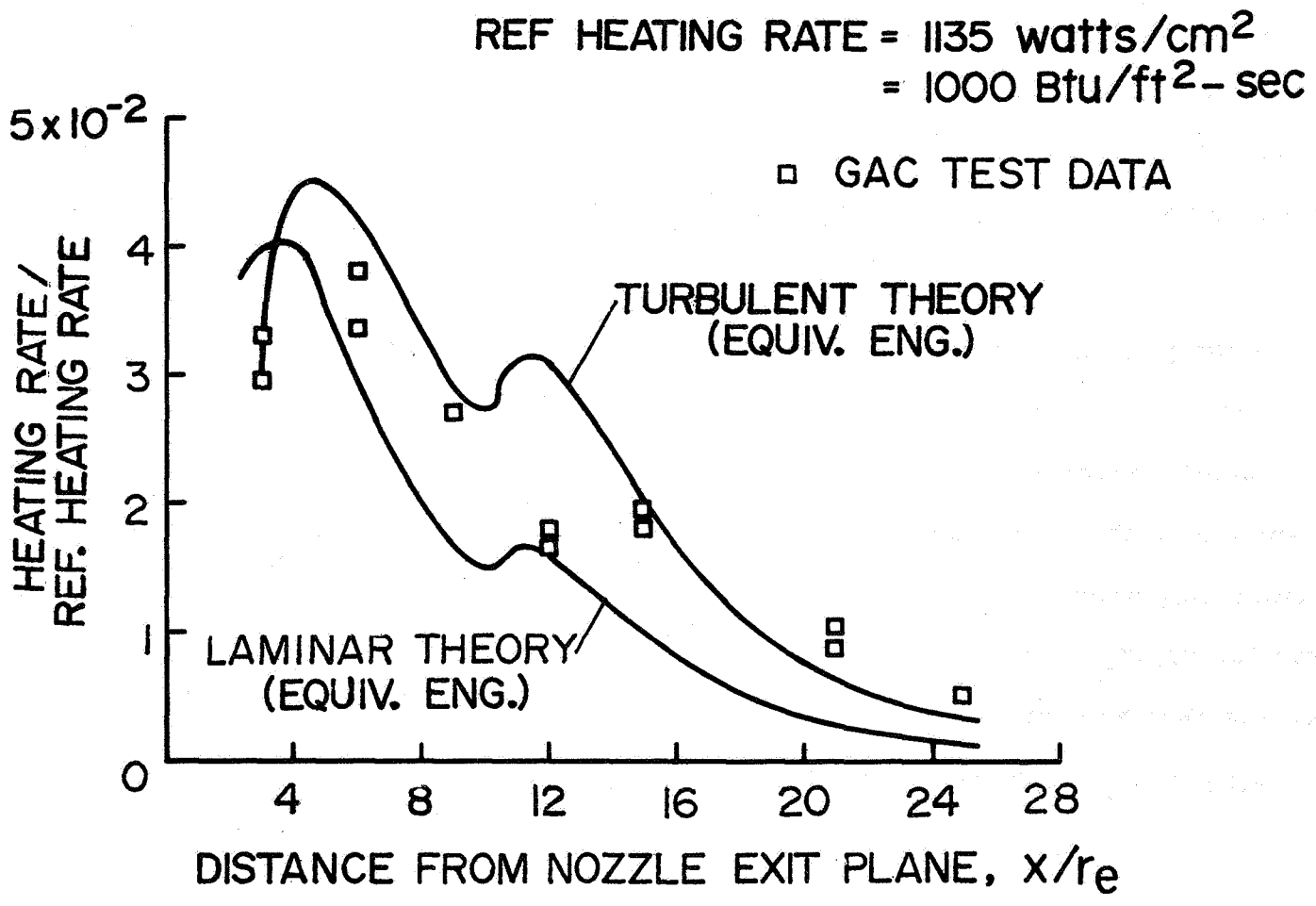

Figure 7

ANALYTICAL/TEST DATA COMPARISONS FOR THE GAC VERTICAL FIN TEST

(Figure 8)

The vertical fin was mounted on the flat plate test model. The base of the vertical fin was located at 9.21 nozzle exit radii downstream of the exit plane and had a leading-edge radius of 0.32 cm. The experimental and analytical heating rate distributions along the fin leading edge are shown in figure 8 for the two engines firing. The analytical results were calculated using laminar yawed infinite cylinder theory. The experimental heating rates in the region near the top of the fin agree with the theory. Following the technique of Bushnell (ref. 13), the interference heating on the vertical fin near the root was calculated. In this method (ref. 13), the inviscid flowfield properties on the flat plate ahead of the vertical fin are used in the laminar yawed infinite cylinder theory. The results are shown in figure 8.

The nozzle internal shocks intersect in the plume flowfield ahead of the vertical fin. This shock intersection region would intersect the vertical fin between y/r_e = 1 and 5. Higher plume static pressures will exist in this region of the flow field compared to the equivalent engine plume, (which was used in the calculations) and could account at least partially for the disagreement noted in this region. In addition, it is possible that this region could be a region of locally high turbulence which was generated by the shock intersection. If free-stream turbulence is present, then this effect alone could account for the disagreement noted (ref. 14).

ANALYTICAL / TEST HEATING RATE COMPARISONS FOR THE GAC VERTICAL FIN TEST (TWO ENGINES FIRING)

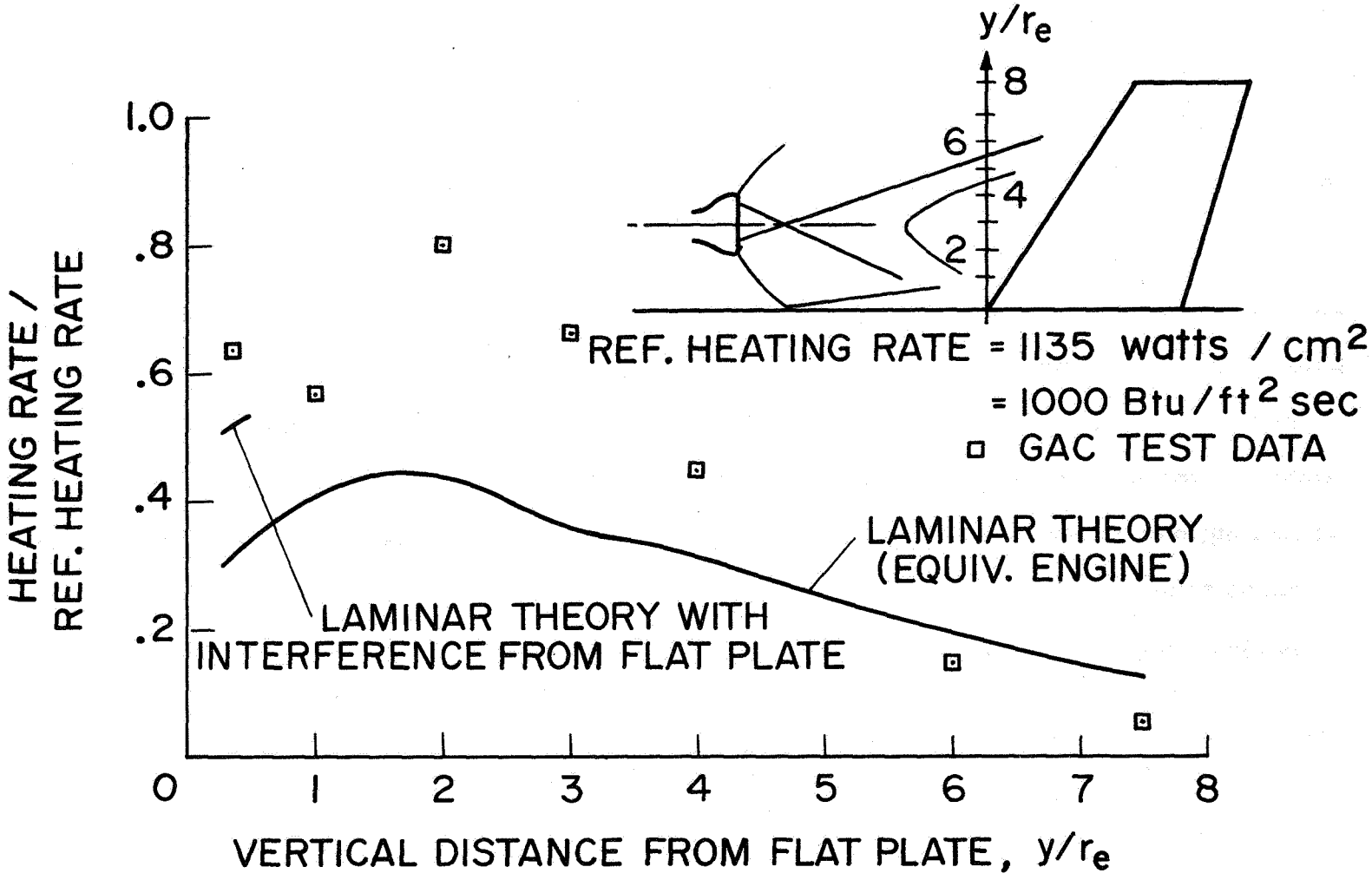

Figure 8

ORBITER ENGINE EXHAUST PLUME SURVEYS CONDUCTED IN THE MSFC IBFF TEST FACILITY

(Figures 9 and 10)

Radial plume surveys of the multiple and equivalent engine exhaust plumes were made at several plume axial stations. Presented in figure 9 are the pitot total-pressure radial surveys at a plume axial station of $X/D_e = 15$ and include data for both the equivalent engine and the multiple engines in the horizontal and vertical arrangements. The analytical results are for the equivalent engine exhaust plume. Overall good agreement was obtained between the theoretical and experimental horizontal and equivalent engine exhaust plume data. Very good agreement is noted for plume diameters less than 4.0. At plume diameters greater than 3, the experimental data for the vertical engines are lower than the horizontal engines and the analytical results.

Comparison of the equivalent and multiple engine exhaust plume experimental data indicates that over the regions surveyed, the equivalent engine exhaust plume can be used to simulate the horizontal multiple engine exhaust plume. Some localized effects due to the multiple engine exhaust plume shock wave structure exist near the equivalent engine plume axis (geometric center of the multiple engine arrangement). However, these effects rapidly disappear with increasing plume radius.

ORBITER ENGINE EXHAUST PLUME SURVEYS CONDUCTED IN THE MSFC / IBFF TEST FACILITY (PITOT PRESSURES AT $X/D_e = 15$)

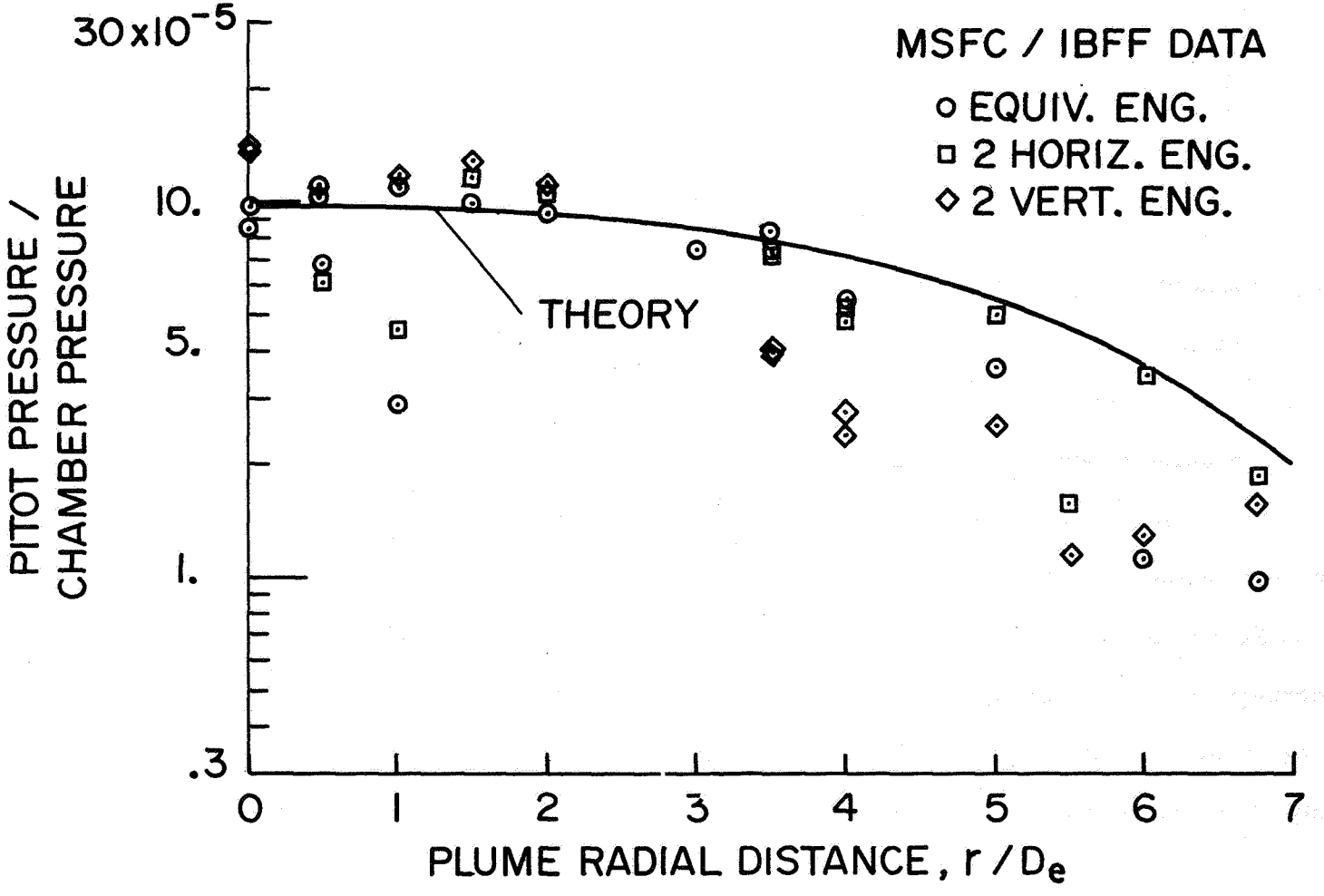

Figure 9

Presented in figure 10 are the stagnation point heating rate radial surveys at a plume axial station of $X/D_e = 15$ and include data for both the equivalent engine and the multiple engines in the horizontal and vertical arrangements. The analytical results are for the equivalent engine exhaust plume. The analytical results were calculated using the Fay and Riddell stagnation point heating theory (ref. 15). Overall good agreement was obtained between the theoretical results assuming a chemically frozen boundary layer on the probes and the experimental data for the equivalent engine. At this axial station, very good agreement between the "equivalent" engine and the two-horizontal engine data is shown indicating that the equivalent engine appears to be a good approximation of the two-horizontal engine configuration. The data point shown for the two vertical engine arrangement at an $r/D_e = 4.5$ is below the equivalent and two-horizontal engine data which is consistent with the pitot pressure data.

ORBITER ENGINE EXHAUST PLUME SURVEY CONDUCTED IN THE MSFC/IBFF TEST FACILITY (STAGNATION HEATING RATES AT $X/D_e = 15$)

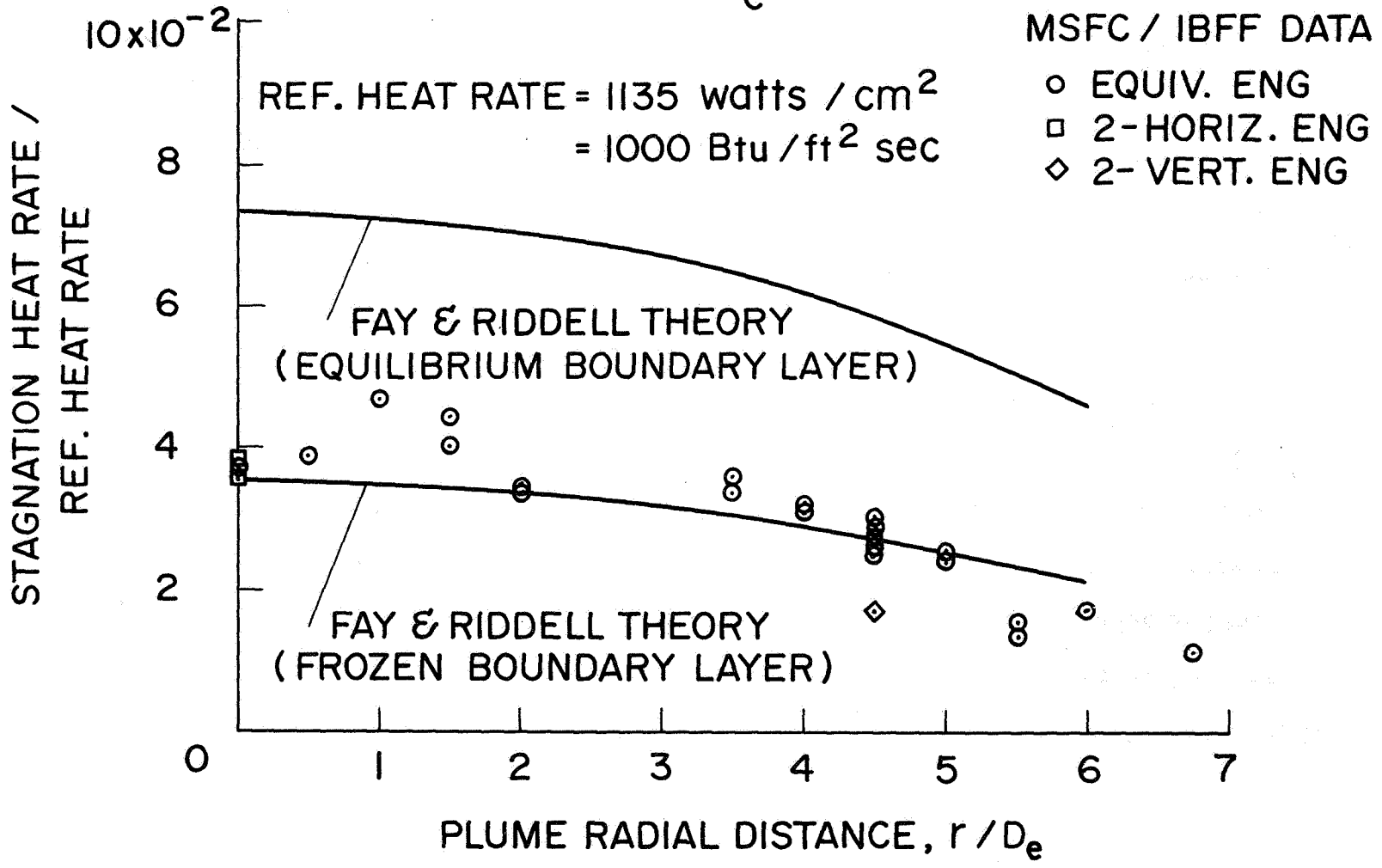

Figure 10

PLUME IMPINGEMENT PRESSURE DISTRIBUTIONS ON THE BOOSTER FIN LEADING EDGE FOR THE MSFC IBFF TESTS

(Figure 11)

The plume impingement pressures on the booster fin leading edge resulting from the equivalent and multiple engine exhaust plume are presented in figure 11 for one test position. For the test position selected the engines were mounted 2.5 exit radii above the fuselage and the vertical fin was located 9.4 exit radii downstream. The analytical impingement pressures are for the "equivalent" engine exhaust plume and were calculated using modified Newtonian impact theory. The multiple engine data are for the horizontal arrangement of the engines only. Impingement pressure tests with the vertical arrangement of the multiple engine configuration are currently being conducted.

The equivalent engine plume centerline (also the multiple engine geometric centerline) intersects the fin centerline approximately 7.6 cm above the fin root chord. This is the region in which the most favorable comparisons between the equivalent and multiple engine plume data occur. Fair agreement between the experimental data and the theory is noted in the outer regions of the plume which occurs near the fin tip chord. There appears to be some fin-booster fuselage interference effects near the fin root chord which is noted by the higher pressures obtained experimentally than those analytically obtained. However, this was not noted on most other test positions.

PLUME IMPINGEMENT PRESSURE DISTRIBUTION ON THE BOOSTER FIN LEADING EDGE FOR THE MSFC/IBFF TESTS

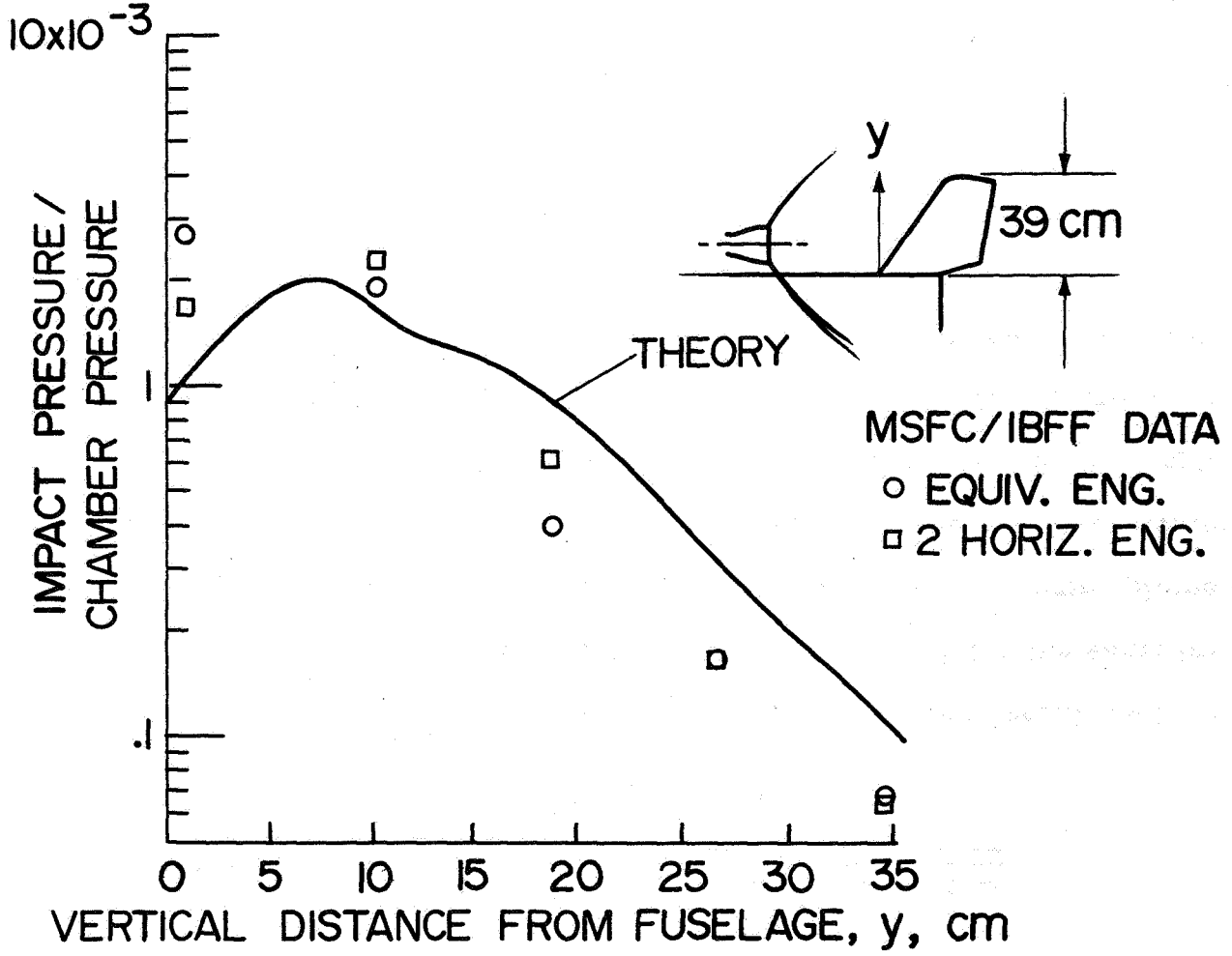

Figure 11

PLUME IMPINGEMENT HEATING RATE DISTRIBUTION ON THE BOOSTER FIN FOR THE MSFC IBFF TESTS

(Figures 12 and 13)

The plume impingement heating rates on the booster fin leading edge resulting from the equivalent and multiple engine exhaust plume are presented in figure 12 for the same test position. The analytical results presented were calculated using the equivalent engine plume and laminar yawed infinite cylinder theory. The experimental heating rates for the equivalent engine agree favorably with the theory. The experimental heating rates for the two engines in the horizontal arrangement tend to be lower than the theory which is consistent with the pressure distribution presented in figure 11. It is planned to repeat this test position in the second phase of the MSFC IBFF tests.

PLUME IMPINGEMENT HEATING RATE DISTRIBUTION ON THE BOOSTER FIN LEADING EDGE FOR THE MSFC/IBFF TESTS

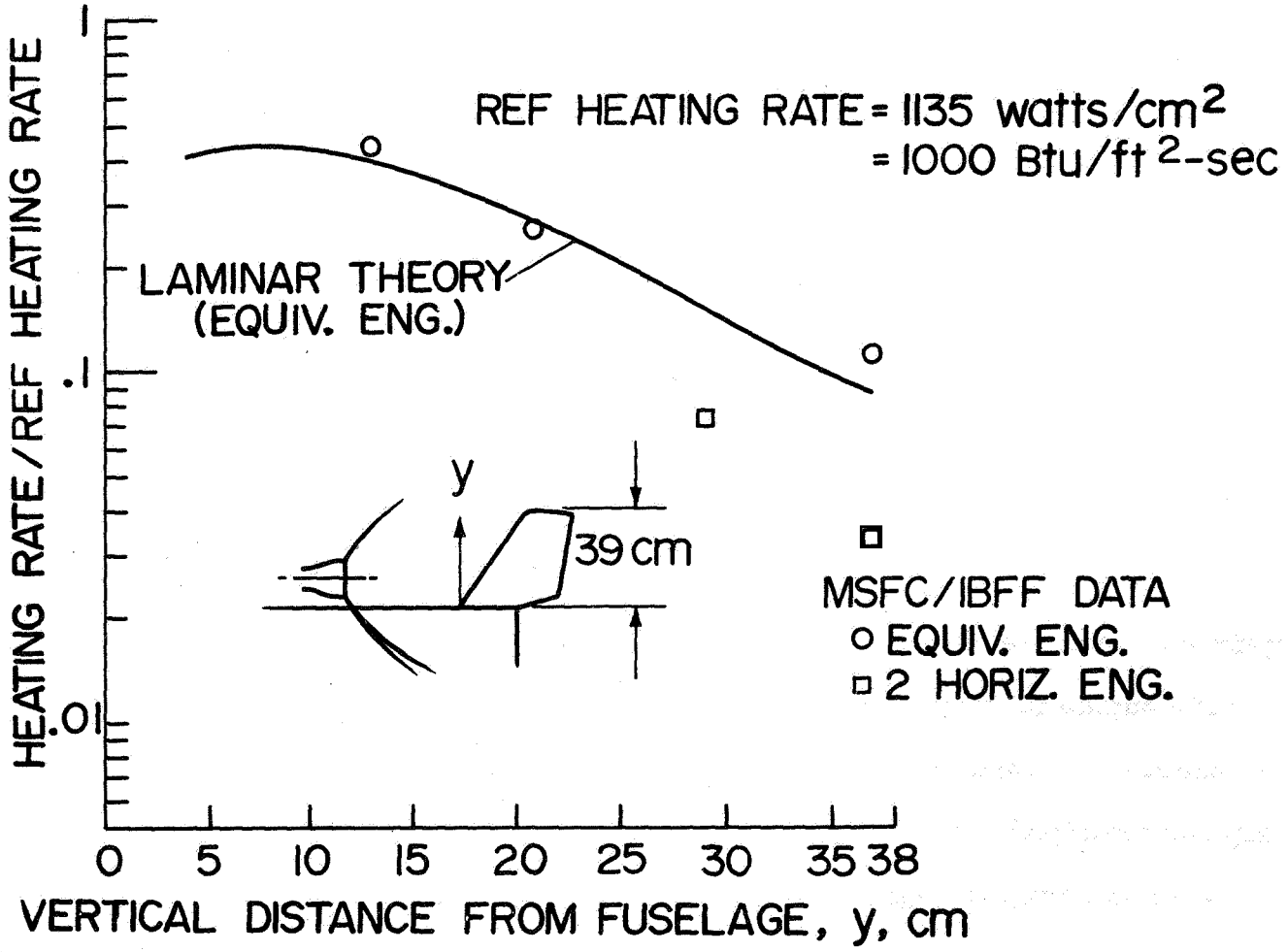

Figure 12

The heating rate distribution along a chord located 20.6 cm above the fuselage are presented in figure 13 for the equivalent and multiple engine arrangements. The analytical results were calculated using the equivalent engine plume and the laminar-yawed-cylinder circumferential-heating-rate-distribution theory (ref. 4). The experimental data for the equivalent engine agree favorably with the theory. The heating-rate data for the horizontal two-engine arrangement again tend to be lower than the equivalent engine data.

PLUME IMPINGEMENT CHORDWISE HEATING RATE DISTRIBUTIONS ON THE BOOSTER FIN FOR THE MSFC/IBFF TESTS

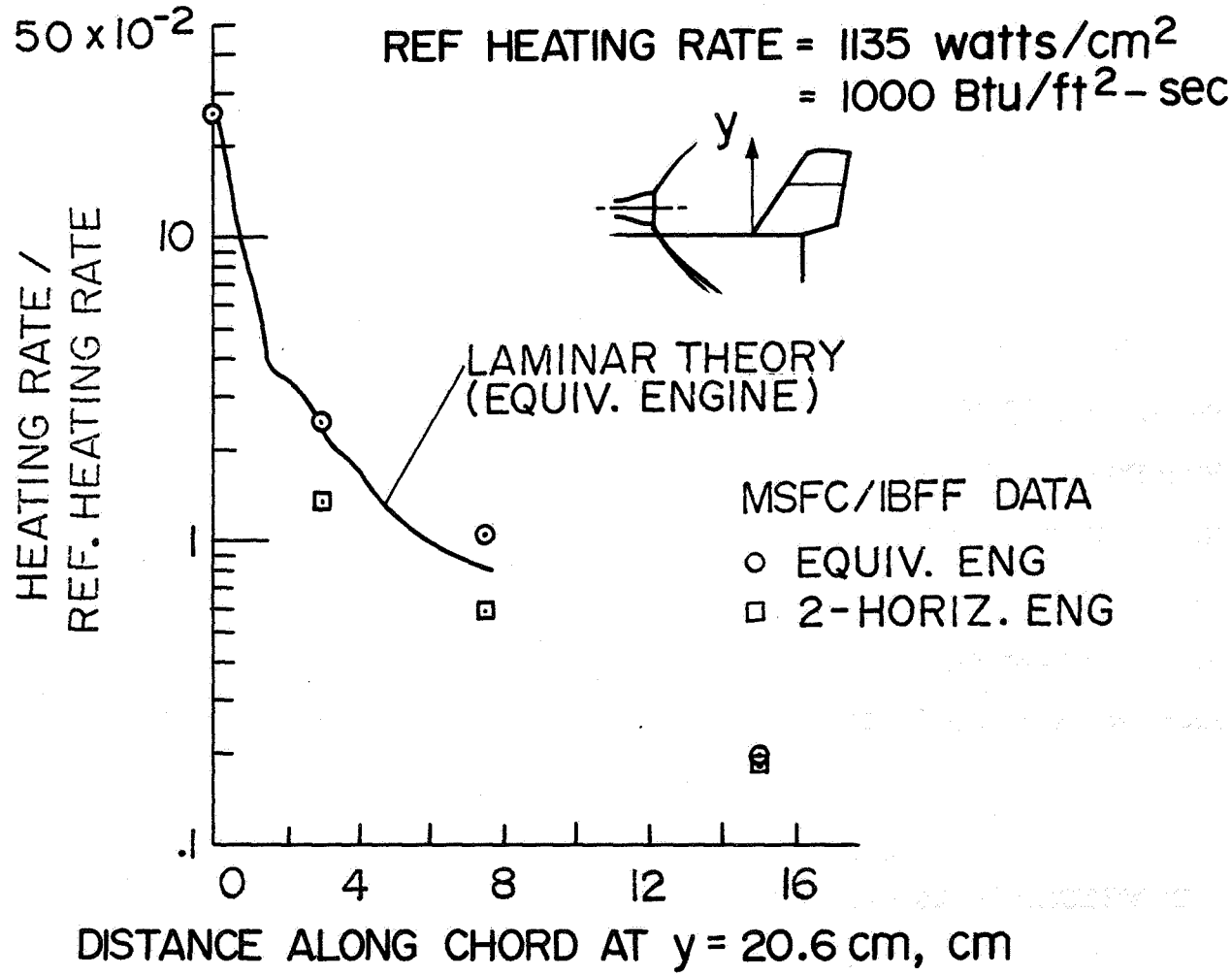

Figure 13

PLUME IMPINGEMENT PRESSURE DISTRIBUTION ALONG THE BOOSTER FUSELAGE STAGNATION LINE FOR THE MSFC IBFF TESTS

(Figure 14)

A comparison of the equivalent and multiple engine plume impingement pressures along the booster fuselage stagnation line is shown in figure 14. Analytical results were calculated using the equivalent engine plume and modified Newtonian impact theory (ref. 4). The analytical results, in general, predict the experimental trends and exhibit good agreement with the experimental data. However, near the fin-fuselage intersection region the experimental data for the horizontal two-engine configuration are higher than the equivalent engine data. In the initial impingement region, good agreement is evident between the analytical results and the experimental data for the horizontal two-engine configuration.

PLUME IMPINGEMENT PRESSURE DISTRIBUTION ALONG THE BOOSTER FUSELAGE STAGNATION LINE FOR THE MSFC/IBFF TEST

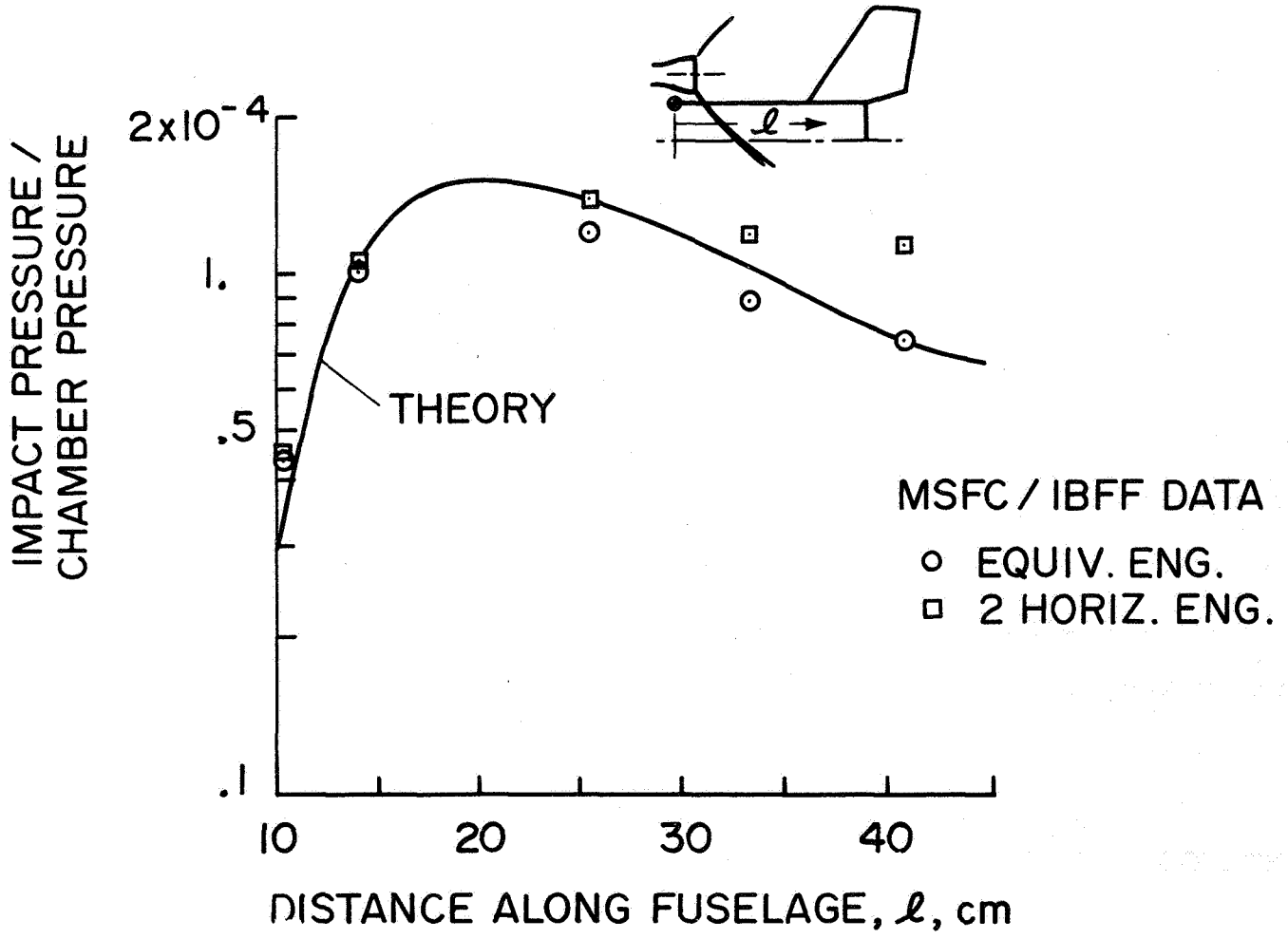

Figure 14

PLUME-IMPINGEMENT HEATING-RATE DISTRIBUTIONS ALONG THE BOOSTER FUSELAGE STAGNATION LINE FOR THE MSFC IBFF TESTS

(Figure 15)

A comparison of the equivalent and multiple engine plume-impingement heating rates along the booster fuselage stagnation line is presented in figure 15. The analytical results were calculated using the equivalent engine plume and laminar yawed infinite cylinder theory (ref. 7). The analytical results in general are in good agreement with the experimental results and are consistently above the experimental data. Good agreement is evident between the test data for the equivalent engine and the two-horizontal engine configuration.

PLUME IMPINGEMENT HEATING RATE DISTRIBUTION ON THE BOOSTER FUSELAGE STAGNATION LINE FOR THE MSFC/IBFF TEST

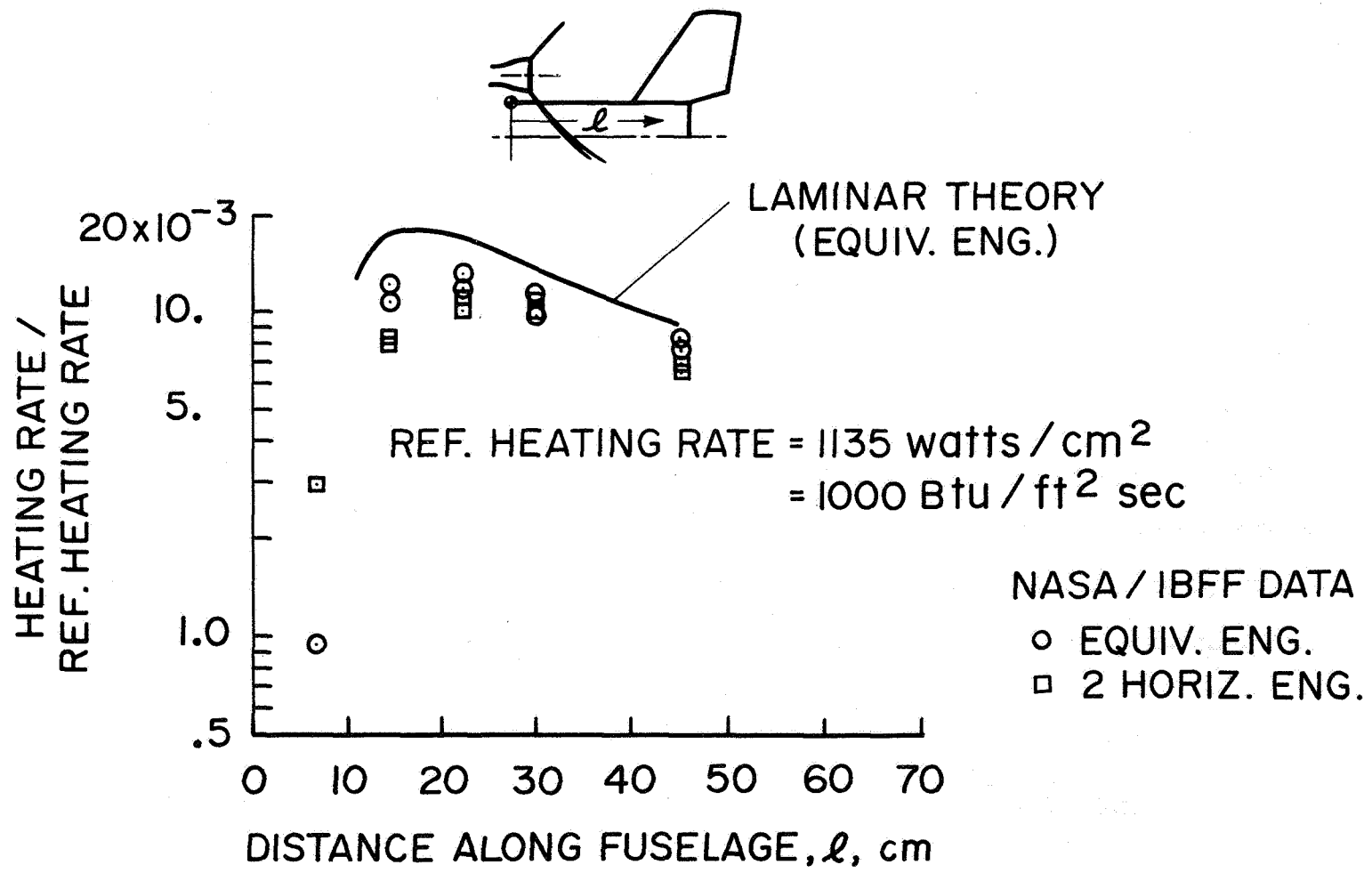

Figure 15

PLUME IMPINGEMENT CIRCUMFERENTIAL PRESSURE DISTRIBUTIONS ON THE BOOSTER FUSELAGE FOR THE MSFC IBFF TESTS

(Figure 16)

Circumferential distributions of the equivalent and multiple engine exhaust plume impingement pressures on the booster fuselage at ℓ = 41 cm are presented in figure 16. Good agreement is obtained between the equivalent engine analytical and experimental data. The equivalent engine data also compare favorably with the multiple engine impingement pressure data. For the test position shown, the plume stagnation line occurs on the booster fuselage upper surface at ϕ = 0 deg and is the location at which the most notable differences in the equivalent and multiple engine occur.

PLUME IMPINGEMENT CIRCUMFERENTIAL PRESSURE DISTRIBUTION ON THE BOOSTER FUSELAGE FOR THE MSFC / IBFF TEST

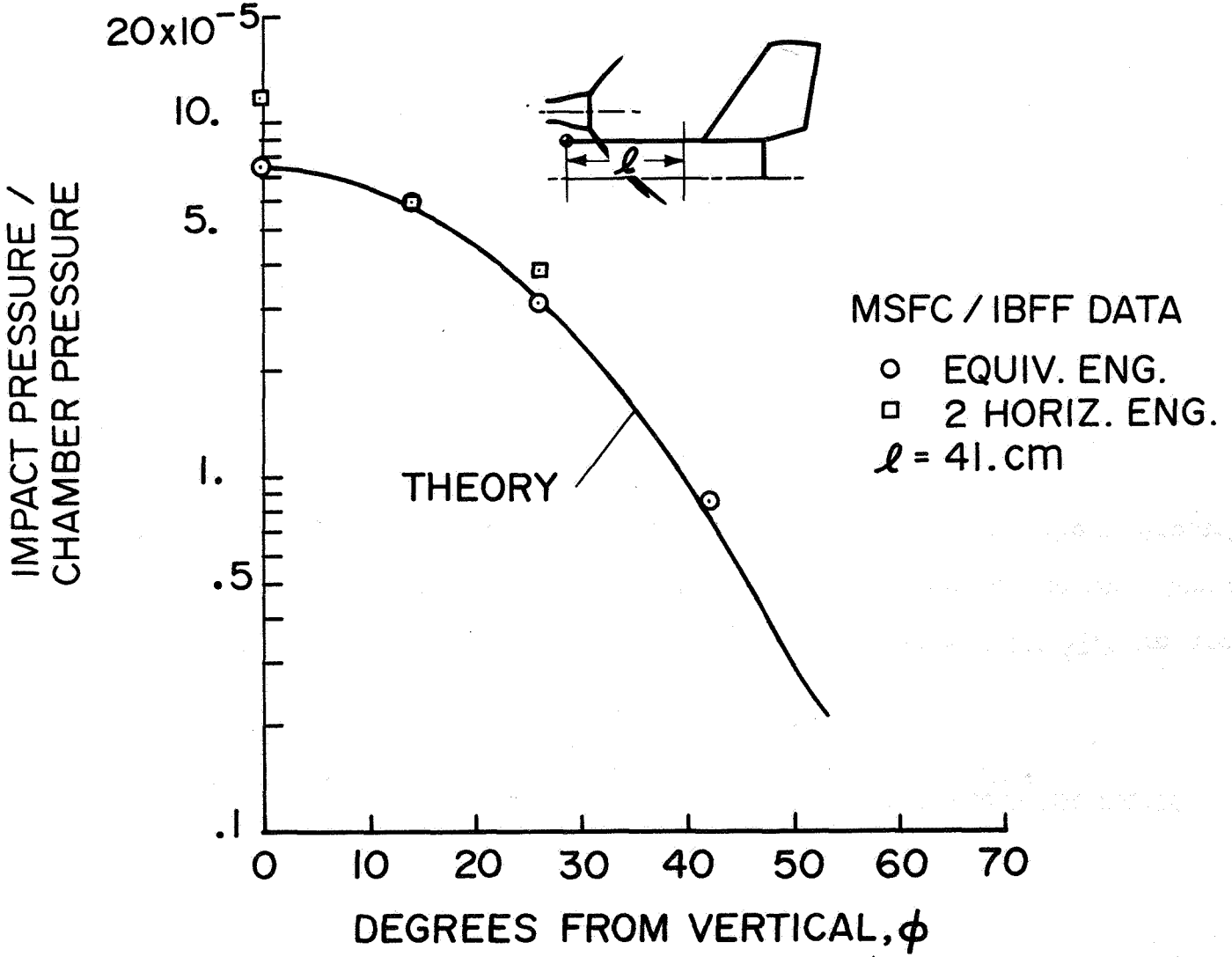

Figure 16

PLUME IMPINGEMENT CIRCUMFERENTIAL HEATING RATE DISTRIBUTIONS ON THE BOOSTER FUSELAGE FOR THE MSFC IBFF TESTS

(Figure 17)

Circumferential heating rate distributions on the booster fuselage at L = 37.2 cm are presented in figure 17. Good agreement is obtained between the equivalent engine analytical and experimental data. The equivalent engine data also compare favorably with the horizontal two-engine data.

PLUME IMPINGEMENT CIRCUMFERENTIAL HEATING RATE DISTRIBUTIONS ON THE BOOSTER FUSELAGE FOR THE MSFC/IBFF TEST

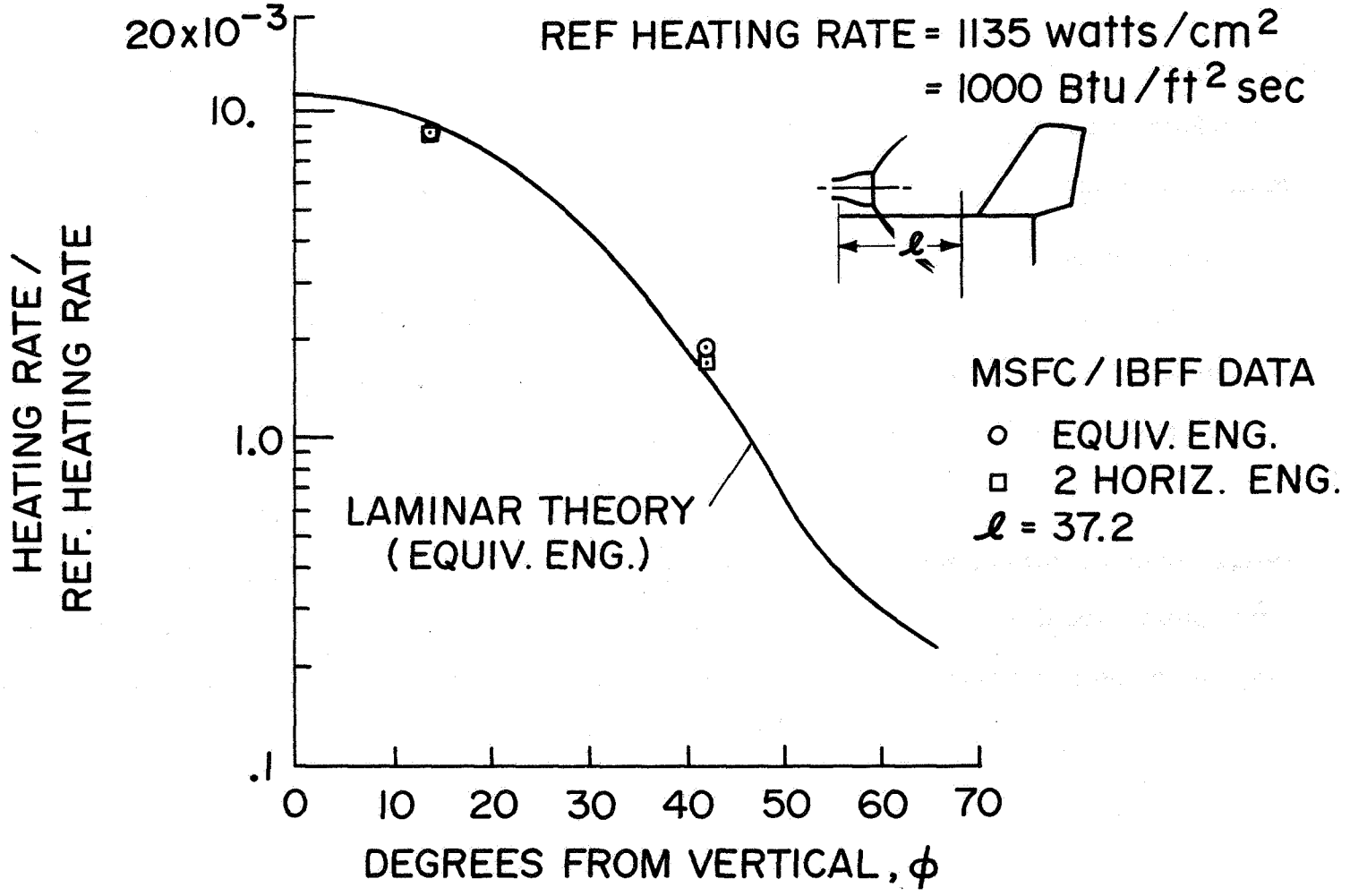

Figure 17

CONCLUSIONS

Preliminary results from the Space Shuttle nominal staging tests indicate that the equivalent engine simulation is a reasonable approximation to the two-engine configuration and can be used in preliminary studies. However, further tests should be conducted for current orbiter main stage engine configurations to verify the plume model.

The integrated plume impingement forces and moments obtained using the equivalent exhaust plume should give realistic estimates of the forces and moments resulting from the multiple engine exhaust plume. Where localized effects are important in predicting heating rates, the test results should be utilized to update the plume and plume impingement models.

Nominal staging test results so far have indicated the booster models experienced laminar-boundary-layer convective heating. However, full-scale surfaces subject to plume impingement are expected to experience turbulent boundary layer convective heating. Therefore, further tests at higher Reynolds numbers are needed to simulate full-scale vehicle plume impingement heating.

REFERENCES

1. Jarvis, Leng, C. W. Osonitsch and W. L. Konopka, "Experimental Study of Plume Impingement Heating from Orbiter Main Engines," GAC 552-1200RD-31, Grumman Aircraft Company, Bethpage, N. Y., May 1971.

2. Prozan, R. J., "Solution of Non-Isoenergetic Supersonic Flow by Method-of-Characteristics, Vol. III, Final Report," LMSC-HREC D162220-III, Lockheed Missiles & Space Company, Huntsville, Ala., July 1971.

3. Smith, S. D., and A. W. Ratliff, "Rocket Exhaust Plume Computer Program Improvement, Vol. I — Final Report," LMSC-HREC D162220-I, Lockheed Missiles & Space Company, Huntsville, Ala., June 1971.

4. Wojciechowski, C. J., and M. M. Penny, "Development of a High Altitude Plume Impingement Analysis for Calculating Heating Rates, Forces and Moments Acting on Bodies Immersed in Rocket Exhaust Plumes," LMSC-HREC D162867-I, Lockheed Missiles & Space Company, Huntsville, Ala., March 1971.

5. Penny, M. M., and C. J. Wojciechowski, "User's Manual and Description of a Computer Program for Calculating Heating Rates, Forces, and Moments Acting on Bodies Immersed in Rocket Exhaust Plumes," LMSC-HREC D162867-2, Lockheed Missiles & Space Company, Huntsville, Ala., March 1970.

6. McBride, Bonnie, and S. Gordon, "Preliminary Description of CEC, A Computer Program for Calculation of Chemical Equilibrium Compositions with Applications," NASA-Lewis Research Center, Cleveland, Ohio, May 1969.

7. Beckwith, I. E., "Similar Solutions for the Compressible Boundary Layer on a Yawed Cylinder with Transportation Cooling," NASA TR R-42, 1959.

8. Beckwith, I. E., and J. J. Gallagher, "Local Heat Transfer and Recovery Temperatures on a Yawed Cylinder at a Mach Number of 4.15 and High Reynolds Numbers," NASA TR R-104, 1961.

9. Wojciechowski, C. J., and R. J. Rader, "A Method for Calculating Stagnation Region Convective Heat Transfer to Arbitrary Surfaces Immersed in the Space Shuttle Attitude Control System Plumes," LMSC-HREC D162334, Lockheed Missiles & Space Company, Huntsville, Ala., May 1970.

10. Eckert, E. R. G., "Engineering Relations for Heat Transfer and Friction in High-Velocity Laminar and Turbulent Boundary-Layer Flow over Surfaces with Constant Pressure and Temperature," Trans. ASME, Vol. 78, No. 6, August 1956, pp. 1273-1283.

11. Vaglio-Laurin, R., "Laminar Heat Transfer on Blunt-Nosed Bodies in Three-Dimensional Hypersonic Flow," WADC TN 58-147, Wright-Patterson AFB, Ohio, May 1958.

12. Vaglio-Laurin, R., "Turbulent Heat Transfer on Blunt-Nosed Bodies in Two-Dimensional and General Three-Dimensional Hypersonic Flow," J. Aerospace Sci., January 1960.

13. Bushnell, Dennis M., "Interference Heating on a Swept Cylinder in Region of Intersection with a Wedge at Mach Number 8," NASA TN D-3094, 1965.

14. Weeks, Thomas M., "Influence of Freestream Turbulence on Hypersonic Stagnation Zone Heating," AFFDL-TR-67-195, Wright-Patterson AFB, Ohio, May 1968.

15. Fay, J. A., and R. R. Riddell, "Theory of Stagnation Point Heat Transfer in Dissociated Air," J. Aeron. Sci., Vol. 25, No. 2, February 1958.

CONVECTIVE HEATING MEASUREMENT BY MEANS OF AN INFRARED CAMERA

By Dale L. Compton
NASA Ames Research Center, Moffett Field, California

INTRODUCTION

As reentry configurations become more sophisticated, the convective heating patterns on these configurations tend to become both more complex and more sensitive to free-stream conditions. There is, therefore, a need to develop rapid and accurate wind tunnel techniques to measure convective heating distributions. One such technique is described in the present paper. Its essence is the measurement of infrared emission from the surface of a wind tunnel model as a function of time by means of an infrared-sensitive imaging camera. Prior calibration of the infrared camera relates the emission to the surface temperature of the model. The time history of the surface temperature can then be related to the heating rate by standard techniques. The output of the camera is an electrical signal that is tape-recorded in analog form, then digitized and processed by computer, so that automated and relatively rapid data reduction can be accomplished. In addition, the camera produces real-time visual displays of the infrared emission as pictures on an oscilloscope screen. These pictures give immediate indications of hot and cool spots on the model.

FIGURE 1

The infrared imaging camera is an AGA Corporation Thermovision, model 661. The infrared detector (indium antimonide, 2-5 micron spectral range) is focused on the field of view by means of a lens and two mirrors, as shown for a typical focal distance in Fig. 1. The image of the detector is swept through the field of view horizontally at a rate of about 1600 sweeps/second by means of a rotating prism, and vertically at a rate of about 16 sweeps/second by means of a tilting mirror. This produces 16 pictures/second with about 83 lines in each picture since 17 of the horizontal line sweeps occur while the mirror is returning to its starting position at the top of the picture. As an alternative mode of operation, the motion of the tilting mirror can be stopped to give a line-scan mode in which the same line is swept repetitively 1600 times/second.

As presently configured, the camera has an output signal-to-noise ratio of unity for a temperature change of about 2° C when the camera is viewing a blackbody near a temperature of 23° C. It has a maximum spatial resolution of about 55 elements/line, as determined by measuring the minimum distance between two signal sources such that the camera can detect that there are in fact two separate sources.

Reference 1 gives both a more detailed description of the camera and a description of its initial use in measuring aerodynamic heating.

SCHEMATIC DRAWING OF CAMERA OPTICS

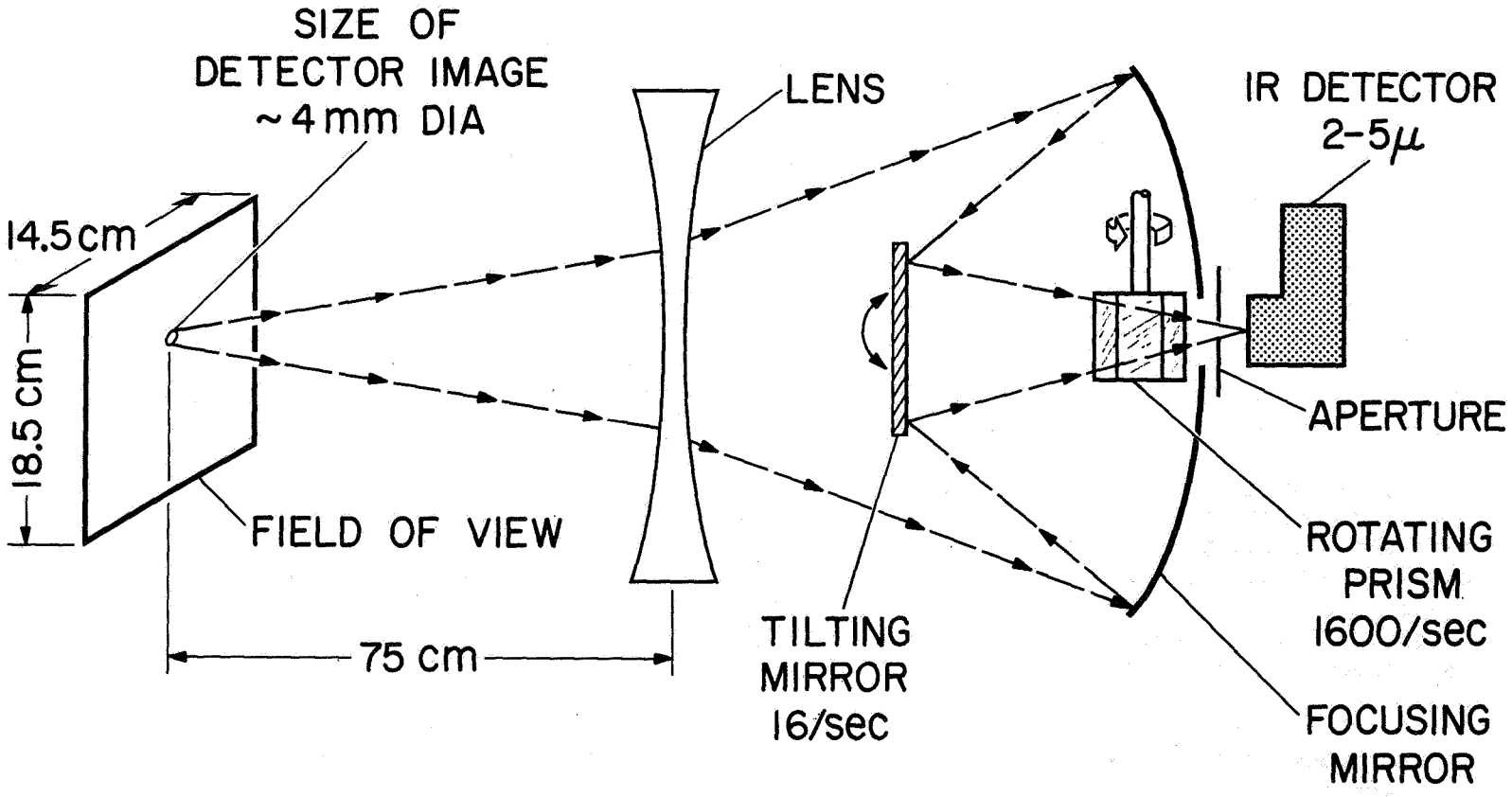

Figure 1

FIGURE 2

Calibration of the camera is performed by using an infrared energy source with surface-emissivity characteristics the same as those of the wind tunnel model to be tested. Both source and model are sprayed with a high-emissivity flat-black paint, 3M Nextel. The paint thickness required is about 0.05 mm, and the resulting surface is slightly grainy in appearance. The paint stands up well under wind tunnel tests and its thermal characteristics have proved unimportant insofar as obtaining heating rate is concerned for tests lasting more than about one second.

A typical calibration curve is shown in Fig. 2, where the voltage output from the camera is plotted as a function of source temperature. (Note that this curve is nonlinear.) Also plotted is the predicted temperature variation computed on the basis of a blackbody source adjusted for the relative spectral sensitivity of the detector. The prediction is matched to the measurements at a temperature of 123° C. The good correspondence between the shapes of predicted and measured curves lends confidence to the calibration. Calibrations are performed with all windows and mirrors in the optical path that are to be used in the actual wind tunnel tests. Repeatability between calibrations has been within about one percent.

The calibration described above is performed for a single position of the scan point in the field of view. The sensitivity of the camera (but not the shape of the calibration curve) depends, however, on the position of the scan point, with higher sensitivities occurring near the center of the field. An auxiliary calibration is performed therefore to obtain an additional position-dependent calibration factor, which is then used during data reduction to appropriately adjust the voltage-temperature calibration.*

---

*This dependence of sensitivity on the position of the scan point in the field lessens the accuracy of the method used in Ref. 1 to obtain heating rate. There, the heating rate was obtained from motion pictures of the visual display when that display contained the so-called "isotherm" contour provided by the manufacturer as part of the camera electronics package. Since the isotherm contour is in fact an isovoltage contour, use of this method is accurate only for part of the field of view.

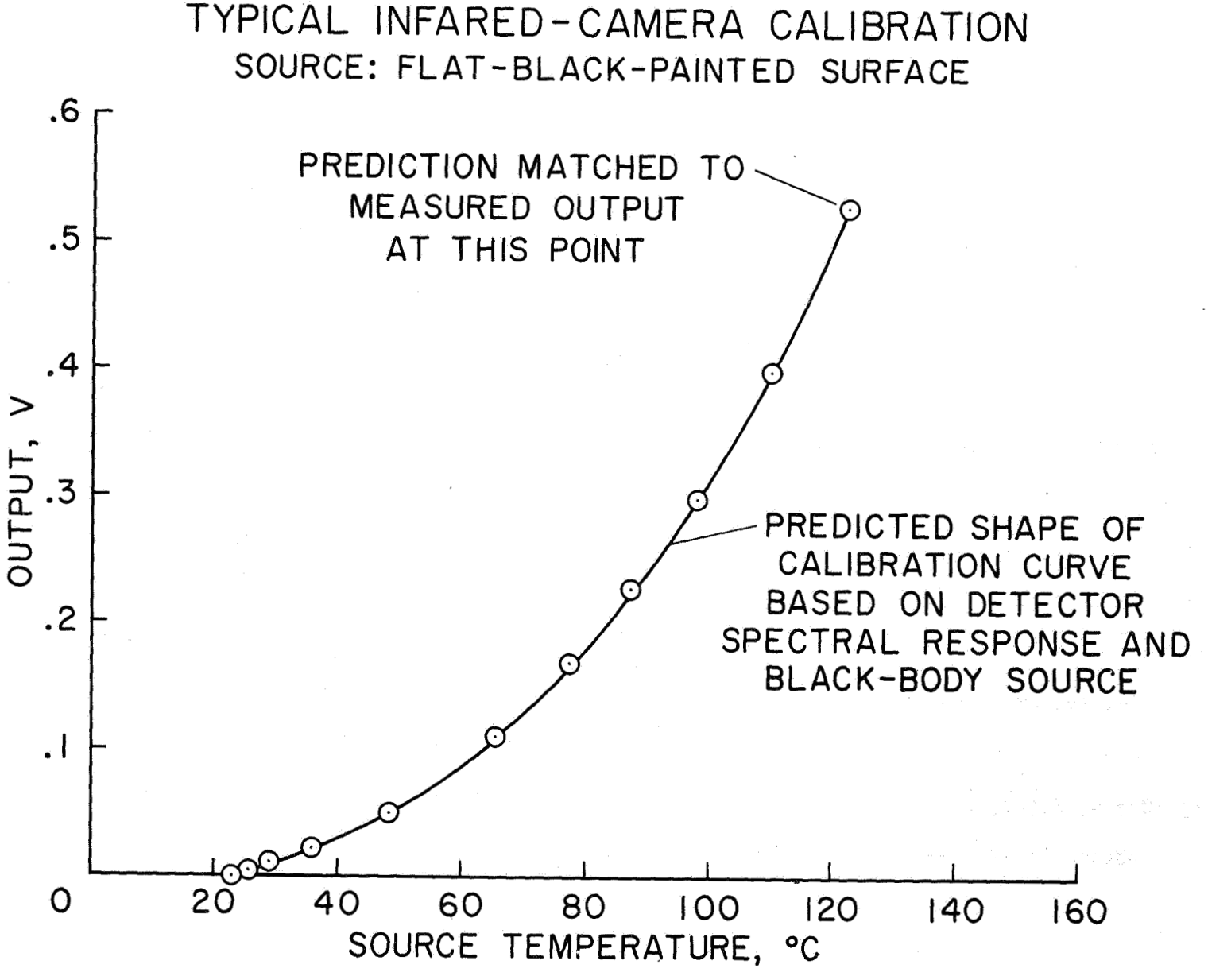
TYPICAL INFARED-CAMERA CALIBRATION
SOURCE: FLAT-BLACK-PAINTED SURFACE
PREDICTION MATCHED TO MEASURED OUTPUT AT THIS POINT
PREDICTED SHAPE OF CALIBRATION CURVE BASED ON DETECTOR SPECTRAL RESPONSE AND BLACK-BODY SOURCE
OUTPUT, V
.6
.5
.4
.3
.2
.1
0
20
40
60
80
100
120
140
160
SOURCE TEMPERATURE, °C

Figure 2

FIGURE 3

An automated data-handling scheme has been developed to reduce the raw analog voltage data to heating rate distributions. The steps in the scheme are shown schematically in Fig. 3. The data are first recorded on analog tape. Then a digital tape suitable for use on standard digital computing equipment is produced from the analog tape. To produce this digital tape, the analog tape is replayed more slowly than it was recorded and the data are digitized continuously at a rate that produces 68 digital words along each scan line in the picture. This yields at least one digital point for each spatial resolution element. The amount of data produced is large, about 130,000 digital words/second of wind tunnel run time.

The digital tape is read by an IBM 360/67 computer, and computer routines have been written to organize the data so that standard heating rate reduction can be accomplished. A heating rate routine is available for thin-skin models; another for semi-infinite models is currently being written. Computation times have not become excessive - 10 to 15 minutes/run are typical.

Contour plots of the heating rate distribution are produced on an SC-4020 plotter. The outline of the model must then be superposed by hand on these plots.

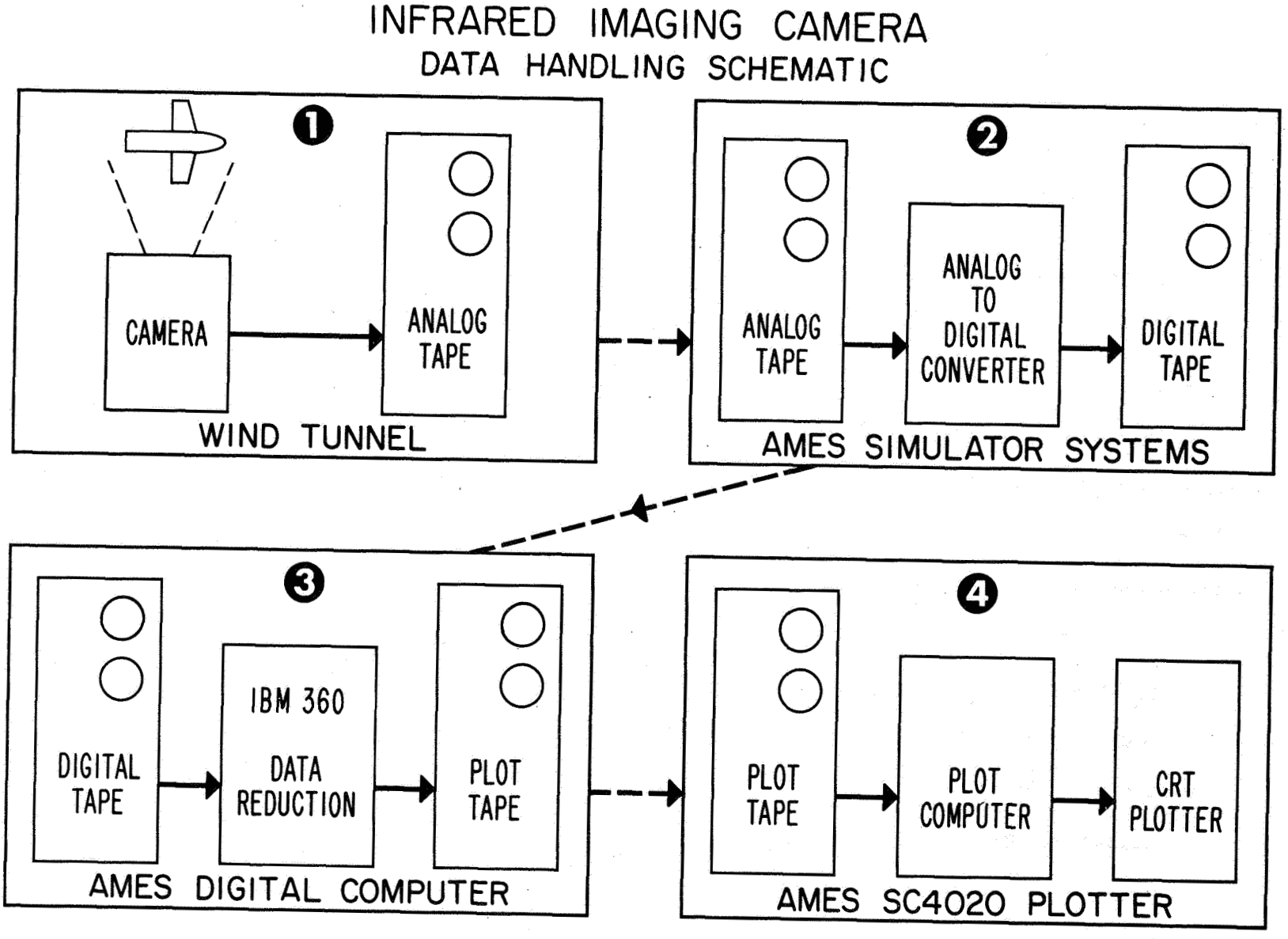
INFRARED IMAGING CAMERA
DATA HANDLING SCHEMATIC
1
CAMERA
ANALOG TAPE
WIND TUNNEL
2
ANALOG TAPE
ANALOG TO DIGITAL CONVERTER
DIGITAL TAPE
AMES SIMULATOR SYSTEMS
3
DIGITAL TAPE
IBM 360
DATA REDUCTION
PLOT TAPE
AMES DIGITAL COMPUTER
4
PLOT TAPE
PLOT COMPUTER
CRT PLOTTER
AMES SC4020 PLOTTER

Figure 3

FIGURE 4

Figure 4 shows a comparison between heating rates measured by means of both the infrared camera and thermocouples. The model in this test was a space-shuttle-orbiter body with a thin skin and the test was performed in the Ames 3.5-foot wind tunnel. The camera was used in the line-scan mode. Thermocouples were located beneath the skin of the model along the scan line. Two sets of measurements, labeled "automated data reduction" and "hand data reduction," are shown for the infrared camera. The former set was obtained by the automated procedure described in the preceding section. Each point of the digital data has been connected to the next by a straight line segment. The short-period fluctuations in these results are due primarily to noise introduced when the data were recorded on analog tape and when the data were digitized. At present, this noise probably limits the accuracy of the technique to about ±10% at best. The measurements labeled "hand data reduction" were obtained by means of photographs taken of a direct oscilloscope display of the camera output. Both sets of infrared camera measurements are in good agreement with the thermocouple data.

COMPARISON OF HEATING RATES MEASURED BY MEANS OF THERMOCOUPLES AND AN INFRARED IMAGING CAMERA

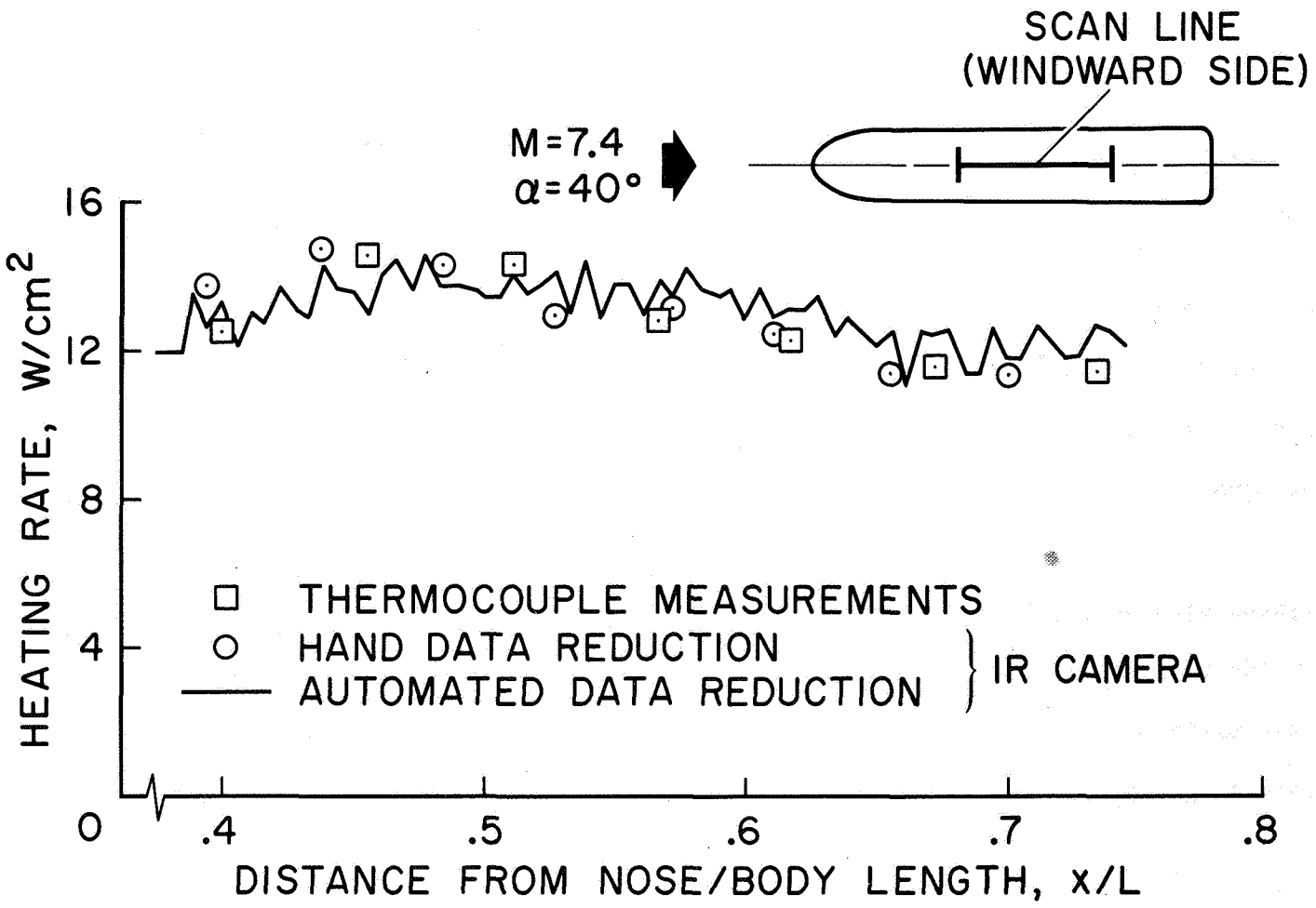

Figure 4

FIGURE 5

The system has been used most frequently and with best success in the Ames 3.5-Foot Hypersonic Wind Tunnel, where run times are typically the order of a few seconds; hence there are several tens of complete pictures per run. The wind tunnel flow must not radiate in a spectral region in which the detector is sensitive, and the 3.5-foot wind tunnel satisfies this requirement.

Figure 5 shows data from a typical run. The model is the same as in Fig. 4. An unintentional single roughness element, just upstream of the field of view of the camera, has tripped the laminar boundary layer and caused a turbulent wedge with its higher attendant heating to form. This roughness element, caused by impact damage on a previous run, was small enough to have easily escaped notice otherwise, since the model also had intentional roughness.

Figure 5(a) shows a photograph of the viewing screen of the camera. Lighter regions have higher temperatures, and the turbulent wedge stands out clearly. The hot regions on the sides of the model are produced by pieces of tape.

Figure 5(b) shows a computer-generated temperature plot from this run, and Fig. 5(c) shows a corresponding heat transfer plot. The turbulent wedge is evident in both of these plots.

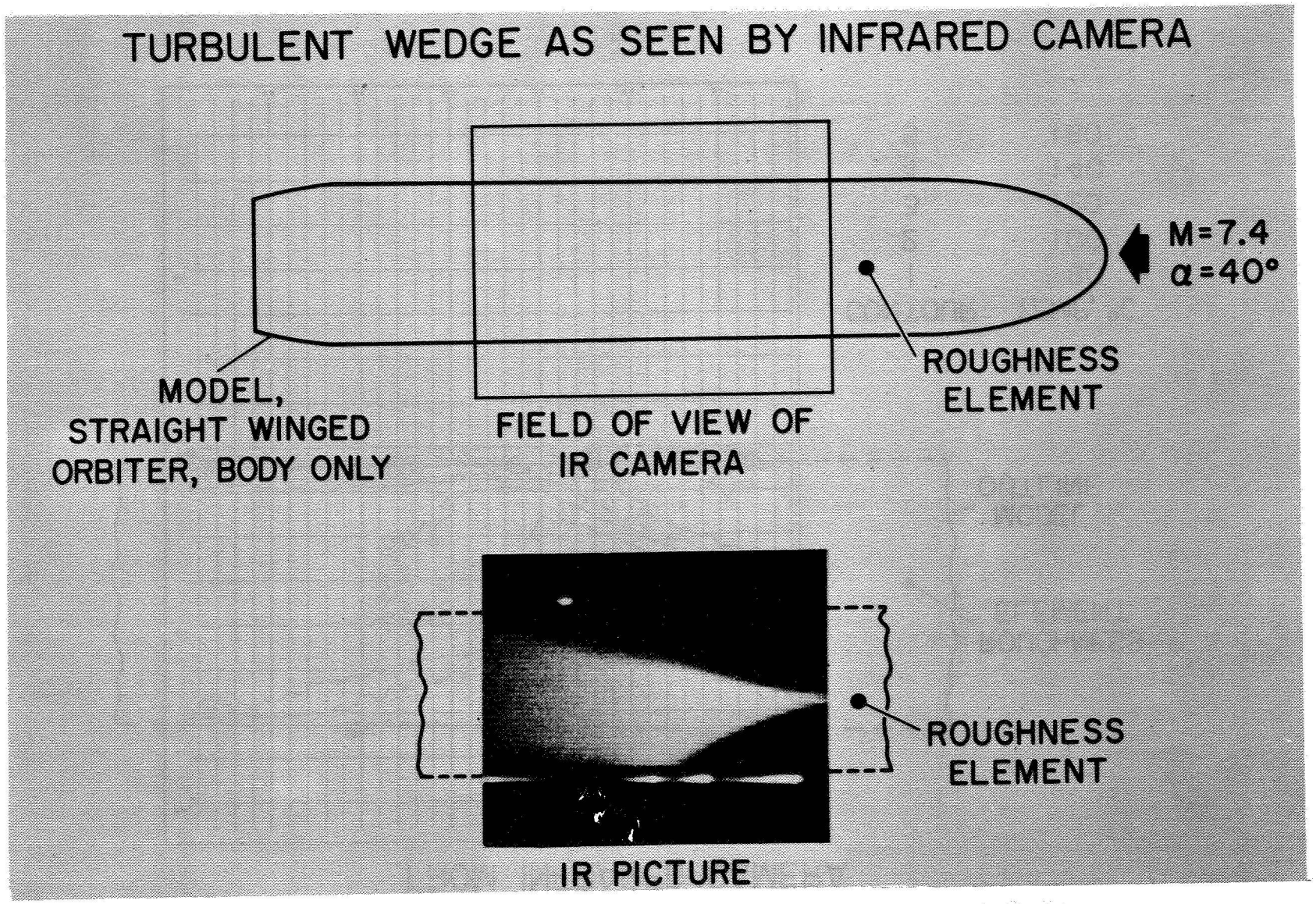
TURBULENT WEDGE AS SEEN BY INFRARED CAMERA
M=7.4
α=40°
ROUGHNESS ELEMENT
MODEL, STRAIGHT WINGED ORBITER, BODY ONLY
FIELD OF VIEW OF IR CAMERA
ROUGHNESS ELEMENT
IR PICTURE

Figure 5(a)

COMPUTER GENERATED TEMPERATURE CONTOURS FROM INFRARED CAMERA

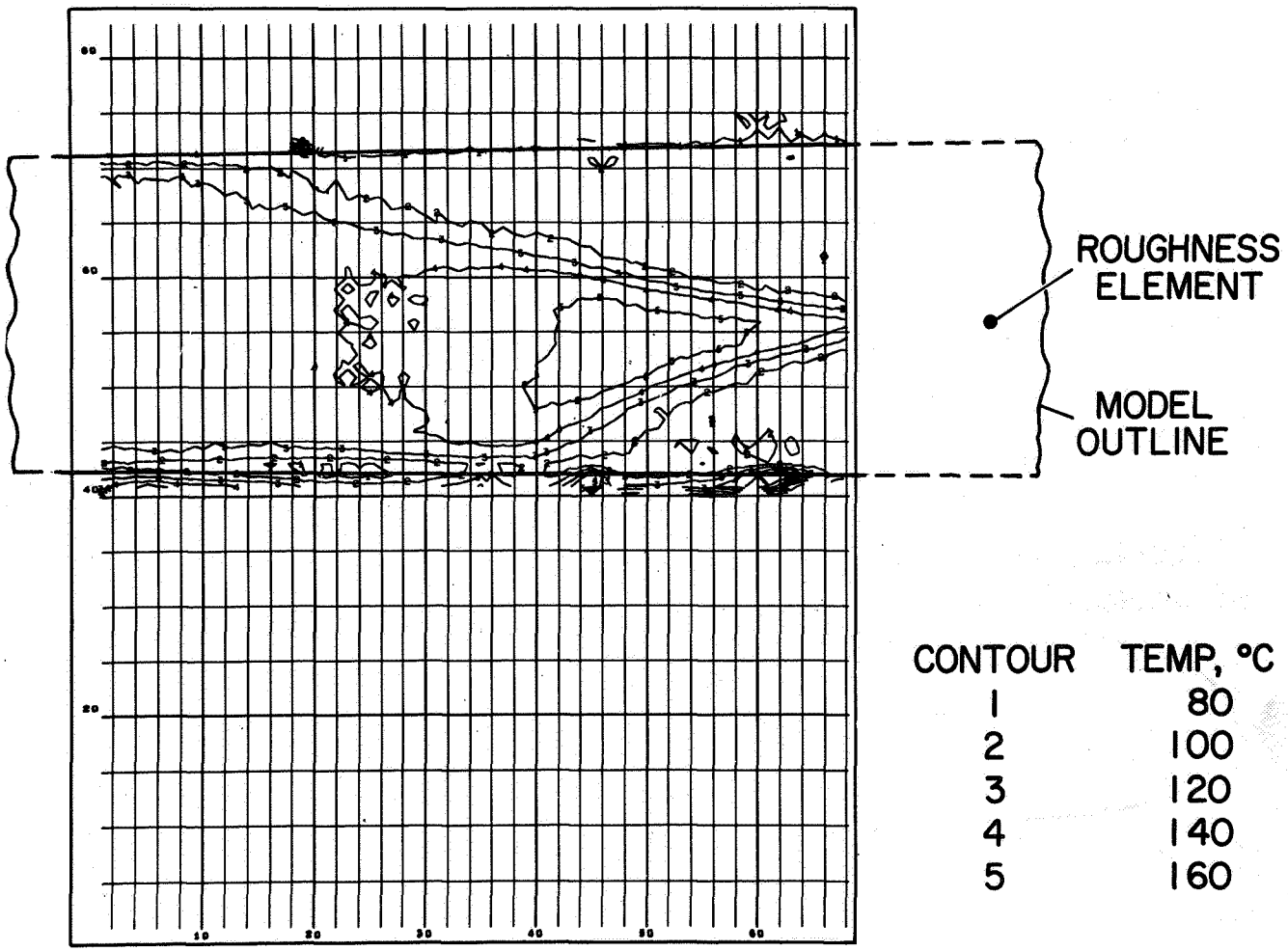

CONTOUR	TEMP, °C
1	80
2	100
3	120
4	140
5	160

Figure 5(b)

COMPUTER GENERATED CONTOUR PLOT OF HEATING RATE

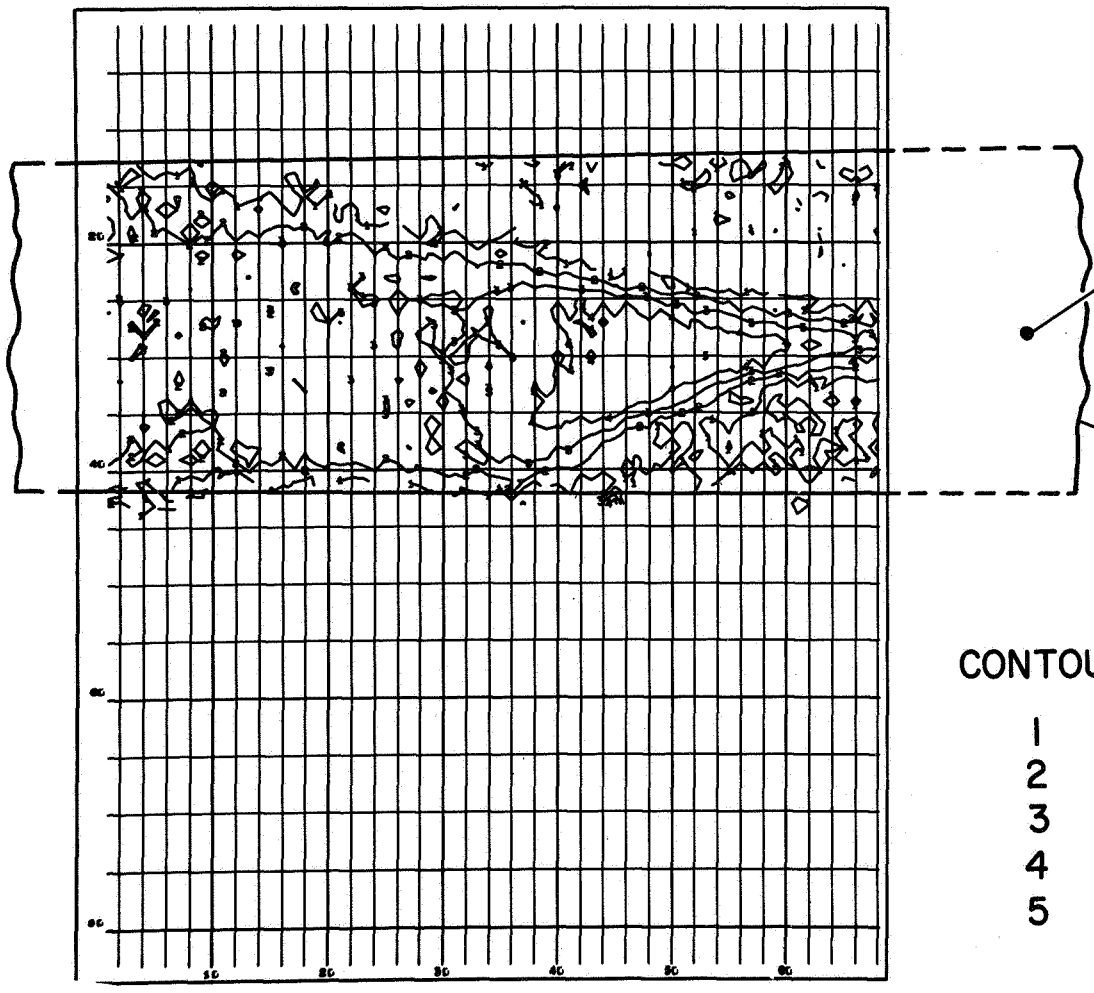

CONTOUR	HEATING RATE W/cm^2
1	6
2	8
3	10
4	12
5	14

Figure 5(c)

FIGURE 6

The camera has also been used to view models in a shock-tube-driven wind tunnel - the Ames Hypervelocity Free-Flight Aerodynamic Facility. Two types of operation have been tried. In the first of these, the line scan mode of the camera is used while the tunnel is actually running so that several line scans are obtained during the few milliseconds of flow time. Radiation, believed to be from hot dust in the flow, has proved to be a problem however and, so far, has prevented the obtaining of any useful data. Better success has been achieved in this particular shock tunnel by stopping the flow suddenly with a plug valve in the nozzle and then viewing the heated model during the relatively quiescent period immediately following flow stoppage. There is just sufficient time to obtain one complete picture scan before returning shock waves interfere with the view.

A picture of the infrared emission obtained by means of this latter technique is shown in Fig. 6. Here an interference-heating pattern on the windward side of the wing of a delta-winged orbiter is visible in the infrared photograph.

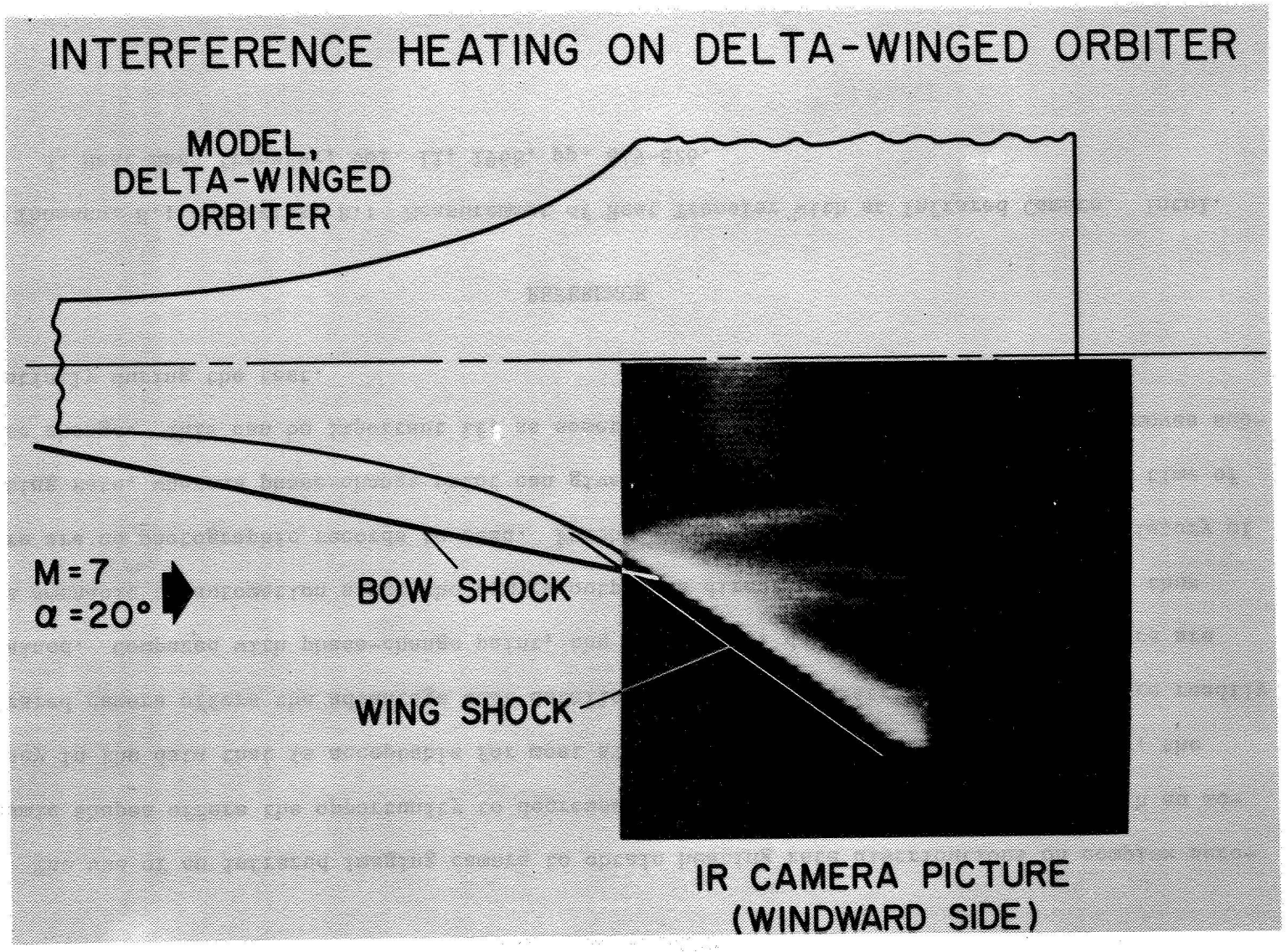
INTERFERENCE HEATING ON DELTA-WINGED ORBITER
MODEL, DELTA-WINGED ORBITER
M = 7
α = 20°
BOW SHOCK
WING SHOCK
IR CAMERA PICTURE (WINDWARD SIDE)

Figure 6

CONCLUDING REMARKS

The use of an infrared imaging camera to obtain heating rate distributions on complex aerodynamic shapes offers the opportunity to decrease data reduction time substantially with an accuracy in the data that is acceptable for most situations. Compared with thermocouples, the infrared camera offers the advantage that detailed heating rate distributions can be more readily obtained. Compared with phase-change paint, the problems of data handling for the camera are more amenable to automation since the camera output is directly in the form of voltage; thus there are no photographic records to read. Furthermore, the camera can give the time history of heating rate, whereas phase-change paint can give only the time-averaged rate up to the time of phase change. This can be important if, as sometimes happens, transition on the model moves substantially during the test.

REFERENCE

1. Thomann, H.; and Frisk, R.: Measurement of Heat Transfer with an Infrared Camera. Intnl. J. Heat Mass Transfer, vol. 11, 1968, pp. 819-826.

HEAT-TRANSFER TESTING PROCEDURES IN PHASE B SHUTTLE STUDIES WITH EMPHASIS ON PHASE-CHANGE DATA IMPROVEMENT

By David A. Throckmorton
Langley Research Center

INTRODUCTION

The recent development of the phase-change coating technique for measuring quantitative aerodynamic heat-transfer data resulted in its rapid adoption for extensive use in the phase B shuttle heating studies. However, procedures which have been utilized in application of the phase-change technique and certain factors which may significantly affect data accuracy require further discussion. These factors include variation of thermal properties of phase-change model material, sensitivity of measured heat-transfer coefficients to the assumed value of the adiabatic to total temperature ratio, and wall-temperature effects. These sensitivities are illustrated in sample calculations for a shuttle geometry. Factors which may affect the visual clarity and interpretation of phase-change data are discussed, and a method of improving photographic-data quality through the use of polarized light is presented.

SYMBOLS

c_p	specific heat of model material
h	heat-transfer coefficient
h_o	stagnation-point heat-transfer coefficient
h_{ref}	stagnation-point heat-transfer coefficient for a sphere with radius of 0.3048 meter (1 foot)
k	thermal conductivity of model material
L	length
M_∞	free-stream Mach number
R_D	free-stream Reynolds number based on diameter
T	temperature
T_{aw}	adiabatic wall or recovery temperature
T_i	model initial temperature

T_{pc} phase-change-coating melt temperature

T_t total temperature of free stream

T_w wall temperature

t time

x longitudinal distance from body

α angle of attack

β parameter in phase-change data-reduction equation

δ flow deflection angle

θ angle

λ thickness of model wall

ρ density of model material

HEAT-TRANSFER DATA REDUCTION

(Figure 1)

Those equations (fig. 1) which are used to determine quantitative values of heat-transfer coefficient, by using either the phase-change coating or thermocouple technique, result from the solution of the equation governing the one-dimensional transient conduction of heat into a solid body with application of the appropriate boundary and initial conditions. For the thin-skin technique, the equation results from the application of boundary conditions consistent with the conduction of heat into a finite solid of known thermal properties. For the phase-change technique, the equation results from the application of boundary conditions consistent with the conduction of heat into a semi-infinite solid also of known thermal properties. Both techniques assume an initial step input in heat-transfer coefficient to a value which is constant with time.

Thermal properties of the materials utilized in the construction of thin-skin models are usually well known and show little variation with material specimen. For phase-change model materials, however, the values of material specific heat and thermal conductivity, which are reflected in the thermal properties parameter $\sqrt{\rho c_p k}$, have been shown to vary substantially with material batch and must be determined for each model which is constructed in order to obtain accurate data utilizing the technique.

Reduction of data by using both techniques requires determination of a value of adiabatic wall or recovery temperature which, with wall temperature, reflects the driving or forcing function of the heat transfer from the gas stream to the model. It has become common practice in reducing heating data to use a constant recovery temperature based upon an assumed value of the ratio of recovery to total temperature. This practice results in a time savings in data reduction; however, it introduces an inaccuracy in the resulting data in that the true value of T_{aw} varies from point to point on a model as a function of configuration geometry, angle of attack, and free-stream Mach number, which reflect themselves in the local properties of the flow at any point.

The solutions for both techniques assume that the heat-transfer coefficient is constant with time. For the thin-skin technique, this assumption is valid in that test times are short, the model remains essentially at a constant temperature, and therefore, the heat-transfer coefficient over the short duration of a transient test is constant. However, for the phase-change technique, with test times of 10 seconds or more, the heat-transfer coefficient is not constant because the level and distribution of temperature along the surface of the model change rapidly with time during the test. This is a result of the very nature of the phase-change technique which requires a temperature gradient along the surface of the model to produce a melt line of the phase-change coating and thereby reveal a contour of constant heat transfer indicated by the location of this line.

HEAT-TRANSFER DATA REDUCTION

THIN SKIN:

$$h = \frac{1}{T_{aw} - T_w} \frac{\partial T}{\partial t} \rho c_p \lambda$$

PHASE CHANGE:

$$h = \frac{\beta}{\sqrt{t}} \sqrt{\rho c_p k}$$

WHERE $e^{\beta^2} \operatorname{erfc}(\beta) = 1 - \frac{T_{pc} - T_i}{T_{aw} - T_i}$

Figure 1

VARIATION OF MATERIAL THERMOPHYSICAL PROPERTIES WITH SAMPLE

(Figure 2)

Thermophysical properties of STYCAST 2762, the material most frequently used for construction of phase-change models, indicate extreme sample-to-sample variations. Data presented in figure 2 represent measurements on a series of models which were fabricated for testing during early Phase B configuration screening. For the particular test program, 44 models were constructed and the material density and thermal conductivity were measured on 16 of the models. Values of specific heat were obtained on only two of the models. From these measurements, average values of density, thermal conductivity, and specific heat were determined and these values then applied to reduce data obtained on all 44 models. Due to the extreme variation of actual thermal properties, the average value utilized to reduce all data resulted in extreme data scatter and large inaccuracies in a substantial portion of the data obtained. In order to obtain accurate data by utilizing the phase-change technique, the value of the thermal properties of each model must be known precisely. For current-generation model materials, each model should have thermal properties measured and those properties utilized in the reduction of data on that particular model.

Further complicating the problem, material thermal properties are a function of material temperature and also vary with the cure cycle to which a model is subjected in order to insure material strength. For this reason, it is essential that the specimen which is being used for measurement of material thermal properties be subjected to a cure cycle identical with that of the model in question. Nonhomogeneity of model materials has also been cited as a problem which results in nonuniform values of the thermal properties on the interior of a model.

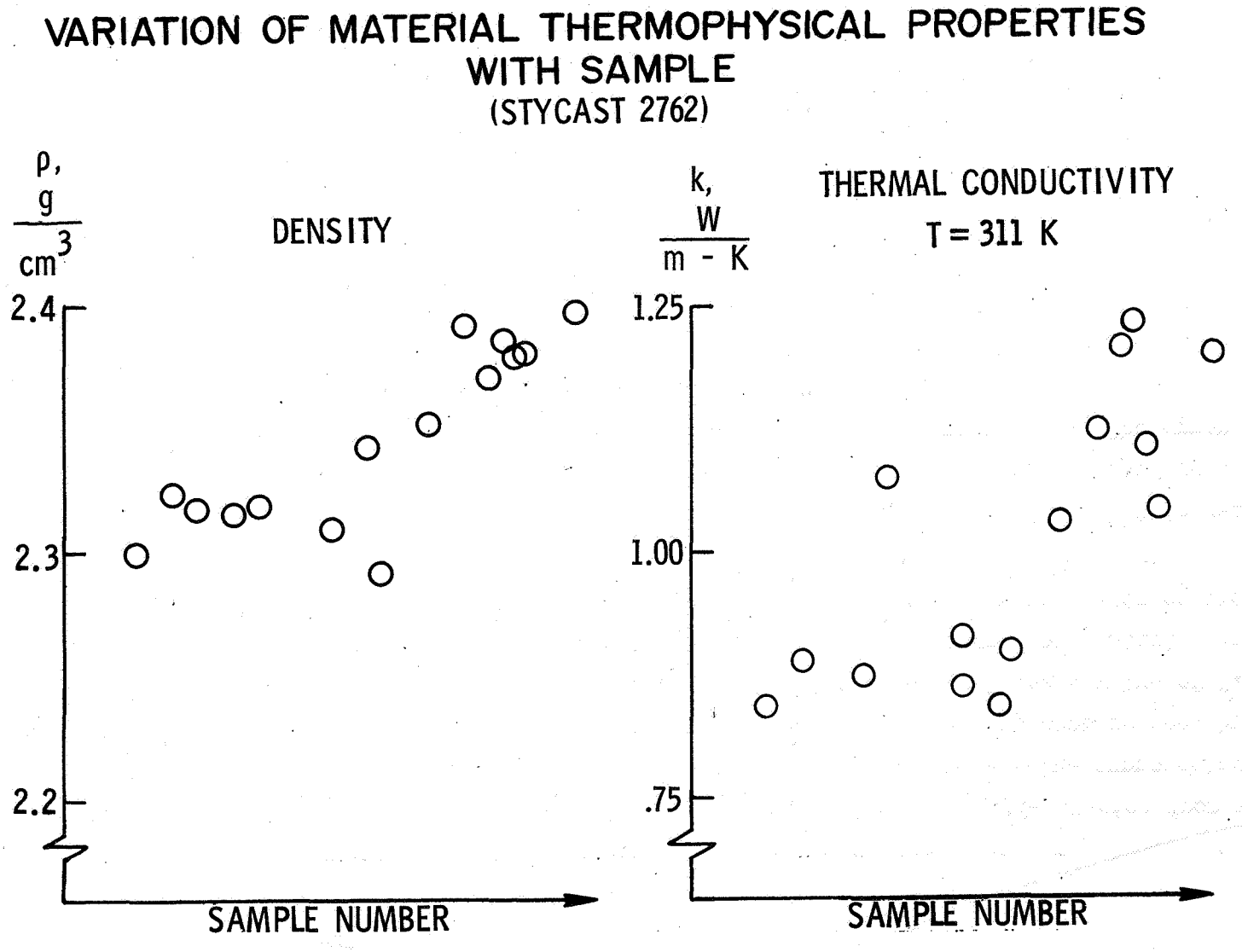
VARIATION OF MATERIAL THERMOPHYSICAL PROPERTIES WITH SAMPLE
(STYCAST 2762)
ρ, g/cm³
DENSITY
2.4
2.3
2.2
SAMPLE NUMBER
k, W/m - K
THERMAL CONDUCTIVITY
T = 311 K
1.25
1.00
.75
SAMPLE NUMBER

Figure 2

VARIATION OF ADIABATIC WALL TEMPERATURE WITH FLOW DEFLECTION ANGLE

(Figure 3)

For the simple case of two-dimensional flow past a wedge, the value of T_{aw}/T_t varies from a minimum of approximately 0.86, when the surface is parallel to the free stream, to a value approaching 1 at deflection angles greater than 60°. (See fig. 3.) Some Phase B heating data have been reduced by assuming a T_{aw}/T_t value of 1, some by assuming a value of 0.9 and some by assuming a value of 0.95. Data based upon an assumption of $T_{aw}/T_t = 1$ is not comparable with those reduced by utilizing an assumption of $T_{aw}/T_t = 0.9$, nor is it completely satisfactory to compare data on the basis of the same assumption of T_{aw}/T_t.

Rigorously, the only valid comparison is that with the correct value of T_{aw}/T_t, but this value varies with angle of attack, Mach number, and the particular geometry in question. The difficulty of this calculation has led to the use of an assumed value of adiabatic wall temperature. The error introduced by utilizing such an assumption is illustrated in figure 4.

VARIATION OF ADIABATIC WALL TEMPERATURE WITH FLOW DEFLECTION ANGLE

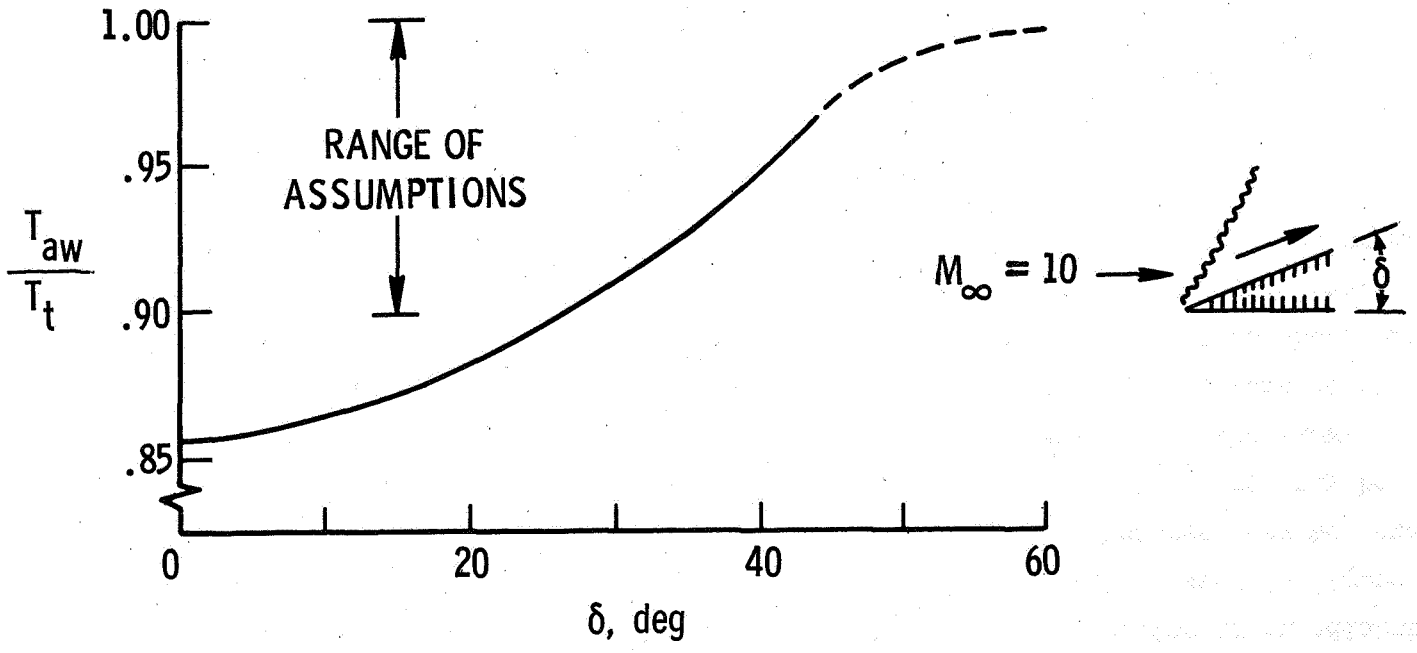

Figure 3

EFFECT OF ADIABATIC-WALL-TEMPERATURE ASSUMPTION ON COMPUTED HEAT-TRANSFER COEFFICIENTS

(Figure 4)

The error in computed heat-transfer coefficient introduced by the assumption of an adiabatic wall temperature, based on a constant recovery to total temperature ratio, is illustrated in figure 4. For phase-change testing, the error is not only a function of the assumed ratio of recovery to total temperature but also varies with phase-change and model initial temperatures. This error may be quite large, especially as phase-change temperature approaches the total temperature of the flow. This same error is also introduced into data obtained with the thin-skin technique; however, because the ratio of wall to total temperature is relatively small, the error is of less significance than those encountered using high-temperature paint. The curve indicating a phase-change to total temperature ratio of 0.31 very closely approximates the cold-wall condition which is encountered in a thin-skin measurement test ($T_t \approx 1000$ K).

EFFECT OF ADIABATIC-WALL-TEMPERATURE ASSUMPTION ON COMPUTED HEAT-TRANSFER COEFFICIENT

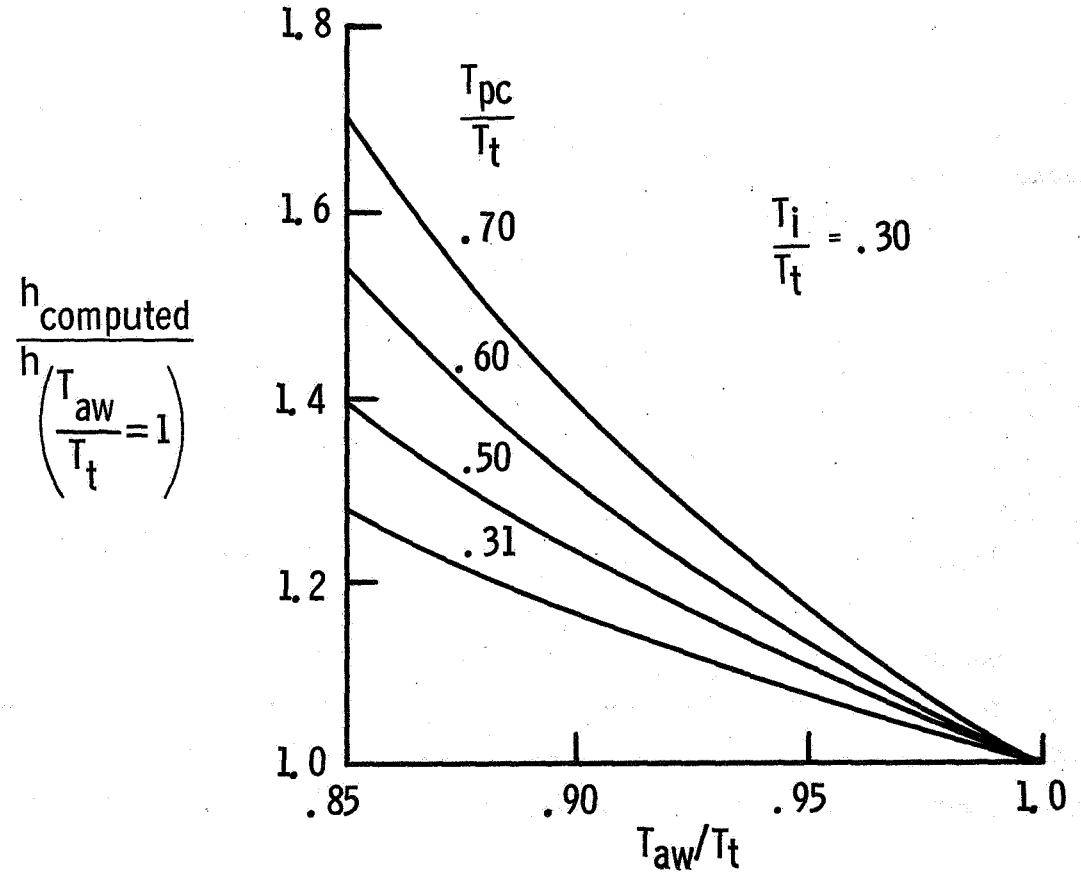

Figure 4

APPLICATIONS OF ADIABATIC-WALL-TEMPERATURE ASSUMPTION TO PHASE B DATA

(Figure 5)

The impact of the T_{aw}/T_t assumption on published Phase B data is now illustrated. The two sets of data shown in the left-hand portion of the figure were obtained in the Langley continuous-flow hypersonic tunnel (CFHT) and the Langley Mach 8 variable-density hypersonic tunnel (VDT) by Raymond S. Raparelli of the North American Rockwell Corp. (NAR). CFHT data were reduced with the assumption that $T_{aw}/T_t = 0.9$, and VDT data were reduced with the assumption that $T_{aw}/T_t = 1$. The differences in the values of measured heat-transfer coefficient determined by utilizing the different assumptions of T_{aw}/T_t are substantial. In the right-hand portion of the figure, the same data have been reduced by utilizing a value of T_{aw}/T_t which is approximate for the lower surface center line of that vehicle at the given angle of attack. When both sets of data are reduced by utilizing the approximate value of the adiabatic wall temperature, the extreme scatter between the sets of data is no longer evident.

It should again be recognized that, rigorously, the only valid comparison is that between data which have been reduced by utilizing the correct value for the adiabatic wall temperature at each point on the body in question. This requires knowledge of the local flow field or a standard methodology with which to express the conditions of the local flow. Use of an approximate recovery temperature should yield data of acceptable accuracy for most engineering applications.

APPLICATION OF ADIABATIC-WALL-TEMPERATURE ASSUMPTION TO PHASE B DATA

WINDWARD CENTER-LINE HEATING TO NAR O_1 DELTA ORBITER;
PHASE-CHANGE TEST; $\alpha = 30^0$

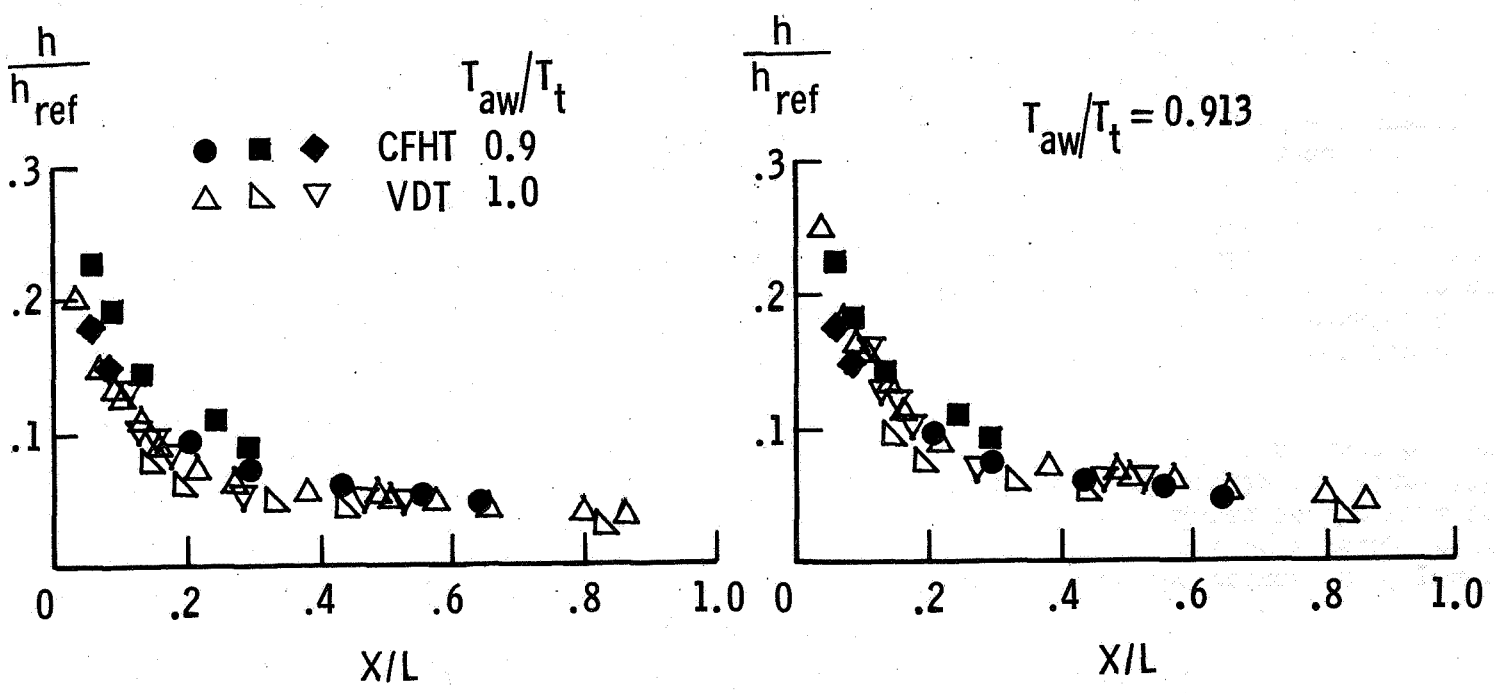

Figure 5

WALL-TEMPERATURE EFFECTS ON HEAT-TRANSFER COEFFICIENT

(Figure 6)

One of the assumptions made in order to derive the equation utilized for the reduction of phase-change data is that the model experiences a step input in heat-transfer coefficient to a value which is constant with time. In a phase-change testing situation, this assumption is violated as the wall temperature of the model and the temperature distribution along the model are continually changing with time. For this reason, the effects of wall temperature on the heat-transfer coefficient must be investigated in order to determine the validity of that assumption.

The trends imposed on the heat-transfer coefficient due to the wall-temperature effect during a phase-change test are illustrated in figure 6. The curves represent the computed heat transfer to the windward center line of a shuttle configuration when the surface temperature and distribution are as shown. The nonisothermal wall condition represents the temperature distribution which the model would experience were it subjected to the heat transfer shown for $T_w = 311$ K for a period of 10 seconds (RTV-type material). The effect of increased surface temperature is to decrease the convective heat-transfer coefficient; however, a negative temperature gradient along the surface increases the heat-transfer coefficient. The combined effects of increased surface temperature and negative temperature gradient along the surface of the model are small (on the order of 5 percent). However, for a geometry such as a hemisphere, where the heat-transfer gradient along the surface is large, the magnitude of these effects has been shown to be on the order of 30 percent. For phase-change testing, wall-temperature effects are at a minimum when the high heat-transfer contours are generated because test time is short and temperature gradients small, and the effects are at a maximum when the low heat-transfer contours are generated because test times are long and temperature gradients large.

WALL-TEMPERATURE EFFECTS ON HEAT-TRANSFER COEFFICIENT

WINDWARD CENTER LINE; NAR 134-B DELTA ORBITER; $\alpha = 30^0$

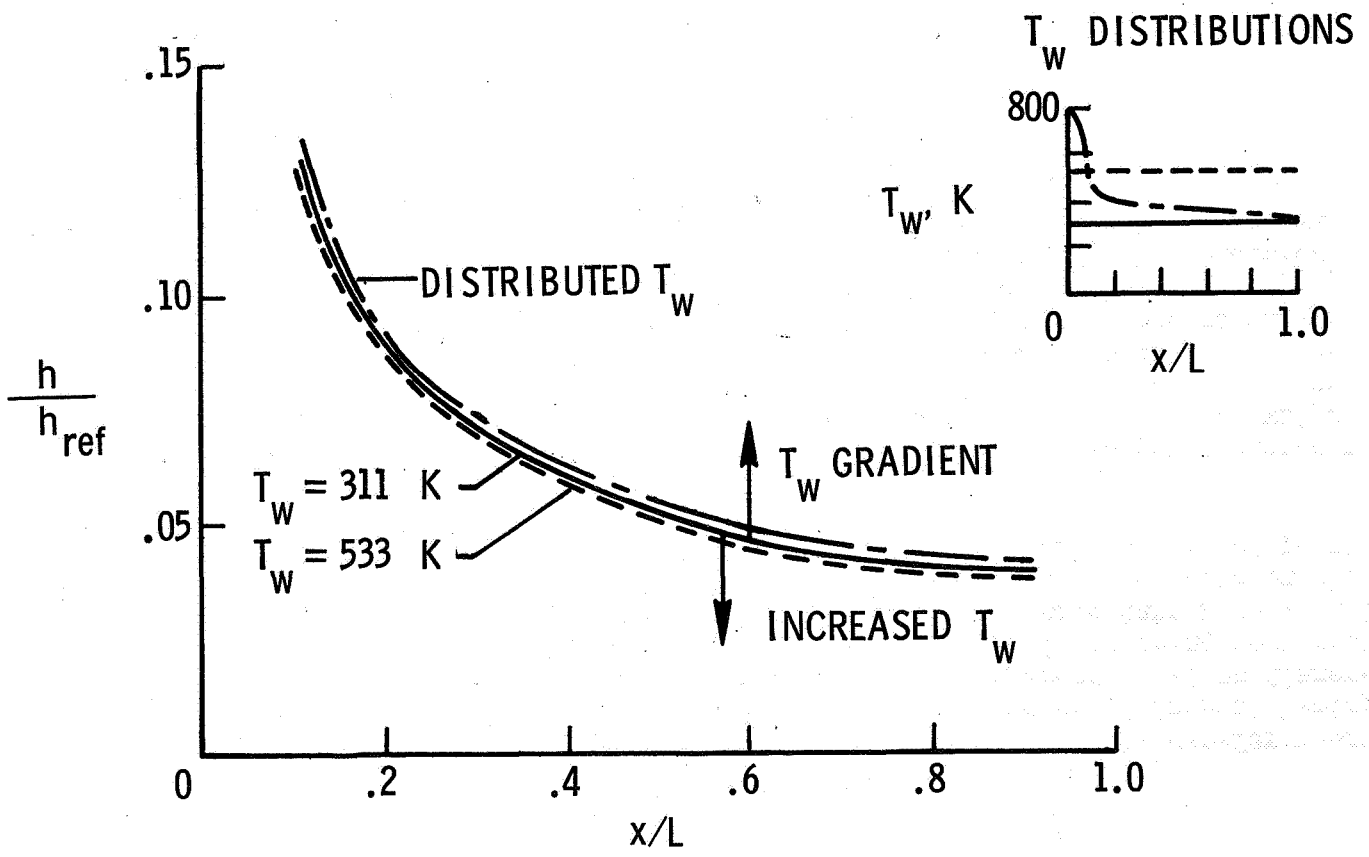

Figure 6

MEASURED HEAT-TRANSFER DISTRIBUTION ON A HEMISPHERE

(Figure 7)

Wall-temperature effects on phase-change test data have been observed in heat-transfer measurements on hemispheres at Mach 10. Data have been obtained on 12.7-centimeter-diameter (5 inches) hemispheres, by utilizing both the thin-skin and phase-change techniques, at Reynolds numbers based on diameters of 0.417×10^6 and 0.833×10^6. Phase-change data obtained by using coatings of differing temperature ratings are indicated by the various open symbols. Observation of the phase-change data reveals a layering effect with paint melt temperature which is a consequence of the wall-temperature effects on the phase-change test. Differences between thin-skin and phase-change data are primarily attributed to the wall-temperature effects on the phase-change data.

Although the magnitude of variation in measured heat transfer encountered in phase-change testing due to wall-temperature effects may seem insignificant in contrast to those other factors which affect the accuracy of the phase-change technique, the importance of these variations becomes apparent when one attempts to take the data obtained in earth-bound experimental facilities and extrapolate those data to flight conditions. Large spatial temperature gradients which exist on a phase-change model will not exist on a full-scale flight vehicle; this vehicle will be more nearly isothermal. However, if data obtained in ground-based facilities are to be used in direct extrapolation to flight conditions or used in theoretical verification, one must be aware of the surface conditions to which the model was subjected in obtaining these data so that accurate predictions to the flight conditions may be made.

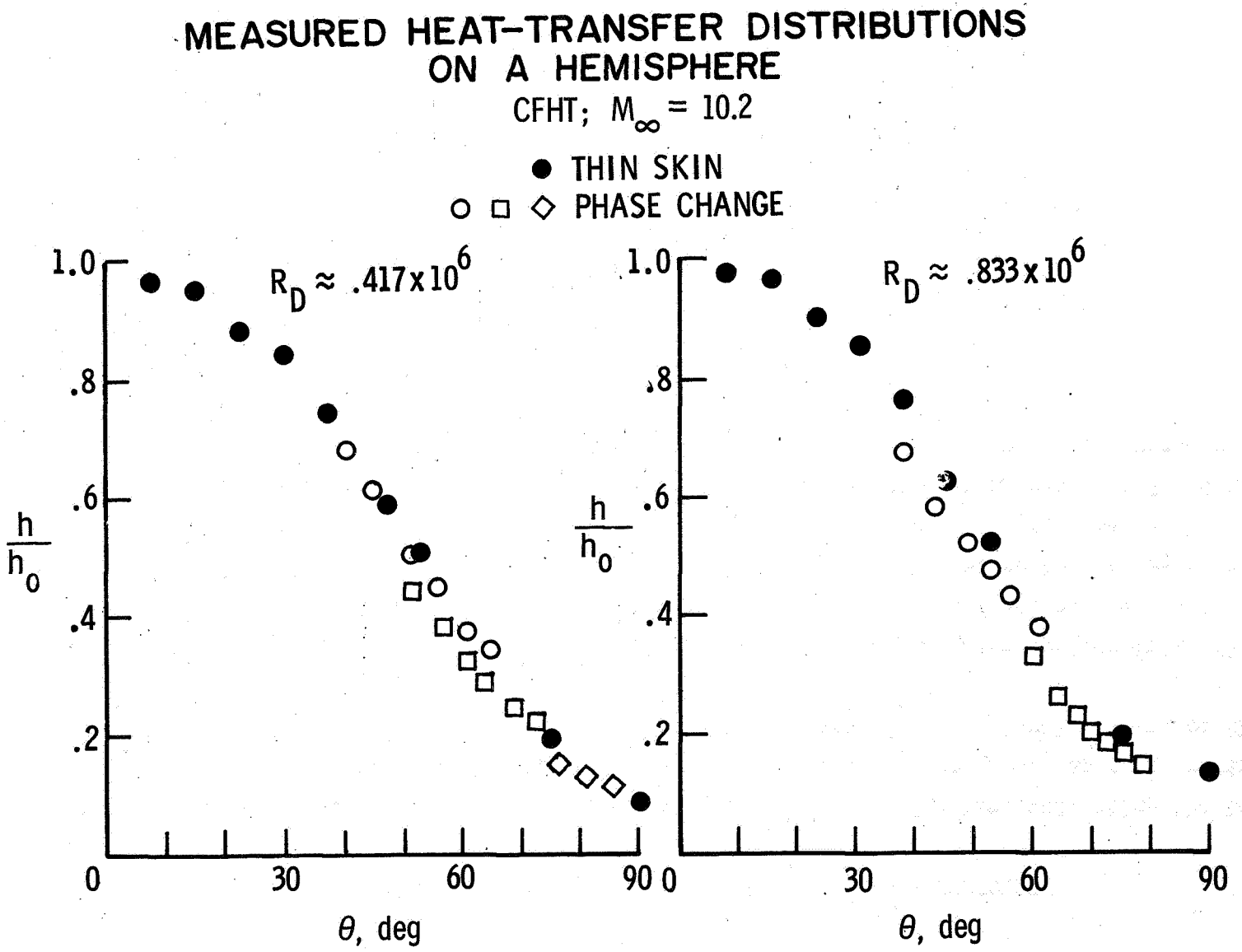
MEASURED HEAT-TRANSFER DISTRIBUTIONS
ON A HEMISPHERE
CFHT; M_∞ = 10.2
● THIN SKIN
○ □ ◇ PHASE CHANGE
$R_D \approx .417 \times 10^6$
$R_D \approx .833 \times 10^6$
$\frac{h}{h_0}$
1.0
.8
.6
.4
.2
0
30
60
90
θ, deg

Figure 7

FACTORS AFFECTING THE VISUAL CLARITY OF PHASE-CHANGE CONTOURS

(Figure 8)

Reduction of phase-change data requires the visual identification of a line indicating the locus of points at which the phase change of a temperature-sensitive coating is occurring at a given time. The identification of the location of this line may vary with observer as the visual clarity of the photographic data is subject to wide variation.

Factors which may significantly affect the clarity of the photographic data include (fig. 8)

(1) Uneven application of the phase-change coating material along the surface of the model

(2) Glare resulting from reflections of the incident light on surfaces where the phase-change material has become liquid yet has not been swept away due to the shear of the airstream

(3) Difficulty in distinguishing those areas where the phase-change coating has melted and has been swept away by shear forces from those areas where the coating has changed phase yet remains on the surface as a clear liquid

(4) Reflections and scattering of the incident light by the tunnel window

(5) Nonuniform and ambient illumination of the model

FACTORS AFFECTING VISUAL CLARITY OF PHASE-CHANGE CONTOURS

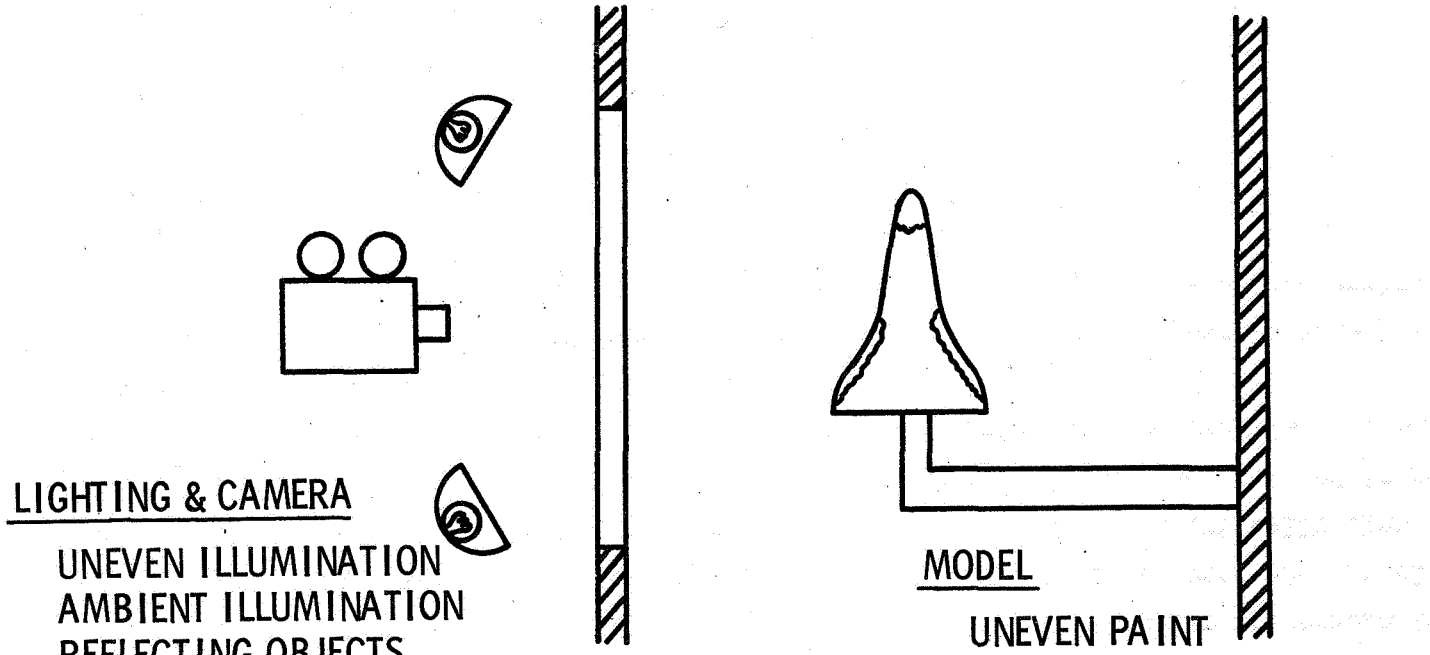

Figure 8

POLARIZED LIGHT FOR IMPROVED DATA QUALITY

(Figure 9)

A photographic technique has been proposed for data acquisition utilizing polarized light to significantly improve the quality of the photographic data. The technique involves polarizing the incident light in a horizontal plane while allowing only vertically polarized light to enter the camera lens. In this manner, specular reflections from the model surface are significantly reduced and the clarity of the phase change data dramatically improved. This type technique requires an optically flat tunnel window in order to maintain the polarization of the light as it enters the test section and is returned from model to camera. A window which is not optically flat, or a window of tempered glass is unacceptable for such a technique as it will depolarize the light.

Studies have indicated that the use of such a technique for acquisition of phase-change photographic data may make feasible the use of automatic machine reduction of the phase-change contour plots.

POLARIZED LIGHT FOR IMPROVED DATA QUALITY

- SIGNIFICANT REDUCTION OF SPECULAR REFLECTIONS
- LOWER CONTRAST BETWEEN MELTED AND "SWEPT-CLEAN" REGIONS
- INCREASED CONTRAST BETWEEN MELTED AND UNMELTED REGIONS
- PRACTICALITY OF AUTOMATED DATA REDUCTION

Figure 9

CONCLUSIONS

The preceding discussion leads to the following conclusions:

1. Thermophysical properties of phase-change model materials must be known precisely for each model tested.

2. Heat-transfer data must be utilized only in the context of the assumptions applied to reduce those data.

3. For long run times and/or certain geometries, wall-temperature conditions may significantly affect data obtained by using the phase-change technique.

4. Use of a polarized lighting technique significantly increases phase-change data quality and may result in practicality of automatic data reduction.

EVALUATION OF BOUNDARY-LAYER-TRANSITION CRITERIA FOR SPACE SHUTTLE ORBITER ENTRY

By Vernon T. Helms III

NASA Langley Research Center
Hampton, Virginia

INTRODUCTION

Approximately a year ago a study was initiated at the Langley Research Center to determine the impact of boundary-layer-transition criteria on thermal protection system requirements. The scope of this investigation covered a wide range of transition criteria which was expanded as new recommendations were made by the NASA shuttle contractors. Effects of the local flow assumptions were also evaluated. Concurrently, an experimental investigation was conducted by Mr. George C. Ashby, Jr. of the Langley staff to establish the appropriate procedure to follow in defining local boundary-layer edge Mach number variation (ref. 1). In addition, a variety of trajectory shaping approaches, all yielding significant cross range, have been investigated.

This paper summarizes the results of this study. Results include the influence of the various transition criteria on surface temperature, heating rate, and heat load distributions over the bottom center line of a typical delta-wing vehicle for several trajectory shaping techniques.

HEATING METHOD, BOUNDARY-LAYER TRANSITION AND FLOW-FIELD ASSUMPTION

As shown in figure 1, a modified version of the Miniver aerodynamic-heating computer program (ref. 2), developed by the McDonnell Douglas Corporation (MDC), was used in performing this study. The heating prediction technique applied was a combination of Eckert's reference enthalpy for laminar flow and the method of Spalding and Chi for turbulent-heating calculations. A linear interpolation of heating with distance in the transition region has been assumed, with the fully turbulent onset Reynolds number being double that for transition. The virtual origin of the turbulent boundary layer was taken to be at transition onset.

This report presents a comparison of six transition criteria which cover a range of transition Reynolds numbers from 0 to well over 6.0×10^6. These criteria include fully turbulent flow throughout the entry, length transition Reynolds number of 0.25×10^6 and 1.0×10^6, the criteria developed by the McDonnell Douglas Corporation (the criteria currently recommended by the Aerothermodynamic/Configurations Working Group's Thermal Panel), and the two criteria used by North American Rockwell (NAR) in 1970 and 1971. Local flow conditions were computed by assuming a sharp-cone flow field, and the real-gas delta-wing cross-flow correction of Baranowski was applied.

The vehicle parameters used in Miniver were those of the McDonnell Douglas high-cross-range orbiter, base line November 1970. The maximum center-line running length of this vehicle is approximately 50.3 meters.

HEATING METHOD, BOUNDARY-LAYER TRANSITION, AND FLOW-FIELD ASSUMPTION

MINIVER AERODYNAMIC HEATING COMPUTER PROGRAM

HEATING METHOD

- LAMINAR FLOW- ECKERT'S REFERENCE ENTHALPY
- TURBULENT FLOW - SPALDING AND CHI

BOUNDARY-LAYER TRANSITION

- FULLY TURBULENT $R_e = 2\,R_{e,tr}$
- VIRTUAL ORIGIN OF TURBULENT BOUNDARY LAYER AT TRANSITION ONSET

TRANSITION CRITERIA

- FULLY TURBULENT FLOW THROUGHOUT ENTRY
- $R_{e,tr} = 0.25 \times 10^6$
- $\dfrac{R_{e,\theta}}{M_e\left(\frac{R_e}{x}\right)^{0.2}} = f(\alpha)$ (MDC)
- $R_{e,tr} = 1.0 \times 10^6$
- R_e vs. M_e (NAR, 1970)
- $\dfrac{R_{e,\theta}}{M_e} = 225$ (NAR, 1971)

FLOW FIELD

- SHARP-CONE FLOW

CROSS FLOW

- BARANOWSKI REAL-GAS DELTA-WING METHOD

Figure 1

DELTA-WING ORBITER, M_∞ = 20.3 IN HELIUM

The justification for using a sharp-cone flow field in this report is illustrated in figure 2. The experimental results represent measurements of the boundary-layer edge Mach number at various flow deflection angles on a delta-wing orbiter model at a Mach number of 20.3 in helium. A comparison of the measured edge Mach number with those predicted by the tangent-wedge and tangent-cone theories and also by Newtonian surface pressure indicates that the tangent-cone theory best approximates the measured values at deflection angles up to that for conical shock detachment. Similar results were obtained for the delta-wing orbiter model in air at a Mach number of 6.8 and for a straight-wing model in helium at a Mach number of 20.3.

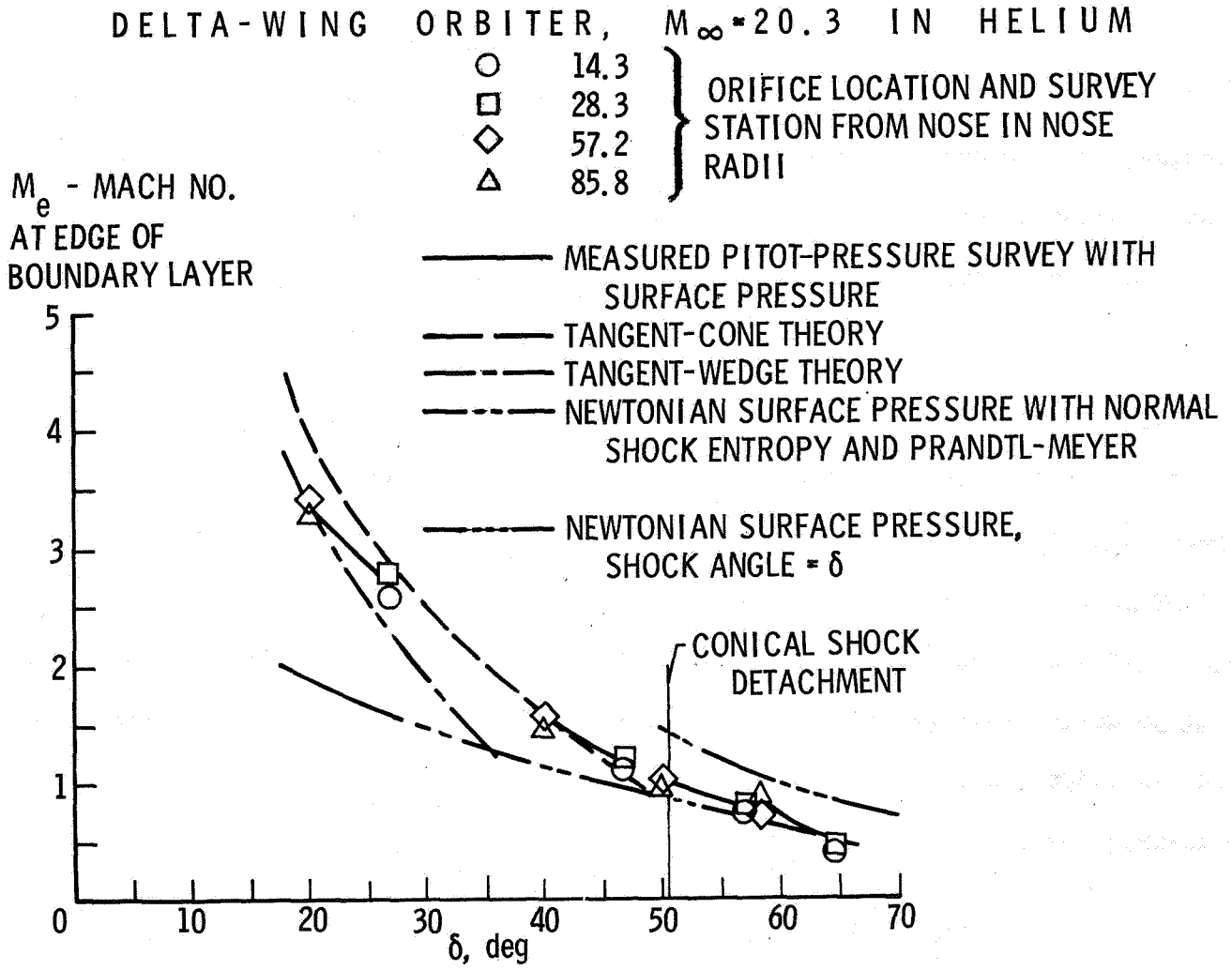
DELTA-WING ORBITER, M_∞ = 20.3 IN HELIUM
14.3
28.3
57.2
85.8
ORIFICE LOCATION AND SURVEY STATION FROM NOSE IN NOSE RADII
M_e - MACH NO. AT EDGE OF BOUNDARY LAYER
MEASURED PITOT-PRESSURE SURVEY WITH SURFACE PRESSURE
TANGENT-CONE THEORY
TANGENT-WEDGE THEORY
NEWTONIAN SURFACE PRESSURE WITH NORMAL SHOCK ENTROPY AND PRANDTL-MEYER
NEWTONIAN SURFACE PRESSURE, SHOCK ANGLE = δ
CONICAL SHOCK DETACHMENT
0
1
2
3
4
5
10
20
30
40
50
60
70
δ, deg

Figure 2

ALTITUDE-VELOCITY PROFILE AND ANGLE-OF-ATTACK TIME HISTORY

The altitude-velocity profiles and angle-of-attack time histories of the three high-cross-range trajectories used in this report are shown in figure 3. The constant α trajectory enters at an angle of attack of 22° and an entry angle of -1.64° from an orbital inclination of 55° with a resulting cross range of 1750 n.mi. The $C_{L,max}$ entry trajectory enters at a 53° angle of attack, and at 275 seconds after entry, α is stepped down to 30°. A cross range of 1850 n.mi. is accomplished with an entry angle of -1.55° from an orbital inclination of 55°. Modulated angle-of-attack trajectory assumes entry at an angle of -1.6° from an equatorial orbit yielding a cross range of 1500 n.mi. In this case, the angle of attack is modulated from an initial value of 45° down to 15° at the terminal portion of the entry.

These trajectories, encompassing three alternate trajectory shaping approaches, provide an excellent basis for comparing the effects of the various transition criteria on center-line heating characterisitcs. That is, trajectory shaping effects can be minimized by comparison, and definite conclusions may be drawn concerning the effects of transition criteria. In addition, the results will cover the operational angle-of-attack range of primary interest for the shuttle.

ALTITUDE-VELOCITY PROFILE AND ANGLE-OF-ATTACK TIME HISTORY

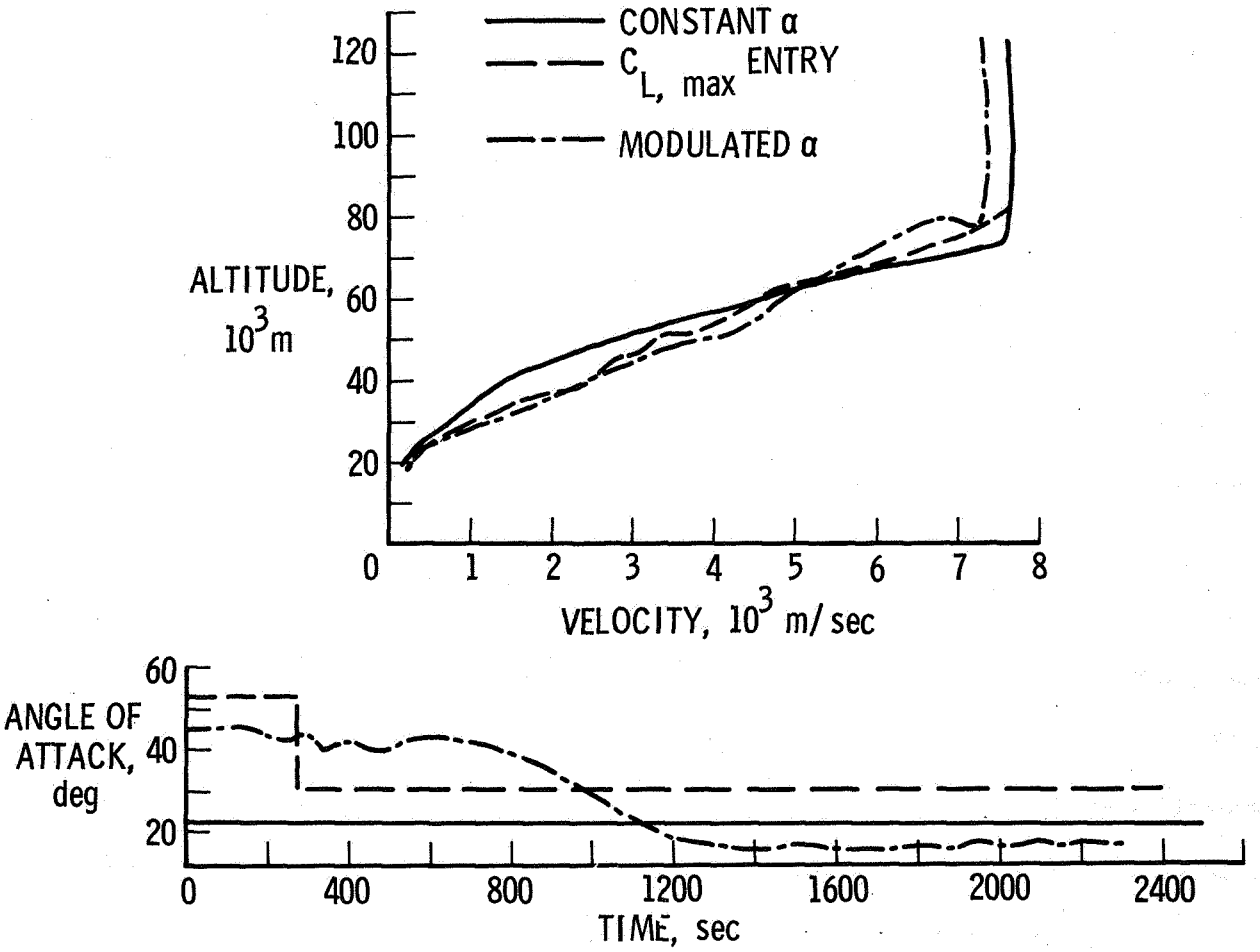

Figure 3

TRANSITION ONSET LOCATION - EDGE MACH NUMBER EFFECTS

Although this paper deals primarily with the oblique shock flow, an evaluation of the effect of boundary-layer transition on center-line heating has also been made by using normal-shock properties with modified Newtonian local pressures. Figure 4 shows the location of transition onset for the constant α trajectory as a function of entry time for three length Reynolds number transition criteria in a conical and normal-shock flow field. Transition occurs much earlier in the trajectory for the conical flow than for the normal-shock case. There is also a large portion of the center line in the oblique-shock case over which there is a relatively small difference in the time of transition onset for Reynolds numbers up to 1.0×10^6. There is, in general, a large difference in the time of transition over most of the center line for the normal-shock flow field. These results demonstrate that the peak heating levels and total heat loads for a conical flow field are affected much less by the transition criteria than is the case for the normal shock. Similar results were obtained with the $C_{L,max}$ entry and modulated α trajectories.

TRANSITION ONSET LOCATION - EDGE MACH NUMBER EFFECTS
CONSTANT α TRAJECTORY

CURVE	TRANSITION CRITERIA
1	$R_{e,tr} = 0.25 \times 10^6$
2	$R_{e,tr} = 1.0 \times 10^6$
3	R_e vs. M_e

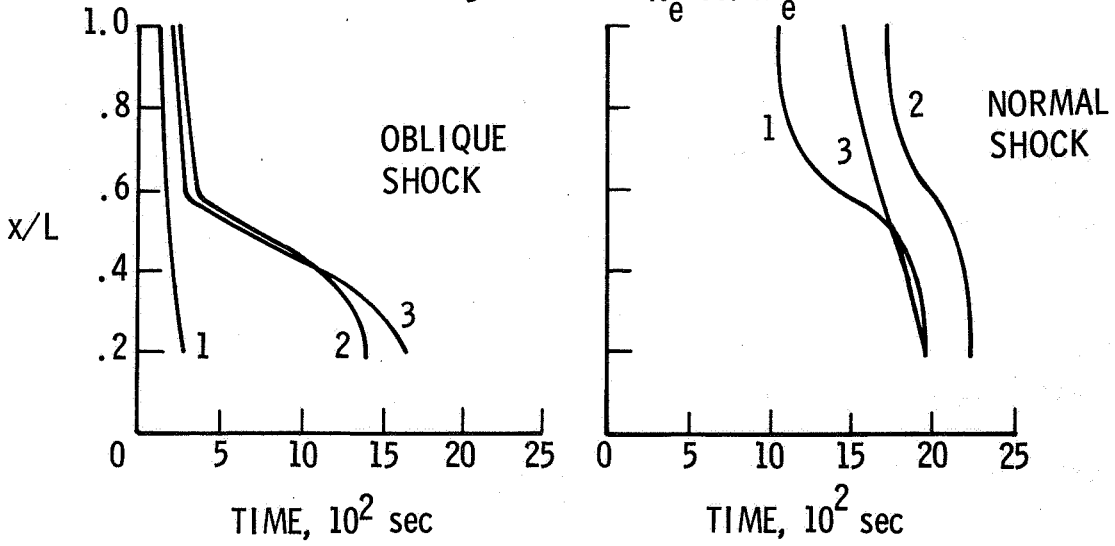

Figure 4

TRANSITION ONSET LOCATION

In comparing the time of transition onset for each transition criteria on these three trajectories in figure 5, certain similarities become apparent. The criteria of $R_{e,tr} = 0.25 \times 10^6$ and $\frac{R_{e,\theta}}{M_e\left(\frac{R_e}{x}\right)^{0.2}} = f(\alpha)$ tend to predict transition onset at a given location at approximately the same time (some differences are indicated for the modulated α case). Similarly, the criteria of $R_{e,tr} = 1.0 \times 10^6$ and R_e vs. M_e agree closely. However, in each case, the $\frac{R_{e,\theta}}{M_e} = 225$ transition criteria predicts the latest time of transition onset, therefore, providing the least severe thermal environment of the criteria evaluated.

TRANSITION ONSET LOCATION
OBLIQUE SHOCK

CURVE	TRANSITION CRITERIA
1	$R_{e,tr} = 0.25 \times 10^6$
2	$\frac{R_{e,\theta}}{M_e \left(\frac{R_e}{x}\right)^{0.2}} = f(\alpha)$
3	$R_{e,tr} = 1.0 \times 10^6$
4	R_e vs. M_e
5	$\frac{R_{e,\theta}}{M_e} = 225$

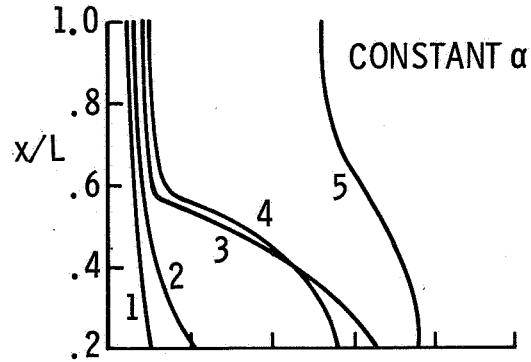

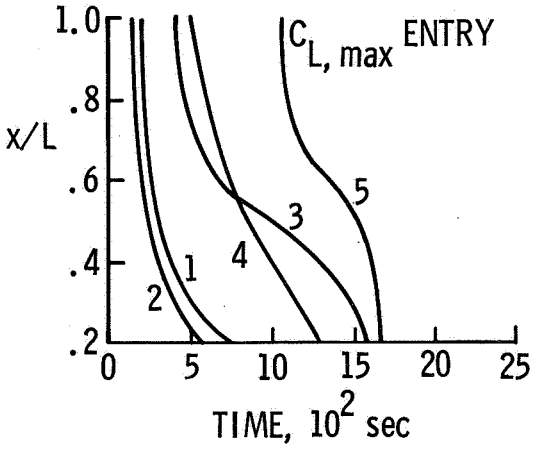

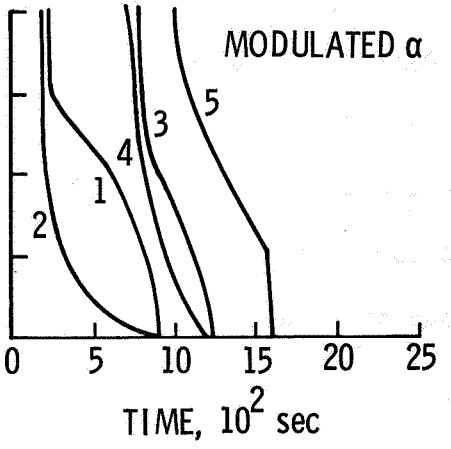

Figure 5

CENTER-LINE WALL TEMPERATURE AT x/L = 0.6

The effect of three transition criteria on the temperature-time histories at the 0.6 center-line location is illustrated in figure 6 for each of the three trajectories. These criteria are representative of those which predict transition at early, intermediate, and late trajectory times. These plots show that even though there is a large time differential in the prediction of transition onset, the peak temperature for this group of transition criteria is affected only to a relatively small degree at this location, especially for transition Reynolds numbers up to approximately $1.0 = 10^6$.

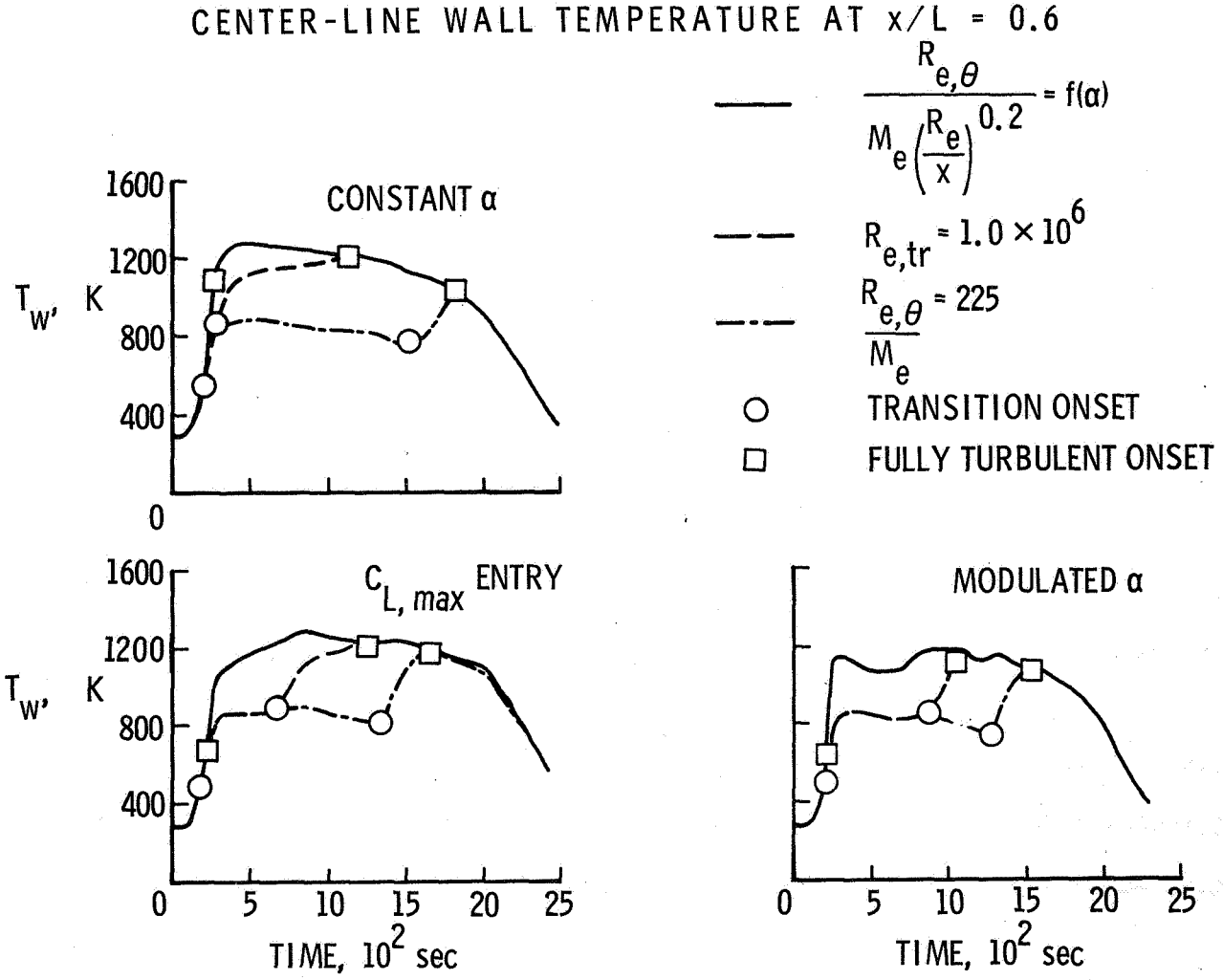
CENTER-LINE WALL TEMPERATURE AT x/L = 0.6
$\frac{R_{e,\theta}}{M_e\left(\frac{R_e}{x}\right)^{0.2}} = f(\alpha)$
$R_{e,tr} = 1.0 \times 10^6$
$\frac{R_{e,\theta}}{M_e} = 225$
TRANSITION ONSET
FULLY TURBULENT ONSET
CONSTANT α
$C_{L,max}$ ENTRY
MODULATED α
T_w, K
1600
1200
800
400
0
0
5
10
15
20
25
TIME, 10^2 sec

Figure 6

CENTER-LINE HEATING RATE AT $x/L = 0.6$

The heating-rate time histories in figure 7 correspond to the temperature-time histories in the previous figure and show the effect on total heat load of each of the three transition criteria listed. The most conservative of these criteria, $\frac{R_{e,\theta}}{M_e\left(\frac{R_e}{x}\right)^{0.2}} = f(\alpha)$, predicts heating rates (and hence heat loads) significantly larger than those predicted by the least conservative criterion, $\frac{R_{e,\theta}}{M_e} = 225$. The criterion of $R_{e,tr} = 1.0 \times 10^6$ predicts heat loads that are intermediate in value to those of the other two transition criteria.

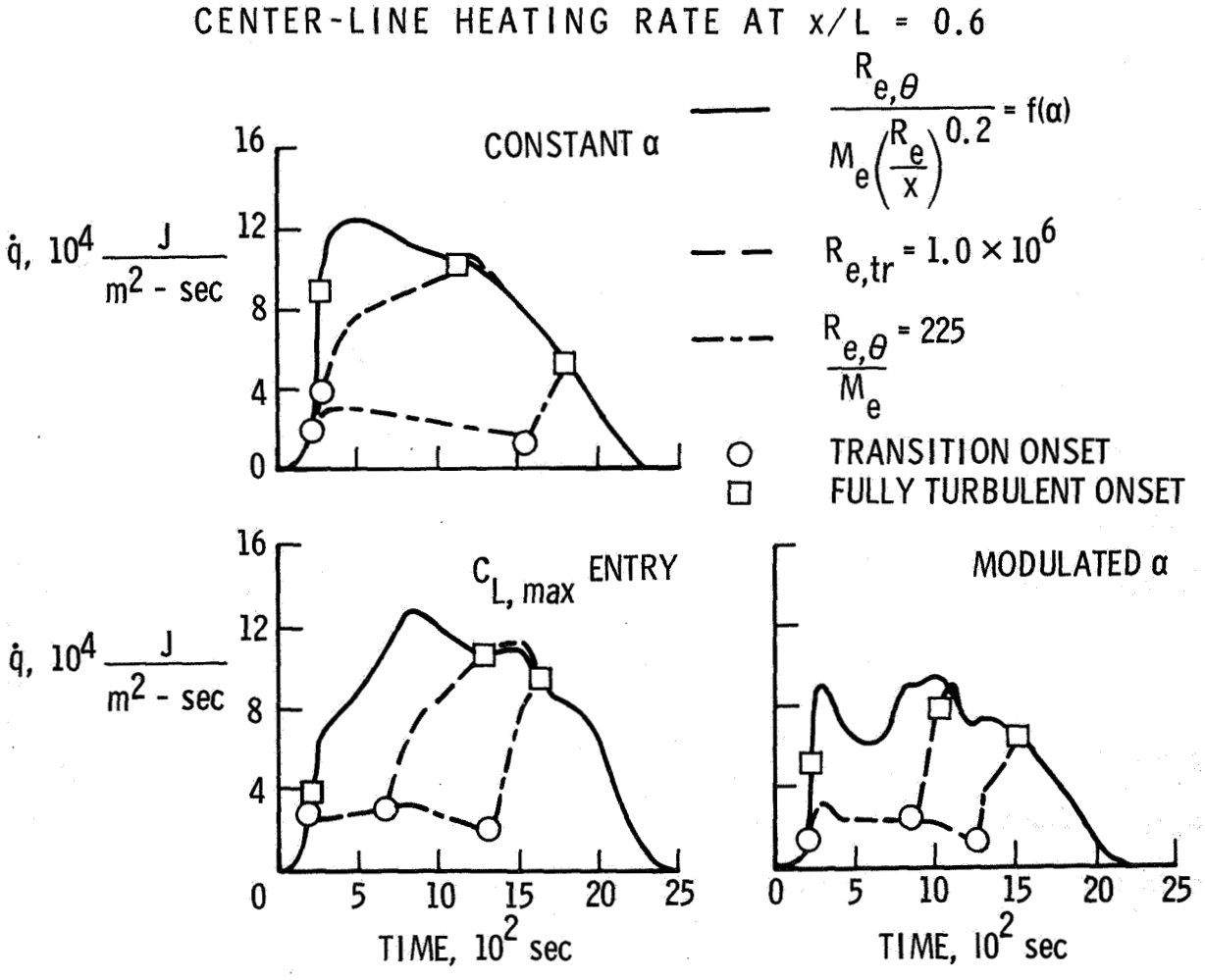
CENTER-LINE HEATING RATE AT x/L = 0.6
$\frac{R_{e,\theta}}{M_e\left(\frac{R_e}{x}\right)^{0.2}} = f(\alpha)$
$R_{e,tr} = 1.0 \times 10^6$
$\frac{R_{e,\theta}}{M_e} = 225$
TRANSITION ONSET
FULLY TURBULENT ONSET
CONSTANT α
$C_{L,max}$ ENTRY
MODULATED α
$\dot{q}$, $10^4 \frac{J}{m^2 - sec}$
16
12
8
4
0
5
10
15
20
25
TIME, 10^2 sec

Figure 7

CENTER-LINE HEAT LOAD

The heat-load distribution along the vehicle center line as predicted by each of the six transition criteria examined is presented in figure 8 for all three trajectories. In each case, the heat loads predicted by the criteria of $R_{e,tr} = 0.25 \times 10^6$, $\frac{R_{e,\theta}}{M_e\left(\frac{R_e}{x}\right)^{0.2}} = f(\alpha)$, and fully turbulent flow have similar values, especially at center-line locations aft of 0.6. These three criteria are more conservative than those of $R_{e,tr} = 1.0 \times 10^6$ and R_e vs. M_e, which also predict similar values of heat load. The $\frac{R_{e,\theta}}{M_e} = 225$ transition criterion is the least conservative of all.

There is a general trend for the heat loads predicted by criteria with transition Reynolds numbers less than 1.0×10^6 $\left(\text{i.e., fully turbulent flow, } \frac{R_{e,\theta}}{M_e\left(\frac{R_e}{x}\right)^{0.2}} = f(\alpha), \text{ and } R_{e,tr} = 0.25 \times 10^6\right)$ to begin to converge near the 0.6 center-line location. It appears that the heat loads for most center-line locations aft of 0.6 would be nearly equal for criteria with a maximum transition Reynolds number of approximately 0.50×10^6.

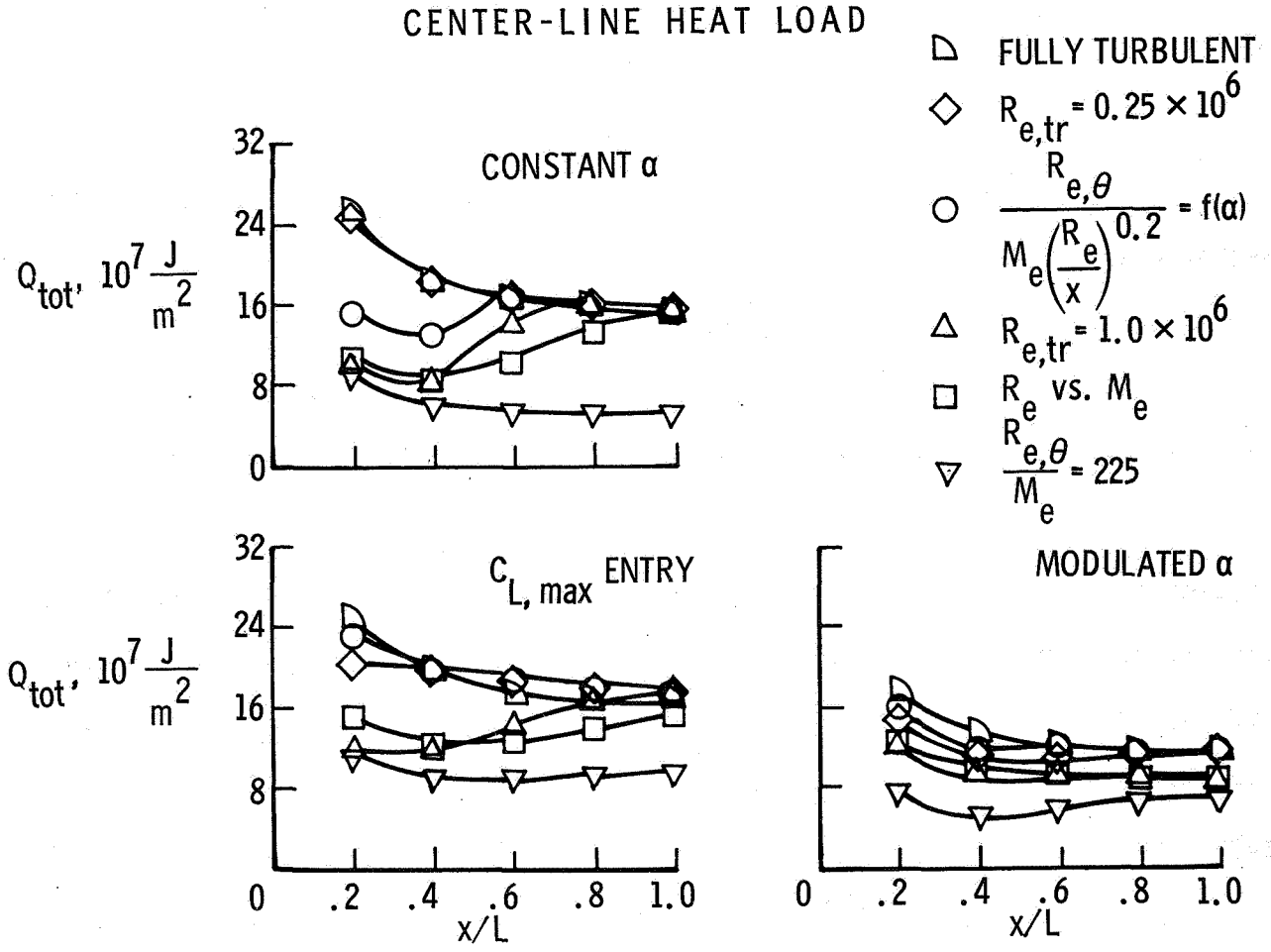
CENTER-LINE HEAT LOAD
FULLY TURBULENT
$R_{e,tr} = 0.25 \times 10^6$
$\frac{R_{e,\theta}}{M_e\left(\frac{R_e}{x}\right)^{0.2}} = f(\alpha)$
$R_{e,tr} = 1.0 \times 10^6$
R_e vs. M_e
$\frac{R_{e,\theta}}{M_e} = 225$
CONSTANT α
$C_{L,max}$ ENTRY
MODULATED α
Q_{tot}, $10^7 \frac{J}{m^2}$
32
24
16
8
0
.2
.4
.6
.8
1.0
x/L

Figure 8

MAXIMUM CENTER-LINE WALL TEMPERATURE

Presented in figure 9 is the maximum wall-temperature distribution along the vehicles center line for the six transition criteria on all three trajectories. The trends and similarities in the predictions using these criteria are the same as those noted for the center-line total heat load distribution. However, those trends are less obvious here because the relative differences in the predicted maximum wall temperature due to the use of various transition criteria are much less than those produced in the value of total heat loads.

As was the case for the total heat load distribution, there is a general trend for the predicted values of maximum wall temperature to converge near the 0.6 center-line location, and depending upon the trajectory at locations forward of this point, for those criteria with low to moderate values of transition Reynolds number. The maximum wall temperatures for center-line locations aft of 0.6 would be very nearly equal for criteria with a maximum transition Reynolds number of from 1.0×10^6 to 1.5×10^6.

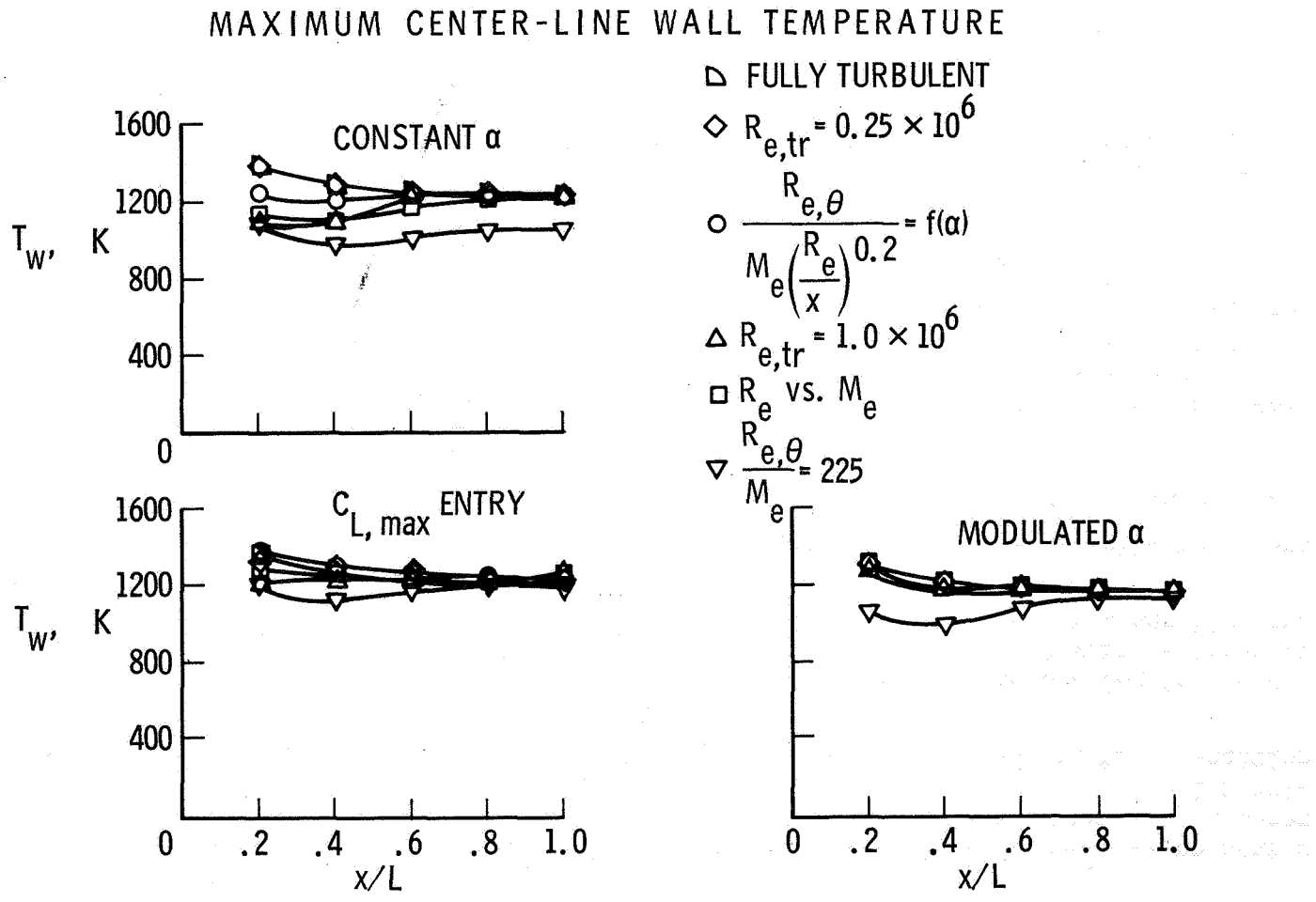
MAXIMUM CENTER-LINE WALL TEMPERATURE
FULLY TURBULENT
◇ $R_{e,tr} = 0.25 \times 10^6$
○ $\frac{R_{e,\theta}}{M_e\left(\frac{R_e}{x}\right)^{0.2}} = f(\alpha)$
△ $R_{e,tr} = 1.0 \times 10^6$
□ R_e vs. M_e
▽ $\frac{R_{e,\theta}}{M_e} = 225$
CONSTANT α
MODULATED α
$C_{L,max}$ ENTRY
T_w, K
1600
1200
800
400
0
.2
.4
.6
.8
1.0
x/L

Figure 9

SUMMARY AND CONCLUDING REMARKS

A comparison has been made of the effect of boundary-layer transition on center-line heating in a conical and a normal-shock flow field. It has been shown that the time of transition onset (and, hence, the heating parameter) is significantly influenced by the choice of transition criterion in the normal-shock flow but that this parameter is much less sensitive to the transition criterion in a conical flow field.

An evaluation of the effects of boundary-layer transition on center-line heating in the conical flow field has shown that the temperatures are less affected by the use of various transition criteria than are heat loads. This difference is due to the delay in the time of transition onset predicted by those criteria with high transition Reynolds numbers.

The criteria which predict the most severe thermal environment are those of fully turbulent flow throughout the entry, $R_{e,tr} = 0.25 \times 10^6$ and $\frac{R_{e,\theta}}{M_e\left(\frac{R_e}{x}\right)^{0.2}} = f(\alpha)$. Because transition occurs early in the trajectory for each of these criteria, they tend to predict similar values of maximum temperature and total heat load especially at center-line locations aft of 0.6. Transition occurs later in the trajectory for the criteria of $R_{e,tr} = 1.0 \times 10^6$ and R_e vs. M_e, but these two also predict similar values of maximum temperature and heat load. These heating parameters are intermediate in value to those predicted by the other four transition criteria, with the criterion of $\frac{R_{e,\theta}}{M_e} = 225$ being the least conservative of all.

Evaluation of center-line heating generated by various trajectory shaping approaches has shown that the maximum surface-temperature distribution was not significantly affected by the shaping technique. However, the heat-load distribution is influenced, particularly on the forward portion of the vehicle.

SYMBOLS

$C_{L,max}$	maximum lift coefficient
L	length of vehicle, measured on center line
M_e	boundary-layer edge Mach number
M_∞	free-stream Mach number
Q_{tot}	total heat load
$\dot{q}$	heating rate
R_e	boundary-layer edge Reynolds number based on length
$R_{e,tr}$	transition Reynolds number
$R_{e,\theta}$	momentum-thickness Reynolds number
T_w	wall temperature
x	center-line running length
α	angle of attack
δ	local flow deflection angle

USGPO-1972/735-025/1051-3-1

REFERENCES

1. Ashby, George C., Jr.: Experimental Boundary-Layer Edge Mach Numbers for Two Space Shuttle Orbiters at Hypersonic Speeds. NASA TN D-6574, 1972.

2. Hender, D.: A Miniature Version of the JA70 Aerodynamic Heating Computer Program, H800 (Miniver). Rep. No. 60462, McDonnell Douglas Corp., June 1, 1970.

"The aeronautical and space activities of the United States shall be conducted so as to contribute . . . to the expansion of human knowledge of phenomena in the atmosphere and space. The Administration shall provide for the widest practicable and appropriate dissemination of information concerning its activities and the results thereof."

—NATIONAL AERONAUTICS AND SPACE ACT OF 1958

NASA SCIENTIFIC AND TECHNICAL PUBLICATIONS

TECHNICAL REPORTS: Scientific and technical information considered important, complete, and a lasting contribution to existing knowledge.

TECHNICAL NOTES: Information less broad in scope but nevertheless of importance as a contribution to existing knowledge.

TECHNICAL MEMORANDUMS: Information receiving limited distribution because of preliminary data, security classification, or other reasons.

CONTRACTOR REPORTS: Scientific and technical information generated under a NASA contract or grant and considered an important contribution to existing knowledge.

TECHNICAL TRANSLATIONS: Information published in a foreign language considered to merit NASA distribution in English.

SPECIAL PUBLICATIONS: Information derived from or of value to NASA activities. Publications include conference proceedings, monographs, data compilations, handbooks, sourcebooks, and special bibliographies.

TECHNOLOGY UTILIZATION PUBLICATIONS: Information on technology used by NASA that may be of particular interest in commercial and other non-aerospace applications. Publications include Tech Briefs, Technology Utilization Reports and Technology Surveys.

Details on the availability of these publications may be obtained from:

SCIENTIFIC AND TECHNICAL INFORMATION OFFICE

NATIONAL AERONAUTICS AND SPACE ADMINISTRATION

Washington, D.C. 20546